

Cyclometalated Ruthenium Complexes for Dye-Sensitized Solar Cells

THÈSE N° 8298 (2018)

PRÉSENTÉE LE 9 FÉVRIER 2018

À LA FACULTÉ DES SCIENCES DE BASE

LABORATOIRE DE PHOTONIQUE ET INTERFACES

PROGRAMME DOCTORAL EN CHIMIE ET GÉNIE CHIMIQUE

ÉCOLE POLYTECHNIQUE FÉDÉRALE DE LAUSANNE

POUR L'OBTENTION DU GRADE DE DOCTEUR ÈS SCIENCES

PAR

Sadig AGHAZADA

acceptée sur proposition du jury:

Prof. M. Mazzanti, présidente du jury

Prof. M. K. Nazeeruddin, Prof. M. Graetzel, directeurs de thèse

Prof. C. Housecroft, rapporteuse

Prof. C. Barolo, rapporteur

Prof. A. Hagfeldt, rapporteur



ÉCOLE POLYTECHNIQUE
FÉDÉRALE DE LAUSANNE

Suisse
2018

Abstract

The transition towards carbon-free sources of energy is vital for humankind. This process is feasible through the extensive use of photovoltaic technologies, which may convert solar energy into electrical and chemical energy. In the last half-century, many competitive technologies were developed. One promising type of solar cell is Dye-Sensitized Solar Cell (DSC), which differ from other solar cells in many ways. DSCs can be produced in different colors and used as constructing components of urban buildings. Additionally, DSCs have inner beauty related to their working principle. The processes of light absorption and charge transport are spatially separated in many ways reminiscent of water oxidation in Photosystem II in nature.

Historically, DSCs were developed with an electrolyte based on an iodine-iodide redox shuttle. However, the overall performance of these solar cells is restricted due to the high loss of potential imparted by multistep dye regeneration by iodide. Shift to the outer-sphere one-electron redox couple, such as $\text{Co}^{3+/2+}$ imine complexes, boosted the field, and new record efficiencies were achieved. Still, new redox mediators failed to provide reasonable power conversion efficiencies using the classic ruthenium sensitizers with isothiocyanate ligands. Poor performance is related to high charge recombination rates. To tackle this problem, I present my research on new cyclometalated ruthenium (II) complexes as sensitizers for DSCs that employ cobalt-based electrolytes. I introduce *tris*-heteroleptic cyclometalated Ru (II) complexes, which have various organic substituents. Optical and electrochemical analyses are conducted before applying the new sensitizers in state-of-the-art solar cells. In this work, a record-high power conversion efficiency of 9.4 % was obtained with a ruthenium sensitizer and a cobalt-based redox shuttle. Transient absorbance spectroscopy, electrochemical impedance spectroscopy, and transient photovoltage and photocurrent decay measurements were conducted to reveal the main factors that limit the performance of the solar cells. The role of dye-loading, which is generally ignored in the field, was shown to be crucial. Additionally, it was shown that organic substituents that are usually attached to improve the photophysical properties of sensitizers cause irreversible sensitizer electrochemical oxidation.

Further, in this thesis, I discuss the role of sulfur atoms in the sensitizer structure on the performance of the solar cell. The role of sulfur atoms in facilitating both beneficial regeneration and detrimental recombination with iodine-based electrolytes was shown previously. This dual behavior is

puzzling when sulfur-containing moieties are used in new sensitizer design. I introduce a study of state-of-the-art solar cells that employ an iodine-based electrolyte and a series of ruthenium complexes of close structure with or without a sulfur atom in their structure. By means of transient absorbance and electrochemical impedance spectroscopies, I untangle two parallel roles of sulfur and determine which is dominant in gauging solar cell performance.

Next, I introduce new ruthenium complexes that contain a bidantate ligand coordinating to the ruthenium with both a cyclometalated carbanion and an N-heterocyclic carbene ligand $C^{\wedge}C_{\text{NHC}}$. *Bis*-heteroleptic complexes of ruthenium with new NHC $^{\wedge}C$ ligands and with 2,2'-bipyridine or its 4,4'-di(carboxymethyl)-substituted analogue were synthesized and characterized for the first time. Structural, optical and electrochemical analyses are discussed. One of the main advantages of the new sensitizers is their broad absorption spectra and their absolutely reversible oxidation. Although these sensitizers are promising for DSC application, the final sensitizers with acid anchor groups are insoluble in many organic solvents and are not discussed.

In the last section, I discuss new *bis*-heteroleptic cyclometalated ruthenium complexes with two tridentate ligands. Ligands that form six-membered metallocycles have recently attracted attention. Among those ligands, 2,6-di(quinolin-8-yl)pyridine was shown to form ruthenium complexes with broad absorption spectra and a prolonged excited state lifetime. To examine whether these advantageous features of ruthenium complexes with new extended ligands will translate into successful performance in DSCs, I have featured a ligand with an anchor and synthesized new complexes. Interestingly, new coordinating mode for this ligand was discovered. Structural, optical and electrochemical analyses are provided. Solar cells are manufactured and analyzed.

Finally, I briefly summarize the obtained results.

Keywords

Dye-Sensitized Solar Cells, Sensitizers, Ruthenium Complexes, Cyclometalation.

Résumé

La transition vers des sources d'énergie sans carbone est vitale pour l'humanité. Cette transition est possible grâce à l'utilisation des technologies photovoltaïques, qui convertit l'énergie solaire en électricité et énergie chimique. Depuis cinquante ans, plusieurs technologies rivales ont été développées. L'une d'entre elles, très prometteuse, est la cellule solaire à pigment photosensible (DSC). Cette dernière est différente des autres technologies solaires. Les DSC peuvent être produites de différentes couleurs et utilisées comme composant de construction pour des projets urbains. De plus, les DSC ont une certaine beauté intérieure de par leur mode de fonctionnement. Les processus d'absorption de la lumière et de transport de charges sont séparés spatialement, de manière très similaire à l'oxydation de l'eau dans le Photosystème II de la nature. Historiquement, les DSC ont été développées avec un électrolyte basé sur une navette redox iode-iodure. Cependant, les performances globales de ces cellules solaires sont restreintes à cause de la forte perte de potentiel dû à la régénération, en plusieurs étapes, du pigment par l'iodure. L'utilisation de couple redox avec un électron dans la sphère externe, comme les complexes $\text{Co}^{3+/2+}$ imine, a relancé le domaine, et de nouveaux records d'efficacité furent atteints. Même avec cette avancée, de nouveaux médiateurs redox n'arrivent pas à donner une conversion de puissance raisonnable en utilisant les pigments photosensibles classiques à base de ruthénium complexé avec de l'isothiocyanate. Les mauvaises performances sont dues au fort taux de recombinaison des charges. Pour m'attaquer à ce problème, je présente ma recherche sur de nouveaux complexes de ruthénium (II) cyclometallé comme pigment pour des DSC utilisant des électrolytes à base de cobalt. J'introduis les complexes Ru (II) cyclometallés *tris*-hétéroléptique, avec divers substituant organiques. Les caractérisations optiques et électrochimiques ont été conduites avant l'utilisation de ces pigments dans des cellules solaires de dernières générations. Lors de ce travail, un record d'efficacité de 9,4 % a été atteint avec un pigment au ruthénium et une navette redox à base de cobalt. Des mesures spectroscopiques d'absorption transitoire, d'impédance électrochimique ainsi que de photo-voltage transitoire et de décroissances de photo-courants ont été faites afin de révéler les facteurs principaux limitant les performances de la cellule solaire. Le rôle de l'application du pigment dans la cellule et généralement ignoré dans le domaine, mais il s'est avéré être crucial. De plus, il a été montré que les substituant organiques qui sont habituellement attachés pour améliorer les propriétés photo-physiques des pigments, cause une oxydation électrochimique irréversible de ce dernier.

Plus tard dans cette thèse, je discute le rôle qu'ont les atomes de soufres, de la structure du pigment, sur la performance des cellules solaires. Il a été démontré précédemment que ces derniers facilitent la régénération, voulue, mais également la recombinaison non voulue avec les électrolytes à base d'iode. Cette ambivalence est déroutante quand des molécules contenant des atomes de soufre sont utilisées dans le design de nouveaux pigments. Je présente une étude sur des cellules solaires de pointes utilisant un électrolyte à base d'iode et une série de complexes de ruthénium à structures fermées avec et sans soufre dans leur structure. En utilisant la spectroscopie par absorption transitoire ainsi que par impédance électrochimique, j'ai désintrié les deux rôles du soufre, et déterminé lequel est dominant dans la mesure des performances des cellules solaires.

Par la suite, j'introduis un nouveau complexe de ruthénium qui contient un ligand bidenté coordonné au ruthénium avec un cabanion cyclometallé et un ligand carbène N-hétérocyclique C^{NHC} . Des complexes de ruthénium *bis*-hétéroléptiques avec de nouveaux ligands NHC C et avec 2,2'-bipyridine ou sont analogue 4,4'-di(carboxyméthyl)-substitué ont été synthétisés et caractérisés pour la première fois. L'analyse de la structure et des propriétés optiques ainsi qu'électrochimiques sont discutées. L'un des principaux avantages de ce nouveau pigment est leur large spectre d'absorption ainsi que leur oxydation totalement réversible. Bien que ces pigments soient prometteurs pour une utilisation dans les DSC, le pigment final avec son groupe acide d'attache est insoluble dans beaucoup de solvants et n'est donc pas discuté.

Dans la dernière section, je discute de nouveaux complexes de ruthénium *bis*-hétéroléptique cyclometallé avec deux ligands tridentés. Ces derniers, formant des métallocycle à six membres, ont récemment attiré l'attention. Il a été montré que, dans ceux-ci, le 2,6-di(quinolin-8-yl)pyridine forme, avec le ruthénium, un complexe à large spectre d'absorption et un temps de vie de l'état excité prolongé. Afin d'examiner si les nouvelles propriétés avantageuses de ces complexes de ruthénium avec ces nouveaux ligands se traduisent par une amélioration des performances dans les DSC, j'ai agrémenté un ligand avec un groupe d'attache et synthétisé un nouveau complexe. Curieusement, de nouveaux modes de coordination de ces ligands ont été découverts. Les analyses structurales, optiques et électrochimiques sont données. Des cellules solaires ont été construites et analysées.

Finalement, je résume de manière succincte les résultats obtenus.

Mots-clés

Cellules solaires à pigment photosensible, pigment photosensible, complexe de ruthénium, Cyclomé-talation

Contents

Abstract	i	
Résumé	iii	
Contents	v	
Chapter 1	Introduction	7
1.1	Energy problems to solve.....	7
1.2	Sunlight.....	8
1.3	Evolution of photovoltaic technologies	9
1.4	Working principle of p-n junction solar cells.....	10
1.5	Dye-Sensitized Solar Cells	11
1.6	Characterization techniques	13
1.7	Processes at the photoanode	18
1.8	Sensitizers	20
1.9	Ruthenium sensitizers.....	22
1.10	Cyclometalated Ruthenium (II) complexes	27
1.11	Organic and copper-based sensitizers	31
1.12	Motivation	33
Chapter 2	Ligand Engineering for the Efficient Dye-Sensitized Solar Cells with Ruthenium Sensitizers and Cobalt Electrolytes	35
2.1	Introduction.....	35
2.2	Results and Discussion	37
2.3	Conclusion.....	49
Chapter 3	Cyclometalated Ruthenium Sensitizers with Arylamine Donors	51
3.1	Introduction.....	51
3.2	Results and Discussion	52
3.3	Conclusion.....	62
Chapter 4	Unraveling the Dual Character of Sulfur Atoms on Sensitizers in Dye-Sensitized Solar Cells	63
4.1	Introduction.....	63
4.2	Result and Discussion	65
4.3	Conclusion.....	71
Chapter 5	Cyclometalated ruthenium complexes with N-heterocyclic carbene ligands.	73
5.1	Introduction.....	73
5.2	Results and discussion.....	75

5.3	Conclusion	85
Chapter 6	Bis-Tridentate Cyclometalated Ruthenium Complexes with Extended Anchoring Ligand	87
6.1	Introduction	87
6.2	Result and Discussion	88
6.3	Conclusion	96
Chapter 7	General Conclusion	99
Chapter 8	Appendix	103
8.1	Appendix to chapter 2	103
8.2	Appendix to chapter 3	150
8.3	Appendix to chapter 5	176
8.4	Appendix to chapter 6	201
References	217	
Acknowledgements		236
Curriculum Vitae		237

Chapter 1 Introduction

1.1 Energy problems to solve

Starting from the mid-XVIII century, the Industrial Revolution changed the fate of humanity. To drive this revolution, wood, coal, and later oil were used extensively as sources of energy. Even today, up to 80 % of the energy produced worldwide comes from fossil fuels.¹ However, the shift toward renewable sources of energy, such as solar and wind energy, is crucial for the following reason. The extensive use of fossil fuels has resulted in rising global CO₂ concentrations in the atmosphere and in the ocean. At the beginning of this decade, the concentration of CO₂ in the atmosphere exceeded 400 ppm, which is a record value for the last several million years (Figure 1.1).² The rise of CO₂ concentrations and the global warming of the planet are causing a change in the ocean habitat and may also cause ocean level to rise.³⁻⁶ Additionally, the projected worldwide consumption of energy is expected to rise further, mostly due to increased living standards in less developed countries. By 2050, approximately 14 TW of additional power will be needed.^{7,8} Although newly discovered deposits of oil and gas together with previously known deposits may provide enough fossil fuels to meet demand for the coming century, the use of those fossil fuels will cause the CO₂ concentration in the atmosphere to increase further. In addition to these environmental reasons, the uneven distribution of oil and gas between countries causes many wars.

Nuclear energy is another powerful energy source. However, considering that with over 440 reactors worldwide, nuclear power plants provided only ~11 % of the world's energy production in April 2017, it is difficult to imagine how many additional reactors should be built to meet increasing energy demands.⁹ Moreover, disasters at Chernobyl and Fukushima-Daiichi reduced positive attitudes about the nuclear power plants.

Wind energy may satisfy a large portion of the increasing energy demand. The potential of wind energy is well observed in Denmark, where approximately 40% of electricity consumption is covered by wind power.¹⁰ However, on a large scale, there is no technology that can compete with solar panels. Within one hour, the Earth receives enough energy from the sun to satisfy our annual energy consumption.^{7,8} Converting a small amount of this energy into electricity or into chemical fuel would be enough to meet the increasing energy demand.

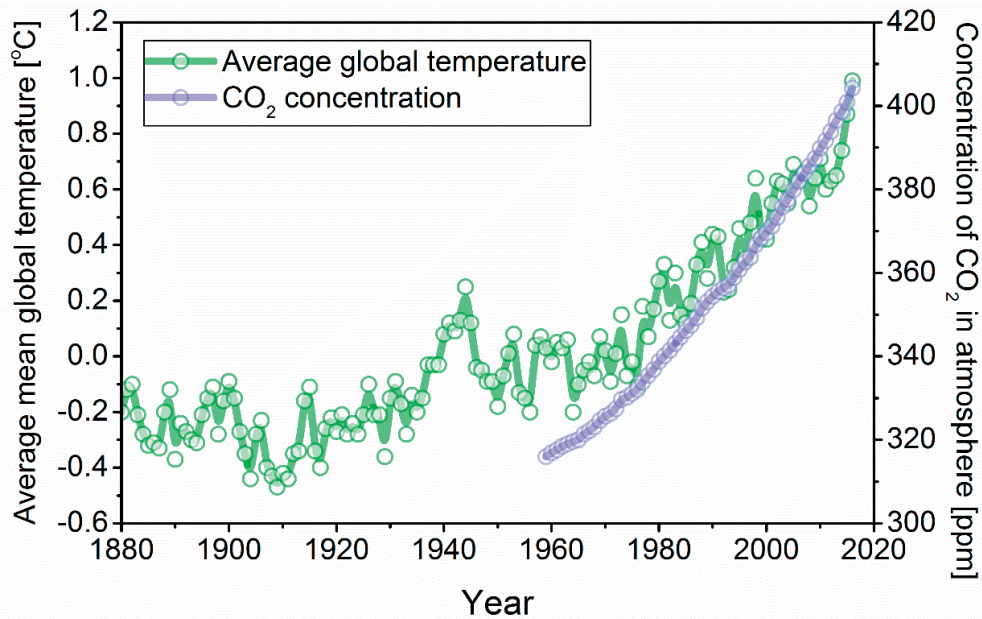


Figure 1.1. The rise in average global temperatures and CO₂ concentrations in the atmosphere. The graph was built based on data from NASA's Goddard Institute for Space Studies (NASA/GISS) and from Dr. Pieter Tans, NOAA/ESRL (www.esrl.noaa.gov/gmd/ccgg/trends/) and Dr. Ralph Keeling, Scripps Institution of Oceanography (scrippsco2.ucsd.edu/).

1.2 Sunlight

The sun can be treated as a blackbody with a surface temperature of approximately 5800 K, and the solar spectrum can be described with Planck's blackbody radiation distribution. Due to scattering and absorption by components present in Earth's atmosphere, the intensity of the solar spectrum is reduced and its shape is changed (Figure 1.2). The degree of spectral intensity reduction can be represented in terms of the air mass coefficient. Air Mass 1 (AM 1) describes the solar spectrum recorded when the sun is at zenith, which means that the optical length for the solar photons is the real thickness of Earth's atmosphere. Before entering the atmosphere, the solar irradiation power is described as AM 0. When the sun is 48.2 degrees off the zenith, the optical path is 1.5 times longer than the real thickness of the atmosphere, thus AM 1.5 attenuated solar spectra will be recorded.¹ As presented in Figure 1.2, in contrast to AM0, the solar spectra recorded at the Earth's surface possess bands caused by absorption by molecules present in the atmosphere. Most important among those molecules is O₃ present in Earth's stratosphere, which absorbs the ultraviolet portion of solar radiation. Additionally, AM 1.5 Direct and AM 1.5 Global solar spectra can be differentiated, with the former presenting only the direct and circumsolar irradiation and the latter also including additional diffuse irradiation. Integrating the

¹ Air mass is equal to the ratio of the optical path to the optical path when the sun is at zenith, and this value will be equal to $1/\cos(\theta)$, where θ is the zenith angle. In this equation, the atmosphere is considered to be flat. For an exact result, an equation that takes into account atmospheric curvature should be used. At $\theta = 48.2$, $AM \approx 1/\cos(48.2) = 1.5$.

AM 1.5 G spectrum result in irradiation power of 1000.4 Wm^{-2} . Considering that most human habitats are at latitudes with yearly and weather average solar irradiation equivalent to the solar irradiation at AM 1.5, this value was chosen as the standard, and all solar cells and panels must be characterized at AM 1.5 solar irradiance.

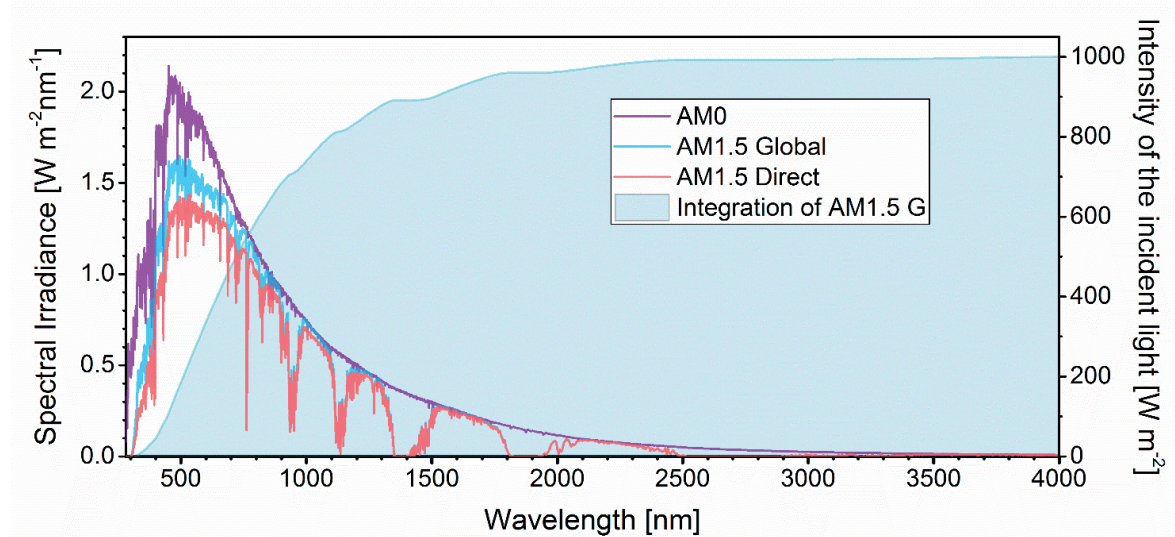


Figure 1.2. Spectral distribution of the solar irradiance above the Earth's atmosphere (AM0), and on the Earth's surface, presenting the difference between direct (AM1.5 Direct) and global irradiation (AM1.5 Global). The integration of AM1.5 G gives the intensity of irradiation as a function of wavelength.

1.3 Evolution of photovoltaic technologies

The photovoltaic effect was reported for the first time by the French scientist Alexandre-Edmond Becquerel in 1839.^{11,12} In his work, a platinum electrode coated with silver chloride and immersed in an acid electrolyte generated current and voltage upon illumination. More than 30 years later, Willoughby Smith reported his study on the resistance of selenium bars with two platinum contacts.¹³ In this work, a change in selenium resistivity was observed upon illumination. This result represented the first observation of the photovoltaic effect in a semiconductor. In a further study, William Grylls Adams and Richard Evans Day also showed reduced selenium resistivity under illumination. Moreover, those authors observed that under illumination, the current flows in a manner opposite to the current from a battery.¹⁴ However, in 1883, Charles Fritts showed that a layer of selenium covered with a thin layer of gold may be used as a solar cell. Such cells were installed on some roof tops in New York.¹⁵ Afterwards, the photovoltaic effect was shown with many different materials.

During the 20th century, the progress in photovoltaics was accelerated by many factors, such as the development of quantum mechanics, solid state physics and material sciences. The process developed by Jan Czochralski enabled the growth of extra pure silicon ingots. Russel Ohl's 1939 discovery of the

photovoltaic performance of cracked silicon crystals¹⁶ and Vadim Lashkaryov's discovery of a p-n junction in Cu₂O photocells created a foundation for further discoveries.¹⁷ Fifteen years later, D. M. Chapin, C. S. Fuller and G. L. Pearson at Bell Laboratories achieved a power conversion efficiency of 6 % with p-n junction solar cells.¹⁸ Afterwards, in their seminal work, William Shockley and Hans Queisser determined the theoretical limit for solar cells.¹⁹ Purer materials were used later to increase the charge extraction efficiency, and additional engineering of the surface efficiently directed the light into the material, resulting in power conversion efficiencies exceeding 26 %, which is very close to the theoretical limit of 29 % for silicon with a bandgap of 1.1 eV.²⁰

An alternative to monocrystalline silicon is gallium arsenide. Solar cells on GaAs were first developed by the group of Zhores Alferov in the 1970's, and GaAs solar cells soon overcame monocrystalline Si solar cells in terms of efficiency.²¹ Later, GaAs was used to power spacecrafts instead of Si.² Today, single junction GaAs shows efficiencies of over 28 %, which is close to the theoretical limit.²² However, both, monocrystalline silicon and GaAs solar cells require energy-expensive and vacuum-assisted manufacturing processes, which makes them relatively expensive. Recently, due to increased production at relatively low demand, the price of monocrystalline Si solar cells has dropped, leading to grid parity for many countries. However, the drop in monocrystalline silicon solar panel prices in the last decade has occurred faster than the learning curve established during the last half-century, which indicates that this drop may be artificial. Considering that China is the biggest producer of solar panels and that Chinese companies are governmentally subsidized and compete with each other, it is possible that the market price of solar panels is lower than the production price.

1.4 Working principle of p-n junction solar cells

Dye-Sensitized Solar Cells (DSCs) will be discussed in later sections. However, to underline the differences between the working principle of DSCs and p-n junction solar cells, it is worth shortly describing the latter here. Doped semiconductors have different Fermi energy level positions. For a p-type and n-type semiconductor, the Fermi energy level will be close to the valence and conduction band, respectively. When these two types of materials are brought into contact, via thermalization, the majority charge carriers will diffuse in opposite directions, resulting in bent conduction, valence bands and a depletion region, as illustrated in Figure 1.3. The bending causes a drift of minority carriers in the direction opposite to the diffusion of majority carriers. The Fermi energy level is equilibrated when the currents from diffusion and the drift of carriers are equal. The initial positions of the Fermi energy

² Today, multijunction solar cells based on GaAs, InGaP and Ge are used. Their efficiencies exceed 38 % under AM 1.5 G illumination.

levels in two materials determine the scale of band-bending and the built-in potential. Upon illumination, the concentration of minority carriers is strongly enhanced, resulting in a dominant drift current, and if the p- and n-sides are externally short-circuited, the provided current, which is called the short-circuit current (J_{sc}), will flow through the circle. Analogously, if the device is externally open-circuited, it will provide a voltage called an open-circuit voltage (V_{oc}).

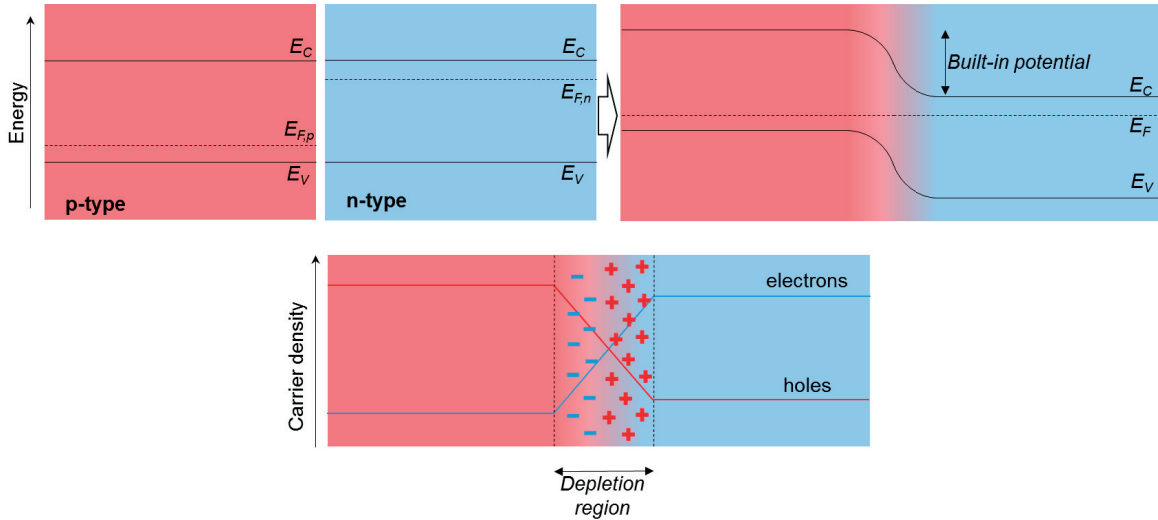


Figure 1.3. An illustration of a p - n junction. The top image shows the bending of the conduction and valence bands and the equilibration of Fermi energy level, and the bottom image shows the changes in the majority carrier densities and the depletion region.

1.5 Dye-Sensitized Solar Cells

1.5.1 Brief history

The concept of sensitization was known from the 19th century due to progress in photographic technology. To generate sensitivity to visible light in photographic plates, in 1873, Hermann Wilhelm Vogel treated silver halide with different dyes.²³ Later, in 1887, James Moser combined the ideas of Antoine C. Becquerel and A. Edmond Becquerel on photo-electrochemical solar cells with the idea of H. W. Vogel and reported for the first time a dye-sensitized photo-electrochemical solar cell.²⁴ In the 1960s, Namba S., Hishiki Y., Gerischer H., Hauffe K., Tributsch H., and others extensively studied the sensitization of ZnO crystals with a monolayer of dye.^{25–27} However, the amount of adsorbed dye was not sufficient to achieve light-harvesting efficiencies higher than 1 %. To increase the light harvesting efficiency, materials of high surface area were needed. In the 1980s Michael Grätzel and his group made big advancements with sensitization efficiencies by using nanostructured anatase with roughness factors reaching 300 and a fractal-type texture.²⁸ Finally, in 1991, Brian O'Regan and Michael Grätzel introduced a mesoporous titania film, which provided DSCs with a power conversion efficiency of 7 %.²⁹

The impact of this work is enormous not only in the field of dye-sensitized solar cells but also in many other research fields.

1.5.2 Working concepts of DSCs

First, it is worth mentioning the building blocks of a DSC in its most conventional configuration. The DSC is made by sandwiching a liquid electrolyte between two electrodes, namely a photoanode and a cathode (Figure 1.4(A)). The photoanode consists of the conducting glass covered with a blocking and mesoporous films of oxide. To absorb visible light, the mesoporous film is sensitized with a dye molecule. The cathode is obtained by covering the conducting glass with a catalyst. The choice of catalyst may vary depending on the electrolyte composition. The electrolyte contains a redox couple with various additives introduced to optimize the solar cell performance.

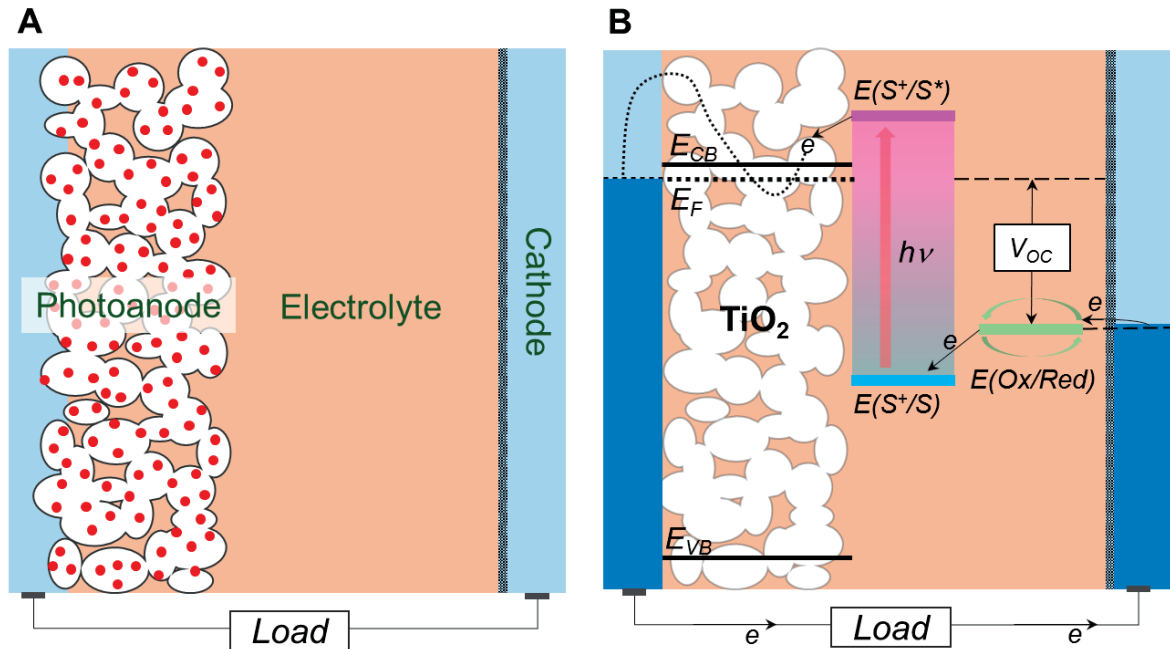


Figure 1.4. Schematic representation of a DSC. (A) illustrates the general components of a DSC, while (B) presents the working principle of DSCs.

In an ideal situation, the light excites the dye molecule on the surface of titania to its excited state (Figure 1.4(B)). Then, the photoexcited molecule injects its electron into the conduction band of the semiconductor, and a hole remains on the molecule. The electron travels through the mesoporous film and then through the external circuit to reach the cathode. In parallel, the oxidized dye molecule is restored back to the ground state by the reduced component of the mediator present in the electrolyte. Thus, the hole extracted into the electrolyte diffuses towards the counter electrode and recombines with an electron, providing a current. The Nernst potential of the redox mediator in the electrolyte will define the electron Fermi level for the cathode. Considering that V_{oc} is determined by the difference

between the two electron Fermi levels on the photoanode and the cathode, in DSCs V_{OC} is defined as the difference between the E_F of titania and the redox mediator Nernst potential.

The research in this area would not be interesting without malignant processes that restrict the performance of DSCs. After photoexcitation, a dye molecule may recombine to its ground state without injecting an electron. Additionally, an electron in the conduction band or in the trap states within the titania bandgap may recombine with a photooxidized dye molecule or with an oxidized component of a redox mediator. Among these two possibilities, the latter is usually most damaging to performance. These processes will be discussed in section 1.7.

1.6 Characterization techniques

1.6.1 Current density – voltage measurement

The main parameters of solar cells can be obtained by applying the forward bias (V) and measuring the current-density (J) flowing through the device at different illumination intensities in a so-called J - V measurement. In the dark, a solar cell can be represented as a diode, which lets the current flow in one direction. This current is called a dark current J_{dark} . Under illumination, additional current flows in the opposite direction J_{light} . In total, the solar cell can be represented as a parallelly connected source of solar current and of diode (Figure 1.5A). The dark current through the diode can be described with the ideal diode equation (1).

$$J_{dark} = J_0(e^{qV/k_B T} - 1) \quad (1)$$

Under illumination, J_{light} will add up, and the *ideal* solar cell's J - V curve will be described by equation (2).

$$J = J_{light} - J_{dark} = J_{light} - J_0(e^{qV/k_B T} - 1) \quad (2)$$

However, in reality, devices are not ideal. First, a diode non-ideality factor m should be introduced. Second, there is always a leakage or *shunt current* due to recombination channels in the solar cell. Considering this factor, we obtain equation (3).

$$J = J_{light} - J_{dark} - J_{shunt} = J_{light} - J_0(e^{qV/mk_B T} - 1) - \frac{V}{R_{shunt}} \quad (3)$$

Finally, there is a drop in the potential within a device due to the series resistance. Considering this, we obtain the final equation (4).

$$J = J_{light} - J_{dark} - J_{shunt} = J_{light} - J_0(e^{q(V+JR_{series})/mk_B T} - 1) - \frac{V + JR_{series}}{R_{shunt}} \quad (4)$$

The schematic representation of an equivalent circuit for a solar cell is presented in Figure 1.5(A), and J - V curves for a solar cell in the dark and under illumination are presented in Figure 1.5(B). With

respect to DSCs, in the dark, when a small forward bias is applied, the mesoporous oxide is not conductive, and a very small current leaks through the device. However, at high applied voltages, the Fermi energy level is close enough to the conduction band edge, giving the material a high conductivity and resulting in an exponential growth of the diodic current.

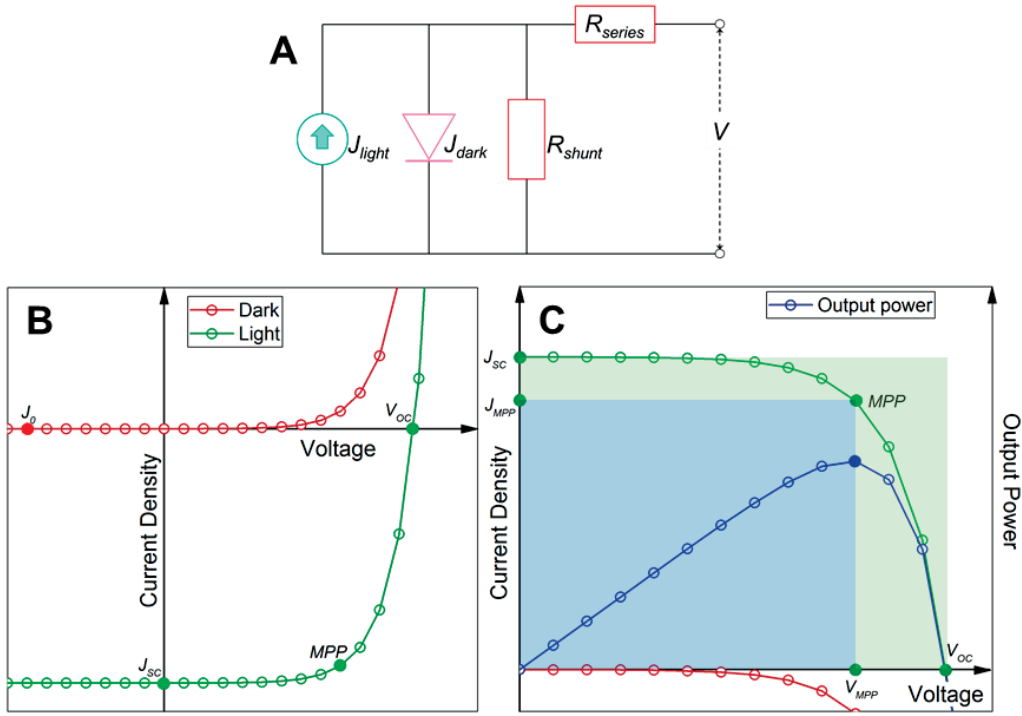


Figure 1.5. (A) Schematic circuit representing a solar cell; (B) J-V curve for a solar cell in the dark and under illumination; (C) the same concept as in (B) represented in a way frequently seen in the DSC literature. The fill factor is represented as the ratio of the small blue area to the bigger green area. Additionally, the curve showing the output power from the solar cell as a function of the voltage in a solar cell is shown.

Under illumination, a strong current from a solar cell that flows in the direction opposite to the diodic current is generated, and the J - V curve shifts towards the fourth quadrant of the voltage – current-density graph. For convenience, this graph is usually turned around the voltage axis (Figure 1.5(C)). When no external forward bias is applied to the DSC, the device is in *short-circuit* and provides the highest current density. In this situation, the Fermi energy level across the whole device is equilibrated, and besides tiny diodic and shunt currents, all the electrons injected from the photoexcited sensitizers are collected to provide the *short-circuit current density* J_{sc} . At a high enough applied voltage, the sum of the diodic and shunt currents is equal to the current from the solar cell, resulting in zero net current. For the DSC, at this point, all the photoinjected electrons recombine with the electrolyte, and the difference between the Fermi energy levels of two electrodes is equal to the *open-circuit voltage* V_{oc} . As the power provided by the device is equal to the product of the produced current and voltage, at some

point on the J - V curve, the $P = J \cdot V$ will reach its maximum value (Figure 1.5(C)). This point on the J - V curve is called the *maximum power point* and determined with the maximum power point current density J_{MPP} and the voltage V_{MPP} . For a high output power, the “squareness” of the J - V curve should also be high; in other words, its *fill factor* (FF), defined as in equation (5), should be high.

$$FF = \frac{J_{MPP} V_{MPP}}{J_{SC} V_{OC}} \quad (5)$$

The power conversion efficiency (PCE or η) of a solar cell is determined as the ratio of the output power to the input power, as shown in equation (6). The input power is determined by the solar irradiation power, and for the AM 1.5 G, this value is equal to 1 kW m^{-2} or 0.1 W cm^{-2} .

$$PCE = \frac{P_{out}}{P_{in}} \cdot 100\% = \frac{J_{MPP} V_{MPP}}{P_{in}} \cdot 100\% = \frac{J_{SC} V_{OC} FF}{P_{in}} \cdot 100\% \quad (6)$$

As was shown in equation (4), the values of the series and shunt resistances (R_{series} and R_{shunt}) influence the shape of the J - V curve and thus the fill factor and efficiency of a solar cell. In Figure 1.6 the effect of these resistances on the J - V curve is shown. Under ideal conditions, a high shunt resistance and a low series resistance are desired. The main cause of a small shunt resistance and a high leakage current is the presence of pinholes within the blocking layer, which is meant to protect the conductive glass from the electrolyte. The main components of a series resistance are the sheet resistance of the conductive glass and the connections.

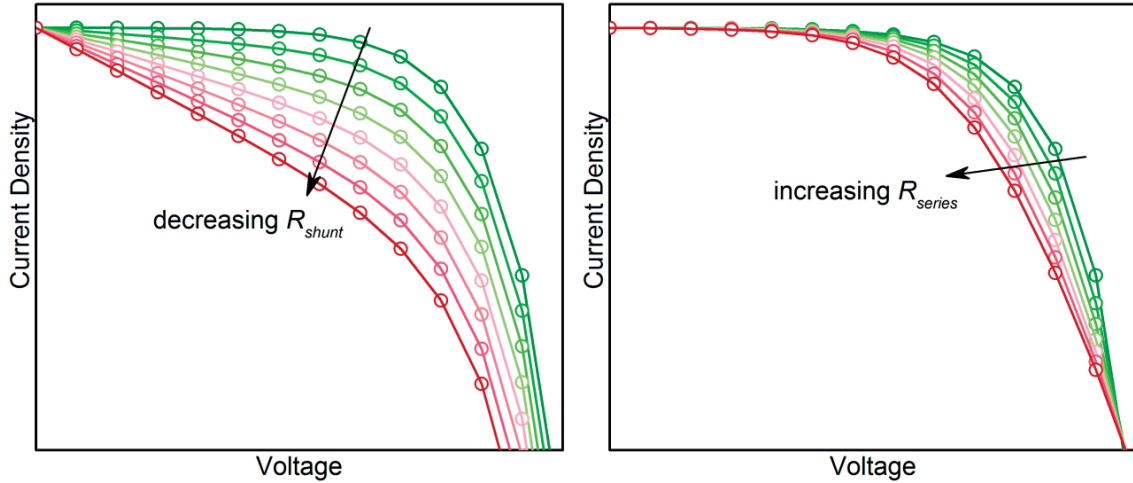


Figure 1.6. The effect of decreasing shunt resistance R_{shunt} and increasing series resistance R_{series} on the J - V curve (or *fill factor*) of a solar cell under illumination.

1.6.2 External and internal quantum efficiency measurements

The efficiency with which a solar cell converts the incident photon of a known wavelength into the electron collected in the external circuit is called the *external quantum efficiency* (EQE) or *incident photon-to-*

current conversion efficiency (IPCE). For the incident photon to result in electron in the external circuit, it should be first absorbed. The photoexcited sensitizer should then inject the electron into the mesoporous oxide, and this electron should be collected. Thus, the EQE is a product of the device's *light-harvesting efficiency (LHE)*, *injection efficiency (φ_{inj})*, and *charge collection efficiency (η_{col})* as shown in equation (7).

$$IPCE(\lambda) = LHE(\lambda) \cdot \varphi_{inj}(\lambda) \cdot \eta_{col} \quad (7)$$

The *internal quantum efficiency (IQE)* indicates the efficiency of converting the absorbed photon into an electron in the outer circuit. This term is also frequently referred to as the *absorbed photon-to-current conversion efficiency (APCE)*. The factor that differentiates the *IPCE* and *APCE* is the *LHE* (8).

$$APCE(\lambda) = \frac{IPCE(\lambda)}{LHE(\lambda)} = \varphi_{inj}(\lambda) \cdot \eta_{col} \quad (8)$$

To conduct the *IPCE* measurement, a solar cell at short circuit is illuminated with monochromatic light of a known flux, and the photocurrent is measured. Since the photon flux is much lower in the *IPCE* measurement than in the *J-V* measurement, 5 – 10 % white light bias is necessary. Afterwards, the integration of the product of the *IPCE* and the solar spectra ($F_{AM1.5G}(\lambda)$) should ideally provide a photocurrent density that matches the J_{SC} obtained from the *J-V* measurement (eq. (9)).

$$J_{SC} = \int_{\lambda_1}^{\lambda_2} e^- \cdot IPCE(\lambda) \cdot F_{AM1.5G}(\lambda) d\lambda \quad (9)$$

As mentioned above, the *LHE* is one of the factors that determines the *IPCE*. To measure the *LHE* of a film, one can measure the absorbance of a thinner transparent sensitized film and then scale that value based on the thickness of the film used in the dye cell. Otherwise, it is possible to estimate the absorbance of the film knowing the absorption spectra of the sensitizer and the amount loaded onto the semiconductor surface. In Figure 1.7(A) the absorption spectra for three sensitizers of the same extinction coefficient and broadness but different absorption maxima wavelengths are modeled as a normal curve. The fourth much broader absorption spectrum of the same covering area as 1, 2, and 3 is also modeled. Considering a dye-loading value of $1 \cdot 10^{-7}$ mol cm⁻², the absorbance of the film was calculated. Afterwards, together with the photon flux from the AM 1.5 G solar spectrum, the number of harvested photons of known wavelength for each modeled sensitizer was calculated. Integrating these curves considering the charge of an electron and considering the injection and collection efficiency to be 1, the J_{SC} provided by these sensitizers were estimated. With a nearly four times lower extinction coefficient than the other three sensitizers, sensitizer 4 provides a much higher J_{SC} than the others, which underlines the importance of broad absorption bands. In contrast to many other sensitizers, ruthenium complexes possess very broad metal-to-ligand charge transfer bands that are useful for DSCs as will be discussed later.

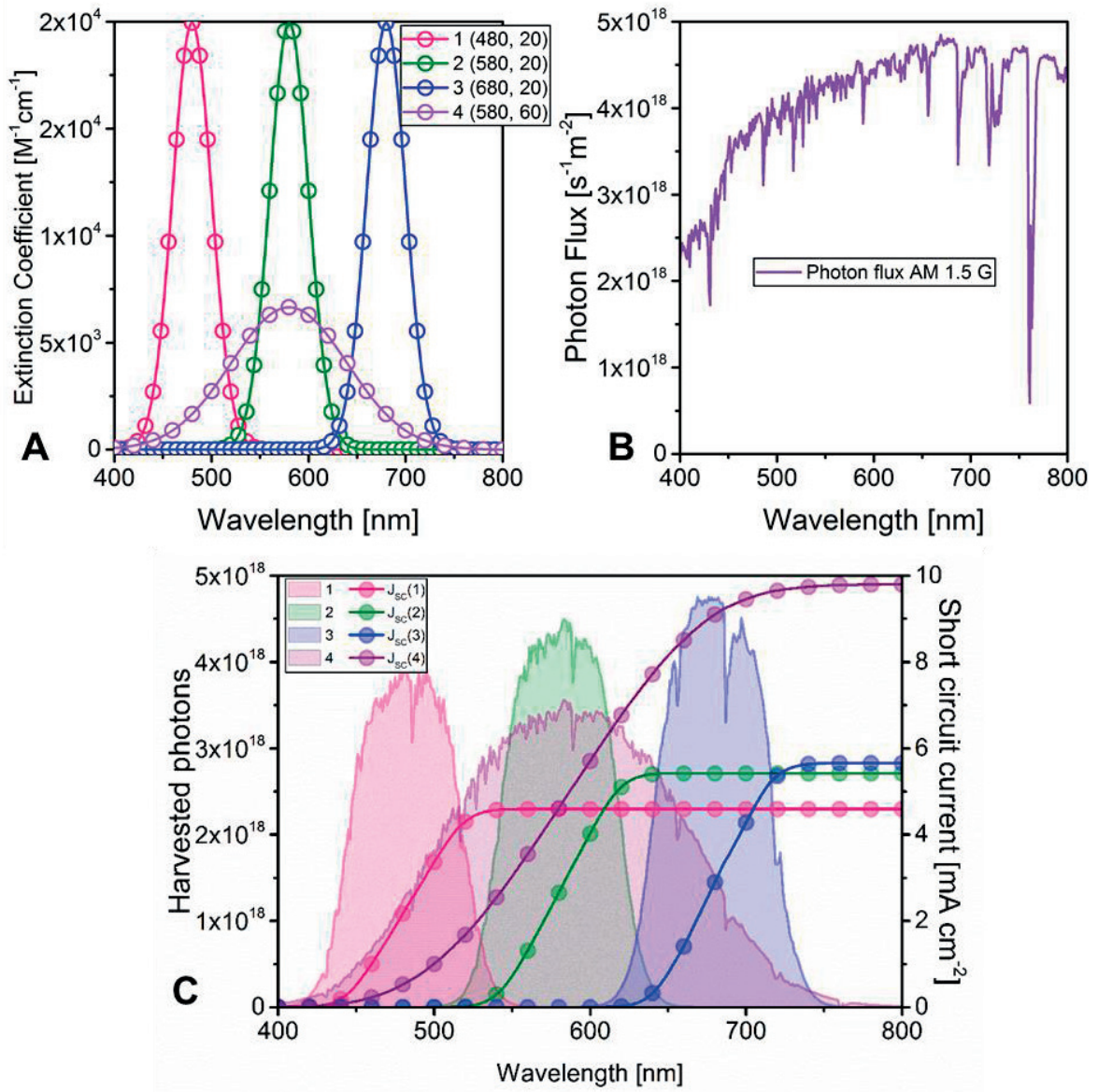


Figure 1.7. (A) Simulated absorption spectra for four sensitizers. Normalized curves of different mean values and standard deviations were used. The area under all four curves is similar. (B) AM 1.5 G solar spectrum showing the photon fluxes at fixed wavelengths. (C) Four spectra showing the numbers of absorbed photons at each wavelength. These curves were obtained by multiplying the *LHE* and the photon flux shown in (B). The *LHE* for each sensitizer was estimated according to $LHE(\lambda) = 1 - 10^{-\Gamma\sigma(\lambda)}$, where Γ is the number of moles of sensitizer per square centimeter of projected surface area of sensitized film (taken as $1 \times 10^{-7} \text{ mol cm}^{-2}$), and $\sigma(\lambda)$ is the absorption cross-section in units of $\text{cm}^2 \text{ mol}^{-1}$ obtained by multiplying the extinction coefficient by $1,000 \text{ cm}^3 \text{ L}^{-1}$. The short-circuit currents provided by each sensitizer were obtained by integrating the number of absorbed photons considering the charge of electrons. Full injection and collection were considered for all cases.

1.7 Processes at the photoanode

The main processes that occur at the photoanode are discussed below and summarized in Figure 1.8.

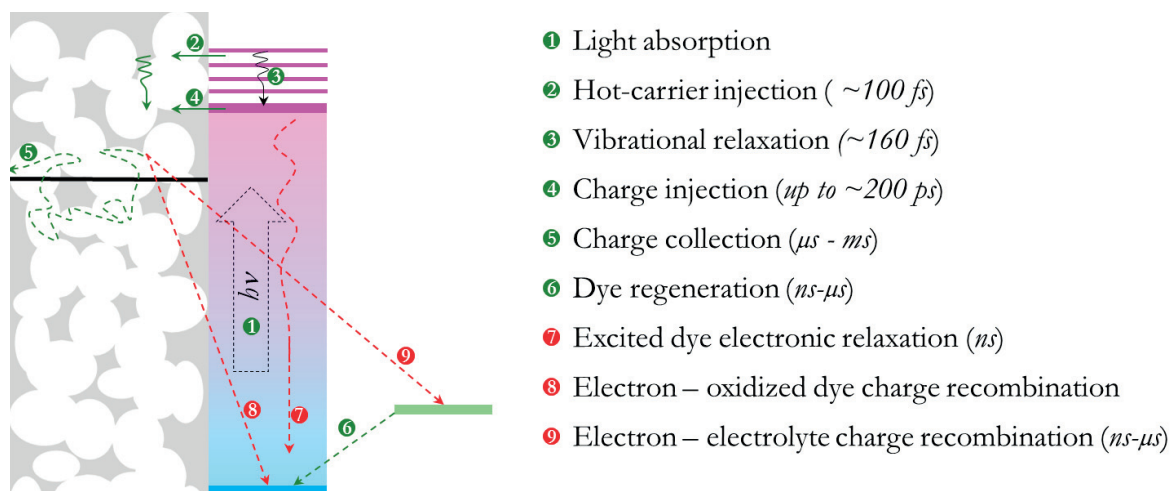


Figure 1.8. Main processes that occur at the photoanode in DSCs. The presented data were obtained from review articles.^{30–32}

1.7.1 Charge injection

There is no consensus in the literature concerning the timescales and efficiencies of electron injection from the excited sensitizer into the conduction band of titania. The main logic popular in the DSC literature is that with ruthenium complexes as sensitizers, the excited dye molecule injects its electron into the conduction band of titania on the femtosecond-to-picosecond timescale.^{33–36} To estimate the injection efficiency, the injection lifetime should be compared with the excited dye lifetime measured on the semiconductor, where the injection cannot happen. Due to the much longer excited state lifetime for ruthenium complexes, it is believed that the injection efficiency should be quantitative. However, most studies with sensitized films are conducted in incomplete solar cells with a definite density of electrons in titania.^{33–35} In a complete solar cell, Koops et al. found an ~ 200 ps injection half-time, which is much longer than previously believed and which results a charge injection efficiency of only 84 %.³⁷

Due to high spin-orbit coupling, after excitation, ruthenium complexes may undergo intersystem crossing (ISC) from an excited singlet state to a triplet state. This ISC occurs on an ~ 100 fs timescale.³⁸ From which state injection occurs is not completely clear. Many articles claim that ISC occurs quantitatively before injection. However, at room temperature, molecular vibrations will happen in 160 fs,^{39,40} and a longer timescale is necessary for thermalization and intersystem crossing.^{34,35,41} Thus, it is possible that ultrafast injection on the femtosecond timescale occurs from the vibrationally hot states of the excited singlet state.

1.7.2 Dye regeneration

Depending on the employed redox mediator, the regeneration half-time may vary. Most of the studies conducted with an N3 sensitizer and an iodine-based electrolyte report that regeneration occurs on the 100 ns to 1 μ s timescale.^{42,43} However, the exact mechanism of regeneration in this system is not clear. In the first step, a photo-oxidized ruthenium complex likely reacts with two iodide anions to produce $I_2^{\cdot-}$. Although third-order reactions in chemistry are little probable, studies have shown that the iodide concentration in the Helmholtz layer is high due to the pairing of iodide ions with the titania surface.⁴⁴ However, due to the lack of electrochemical studies conducted in organic solvents, it is difficult to draw a clear conclusion.

With one electron outer-sphere redox mediator, dye regeneration is straightforward, and the regeneration efficiency generally depends on the change in Gibbs' free energy upon electron transfer. Some redox mediators, like those based on $Co^{3+/2+}$ polypyridile complexes, may require a stronger driving force for regeneration due to additional reorganization energy for spin flip,⁴⁵ and some mediators may require very little driving force, like those based on $Cu^{2+/1+}$.^{46,47} Generally, for these systems, regeneration half-times on the microsecond timescale were shown.

1.7.3 Charge collection

Since the titania nanoparticles used to make a film are too small for any band bending, photo-injected electrons do not have a preferential direction for drift. In addition, diffusion is not a determining factor for charge collection, the nanoparticles are sensitized and, in a working device, each nanoparticle has 20 injected electrons on average. Approximately, 90 % of injected electrons fill up the trap states, while the rest are in the conduction band.³² Thus, electrons in the conduction band experience transport in random directions, with occasional trapping and de-trapping.^{48,49} For efficient electron collection, the electron diffusion length L_n must be higher than the film thickness L . Analogously, one may compare the electron lifetime τ_n with the characteristic transport time τ_d , which relates the electron diffusion coefficient D_n and the active film thickness L . The electron lifetime is related to the diffusion length in the same way the transport time is related to the film thickness ($\tau_n = L_n^2/D_n$; $\tau_d = L^2/D_n$).⁵⁰ The electron lifetime usually describes the electron recombination with an oxidized component of a redox shuttle. Recombination with the photooxidized sensitizer is usually negligible, since its regeneration occurs on a much faster timescale. Recombination in state-of-the-art solar cells that employ iodine-based electrolytes occurs on the microsecond timescale, which is long enough to allow most of the electrons to reach the contact.^{51,52} With other redox shuttles, like those based on $Co^{3+/2+}$ and $Cu^{2+/1+}$ couple, recombination is much faster; however, through the judicious design of the sensitizer, surface protection and an increased recombination lifetime can be achieved.⁵³

In comparison to many other technologies, DSCs are usually manufactured with analytically low grade materials. Additionally, considering the complexity of the processes that occur in DSCs, a question comes to mind. Why does a DSC not only work but also provide high power conversion efficiencies? The answer probably lies in the perfect timing of different processes. An analogy could be made to Photosystem II, for which many consequent steps also occur with perfect timing.

1.8 Sensitizers

(It worth noting that the oxidation potentials mentioned below are implied versus the normal hydrogen electrode (NHE) potential unless otherwise noted)

For an efficient DSC, a sensitizer should meet the following requirements.

1. The sensitizer should possess an anchoring group, which should enable its chemisorption onto the mesoporous oxide. Most of the developed sensitizers possess carboxylic and phosphonic acid anchors; however, impressive results were recently presented with silyl-anchors.⁵⁴
2. For efficient dye-regeneration, the oxidation potential of the sensitizer should be higher than the oxidation potential of the redox couple that *immediately* regenerates it. Efficient regeneration implies two orders faster regeneration than charge recombination with a photooxidized sensitizer. For a DSC with an electrolyte based on an outer-sphere one-electron redox mediator like $[\text{Co}(\text{bpy})_3]^{3+/2+}$ and $[\text{Cu}(\text{bpy})_2]^{2+/1+}$, the regeneration kinetics are well described by the Marcus electron transfer theory, where the two main factors that determine the rate are the driving force, $\Delta G = -nF\Delta E$, and the reorganization energy, $\lambda = \lambda_{\text{inner}} + \lambda_{\text{out}}$. Thus, depending on the nature of the redox mediator, the necessary driving force may vary to cover the reorganization energy. On the other hand, the exact couple that participates in direct regeneration in the iodine-based electrolyte is not yet established and may vary depending on the sensitizer.
3. The sensitizer's excited state oxidation potential should be more cathodic than the conduction band edge of titania. As Gerischer developed, the rate of electron injection from a sensitizer into the electrode is described in equation (10),

$$k_{\text{inj}} \propto \int \kappa_{\text{don}}(E)D(E)W_{\text{don}}(E)dE \quad (10)$$

where $\kappa_{\text{don}}(E)$ is the transfer frequency as a function of E , $D(E)$ is the density of empty electron states (DOS) within the semiconductor, and $W_{\text{don}}(E)$ is the donor distribution function for sensitizers.^{55–57} Thus, for the fast charge injection, the density of donor states, $W_{\text{don}}(E)$, which, in our case, is the population density of the vibrational states for the excited sensitizer S^* , and DOS should overlap in energy. As illustrated in Figure 1.9, W_{don} reaches its maxima at potentials by λ/e below the sensitizers excited state potential, which implies that for fast injection the excited state potential should be at least few hundred mV more cathodic than the conduction band edge of mesoporous titania.

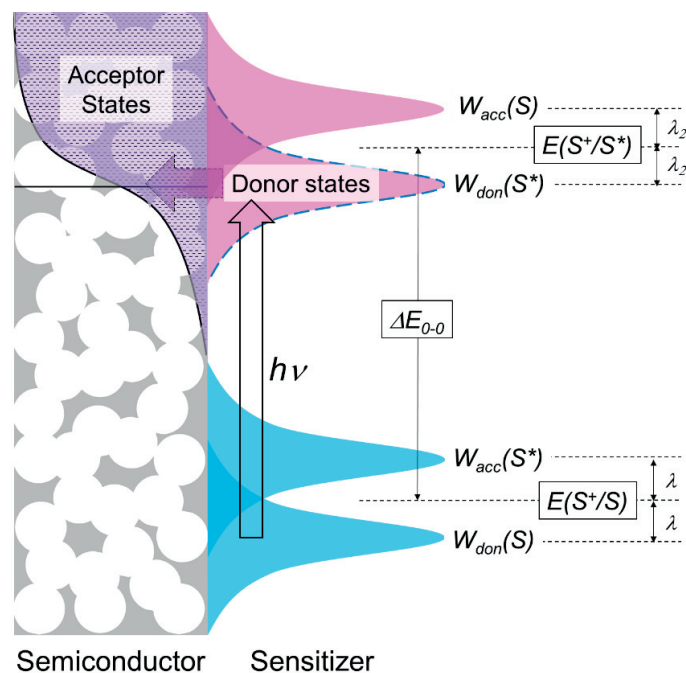


Figure 1.9. A Gerischer diagram illustrating electron injection from the photo-excited sensitizer into acceptor states within titania.^{55–57}

4. The absorption spectrum for a sensitizer should be intense to absorb most of the light on a thin layer of sensitized mesoporous titania. Roughly, extinction coefficients more than $10^4 \text{ M}^{-1}\text{cm}^{-1}$ are desired. However, sensitizers with lower extinction coefficients still work well when a thicker mesoporous layer is used.

5. For a record efficient DSC, a sensitizer should absorb all the photons up to 940 nm, which implies very high HOMO energies and very low LUMO energies. Thus, for this sensitizer, the overpotential required for efficient regeneration and charge injection should be exceptionally small.⁵⁸

6. For an efficient sensitizer, the HOMO and LUMO should be spatially separated, with the LUMO close to the part of molecule with the anchoring group and the HOMO on the part further away from the oxide surface. The closeness of the LUMO to the oxide surface is advantageous for efficient charge injection, while a HOMO far away from the semiconductor surface is useful for two reasons. First, it is necessary to hamper the rate of malignant charge recombination with the photooxidized sensitizer, and second, it increases the visibility of a hole for the electron donor in the electrolyte.

7. The sensitizer should be photochemically and electrochemically stable. For the DSC to be stable for 20 years, the oxidation – back-reduction turnover number for the sensitizer should reach 10^6 .⁵⁹

Many sensitizers have been developed for DSC applications. Below, I will primarily describe ruthenium (II)-based sensitizers and will only briefly describe organic and copper-based sensitizers.

1.9 Ruthenium sensitizers

The origin of Metal-to-Ligand Charge Transfer (MLCT)

The distinguishing feature of ruthenium (II) polypyridine complexes is their characteristic metal-to-ligand charge transfer band. In a vacuum, a ruthenium (II) ion possesses 6 electrons that occupy five degenerate 4d atomic orbitals. Higher in energy, there are 5s and triply degenerate 5p empty orbitals. Generally, these nine orbitals and the ligands determine the bonding and photophysical properties of the final molecule to be constructed.

First, let us consider how in the octahedral environment (O_h point group), six identical σ -symmetry ligands interact with central metal orbitals. In the octahedral point group, the s orbital will gain A_{1g} , three p orbitals will have T_{1u} , and five d orbitals will split into a set of orbitals with T_{2g} for d_{xy} , d_{xz} , and d_{yz} , and E_g character for d_{z^2} and $d_{x^2-y^2}$. Using the character table for the O_h point group, one can build a reducible representation of six ligand σ group orbitals - Γ_σ . Then, using a reduction formula, Γ_σ can be decomposed into a set of irreducible representations $\Gamma_\sigma = A_{1g} \oplus E_g \oplus T_{1u}$. Afterwards, using the projection operators, we can find a symmetry-adapted linear combination (SALC) of orbitals, which are the bases for these irreducible representations. The symmetry-adapted linear combination of six σ -donating ligands is presented in Figure 1.10 and an interaction diagram with the metal center is constructed. Only orbitals of the same symmetry are interacting, resulting in bonding and antibonding molecular orbitals. All of the metal orbitals except those with a T_{2g} character have ligand-based couples to interact. Thus, the t_{2g} orbitals remain as nonbonding. In the case of Ru(II) with σ -donating ligands (we may choose NH_3 as an example), all the bonding orbitals will be filled by electrons from the donor ligands, and six electrons from the ruthenium will occupy the t_{2g} orbitals. Considering that the bonding orbitals are too deep in energy, they do not play any crucial role in the photophysical and electrochemical properties of the complex. However, the positions of non-bonding t_{2g} and antibonding e_g^* orbitals are one of the most important factors for the complex. Thus, this diagram implies that the donating nature of σ -ligand orbitals affects only the e_g^* orbital and that by varying the basicity of ligand orbitals and the efficiency of overlap with the central atom orbitals, only the e_g^* orbital energy can be controlled.

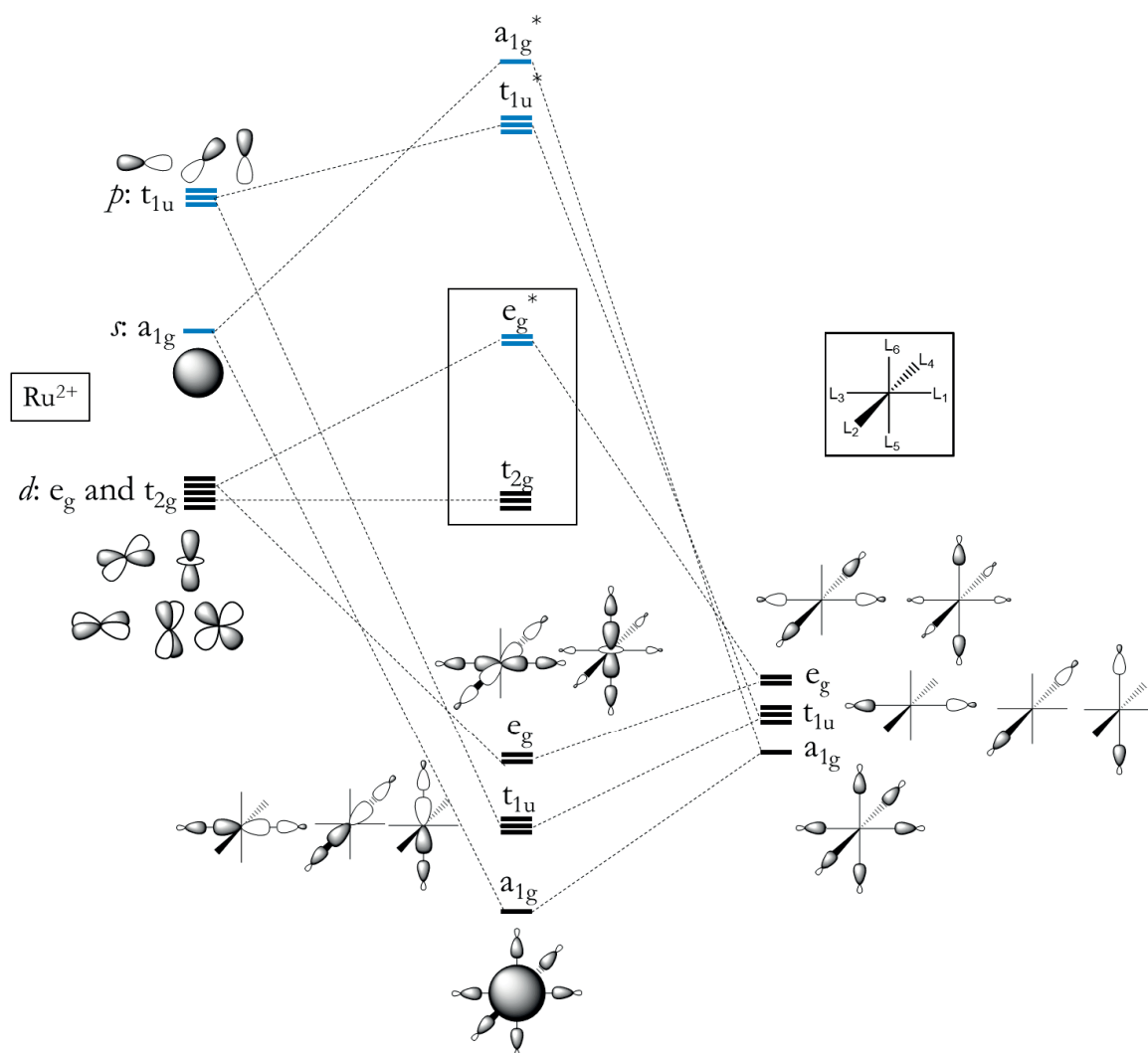


Figure 1.10. An interaction diagram of Ru^{2+} ions with six identical σ -ligands in an O_h symmetry point group. Bonding interactions of a symmetry-adapted linear combination of ligand donor orbitals with metal orbitals are presented. Black and blue bars represent doubly filled and empty orbitals, respectively.

The next step is to introduce a π -interaction with the ligand π -orbitals. A $[\text{Ru}(\text{bpy})_3]^{2+}$ ($\text{bpy} = 2,2'$ -bipyridine) can be considered as an example. In addition to the σ -donation from the six nitrogens, this molecule has an aromatic orbitals on each ring, which may interact with the central atom. Instead of building a D_3 symmetry-adapted linear combination of ligand π -orbitals and constructing their interaction with a central atom, we could check how ligand π -orbitals are interacting with the central atom orbitals qualitatively. Among the t_{2g} and e_g^* orbitals that already formed as a result of interactions with σ -ligands, only t_{2g} may π -interact with the ligand orbitals. In Figure 1.11(A), a perturbation of t_{2g} orbitals as a result of the interaction with the π -acidic and π -basic ligands is presented. Both types of ligands could be present in sensitizers, with pyridine, NCS, and cyclometalated ligands as π -basic ligands, and NHC-carbenes as π -acidic ligands. In the case of pyridine-type ligands, the bonding t_{2g} orbitals will be

filled with the ligand orbitals and the antibonding orbitals will be filled with six electrons from the Ru(II). Since the energy difference between the metal and ligand t_{2g} orbitals is usually high, the π -bonding is usually weak, resulting in the bonding and antibonding t_{2g} orbitals having primarily ligand and metal orbital nature, respectively. Consequently, the metal-to-ligand charge transfer occurs from the generally metal-based t_{2g}^* orbitals to the ligand-based π^* orbitals.

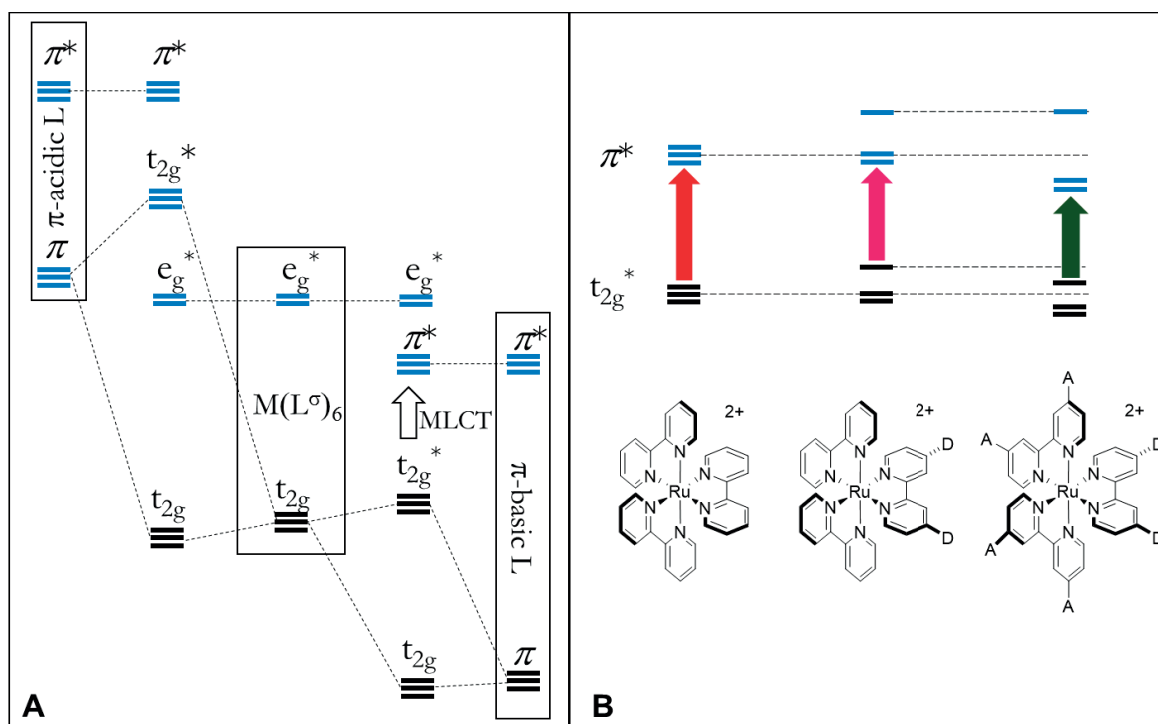


Figure 1.11. (A) An interaction of π -acidic and π -basic ligand orbitals with metal-based orbitals formed as a result of the interaction with six σ -ligands (*vide supra* Figure 1.10). (B) The effect of π -donor and π -acceptor substituents on the molecular orbital energies in heteroleptic ruthenium (II) complexes. D and A stand for π -donating and accepting substituents. The black and blue bars represent doubly filled and empty orbitals, respectively.

As follows from the interaction diagram in Figure 1.11(A), by tuning the π -basicity of the ligand orbitals, one may control the t_{2g}^* orbital energy and thus control the MLCT band energy. However, complete control over MLCT band position is not possible, since the π^* -orbital energy changes in accord with the π -orbital energy. In heteroleptic complexes, various ligands with different π -basicity can be used to bypass this problem, as illustrated in Figure 1.11(B) with derivatives of $[Ru(bpy)_3]^{2+}$. When the π -basicity values of various ligands are differentiated, the highest energy t_{2g}^* and the lowest energy π^* orbitals originate from the ligands of the highest and lowest π -basicity values, respectively. Thus, primarily the strongly π -donating ligands control the position of the t_{2g}^* orbital, while weaker π -donating ligands are responsible for the π^* -orbitals that participate in the lowest-energy MLCT band.

In addition to controlling the energy of the MLCT band, differentiation of ligands also attribute directionality to the MLCT band. This directionality of the MLCT bands in heteroleptic ruthenium complexes is one of the factors that determines their success in DSCs (*vide supra* requirements for sensitizers point 6 in section 1.8).

N3 sensitizer and its derivatives

Although the first breakthrough in DSCs was made with the trinuclear ruthenium complex,^{29,60,61} the N3 sensitizer that was introduced in 1993 has set a new trend in sensitizer design (Figure 1.12).⁶² This complex was synthesized in a two-step procedure from a commercially available $\text{RuCl}_3 \cdot x\text{H}_2\text{O}$ and provided a *PCE* of 10 %. Later studies revealed that few uppermost filled orbitals are shared between the Ru t_2 and NCS ligands' π and π^* -orbitals, while the first few empty orbitals are delocalized over anchoring 2,2'-bipyridine-4,4'-dicarboxylic acid ligands.⁶³ Later, it was found that the N3 dye's double deprotonated analogue N719 provides a *PCE* of over 11 %, as a result of a higher V_{oc} than obtained with the N3 dye. Additional TD-DFT calculations revealed that although the absorption spectrum of N719 is blue-shifted in comparison to that of N3, the higher lying LUMO of N719 ensures more efficient charge injection than for N3.⁶³ One of the disadvantages of the N3 and N719 complexes is their relatively low extinction coefficients. To improve the photophysical properties of NCS-based ruthenium complexes, *tris*-heteroleptic analogues of the N3 sensitizer, in which one of the bipyridine ligands possesses various substituents in the 4 and 4'th positions, were introduced. The most common *tris*-heteroleptic analogues are presented in Figure 1.12, including Z907, C101, C104, C106, K19, K106, CYC B3, and many others.⁶⁴⁻⁶⁷ In the most common case, these complexes are synthesized in an one-pot reaction, starting from a ruthenium(II) benzene (or p-cymene) dichloride dimer and introducing two ligands and an isothiocyanate salt. Thus, these complexes have two donating NCS ligands, an anchoring 4,4'-dicarboxy-2,2'-bipyridine ligand, and an auxiliary 4,4'-diR-2,2'-bipyridine ligand. Substituents on the auxiliary ligand may help to boost the extinction coefficient of sensitizers, and thus thinner mesoporous titania films, which are preferential to avoid extensive charge recombination, could be used. Additionally, substituents may help in preventing dye-aggregation, which can be detrimental to efficient charge injection. Although hundreds of heteroleptic complexes have been synthesized, they rarely provide better *PCEs* than N719.

An analogous sensitizer with a tridentate anchoring ligand as a derivative of 2,2':4',2''-terpyridine and three donating isothiocyanate ligands were also synthesized. This sensitizer is called a *black dye* due to its appearance in the solid state.⁶⁸ Extended π -conjugation in terpyridine in comparison to bipyridine results in a panchromatic absorption spectrum and very efficient solar light harvesting, resulting in a *PCE* of 10.4 % in a device.

One of the requirements of a sensitizer is that it should be stable to electrochemical oxidation, which is not the case with the isothiocyanate-ligated ruthenium sensitizers. The lability of isothiocyanate ligands, when the ruthenium complex is in the oxidized state is known in the literature.^{69–71} To overcome this problem, new ruthenium complexes with chelating donating ligands were developed.

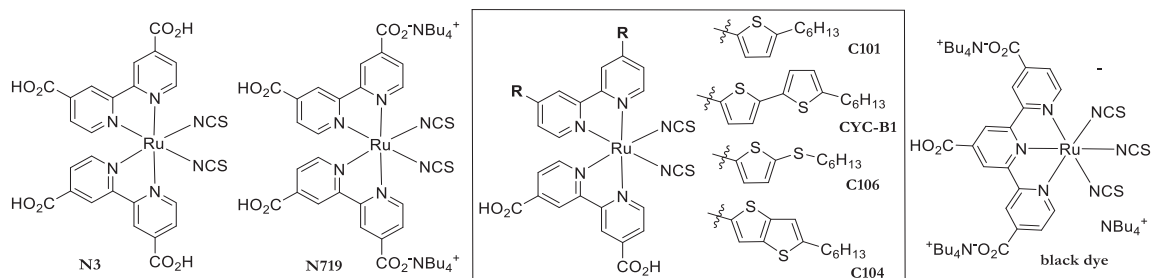


Figure 1.12. Some efficient ruthenium (II) complexes with isothiocyanate ligands.

Ruthenium complexes with pyridine-pyrazolyl ligands

Ruthenium complexes with 2-pyrazolyl-pyridine (PzPy) and its derivatives as ligands are good alternatives to complexes with isothiocyanate ligands, as in addition to eliminating non-chelating labile ligands, these complexes possess high extinction coefficients. Many *bis*-heteroleptic complexes with two PzPy ligands and one 2,2'-bipyridine-4,4'-carboxylic acid anchoring ligand with no overall charge were synthesized (Figure 1.13)^{72,73}. The photophysical properties of Ru complexes with PzPy ligands can be tuned by changing the pyrazole ligand to 1,2,4-triazole and fine-tuned by introducing substituents on two pyridine rings or changing them to isoquinolin-2-yl ligands. Although most of the characterized complexes have two pyrazolyl ligands in *trans* position to each other, in some cases, two other geometrical isomers were also separated and their different photophysical properties and performance in the solar cells were shown. In Figure 1.13, a few of the complexes with PzPy ligands are presented. Although with iodine-based electrolytes in DSCs, Ru complexes with PzPy ligands generally present lower efficiency values than complexes with isothiocyanate ligands, with cobalt-based ligands, the former complexes provide record high efficiencies for the reasons described in Chapter 2.

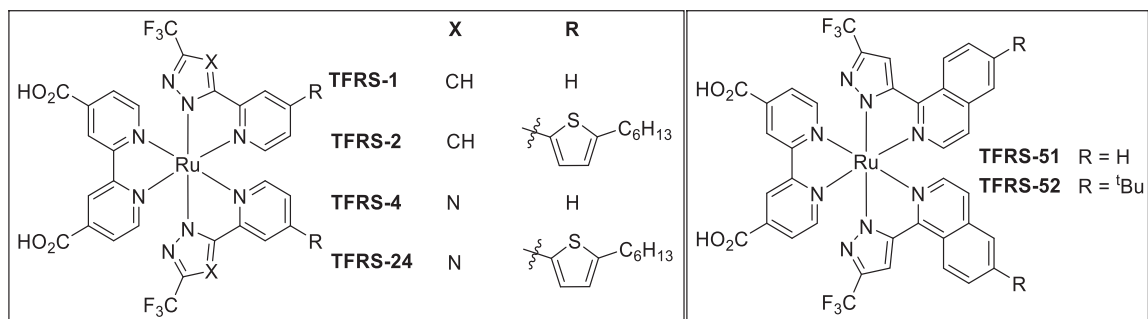
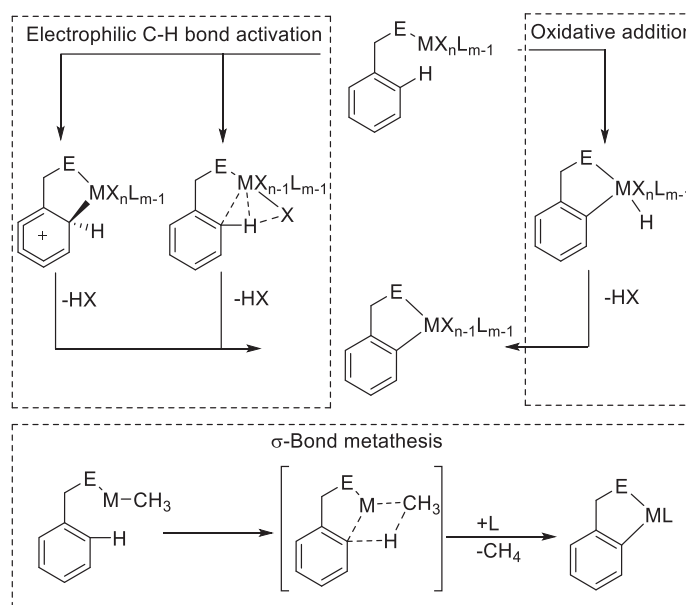


Figure 1.13. Some Ruthenium complexes with 2-pyrazolylpyridine or 2-(1,2,4-triazol-5-yl)pyridine ligands.

1.10 Cyclometalated Ruthenium (II) complexes

Cyclometalated complexes are those that possess a metallocycle with a metal-carbon σ -bond.⁷⁴ Cyclometalation reactions were first developed in 1960s, and this field later grew into a major part of organometallic chemistry.⁷⁴⁻⁷⁶ The main mechanism of cycloruthenation may differ depending on the ligand and source of ruthenium; in many cases, it is difficult to establish which mechanism takes place.^{74,77} Most cyclometalation reactions occur through three different mechanisms: electrophilic C-H bond activation, oxidative addition, and σ -bond metathesis (Scheme 1.1).⁷⁴

Scheme 1.1. Possible mechanism of cyclometalation. This scheme was drawn according to a published work.⁷⁴



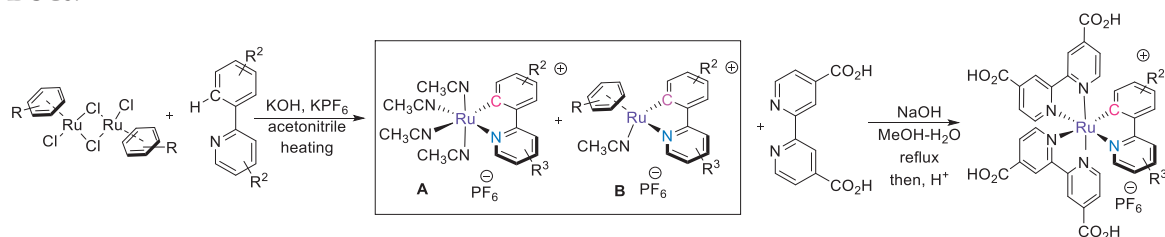
The electrophilic C-H bond activation mechanism is characteristic of the late-transition metals of an electron-poor nature. This mechanism occurs through two pathways: (i) through the formation of arenium intermediate or (ii) through the formation of an agostic C-H bond.⁷⁴ The first pathway is usually activated with electron-releasing substituents on the aryl ring, while for the second pathway, the effect of substituents is negligible. The (η^6 -arene)dichloridoruthenium dimer that is used extensively in this work (Chapters 1, 2) is thought to react through the electrophilic arenium intermediate, as the reaction with a cyclometalating ligand is facilitated by electron-releasing substituents on the aromatic ligand.⁷⁸ Although the oxidative addition mechanism is close to the agostic pathway of the electrophilic substitution mechanism, oxidative addition occurs via the occupation of C-H σ^* orbitals. Thus, this mechanism is more probable for electron-rich metal centers. This pathway is believed to take place when $\text{Ru}(\text{bpy})_2\text{Cl}_2$ or $\text{Ru}(\text{tpy})\text{Cl}_3$ is cyclometalated first by halogen abstraction and the reduction of ruthenium and then via the reaction with a cyclometalating ligand.⁷⁹⁻⁸¹ For the cyclometalation of

$\text{Ru}(\text{tpy})\text{Cl}_3$ with pyrazolylmethylbenzenes an agostic intermediate was even characterized spectroscopically.⁸² The third mechanism, σ -bond metathesis, predominantly occurs for the high-valent early transition elements. Methathesis requires the presence of metal-alkyles or metal hydrides, which is not usually the case for the ruthenium complexes described in this work.

To understand the effect of cyclometalation on the characteristics of ruthenium complexes, it is worthwhile to compare the features of $[\text{Ru}(\text{bpy})_3]^{2+}$ and $[\text{Ru}(\text{bpy})_2(\text{ppy})]^{1+}$ ($\text{ppy} = 2\text{-phenylpyridine}$). In cyclometalated complexes, the Ru-C bond is usually shorter than the Ru-N bond, and the Ru-N bond in the *trans* position to the Ru-C bond is usually elongated.^{83,84} The elongation of the latter bond might occur due to the strong trans-effect of the carbanion. In comparison to $[\text{Ru}(\text{bpy})_3]^{2+}$, in the absorption spectrum of $[\text{Ru}(\text{bpy})_2(\text{ppy})]^{1+}$, the MLCT bands are strongly red-shifted. In a methanol solution, for $[\text{Ru}(\text{bpy})_3]^{2+}$, the MLCT band's maximum is at 452 nm, while for $[\text{Ru}(\text{bpy})_2(\text{ppy})]^{1+}$, the maxima are at 543 and 486 nm.^{80,85} Thus, changing one pyridine ligand to the negatively charged carbanion results in a nearly 100 nm red-shift of the absorption spectrum. In comparison to $[\text{Ru}(\text{bpy})_3]^{2+}$, both the oxidation and first reduction potentials for $[\text{Ru}(\text{bpy})_2(\text{ppy})]^{1+}$ are cathodically shifted by 690 and 320 mV, respectively. Thus, cyclometalation strongly affects the position of the t_2 orbitals and less strongly affects the position of the lowest unoccupied π^* orbital.

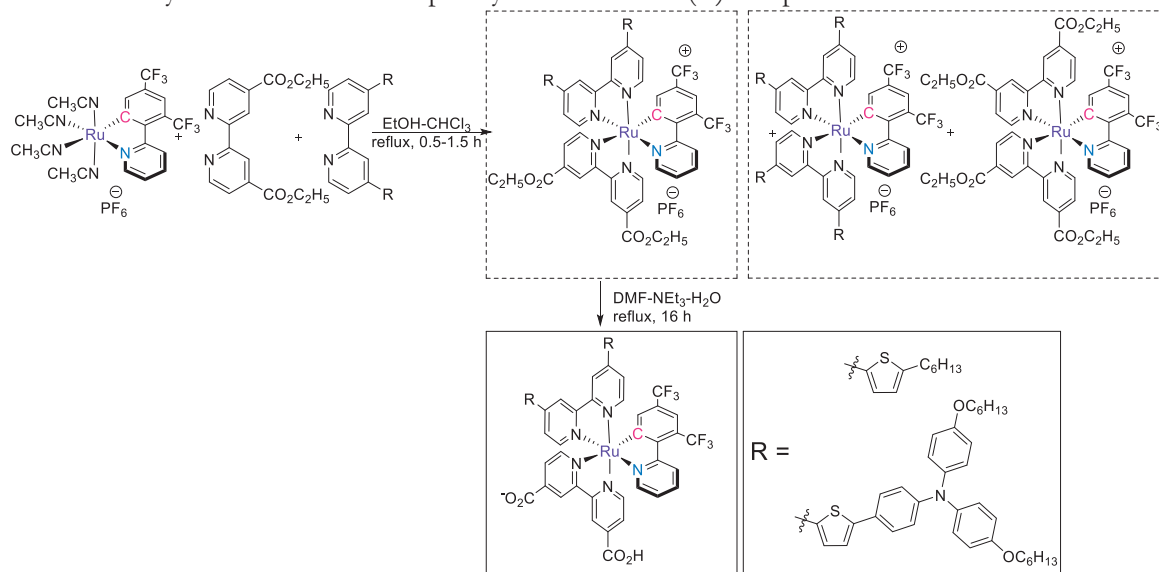
The first sensitizer for DSCs based on cyclometalated ruthenium complex was introduced in 2009 by Takeru Bessho et al.⁸⁶ In this work, the cyclometalation was conducted by reacting $\text{Ru}(\text{bpy}(\text{CO}_2\text{H})_2)_2\text{Cl}_2$ with 2-(2,4-difluorophenyl)pyridine in ethylene glycol at 170 °C. According to the ^1H NMR, the final sensitizer was obtained in its doubly deprotonated state, with one tetrabutylammonium cation. DSCs manufactured with this sensitizer and an iodine-based electrolyte provide a *PCE* of 10.1 %. Later, Paolo Bomben et al. reported a series of *bis*-heteroleptic cyclometalated ruthenium complexes as potential sensitizers for DSCs.⁸⁷ In this work, 2-phenylpyridine ligands with various electron donor and acceptor substituents on the phenyl ring were synthesized. Afterwards, these ligands were coordinated to the ruthenium, in a procedure developed by James Boncella and later optimized by Michel Pfeffer.^{78,88–90} In this procedure, a ligand is reacted with a (η^6 -arene)dichloridoruthenium dimer, where the arene is usually *p*-cymene or benzene, in the presence of potassium hydroxide and potassium hexafluorophosphate in acetonitrile. Depending on the reaction temperature and time and the type of arene, two possible products are possible, which are shown as **A** and **B** in Scheme 1.2. Although with *p*-cymene as a capping ligand, **B** is the main product after heating in acetonitrile at 45 °C for 2 days, with the benzene-capped ruthenium synthon, the ligand dissociation is complete and **A** is the only product.⁷⁷ Both products **A** and **B** have a yellowish color and can be purified easily via column chromatography using basic alumina.

Scheme 1.2. One approach to synthesize *bis*-heteroleptic cyclometalated ruthenium (II) complexes for DSCs.



The reaction of a mixture of **A** and **B** with two equivalents of 4,4'-dicarboxy-2,2'-bipyridine in the presence of sodium hydroxide results in the final complex. Various substituents on the cyclometalated benzene ring resulted in oxidation potentials in the range of 0.61 – 1.21 V. Moreover, the effect of the substituents in the *para*- position to the carbanion is stronger than the effect of substituents in the *meta*- position. Additionally, by the means of the density functional theory (DFT) calculation, the authors showed that the HOMO of the molecule is not only localized on the Ru t_2 orbitals but also delocalized over the cyclometalated benzene ligand with electron-releasing substituents.

Later, Bomben et al. introduced *tris*-heteroleptic cyclometalated ruthenium(II) complexes. To synthesize these complexes, the first cyclometalation was conducted as shown in Scheme 1.2, and product **A** was obtained. Product **A** was then reacted with a mixture of one equivalent of anchoring and auxiliary ligands, as presented in Scheme 1.3.^{91,92} This reaction results in three products, two *bis*-heteroleptic and one *tris*-heteroleptic, which can be separated using silica column chromatography. The *tris*-heteroleptic product is then hydrolyzed to obtain the final sensitizer. In these two sensitizers, in order to anodically shift the oxidation potential of the sensitizer, two trifluoromethyl groups were introduced onto the cyclometalating benzene ring. The introduction of substituents onto the auxiliary bipyridine ligand resulted in strongly enhanced molar extinction coefficients, reaching $30 \times 10^3 \text{ M}^{-1} \text{ cm}^{-1}$. The highest *PCE* achieved with these sensitizers in solar cells with an iodine-based electrolyte was 7.3 %, which is much lower than the *PCE* achieved with *bis*-heteroleptic complexes. However, considering that DSC performance is strongly dependent on the experience of the manufacturer and the materials used in different laboratories, the question of which type of sensitizer is better for DSC performance is tricky.

Scheme 1.3. Synthesis of *tris*-heteroleptic cyclometalated Ru(II) complexes.

To synthesize a ruthenium complex compatible with a cobalt-based electrolyte in a DSC, Lauren Polander et al. developed a new design approach⁹³. It was necessary to functionalize the donating ligand with long alkyl chains in order to sterically hinder the cobalt complex in an electrolyte from approaching too close the oxide surface. At the same time, the oxidation potential of the sensitizer had to be kept deep enough for efficient regeneration, which would not be the case with the alkyl-substituted cyclometalated benzene ring. The authors cunningly solved this problem by using a pyridine ring substituted with two alkoxy- chains instead of benzene with two trifluoromethyl groups. The electron-accepting nature of the pyridine ring was balanced with two π -donating alkoxy chains, resulting in oxidation potentials suitable for DSC application (Figure 1.14). Two ruthenium complexes with methoxy and dodecyloxy substituents on the cyclometalated pyridine ring were introduced. Both sensitizers were tested with a cobalt-based electrolyte. Changing the methoxy substituents to the long dodecyloxy substituents resulted in a *PCE* increase from 4.7 to 8.6 %. This work showed that through rational ligand design, one may improve the compatibility of ruthenium-based sensitizers with a cobalt-based electrolyte.

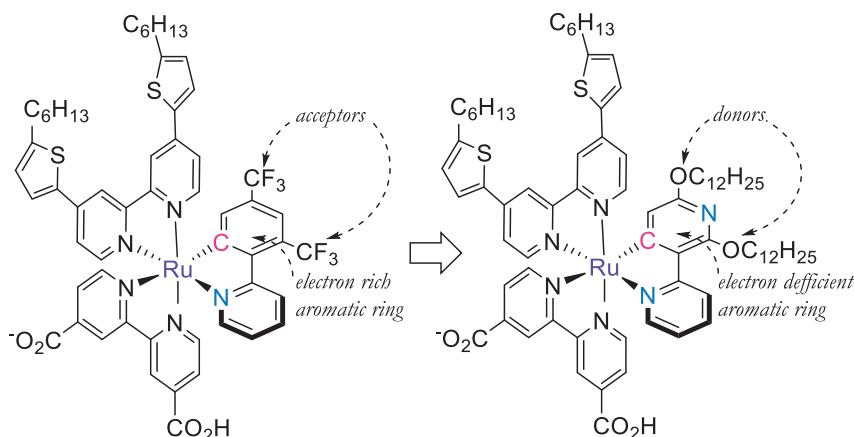


Figure 1.14. New ligand design introduced for sensitizers compatible with a cobalt-based electrolyte in a DSC.

1.11 Organic and copper-based sensitizers

The introduction of organic sensitizers revived the field of DSCs. Most of the organic sensitizers consist of three parts, a donor (D), π -bridge (π), and acceptor (A). The molecular structures of some of these components are presented in Figure 1.15. These parts can be combined as D- π -A or D-A- π -A to obtain a sensitizer, which will be attached to the semiconductor surface through the side A group. Thus, by modifying the nature of all the components, together with the length of the π -bridge, one may design a sensitizer with almost any photophysical properties and any geometrical shape. The intense absorption band of these types of molecules arises from the charge transfer (CT) from the donor to the acceptor moieties. Control over the CT band's position is possible by changing the electron-releasing and electron-accepting nature of the donor and acceptor groups, respectively, along with the nature and the length of the π -bridge. Some of the best organic sensitizers are shown in the Figure 1.15. Most organic dyes possess cyanoacrylic or carboxylic acid groups as an anchor. However, Kenji Kakiage et al. recently reported a new sensitizer, ADEKA-1, which has a silyl anchoring group. A DSC sensitized with a mixture of ADEKA-1 and LEG4 provides a record *PCE* of 14.3%.⁵⁴ The π -bridge can also be changed to a chromophore (C), as is the case with porphyrin sensitizers. One of the biggest advantages of porphyrin sensitizers is their intense Soret and Q-bands in the absorption spectrum. A porphyrin ring with D and A groups and side substituents to prevent dye aggregation provided a *PCE* of 13%.

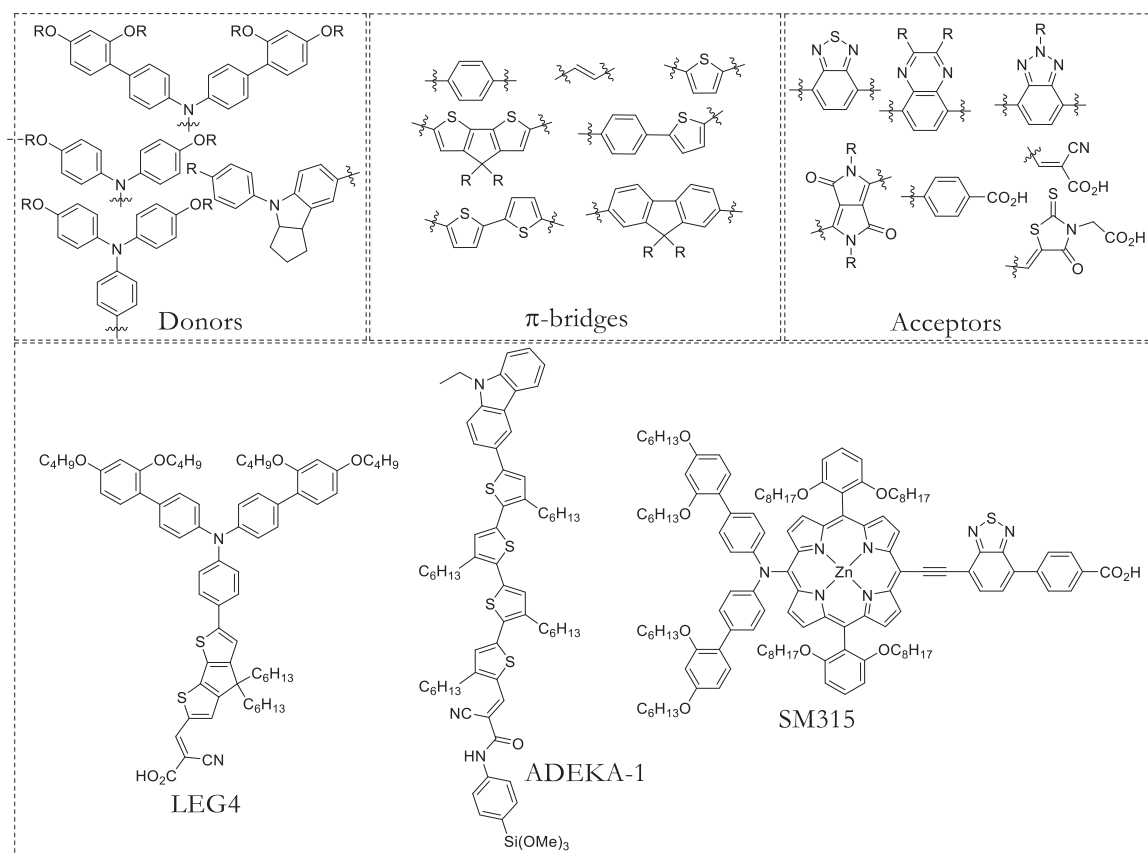


Figure 1.15. Top: Donors, π -bridges and acceptors frequently used to design organic sensitizers. Bottom: Three very important organic sensitizers.

Another class of sensitizers worth mentioning are those based on copper (I) complexes with *bis*-diimine ligands.⁹⁴ As in ruthenium complexes, the main absorption band in the visible spectra of Cu(I) complexes has an MLCT nature but with a lower extinction coefficients. Photoexcited copper complexes formally have Cu(II) in the d^9 configuration, which in contrast to the Cu(I) ground state, prefers a square-planar coordination due to Jahn-Teller effect. Thus, strong distortion of the Frank-Condon excited states leads to high reorganization energies, rapid deactivation and irreversible oxidation. This problem was ingeniously solved by inserting substituents that prevent ligand flattening.^{95,96} Although the synthesis of homoleptic Cu(I) complexes is straightforward, that is not the case with heteroleptic complexes, which are needed for charge transfer directionality. Due to the lability of diimine ligands in Cu(I) complexes, their exchange results in a statistical mixture of heteroleptic and homoleptic complexes.⁹⁷ This problem was also solved by functionalizing the mesoporous oxide surface with the anchoring diamine ligand and then reacting it with the Cu(I) source and the donating ligand.^{97,98} However, in my opinion, this feature will restrict the use of Cu(I) sensitizers in DSCs with liquid electrolytes. Most highly efficient DSCs are made of acetonitrile or 3-methoxypropionitrile, which may capture the copper ions and result in free homoleptic complexes in the electrolyte. One way

to resolve this issue is to reuse the electrode by dipping it into a solution containing Cu(I) and a donating ligand.⁹⁴ The PCE of state-of-the-art DSCs with Cu(I) sensitizers is still approximately 4-5 %, and advances in this field are necessary to obtain inexpensive and efficient sensitizers.⁹⁹

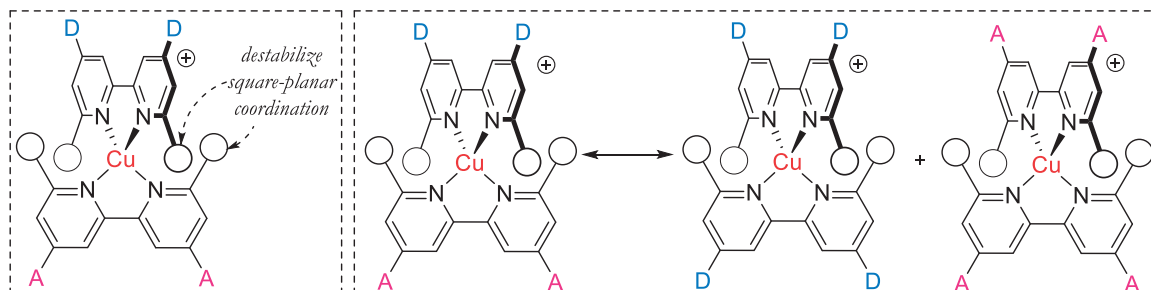


Figure 1.16. Left: the general structure of Cu(I) sensitizers for DSCs. Circles represent substituents that prevent ligand flattening when the metal center is oxidized to Cu(II). Right: the lability of ligands results in the formation of homoleptic complexes.

1.12 Motivation

In August 2013, when I started pursuing my Ph.D. degree, the laboratory of photonics and interfaces at EPFL had recently showed that newly designed cyclometalated ruthenium (II) complexes show *PCE* values of over 8 % in DSCs with a cobalt-based electrolyte.⁹³ This report was tremendously important to me. Ruthenium sensitizer, with its broad absorption spectrum, and cobalt-based electrolyte, which is known to provide high open-circuit voltages, were combined in one system. Generally, this report defined the starting project of my Ph.D.

In **Chapter 2**, I introduce six new *tris*-heteroleptic cyclometalated ruthenium complexes with different substituents on the auxiliary ligands. All the substituents were derivatives of thiophene and benzene and were introduced to increase the sensitizer extinction coefficient. All of the sensitizers were characterized, and solar cells with $[\text{Co}[\text{phen}]_3]^{3+/2+}$ -based redox shuttles and with new sensitizers were manufactured. In this work, we achieved record high *PCE* values for solar cells with a ruthenium sensitizer and a cobalt-electrolyte system. Spectroelectrochemical analyses of sensitizers in solution and in solar cells were conducted to analyze the electrochemical reversibility of new sensitizers. Transient absorbance spectroscopy and electrochemical impedance analyses were conducted to elucidate the observed trends in *PCE* values. Finally, the importance of dye-loading is emphasized.

In **Chapter 3**, we perform further investigations with cyclometalated *tris*-heteroleptic ruthenium complexes. In this work, we introduce arylamine-based donors onto the auxiliary ligands. We investigate the spectroelectrochemical characteristics of new sensitizers and discuss the reversibility of electrochemical oxidation. Further, solar cells with a cobalt-based electrolyte are introduced and their performance is explained based on transient photocurrent and voltage decay measurements.

In **Chapter 4**, we investigate the role of sulfur atoms in the dye structure and how the presence of sulfur atoms influences sensitizer performance in DSCs with an iodine-based electrolyte. Previous studies showed that sulfur atoms in a sensitizer may boost both the regeneration and recombination rates. However, all of these previous studies were conducted for unique systems that were composed to investigate either the recombination or regeneration rate. We fabricated state-of-the-art solar cells with sensitizers with and without sulfur atoms in their structures and analyzed performance. Transient absorption spectroscopy, together with electrochemical impedance spectroscopy, revealed which of the two consequences of sulfur atom presence is more crucial in determining the performance of a solar cell.

Concluding Chapters 2 and 3, I noticed that in addition to the desired effects, the chosen design approach also brings other unexpected detrimental features that restrict performance. At this stage, I was determined to discover new coordination environments to achieve complexes with photophysical properties suitable for DSCs. In **Chapter 5**, I introduce a novel ruthenium complex. In these *bis*-heteroleptic complexes, the ruthenium center was coordinated with both a cyclometalated carbanion and an N-heterocyclic carbene NHC⁺ ligand and two 2,2'-bipyridine or 4,4'-dimethoxycarbonyl-2,2'-bipyridine ligands. Structural, optical and electrochemical analyses are presented to support the potential use of these complexes in DSCs.

In **Chapter 6**, I introduce new extended ligands. This work was inspired by a recent growing interest in 2,6-bis(quinolin-8-yl)pyridine, which is a tridentate ligand that forms six-membered metallocycles. The advantages of this ligand over terpyridine in the resulting ruthenium complexes with a prolonged excited state lifetime and a bathochromically shifted absorption spectrum were shown. We have modified this ligand with an anchor, and together with another donating tridentate cyclometalated ligand, we have synthesized heteroleptic complexes. Structural, electrochemical and optical analyses were conducted. Finally, solar cells were manufactured and investigated.

Thus, the next five chapters present my research on ruthenium complexes. Afterwards, in **Chapter 7**, I present a general conclusion. **Chapter 8** presents all the supporting material for Chapters 2-6. All the research presented in this work has either been published or submitted for publication. The main body of each chapter is based on the respective article, with slight modifications to the text and figures.

Chapter 2 Ligand Engineering for the Efficient Dye-Sensitized Solar Cells with Ruthenium Sensitizers and Cobalt Electrolytes

This chapter is based on the following published article:

Sadig Aghazada, Peng Gao, Aswani Yella, Gabriele Marotta, Thomas Moehl, Joël Teuscher, Jacques-E. Moser, Filippo De Angelis, Michael Grätzel, Mohammad Khaja Nazeeruddin, *Inorg. Chem.*, **2016**, *55*, 6653-6659, DOI: 10.1021/acs.inorgchem.6b00842

In this work with the help from Dr. Peng Gao, I have designed all the molecules, then synthesized and fully characterized them. Dr. Aswani Yella fabricated solar cells, Dr. Joël Teuscher conducted laser measurements, Dr. Thomas Moehl measured electrochemical impedance, Dr. Gabriele Marotta conducted DFT calculations. With help from all the authors, I have analysed all the results and wrote the manuscript. Drs. Jacques-E. Moser, Filippo De Angelis, Michael Grätzel and Mohammad Khaja Nazeeruddin supervised the process.

Over the past 20 years, ruthenium(II)-based dyes have played a pivotal role in turning dye-sensitized solar cells (DSCs) into a mature technology for the third generation of photovoltaics. However, the classic I_3^-/I^- redox couple limits the performance and application of this technique. Simply replacing the iodine-based redox couple by new types like cobalt(3+/2+) complexes was not successful because of the poor compatibility between the ruthenium(II) sensitizer and the cobalt redox species. To address this problem and achieve higher power conversion efficiencies (PCEs), we introduce here six new cyclometalated ruthenium(II)-based dyes developed through ligand engineering. We tested DSCs employing these ruthenium(II) complexes and achieved PCEs of up to 9.4% using cobalt(3+/2+)-based electrolytes, which is the record efficiency to date featuring a ruthenium-based dye. In view of the complicated liquid DSC system, the disagreement found between different characterizations enlightens us about the importance of the sensitizer loading on TiO_2 , which is a subtle but equally important factor in the electronic properties of the sensitizers.

2.1 Introduction

The global challenge to develop carbon-neutral renewable energy sources can be addressed by harnessing solar power using photovoltaics.⁷ As an alternative to conventional solar cells, third-generation photovoltaic devices with dye-sensitized solar cells at the forefront have been extensively studied.²⁹ In standard DSCs, mesoporous TiO_2 is sensitized by a ruthenium(II) complex or an organic dye, and

I_3^-/I^- is widely employed as the most effective redox couple.^{62,100} Congruence between the dye molecule chemisorbed on a mesoporous oxide and redox pair in the electrolyte in DSCs should be fine-tuned to obtain fast dye regeneration and ideally slow charge recombination. The present certified record power conversion efficiencies of up to 11.1% were achieved with I_3^-/I^- and heteroleptic ruthenium dyes.^{64,68,101} However, regeneration of a ruthenium(II) complex by electron donation from the I_3^-/I^- redox couple entails a loss of around 500 mV, with over 300 mV of that being directly related to the complicated sequence of reactions associated with the two-electron oxidation of iodide that do not involve the sensitizer molecule.^{49,57,102} The estimated lowest potential loss for the ruthenium metal complex/iodide system is around 750 mV, which limits the maximum obtainable conversion efficiency to 13.4%.^{58,102}

To boost the efficiencies further, redox couples with a smaller loss in potential were introduced. Among the one-electron redox pairs,^{103,104} cobalt(3+/2+) is the most promising for the following two reasons: (i) DSCs with organic dyes and cobalt electrolytes are more stable in comparison to the cells with other one-electron shuttles;¹⁰⁵ (ii) it is possible to obtain cobalt complexes with various redox potentials just by ligand modification.^{106,107} It is worth noting that the recent advances with copper(2+/1+) phenanthroline-based electrolytes may result in an improved performance.^{108,109} Contrary to the reduction of I_3^- , the unwanted recapture of the conduction band electrons by the cobalt(3+) complex is a simple one electron outer-sphere redox reaction, which can attain fast rates depending on the driving force, even though the cobalt(3+/2+) self-exchange reaction is slow due to spin change. This is prominent, in particular, for conventional ruthenium dyes such as N3, N719, and N749.^{91,110–113} This caveat was ascribed to (i) the net negative charge on NCS-containing complexes causing coulombic attraction between the positively charged cobalt complex and sensitizer, which results in adsorption of the cobalt complexes on the semiconductor surface;⁴⁵ and (ii) the quenching of the triplet metal-to-ligand charge-transfer (³MLCT) state of ruthenium dyes by cobalt(3+) species, giving rise to a lower photocurrent.¹¹⁴ To alleviate this problems, new ruthenium-free dye structures were accommodated with long alkyl or alkoxy chains to keep the redox pairs away from the surface.^{105,115,116} In this manner, PCEs of over 14% and open-circuit voltages higher than 1 V were achieved by employing bulky D- π -A dyes with a cobalt-based electrolyte.^{54,117–119} A similar strategy was introduced for ruthenium dyes to improve their compatibility with the cobalt-based electrolyte.^{72,93,120}

On the other hand, the bulky nature of the cobalt-based complexes compels one to use thinner mesoporous films in order to avoid mass-transport limitations of the photocurrent. This, in turn, requires the use of dyes with higher extinction coefficients. Ruthenium(II)-based sensitizers generally suffer from relatively low extinction coefficients, which motivated us to design and synthesize new

cyclometalated *tris*-heteroleptic ruthenium(II) complexes.⁸⁶ Through modification of the auxiliary ligands by attaching polyaromatic moieties, we can fine-tune the photophysical properties of the complexes, especially the extinction coefficient, and consequently the incident photon-to-current conversion efficiency (*IPCE*) in a device. It is known that the highest occupied molecular orbital (HOMO) in a cyclometalated ruthenium(II) complex involves the auxiliary ligand to a lesser degree than the cyclometalated ligand.^{91,93} This provides a wide window for modification of the auxiliary ligand without destabilization of the HOMO's energy.

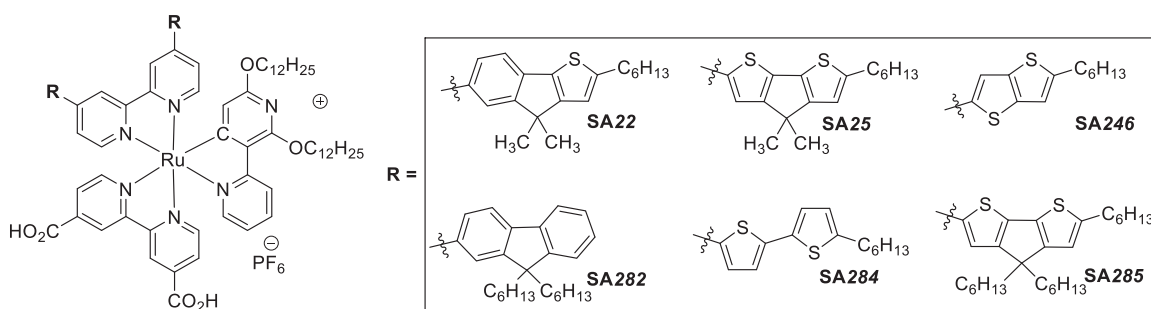


Figure 2.1. Molecular structures of cyclometalated Ru(II) complexes.

Here, we introduce six new *tris*-heteroleptic cyclometalated ruthenium(II) dyes (**SA22**, **SA25**, **SA246**, **SA282**, **SA284**, and **SA285**; Figure 2.1). All of these complexes possess the same anchoring ligand, 4,4'-dicarboxy-2,2'-bipyridine, and the same cyclometalated ligand as previously optimized.⁹³ 2,2'-Bipyridines substituted in the 4 and 4' positions with polyaromatic rings were used as auxiliary ligands. With these sensitizers, we systematically investigated the influence of the auxiliary ligand by optical and electrochemical measurement, theoretical calculation, transient absorbance spectroscopy (TAS), and electrochemical impedance spectroscopy (EIS). In the presence of cobalt(3+/2+) *tris*-phenantroline-based redox electrolytes, the highest PCE came from **SA246**, which possesses an insignificant absorption spectrum and the lowest electron lifetime. These contradictory results motivated us to unravel the critical parameters among the intricate effect of the kinds of factors. Through desorption experiments, we show that a proper substitution on the auxiliary ligands can dramatically increase the dye loading, which will play a decisive role in boosting the current density and *quasi*-Fermi level of TiO₂ and lead to an overtaking efficiency.

2.2 Results and Discussion

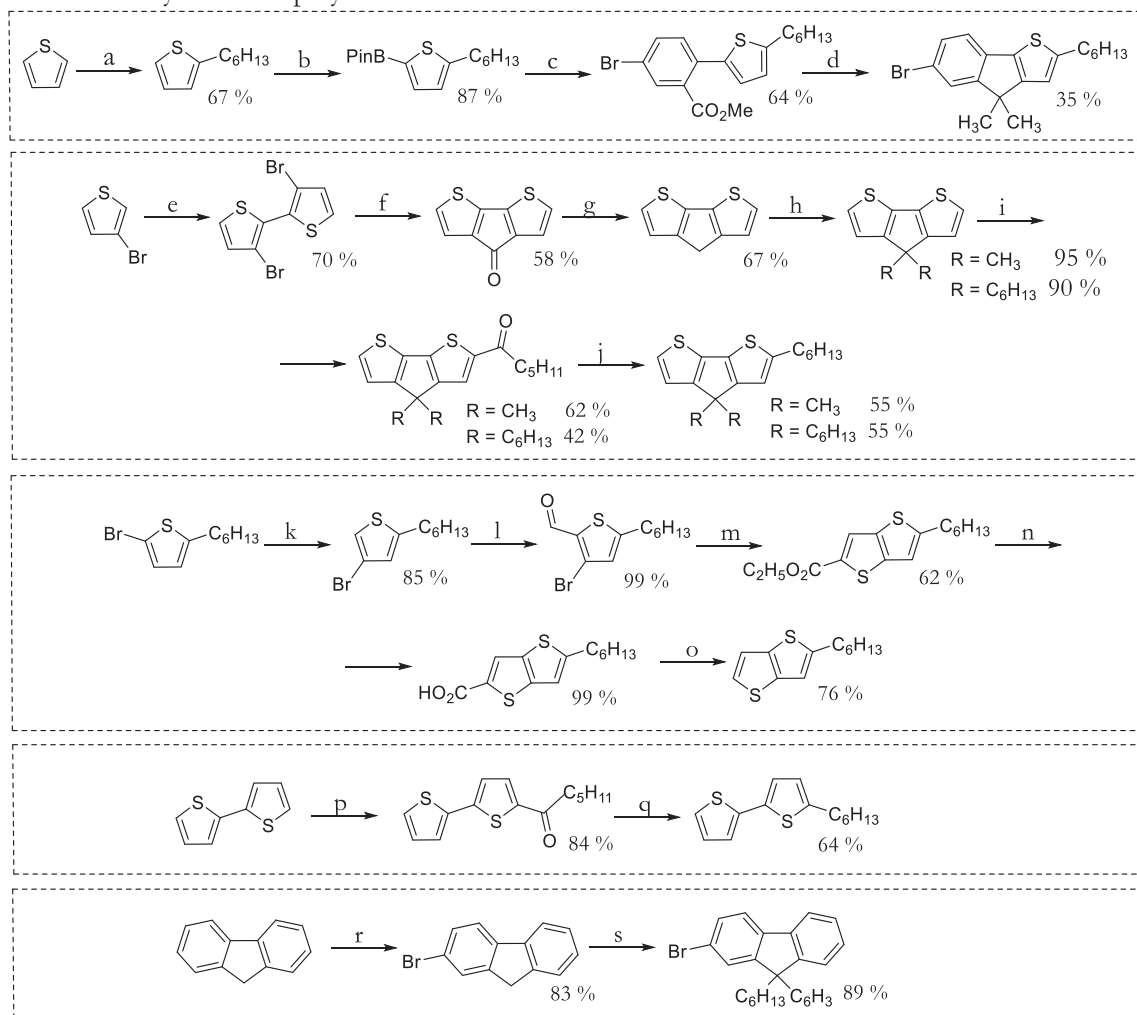
2.2.1 Synthesis of ligands and *tris*-heteroleptic ruthenium complexes

Our group has previously reported 2,6-didodecyloxy-3,2'-bipyridine as a superior cyclometalating ligand over 2,6-dimethoxy-3,2'-bipyridine because of its ability to keep the redox shuttle away from

the semiconductor surface.⁹³ To synthesize the auxiliary ligands, we first prepared 6 different polyaromatic compounds based on indenothiophene (*it*), cyclopentadithiophene (*cpdt*), thienothiophen (*tt*), bi-thiophene (*bt*) and fluorene (*f*) (Scheme 2.1). From the obtained materials, their boronic ester or tributyltin adduct were synthesized, and attached to the the 4 and 4'th position of 2,2'-bipyridine in their Suzuki-Miyaura or Stille coupling reactions with 4,4'-dibromo-2,2'-bipyridine (Scheme 2.2).

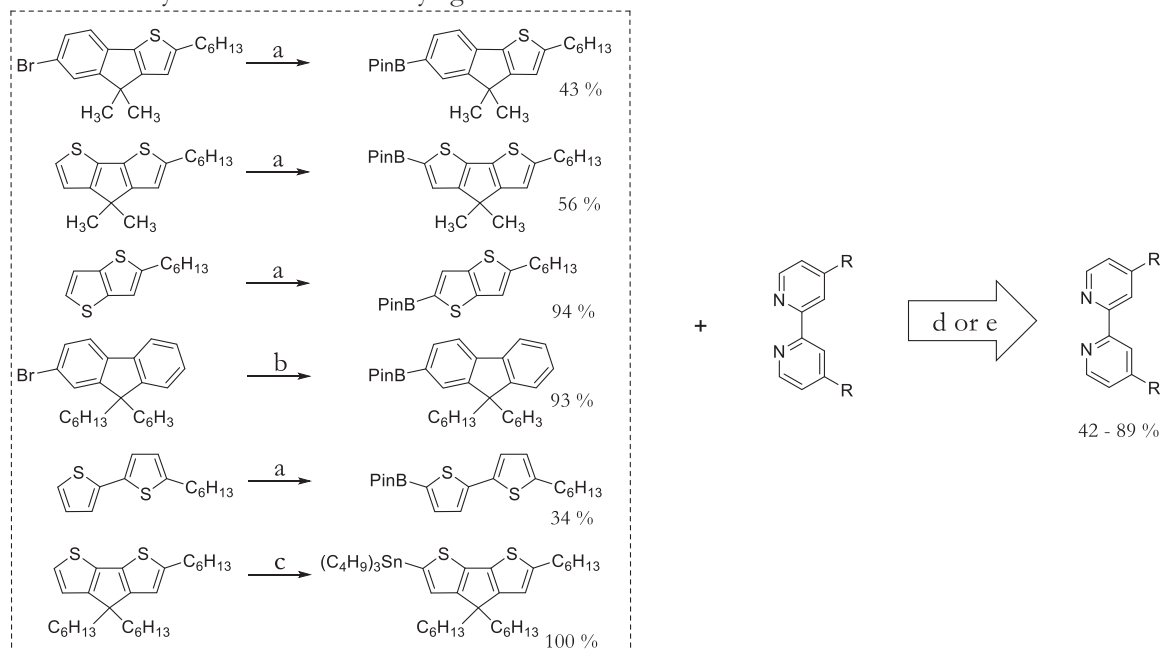
For the synthesis of *tris*-heteroleptic cyclometalated ruthenium(II) complexes, we adopted the procedures developed by Bomben et al., which starts from reacting the cyclometalating ligand with $[\text{Ru}(\text{C}_6\text{H}_6)\text{Cl}_2]_2$ or $[\text{Ru}(\text{p-Cymene})\text{Cl}_2]_2$ (Scheme 2.3).⁸⁷ After that, the intermediates were coordinated with the auxiliary and anchoring ligands in a one-pot reaction, resulting in three products: two cyclometalated *bis*-heteroleptic complexes and one *tris*-heteroleptic complex. It is worth mentioning that from the two possible isomers, where the cyclometalated ligand is in the *trans* position to the auxiliary or anchoring ligand pyridines, the former one is usually formed, as was shown from the single-crystal X-ray diffraction structures.^{91,93} Thus, the new ruthenium(II) complexes were separated and hydrolyzed to yield the final dye. All intermediates were characterized by ¹H NMR and the final complexes by ¹H NMR, ¹³C 135 DEPT NMR, and high-resolution mass spectrometry. The results are provided in the Appendix.

Scheme 2.1. Synthesis of polyaromatic substituents.



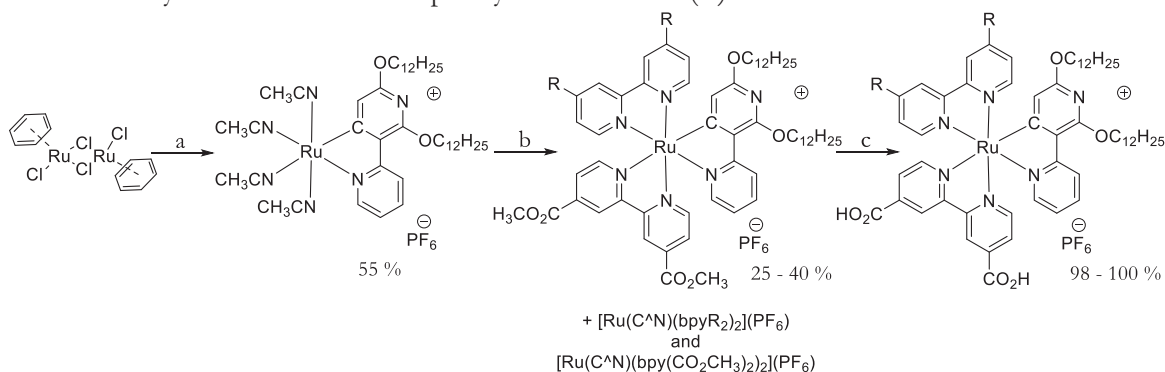
All reactions were conducted under N_2 atmosphere: (a) i. BuLi (2.5 M in hexanes), THF, $-78^\circ C$, 2 h; ii. $C_6H_{13}Br$; (b) i. BuLi (2.5 M in hexanes), THF, $-78^\circ C$, 2 h; ii. 2-Pr^tOBPin; (c) methyl 5-bromo-2-iodobenzoate, $Pd(PPh_3)_4$, toluene - 2M aqueous K_2CO_3 , $85^\circ C$, 48 h; (d) i. CH_3MgBr , THF, RT, overnight; ii. HCl; iii. $CH_3CO_2H - H_2SO_4$, reflux, 6 h; (e) i. LDA, THF, $-78^\circ C$, 1 h; ii. $CuCl_2$, $-78^\circ C$, 1 h, then RT, 5 h; iii. NH_4Cl_{aq} ; (f) i. BuLi (2.5 M in hexanes), THF, $-78^\circ C$, 30 min; ii. N,N-dimethylcarbamoyl chloride, $-78^\circ C$ to $0^\circ C$, 3 h; iii. NH_4Cl_{aq} ; (g) KOH, $N_2H_4 \cdot H_2O$, ethylene glycol, $200^\circ C$; (h) KOH, KI, CH_3I (or $C_6H_{13}Br$), RT, 12 h; (i) i. hexanoyl chloride, DCM, RT; ii. $AlCl_3$, $0^\circ C$ to RT, 24 h; iii. HCl; (j) i. $LiAlH_4 - AlCl_3$, diethyl ether, $0^\circ C$, 4 h; ii. H_2O ; (k) i. LDA, THF, $0^\circ C$ to RT, 18 h; ii. H_2O ; (l) i. LDA, THF, $0^\circ C$, 1 h; ii. DMF, $0^\circ C$ to RT, 5 h; iii. H_2O ; (m) K_2CO_3 , ethyl 2-sulfanilacetate, DMF, RT, 3 days; (n) $LiOH \cdot H_2O$, THF - H_2O ; reflux, 6 h; ii. HCl; (o) CuO, quinoline, reflux, 1 h; (p) i. hexanoyl chloride, DCM, RT; ii. $AlCl_3$, $0^\circ C$ to RT, 24 h; iii. HCl; (q) i. $LiAlH_4 - AlCl_3$, diethyl ether, $0^\circ C$ to RT, 4 h; (r) NBS, acetone, reflux, 3 h; (s) $C_6H_{13}Br$, $KOBu^t$, DMF, $60^\circ C$, 6 h.

Scheme 2.2. Synthesis of the auxiliary ligands.



All reactions were conducted under N_2 atmosphere: (a) i. BuLi (2.5 M in hexanes), THF, -41 or -78 °C, 2 h; ii. 2-PrⁱOⁱBPin; iii. H₂O; (b) B₂Pin₂, KOAc, Pd(dppf)Cl₂, dioxane, 80 °C, 6 h; (c) i. BuLi (2.5 M in hexanes), THF, -78 °C, 2 h; ii. (C₄H₉)₃SnCl; (d) Pd(PPh₃)₄, toluene - 2M aqueous K₂CO₃, 80 °C, 24 h; (e) Pd(PPh₃)₄, DMF, 80 °C, 12 h.

Scheme 2.3. Synthesis of tris-heteroleptic cyclometalated Ru(II) sensitizers.



All reactions were conducted under N_2 atmosphere: (a) cyclometalating ligand, KOH, KPF₆, acetonitrile, 45 °C, 72 h; (b) anchoring ligand, auxiliary ligand, ethanol - chloroform, reflux, 6 h; (c) NEt₃ - H₂O - DMF, reflux, 18 h.

2.2.2 Optical and Electrochemical Properties of Sensitizers

Figure 2.2(A,B,C) show the absorption spectra of the **SA** dyes in dichloromethane (DCM). All sensitizers have a set of $\pi-\pi^*$ transitions in the UV and near-UV regions. In the visible region, all dyes have characteristic metal-to-ligand charge-transfer (MLCT) bands. The extinction coefficient for the MLCT bands around 600 nm varies from $15 \times 10^3 \text{ M}^{-1} \cdot \text{cm}^{-1}$ (for **SA22**) to $24 \times 10^3 \text{ M}^{-1} \cdot \text{cm}^{-1}$ (for **SA285**). Except **SA22** and **SA284**, all other dyes have more intense absorption bands than the sensitizer

3b reported in ref⁹³, which has hexylthiophene substitution on the auxiliary ligand. Moreover, except **SA282**, in the presented sensitizers, the low-energy MLCT band is red-shifted by 5–15 nm. **SA22** and **SA282** have similar shapes of absorption spectra. However, in the case of **SA22** with the indenothiophene-substituted auxiliary ligand, the MLCT bands are red-shifted compared to that of **SA282** with fluorene moieties on the auxiliary ligands. Despite the substantial MLCT band shift between **SA22** and **SA282** (≈ 21 nm), the steeper drop of the MLCT band in long wavelengths in **SA22** compared to **SA282** results in a similar E_{0-0} value (1.77 eV; Table 2.1). **SA246** and **SA284** with thienothiophene and bithiophene moieties, respectively, also have similar shapes of absorption spectra, with that of **SA284** having more red-shifted bands in the near-UV region. **SA25** and **SA285** exhibit similar absorption spectra because of the same cyclopentadithiophenes. However, **SA285**, with longer alkyl chains on the cyclopentadithiophene moieties, has a higher extinction coefficient for the MLCT band than **SA25**.

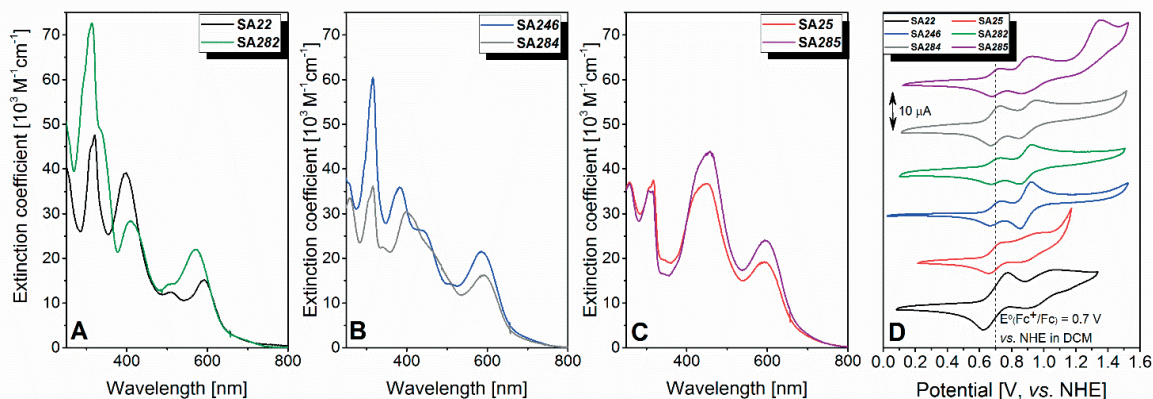


Figure 2.2. (A, B, and C) UV-vis absorption spectra of 10^{-5} M DCM solution of SA dyes; (D) Cyclic voltammograms obtained in 0.1 M NBu_4PF_6 solution in DCM. To reference the oxidation potentials, ferrocene was added as an internal standard. Corrected voltammograms with ferrocene oxidation potential fixed at 0.7 V *vs.* NHE are presented.

Figure 2.2(D) presents the cyclic voltammograms of the SA dyes. From the intersection of normalized absorbance and emittance (Figure 2.3(A)), E_{0-0} was calculated, and the excited-state oxidation potentials were calculated by subtracting E_{0-0}/e from the groundstate oxidation potentials. Table 2.1 and Figure 2.4 summarize the obtained optical and electrochemical data.

All dyes have oxidation potentials between 0.88 and 0.92 V *vs.* NHE, which are higher than the $[\text{Co}(\text{phen})_3]^{3+/2+}$ standard oxidation potential (0.62 V) by at least 260 mV. This difference should create enough driving force for efficient dye regeneration. **SA22** and **SA282** have similar E_{0-0} values, which ideally should lead to identical MLCT band positions. The ground-state oxidation potential of **SA285** (0.89 V) is surprisingly lower than that of **SA25** (0.92 V) by 30 mV. Because of the same E_{0-0} values,

the difference is maintained in the excited state. All presented sensitizers have the excited-state oxidation potentials in the range of -0.79 to -0.89 V *vs.* NHE, which should guarantee an efficient charge injection into the titania conduction band.

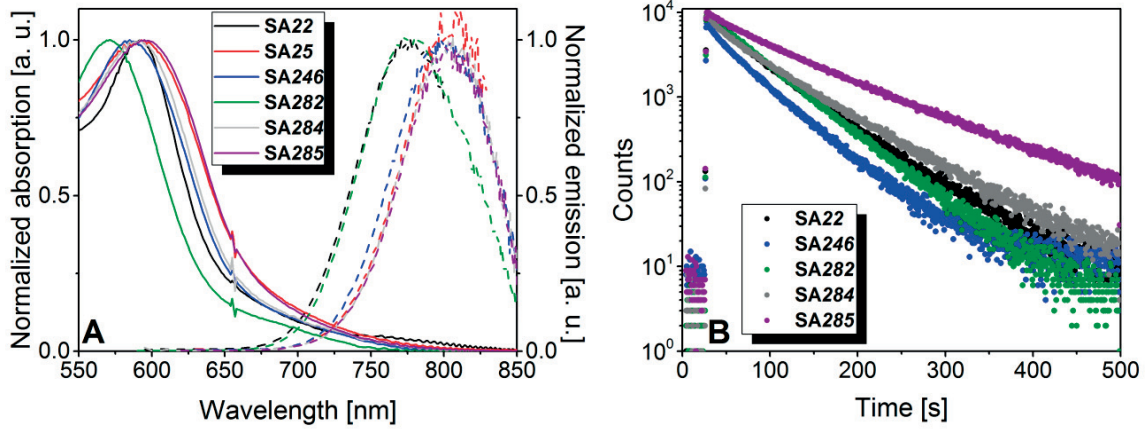


Figure 2.3. (A) Normalized absorption and emission spectra of SA dyes in DCM solution; (B) time-correlated single photon counting measurements for SA dyes in DCM solution. Decays were fitted with single exponential to obtain the excited state lifetime.

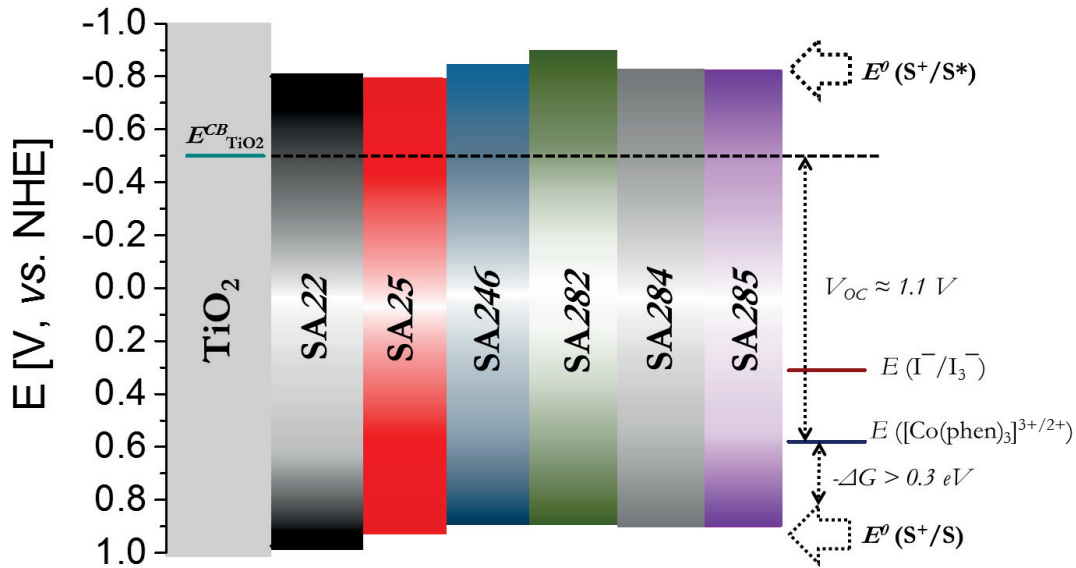


Figure 2.4. The energy diagram representing sensitizers' ground (GS) and excited states (ES) oxidation potentials and redox couples' Nernst potentials with respect to the conduction band of TiO₂. Sensitizer's GS oxidation potential was determined from the CV measurements, and ES oxidation potential was obtained by subtracting $E_{0,0}/e$ from the GS oxidation potential. Redox couple Nernst potentials are shown considering concentrations in Z960¹²¹ iodine based electrolyte and in optimized cobalt-based electrolyte.

Table 2.1. Photophysical and Electrochemical Properties of Dyes

	^[a] λ_{abs}/max , [nm] ($\epsilon \cdot 10^{-3}$ [M ⁻¹ ·cm ⁻¹])	^[b] $E^0(S^+/S)$ [V, <i>vs.</i> NHE]	^[a] λ_{em}/max , nm (in DCM/on TiO ₂)	^[c] $\tau_{1/2}$ [ns]	^[d] E_{0-0} [eV] (in in DCM/on TiO ₂)	^[e] $E^0(S^+/S^*)$ [V, <i>vs.</i> NHE]
SA22	592 (15.2), 511 (12.5), 399 (39.2)	0.97	771/776	46	1.77/1.77	-0.80
SA25	593 (19.3), 448 (36.7)	0.92	808/811	-	1.71/1.71	-0.79
SA246	585 (21.5), 431sh (26.4), 382 (36)	0.88	798/814	38	1.72/1.71	-0.84
SA282	571 (22), 508sh (14.2), 411 (28.2)	0.88	775/798	48	1.77/1.74	-0.89
SA284	592 (16.3), 398 (30.4)	0.89	803/810	44	1.71/1.70	-0.82
SA285	595 (24.1), 456 (44)	0.89	804/822	82	1.71/1.67	-0.82
3b ⁹³	580 (19.6), 507 (14.1), 418 (23.4)	0.86	789/-	-	1.76/-	-0.90

^[a]Absorption and emission spectra were measured in DCM at RT. ^[b]Oxidation potentials were determined from cyclic voltammetry in 0.1 M NBu₄PF₆ in DCM. Working electrode was glassy carbon, counter and reference electrodes were Pt wires and Ferrocene (Fc) was used as an internal standard. To calculate the potentials versus NHE, 0.7 V as Fc oxidation potential was used. ^[c]Excited state lifetime in DCM solution were determined from fluorescence TCSPC measurements. ^[d] E_{0-0} was determined from the intersection of normalized absorption and emission spectra. ^[e]Excited dyes oxidation potentials were calculated by subtracting E_{0-0}/e from the ground state oxidation potential.

One of the desired properties of a DSC sensitizer is its capability of sustaining numerous oxidation–reduction cycles under long-term operation, e.g., turnover numbers reaching 100 million for an outdoor lifetime of 20 years. Isothiocyanate ligands employed often for ruthenium(II) complexes cannot survive because of ligand exchange by electrolyte components such as *tert*-butylpyridine.¹²²

In this regard, cyclometalated ruthenium(II) complexes were introduced as being potentially more stable, by ruling out the possibility of ligand exchange. However, on the basis of cyclic voltammetry measurements, our ruthenium(II) complexes are *quasi*-reversible because the obtained oxidative and reductive wave peak separations are usually around 120 mV.^{68,86,87,91,92}

To understand the origin of the electrochemical irreversibility in cyclometalated ruthenium dyes, we conducted spectroelectrochemical measurements in solution and in the complete device without a redox pair. We focused on the bands above 300 nm. In solution (Figure 2.5), none of these six complexes showed complete reversibility of both the π – π^* and MLCT bands. Among them, **SA22** and **SA246** showed the best reversibility. However, these results should not be discouraging because dye

features on titania may strongly change. In complete devices, **SA22**, **SA282**, and **SA284** showed reversible behavior only for the $\pi-\pi^*$ transitions. Conversely, **SA25**, **SA246**, and **SA285** have reversible MLCT bands in a device, but the $\pi-\pi^*$ transitions around 450 nm become extinct, indicating that the coordination core is more stable than the polyaromatic substituents (Figure 8.43(C)).

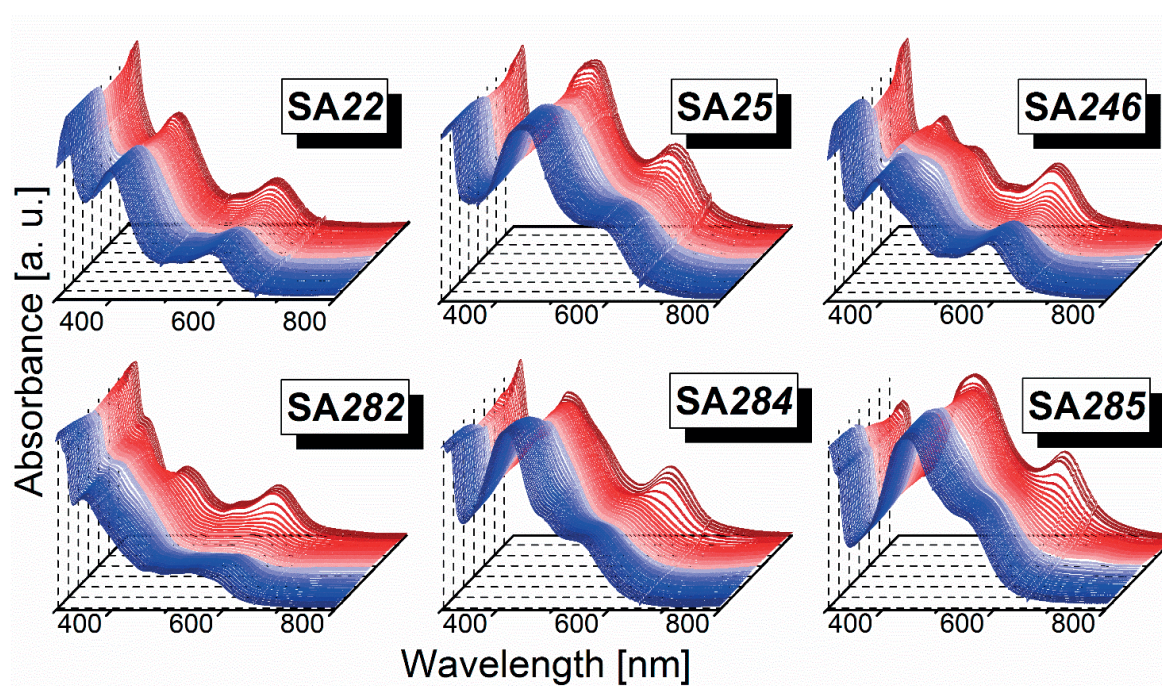


Figure 2.5. Spectroelectrochemical measurements in 0.1 M NBu_4PF_6 DCM solution of SA dyes. Color change from the red to the pale red and then to the blue visualize the change in spectra during the oxidation and back-reduction respectively. First anodic voltage (50 mV higher than dye's oxidation wave maximum potential) was applied and the absorption spectra were measured every 10 sec. 16 times, then the cathodic voltage (50 mV lower than dye's reduction wave maximum potential) was applied and the absorption spectra were measured in every 10 sec. for 16 – 20 times.

2.2.3 Computational Analysis

In Figure 8.44, the optimized geometries of studied **SA** dyes are shown. All of them have the typical geometry of ruthenium *tris*-bipyridine complexes. These optimizations were carried out for the isomers, which have a cyclometalated pyridine ring in the position *trans* to one of the anchoring carboxypyridine rings. It is worth noting that calculated molecular volumes meet expectations, and **SA246** and **SA284** with the least number of substituents have the lowest molecular volumes (Table 8.1).

Among the entire series of **SA** dyes, the first few unoccupied molecular orbitals have very close energies (Table 8.2) and are localized on the anchoring ligand, as can be observed from the isodensity plots in Figure 8.45 and Figure 8.46. However, the few uppermost occupied orbitals present variation in the energies mainly because of localization on the different substituents. In particular, **SA25** and

SA285 exhibit the highest HOMO energy with a consequent decrease of the HOMO–LUMO energy gap. As expected, the three uppermost occupied orbitals are not localized on the metal t_2 orbitals, but are also partially delocalized through the auxiliary ligand, the degree of which depends on the different substituents. In **SA25** and **SA285**, both cyclopentadithiophene moieties on the auxiliary ligands contribute to a major fraction of the HOMO. In **SA22**, **SA246**, and **SA284**, only one donating moiety on the auxiliary ligands, which is in the *trans* position to the anchoring carboxypyridine ring, owns a fraction of the HOMO. Fluorene moieties on the auxiliary ligand in **SA282** do not possess any substantial fraction of the HOMO (Figure 8.45). These observations imply that among all of these substituents on the auxiliary ligands, cyclopentadithiophene and fluorene own the strongest and weakest donating power respectively, considering that the dihedral angles between the substituents and pyridine rings of the auxiliary ligand may also play a role. Because the dihedral angles between the indenothiophene or fluorene moieties and pyridine planes are close values according to the density functional theory (DFT) calculations (36 and 38°, respectively; Table 8.1), the red-shifted spectrum of **SA22** (or **SA285**) with respect to **SA282** is more reasonably due to the higher donating power of indenothiophene than fluorene. Although the shapes of theoretical spectra do not perfectly follow the experimental results (Figure 8.47), the absorption maxima and the main calculated transitions (Table 8.4) are in perfect agreement with the experimental optical data.

2.2.4 Transient Absorption Spectroscopy (TAS)

To evaluate the influence of different substituents on the lifetimes of the photooxidized dyes in the environment of cobalt-based electrolytes, we performed TAS measurements on unbiased devices. Measurements were carried out on two different types of cells containing (a) redox-inactive acetonitrile containing lithium salt and 4-*tert*-butylpyridine and (b) a cobalt-based electrolyte. Dye molecules were excited with a low-intensity pulsed laser at 510 nm to ensure an average of less than one injected electron per nanoparticle, i.e., typically $40 \mu\text{J}\cdot\text{cm}^{-2}$. The probe was monitored at 900 nm, following the oxidized dye signature, and transient absorbance decay was fitted with a monoexponential function (Figure 8.48).

We find a regeneration yield of above 94% for all dyes, except **SA282** and **SA285**. A low regeneration yield for **SA282** and **SA285** is reasonable considering the steric hindrance of their hexyl chains, which drastically affect the regeneration lifetime. We also observe that, for most of the dyes, regeneration does not seem complete and the dynamics reach a plateau, suggesting remaining oxidized species in the system. It is worth noting that, to estimate the regeneration efficiency, we consider that electron recombination with photooxidized dye, and dye regeneration with the electrolyte rates follow first-

order dynamics on the reductant concentration, thus the regeneration efficiency can be calculated according to equation (11),

$$\eta_{reg} = \frac{\tau_{rec}}{\tau_{rec} + \tau_{reg}} \quad (11)$$

where τ_{rec} is the electron - oxidized dye recombination lifetime, and τ_{reg} the oxidized dye regeneration lifetime in the presence of an electrolyte (Table 8.6). This procedure may not exactly represent the situation in a device under full sun illumination considering the following facts: (a) dye regeneration is not necessarily a first-order reaction;¹²³ and (b) the electron density in TiO₂ created by the laser pulse is not comparable to the electron density in the performing device at maximum power point.^{122,124} The second fact may bring an overestimated lifetime of photooxidized dyes in the devices with a redox-inactive electrolyte at a low-light regime. Although not exactly picturing devices in working conditions, we use these data as an approximation of the charge-transfer dynamics.¹²⁵

2.2.5 Electrochemical Impedance Spectroscopy (EIS)

The V_{OC} trends of the devices with various dyes can be predicted by EIS analysis on complete devices in the dark. The Nyquist plots were fitted according to the transmission-line model developed by Bisquert et al., and the main parameters were extracted.^{52,126} They comprise the charge-transfer resistance, R_n , representing the charge recombination resistance for the electrons in the TiO₂ conduction band with the oxidized form of the redox couple, the chemical capacitance, C_μ , representing the density of states (*DOS*) accessible to electrons in the TiO₂ nanocrystals, and the transport resistance, R_{trans} , representing the resistance for the transport of the electrons through the mesoporous TiO₂ network. Using the obtained charge recombination (R_n) and transport (R_{trans}) resistances along with the chemical capacitance (C_μ) of the titania, one can calculate the electron lifetime (τ_n) and transport time (τ_{trans}) according to equations (12) and (13).

$$\tau_n = R_n \cdot C_\mu \quad (12)$$

$$\tau_{trans} = R_{trans} \cdot C_\mu \quad (13)$$

The main parameters from the EIS fitting of cobalt-based devices are shown in Figure 2.6. The cobalt-based devices showed pronounced changes in the conduction-band edge position. It is interesting to note that the highest chemical capacitance, and so the lowest conduction band, and the highest electron lifetimes were observed for **SA22**, followed by **SA285**, while the lowest values of the electron lifetime were obtained for **SA246** and **SA282**. The differences in V_{OC} due to the conduction-band shift and electron lifetime were estimated in reference to the values obtained with **SA22** and are presented in Table 2.2.

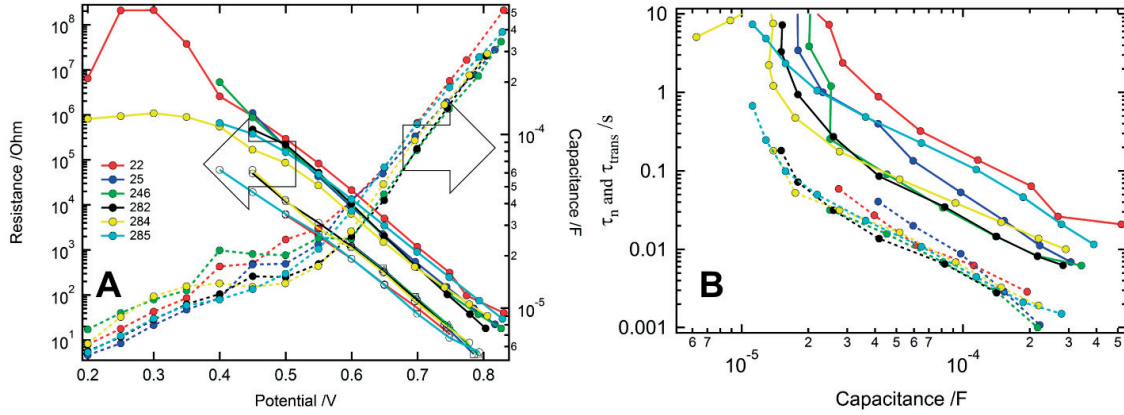


Figure 2.6. The key parameters extracted from EIS analyses of the cobalt-based devices: (A) recombination resistance (solid figures with solid lines); transport resistance (hollow figures with solid lines) and capacitance (solid figures with dashed lines) over potential; (B) the electron recombination lifetime (solid lines) and transport lifetime (dashed lines) as a function of capacitance. In all figures, lines with red, blue, green, black, yellow and cyan colors refer to the devices with SA22, SA25, SA246, SA282, SA284 and SA285 respectively.

Table 2.2. Comparison of the V_{OC} differences estimated from the EIS analyses and obtained from the J-V measurements for the cobalt-based electrolytes.

Dye	^a ΔE^{CB} [mV]	^b τ_n [s] / in parenthesis ΔV due to the changes in τ_n in respect to the τ_n for SA22 [mV]	^c Estimated $\Delta V_{OC} = \Delta E^{CB} + \Delta V$ (due to $\Delta\tau_n$)	^d ΔV_{OC} [mV]
SA22	0	0.180	-	0
SA25	24	0.052 (-32)	-8	-17
SA246	40	0.024 (-52)	-12	18
SA282	22	0.025 (-51)	-27	-33
SA284	23	0.035 (-43)	-20	-33
SA285	15	0.120 (-11)	4	-20

^aThe shift in the conduction band edge was estimated from the EIS analyses; ^bThe change in the voltage due to the change in electron lifetime was calculated using diode equation. ^cTotal estimated change in V_{OC} due to the conduction band edge difference and electron lifetime. ^dThe difference in V_{OC} obtained from the J-V measurements (*vide infra*). All values are brought in reference to the case with SA22. Positive values indicate the rise in V_{OC} .

2.2.6 Photovoltaic Performance

To evaluate the influence of ligands on the photovoltaic performance of ruthenium sensitizers, we put the complete devices with the cobalt-based electrolytes under photovoltaic characterization and present the results in Table 2.3 and Figure 2.7. In the case of the DSCs with cobalt-based electrolytes, both J_{SC} and V_{OC} vary significantly between 9 and 14 $\text{mA}\cdot\text{cm}^{-2}$ and 794 and 845 mV with the following trends: for J_{SC} , SA282 < SA25 < SA284 < SA285 < SA22 < SA246; for V_{OC} , SA282 = SA284 < SA285

< **SA25** < **SA22** < **SA246** (Figure 2.7 and Table 2.3). The sensitizer **SA246** showed the best *IPCE*, which is in agreement with the measured J_{SC} value and a record high performance for the ruthenium-cobalt system. Inconsistencies are found in both J_{SC} and V_{OC} , especially with **SA246**, which has relatively blue-shifted absorption spectrum and the lowest electron lifetime. An unexpected trend in the V_{OC} and J_{SC} values indicating some more vital parameters is controlling the photovoltaic performance.

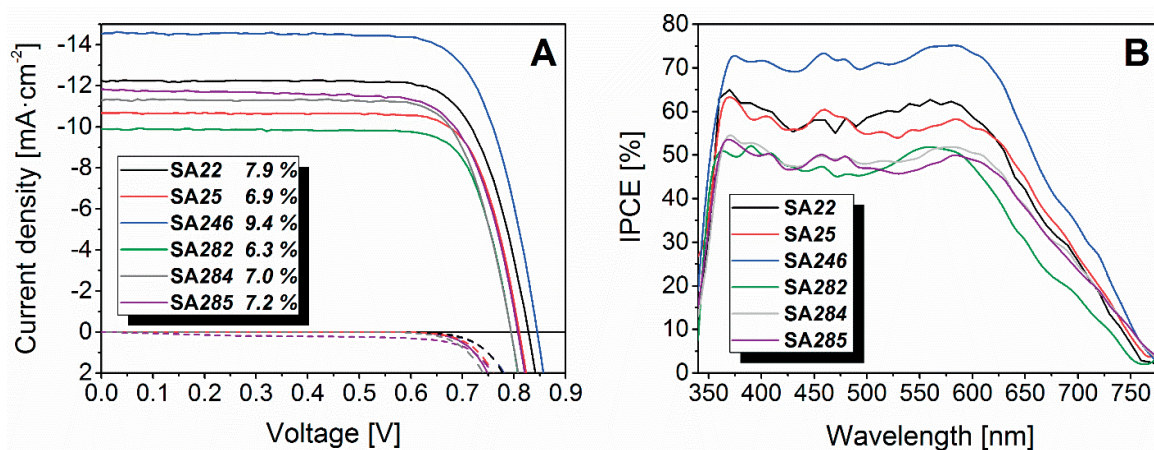


Figure 2.7. (a) J-V curves and (b) IPCE curves for DSCs based on cobalt electrolytes and cyclometalated ruthenium dyes SA22, SA25, SA246, SA282, SA284 and SA285.

Table 2.3. Photovoltaic Performance of Iodine and Cobalt Based DSCs with SA Dyes.

^[a] dye	Electrolyte	J_{SC} [mA/cm ²]	V_{OC} [mV]	<i>FF</i> [%]	<i>PCE</i> (0.1 Sun) [%]	<i>PCE</i> (1 Sun) [%]
SA22	^[b] [Co(phen) ₃] ^{3+/2+}	12.25	827	75.5	8.4	7.9
SA25	^[b] [Co(phen) ₃] ^{3+/2+}	10.68	810	77.9	7.4	6.9
SA246	^[b] [Co(phen) ₃] ^{3+/2+}	14.55	845	74.7	9.4	9.4
SA282	^[b] [Co(phen) ₃] ^{3+/2+}	9.89	794	78.5	6.7	6.3
SA284	^[b] [Co(phen) ₃] ^{3+/2+}	11.28	794	76.9	7.2	7.0
SA285	^[c] [Co(phen) ₃] ^{3+/2+}	11.85	807	73.6	6.1	7.2

^[a]All cells were measured under AM 1,5 simulated solar light irradiation with power 100 mW cm⁻² at room temperature; ^[b]Cobalt based electrolyte: 0.25 M [Co(II)(phen)₃](TFSI)₂, 0.05 M [Co(III)(phen)₃](TFSI)₃, 0.25 M 4-(5-nonyl)pyridine (NP) and 0.1 M LiTFSI; ^[c]Cobalt based electrolyte: 0.25 M [Co(II)(phen)₃](TFSI)₂, 0.05 M [Co(III)(phen)₃](TFSI)₃, 0.5 M 4-(5-nonyl)pyridine (NP) and 0.1 M LiTFSI.

Despite the indistinctive molar extinction coefficient and moderate absorption range, the high J_{SC} values for the devices with **SA246** over other sensitizers is a baffling result. To explain this result, we analyzed the amount of dye adsorbed on the surface. One way to evaluate the absolute dye loading is the desorption experiment of sensitized titania films (Figure 2.8). The amount of **SA246** adsorbed on titania is drastically higher in comparison to other dyes. It is worth noting that **SA285** also provides

high dye loading; however, because of inefficient dye regeneration (*vide supra*), **SA285** fails to yield high *PCEs*. The high dye-loading of **SA246** increases the absorbance (optical density) of the sensitized titania films, which, in turn, boosts the J_{SC} more than the other sensitizers with even higher molar extinction coefficients and a wider absorption spectra. This effect has already been indicated by the *IPCE* spectra (Figure 2.7(B)).

At the same time, it is quite unexpected that the device with **SA246** gave the highest V_{OC} even though it possesses the lowest electron lifetime and therefore the highest recombination. It is known that the long electron lifetime is necessary but not sufficient condition to lead to the high V_{OC} . We have to take the change in J_{SC} under light into consideration, which has been completely neglected in ESI analyses; e.g., the inversed correlation of the electron lifetime and V_{OC} in the case of **SA22** and **SA246** can be explained by the higher J_{SC} in the case of **SA246**. Higher J_{SC} will induce a higher steady-state electron density in titania in the performing device, which yields an upwardly shifted *quasi-Fermi level* $E_{F,n}^*$ and, hence, a higher V_{OC} . In this case, the rise in V_{OC} compensates for the loss due to high electron recombination rate.

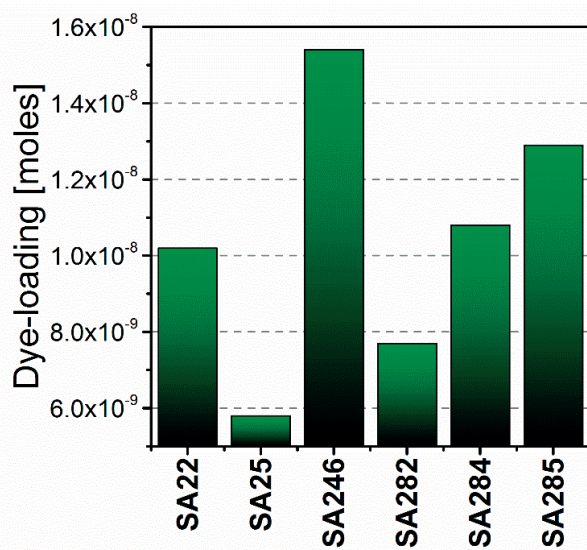


Figure 2.8. Dye-loading values obtained by desorption of SA dyes from the titania films.

2.3 Conclusion

Six new cyclometalated *tris*-heteroleptic ruthenium complexes were synthesized and characterized in the course of ligand engineering compatible with cobalt-based electrolytes in DSCs. The substituents on the auxiliary ligand were the focus of this study. Various substituents result in different photophysical properties and different performances in the DSCs. With the cobalt-based devices, the record efficiency to date featuring ruthenium-based dyes was obtained for **SA246** as 9.4%. The highest

efficiency is explained by the higher dye-loading, a factor that is normally neglected by the designers. The high absolute dye-loading increases the optical density, which can lead to a higher photocurrent and voltage. This effect can even overwhelm the influence of the recombination rate. Provided in this work, different analyses indicate the complexity of the processes taking place and underline the compromise between various parameters to be considered from the sensitizer-design viewpoint. For the cobalt-based devices, the sensitizer molecule should have small enough size to maintain (i) efficient dye regeneration and (ii) high dye loading and, at the same time, (iii) a bulky periphery to keep the redox mediator away from the semiconductor surface. These results could be very instructive for further dye engineering to reach even higher *PCEs*.

Chapter 3 Cyclometalated Ruthenium Sensitizers with Arylamine Donors

This chapter is based on the following published article:

Sadig Aghazada, Yameng Ren, Peng Wang, Mohammad Khaja Nazeeruddin, *Inorg. Chem.*, DOI: 10.1021/acs.inorgchem.7b02164

In this work I have designed, synthesized and characterized all the compounds. Dr. Yameng Ren fabricated and characterized solar cells. I have analysed all the results and wrote the article. Drs. Peng Wang and Mohammad Khaja Nazeeruddin supervised the process.

Three new *tris*-heteroleptic complexes of ruthenium (II) were designed by coordinating the metal center with cyclometalating, anchoring, and auxiliary ligands with different donor substituents. N-Hexylcarbazole, N-hexylphenothiazine, and N-hexyldiphenylamine donor moieties were used as substituents on the auxiliary ligands for **SA633**, **SA634**, and **SA635**, respectively. Complexes were characterized by ^1H , ^{13}C , and 2D-COSY NMR techniques. These complexes provide power conversion efficiencies in the range of 7.6–8.2 % when they are employed in state-of-the-art dye-sensitized solar cells (DSCs) with cobalt electrolyte. Various electrochemical and transient techniques were used to unveil the unexpected differences in the performance of these very similar sensitizers

3.1 Introduction

To understand the main structural characteristics of ruthenium sensitizers that limit the *PCEs* in DSCs with cobalt-based electrolyte, we have designed three new *tris*-heteroleptic cyclometalated ruthenium(II) complexes with various aromatic moieties of different electron-releasing power (Figure 3.1). The choice of donor groups was also limited to a few groups with very similar structures to level off the effect of different dye loadings on the performance of solar cells. Ruthenium complexes bearing different amine-based aromatic substituents have been studied in DSCs, but these complexes were usually based on NCS and were always investigated with iodine-based electrolytes. Many works have investigated the “antenna” effect of donor groups and the role of hole extraction in solar cell performance.^{66,73,127–130}

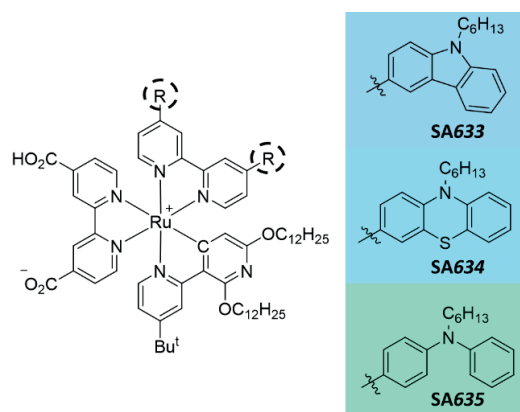
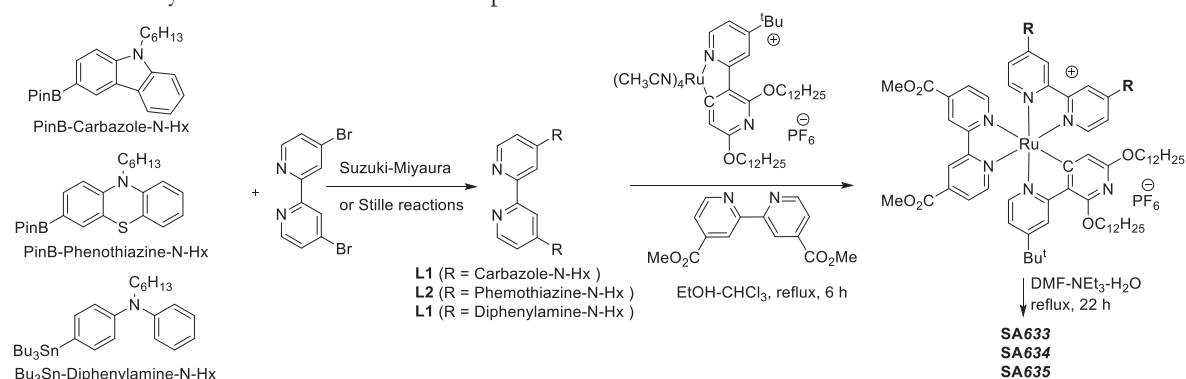


Figure 3.1. Sensitizers introduced in this chapter.

3.2 Results and Discussion

Scheme 3.1 illustrates the synthesis of the complexes. First, the cyclometalating ligand was synthesized in a way similar to published methods.^{93,131} The ancillary ligands were synthesized by Stille or Suzuki–Miyaura coupling of the tributyltin or boronic ester adducts of the donor groups with 4,4'-dibromo-2,2'-bipyridine. The *tris*-heteroleptic complexes were synthesized in three steps. First, cyclometalation was carried out with $[\text{Ru}(\text{C}_6\text{H}_6)\text{Cl}_2]_2$, and $[\text{Ru}(\text{C}^{\wedge}\text{N})(\text{CH}_3\text{CN})_4](\text{PF}_6)$ was obtained.^{87,90,132} This complex was reacted with a 1:1 mixture of ancillary (bpyR_2) and 4,4'-dimethoxycarbonyl-2,2'-bipyridine ($\text{bpy}(\text{CO}_2\text{Me})_2$), which resulted in three compounds (two *bis*-heteroleptic and one *tris*-heteroleptic).^{91,92} The *tris*-heteroleptic product was separated by column chromatography and hydrolyzed to obtain the final sensitizer. It is worth noting that neutral complexes with one deprotonated carboxylic acid group were obtained. All of the products were characterized by means of ^1H , ^{13}C , ^{31}P , and COSY NMR, and all the results are provided in the Appendix (check section 8.2).

Scheme 3.1. Synthesis of Ruthenium Complexes



The absorption spectra of the sensitizers in DCM show four apparent bands in the visible region of the solar spectrum, which could all be related to different metal-to-ligand charge transfer (MLCT) transitions (Figure 3.2(A)). The band of the lowest energy for all three sensitizers is broad and extends up to 750 nm. From **SA633** to **SA634** and **SA635**, there is a small bathochromic shift of the lowest intense energy band from 572 nm to 578 and 579 nm. Moreover, the extinction coefficient of this band changes from $21.2 \times 10^3 \text{ M}^{-1}\text{cm}^{-1}$ to 23.9×10^3 and $22.3 \times 10^3 \text{ M}^{-1}\text{cm}^{-1}$ (Table 3.1). Around 400 nm, the bands for **SA633** and **SA634** have intensities of around $36 \times 10^3 \text{ M}^{-1}\text{cm}^{-1}$, but **SA635** has the most intense band with an extinction coefficient of $51.1 \times 10^3 \text{ M}^{-1}\text{cm}^{-1}$. Moreover, from **SA633** to **SA635** and **SA634**, there is a strong red shift of this band, with no clear reason behind it. Thus, these sensitizers almost completely cover the whole visible spectrum owing to the broad nature of the MLCT bands, which should lead to high light-harvesting efficiency.

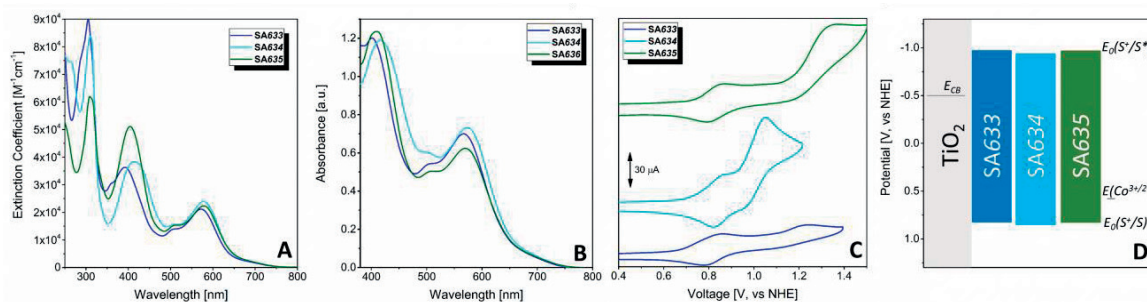


Figure 3.2. (A) Absorption spectra of **SA633**, **SA634**, and **SA635** solutions in DCM. (B) Absorption spectra of sensitized mesoporous titania films (4 μm thick). (C) Cyclic voltammograms of sensitizers measured in 0.1 M DMF solution of (NBu₄)(PF₆). Ferrocene was used as an internal standard, and its oxidation potential was located at 0.63 V *vs* NHE. The cyclic voltammograms without ferrocene are presented. (D) Energy diagram of **SA633**, **SA634**, and **SA635** sensitizers in DSCs using [Co(phen)₃]^{3+/2+} as a redox mediator. The excited-state oxidation potentials for all three sensitizers were obtained by extracting the E_{0-0}/e value from the ground-state oxidation potential

Table 3.1. Photophysical and Electrochemical Data for **SA633**, **SA634**, and **SA635**.

	λ_{max}^{abs} [nm] ($\epsilon \cdot 10^{-3}$ [M ⁻¹ cm ⁻¹])	λ_{max}^{PL} [nm] ^[a]	E_{0-0} [eV] ^[b]	$E_0^{S+/S}$ [V <i>vs</i> NHE], ($V_A - V_C$ [mV]) ^[c]	E_0^{S+/S^*} [V <i>vs</i> NHE] ^[d]
SA633	572 (21.2)	622	1.79	0.82, (69)	-0.97
SA634	578 (23.9)	630	1.78	0.85, (66) and 1.0, (100)	-0.93
SA635	579 (22.3)	625	1.80	0.82, (79)	-0.97

^[a]Measured in 10⁻⁵ DCM solution. ^[b]Determined from the intersection of normalized emission and absorption spectra. ^[c]Were determined from the CV measurements in 0.1 M NBu₄PF₆ solution in DMF under argon atmosphere. Ferrocene was used as an internal standard and its oxidation potential was fixed at 0.62 V *vs* NHE. The shift between the anodic and cathodic wave maximums is shown in brackets. ^[d]Excited-state oxidation potential is determined by extracting the E_{0-0}/e value from the ground-state oxidation potential.

From the photoluminescence measurements in DCM, a weak emission for all three complexes was detected with maximum values occurring at 622, 630, and 625 nm for **SA633**, **SA634**, and **SA635**, respectively (Figure 3.3). E_{0-0} values in the range of 1.78–1.80 eV were determined from the intersection of the normalized absorption and emission spectra.

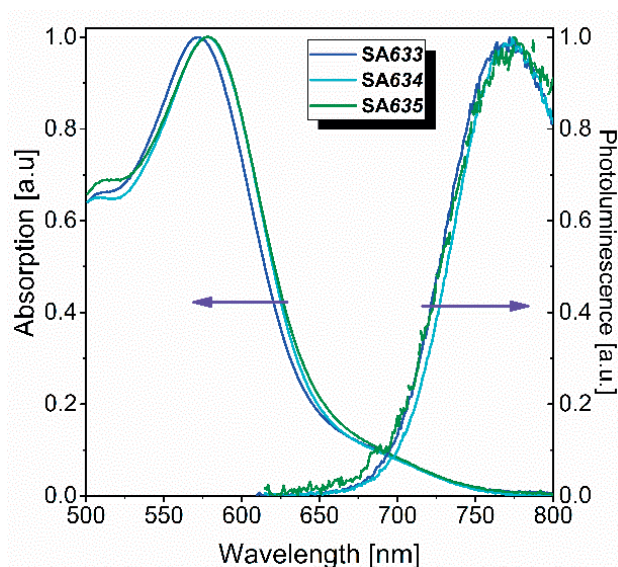


Figure 3.3. Normalized absorption and emission spectra of sensitizers in DCM.

The cyclic voltammograms of the new sensitizers were obtained in a 0.1 M NBu_4PF_6 solution in DMF under an argon atmosphere. Analogous measurements in DCM were unsuccessful (Figure 3.2(C)). Ferrocene was used as an internal standard, and its oxidation potential was fixed at 0.63 V vs NHE. In the electrochemical window of DMF, all three sensitizers show two oxidations. The first oxidation potentials for **SA633**, **SA634**, and **SA635** were found at 0.82, 0.85, and 0.83 V *vs* NHE respectively. Considering the very small dependence of the values on the substituents on the auxiliary ligand, the first oxidation for all three sensitizers was attributed to the $\text{Ru}^{3+/2+}$ redox reaction.

The second oxidation for **SA634** with the phenothiazine substituent was observed at 1.0 V *vs* NHE, while for **SA633** and **SA635**, the second oxidation potentials were not determined due to irreversibility. However, the anodic waves appear at potentials higher than that for **SA634** (1.22 and 1.36 V *vs* NHE for **SA633** and **SA635**). The second oxidation of the sensitizer was attributed to the possible oxidation of donor moieties at the ancillary ligand. Considering their more positive value, we do not expect any efficient charge extraction from the metal center after photo-oxidation, except partially in **SA634**. More electron-donating moieties should be attached to enable efficient hole extraction toward the periphery of a ligand.¹²⁹

We have conducted DFT calculations to support our referencing of the first and second oxidation waves to ruthenium and ligand oxidations, respectively (check the appendix, section 8.2.2). As shown in Figure 8.73, the HOMO, HOMO-1, and HOMO-2 for **SA633** and **SA635** generally have Ru t_2 orbital character (considering the ideal octahedral coordination) with little composition on the cyclometalated ligand. Additionally, HOMO-2 for **SA635** has little composition from the diphenylamine substituents. In contrast to **SA633** and **SA635**, all three of the uppermost occupied orbitals of **SA634** have a significant contribution from the phenothiazine substituents. This contribution is highest for the HOMO-1, which is the result of the stronger donating character of the phenothiazine moiety in comparison to that for carbazole and diphenylamine. However, as shown in the cyclic voltammograms, higher π -donating character of phenothiazine moieties does not push the Ru^{3+/2+} redox potential toward more negative values.

Generally, the oxidation potential of Ru^{3+/2+} redox for these three sensitizers does not depend on the π -electron-releasing power of the donor moieties, which is due to the twisting between the donor moiety and bipyridine planes resulting in no conjugation between them. The excited-state oxidation potentials were determined according to equation (14) from the obtained ground-state oxidation potentials and E_{0-0} values. The excited-state oxidation potentials for all three dyes were found between -0.93 and -0.97 V *vs* NHE. These values are ~ 400 mV more negative than the conduction band edge for the mesoporous titania used in conventional DSCs and should provide enough driving force for efficient charge injection from the photoexcited sensitizer into the conduction band of titania (Figure 3.2(D)).

$$E_0^{S^+/S^*} = E_0^{S^+/S} - E_{0-0}/e \quad (14)$$

One of the main requirements for the sensitizers in DSCs is stability toward the redox processes, and they should not degrade when they are photo-oxidized. This implies that their oxidation should be perfectly reversible. Irreversible photooxidation is a disadvantage of NCS-ligated ruthenium sensitizers, which undergo ligand substitution.⁶⁹⁻⁷¹ In previous work, we showed that cyclometalating complexes also suffer from redox irreversibility, but this was generally attributed to the degradation of polyaromatic moieties attached to the ancillary ligand.¹³¹

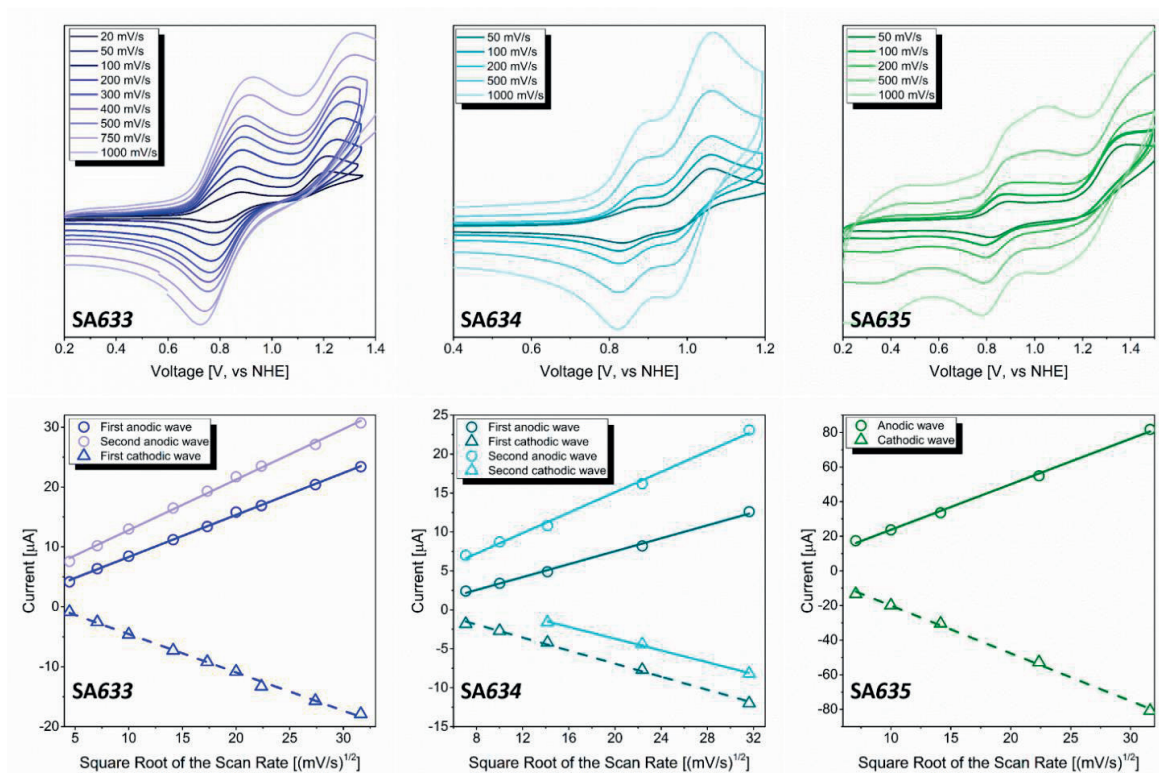


Figure 3.4. Cyclic voltammograms of SA633, SA634, and SA635 at different scan rates in 0.1 M NBu₄PF₆ solution in DMF and Randles–Sevcik analyses showing a linear change of maximum current value over square root of the scan rate.

We have conducted Randles–Sevcik analyses to analyse the redox reversibility of new sensitizers.¹³³ The Randles–Sevcik equation defined at room temperature in equation (15),

$$i_p = 268715n^{3/2}AC(D\nu)^{1/2} \quad (15)$$

where i_p is the current at the wave maximum, A is the electrode area, C is the concentration of the component undergoing redox, D is the diffusion constant of the studied molecule, n is the number of electrons transferred in one redox event, and ν is the scan rate. According to this equation, there should be a linear rise in the current maximum for the reversible redox when it is plotted vs the square root of the scan rate. For **SA634**, the Randles–Sevcik analysis showed perfect reversibility for both oxidation waves, which we related to the oxidation of the ruthenium and one phenothiazine substituent (Figure 3.4). Perfect reversibility is also observed for the oxidation of Ru in **SA633**. However, a definitive conclusion cannot be obtained for the second oxidation, due to the shape of the anodic wave and undeveloped cathodic wave, as well as the perfect linear rise of the maximum current over the square root of the scan rate for the anodic wave. For **SA635**, although Randles–Sevcik analysis shows a linear dependence, the shape of the voltammogram changes drastically when it is measured at different scan rates.

To unravel the ambiguous results from the solution CV analysis, the Randles–Sevcik analysis was conducted for the sensitized mesoporous titania films in 1-ethyl-3-methylimidazolium *bis*(trifluoromethylsulfonyl)imide. In this experiment, perfect reversibility was observed for **SA635**. For **SA633** and **SA634**, the results are not completely clear (Figure 3.5). Thus, considering the general inconsistencies between changing shapes of voltammograms and results of Randles-Sevcik analyses, we avoid decisive conclusion.

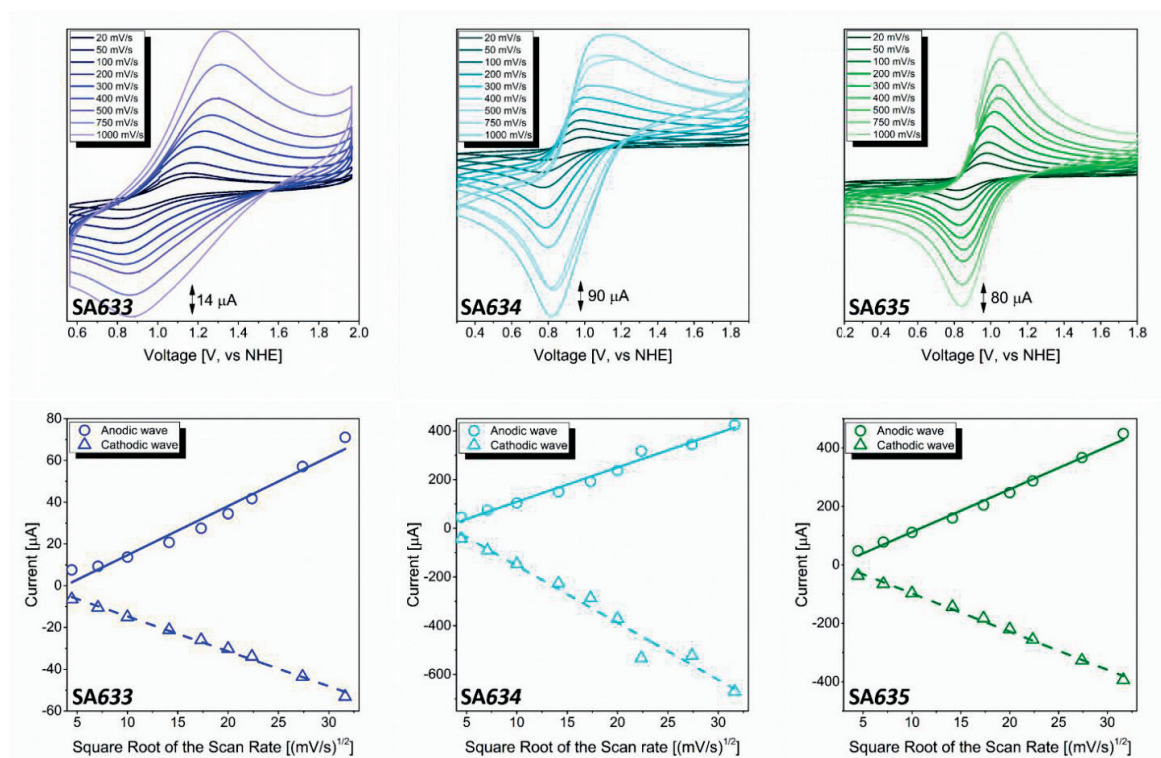


Figure 3.5. Cyclic voltammograms of SA633, SA634, and SA635 sensitized titania films on ITO covered glass at different scan rates in a neat 1-Ethyl-3-methylimidazolium *bis*(trifluoromethylsulfonyl)imide and Randles-Sevcik analyses showing a linear change of maximum current value over square root of the scan rate.

Additionally, in a perfectly reversible redox, the anodic and cathodic currents should have comparable values. For these sensitizers, the comparison of the values of anodic and cathodic waves is difficult due to the overlap of the first and second anodic waves. To show whether these sensitizers are stable in the oxidized state and may quantitatively regenerate, we have conducted spectroelectrochemical analyses in 0.1 M NBu_4PF_6 solution in DMF under an ambient atmosphere (Figure 3.6). After each voltage step was applied for 60 s, the absorption spectra were measured in the following 5 s. For all of the sensitizers, increasing the potential results in reduction of the MLCT band around 575 nm and in the formation of a new absorption band in the IR region. In this process, the high energy bands also change their shapes and positions.

The spectra measured at high voltages do not show the gradual changes and do not cross the isosbestic points formed by the spectra that were observed when more negative voltages are applied. This is the result of partial second oxidation, which presumably leads to a slow degradation of the complex. In the backward run, the MLCT bands for **SA634** and **SA635** recovered completely, while just $\sim 90\%$ was recovered for **SA633**. Moreover, the initial shapes of the spectra were also recovered, with a red shift of $\sim 5\text{--}10\text{ nm}$ of the recovered lowest energy MLCT band.

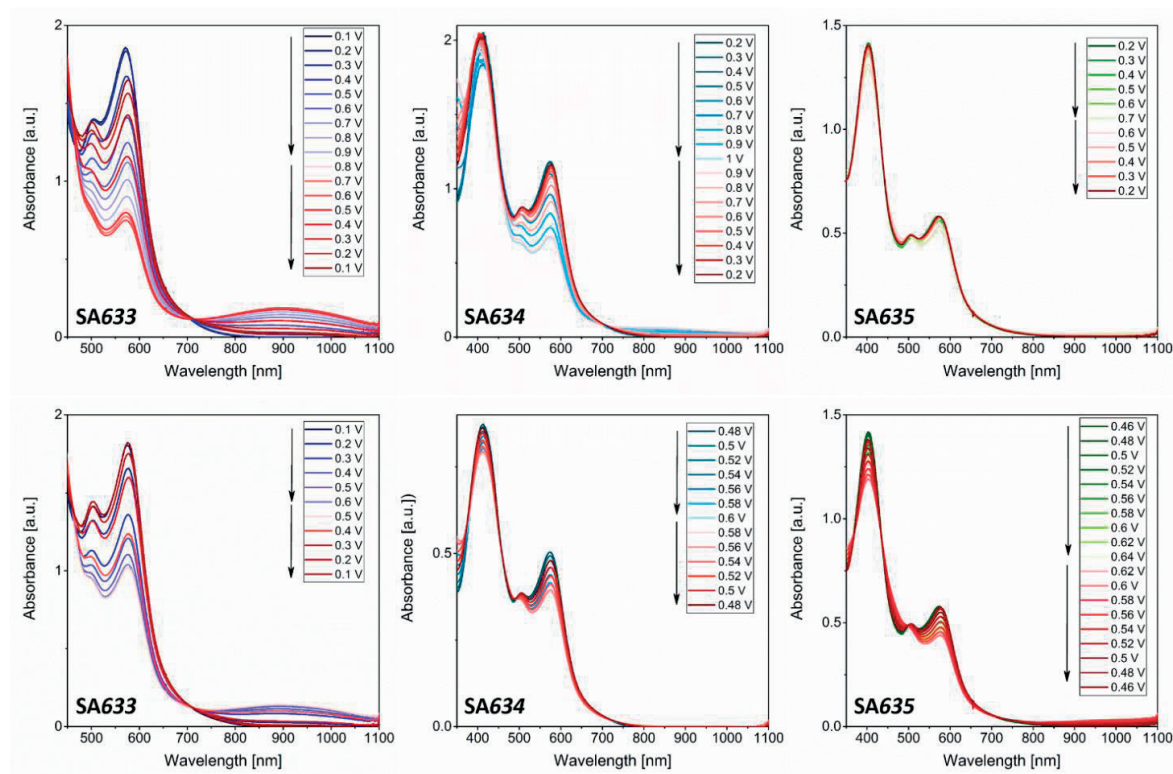


Figure 3.6. Spectroelectrochemical analyses of **SA633**, **SA634**, and **SA635** in 0.1 M solution of NBu_4PF_6 in DMF. No preliminary deoxygenation was carried out. The absorption spectra were measured after applying each voltage step for 60 s. The top three graphs show the destructive effect of the second oxidation. The bottom three graphs show perfect reversibility for the single oxidation of sensitizers.

The destroyed isosbestic points and the small red shift of the MLCT bands indicate that, at high voltages, the oxidation of donor moieties on the ancillary ligands leads to structural changes where the coordination core is saved. When the spectroelectrochemical analyses were carried out at a less positive voltages to avoid the second oxidation, clean isosbestic points were obtained with a full recovery of the initial spectra at the opposite voltage run. This further supports that the first oxidation is fully reversible and that the second oxidation is detrimental. Moreover, the attached instability undermines the direction of research on the design of new ruthenium complexes mostly comprising the attachment of various substituents on one of the bipyridine ligands.⁶⁷ This work shows that substituents on derivatives

of diphenylamine should play a negative role in the long-term sensitizer performance. This was also observed in our previous work on complexes with substituents based on thiophene. However, only a single oxidation is taking place in a DSC and the photooxidized dye is in a reducing environment. Thus, this destructive pathway should not influence the *PCE* in the short term.

DSCs were assembled using **SA633**, **SA634**, and **SA635** as sensitizers. The working electrode was fluorine-doped tin oxide with a 4.5 μm layer of transparent titania and an additional 5 μm scattering layer on top. Films were sensitized in dye solutions of similar concentration of 0.2 mM. The $[\text{Co}(\text{phen})_3]^{3+/2+}$ redox couple was used as a mediator with a 1:4 molar ratio of 3+ to 2+ species. Photocurrent density–photovoltage (J – V) curves were obtained under AM 1.5 G irradiation of devices with an active area of 0.16 cm^2 (Figure 5(A)), and all of the measured parameters are summarized in Table 3.2.

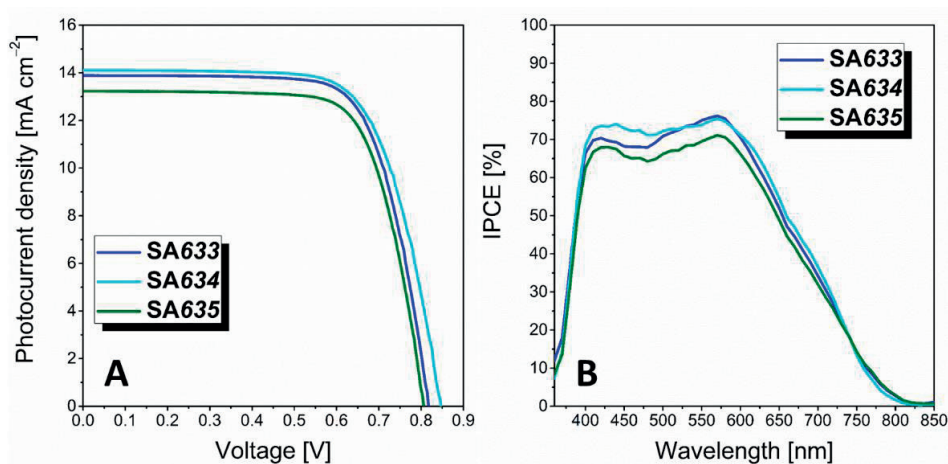


Figure 3.7. (A) Current density–voltage (J – V) curves recorded under simulated AM 1.5 G sunlight (100 mW cm^{-2}). The aperture area of the black metal mask was 0.16 cm^2 . Antireflection film was used on the back of the counter electrode. (B) Incident photon to current conversion efficiency (*IPCE*) at a set of wavelengths (λ) of incident monochromatic lights. The measurements were carried out at intervals of 10 nm for incident monochromatic light under a constant white light bias (10 mW cm^{-2}). Antireflection film was used on the back of the counter electrode

Table 3.2. Photovoltaic Parameters of Four Cells Measured Under Simulated AM 1.5 G Sunlight (100 mW cm^{-2}).

	J_{SC}^{IPCE} [mA cm^{-2}] ^[a]	J_{SC} [mA cm^{-2}]	V_{OC} [mV]	<i>FF</i> [%]	<i>PCE</i> [%]
SA633	13.70 ± 0.05	13.68 ± 0.04	819 ± 2	71.5 ± 0.2	8.0 ± 0.1
SA634	13.91 ± 0.04	13.89 ± 0.03	845 ± 2	70.0 ± 0.1	8.2 ± 0.1
SA635	13.06 ± 0.04	13.03 ± 0.03	809 ± 2	72.1 ± 0.1	7.6 ± 0.2

^[a] J_{SC}^{IPCE} was computed via wavelength integration of the product of the *IPCE* curve measured at the short circuit and the standard AM1.5G emission spectrum (ASTM G173-03).

The J_{sc} value increases from 13.03 mA cm^{-2} for **SA635** to 13.68 and 13.89 mA cm^{-2} for **SA633** and **SA634**, respectively. The V_{oc} value rises in the same order from 809 to 819 and 845 mV . With small differences in the fill factor, **SA633**, **SA634**, and **SA635** provide $PCEs$ of 8.0 , 8.2 , and 7.6% . The incident photon-to-current conversion efficiency ($IPCE$) results are presented in Figure 3.6(B). We obtained the short-circuit currents by integrating the product of the $IPCE$ curve with the AM 1.5 G solar spectrum, and the results are in agreement with the values obtained from the $J-V$ measurements. In comparison to the absorption spectra, the $IPCE$ spectra have a red-shifted onset to 820 nm . The $IPCE$ spectra also indicate that the higher $IPCE$ values in the range of 420 and 620 nm are responsible for the higher photocurrent of the devices with **SA634** and **SA633** in comparison with that for **SA635**.

To understand the reasons behind the obtained photocurrents and voltages, we have measured the charge extraction (CE)¹³⁴ and transient photovoltage decay (TPD)¹³⁵ of the final devices (Figure 6). The charge extraction measurements for all three sensitizers show the same profile over the voltage range, which indicates that the distribution of trap states within the band gap does not depend on the sensitizer used (Figure 3.8(A)). The similar distribution of trap states also indicates that the adsorption modes of these three sensitizers are somehow similar. Moreover, the position of the conduction band edge (E_{CB}) should be similar for all the devices, and thus, the change in V_{oc} should not be due to the variations in the E_{CB} position.

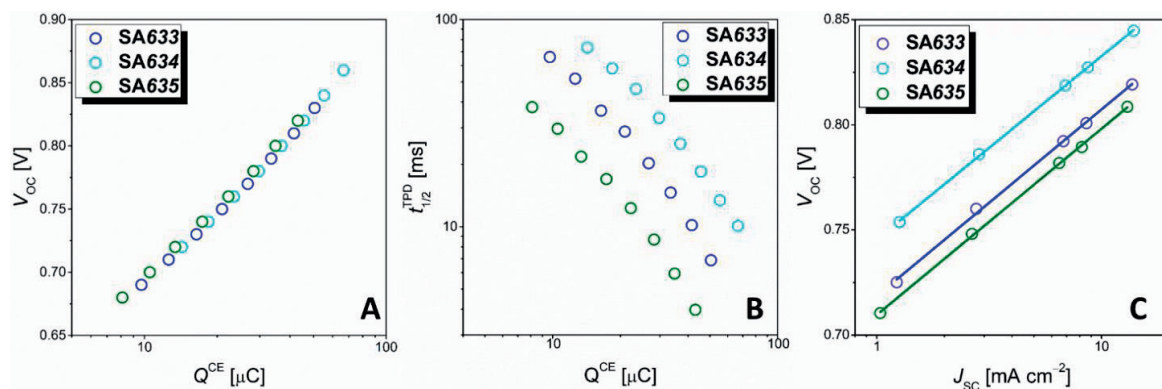


Figure 3.8. (A) Charge extracted from a dye-grafted titania film (Q^{CE}) as a function of open-circuit photovoltage (V_{oc}). (B) Plots of half-lifetime ($t_{1/2}^{TPD}$) of electrons in the conduction band and traps under the conduction band of titania vs Q^{CE} . (C) Dependence of open-circuit photovoltage (V_{oc}) on short-circuit photocurrent density (J_{sc}). The solid lines are displayed as a visual aid.

TPD measurements of the devices with these three dyes reveal very different electron lifetimes at similar capacitances. Solar cells with **SA635** show the poorest electron lifetime, while for devices with **SA633** and **SA634**, the electron lifetimes are nearly 2 and 4 times longer than that with **SA635** at the same capacitance (Figure 3.8(B)). Thus, the difference in open-circuit voltage could result from two components. First, the current induced an increase in V_{oc} . Second, the different electron lifetimes lead

to different steady-state concentrations of electrons in trap states and thus different values of Fermi energy.

Equation (16) can be used to calculate the current-induced buildup in V_{oc} , which is the result of the diode equation,

$$V_{oc}(2) - V_{oc}(1) = \frac{k_B T m}{q} \log \frac{J_{sc}(2)}{J_{sc}(1)} \quad (16)$$

where k_B , T , q , and m are the Boltzmann constant, temperature, electron charge, and nonideality factor, respectively. This equation indicates that at room temperature the V_{oc} value in the ideal case ($m = 1$) should increase by 59 mV when J_{sc} is increased by 10 times.

The $J-V$ curves were measured at different light intensities obtained using various meshes. The linear fit results in rise of *ca.* 87 mV in V_{oc} when J_{sc} increases 10 times for all sensitizers (Figure 3.8(C)). From this result, we can use equation (16) to calculate the gain in V_{oc} for the solar cells with **SA633** and **SA635** in reference to that for **SA635** due to higher photocurrents with former two sensitizers. A current-favored buildup in the photovoltage occurred below 3 mV.

Equation (17) can be used to calculate the change in V_{oc} due to different electron recombination lifetimes. The calculated change in V_{oc} was substantial and was in good agreement with the values obtained from $J-V$ measurements (Table 3.3). This indicates that the processes discussed above completely explain the difference in the obtained voltages and PCEs.

$$V_{oc}(2) - V_{oc}(1) = \frac{k_B T m}{q} \log \frac{t_{1/2}^{TPD}(2)}{t_{1/2}^{TPD}(1)} \quad (17)$$

Table 3.3. Comparison of Calculated Differences in V_{oc} Due to Different Short-Circuit Current Densities and Electron Recombination Lifetimes with the Differences in V_{oc} from the $J-V$ Measurements.^[a]

	ΔV_{oc} (photocurrent) [mV]	ΔV_{oc} (electron lifetime) [mV]	ΔV_{oc} (total) [mV]	ΔV_{oc} (from $J-V$) [mV]
SA633	~2	~14	~16	10
SA634	~2.5	~24	~26.5	37
SA635				

^[a]Values for devices with SA633 and SA635 are referenced vs values for a device with SA635.

All three sensitizers have very similar spectral, electrochemical, and structural characteristics: (a) absorption spectra with negligible variations in extinction coefficients, (b) position of ground and excited oxidation potentials, and (a) structures with tiny variations. Therefore, these sensitizers are expected

to provide the same *PCEs* in DSCs, which is not the case. By comparison of the absorption spectra of sensitized films (Figure 3.2(B)) we may judge the relative dye loading. By dividing the intensity of MLCT bands from the spectra of sensitized films by the extinction coefficients of these bands in solution, we approximate that the amounts of **SA634** and **SA633** loaded on the titania are 10 and 18 % more than the amount of loaded **SA635**. Increased dye loading may result in better protection of the surface and thus in greater electron lifetimes. In this case, the dye-loading factor may explain the higher electron lifetime in devices with **SA633** than with **SA635**, but why **SA634** would provide an even higher electron lifetime is still an open question.

3.3 Conclusion

Three new cyclometalated *tris*-heteroleptic ruthenium sensitizers with different donor substituents were synthesized and characterized. All of these sensitizers showed reversible metal oxidation and irreversible ligand oxidation as a result of slow degradation. DSCs employing these sensitizers together with $[\text{Co}(\text{phen})_3]^{3+/2+}$ -based electrolyte provide good *PCEs* of up to 8.2 % under AM 1.5 G irradiation. Among these sensitizers, **SA634** with a phenothiazine substitution resulted in the best performance, while **SA635** with a diphenylamine group provided the lowest performance. The difference in the performance of these sensitizers in DSCs is generally attributed to the different electron lifetimes.

Chapter 4 Unraveling the Dual Character of Sulfur Atoms on Sensitizers in Dye-Sensitized Solar Cells

This chapter is based on the following published work:

Sadig Aghazada, Peng Gao, Aswani Yella, Thomas Moehl, Joël Teuscher, Jacques-E. Moser, Michael Grätzel, Mohammad Khaja Nazeeruddin, *ACS Appl. Mater. Interfaces*, **2016**, *8*, 26827-26833, DOI: 10.1021/acsami.6b08882

In this work, I have designed the experiments. Dr. Aswani Yella fabricated devices, Dr. Thomas Moehl measured electrochemical impedance, and Dr. Joël Teuscher conducted laser measurements. Drs. Jacques-E. Moser, Michael Grätzel and Mohammad Khaja Nazeeruddin supervised the process.

Cyclometalated ruthenium sensitizers have been synthesized that differ with number of thiophene units on the auxiliary ligands. Sensitizers possessing four (**SA25**, **SA246**, and **SA285**) or none (**SA282**) sulfur atoms in their structures, were tested in solar cell devices employing I_3^-/I^- redox mediator, enabling an estimation of the influence of sulfur–iodine/iodide interactions on dye-sensitized solar cell (DSC) performance. Power conversion efficiencies over 6% under simulated AM 1.5 illumination (1 Sun) were achieved with all the sensitizers. Consistently higher open-circuit voltage (V_{oc}) and fill factor (FF) values were measured using **SA282**. Scrutinizing the DSCs with these dyes by transient absorption spectroscopy (TAS) and electrochemical impedance spectroscopy (EIS) indicate that sulfur atom induced recombination cancels favorable increased regeneration, resulting in decreased power conversion efficiencies ($PCEs$). The data indicate that, to reduce charge recombination channels, if possible, the use of sulfur containing aromatic rings should be avoided in the dye structure when I_3^-/I^- redox mediator is used.

4.1 Introduction

Processes taking place on different parts of DSCs were extensively studied.³¹ Among the pertinent problems, electron–hole recombination on the working electrode remains the main factor limiting the power conversion efficiency.⁵¹ The charge recombination may take place with two electron sinks: photooxidized sensitizer and the oxidized component of a redox mediator.³⁰ Among these two, the recombination of the conduction band and trap state electrons with the oxidized redox component is

more devastating.¹³⁶ In the DSCs, employing cobalt(III/II) redox mediator in the electrolyte, the strategy to diminish charge recombination is that sensitizers are endowed with bulky alkyl chains to keep cobalt(3+) ions away from the surface.^{93,117,137–141} However, there is no such a universal rule for the DSCs employing I_3^-/I^- mediator, making it hard to foresee the sensitizer's ability to prevent recombination. In the sensitizer design one would greatly benefit from any rule of thumb about how the sensitizer structure affects the recombination rate.

Many works have shown that the sulfur atoms in a dye structure prone to induce dye–iodine interaction, which increases iodine concentration in the vicinity of mesoporous oxide resulting in a higher recombination.^{142–146} Using TG6 and K19 ruthenium based sensitizers (Figure 4.1), which have sulfur and oxygen atoms on the ancillary bipyridine ligand respectively, O'Regan et al. studied the change in the open-circuit voltage (V_{oc}) in the DSCs. The DSC with TG6 exhibited 20 mV lower V_{oc} than the DSC with K19.¹⁴⁷ With all the rest of the parameters identical, this result was solely related to the 2.3 times lower recombination lifetime in the case of TG6. The same effect was shown to take place for the donor (D)– π –acceptor (A) organic dyes, where additional thiophene (T3 in comparison to T1 in Figure 4.1) moiety in the π -bridge results in V_{oc} reduction.^{148–150} Calculations indicate that iodine molecules preferentially bind to the sulfur atoms in the thiophenes. On the other hand, Robson et al. established that substituting oxygen in the hexyloxy groups on the donor part of sensitizer (Dye-O) to the sulfur (Dye-S) (Figure 4.1) results in increased *PCE*, due to an increase in V_{oc} of 64 mV.¹⁵¹ This is understood by faster regeneration in the case of Dye-S and no substantial difference in recombination rates between Dye-S and Dye-O. Moreover, recently, the role of halogen bonding in increased dye regeneration rate was also established.¹⁵²

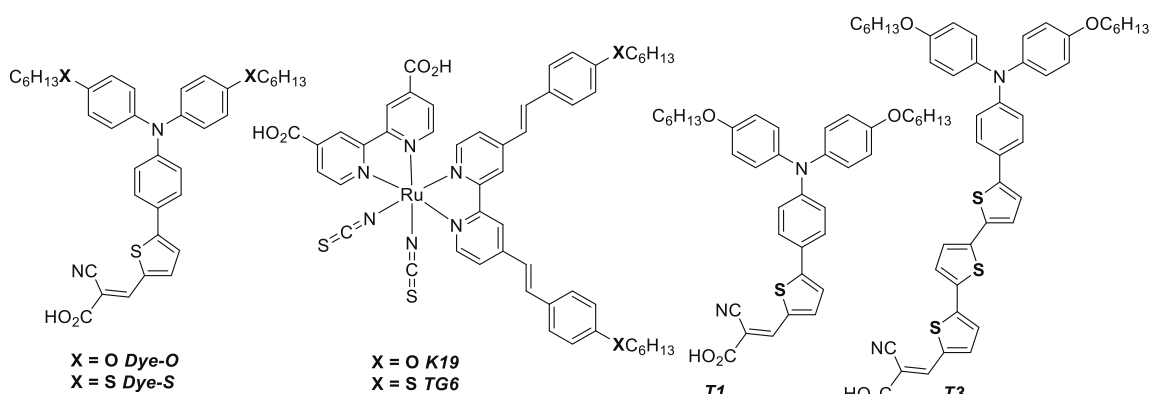


Figure 4.1. Molecular structures of some ruthenium isothiocyanate complexes and D- π -A organic molecules studied in literature.

4.2 Result and Discussion

Thiophene and other sulfur-containing aromatic and polyaromatic rings enable wide-range tuning of spectral and electrochemical properties of a material.^{100,153} It is not surprising that the majority of sensitizers possess one or more sulfur containing aromatics. Considering the role of sulfur atoms in initiating both favorable regeneration and unfavorable recombination processes, predictions on whether addition of a sulfur atom into the structure will increase or decrease V_{OC} are hard to make. To address this issue, we developed four ruthenium sensitizers and assembled DSCs (Figure 4.2). All four sensitizers possess similar cyclometalating and anchoring ligands, but different ancillary ligands. Polyaromatic moieties on the bases of cyclopentadienedithiophene (**SA25**, **SA285**), thienothiophene (**SA246**), and fluorene (**SA282**) were attached to the corresponding ancillary ligands. One of the sensitizers has no sulfur atom in its structure, and the rest possess four sulfur atoms, making a reasonable comparison (more details in section 2.2).

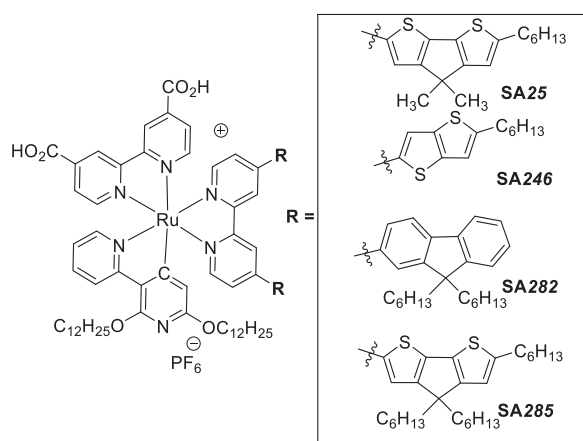


Figure 4.2. Molecular structures of cyclometalated ruthenium(II) complexes employed as sensitizers in DSCs in this work.

To relate the V_{OC} change solely to the role of sulfur atoms, we have to first exclude other possible causes. Generally, the V_{OC} is a difference between the *quasi*-Fermi energy level ($^*E_{F,n}$) for electrons in mesoporous oxide (TiO_2) and the oxidation potential of the redox couple.³² Trap and conduction band state distributions are important factors determining the steady-state concentration of electrons and thus the $^*E_{F,n}$. Since V_{OC} is achieved when the flux of injected electrons is equal to the flux of recombined electrons, for a reasonable comparison, the electron recombination flux should follow the same kinetics. In our discussion we need to consider these points.

Optical and electrochemical properties of SA sensitizers supported with quantum-mechanical calculations are thoroughly discussed in 2.2.2 and summarized in Figure 4.3.¹³¹ The absorption spectra red shift in the order **SA282** < **SA246** < **SA284** < **SA285** (Figure 4.3(A)). Oxidation potentials for the

series vary around 0.9 V *versus* normal hydrogen electrode (NHE), which should guarantee an analogous regeneration mechanism with iodide. From the E_{0-0} values, the estimated excited state oxidation potentials are negative enough to guarantee an efficient excited electron injection (Figure 4.3(B)). It is worth mentioning that according to density functional theory (DFT) calculations, the highest occupied molecular orbital (HOMO) is localized purely on the Ru t_2 orbitals only for **SA282**. For **SA246** the HOMO is distributed also over one side of the ancillary ligand, while for **SA25** and **SA285** it is distributed over both sides. The lowest unoccupied molecular orbital (LUMO) is localized on the anchoring ligand for all four sensitizers (see paragraph 2.2.3).

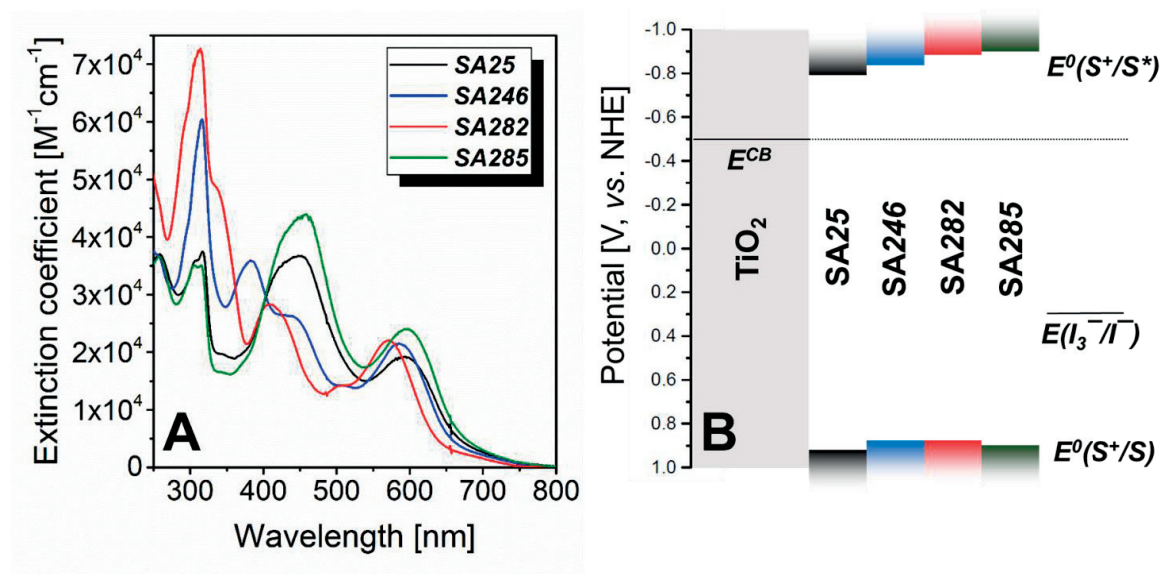


Figure 4.3. (A) Absorption spectra of SA dyes in 10^{-5} M DCM solution; (B) energy diagram showing the sensitizers' ground and excited state oxidation potentials along with iodine's oxidation potential in Z960 electrolyte.

The DSCs employing SA sensitizers and iodine based electrolyte were assembled. The electrolytes were optimized based on Z960 to achieve high efficiencies, and devices were fabricated analogously to those described in chapter 2 (check section 8.1.5). The electrolytes consisted of 1.0 M 1,3-propylmethylimidazolium iodide (PMII), 50 mM LiI, 30mM I_2 , 0.5 M *tert*-butylpyridine (*t*BP) and 0.1 M guanidinium thiocyanate (GNCS) in acetonitrile. The $J-V$ curves are presented in Figure 4.4. Usually in the DSCs a dye with more red-shifted absorption spectrum provides higher photocurrent. However, that is not the case for this series of sensitizers. The short-circuit current varies in the range 14–16 $mA cm^{-2}$ and increases in the following order: **SA282** < **SA25** < **SA285** < **SA246** (Table 4.1). The open-circuit potential varies in a big range from 570 to 694 mV, with the order **SA25** < **SA285** < **SA246** < **SA282**. Interestingly, the **SA282** sensitizer provides the highest V_{OC} and the lowest J_{SC} , but still leading to the best performing DSC with a PCE of 7.2%.

Table 4.1. Photovoltaic performance of DSCs.

	J_{sc} [mA cm^{-2}] [a]	V_{oc} [mV]	FF [%]	PCE (0.1 Sun) [%]	PCE (1 Sun) [%]
SA25	13.98	570	62.4	6.8	6.6
SA246	15.32	647	70.6	6.7	7.1
SA282	13.84	694	73.8	7.1	7.2
SA285	14.71	634	69.9	6.9	6.7

[a] Cell active area was 0.28 cm^2 and during the measurements a black mask with an open area 0.159 cm^2 was used.

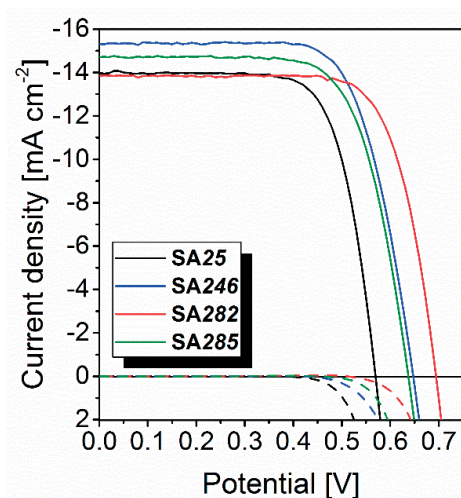


Figure 4.4. Photocurrent density versus applied voltage under AM 1.5 G irradiance (solid lines) and in the dark (dashed lines).

To understand this phenomenon, all DSCs were studied by the means of transient absorption spectroscopy (TAS) (Figure 4.5). Two sets of devices, with and without redox mediator in the electrolyte, have been prepared. Sensitizer in the unbiased DSC was excited with low intensity, ca. $40 \mu\text{J cm}^{-2}$, with pulsed laser light at 510 nm, to result in no more than one electron per nanoparticle. The probe was monitored at 900 nm, based on the oxidized dye absorption spectra. Care needs to be taken, since this condition is far from the maximum power point condition, where the electron density reaches 20 electrons per particle.³² In the first set of devices, lacking redox mediator, the only process to be considered to fit the transient absorbance decay is electron recombination with the photooxidized sensitizer ($\tau_1 = 1/k_1$). Thus, from the monoexponential fitting, the photooxidized sensitizer's lifetime was obtained. In the presence of the redox couple, the transient absorbance spectra decay much faster, which is due to the fast photooxidized dye regeneration. The photooxidized dye lifetime then is determined not only by recombination, but also by regeneration: $\tau_{\text{reg}} = 1/(k_1 + k_{\text{reg}})$. Thus, the regeneration yield can be estimated as $\eta = \tau_1/(\tau_1 + \tau_{\text{reg}})$. Except for **SA282** and **SA285**, all sensitizers regenerate with at least 96%

efficiency. **SA282** regenerates with 63% and **SA285** with 73% yield. These results are not surprising, considering that sulfur atoms in the sensitizer structure catalyze regeneration with iodide. Sluggish regeneration of **SA282** compared to other sensitizers is due to the absence of any sulfur atoms in the structure. If compared to **SA246**, which has a similar oxidation potential, we may notice that the drop in the regeneration yield is huge. This result underlines the importance of sulfur atoms in efficient regeneration.¹⁵⁴ For the case of **SA285**, comparison to **SA25** would be more reasonable, since they both have the same substituents but with different alkyl chain lengths. The drop in the regeneration efficiency for **SA285** in comparison to **SA25** could be due to longer alkyl chains in former, which prevent efficient interaction between the sensitizer and iodide.

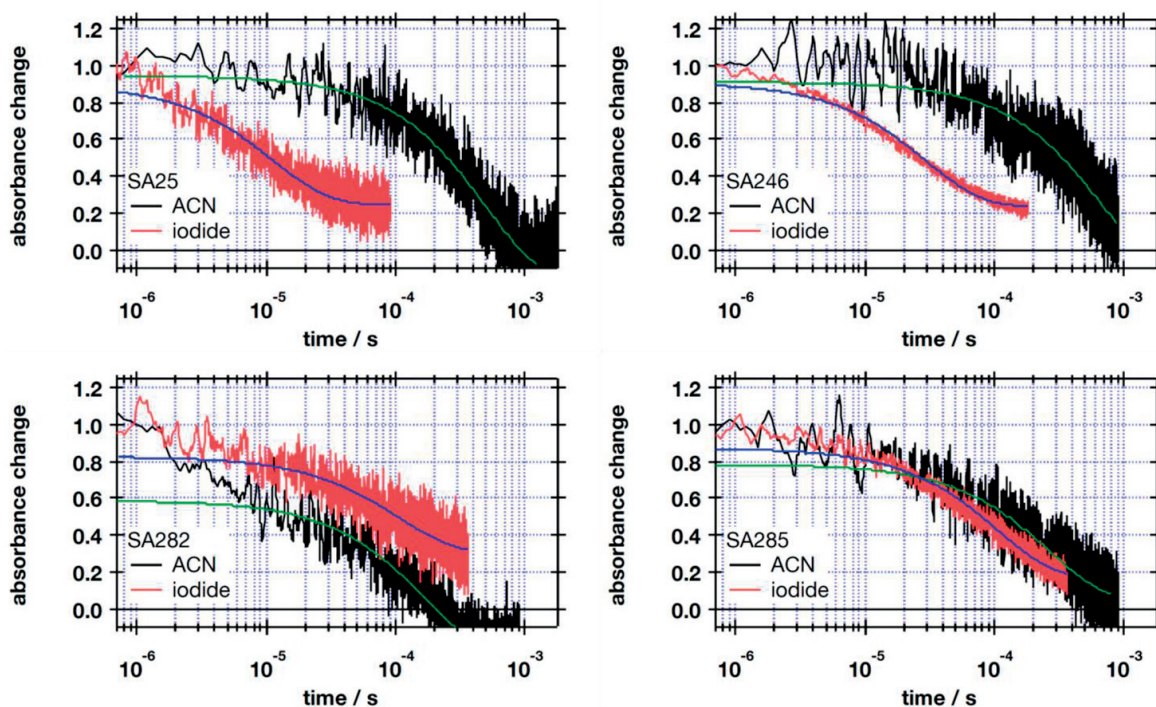


Figure 4.5. Normalized nanosecond transient absorbance decays. Red and black decays refer to the cells with and without the redox mediator. Green and blue lines are fits.

Thus, the transient absorption measurements confirmed that the presence of the sulfur atoms on the aromatic substituents potentiate faster, thus more efficient sensitizer regeneration with iodide. However, since the regeneration with iodide is considered to take place through an inner-sphere electron transfer mechanism, we may not completely exclude the role of the frontier orbitals, meaning the HOMO of reductant and the LUMO of oxidant.^{155,156} In our case, the LUMO of photooxidized dye, which is qualitatively related to the HOMO of neutral dye in comparison to other sensitizers, is localized on the ruthenium t_2 orbitals for **SA282** and is not distributed over the ligands, making it difficult to achieve an efficient overlap with the reductant's HOMO.

To investigate the internal electronic features of the optimized DSCs, we conducted electrochemical impedance spectroscopy (EIS) measurements in the dark and at different forward biases applied. Transmission line models developed by Bisquert et al. were used to fit the impedance spectra.^{52,126} The main parameters such as the titania charge recombination resistance R_{cr} and chemical potential C_{μ} , describing the density of states accessible for electrons, were extracted. According to the equation $\tau = RC_{\mu}$, the apparent electron recombination (τ_{rec}) lifetime was obtained.

In Figure 4.6(A) the charge density, calculated from the chemical potential, for four DSCs as a function of applied voltage are presented. Since there is no substantial difference between them, we may conclude that the conduction band positions for four DSCs with SA dyes are identical. From this point, we may conclude that for this series of four sensitizers the DSC voltage difference is not due to conduction band change. The shift in the conduction band position is usually caused by different components in electrolyte or by the adsorption mode of the sensitizer. Considering that here we analyze DSCs with similar electrolyte compositions and that investigated sensitizers have close structures, a similar conduction band position was anticipated. In Figure 4.6(B) the recombination lifetime versus capacitance is presented. Depending on the sensitizer, the recombination lifetime changes dramatically. As we can see, the highest recombination lifetime was achieved with **SA282** and the lowest one was achieved with **SA25**. We need to note here that the lifetimes obtained from the EIS measurements, which were conducted in the dark with applied bias close to the open circuit voltage, are usually higher than the lifetimes obtained from the EIS measurements at V_{OC} under 1 Sun illumination.

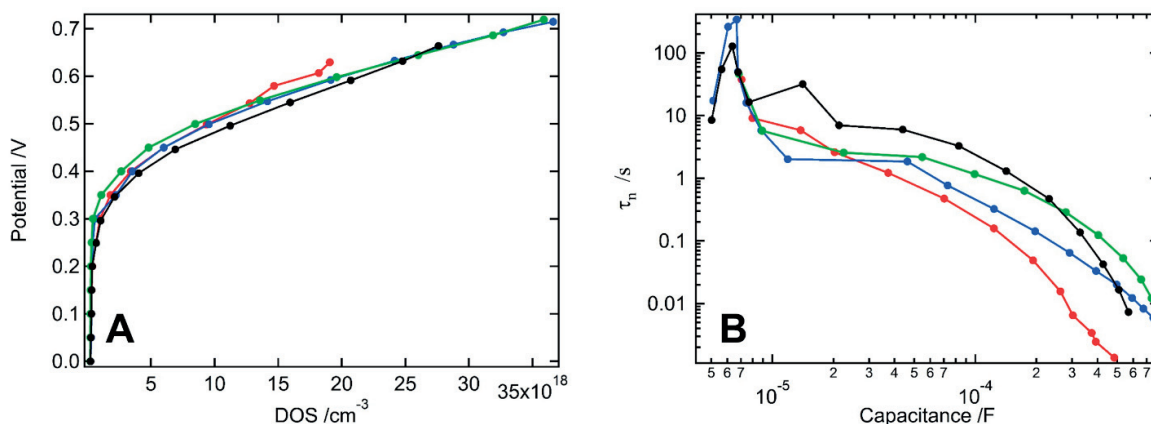


Figure 4.6. (A) Density of states; and (B) electron lifetimes obtained from the EIS analyses for SA25 (red), SA246 (blue), SA282 (green), and SA285 (black).

The main difference between these two cases is that the photooxidized dyes in the latter case can be regenerated with iodide and result in a gradient of I_3^- concentration between two electrodes with

higher concentration in the vicinity of titania. In the former case there is no electrolyte gradient present.¹⁵⁷ Thus, electron recombination lifetimes obtained from EIS in the dark under forward bias should be treated with care. Nevertheless, these values can be used for estimation. Since electron recombination lifetimes vary among four DSCs under similar forward biases, the steady-state concentration of electrons in TiO₂ should be different. The relative change in V_{OC} caused by $E_{F,n}$ due to the changes in the recombination lifetimes were calculated as described in previous chapter, and the total change of V_{OC} , as a result of conduction band shift and various electron recombination lifetimes, are brought in Table 4.2 together with the values obtained from $J-V$ measurements. Very good agreement between the predictions from the EIS measurements and $J-V$ measurements were obtained. From here, we may conclude that higher V_{OC} achieved with **SA282** is the result of increased electron recombination lifetime. This point is in agreement with previous studies, which indicate that sulfur-containing sensitizers catalyze electron recombination. However, we need to show that the various electron recombination lifetimes are not due to present pinholes on the sensitized mesoporous semiconductor.

Table 4.2. Comparison of the change in V_{OC} values estimated from EIS analyses and obtained from the $J-V$ measurements.

	ΔE_{CB} [mV]	ΔV (due to τ_{rec}) [mV] ^[b]	$\Delta V_{OC} = \Delta V + \Delta E_{CB}$ [mV]	ΔV_{OC} (from $J-V$) [mV]
SA25 ^[a]	-	-	-	-
SA246	-9	68	59	77
SA282	-2	99	97	124
SA285	-31	78	47	64

^[a]Values for all devices are brought in reference to the those obtained with SA25. ^[b]In the equation $\Delta V_{OC} = (k_B T/q) \ln[\tau_{rec}(S2)/\tau_{rec}(S1)]$, $\tau_{rec}(S1)$ was taken for SA25.)

To analyze this aspect, we conducted X-ray photoemission spectroscopy (XPS) measurements with bare and sensitized mesoporous semiconductor films (Figure 4.7). We compared the drop in the Ti 2p_{3/2} and Ti 2p_{1/2} signal intensities in reference to the ones obtained for the bare titania film, with the assumption that the efficient coverage should decrease the signal intensity. When full coverage is present, the factor influencing the signal damping is the thickness of the adsorbed layer. Here, considering that SA dyes possess alike sizes and structures, we assume that the layer thickness varies negligibly. For the cobalt based electrolytes, where there is no dye redox mediator interaction discussed in the literature, it was shown that the effective coverage correlates with the open-circuit voltage, and low voltages were related to a thinner monolayer.^{158,159} Since the sizes of sensitizers presented in this work do not vary strongly, weaker damping of the photoemission signals could be related to the presence of pinholes in the sensitizer monolayer.

The best surface protection is achieved with sensitizer **SA285** and the worst is achieved with **SA25**. **SA246** and **SA282** result in a similar damping. These results indicate that the changes in voltages for **SA246** and **SA282** are not due to present pinholes. For **SA25** the drastically lower V_{OC} could be related to both the increased recombination via sulfur-iodine interaction and pinholes present on the adsorbed surface.

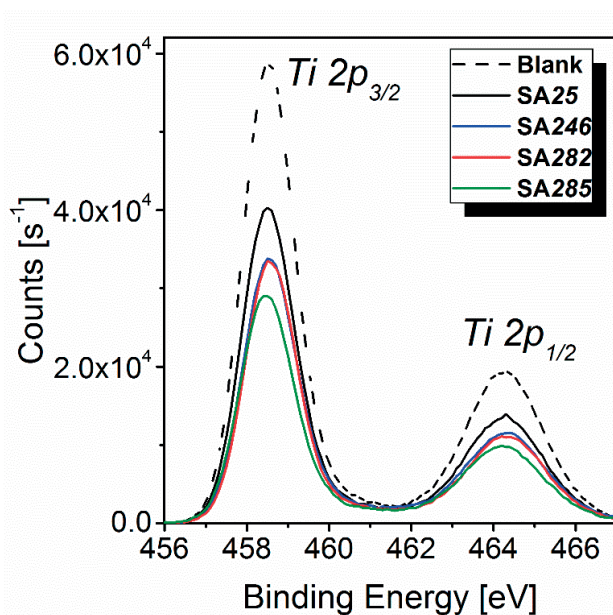


Figure 4.7. Ti 2p XPS spectra of bare (blank) and sensitized titania films.

4.3 Conclusion

Thus, we have studied the influence of sulfur–iodine/iodide interactions on DSC performance with four cyclometalated ruthenium(II) sensitizers employing iodine-based electrolyte. The dual role of sulfur atom containing aromatic substituents in the photovoltaic performance have been analyzed and explained on the basis of transient absorption, electrochemical impedance, and X-ray photoemission spectroscopies. We observed the trade-off between strongly enhanced dye regeneration and increased recombination owing solely to the sulfur atom substituents, and in total it has a drastic negative effect on the photovoltaic performance. Without a sulfur atom in its structure, **SA282** provides the highest efficiency due to the much increased electron recombination lifetime, which suppressed the negative effect of a blue-shifted absorption spectrum and lowest dye regeneration yield. Thus, based on this study, the introduction of sulfur-containing aromatic rings in a sensitizer should be rechecked because it might not benefit to the total performance of the final devices.

Chapter 5 Cyclometalated ruthenium complexes with N-heterocyclic carbene ligands.

This chapter is based on the following published article:

Sadig Aghazada, Iwan Zimmermann, Valeriu Scutelnic, Mohammad Khaja Nazeeruddin, *Organometallics*, **2017**, *36*, 2397-2403, DOI: 10.1021/acs.organomet.7b00354

In this work, I have designed, synthesized, and characterized all the compounds. Dr. Iwan Zimmermann has conducted single crystal measurements and analyses, Mr. Valeriu Scutelnic has conducted DFT calculations. I have analysed all the results and wrote the manuscript. Dr. Mohammad Khaja Nazeeruddin supervised the process.

In the search of new ligand environment for the ruthenium (II) complexes with pyridine-type ligands, we developed seven new cyclometalated ruthenium complexes with N-heterocyclic carbenes (NHCs). In a two-step procedure, we synthesized complexes with the general formula $[\text{Ru}(\text{NHC}^{\wedge}\text{C})(\text{bpyR}_2)_2](\text{PF}_6)$, where $\text{NHC}^{\wedge}\text{C}$ is a bidentate ligand coordinating with the carbene and cyclometalated carbanion; bpyR_2 is either 2,2'-bipyridine, when $\text{R} = \text{H}$, or 4,4'-dimethoxycarbonyl-2,2'-bipyridine, when $\text{R} = \text{CO}_2\text{Me}$. To investigate the photophysical properties of these complexes, various NHC and cyclometalated ligands of different electron donating potency were used. The new compounds were characterized by ^1H , ^{13}C , and COSY NMR methods, cyclic voltammetry, absorption spectroscopy, and single crystal X-ray crystallography. These complexes exhibit perfect redox reversibility, and in contrast to the reported analogues without cyclometalation, they do not have photoemission in solution.

5.1 Introduction

To achieve high power conversion efficiencies in DSCs, many sensitizers based on ruthenium(II) complexes have been developed with the N3 dye and its *tris*-heteroleptic analogues in the forefront.^{62,67} These complexes have the general formula $[\text{Ru}(\text{bpy}(\text{CO}_2\text{H})_2)(\text{bpyR}_2)(\text{NCS})_2]$ and possess 4,4'-dicarboxy-2,2'-bipyridine as an anchoring ligand, two isothiocyanate donating ligands, and the 4,4'-*bis*-substituted-2,2'-bipyridine auxiliary ligand. By attaching various substituents onto the 4 and 4' positions of the auxiliary bipyridine ligand, one can fine-tune the spectral and electrochemical properties of these sensitizers. However, these bulky substituents on the auxiliary ligand result in an increased molecular size of the sensitizer, which leads to lower dye uptake onto the semiconductor and thus leads to

lower power conversion efficiencies (*PCEs*) as was discussed in chapters 2 and 3.^{67,160} Alternative ruthenium photosensitizers for DSCs based on pyridine-azolates such as TFRS-1 or cyclometalated ligand also provide good *PCEs*.^{72,73,87,161} However, new sensitizers rarely show better performance in DSCs than those reported for the classic N3, C101, or N719 dyes. This situation motivated us to investigate a different ligand environment in search of a small molecule with a broad and intensive absorption spectrum, proper oxidation potential, and reversible redox behavior.

Considering the labile nature of the monodentate ligands, we excluded isothiocyanate ligands in our search for new structures.^{69,70} Instead, to increase the ground state energy, we prefer to employ bidentate or tridentate cyclometalated ligands with a $[\text{Ru}(\text{ppy})(\text{bpy})_2]^+$ or $[\text{Ru}(\text{dpb})(\text{tpy})]^+$ (ppy = 2-phenylpyridine, dpb = 1,3-di(pyridine-2-yl)benzene) as a starting point. The effect of the substituents attached on the cyclometalated ligand of the $[\text{Ru}(\text{ppy})(\text{bpy})_2]^+$ derivatives has been studied by Bomben et al., who showed that the cyclometalating ligand and the Ru t_{2g} orbitals share the great part of the occupied frontier orbitals (octahedral environment considered).⁸⁷ A similar result for the $[\text{Ru}(\text{dpb})(\text{tpy})]^+$ - type complexes was also shown.^{162–164}

During the course of designing sensitizers, we and others have modified the cyclometalating ring of ppy as well as the auxiliary ligand to achieve sensitizers with a span of spectral and electrochemical parameters. However, due to the small role of the pyridine ring of the ppy ligand in frontier orbitals, its modification does not lead to a clear tuning of spectral and electrochemical features of a sensitizer.¹⁶⁵ In this regard, N-heterocyclic carbenes (NHC) are good alternatives to pyridine type ligands (Figure 5.1). Their strong σ -donation to the transition metal and π -back bonding result in thermodynamically strong and kinetically inert bonds. Moreover, NHCs are strong electron donors that are superior to phosphines and are more likely to contribute to the occupied frontier orbitals.¹⁶⁶ This means that one may control the optical and electrochemical features of the complex via structural modifications of the NHC ligand.

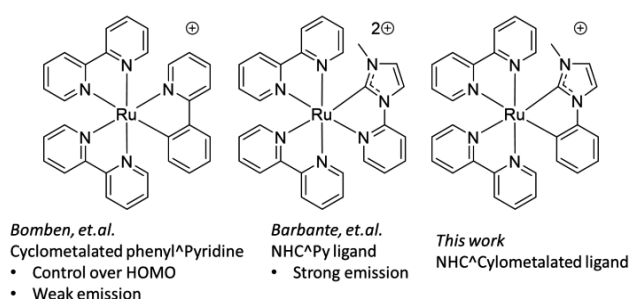


Figure 5.1. Ruthenium complexes relevant to this chapter.

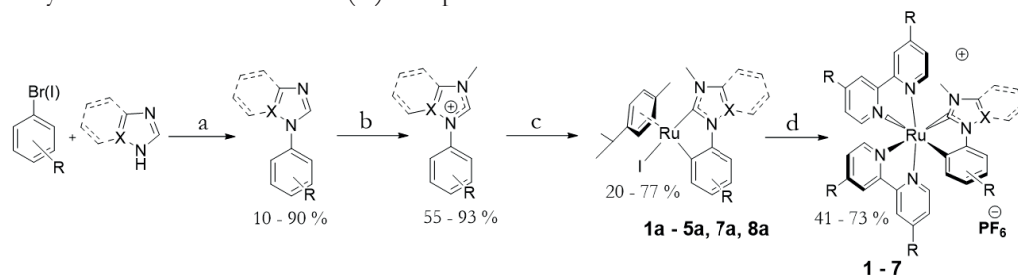
NHCs are usually obtained by deprotonating N-heterocycles. Syntheses of the latter are well developed thus offering chemists a library for designing possible NHC ligands. Only a few ruthenium(II) complexes with the NHC ligand have been studied as photosensitizers, and many have been studied for catalysis applications.^{167–170} In some reports, the *bis*-heteroleptic ruthenium complexes of $[\text{Ru}(\text{NHC}^{\wedge}\text{N})(\text{bpy})_2]^+$ type are investigated in regard to their photoluminescence efficiency.^{171–173} In the same course, surprisingly long excited state lifetime for the $[\text{Ru}(\text{NHC}^{\wedge}\text{N})_3]^{2+}$ was shown.¹⁷⁴ Among the complexes with two tridentate ligands, a similar increase of the excited state lifetime due to NHC ligand was observed.¹⁷⁴ Moreover, Zhang et.al. prepared a ruthenium(II) complex employing the *bis*-NHC NHC[^]C[^]NHC ligand with a cyclometalating benzene ring in between.¹⁷⁵ However, there are no similar structures employing both the cyclometalating and NHC ligands within the bidentate ligand. Our goal is to expand this study on another class of complexes. Thus, we have designed and synthesized 7 novel *bis*-heteroleptic ruthenium(II) complexes with both, cyclometalated and NHC ligands, and with the general formula of $[\text{Ru}(\text{NHC}^{\wedge}\text{C})(\text{bpyR}_2)_2](\text{PF}_6)$. In this work, we investigate the synthesis, crystal structures, and spectral and electrochemical properties of the series of molecules together with their quantum mechanical calculations.

5.2 Results and discussion

Scheme 5.1 shows the synthesis of the ligands and the complexes. The imidazolium salts were obtained first from the Ullmann coupling of an imidazole or its derivatives with aryl halides followed by methylation of the free nitrogen. The final complexes were synthesized in a two-step procedure from the imidazolium salt and $[\text{Ru}(\text{p-cymene})\text{Cl}_2]_2$. First, $[\text{Ru}(\text{p-cymene})\text{Cl}_2]_2$ was reacted with the ligand in the presence of cesium carbonate as a base in dry THF. The $[\text{Ru}(\text{p-cymene})(\text{NHC}^{\wedge}\text{C})\text{I}]$ complexes were obtained (**1a–8a**) as orange products, which are easily purified by column chromatography on neutral alumina. Then, $[\text{Ru}(\text{p-cymene})(\text{NHC}^{\wedge}\text{C})\text{I}]$ complexes were reacted with two equivalents of 2,2'-bipyridine in the presence of AgPF_6 for halogen abstraction to yield $[\text{Ru}(\text{NHC}^{\wedge}\text{C})(\text{bpy})_2](\text{PF}_6)$ (**1–5**) complexes as mauve products. To ensure full counteranion exchange, all of the final products were washed with saturated aqueous solution of NH_4PF_6 . An analogous reaction with 4,4'-dimethoxycarbonyl-2,2'-bipyridine ($\text{bpy}(\text{CO}_2\text{Me})_2$) resulted in green complexes **6** and **7** with the general formula $[\text{Ru}(\text{NHC}^{\wedge}\text{C})(\text{bpy}(\text{CO}_2\text{Me})_2)_2](\text{PF}_6)$. All the final complexes were obtained with good yields, except for the complex with dimethoxy-pyridine cyclometalating ligand (**4**). Although the reaction mixture of **7a** and **8a**, which contains 3,5- or 2,4-dimethoxyphenyl-pyridine ligands, with bpy was deep mauve, indicating on the product formation, the products completely decomposed during alumina (neutral, basic) and silica column chromatography purification. This outcome could be understood based on the elec-

tron-rich character of the dimethoxy-substituted cyclometalating ligands leading to the product oxidation. Substitution of bpy to electron deficient 4,4'-dimethoxycarbonyl-2,2'-bipyridine resulted in a stable complex **7**.

Scheme 5.1. Synthesis of the ruthenium (II) complexes.



	NHC-Cyclometalated ligands						
[Ru(p-Cy)(NHC^C)I]	1a	2a	3a	4a	5a	7a	8a
[Ru(NHC^C)(bpy) ₂]PF ₆ R = H	1	2	3	4	5	x	x
[Ru(NHC^C)(bpy(CO ₂ Me)) ₂]PF ₆ R = CO ₂ Me	6					7	

a. CuI, KOH, DMSO, 110 °C, 24 h; b. MeI, THF, 130 °C, 12 h; c. [Ru(p-cymene)Cl₂]₂, Cs₂CO₃, THF, reflux, 6 - 12 h; d. bpy or 4,4'-dimethoxycarbonyl-bpy, AgPF₆, reflux, 12 h.

All of the intermediate and the final complexes were characterized by high resolution mass spectroscopy and by ¹H and ¹³C NMR. The ¹H NMR shows the effect of the NHC ligand on the proton chemical shifts. Figure 5.2 assigns the NMR spectra based on 2D COSY spectra for complexes **1** and **3**. In comparison to **1**, almost all of the signals for the **3** are shifted downfield. This result is due to more electron deficient character of triazole compared to imidazole.

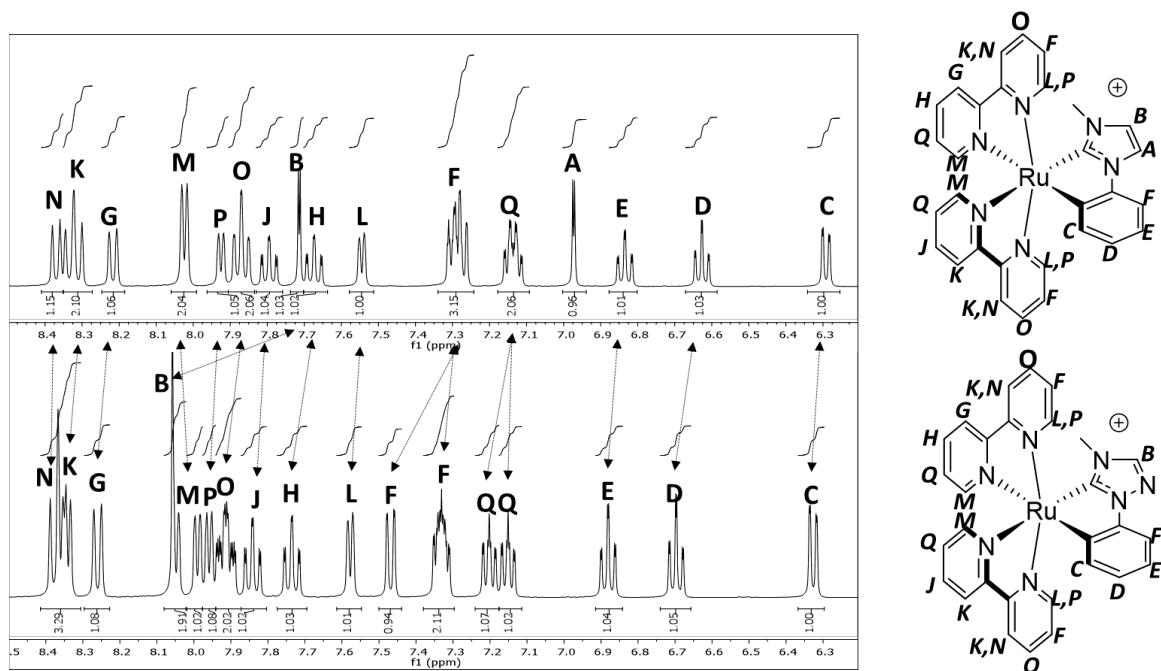


Figure 5.2. ^1H NMR spectra of complexes **1** (top) and **3** (bottom) measured in d_3 -acetonitrile. Arrows indicate how NHC ligands affect signal position.

Single crystals of three intermediate cyclometalated complexes **1a**, **2a** and **3a** and of the final complexes **1** and **6** were obtained by slow diffusion of hexane into a concentrated DCM solution of the complexes at room temperature.

Compound **1a**, **2a** and **3a** crystallize in the space groups $Pna2_1$ (orthorhombic), $P2_1/c$ (monoclinic), and $P2_12_12_1$ (orthorhombic), respectively. The structure for **3a** is noncentrosymmetric, while compound **1a** has been refined as racemic twins. The structure representations of the asymmetric units for the three complexes are shown in Figure 5.3. The crystal structure consists of a neutral complex of Ru connected to iodine, p-cymene and 1-phenyl-3-methylimidazole-2-ylidene for **1a**, 1-phenyl-3-methylbenzimidazole-2-ylidene for **2a** and 1-phenyl-4-methyltriazole-5-ylidene for **3a** as the bidentate ligands. The p-cymene is η^6 coordinated to Ru forming a semi-sandwiched arrangement, while NHC \wedge C ligands are bound by cyclometalation forming a five-membered ruthenacycle. The ruthenium complex adopts a three-legged piano-stool structure with the two carbon atoms from the ruthenacycle and the iodine atoms as the legs. The average ruthenium aryl π interactions are around 1.74 Å, while Ru-C bond lengths are in the range from 2.003(3) Å to 2.079(16) Å (Table 8.7). Moving from **1a** to **3a** and **2a** the Ru – NHC carbon bond length is decreasing. We assume that this change is a consequence of stronger π -back-bonding in the latter two complexes due to a more electron deficient character of benzimidazole and triazole in reference to imidazole.

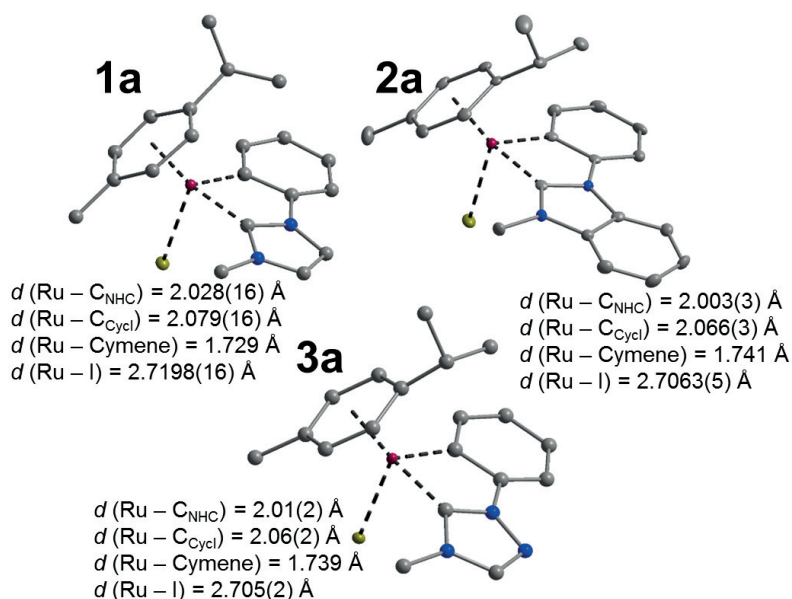


Figure 5.3. Structure representations of the asymmetric unit of compounds **1a**, **2a**, and **3a**. Color code: Ru – violet; I – green; N – blue; C – grey. Hydrogen atoms are omitted for clarity.

Compounds **1** and **6** crystallize in the triclinic space group $P_{\bar{1}}$. The crystal structure of **1** is considerably more complicated than that of **6** due to a larger unit cell, disorder, and the presence of solvent molecules. The unit cell of **1** has almost twice the volume of the one for **6**, and its asymmetric unit contains two complex cations, three PF_6^- counterions (one half occupied and another one laying on the inversion center), and two heavily disordered dichloromethane solvent molecules (Figure 5.4(A)). The asymmetric unit for **6**, shown in Figure 5.4(B), contains a complex cation and a PF_6^- counterion. The cationic complex consists of a Ru bound to $\text{C}^{\wedge}\text{C}$ by cyclometalation and is further complexed by two 2,2'-bipyridine or 4,4'-dimethoxycarbonyl-2,2'-bipyridine ligands by *bis*-chelation for **1** and **6**, respectively. The coordination of the Ru atom is found to be distorted octahedral with Ru–C bond lengths in the range of 2.002(7) Å to 2.168(11) Å and Ru–N bond lengths between 2.017(5) Å and 2.251(8) Å. Moving from complex **1** to **6**, all the bond lengths between Ru and ligands significantly decrease. The more electron withdrawing nature of $\text{bpy}(\text{CO}_2\text{Me})_2$ in comparison to bpy ligands may increase a positive charge on the Ru center, which in turn may cause bond contraction. The packing of compound **6** is shown in Figure 5.5, where ruthenium complexes arrange in double chains by π – π stacking of the organic ligands running along *a*-direction. The PF_6^- counterions are located between those chains. Crystallographic data were submitted to Cambridge Crystallographic Data Centre (CCDC 1529867–1529871 for complexes **1a**, **2a**, **3a**, **1**, and **6**).

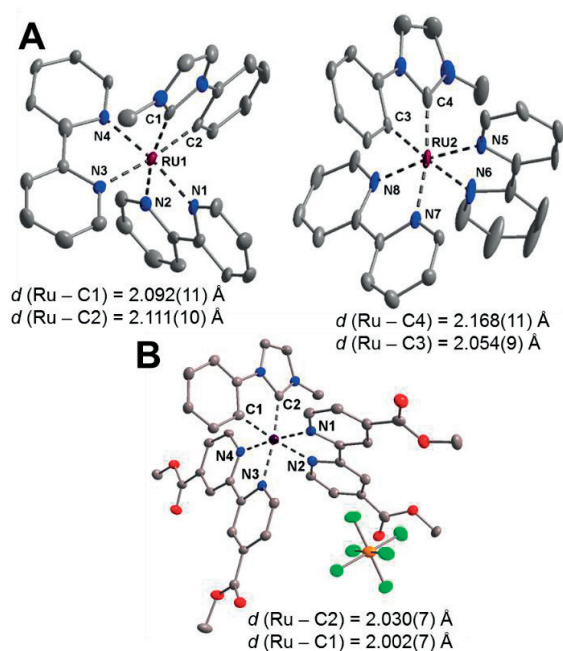


Figure 5.4. Structure representations of the asymmetric unit (A) of compound **1** (PF_6^- ions, solvent molecules as well as hydrogen atoms are omitted for clarity); and (B) of compound **6** (hydrogen atoms are omitted for clarity). Color code: Ru – violet; N – blue; C – grey; O – red; P – orange; and F – green.

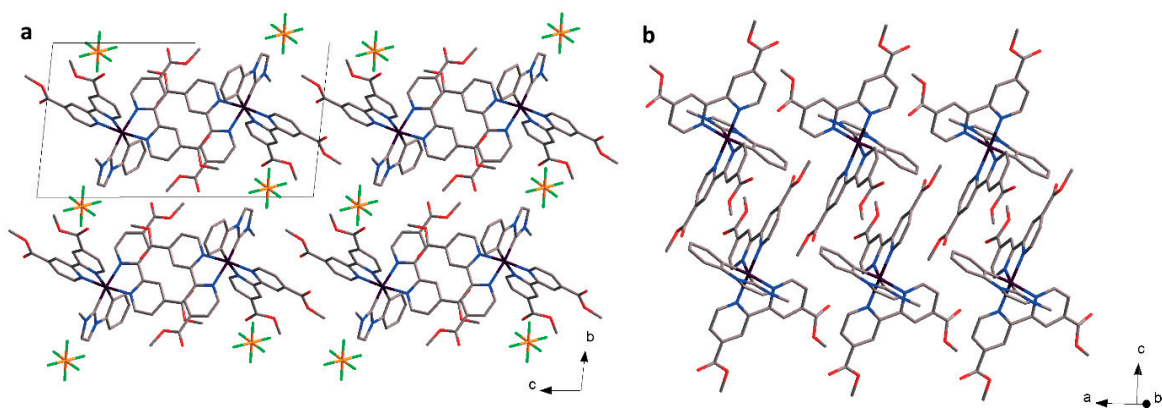


Figure 5.5. Overview of the molecular packing of compound **6**. (a) View along a ; and (b) view parallel to a . Color code: Ru – violet; N – blue; C – grey; O – red; P – orange; and F – green.

The absorption spectra of the 10^{-5} M acetonitrile solution of the final complexes were measured and are presented in Figure 5.6. All of the spectra consist of three apparent bands in the visible and UV region with the extinction coefficients from 8×10^3 to $17 \times 10^3 \text{ M}^{-1} \text{ cm}^{-1}$. Two low energy bands can be related to the metal-to-bipyridine ligand charge transfer, and the band around 350 nm can be related to the metal-to-NHC π ligand charge transfer. Moreover, all the spectra feature a broad and low energy band of unknown origin. The effect of the NHC ligands can be determined by comparing the spectra

for **1**, **2**, and **3** (Figure 5.6(A)). The imidazole-based carbene has more electron-rich character in comparison to the benzimidazole and triazole-based carbenes. This results in a 24 nm red-shifted band for **1**. We expect that the role of imidazole in the band shift must be due to the increased electron density on the ruthenium center. In Figure 5.6(B), we compare the spectra for **1**, **4**, and **5** with various cyclometalated rings and with the same imidazole NHC. Generally, all three spectra have similar shapes. Moving from the phenyl ligand to the 3,5-dimethoxy-4-pyridyl and 3-carboxymethyl phenyl ligands results in a blue-shifted spectrum by 16 and 11 nm, respectively. This is due to electron deficient character of the latter two ligands.

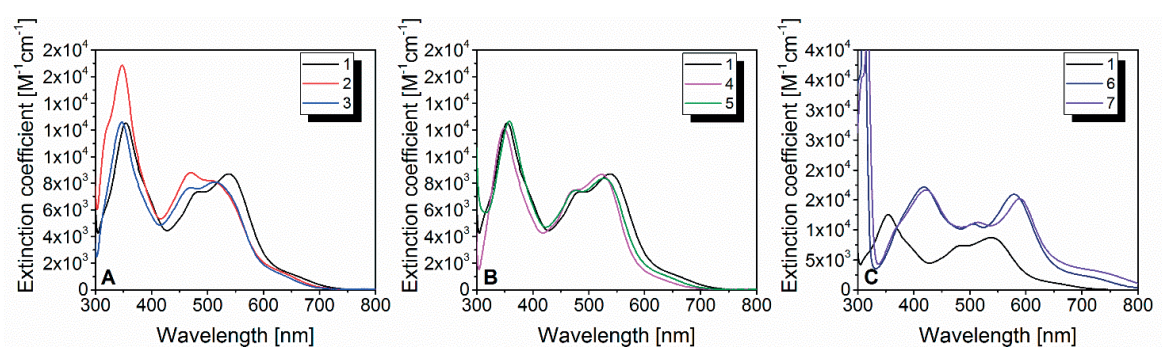


Figure 5.6. Absorption spectra of 10⁻⁵ M acetonitrile solution of cyclometalated ruthenium NHC complexes.

For the dye cell application, the sensitizer is needed to possess an anchoring moiety. Various groups like carboxylic or phosphonic acids may facilitate molecule binding to the surface. These groups are also known to have strong electron withdrawing properties, and thus their introduction may greatly red-shift the absorption spectra. The substitution of the bpy ligands with bpy(CO₂Me)₂ ligands for the complexes **6** and **7** resulted in great *batho*- and *hypsochromic* shifts of the absorption spectra (Figure 5.6(C)). Due to the very broad MLCT bands of **6** and **7**, most of the visible region of the solar spectrum is covered. When compared to the N3 sensitizer, the low energy absorption band of **6** is red-shifted by 45 nm with little increase of the extinction coefficient. This feature of complexes **6** and **7** makes them very good starting molecules for DSC photosensitizer design.

Long excited state lifetimes are usually desired for photosensitizers to facilitate the main process of photosensitization. This implies a measurable steady state photoluminescence. Nevertheless, in the DSCs, electron injection from an excited sensitizer to the conduction band of semiconductor takes place on a femtosecond time scale, and short excited state lifetimes are not considered to be a limiting factor.^{37,176} On the other hand, for organic catalysis applications, the photoredox catalyst should have a long excited state lifetime for the bimolecular reaction step to occur.¹⁷⁷ Unfortunately, none of our seven complexes exhibit any emission at room temperature in deoxygenated acetonitrile solution. The

main cause of ruthenium complexes' low photoluminescence quantum yield is a thermally accessible ^3MC state leading to the fast nonemissive quenching.^{178,179} In the MC state, the excited electron occupies the e_g orbitals, which are metal–ligand bond directed, and due to such an orbital composition, the MC states usually cause a fast nonemissive excited state decay.^{180–184} NHC ligands are strong field ligands, which cause the e_g orbitals to increase in energy. Introducing three NHC ligands instead of the three pyridines of $[\text{Ru}(\text{bpy})_3]^{2+}$ results in the exceptionally long excited state lifetime.^{185,186} Moreover, very long excited state lifetimes of the iron(II) complexes with NHC ligands were observed.^{186,187} Thus, the nonemissive nature of our complexes, which possess both NHC and cyclometalated ligands, is probably not due to deactivation through the ^3MC state, which is inaccessible at room temperature. As Christoph Kreitner and Katja Heinze propose, the inefficient emission in this type of complex could be due to tunneling into high-energy vibrationally excited singlet states.¹⁶⁴

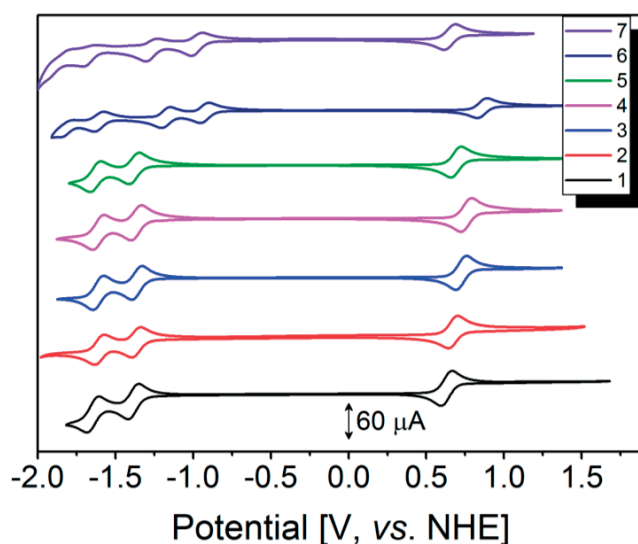


Figure 5.7. Cyclic voltammograms of the new ruthenium complexes measured in 0.1 M NBu_4PF_6 acetonitrile solution under argon atmosphere with a scan rate of 50 mV s^{-1} . A glassy carbon working electrode and platinum counter and reference electrodes were employed. Ferrocene was used as an interval standard, and its oxidation potential was positioned at 0.63 V vs. NHE . Corrected voltammograms without ferrocene are presented.

Cyclic voltammetry measurements of the ruthenium complexes were conducted in acetonitrile under argon atmosphere. Ferrocene was used as an internal standard. Figure 5.7 presents the cyclic voltammograms, and all the oxidation potentials are summarized in Table 5.1. In the electrochemical window of acetonitrile, all of the complexes undergo a single one-electron oxidation, which is related to the $\text{Ru}^{3+/2+}$ redox couple, where the metal center loses its electron. Complexes **1–5** possess two one-electron reductions, while complexes **6** and **7** undergo four one-electron reduction processes. Such a

difference is due to a more electron deficient character of $\text{bpy}(\text{CO}_2\text{Me})_2$ in comparison to bpy , which enables in total quadruply-reduced species with one electron per pyridyl ring.

When complexes **1**, **2**, and **3** are compared, the oxidation potentials of **2** and **3** are 40 and 100 mV higher than the oxidation potential of **1**. This fact indicates how the NHC ligand affects the oxidation potential - a more electron deficient ligand leads to a more positive oxidation potential. Moreover, this result is consistent with the optical spectra, where **1** has a more red-shifted band in comparison with **2** and **3**, when a similar excited state energy is considered. Similarly, the comparison of **1**, **4**, and **5** shows the effect of the cyclometalating ring, where the less electron donating 4-pyridyl (**4**) or 3-carboxy methyl-benzene (**5**) rings result in a more positive oxidation potentials than for **1**. This possibility to introduce various substituents on the cyclometalated ring along with the possibility to vary the NHC ligand give chemists better control on the oxidation potentials. Substituting bpy by $\text{bpy}(\text{CO}_2\text{Me})_2$ pushes the oxidation potential by up to 230 mV from 0.63 V for **1** to 0.86 V for **6**. This can be explained by the stronger electron withdrawing power of $\text{bpy}(\text{CO}_2\text{Me})_2$. In complex **7**, the oxidation potential is decreased back to 0.65 mV as an outcome of the methoxy substitutions. The reduction potentials for the complexes **1–5** have roughly the same values.

Table 5.1. Electrochemical properties of **1–7** and $[\text{Ru}(\text{ppy})(\text{bpy})_2](\text{PF}_6)$ ^[a]

E^0 , V	1	2	3	4	5	6	7
E^0_{ox}	0.63 (71)	0.67(59)	0.73(68)	0.76(68)	0.69(66)	0.86(60)	0.65 (70)
$E^0_{\text{red 1}}$	-1.39(61)	-1.37(54)	-1.36(62)	-1.37(64)	1.38(64)	-0.93(54)	-0.97(68)
$E^0_{\text{red 2}}$	-1.64(84)	-1.60(60)	-1.61(71)	-1.61 (71)	-1.63(69)	-1.18(53)	-1.28(72)
$E^0_{\text{red 3}}$						-1.61(60)	-1.66(85)
$E^0_{\text{red 4}}$						-1.81(88)	

^[a]In parentheses the difference between the oxidation and reduction wave maxima for each redox are brought. Measurement conditions are the same as described in Figure 5.7.

For a photosensitizer to function for a long time it should bear many oxidation–reduction cycles. For example, in DSCs with 20 years of lifetime, a sensitizer should withstand nearly 10^6 photooxidation - reduction cycles.⁵⁹ Thus, redox reversibility is an essential requirement for a photosensitizer. Photosensitizers for DSC application that feature isothiocyanate ligands undergo an irreversible oxidation. This irreversibility was related to the ease of the isothiocyanate ligand cleavage when Ru^{2+} is oxidized to Ru^{3+} . Moreover, for the cyclometalated ruthenium sensitizers the $\text{Ru}^{3+/2+}$ redox process is usually quasi-reversible.^{92,131}

To examine the $\text{Ru}^{3+/2+}$ redox reversibility for our new complexes, we conducted Randles–Sevcik analysis.¹³³ In the Randles–Sevcik equation at 298 K shown in equation (18),

$$i_p = 268\,715\,ACD^{1/2}n^{3/2}v^{1/2} \quad (18)$$

i_p is the current density in A cm^{-2} , A is the working electrode area in cm^2 , C is the bulk concentration of molecule undergoing redox process in mol cm^{-3} , D is a diffusion coefficient in cm^2s^{-1} , n is the number of electrons transferred in one redox process, and v is a voltage scan rate in Vs^{-1} . Thus, for the reversible redox process, the current density maximum should grow linearly versus the square root of the scan rate. We have measured cyclic voltammograms at 50, 100, 200, 500, and 1000 mVs^{-1} and plotted the cathodic and anodic peak currents versus the square root of the scan rate.

In Figure 5.8, the CVs at different scan rates for complex **1** are presented, and the results of the Randles–Sevcik analysis along with the linear fit for all the complexes are presented. The CVs for complexes **2–7** are presented in Figure 8.95. All results were fitted with an R^2 factor over 99%. These results indicate that the redox process is reversible, and the current is limited by the mass transport to the electrode. Such a reversible behavior renders the NHC-cyclometalated complexes as good photosensitizers for DSC and other applications.

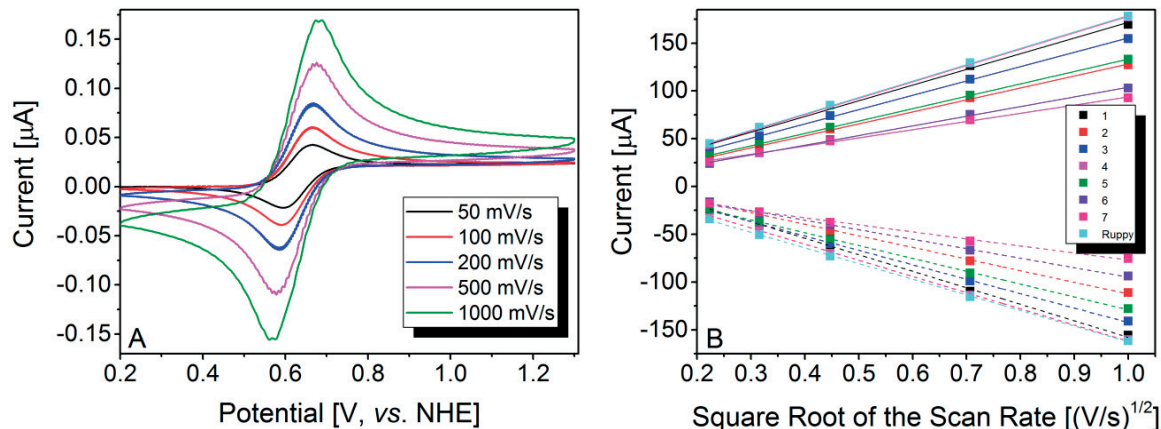


Figure 5.8. (A) Cyclic voltammograms of the first oxidation of complex **1** measured in the same system as described in Figure at different voltage sweep rates; (B) Randles–Sevcik analyses of first oxidation for all the complexes. Solid and dashed linear fits are for the oxidation wave and back-reduction wave respectively.

Computational analysis of the ruthenium complexes was carried out with Gaussian 09 software package¹⁸⁸ using the functional mPW1PW91¹⁸⁹. Geometries in the ground state were optimized using LANL2DZ¹⁹⁰ basis set and effective core potential (ECP) for ruthenium and 6-31G* for nonmetal atoms¹⁹¹. Single point energy calculations were performed at the optimized geometries employing the Stuttgart-Dresden SDD¹⁹² basis set and quasirelativistic effective core potential for ruthenium atom and

TZVP¹⁹³ for nonmetal atoms. Solvation effects of acetonitrile were taken into account with implicit solvent model COSMO¹⁹⁴. Frontier molecular orbitals of the ground state were plotted with GaussView 5.0.8. Vertical singlet-singlet excitations were computed within the frame of time-dependent density functional theory (TD-DFT).^{195,196} Frontier molecular orbital plots for complex **1** are presented in Figure 5.9. For complexes **2** and **3**, which have benzimidazolidene and triazolidene substituents instead of imidazolidene, no substantial change in the frontier orbitals was observed (Figure 8.96 and Figure 8.97). For complexes **1** - **3**, three occupied frontier orbitals HOMO, HOMO-1 and HOMO-2 are generally metal based originating from the t_{2g} orbitals of metal center in octahedral environment. The NHC ligand partially shares the HOMO-2 and HOMO orbitals with the former delocalized over NHC ligand and the latter on the cyclometalated ligand. On the other hand, LUMO, LUMO+1 and LUMO+2 are all mostly delocalized over two bipyridine ligands; the first two have some contribution from the ruthenium d orbitals. Such a distribution of frontier orbitals supports the description of cyclic voltammograms where the molecule oxidation was related to the $\text{Ru}^{3+/2+}$ couple, and its reduction was related to the bipyridine receiving extra electrons. Moreover, the changes in the HOMO and LUMO energies moving from **1** to **2**, and **3** are in agreement with the oxidation and reduction potentials (Table 8.10). Thirty excitations were first calculated from the TD-DFT calculations in the acetonitrile medium. Although the calculated UV-Vis spectra are in good agreement with the experimental spectra, the calculated spectra were somewhat blue-shifted (Figure 8.98).

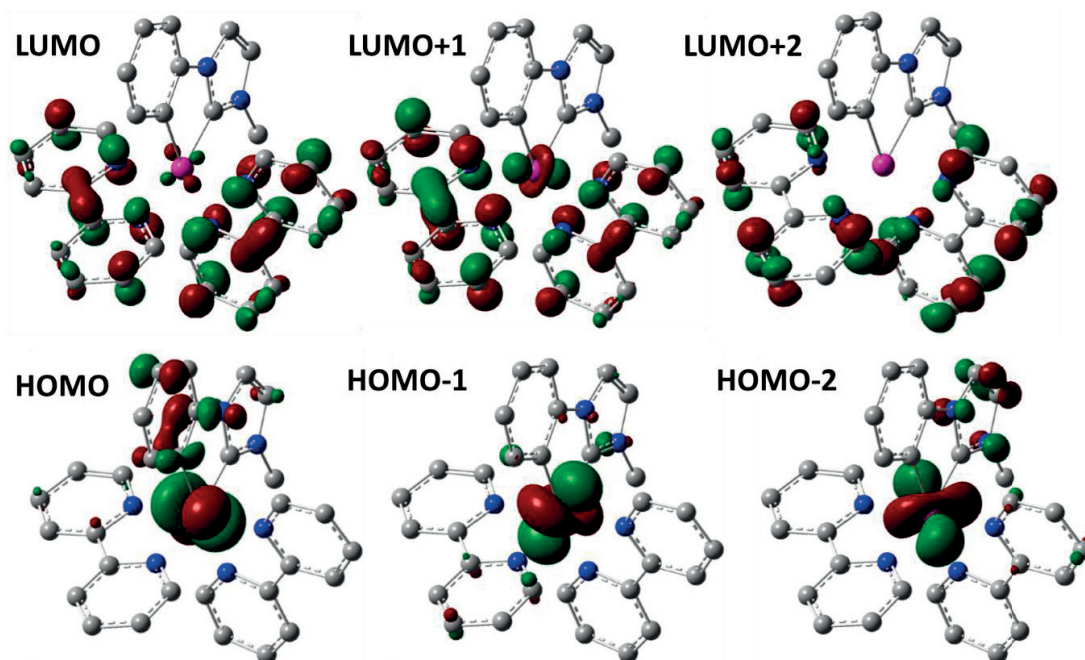


Figure 5.9. Frontier molecular orbitals of **1** (mPW1PW91/SDD, TZVP in acetonitrile).

5.3 Conclusion

A series of ruthenium complexes, $[\text{Ru}(\text{NHC}^{\wedge}\text{C})(\text{bpyR}_2)_2](\text{PF}_6)$, where ruthenium is coordinated by both NHC and cyclometalating ligands, were synthesized using a double step process that introduced $\text{NHC}^{\wedge}\text{C}$ and bpyR_2 ligands consecutively. To the best of our knowledge, these molecules are the first examples of Ru(II) complexes where, along with bipyridine derivatives, the bidentate $\text{NHC}^{\wedge}\text{C}$ ligand is also attached to the metal. By changing both the cyclometalating and the NHC ligands, spectral and electrochemical properties were finetuned. Spectral and electrochemical data together with quantum mechanical calculations show that the NHC ligands share the highest occupied frontier orbitals as well. Finally, complexes $[\text{Ru}(\text{NHC}^{\wedge}\text{C})(\text{bpy}(\text{CO}_2\text{Me})_2)_2](\text{PF}_6)$ with methylcarboxy groups attached to the 2,2'-bipyridine feature very broad absorption spectra covering the entire visible region of the solar spectrum, which underpins this type of complex as promising candidates for DSC applications.

Chapter 6 Bis-Tridentate Cyclometalated Ruthenium Complexes with Extended Anchoring Ligand

This chapter is based on the following article:

Sadig Aghazada, Iwan Zimmermann, Yameng Ren, Peng Wang, Mohammad Khaja Nazeeruddin, *Submitted*

In this work, I have designed, synthesized and characterized all the molecules. Dr. Iwan Zimmermann conducted single crystal analyses. Dr. Yameng Ren fabricated and characterized solar cells. Drs. Peng Wang and Mohammad Khaja Nazeeruddin supervised the work.

Ruthenium polypyridine complexes with six-membered chelating rings have recently received significant attention due to broad absorption spectra and improved photophysical characteristics. We have synthesized three new heteroleptic bis-tridentate cyclometalated ruthenium complexes, named **1a**, **2a**, and **3a**, with the donating and accepting ligands. The **2a** and **3a** complexes contain 2,6-di(quinolin-8-yl)-4-methoxycarbonylpyridine (*dqpCO₂Me*), and the **1a** - 2,2':6',2''-terpyridine-4'-ethoxycarbonyl (*tpyCO₂Et*) accepting ligands. The ester groups in **1a** and **2a** were hydrolyzed to obtain sensitizers **1** and **2**, which were used in dye-sensitized solar cell (DSC) application. Interestingly, the binding mode of the accepting ligand was found to differ in **3a** and **2a**. NMR spectra and single crystal XRD data reveal that in **3a** one of the quinolines of *dqpCO₂Me* ligand is cyclometalated, while in **2a** the ligand coordinates in an expected fashion similar to *tpyCO₂Et*. Complete ¹H, ¹³C and ¹H-¹H COSY NMR, and high-resolution mass analyses of all complexes were conducted. The performance of dye-sensitized solar cells using complexes **1** and **2** with both iodine- and cobalt-based electrolytes were investigated.

6.1 Introduction

All the highest performing DSCs were achieved by modifying the core of Ru(NCS)₂(bpy)₂ (bpy = 2,2'-bipyridine), cyclometalated [Ru(ppy)(bpy)]⁺ (Hppy = 2-phenylpyridine) or of TFRS sensitizers by attaching various organic chromophores (Figure 6.1).^{67,72,86,92} Our recent studies show that although by these substituents higher efficient DSCs are possible, their redox irreversibility brings additional instability to the molecule.¹³¹ In this regard, search for the new ligand environments for ruthenium complexes with suitable photophysical properties is critical.

A tridentate ligand - 2,6-bis(quinolone-8-yl)pyridine (*dqp*), which forms six membered chelating rings with the metal center has recently been under intense scrutiny.¹⁹⁷⁻²⁰¹ Abrahamson *et. al.* observed that, at room temperature, the homoleptic ruthenium complex $[\text{Ru}(\text{dqp})_2]^{2+}$ with two *dqp* ligands exhibits an excited state lifetime of 3.0 μs , while its $[\text{Ru}(\text{tpy})_2]^{2+}$ (*tpy* = 2,2':6',2''-terpyridine) analogue's excited state lifetime is less than 1 ns.¹⁹⁷ The extended lifetime of the aforementioned complex was related to the increased bite angle, with an electron pair on the nitrogen atom better suited to overlap with the e_g orbitals of ruthenium (octahedral symmetry is considered), causing destabilization of excited metal centered (^3MC) states and thus lowering the probability of non-radiative deactivation of $^3\text{MLCT}$ via these ^3MC states.^{197,202,203} This work has also initiated further investigations on a modified complexes with various substituents on *para*-positions of two coordinating pyridine rings.¹⁹⁹ Asymmetric analogues like $[\text{Ru}(\text{dpb})(\text{dqp})]^+$ or $[\text{Ru}(\text{dqb})(\text{dqp})]^+$ (where *dpb* = 1,3-di(pyridine-2-yl)-4,5-dimethylbenzene, *dqb* = 1,3-di(quinolone-8-yl)benzene) with one cyclometalated ligand, possess very broad absorption spectra with the onset at 780 nm.¹⁹⁸ Moreover, heteroleptic complexes with one *dqp* ligand and various asymmetric cyclometalated ligands also possess broad absorption spectra attractive for DSC application.²⁰¹ We became interested to modify *dqp* coordinated ruthenium complexes with functional substituents, to obtain a sensitizer for DSC application. We chose $[\text{Ru}(\text{dqp})(\text{dpb})]^+$ as a starting core, and attached a benzene ring with two long *alkoxy*- chains to the *para* position of the cyclometalated carbanion, with the purpose of reducing the aggregation and charge recombination with the redox mediator. A carboxylic acid group was introduced at the *dqp* ligand to attach it onto the mesoporous semiconductor. A reference sensitizer with *tpy* instead of *dqp* was also designed.

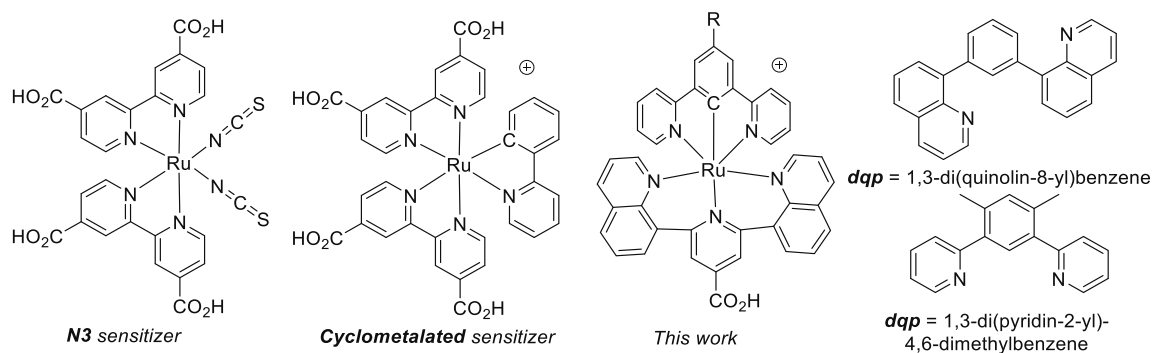


Figure 6.1. Ruthenium sensitizers and ligands in literature and in this work

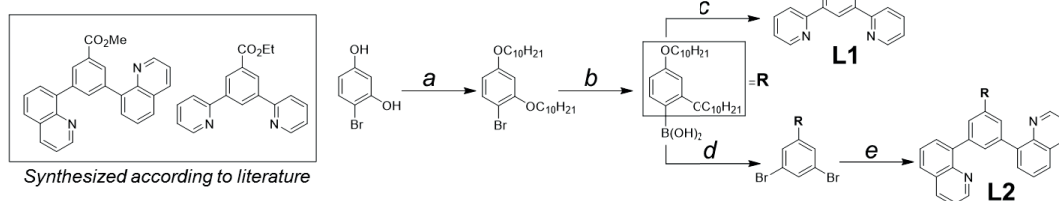
6.2 Result and Discussion

Ruthenium sensitizers with NCN and NNC type of tridentate cyclometalated ligands are known.^{129,204} In this work, we chose the former type of ligands as they are easier to synthesize than the latter. Although, due to lowered symmetry, NNC type of ligands result in more absorption bands than NCN ligated complexes, no clear work showed their better performance in solar cells.^{129,205}

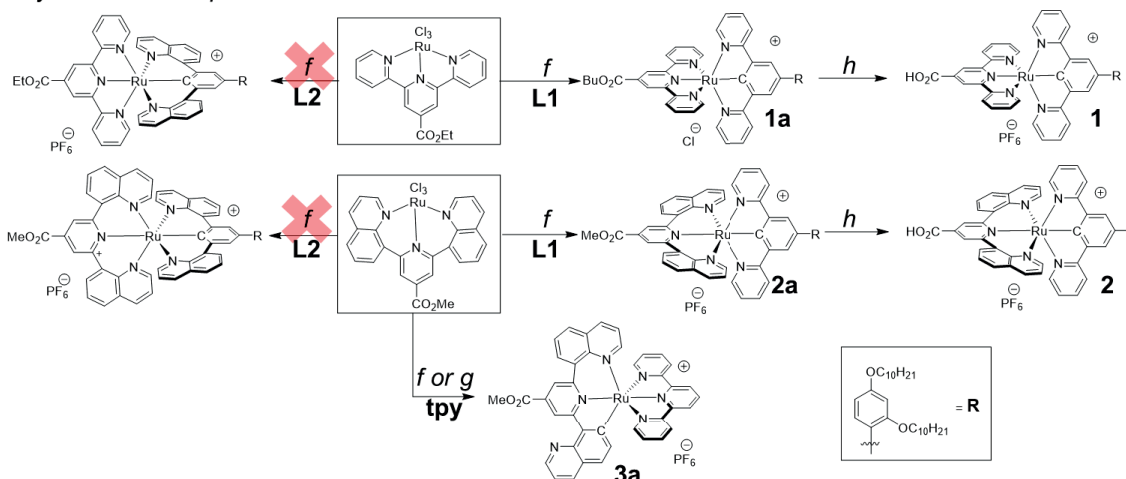
Thus, we chose cyclometalated donating ligand – 1,3-bis(pyridin-2-yl)-benzene featured on the 5th position with a bulky 2,4-bis(decyloxy)benzene substituent. The syntheses of ligands and ruthenium complexes are summarized in Scheme 6.1. To synthesize the ligands, 4-bromoresorcinol was reacted with *n*-bromodecane and 1-bromo-2,4-bis(decyloxy)benzene was obtained, from which the boronic acid adduct R-B(OH)₂ (R = 2,4-bis(decyloxy)phenyl) was obtained. In a Suzuki-Miyaura reaction of latter with 1,3-bis(pyridine-2-yl)-5-bromobenzene, the ligand **L1** was obtained in 58 % yield. Analogously, tributyltin adduct R-SnBu₃ and 1,3-bis(pyridine-2-yl)-5-bromobenzene in Stille reaction in DMF didn't result in any product formation in 24 hours. To obtain the ligand **L2**, first the boronic acid adduct R-B(OH)₂ was reacted with 1 equivalent of 1,3,5-tribromobenzene, and then two other bromides were coupled with 2-(tributylstannyl)pyridine in 76 % total yield. Worth to note, R-SnBu₃ reaction with 1,3,5-tribromobenzene also failed.

Scheme 6.1. Syntheses of ligands and ruthenium complexes

Synthesis of ligands



Synthesis of complexes



(a) C₁₀H₂₁Br, K₂CO₃, DMF, 100 °C (97 %); (b) *n*-BuLi, THF, -78 °C, then B(OPr)₃, -78 °C to RT, 6 h (98 %); (c) 1,3-(pyridin-2-yl)-5-bromobenzene, Pd(PPh₃)₄, toluene – ethanol - 2M aqueous K₂CO₃, reflux, 6 h (58 %); (d) BzBr₃, Pd(PPh₃)₄, toluene - ethanol - 2M aqueous K₂CO₃, reflux, 4 h (79 %); (e) quinolin-8-boronic acid, toluene - ethanol - 2M aqueous K₂CO₃, reflux, 24 h (96 %); (f) AgPF₆ in acetone, reflux, 2 h, then L1 or L2 in ⁿBuOH/^tBuOH - DMF, reflux, 18 h (19 – 42 %); (g) tpy, DMF - ethanol - N-Et-morpholine (h) DMF - NEt₃ - H₂O, reflux, 18, then counter ion exchange (60 – 70 %).

To coordinate **L1** and **L2** ligands to the $\text{RuCl}_3(\text{tpyCO}_2\text{Et})$ and $\text{RuCl}_3(\text{dqpCO}_2\text{Me})$, first, chloride ligands were abstracted by treating $\text{RuCl}_3(\text{tpyCO}_2\text{Et})$ or $\text{RuCl}_3(\text{dqpCO}_2\text{Me})$ with AgPF_6 in acetonitrile, and then the product was reacted with **L1** or **L2** by refluxing it in a mixture of DMF and $t\text{BuOH}$ or $n\text{BuOH}$.^{206,207} Thus, with **L1** and $\text{RuCl}_3(\text{tpyCO}_2\text{Et})$ or $\text{RuCl}_3(\text{dqpCO}_2\text{Me})$ complexes **1a** and **2a** were obtained. However, with **L2** this reaction condition failed. Worth to note that the complexation reaction of $\text{RuCl}_3(\text{tpyCO}_2\text{Et})$ with **L1** was conducted in a mixture of $n\text{BuOH}$ and DMF, which resulted in a complete exchange of $-\text{CO}_2\text{Et}$ group to $-\text{CO}_2\text{Bu}$. For the DSC application, the ester groups in **1a** and **2a** were hydrolyzed and thus final complexes **1** and **2** were obtained. Using ^1H - ^1H COSY NMR all the aromatic proton signals were assigned (check section 8.4.1).

As a reference for the electrochemical and optical measurements, we set a reaction of $\text{RuCl}_3(\text{dqpCO}_2\text{Me})$ with *tpy* with the expectations to obtain $[\text{Ru}(\text{tpy})(\text{dqpCO}_2\text{Me})](\text{PF}_6)_2$ as a non-cyclometalated complex. Both conditions: a reaction of $\text{RuCl}_3(\text{dqpCO}_2\text{Me})$ with *tpy* in refluxing mixture of DMF and methanol in the presence of N-ethyl-morpholine; and a procedure analogous to the synthesis of **1a** and **2a** resulted in a mauve solid product. However, the ^1H NMR of **3a** revealed lower symmetry in a molecule and absence of one aromatic proton. With further analysis of ^1H - ^1H COSY NMR spectra we guessed that one of the quinoline substituents coordinates to the ruthenium via carbanion at 7th position, resulting in a five membered chelating ring (Figure 6.2). Our hypothesis was supported with the MALDI-TOF mass spectrometry where only **3a** as $[\text{Ru}(\text{L1}_{\text{NNC}})(\text{tpy}_{\text{NNN}})]^+$ signal was observed. This outcome is first of its type and was never observed in literature before. Failure to coordinate **L2** and formation of **3a** underline than with polypyridine type of ligands a ruthenium center prefers a five-membered chelating ring over six-membered.

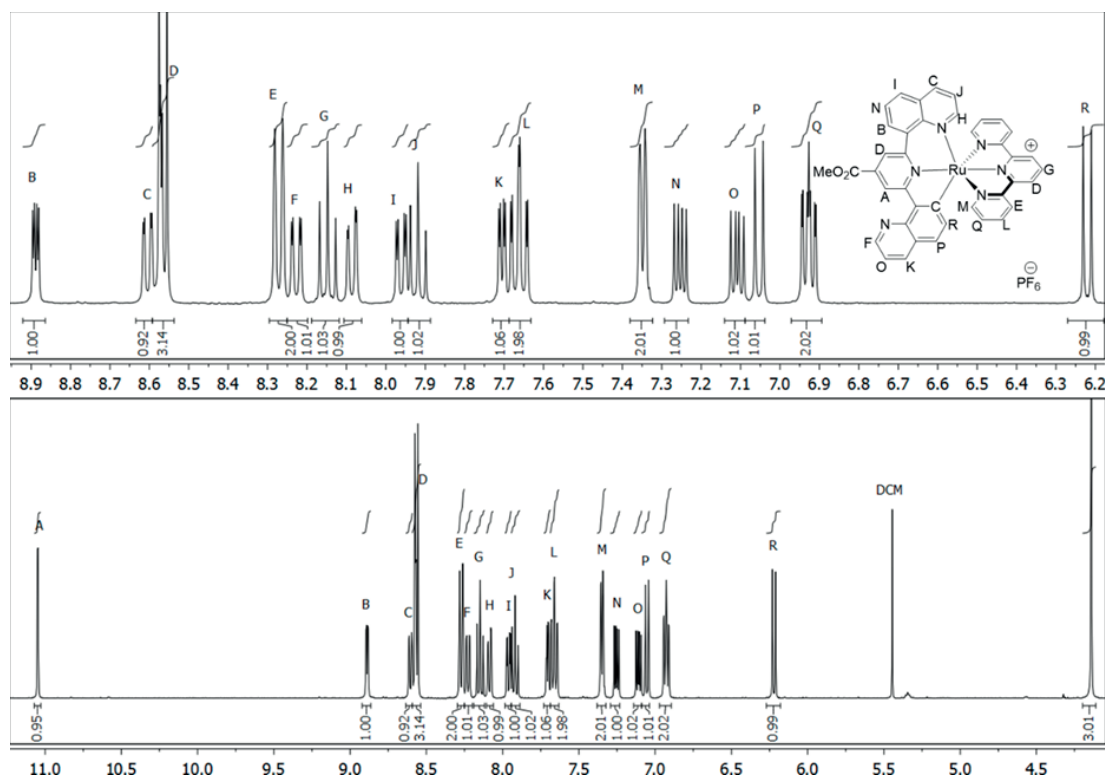


Figure 6.2. 400 MHz ^1H NMR spectrum of **3a** in acetonitrile- d_3 with assigned signals

To further support the proposed structure for **3a**, we grew crystals suitable for single crystal diffraction analysis. By slow diffusion of hexane into a concentrated DCM solution of **3a**, very thin plate-like crystals of rather poor quality were obtained. The ruthenium complex **3a** was shown to crystallize in the triclinic space group P_{-1} (CCDC 1582261). The measured crystal was twinned by a 180-degree rotation along (010). Due to the thin nature and low quality of the crystal, the collected data is of poor quality, explaining the relatively high R1 value of around 12 %. Nevertheless, all atoms could be refined anisotropically including the PF_6^- counter ion as well as the two dichloromethane solvent molecules present in the structure (Figure 6.3). The analysis confirmed the proposed structure with meridional coordination of both tridentate ligand and with one of the quinolines cyclometalated in the 7th position. Another quinoline, which coordinates to the ruthenium atom via its nitrogen, is strongly twisted, with a torsion angle of 41.46° . However, the cyclometalated quinoline is twisted by 9.72° . Six-membered chelating ring results in increased bite angle of 90.9° , which is by 10° higher than the bite angle formed by five-membered chelating rings in this complex. All the Ru-N bonds are in the range of 1.962 – 2.063 Å. However, the Ru-N4 bond length is elongated up to 2.19 Å, which is due to the *trans* influence of the cyclometalated ligand.

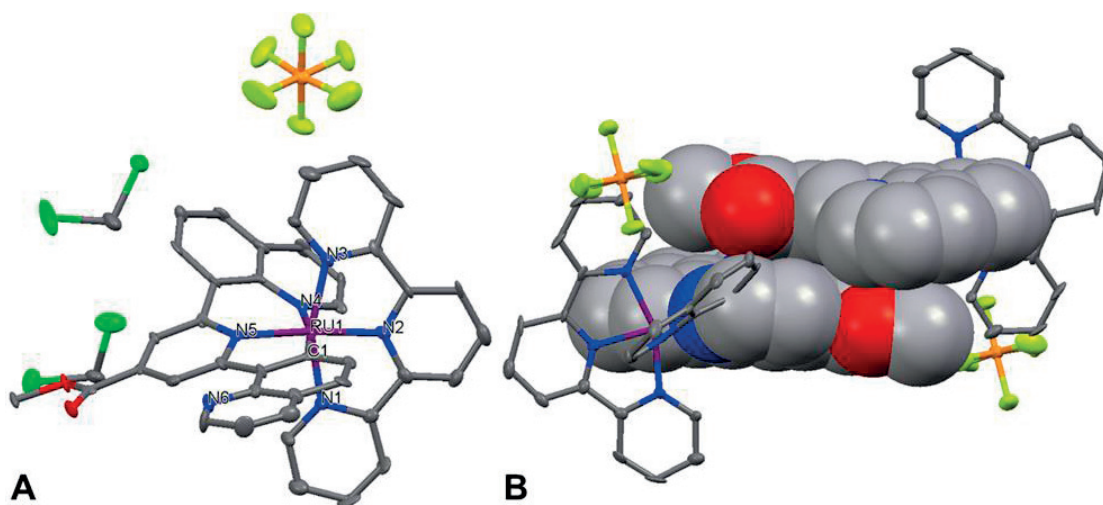


Figure 6.3. (A) Structure of **3a** with two dichloromethane solvent molecules: $3a \cdot 2\text{CH}_2\text{Cl}_2$. Ellipsoids are plotted at 50 % probability level. Color coding: Ru – purple; N – blue; O – red; C – grey; Cl – green; P – orange; F – yellow; (B) partly space-fill model showing face-to-face π -stacking interactions between the two independent cations. Solvent molecules are hidden for clarity. XRD measurements were conducted at 100 K. Selected bond lengths and angles: bond lengths in Å: Ru-N1 – 2.063(9); Ru-N2 – 1.962(8); Ru-N3 – 2.06(1); Ru-N4 – 2.19(1); Ru-N5 – 2.037(8); Ru-C – 2.00(1); angles in °: N2-Ru-N3 – 80.0(4); N2-Ru-N1 – 79.4(4); N4-Ru-N5 – 90.9(4); C1-Ru-N5 – 79.6(4); N1-Ru-N3 – 159.4(4); C1-Ru-N4 – 170.5(4).

Absorption spectra of **1**, **2** and **3a** are presented in Figure 6.4(A). Complexes **1** and **3a** exhibit similar absorption spectra. Both have a close onset around 750 nm and show two apparent bands between 400 nm and 600 nm. The extinction coefficients of the bands in the visible region of the solar spectrum for **3a** is slightly higher than those for **1**, which indicates that aromatic substituent on the donating ligand **L1** does not enhance the intensity of the absorption spectra as it would be expected. The absorption spectrum of **2** has an onset at 780 nm and covers the whole visible region of the solar spectrum. The bathochromic shift of the MLCT bands in **2** in comparison to **1** could be due to both – reduced ligand-based LUMO energy and increased metal-based HOMO energy. The reduction of the LUMO energy in **2** in comparison to **1** is due to increased electron-affinity of the π -system in *dqp* than in *tpy*. An increased HOMO energy in molecule **2** might be due to augmented electron density on the metal center caused by efficient overlap with the ligand orbitals in *dqp*.¹⁹⁸ None of these three complexes exhibit any emission at room temperature in deoxygenated dichloromethane up to 900 nm. As mentioned above, increasing the chelating ring size from five to six is favorable for long-lived and efficient emission. However, cyclometalation usually leads to inefficient emission as the optical bandgap reduces resulting in thermal deactivation.²⁰⁸

Table 6.1. Summarized data from the absorption spectra and cyclic voltammetry of new and known in literature complexes^{162,209,210}

	λ_{max} [nm]/ ϵ^*10^{-3} [M ⁻¹ cm ⁻¹]	E_{ox} , [V, vs. NHE] (ΔE_p) ^[a]	E_{red} , [V, vs. NHE] (ΔE_p) ^[a]
1	562/6.7; 504/9.1	0.72(65); 1.28(90)	-1.35(73)
2	629/6.2; 458/7.8	~0.63 (72)	-1.31(68); -1.57(111)
3a	550/10.0; 527/10.2	0.83(72)	-1.18(64); -1.46(80); -1.86 (114); -2.05(157)
[Ru(tpy) ₂](PF ₆) ₂	475/17	1.52	-1.14; -1.28
[Ru(tpy)(tpyCO ₂ Et)](PF ₆) ₂	484/18.1	1.58	-0.82; -1.22
[Ru(dpb)(tpyCO ₂ Et)](PF ₆)	559/11.1; 500/14.1	0.83	-1.11
^[a] ΔE_p represents the difference between the potentials for the anodic and cathodic current maxima.			

The cyclic voltammograms measured in 0.1 M DMF solution of NBu₄PF₆ reveal one oxidation wave for **3a** and two oxidation waves for **1** and **2** in the electrochemical window of DMF (Figure 6.4(B)). The second oxidation for **2** appears at potentials close to the solvent oxidation, which complicates its analysis. To reference the oxidation potentials, ferrocene was introduced as an internal standard. According to Wadman et al., ester group attached onto 4'' position of one of the terpyridines increases the oxidation potential by 60 mV.¹⁶² Following introduction of cyclometalation, decreases the oxidation potential by 750 mV, reaching 0.83 V in [Ru(dpb)(tpyCO₂Et)]⁺. Surprisingly, the oxidation potential of **1** is 110 mV less than that of [Ru(dpb)(tpyCO₂Et)]⁺, which might be due to the donating nature of 2,4-di(decyloxy)phenyl substituent. In molecule **2**, due to the two six-membered chelating rings, the oxidation potential decreases to 0.63 V, which is in accord with the bathochromic shift of its absorption spectrum in comparison to that of **1**. Interestingly, the oxidation potential for **3a** is higher than that for **1**. Apparently, the sum of effects from quinoline cyclometalation and higher ligand bite angle in **3a** is less prominent than donation from the cyclometalated benzene in **1**. For the molecule **1**, **2** and **3a**, one, two and four reductions respectively were observed. Double reduction in **2** in comparison to single reduction in **1** in the electrochemical window of DMF is due to extended π -system in *dqp* ligand in comparison to the *tpy*. Observation of four reduction waves in **3a** indicates that both ligands, cyclometalated *dqp* and *tpy* receive electrons.

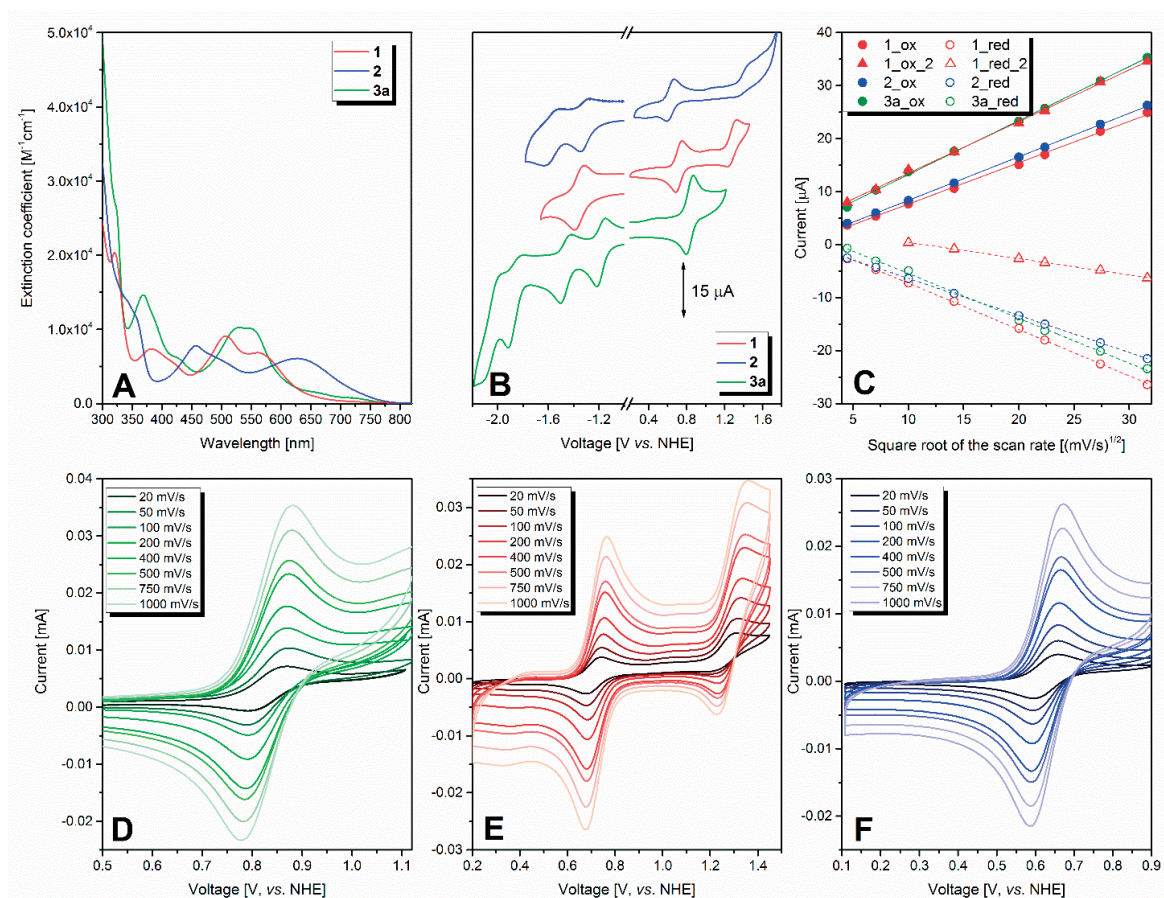


Figure 6.4. (A) Absorption spectra of complexes in 10^{-5} M DCM solution; (B) cyclic voltammograms measured in 0.1 M solution of NBu_4PF_6 in DMF under argon atmosphere. Ferrocene was used as an internal standard and its oxidation potential was positioned at 0.63 V *vs.* NHE. Corrected cyclic voltammograms without Fc are presented. (C) Randles-Sevcik analysis for complexes. (D), (E), and (F) present cyclic voltammograms of 3a, 1, and 2 respectively at different scan rates

The redox reaction of a photosensitizer in DSCs should be completely reversible as a prerequisite for the long-term performance. Both complexes, **1** and **2** undergo two oxidations. However, the second oxidation potential is almost half a volt more anodic than the first one, and only a strong oxidant may doubly oxidize these molecules. Thus, we didn't explicitly investigate the reversibility of the second oxidation. To analyze the reversibility of the first oxidation in all three molecules, we have measured the CVs at different voltage scan rates and conducted Randles-Sevcik analysis. According to the Randles-Sevcik equation, in a reversible system, the maximum current values should rise linearly with the square root of the scan rate. Analyses revealed that molecules **2** and **3a** undergo perfectly reversible first oxidation and in molecule **1** both redox processes are reversible (Figure 6.4(C, D, E, and F)). Thus, in a performing DSC, these sensitizers should be electrochemically stable, which is not the case for many sensitizers providing the record efficient DSCs.

We prepared DSCs employing sensitizers **1** and **2** with both iodine- and cobalt-based electrolytes. For that, anodes, made of conducting glass with a 4.5 μm thick mesoporous titania layer and an additional 5 μm of scattering layer on top, were dipped into a 0.2 mM solution of dye in 1:4 volume mixture of tetrahydrofuran and ethanol for 12 hours. For the counter electrode the conductive glass covered either with platinum or graphite particles for solar cells with iodine- and cobalt-based electrolytes respectively were used. The iodine-based electrolyte consisted of 1.0 M 1,3-dimethylimidazolium iodide (DMII), 0.02 M iodine, 0.05 M lithium iodide, 1 M *tert*-butyl pyridine (TBP), and 0.1 M guanidinium isothiocyanate (GNCS), while the cobalt-based electrolyte consisted of 0.25 M $[\text{Co}(\text{bpy})_3](\text{TFSI})_2$; 0.05 M $[\text{Co}(\text{bpy})_3](\text{TFSI})_3$; 0.25 M TBP; and 0.1 M LiTFSI in acetonitrile (TFSI⁻ = bis(trifluoromethane)sulfonamide anion).

Table 6.2. Average Photovoltaic Parameters of 4 Cells Measured under Simulated AM 1.5G Sunlight (100 mW cm^{-2}).

		1	2
Iodine-based devices	J_{sc}/J_{sc}^{IPCE} [mA cm^{-2}]	5.14 \pm 0.03/4.69 \pm 0.03	3.09 \pm 0.03/2.61 \pm 0.04
	V_{oc} [mV]	714 \pm 2	629 \pm 2
	FF [%]	76.7 \pm 0.1	76.9 \pm 0.1
	PCE [%]	2.8 \pm 0.2	1.5 \pm 0.1
Cobalt-based devices	J_{sc}/J_{sc}^{IPCE} [mA cm^{-2}]	4.46 \pm 0.03/3.73 \pm 0.04	0.78 \pm 0.03/0.62 \pm 0.04
	V_{oc} [mV]	679 \pm 2	512 \pm 2
	FF [%]	70.6 \pm 0.1	45.1 \pm 0.1
	PCE [%]	2.14 \pm 0.15	0.18 \pm 0.02
J_{sc}^{EQE} values were computed via wavelength integration of the product of the EQE curve measured at the short-circuit and the standard AM1.5G solar spectrum (ASTM G173-03) as described in Chapter 1.			

Photocurrent-voltage curves for assembled solar cells reveal a poor performance of these sensitizers with both electrolytes (Figure 6.5 and Table 6.2). With iodine-based electrolyte, sensitizer **1** provides power conversion efficiency (PCE) of 2.8 %, while **2** results in a PCE of only 1.5 %. Poor efficiencies obtained for these devices stem from the low photocurrent density values. Although the film absorption spectrum of **2** is much broader than that of **1**, in DSCs the former provides 40 % lower photocurrent density than the latter (Table 6.2). The photocurrent density values obtained from the J - V measurements are also supported with the incident photon-to-current conversion efficiency ($IPCE$) measurements. With the cobalt-based electrolyte the performance was even worse for both sensitizers. The PCE of DSC with **1** dropped to 2.14 % and with **2** to 0.18 %. In opposite to the $IPCE$ spectrum of

DSC with **1** and iodine-based electrolyte, the *IPCE* spectrum with cobalt-based system an apparent maximum at 400 nm is appearing. The absence of these maxima for the solar cells with iodine-based electrolyte could be due to the parasitic light absorption by iodide-electrolyte at these wavelengths.

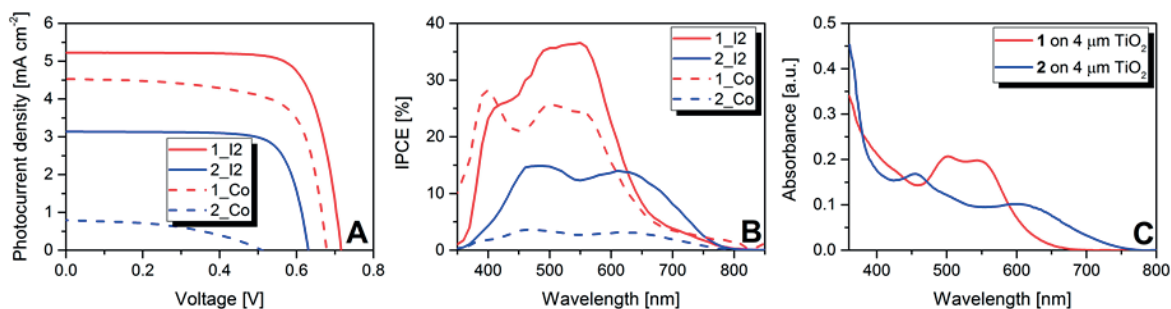


Figure 6.5. (A) *J-V* curves and (B) *IPCE* measurements for solar cells employing iodine- and cobalt-based electrolytes; (C) absorbance of 4 μm sensitized mesoporous films on ITO. Films were prepared in the same way as those for the solar cells.

The main issue restricting an efficient performance of these sensitizers could be their low regeneration rate. As discussed above, both complexes possess negatively shifted oxidation potential, with molecule **2** having more cathodic value than **1**. The regeneration with the cobalt-based electrolyte is well described by the Marcus theory for electron transfer. The driving force for the regeneration is determined as a difference between the Nernst potential of the redox shuttle and the oxidation potential of a sensitizer, while the electron transfer rate is also dependent on the reorganization energy and the electronic coupling between the donor and the electron acceptor. The Nernst oxidation potential for the cobalt-based electrolyte, which contains oxidized and reduced components in a 1:5 ratio is 0.52 V, which is only 200 mV and 110 mV more negative than the oxidation potential for **2** and **1**, respectively. These small driving forces are not enough for an efficient regeneration. As Feldt et. al. showed, with D35 sensitizer and $[\text{Co}(\text{NO}_2\text{-phen})_3]^{3+/2+}$ -based electrolyte, the driving force of 260 mV produced a regeneration with 56 % efficiency.^{105,211} With the iodide-based electrolyte the regeneration is a multistep and still not well understood process, and requires much higher driving force.^{57,144,145} Regarding the charge injection, both sensitizers should be able to efficiently inject the photoexcited electrons, as they possess a more than 450 mV cathodically shifted excited state oxidation potential compared to the conduction band edge of mesoporous titania.

6.3 Conclusion

In summary, we have synthesized and characterized three new cyclometalated ruthenium complexes with and without six-membered chelating rings. In opposite to our expectations, the complex **3a** was formed. This molecule is a first report where the pyridine-type ligand prefers cyclometalation and for-

mation of a five-membered chelating ring rather than coordinating to the metal center through its nitrogen and resulting in a six-membered ring. Although these complexes show: attractive absorption spectra with that of **2** covering all the visible region of the solar spectra; and perfectly reversible oxidation, DSCs with the molecules **1** and **2** provided poor performance. Cathodically shifted oxidation potential of these sensitizers result in low driving force and consequently inefficient regeneration. By further modifications of the coordinating ligands the oxidation potential could be tuned for the efficient solar cells.

Chapter 7 General Conclusion

One of the latest breakthroughs in the field of dye-sensitized solar cells occurred due to the introduction of Co-imine complexes as redox shuttles. With purely organic and porphyrin sensitizers, the new redox shuttle resulted in record high power conversion efficiencies that reached 13 %. However, with the classic ruthenium complexes, the new shuttle failed to perform. The problem of the incompatibility of ruthenium sensitizers and cobalt-based electrolytes in DSCs inspired the main research projects presented within this thesis. This work focuses on new cyclometalated ruthenium complexes that were designed to reach high *PCE* values with primarily cobalt-based electrolytes and partly iodine-based electrolytes.

In **Chapter 2**, I presented six new cyclometalated *tris*-heteroleptic ruthenium complexes, namely **SA22**, **SA25**, **SA246**, **SA282**, **SA284**, and **SA285**. All of the complexes possess the same cyclometalating ligand, 2',4'-bis(dodecyloxy)-2,3'-bipyridine, and anchoring ligand, 4,4'-dicarboxy-2,2'-bipyridine. However, different substituents were installed on the auxiliary ligand. All the substituents are derivatives of thiophene, except for **SA282**, for which a derivative of fluorene is used. Optical and electrochemical analyses were conducted to reveal the effects of different substituents on the photophysical characteristics of sensitizers. Additionally, spectroelectrochemical analyses showed that some substituents impart greater irreversibility to the electrochemical oxidation. Further spectroelectrochemical analyses of solar cells without the redox component revealed better electrochemical reversibility. Manufactured solar cells revealed power conversion efficiencies varying from 6.3 % to a record high of 9.4 %. The general trend in *PCE* values was explained by means of transient absorbance and electrochemical impedance spectroscopies. However, the record high efficiency of 9.4 % that was obtained with **SA246** with a thienothiophene substituent were inexplicable based on the aforementioned measurements. The fact that this sensitizer with one of the highest recombination rates provided the highest voltage and current was surprising. However, dye-loading analysis revealed that **SA246** loads onto the surface nearly two-fold more than other sensitizers; thus, higher photocurrent and voltage values are obtained. In my opinion, this work is extremely important, because it undermines the general trend in sensitizer design to attach bigger and bigger substituents to improve the photophysical

properties. Although with the cobalt-based electrolytes, bulky substituents are necessary to protect the oxide surface from the Co(3+) species, substituents that are too bulky may result in losses in dye-loading. Thus, the sweet point in substituent size should be identified.

To further support our conclusions from Chapter 2, in **Chapter 3**, we introduce three new *tris*-heteroleptic cyclometalated ruthenium complexes, namely **SA633**, **SA634**, and **SA635**. The main purpose of this work was to use redox active substituents on the auxiliary ligand, and carbazole, phenothiazine, and diphenylamine were chosen for **SA633**, **SA634**, and **SA635**, respectively. Spectroelectrochemical analyses indicate that at high enough applied voltages, the organic substituents are oxidized, and the overall oxidation is irreversible. However, at low potential, only the ruthenium center is reversibly oxidized. This finding supports again the claim that organic substituents impart redox irreversibility. Solar cells with new sensitizers, together with the cobalt-based electrolyte, provide power conversion efficiencies in the range of 7.6 – 8.2 %. **SA634** with phenothiazine substituents provided the highest value at 8.2 %. The difference in the performance of these three sensitizers is generally attributed to the different electron lifetimes obtained from transient photovoltage and photocurrent decay measurements.

Having introduced ruthenium complexes in Chapter 2, in **Chapter 4**, we discuss the performance of four sensitizers (**SA25**, **SA246**, **SA282**, and **SA285**) with an iodine-based electrolyte. I present X-ray photoemission analyses of sensitized films to reveal whether the surface is well covered. DSCs were then analysed with transient absorbance and electrochemical impedance spectroscopies. This work confirms both claims in literature: first, that sulfur atoms in the sensitizer structure catalyze dye regeneration; and second, that sulfur atoms also bind iodine/triiodide and thus accelerate charge recombination. The sensitizer **SA282** with no sulfur atom suffered from only 63 % efficient dye-regeneration, while for **SA25** and **SA246** regeneration of 96 % was observed. The bulky nature of the substituents in **SA285** also results in a reduced regeneration efficiency. However, DSCs with **SA282** still provided the highest performance, primarily due to its much lower recombination rates. This work concludes that among the two opposite effects of sulfur atoms in the dye structure on the performance of solar cells, the role of sulfur in enabling detrimental charge recombination overrides its role in advantageous dye-regeneration.

From Chapters 2 and 3, I have concluded that at some point, further complication of the sensitizer structure brings more negative features, such as reduced dye loading and electrochemical irreversibility. Thus, in the search for simpler complexes with new ligand environments, in **Chapter 5**, I introduce new ruthenium complexes with a series of bidentate ligands coordinating

to the ruthenium via both a cyclometalating carbanion and N-heterocyclic carbenes. 2,2'-bipyridine or its 4,4'-bis(methoxycarbonyl)-substituted analogue was used as an accepting ligand. All new complexes have broad absorption spectra and perfectly reversible electrochemical oxidation. One of the advantages of these complexes is the ability to control the ground state oxidation potential not only by changing the nature of the cyclometalated part of the ligand but also by varying the N-heterocyclic carbene part. As a disadvantage, the hydrolyzed sensitizers with carboxylic acid groups are insoluble in most of the organic solvents used to test them in DSCs, and solubilizing groups must be introduced.

In the last section, in **Chapter 6**, *bis*-heteroleptic ruthenium complexes with two tridentate ligands are discussed. Two complexes with similar donating cyclometalated ligands, as a derivative of 1,3-bis(pyridin-2-yl)benzene, and with different accepting ligands were prepared. The main feature that differentiates the two accepting ligands, namely 4'-carboxy-2,2':6',2''-terpyridine (L1) and 2,6-bis(quinolin-8-yl)-4-carboxy-pyridine (L2), is that with the metal center, they form two five- and six-membered chelating rings, respectively. For the comparison, a complex with L2 and terpyridine was synthesized. To our surprise, we discovered that in this complex, one of the quinoline rings is cyclometalated, resulting in one six- and one five-membered chelating rings. This new binding mode for the L2 type of ligands is shown for the first time. Unfortunately, the complexes provided poor performance in DSCs with both iodine- and cobalt-based electrolytes, which we refer to inefficient dye-regeneration due to cathodically shifted oxidation potentials.

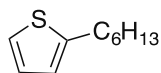
During the last four years of research on DSCs, I concluded that fundamentally new breakthroughs are necessary to improve the DSC technology. These breakthroughs have appeared before; among them are the shift from fractal to mesoporous titania, the change from iodine- to cobalt-based electrolytes, and the evolution of DSCs into organometal halide perovskite solar cells. However, the working principle of the latter technology is more close to the working principle of silicon solar cells rather than DSCs. From this thesis I can claim that the shift to more sophisticated structures is not a good strategy.

Chapter 8 Appendix

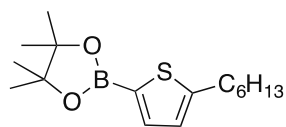
8.1 Appendix to chapter 2

8.1.1 Synthetic Procedures and material characterization

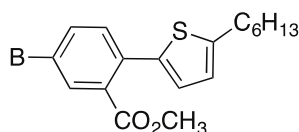
All starting materials were reagent grade and used without further purification. Anhydrous solvents were purchased from Acros Organics (THF, Toluene, acetonitrile, dichloromethane) and used as received. 2',6'-didodecyloxy-2,3'-bipyridine⁹³ and 2-bromo-9,9-dihexyl-9H-fluorene was synthesized according to the reported procedure. Standard flash column chromatography method was used either with silica (Merck: silica gel 60, 230-400 mesh ASTM) or basic alumina (Acros: aluminium oxide, basic Brockmann I, 50-200 μm , 60 A). Analytical thin-layer chromatography was performed on aluminium-backed sheets pre-coated with silica 60 F254 adsorbent (0.25 mm thick; Merck, Germany). All water and air sensitive reactions were performed in oven dried flasks and standard Schlenk techniques were used. NMR spectra have been recorded at ambient temperature in deuterated solvents on a Bruker AVANCE 400 MHz or AVANCE III 400 MHz instruments. Electrospray ionization (ESI) and matrix-assisted laser desorption ionization (MALDI) mass spectrometry data were collected at Swiss Federal Institute of Technology (EPFL).



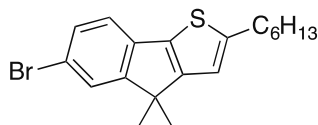
2-hexylthiophene (1).^{212,213} n-BuLi (2.5 M in hexane) (60 mL, 0.15 mol) was added dropwise to the solution of thiophene (15 g, 0.18 mol) in 150 mL of THF at -78 °C. After 45 min. upon addition, 27 g of 1-bromohexane (0.16 mol) were added to the solution. The reaction mixture was then warmed to room temperature, stirred for another 3 h and poured into water. The mixture was extracted with ether, dried over MgSO_4 , and the solvent evaporated. The compound was purified by flash chromatography (silica/hexane). 20 g of pure product (colorless liquid) were obtained (Yield: 67%). ¹H NMR (400 MHz, *Chloroform-d*) δ 7.18 (d, J=4 Hz, 1H), 7.00 (t, J=4 Hz, 1H), 6.87 (d, 4Hz, 1H), 2.91 (t, 2H), 1.8 (p, 2H), 1.5-1.3 (m, 4H), 1 (t, 3H).



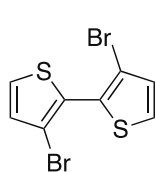
2-(5-hexylthiophen-2-yl)-4,4,5,5-tetramethyl-1,3,2-dioxaborolane (2).^{214,215} A solution of **1** (10 g, 60 mmol) in dry THF (30 ml) was cooled to -78 °C under nitrogen and treated with a 2.5 M solution of BuLi in hexane (27.5 mL, 68 mmol). The temperature was slowly raised to room temperature and the reaction mixture was stirred for 25-30 minutes. The reaction mixture was cooled again to -78 °C and the 2-isopropoxy-4,4,5,5-tetramethyl-1,3,2-dioxaborolane (14 mL, 68 mmol) was added. Then the mixture was stirred for 3 h and the solvent was removed in the vacuo. The crude product was dissolved in CH_2Cl_2 and the solution was washed with water. Dried solution was purified by flash chromatography (silica/ CH_2Cl_2). Then the solvent was evaporate to give 15.2 g of yellow oil (Yield: 87 %). ¹H NMR (400 MHz, *Chloroform-d*) δ 7.5 (s, 1H), 6.9 (s, 1H), 2.8 (t, 2H), 1.7 (p, 2H), 1.4-1.2 (m, 4H), 0.9 (t, 3H).



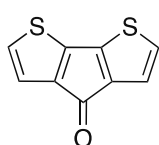
Methyl 2-(5-hexylthiophen-2-yl)-5-bromobenzoate (3).²¹⁶ **2** (4.32 g, 14.7 mmol) methyl-5-bromo-2-iodobenzoate (5 g, 14.7 mmol), K_2CO_3 (5.52 g) were dissolved in toluene (80 ml) and water (20 ml). Then the mixture was degassed with nitrogen for 30 minutes. After, 5 mol % of $Pd(PPh_3)_4$ (0.44 mmol) was added to the mixture. Then the mixture was stirred at 85 °C for 48 h. The reaction progress was checked by TLC (hexane : dichloromethane 3:1). After evaporating the solvent under reduced pressure, water was added and the product was extracted by dichloromethane. Organic layer was dried on magnesium sulfate and the pure product was obtained by column chromatography on silica gel (hexane: dichloromethane 3:1). After drying under high vacuum 3.6 g (64 %) of yellow viscous product was obtained. 1H NMR (400 MHz, *Chloroform-d*) δ 7.82 (d, $J=2,2$ Hz, 1H), 7.58 (dd, $J=8.3, 2,2$ Hz, 1H), 7.34 (d, $J=8,3$ Hz, 1H), 6.85 (d, $J=3.5$ Hz, 1H), 6.73 (d, $J=3.5$ Hz, 1H), 2.83 (t, $J=7.6$ Hz, 2H), 1.71 (p, $J=7.5$ Hz, 2H), 1.43-1.27 (m, 6H), 0.92 (t, 3H).



2-hexyl-6-bromo-4,4-dimethyl-4H-indeno[1,2-*b*]thiophene (4).²¹⁶ To the two-necked flask dropping-glass funnel was attached and system was dried by heating gun and degassed with nitrogen. **3** (4.6 g, 12 mmol) was dissolved in 60 ml of dry THF and $MeMgBr$ (1M in THF, 36 mL, 36 mmol) was dropwise added over 2 hours and reaction mixture was stirred under nitrogen overnight. After reaction mixture was neutralized with 1M HCl and organic products were extracted by dichloromethane, dried over magnesium sulfate and evaporated to the minimal amount. Tertiary alcohol without further purification was used for the next step. 4:1 mixture of glacial acetic acid and 98% sulfuric acid (80 mL) was added; mixture was purged with nitrogen and refluxed for 6 hours. After reaction mixture was cooled down, neutralized with 25 M solution of ammonia, extracted with dichloromethane, dried over magnesium sulfate and purified by flash chromatography (hexane:DCM 4:1). (1.54 g, yield: 35%). 1H NMR (400 MHz, *Chloroform-d*) δ 7.45 (d, $J=1.8$ Hz, 1H), 7.37 (dd, $J=8.0, 1.8$ Hz, 1H), 7.19 (d, $J=8.0$ Hz, 1H), 6.72 (s, 1H), 2.85 (t, $J=7.2$ Hz, 2H), 1.72 (p, $J=7.4$ Hz, 2H), 1.43 (s, 6H), 1.40-1.23 (m, 6H), 0.91 (t, 1H).

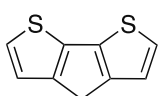


3,3'-dibromo-2,2'-bithiophene (5).²¹⁷ To the stirring solution of 3-bromothiophene (20.0 g; 122.8 mmol) in 150 mL dry tetrahydrofuran at -78 °C freshly prepared lithium diisopropylamide (LDA) (122.8 mmol) in 80 mL of dry THF was added dropwise. After stirring at -78 °C for one hour copper (II) chloride ($CuCl_2$) (33 g; 245 mmol) was added portionwise and the reaction mixture was stirred another one hour at -78 °C and 5 hours at room temperature. Afterwards, the reaction mixture was quenched with saturated aqueous solution of ammonia chloride. Organic phase was extracted with dichloromethane, washed with water and dried over magnesium sulfate and evaporated to minimal amount. Pure product was obtained by column chromatography on silica gel (hexane:DCM 95:5) applying a dry loading of the product in hexane due to bad solubility in hexane. (13.9 g, yield: 70 %). 1H NMR (400 MHz, *Chloroform-d*) δ 7.40(d, $J=5.4$ Hz, 2H), 7.09 (d, $J=5.4$ Hz, 2H).

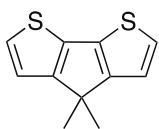


4H-cyclopenta[1,2-*b*:5,4-*b'*]dithiophene-4-one (6).²¹⁸ In the oven dried Schlenk tube **5** (4 g, 12.3 mmol) was dissolved in 30 mL of dry THF under nitrogen. Solution was cooled down to -78 °C and $n-BuLi$ (2.5 M in hexanes, 10 mL, 25 mmol) was dropwise, while colorless mixture became yellowish. Then mixture was stirred for 30 minutes and N,N -dimethylcarbonyl chloride (1.335 g, 12.4 mmol) in 10 mL of dry

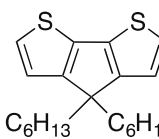
THF was added, mixture warmed up to 0 °C and stirred for 3h. Then aqueous solution of ammonia chloride (4.84 g, in 36 mL of water) was added, during what the mixture becomes intensely red. Organic phase was extracted with hexanes, washed with water and dried over magnesium sulfate. Pure product was obtained after column chromatography on silica gel (hexane:EtOAc 30:1). (1.38 g, yield: 58 %). ¹H NMR (400 MHz, Chloroform-*d*) δ 7.05 (d, J=4.9 Hz, 2H), 7.01 (d, J=4.9 Hz, 2H).



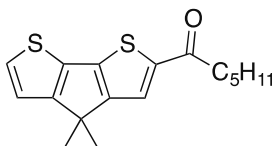
4H-cyclopenta[1,2-*b*:5,4-*b'*]dithiophene (7).²¹⁶ Finely ground potassium hydroxide (0.5 g) was added to the suspension of **6** (0.5 g, 2,6 mmol) in 100 mL of ethylene glycol under nitrogen. Then the mixture was heated to 200 °C and hydrazine hydrate (1 mL) was added dropwise. The mixture was stirred at 200 °C 2 hours more, cooled to room temperature and quenched with water (10 mL). The organic phase was extracted with diethyl ether, washed with water, brine and dried over magnesium sulfate. After evaporating the solvent a crude product was purified by flash chromatography over silica and hexane as an eluent. (279 mg, yield: 67%). ¹H NMR (400 MHz, Chloroform-*d*) δ 7.19 (d, J=4.9 Hz, 1H), 7.10 (d, J=4.9 Hz, 1H), 3.65 (s, 2H).



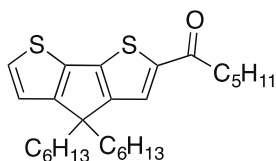
4,4-dimethyl-4H-cyclopenta[1,2-*b*:5,4-*b'*]dithiophene (8).²¹⁶ To the mixture of **7** (450 mg, 2,5 mmol), KI (35 mg), MeI (850 mg, 6 mmol) in DMSO (15 mL), at 0 °C potassium hydroxide (500 mg) in one portion was added. Then the reaction mixture was stirred at room temperature for 12 hours. After, organic phase was extracted with ether and washed several times with water to decrease the amount of DMSO in organic phase. Then, combined organic phases were dried over MgSO₄, evaporated and purified by flash chromatography on silica gel with hexane as an eluent.: (0.49 g, yield: 95 %). ¹H NMR (400 MHz, Chloroform-*d*) δ 7.16 (d, J=4.9 Hz, 1H), 7.00 (d, J=4.9 Hz, 1H), 1.46 (s, 6H).



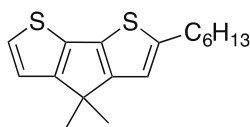
4,4-dihexyl-4H-cyclopenta[1,2-*b*:5,4-*b'*]dithiophene (9).²¹⁶ was synthesized according to the procedure described for **8**. **7** (660 mg, 3.7 mmol), KOH (623 mg, 11.1 mmol), hexylbromide (1.83 g, 11.1 mmol) and KI (15 mg, 0.1 mmol) in 40 mL DMSO was used. For purification a column chromatography on silica (hexane) yielded bright yellow oil. (1.15 g, 90 %). ¹H NMR (400 MHz, Chloroform-*d*) δ 7.15 (d, J = 4.8 Hz, 2H), 6.93 (d, J = 4.9 Hz, 2H), 1.87 – 1.78 (m, 4H), 1.24 – 1.12 (m, 12H), 0.94 (m, 4H), 0.81 (t, J = 6.9 Hz, 6H).



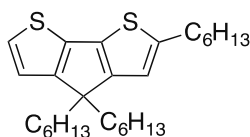
1-(4,4-dimethyl-4H-cyclopenta[2,1-*b*:3,4-*b'*]dithiophen-2-yl)hexan-1-one (10).²¹⁶ In the oven dried two-necked flask **8** (490 mg, 2.37 mmol) was dissolved in dry dichloromethane under nitrogen and hexanoyl chloride was added (320 mg, 2.4 mmol). Then reaction mixture was stirred for 30 minutes, cooled to 0 °C and aluminium chloride (350 mg, 2.62 mmol) was portionwise added. After the reaction mixture was heated up to room temperature and stirred for 24 hours. Then aluminium chloride was quenched with 5 mL of water and mixture was acidified with 2M HCl. Organic phase was extracted with dichloromethane, washed with water and dried over magnesium sulfate. Pure product was obtained after column chromatography on silica gel (hexane:DCM 1:1). (446 mg, yield: 62 %). ¹H NMR (400 MHz, Chloroform-*d*) δ 7.60 (s, 1H), 7.34 (d, J=4.9 Hz, 1H), 7.03 (d, J=4.9 Hz, 1H), 2.88 (t, 2H), 1.76 (p, 2H), 1.49 (s, 6H), 1.47-1.33 (m, 4H), 0.93 (t, 3H).



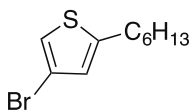
1-(4,4-dihexyl-4H-cyclopenta[1,2-b:5,4-b']dithiophen-2-yl)hexan-1-one (11)²¹⁶ was synthesized according to the procedure described for **10**. 9 (1.15 g, 3.32 mmol), hexanoyl chloride (455 mg, 3.4 mmol), AlCl₃ (465 mg, 3.5 mmol) in 20 ml dry DCM were used. Column chromatography on silica (hex:DCM 2:3) yielded a pure product (620 mg, 42 %). ¹H NMR (400 MHz, *Chloroform-d*) δ 7.53 (s, 1H), 7.31 (d, *J* = 4.9 Hz, 1H), 6.95 (d, *J* = 4.9 Hz, 1H), 2.86 (t, *J* = 7.5 Hz, 2H), 1.84 (dd, *J* = 10.4, 6.2 Hz, 4H), 1.76 (p, *J* = 7.4 Hz, 2H), 1.42 – 1.32 (m, *J* = 5.2 Hz, 4H), 1.21 – 1.06 (m, 12H), 0.97 – 0.87 (m, 7H), 0.79 (t, *J* = 6.8 Hz, 6H).



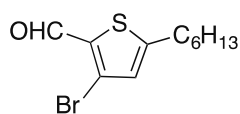
2-hexyl-4,4-dimethyl-4H-cyclopenta[2,1-b:3,4-b']dithiophene (12)²¹⁶ LiAlH₄ (200 mg, 5.26 mmol) and AlCl₃ (666 mg, 5 mmol) were dissolved separately in 6 mL dry ether each under nitrogen at 0 °C and then solutions were combined. Afterwards, **10** (446 mg, 1.47 mmol) in 6 mL of dry ether was added via syringe to the mixture at 0 °C. After, ice bath was taken away and mixture was stirred for 4 hours. Then to quench the reaction 1 mL of ether and 2 mL of 2M HCl was added carefully. Organic phase was extracted with ether washed with water and dried over magnesium sulfate. Pure product was obtained after column chromatography on silica gel (hexane). (234 mg, yield: 55%). ¹H NMR (400 MHz, *Chloroform-d*) δ 7.14 (d, *J* = 4.9 Hz, 1H), 7.03 (d, *J* = 4.9 Hz, 1H), 6.76 (s, 1H), 2.90 (t, *J* = 7.7 Hz, 2H), 1.78 (p, *J* = 7.4 Hz, 2H), 1.50 (s, 6H), 1.48–1.24 (m, 6H), 0.99 (t, 3H).



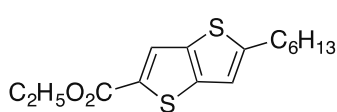
2,4,4-trihexyl-4H-cyclopenta[1,2-b:5,4-b']dithiophene (13). In an oven-dried double-neck flask equipped with a condenser NaBH₄ (190 mg, 5 mmol) was dissolved in dry THF (15 mL) and AlCl₃ (400 mg, 3 mmol) was added portionwise. Afterwards, **11** (444 mg, 1 mmol) in dry THF (10 mL) was added via syringe and the reaction mixture was refluxed for 20 h. Then, the reaction was carefully quenched with icy water, extracted with DCM, washed several times with water and collected organic phases were dried over anhydrous MgSO₄. After separation, a filtrate was evaporated to small amount and loaded into column chromatography on silica (hexane) to obtain the pure product. (237 mg, 55 %). ¹H NMR (400 MHz, *Chloroform-d*) δ 7.12 (d, *J* = 4.8 Hz, 1H), 6.96 (d, *J* = 4.8 Hz, 1H), 6.68 (s, 1H), 2.89 (t, *J* = 7.6 Hz, 2H), 1.88 – 1.82 (m, 4H), 1.75 (p, *J* = 7.4 Hz, 2H), 1.49 – 1.31 (m, 6H), 1.29 – 1.15 (m, 8H), 1.06 – 0.98 (m, 7H), 0.98 – 0.93 (m, 4H), 0.88 (t, *J* = 6.9 Hz, 6H).



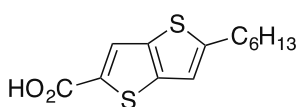
3-bromo-5-hexylthiophene (14)²¹⁹ In the oven-dried Schlenk flask freshly distilled diisopropylamine (22 mL, 156.7 mmol) was dissolved in dry THF (150 mL) and *n*-butyllithium (2.5 M, 43.8 mL) was slowly added via syringe at 0 °C. After 20 minutes, 2-bromo-5-hexylthiophene in dry THF (80 mL) was added via syringe. The reaction mixture was allowed to warm up to room temperature and stirred for 18 hours. Afterwards, the reaction was quenched with water; the organic phase was extracted with dichloromethane and washed several times with deionized water. The organic phase was dried over magnesium sulfate, and concentrated via rotary evaporation. The pure product obtained after column chromatography on silica gel (hexane) (19.25 g, yield: 86 %). ¹H NMR (400 MHz, *Chloroform-d*) δ 7.01 (s, 1H), 6.71 (s, 1H), 2.78 (t, *J* = 7.6 Hz, 2H), 1.66 (p, *J* = 7.7 Hz, 2H), 1.42–1.28 (m, 6H), 0.91 (t, *J* = 6.9 Hz, 3H).



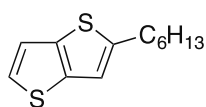
3-bromo-5-hexylthiophene-2-carbaldehyde (15).²²⁰ To the freshly prepared lithium diisopropylamide (77 mmol) in THF (100 mL), **14** (19 g, 77 mmol) was added dropwise at 0 °C. After stirring the reaction mixture for 1 hour, dimethylformamide (6 mL, 77 mmol) was added at 0 °C and the mixture was allowed to warm up to room temperature and stirred for the following 6 hours. Afterwards, the reaction was quenched with water, organic phase was extracted with dichloromethane, washed with deionized water several times and the organic phase was dried over magnesium sulfate, and solvent was evaporated under vacuum to obtain the product (21.17 g, yield: 99 %). ¹H NMR (400 MHz, Chloroform-*d*) δ 9.85 (s, 1H), 6.83 (s, 1H), 2.81 (t, J=7.7 Hz, 2H), 1.65 (m, 2H), 1.70-1.55 (m, 6H), 0.90-0.83 (m, 3H).



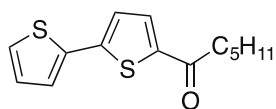
Ethyl 5-hexylthieno[3,2-b]thiophene-2-carboxylate (16).²²⁰ **15** (21 g, 76 mmol) was added to the mixture of potassium carbonate (14 g, 0.1 mol) and ethyl 2-sulfanylacetate (10 g, 0.74 mmol) in dimethylformamide (100 mL) and the reaction mixture was stirred for 3 days at room temperature. Afterwards, the reaction mixture was extracted with dichloromethane and washed numerous times with water to delete as much dimethylformamide as possible. The organic phase was dried over magnesium sulfate, concentrated via rotary evaporation and column chromatography on silica gel (DCM) was used to obtain a pure product (13.5 g, 62 %). ¹H NMR (400 MHz, Chloroform-*d*) δ 7.89 (s, 1H), 6.95 (s, 1H), 4.36 (q, J=7.1 Hz, 2H), 2.88 (t, J=7.6 Hz, 2H), 1.71 (p, J=7.5 Hz, 2H), 1.43-1.24 (m, 9H), 0.89 (m, 3H).



5-hexylthieno[3,2-b]thiophene-2-carboxylic acid (17).²²⁰ **16** (13.5 g, 46 mmol) and lithium hydroxide monohydrate (4.2 g, 100 mmol) were dissolved in a mixture of THF (100 mL) and water (100 mL) and the reaction mixture was refluxed for 6 hours. Afterwards, the solvent was evaporated via rotary evaporation to small amount and concentrated hydrochloric acid was added to obtain a white precipitate. Then the mixture was dissolved in chloroform and washed with deionized water. The organic phase was dried over magnesium sulfate and the solvent was evaporated under vacuum to obtain white product. (12.23 g, yield: 99 %). ¹H NMR (400 MHz, Chloroform-*d*) δ 8.03 (s, 1H), 7.29 (s, 1H), 7.02 (s, 1H), 2.94 (t, J=7.6 Hz, 2H), 1.76 (p, J=7.6 Hz, 2H), 1.47-1.28 (m, 6H), 0.94-0.89 (m, 3H).

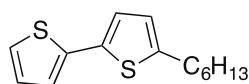


2-hexylthieno[3,2-b]thiophene (18).²²⁰ To the solution of **17** (12 g, 45 mmol) in quinolone (50 mL) copper (II) oxide (1 g) was added and the mixture was refluxed at 260 °C for 1 hour. Afterwards, the mixture was cooled to room temperature, filtered, extracted with dichloromethane and washed with deionized water. The organic phase was dried over magnesium sulphate, and concentrated via rotary evaporation. To obtain pure product, column chromatography on silica gel (hexane) was used (7.7 g, yield: 76 %). ¹H NMR (400 MHz, Chloroform-*d*) δ 7.34 (d, J=5.1 Hz, 1H), 7.26 (d, J=5.2 Hz, 1H), 7.04 (s, 1H), 2.97 (t, J=7.7 Hz, 2H), 1.85-1.77 (m, 2H), 1.54-1.38 (m, 6H), 1.03 (t, J=7.8 Hz, 3H).

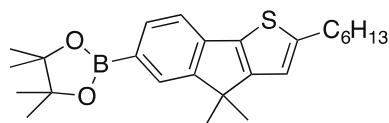


1-([2,2'-bithiophen]-5-yl)hexan-1-one (19)²²¹ was synthesized according to the procedure described for **10**. 2,2'-bithiophene (1.5 g, 9 mmol), hexanoyl chloride (1.24 g, 9.2 mmol), aluminum trichloride (1.24 g, 9.3 mmol) was used. Column chromatography on silica gel (hexane:DCM 2:1 to 1:1) was used to obtain a pure product (2 g, yield: 84 %). ¹H NMR (400 MHz, Chloroform-*d*) δ 7.60 (d, J=3.9 Hz,

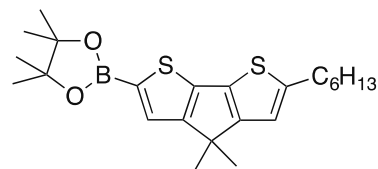
1H), 7.33-7.30 (m., 2H), 7.17 (d, J=4.0 Hz, 1H), 7.06 (dd, J=5.0, 3.8 Hz, 1H), 2.86 (t, J=7.5 Hz, 2H), 1.75 (p, J=7.4 Hz, 2H), 1.36 (m, 4H), 0.91 (t, J=7.1 Hz, 3H).



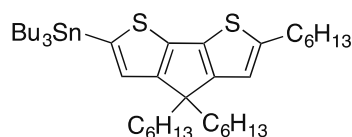
5-hexyl-2,2'-bithiophene (20) was synthesized according to the procedure described for **13**. Sodium borohydride (1.43 g, 37.9 mmol), aluminum trichloride (3 g, 22.7 mmol) and **19** (2 g, 7.57 mmol) was used. The product was purified on column chromatography on silica gel (hexane) and yellow oil was obtained (1.22 g, 64 %). ¹H NMR (400 MHz, Chloroform-*d*) δ 7.17 (d, J=5.1 Hz, 1H), 7.11 (d, J=3.6 Hz, 1H), 7.01 (m, 2H), 6.69 (d, J=3.5 Hz), 2.81 (t, J=7.6 Hz, 2H), 1.70 (p, J=7.5 Hz, 2H), 1.45-1.30 (m, 6H), 0.96-0.88 (m, 3H).



2-(2-hexyl-4,4-dimethyl-4H-indeno[1,2-*b*]thiophen-6-yl)-4,4,5,5-tetramethyl-1,3,2-dioxaborolane (23).²¹⁶ **4** (1.4 g, 3.85 mmol) was dissolved in 30 mL of dry THF in oven dried Schlenk flask under nitrogen. Then the solution was cooled down to -41 °C by the acetonitrile/dry ice cooling bath. *n*-BuLi (2.5 M in hexanes, 1.9 mL, 4.74 mmol) was added via syringe dropwise. Then solution was stirred for 2 hours at -41 °C and 2-isopropoxy-4,4,5,5-tetramethyl-1,3,2-dioxaborolane (0.88 g, 4.74 mmol) was added. After, reaction mixture was heated up to room temperature and stirred overnight. Then organic phase was extracted with dichloromethane, washed with water and dried over magnesium sulfate. Pure product was obtained after flash chromatography on silica gel. (hexane :EtOAc 5:1). (0.695 g, yield: 43 %). ¹H NMR (400 MHz, Chloroform-*d*) δ 7.78 (s, 1H), 7.76 (d, J=7.4 Hz, 1H), 7.36 (d, J=7.4 Hz, 1H), 6.76 (s, 1H), 2.87 (t, J=7.3 Hz, 2H), 1.74 (p, J=7.3 Hz, 2H), 1.47 (s, 6H), 1.39 (s, 12H), 1.49-1.24 (m, 6H), 0.93 (t, 3H).

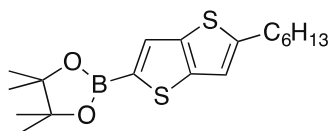


2-(6-hexyl-4,4-dimethyl-4H-cyclopenta[2,1-*b*:3,4-*b'*]dithiophen-2-yl)-4,4,5,5-tetramethyl-1,3,2-dioxaborolane (24).²¹⁶ In the oven dried Schlenk flask **12** (190 mg, 0.65 mmol) was dissolved in 3 mL of dry THF, then solution was cooled down to -41 °C and *n*-BuLi (2.5 M in hexane, 0.314 mL, 0.78 mmol) was dropwise added. After, reaction mixture was stirred at -41 °C for 2 hours, and 2-isopropoxy-4,4,5,5-tetramethyl-1,3,2-dioxaborolane (146 mg, 0.78 mmol) was added. Then, cooling bath was taken away and mixture stirred at room temperature overnight. Organic phase after was extracted with dichloromethane, washed with water and dried over magnesium sulfate. To obtain pure product column chromatography on silica gel was run (EtOAc). (153 mg, 56%). ¹H NMR (400 MHz, Chloroform-*d*) δ 7.51 (s, 1H), 6.72 (s, 1H), 2.85 (t, J=7.7 Hz, 2H), 1.72 (p, J=7.4 Hz, 2H), 1.44 (s, 6H), 1.37 (s, 12H), 1.42-1.39 and 1.36-1.25 (m, 6H), 0.92 (t, J=7.0 Hz, 3H).

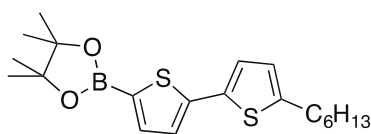


Tributyl(4,4,6-trihexyl-4H-cyclopenta[1,2-*b*:5,4-*b'*]dithiophen-2-yl)stannane (25). In the oven-dried Schlenk flask **13** (248 mg, 0.58 mmol) was dissolved in THF (10 mL) under nitrogen and *n*-BuLi (2.5 M, 0.3 mL, 0.75 mmol) was added via syringe at -78 °C. After stirring at this temperature for 2 hours, tributyltin chloride (244 mg, 0.75 mmol) was added at -78 °C and the reaction mixture was allowed to warm up to room temperature naturally and was stirred for the following 6 hours. Afterwards, the reaction was quenched with water, organic phase was extracted with dichloromethane and washed with deionized water. The organic phase was dried over magnesium sulfate and solvent was evaporated under vacuum. Product was not purified and yield was considered as 100 %, which is consistent with ¹H NMR analysis. ¹H NMR (400 MHz, Chloroform-*d*) δ 6.88 (s, 1H), 6.60 (s,

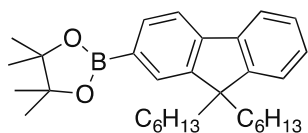
1H), 2.82 (t, $J=7.5$ Hz, 2H), 1.77 (m, 2H), 1.71-1.51 (m, 4H), 1.41-1.24 (m, 4H), 1.2-1.08 (m, 6H), 1.00-0.86 (m, 10H), 0.81 (t, $J=6.9$ Hz, 12H).



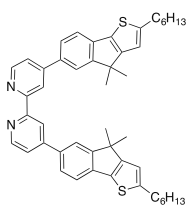
2-(5-hexylthieno[3,2-b]thiophen-2-yl)-4,4,5,5-tetramethyl-1,3,2-dioxaborolane (26) was synthesized according to the procedure described for **24**.²²² **18** (2.27 g, 10.1 mmol), 2.5 M *n*-BuLi solution in hexanes (4.9 mL, 12.15 mmol), 2-isopropoxy-4,4,5,5-tetramethyl-1,3,2-dioxaborolane (2.26 g, 12.2 mmol) in dry THF (20 mL) was used. A flash chromatography on silica (hexanes) was used to obtain the pure product. (3.32 g, 94 %). ¹H NMR (400 MHz, *Chloroform-d*) δ 7.75 (s, 1H), 6.98 (s, 1H), 2.89 (t, $J = 7.5$ Hz, 2H), 1.75 (t, $J = 7.4$ Hz, 2H), 1.48 – 1.32 (m, 18H), 0.96 (m, 3H).



2-(5'-hexyl-[2,2'-bithiophen]-5-yl)-4,4,5,5-tetramethyl-1,3,2-dioxaborolane (27).²²³ In the oven-dried Schlenk flask 5-hexyl-2,2'-bithiophene (1.22 g, 4.9 mmol) was dissolved in dry THF (20 mL) and *n*-butyllithium (2.5 M, 2.4 mL, 5.9 mmol) was added dropwise at -78 °C. After stirring for 2 hours 2-isopropoxy-4,4,5,5-tetramethyl-1,3,2-dioxaborolane (1.1 g, 5.9 mmol) was added at the same temperature and the reaction mixture was stirred for the following 6 hours allowing to warm up to room temperature. Afterwards, the reaction was quenched with water, organic phase was extracted with dichloromethane, washed with deionized water; the organic phase was dried over magnesium sulfate and concentrated via rotary evaporation. The pure product was obtained after flash column on silica (DCM) (625 mg, 34 %). ¹H NMR (400 MHz, *Chloroform-d*) δ 7.55 (d, $J=3.6$ Hz, 1H), 7.19 (d, $J=3.6$ Hz, 1H), 7.07 (d, $J=3.5$ Hz, 1H), 6.70 (d, $J=3.6$ Hz, 1H), 2.80 (t, $J=7.6$ Hz, 2H), 1.70 (p, $J=7.6$ Hz, 2H), 1.49-1.31 (m, 18H), 0.94 (t, $J=7.1$ Hz, 3H).

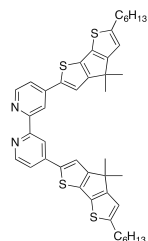


2-(9,9-dihexyl-9H-fluoren-2-yl)-4,4,5,5-tetramethyl-1,3,2-dioxaborolane (28).²²⁴ In the oven dried Schlenk tube 2-bromo-9,9-dihexyl-9H-fluorene (850 mg, 2.06 mmol), 4,4,4',4',5,5,5',5'-octamethyl-2,2'-bi(1,3,2-dioxaborolane) (B₂Pin₂) (574 mg, 2.26 mmol), potassium acetate (606 mg, 6.2 mmol) and [1,1'-bis(diphenylphosphino)ferrocene]dichloropalladium (II) (Pd(dppf)Cl₂) (90 mg, 0.12 mmol) were degassed under vacuum and refilled with nitrogen, then dry 1,4-dioxane (20 mL) was added. The reaction mixture was stirred at 80 °C for 6 hours and then cooled down, extracted with dichloromethane, washed with deionized water. The organic phase was dried over magnesium sulfate, concentrated to small amount via rotary evaporation. The Pure product was obtained after column chromatography on silica gel (Hexane:DCM 1:1). (881 mg, yield: 93 %). ¹H NMR (400 MHz, *Dichloromethane-d*₂) δ 7.87 (m, 2H), 7.84-7.79 (m, 2H), 7.47-7.38 (m, 3H), 2.11(d, $J=8.2$ Hz, 4H), 1.46 (s, 12 H), 1.24-1.07 (m, 16H), 0.85 (t, $J=7.1$ Hz, 6H).

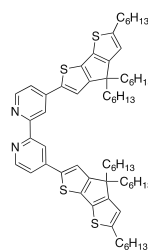


4,4'-bis(2-hexyl-4,4-dimethyl-4H-indeno[1,2-b]thiophen-6-yl)-2,2'-bipyridine (29).²¹⁶ 8 mL of 2M water solution of potassium carbonate and 30 mL of toluene with **23** (600 mg, 1.47 mmol) and 4,4'-dibromo-2,2'-bipyridine (182 mg, 0.58 mmol) were purged for 20 minutes with nitrogen in Schlenk tube. Then Pd(PPh₃)₄ (56 mg, 0.048 mmol) was added; tube was capped and reaction mixture was heated up to 85 °C and stirred for 24 hours. Then mixture was cooled down to room temperature, organic phase was extracted with dichloromethane, washed with water, dried over magnesium sulfate and evaporated to minimal amount. Pure component was obtained by column chromatography

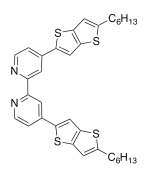
on silica gel (Hexane:EtOAc 1:3). (373 mg, yield: 89 %). $^1\text{H NMR}$ (400 MHz, *Chloroform-d*) δ 8.81 (d, $J=1.3$ Hz, 2H), 8.79 (d, $J=5.2$ Hz, 2H), 7.80 (d, $J=1.7$ Hz, 2H), 7.71 (dd, $J=7.9, 1.7$ Hz, 2H), 7.63 (dd, $J=5.2, 1.9$ Hz, 2H), 7.46 (d, $J=7.9$ Hz, 2H), 6.79 (s, 2H), 2.89 (t, $J=7.7$ Hz, 4H), 1.76 (p, $J=7.4$ Hz, 4H), 1.55 (s, 13H), 1.49-1.24 (m, 12H), 0.94 (t, $J=7.0$ Hz, 6H).



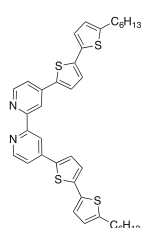
4,4'-bis(6-hexyl-4,4-dimethyl-4H-cyclopenta[2,1-b:3,4-b']dithiophen-2-yl)-2,2'-bipyridine (30).²¹⁶ This compound was synthesized by the procedure absolutely similar for the synthesis of **29**. From **24** (153 mg, 0.36 mmol) product was obtained (120 mg, yield: 83%). $^1\text{H NMR}$ (400 MHz, *Chloroform-d*) δ 8.67-8.62 (m, 4H), 7.63 (s, 2H), 7.46 (d, $J=3.6$ Hz, 2H), 6.74 (s, 2H), 2.86 (t, $J=7.8$ Hz, 4H), 1.73 (p, $J=7.6$ Hz, 4H), 1.49 (s, 12H), 1.45-1.28 (m, 6H), 0.92 (t, $J=6.6$ Hz, 6H).



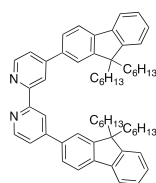
4,4'-bis(6-hexyl-4,4-dihexyl-4H-cyclopenta[2,1-b:3,4-b']dithiophen-2-yl)-2,2'-bipyridine (31).²¹⁶ In the oven-dried Schlenk tube **25** (0.58 mmol), 4,4'-dibromo-2,2'-bipyridine (60 mg, 0.19 mmol) and tetrakis(triphenylphosphine)palladium(0) ($\text{Pd}(\text{PPh}_3)_4$) (33 mg, 0.03 mmol) were degassed under high vacuum and refilled with nitrogen and then dry dimethylformamide (10 mL) was added via syringe and the mixture was stirred at 85 °C for 12 hours. After completion, the reaction mixture was extracted with dichloromethane, washed several times with deionized water, organic phase was dried over magnesium sulfate and concentrated via rotary evaporation. The pure product was obtained after column chromatography on silica (DCM-methanol-triethylamine 98-2-0.1) (120 mg, 62 %). $^1\text{H NMR}$ (400 MHz, *Chloroform-d*) δ 8.64 (m, 4H), 7.56 (s, 2H), 7.46 (d, $J=5.2$ Hz, 2H), 6.65 (s, 1H), 2.86 (t, $J=7.6$ Hz, 4H), 1.85 (dd, $J=11.1, 5.6$ Hz, 8H), 1.71 (p, $J=7.4$ Hz, 4H), 1.44-1.08 (m, 26H), 0.94 (m, 30H), 0.81 (t, $J=6.7$ Hz, 6H). $^{13}\text{C NMR}$ (101 MHz, *Chloroform-d*) 158.84, 157.70, 156.43, 149.63, 148.34, 143.58, 139.62, 139.50, 133.31, 120.35, 119.06, 118.94, 116.11, 54.01, 37.91, 31.78, 31.67, 31.58, 31.06, 29.75, 28.72, 24.54, 22.67, 22.62, 14.10, 14.07. DEPT 135 $^{13}\text{C NMR}$ (101 MHz, *Chloroform-d*) δ =CH-: 149.63, 120.35, 119.06, 118.94, 116.11; -CH₂-: 37.91, 31.78, 31.67, 31.58, 31.06, 29.75, 28.72, 24.54, 22.67, 22.62; -CH₃: 14.10, 14.07.



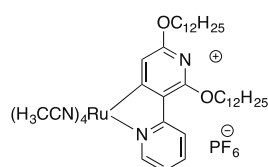
4,4'-bis(5-hexylthieno[3,2-b]thiophen-2-yl)-2,2'-bipyridine (32) was synthesized according to the procedure described for **29**.²²⁵ **26** (3.32 g, 9.5 mmol), 4,4'-dibromo-2,2'-bipyridine (785 mg, 2.5 mmol), $\text{Pd}(\text{PPh}_3)_4$ (250 mg, 0.2 mmol) in 2.5 M aqueous solution K_2CO_3 (10 mL) and toluene (40 mL) was used. After column chromatography (DCM:EtOAc = 9:1) the pure product was obtained. (630 mg, 42 %). $^1\text{H NMR}$ (400 MHz, *Chloroform-d*) δ 8.66 (m, 4H), 7.77 (s, 2H), 7.49 (d, $J = 5.1$ Hz, 2H), 7.26 (s, 2H), 6.98 (s, 2H), 2.90 (t, $J = 7.6$ Hz, 4H), 1.74 (p, $J = 7.5$ Hz, 4H), 1.45 - 1.27 (m, 12H), 0.89 (t, 6H). $^{13}\text{C NMR}$ (101 MHz, *Chloroform-d*) 156.48, 150.49, 149.74, 143.08, 141.02, 139.76, 138.19, 119.54, 118.14, 116.89, 116.54, 31.58, 31.47, 31.31, 28.79, 22.59, 14.11. DEPT 135 $^{13}\text{C NMR}$ (101 MHz, *Chloroform-d*) δ =CH-: 156.48, 150.49, 149.74, 143.08, 141.02, 139.76, 138.19, 119.54, 118.14, 116.89, 116.54; -CH₂-: 31.58, 31.47, 31.31, 28.79, 22.59; -CH₃: 14.11.



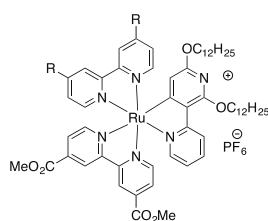
4,4'-bis(5'-hexyl-[2,2'-bithiophen]-5-yl)-2,2'-bipyridine (33) was synthesized according to the procedure described for **29**.²²⁶ **27** (625 mg, 1.66 mmol), 4,4'-dibromo-2,2'-bipyridine (157 mg, 0.5 mmol), Pd(PPh₃)₄ in 2 M solution aqueous potassium carbonate solution (10 mL) and toluene (40 mL) were used. Column chromatography on silica gel (DCM-methanol-NEt₃ 98-2-0.1) was used to obtain pure product (250 mg, 77 %). ¹H NMR (400 MHz, Chloroform-d) δ 8.67 (d, J=5.2 Hz, 2H), 8.63 (d, J=1.7 Hz, 2H), 7.56 (d, J=3.8 Hz, 2H), 7.48 (dd, J=5.2, 1.9 Hz, 2H), 7.13 (d, J=3.9 Hz, 2H), 7.07 (d, J=3.5 Hz, 2H), 6.72 (d, J=3.6 Hz, 2H), 2.81 (t, J=7.6 Hz, 4H), 1.70 (p, J=7.6 Hz, 4H), 1.44-1.27 (m, 12H), 0.93-0.87 (m, 6H). ¹³C NMR (101 MHz, Chloroform-d) 156.48, 149.71, 146.44, 142.20, 139.91, 139.03, 134.23, 126.44, 125.02, 124.11, 123.96, 119.50, 116.87, 31.58, 30.24, 28.78, 22.60, 14.11. DEPT 135 ¹³C NMR (101 MHz, Chloroform-d) δ =CH-: 149.71, 126.44, 125.02, 124.11, 123.96, 119.50, 116.87; -CH₂-: 31.58, 30.24, 28.78, 22.60; -CH₃: 14.11.



4,4'-bis(9,9-dihexyl-9H-fluoren-2-yl)-2,2'-bipyridine (34) was synthesized according to the procedure described for the **29**. **28** (875 mg, 1.9 mmol), 4,4'-dibromo-2,2'-bipyridine (251 mg, 0.8 mmol), Pd(PPh₃)₄ (116 mg, 0.1 mmol) in 2 M aqueous solution of potassium carbonate (10 mL) and toluene (40 mL) was used. Column on silica (DCM:EtAc 9:1) was used to obtain a pure product (490 mg, 74 %). ¹H NMR (400 MHz, Dichloromethane-d₂) δ 8.93 (d, J=1.7 Hz, 2H), 8.81 (d, J=5.1 Hz, 2H), 7.91-7.80 (m, 8H), 7.70 (dd, J=5.1, 1.9 Hz, 2H), 7.46-7.37 (m, 6H), 2.12 (d, J=10.1 Hz, 8H), 1.21-1.05 (m, 24H), 0.79 (t, J=7.0 Hz, 12H), 0.7 (m, 8H). ¹³C NMR (101 MHz, Dichloromethane-d₂) 156.77, 151.78, 151.24, 149.60, 142.34, 140.45, 137.14, 127.59, 126.93, 126.14, 123.05, 121.73, 121.46, 120.23, 120.04, 118.85, 40.38, 31.57, 29.71, 23.87, 22.61, 13.84. DEPT 135 ¹³C NMR (101 MHz, Dichloromethane-d₂) δ =CH-: 149.60, 127.59, 126.93, 126.14, 123.05, 121.73, 121.46, 120.23, 120.04, 118.85; -CH₂-: 40.38, 31.57, 29.71, 23.87, 22.61; -CH₃: 13.84.

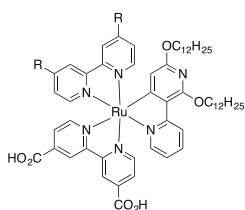


[Ru(C^N)(CH₃CN)₄](PF₆)⁹³ In the oven-dried Schlenk flask [Ru(C₆H₆)Cl(μ-Cl)]₂ (370 mg, 0.74 mmol), 2',6'-dodecyloxy-2,3'-bipyridine (796 mg, 1.5 mmol, 2 equiv.), potassium hydroxide powder (85 mg, 1.5 mmol, 2 equiv) and potassium hexafluorophosphate (554 mg, 3 mmol, 4 equiv) were degassed and flushed with nitrogen. Then, 20 mL of dry acetonitrile was added by syringe. The reaction mixture was heated up to 50 °C and stirred for three days. After, while hot, the reaction mixture was filtered; the filtrate was evaporated and the pure product was obtained after column chromatography on basic aluminium oxide with gradient eluent (acetonitrile in dichloromethane 0-10%). (777 mg, yield: 55%). ¹H NMR (400 MHz, Acetonitrile-d₃) δ 8.89 (d, J=5.4 Hz, 1H), 8.44 (d, J=8.3 Hz, 1H), 7.70 (ddd, J=8.6, 7.4, 1.7 Hz, 1H), 7.06 (ddd, J=7.3, 5.7, 1.5 Hz, 1H), 6.95 (s, 1H), 4.47 (t, J=6.7 Hz, 2H), 4.32 (t, J=6.8 Hz, 2H), 2.51 (s, 3H), 2.16 (s, 3H), 2.03 (s, 6H), 1.89 (p, J=6.9 Hz, 2H), 1.78 (p, J=6.9 Hz, 2H), 1.58-1.23 (m, 40H), 0.88 (t, 6H).



General procedure for the synthesis [Ru(C^N)(L^{aux})(bpy(CO₂Me)₂)](PF₆)⁹³ Auxiliary (**29**, **30**, **31**, **32**, **33** and **34**, 1 equiv.) and anchoring (4,4'-dicarboxy-2,2'-bipyridine methyl ester, 1 equiv.) ligands and 20 mL of absolute ethanol:chloroform (3:1) in the flask with condenser were heated up to 70 °C until all ligands dissolved. Then

$[\text{Ru}(\text{C}^{\wedge}\text{N})(\text{CH}_3\text{CN})_4](\text{PF}_6)$ (1 equiv.) was added and reaction mixture was refluxed for 3 hours under nitrogen. Then mixture was evaporated to the small amount and column chromatography on silica gel with gradient eluent (acetonitrile in dichloromethane 0-10 %) resulted in 3 bands representing the following complexes in the order of decreasing R_f : bis-heteroleptic complex with two auxiliary ligands, tris-heteroleptic complex and bis-heteroleptic complex with two anchoring ligands. We must note that we were not able to separate some of the non-hydrolyzed dyes, especially SA25 from free 4,4'-dimethyldicarboxy-2,2'-bipyridine, which was separated by filtering several times through celite after hydrolysis. This was possible due to bad solubility of 4,4'-dicarboxy-2,2'-bipyridine in dichloromethane.



General procedure for the synthesis of $[\text{Ru}(\text{C}^{\wedge}\text{N})(\text{L}^{\text{aux}})(\text{bpy}(\text{CO}_2\text{H})_2)](\text{PF}_6)$.⁹³

The $[\text{Ru}(\text{C}^{\wedge}\text{N})(\text{L}^{\text{aux}})(\text{bpy}(\text{CO}_2\text{Me})_2)](\text{PF}_6)$ was dissolved in 5 ml of DMF:H₂O:NEt₃ (3:1:1) and reaction mixture was refluxed for one day under nitrogen. Afterwards, the reaction mixture was extracted with dichloromethane and washed with 0.1 % aqueous HPF₆ solution. The organic phase was dried over magnesium sulfate, concentrated to small amount via rotary evaporation and purified on size exclusive column on Sephadex LH-20.

$[\text{Ru}(\text{C}^{\wedge}\text{N})(\mathbf{29})(\text{bpy}(\text{CO}_2\text{Me})_2)](\text{PF}_6)$ (SA20). Was synthesized according to the general procedure. $[\text{Ru}(\text{C}^{\wedge}\text{N})(\text{CH}_3\text{CN})_4](\text{PF}_6)$ (161 mg, 0.17 mmol), **29** (124 mg, 0.17 mmol), 4,4'-dicarboxy-2,2'-bipyridine methyl ester (47 mg, 0.17 mmol) was used. (121 mg, 40%).

¹H NMR (400 MHz, Chloroform-*d*) δ 8.93 (s, 1H), 8.83 (s, 1H), 8.61 (d, $J = 8.4$ Hz, 1H), 8.47 (d, $J = 6.1$ Hz, 1H), 8.44 (d, $J = 7.4$ Hz, 2H), 8.22 (d, $J = 5.6$ Hz, 1H), 8.10 (d, $J = 5.5$ Hz, 1H), 7.75 (s, 1H), 7.71 (d, $J = 6.0$ Hz, 1H), 7.67 (s, 1H), 7.65 – 7.57 (m, 4H), 7.52 (dd, $J = 5.9, 1.9$ Hz, 1H), 7.49 – 7.40 (m, 4H), 7.39 (dd, $J = 6.1, 1.8$ Hz, 1H), 6.84 (t, $J = 6.6$ Hz, 1H), 6.77 (s, 2H), 5.68 (s, 1H), 4.53 – 4.42 (m, 2H), 4.16 (d, $J = 7.4$ Hz, 2H), 4.03 (s, 3H), 3.99 (s, 3H), 2.87 (t, $J = 7.7$ Hz, 4H), 1.92 (m, 2H), 1.79–1.61 (m, 6H), 1.59–1.17 (m, 60H), 0.93–0.82 (m, 12H).

MALDI TOF: $m/z = 1617.6307$ [M]⁺ (calcd for $[\text{RuC}_{116}\text{H}_{119}\text{N}_6\text{O}_6\text{S}_2]^+$: $m/z = 1617.7675$).

$[\text{Ru}(\text{C}^{\wedge}\text{N})(\mathbf{30})(\text{bpy}(\text{CO}_2\text{Me})_2)](\text{PF}_6)$ (SA23). Was synthesized according to the general procedure. **SA-17** (49 mg, 0.05 mmol), **30** (38 mg, 0.05 mmol), 4,4'-dicarboxy-2,2'-bipyridine methyl ester (14 mg, 0.05 mmol) was used. (27 mg, yield: 30 %).

¹H NMR (400 MHz, Chloroform-*d*) δ 8.92 (s, 1H), 8.81 (s, 1H), 8.58 (d, $J = 8.5$ Hz, 1H), 8.43 (d, $J = 6.0$ Hz, 1H), 8.30 (dd, $J = 10.5, 2.0$ Hz, 2H), 8.15 (d, $J = 5.7$ Hz, 1H), 8.03 (dd, $J = 5.7, 1.6$ Hz, 1H), 7.74 (d, $J = 12.7$ Hz, 2H), 7.68 (dd, $J = 5.9, 1.8$ Hz, 1H), 7.63 – 7.55 (m, 1H), 7.44 (d, $J = 6.2$ Hz, 1H), 7.40 – 7.30 (m, 2H), 7.29 – 7.25 (m, 1H), 7.22 (dd, $J = 6.2, 1.9$ Hz, 1H), 6.80 (ddd, $J = 7.3, 5.6, 1.5$ Hz, 1H), 6.73 (d, $J = 2.8$ Hz, 2H), 5.65 (s, 1H), 4.46 (t, $J = 6.6$ Hz, 2H), 4.18 – 4.11 (m, 2H), 4.02 (s, 3H), 4.00 (s, 3H), 2.84 (t, $J = 7.7$ Hz, 4H), 1.91 (p, $J = 6.9$ Hz, 2H), 1.75 – 1.61 (m, 6H), 1.57 – 1.16 (m, 60H), 0.93 – 0.82 (m, 12H).

HRMS (ESI): $m/z = 1629.6686$ [M]⁺, (calculated for $[\text{RuC}_{92}\text{H}_{115}\text{N}_6\text{O}_6\text{S}_4]^+$: $m/z = 1629.6804$).

[Ru(C[^]N)(29)(bpy(CO₂H)₂)](PF₆) (SA22) was synthesized according to the general procedure. **SA-20** (70 mg, 0.04 mmol) was used. (68 mg, 100 %).

HRMS (ESI): $m/z=1589.7490$ [M]⁺, (calculated for [RuC₉₄H₁₁₅N₆O₆S₂]⁺: $m/z = 1589.7363$).

[Ru(C[^]N)(30)(bpy(CO₂H)₂)](PF₆) (SA25) was synthesized according to the general procedure. **SA-23** (27 mg, 0.015 mmol) was used. (26 mg, 100 %).

MALDI TOF: $m/z = 1601.4746$ [M]⁺ (calcd for [RuC₉₀H₁₁₁N₆O₆S₂]⁺: $m/z = 1601.6491$).

[Ru(C[^]N)(32)(bpy(CO₂Me)₂)](PF₆) (SA245) was synthesized according to the general procedure. **32** (100 mg, 0.17 mmol), dimethyl 2,2'-bipyridine-4,4'-dicarboxylate (45.3 mg, 0.17 mmol) and [Ru(C[^]N)(CH₃CN)₄](PF₆) (155.5 mg, 0.17 mmol) were used. (79.4 mg, 29%).

¹H NMR (400 MHz, Chloroform-*d*) δ 8.92 (s, 1H), 8.82 (d, *J* = 1.8 Hz, 1H), 8.60 (d, *J* = 8.4 Hz, 1H), 8.42 (d, *J* = 5.9 Hz, 1H), 8.28 (s, 1H), 8.23 (s, 1H), 8.20 (d, *J* = 5.7 Hz, 1H), 8.06 (d, *J* = 5.6 Hz, 1H), 7.83 (s, 1H), 7.72 (s, 1H), 7.67 (dd, *J* = 6.0, 1.7 Hz, 1H), 7.60 (t, *J* = 7.9 Hz, 1H), 7.54 (d, *J* = 6.1 Hz, 1H), 7.41 – 7.36 (m, 1H), 7.34 – 7.29 (m, 2H), 7.18 (d, *J* = 5.4 Hz, 1H), 6.94 (s, 1H), 6.91 (s, 1H), 6.84 (t, *J* = 6.6 Hz, 1H), 5.66 (s, 1H), 4.52 – 4.40 (m, 2H), 4.23 – 4.07 (m, 2H), 4.03 (s, 3H), 4.00 (s, 3H), 2.90 – 2.81 (m, 4H), 1.91 (p, *J* = 6.9 Hz, 4H), 1.76 – 1.47 (m, 10H), 1.44 – 1.09 (m, 42H), 0.92 – 0.81 (m, 12H).

DEPT 135 ¹³C NMR (101 MHz, Chloroform-*d*) δ =CH-: 155.24, 150.00, 149.92, 149.67, 149.42, 136.11, 127.34, 125.24, 122.57, 122.46, 122.43, 122.16, 121.90, 120.89, 119.87, 119.72, 117.86, 117.62, 116.43, 116.38, 107.21; -CH₂-: 31.94, 31.92, 31.55, 31.54, 31.37, 29.72, 29.68, 29.64, 29.62, 29.57, 29.56, 29.48, 29.39, 29.36, 29.31, 29.27, 29.81, 26.52, 26.12, 22.71, 22.69, 22.59; -CH₃: 53.33, 53.26, 14.14, 14.13, 14.10.

HRMS (ESI): $m/z=1497.6611$ [M]⁺, (calculated for [RuC₈₂H₁₀₃N₆O₆S₄]⁺: $m/z = 1497.5885$).

[Ru(C[^]N)(32)(bpy(CO₂H)₂)](PF₆) (SA246) was synthesized according to the general procedure. SA-245 (75 mg, 0.04 mmol) in DMF:NEt₃:H₂O (3:1:1) (10 mL) was used. (68.5 mg, 98 %).

¹H NMR (400 MHz, Chloroform-*d*) δ 11.16 (s, 1H), 9.93 (s, 1H), 9.82 (s, 1H), 8.63 (d, *J* = 8.5 Hz, 1H), 8.36 – 8.20 (m, 3H), 8.08 (d, *J* = 5.9 Hz, 1H), 8.02 (d, *J* = 5.9 Hz, 1H), 7.83 – 7.75 (m, 2H), 7.70 (s, 1H), 7.58 (d, *J* = 7.0 Hz, 2H), 7.47 (d, *J* = 6.2 Hz, 1H), 7.40 (d, *J* = 5.6 Hz, 1H), 7.29 – 7.24 (m, 1H), 7.18 (d, *J* = 6.2 Hz, 1H), 6.96 (d, *J* = 9.1 Hz, 2H), 6.77 (t, *J* = 6.7 Hz, 1H), 5.72 (s, 1H), 4.54 – 4.43 (m, 2H), 4.17 (m, 2H), 2.95 – 2.84 (m, 4H), 1.92 (q, *J* = 7.3 Hz, 2H), 1.83 – 1.06 (m, 54H), 0.88 (m, 12H).

¹³C NMR (101 MHz, Dichloromethane-*d*₂) δ 167.78, 165.49, 160.85, 159.72, 158.54, 156.16, 155.94, 154.37, 152.29, 149.85, 149.62, 149.37, 148.52, 148.49, 140.65, 140.39, 140.24, 136.72, 138.62, 135.72, 127.11, 126.85, 125.81, 125.78, 124.41, 124.31, 122.91, 122.57, 121.85, 121.77, 120.42, 120.27, 119.34, 119.18, 117.75, 117.58, 116.48, 107.26, 66.06, 65.90, 46.04, 31.93, 31.91, 31.54, 31.42, 31.37, 29.65, 29.72, 29.67, 29.62, 29.56, 29.48, 29.38, 29.35, 29.33, 29.29, 28.79, 26.51, 26.13, 22.71, 22.68, 22.58, 14.14, 14.13, 14.10, 8.45.

DEPT 135 ¹³C NMR (101 MHz, Dichloromethane-*d*₂) δ =CH-: 154.37, 149.85, 149.62, 149.37, 148.52, 135.72, 127.11, 126.85, 124.41, 124.31, 122.57, 121.85, 121.77, 120.42, 119.34, 119.18, 117.75, 117.58, 116.48, 107.26; -CH₂-: 66.14, 65.71, 66.06, 65.90, 46.04, 31.93, 31.91, 31.54, 31.42, 31.37, 29.65, 29.72,

29.67, 29.62, 29.56, 29.48, 29.38, 29.35, 29.33, 29.29, 28.79, 26.51, 26.13, 22.71, 22.68, 22.58; $-CH_3$: 14.14, 14.13, 14.10, 8.45.

HRMS (ESI): $m/z=1469.5587 [M]^+$, (calculated for $[RuC_{80}H_{99}N_6O_6S_4]^+$: $m/z = 1469.5571$).

[Ru(C[^]N)(34)(bpy(CO₂Me)₂)](PF₆) (SA274) was synthesized according to the general procedure. **34** (300 mg, 0.37 mmol), dimethyl 2,2'-bipyridine-4,4'-dicarboxylate (99.5 mg, 0.37 mmol) and $[Ru(C^{\wedge}N)(CH_3CN)_4](PF_6)$ (341 mg, 0.37 mmol) were used. Yield: (216 mg, 31%).

¹H NMR (400 MHz, Chloroform-*d*) δ 8.95 (d, $J = 1.5$ Hz, 1H), 8.85 (d, $J = 1.7$ Hz, 1H), 8.60 (d, $J = 8.1$ Hz, 1H), 8.50 – 8.46 (m, 3H), 8.28 (d, $J = 5.6$ Hz, 1H), 8.12 (dd, $J = 5.7, 1.6$ Hz, 1H), 7.86 (d, $J = 4.3$ Hz, 1H), 7.84 (d, $J = 4.3$ Hz, 1H), 7.79 (dd, $J = 8.0, 1.7$ Hz, 1H), 7.77 – 7.68 (m, 6H), 7.66 – 7.58 (m, 3H), 7.50 (d, $J = 6.1$ Hz, 1H), 7.49 – 7.44 (m, 2H), 7.38 – 7.35 (m, 6H), 6.88 (ddd, $J = 7.3, 5.6, 1.5$ Hz, 1H), 5.67 (s, 1H), 4.53 – 4.41 (m, 2H), 4.26 – 4.10 (m, 2H), 4.04 (s, 3H), 4.01 (s, 3H), 2.07 – 1.98 (m, 8H), 1.96 – 1.86 (m, 2H), 1.75 – 1.63 (m, 2H), 1.62 – 1.49 (m, 4H), 1.47 – 1.18 (m, 34H), 1.14 – 0.96 (m, 22H), 0.91 – 0.83 (m, 8H), 0.77 – 0.69 (m, 12H), 0.66 – 0.55 (m, 6H).

¹³C NMR (101 MHz, Chloroform-*d*) δ 165.21, 164.62, 164.39, 160.66, 159.52, 158.45, 156.84, 155.65, 155.3, 154.64, 152.16, 152.08, 151.25, 151.18, 150.31, 150.07, 149.85, 149.48, 147.96, 147.54, 143.31, 143.14, 140.08, 139.94, 137.05, 136.14, 135.26, 134.93, 134.72, 128.02, 127.89, 127.54, 127.06, 126.99, 126.21, 126.05, 125.13, 124.96, 124.43, 123.00, 122.55, 122.41, 121.27, 120.96, 120.67, 120.62, 120.41, 120.30, 120.27, 120.07, 107.35, 66.09, 65.90, 55.45, 53.34, 53.27, 40.47, 40.43, 31.94, 31.92, 31.54, 31.51, 29.69, 29.66, 29.62, 29.55, 29.53, 29.39, 29.36, 29.32, 26.51, 26.13, 23.82, 22.71, 22.69, 22.59, 22.58, 14.14, 14.13, 14.00.

DEPT 135 ¹³C NMR (101 MHz, Chloroform-*d*) δ =CH-: 155.30, 150.31, 150.07, 149.85, 149.48, 136.14, 128.02, 127.89, 127.54, 127.06, 126.99, 126.21, 126.05, 125.13, 124.96, 124.43, 123.00, 122.55, 122.41, 121.27, 120.96, 120.67, 120.62, 120.41, 120.30, 120.27, 107.35; -CH₂-: 66.09, 65.90, 55.45, 40.47, 40.43, 31.94, 31.92, 31.54, 31.51, 29.69, 29.66, 29.62, 29.55, 29.53, 29.39, 29.36, 29.32, 26.51, 26.13, 23.82, 22.71, 22.69, 22.59, 22.58; -CH₃: 53.34, 53.27, 14.14, 14.13, 14.00.

[Ru(C[^]N)(34)(bpy(CO₂H)₂)](PF₆) (SA282) was synthesized according to the general procedure. SA-274 (215 mg, 0.115 mmol) in DMF:NEt₃:H₂O (3:1:1) (10 mL) was used. Yield: 206 mg, 96 %.

¹H NMR (400 MHz, Dichloromethane-*d*₂) δ 9.80 (s, 1H), 9.69 (s, 1H), 8.65 (d, $J = 8.4$ Hz, 1H), 8.56 (dd, $J = 7.0, 1.9$ Hz, 2H), 8.33 (d, $J = 5.8$ Hz, 1H), 8.01 – 7.93 (m, 2H), 7.89 (d, $J = 8.0$ Hz, 1H), 7.87 (d, $J = 8.0$ Hz, 1H), 7.81 – 7.68 (m, 10H), 7.60 (ddd, $J = 8.7, 7.4, 1.7$ Hz, 1H), 7.53 (dd, $J = 6.1, 1.9$ Hz, 1H), 7.50 (dd, $J = 5.8, 1.4$ Hz, 1H), 7.47 (dd, $J = 6.1, 1.8$ Hz, 1H), 7.43 – 7.35 (m, 7H), 6.76 (ddd, $J = 7.3, 5.6, 1.5$ Hz, 1H), 5.68 (s, 1H), 4.48 (t, $J = 6.8$ Hz, 2H), 4.21 – 4.10 (m, 2H), 2.11 – 1.99 (m, 8H), 1.98 – 1.86 (m, 2H), 1.64 (p, $J = 6.9$ Hz, 2H), 1.60 – 1.50 (m, 4H), 1.48 – 1.17 (m, 34H), 1.16 – 0.95 (m, 22H), 0.94 – 0.80 (m, 8H), 0.79 – 0.68 (m, 12H), 0.68 – 0.54 (m, 6H).

¹³C NMR (101 MHz, Dichloromethane-*d*₂) δ 167.45, 165.59, 160.68, 159.61, 158.41, 156.90, 156.77, 155.86, 154.22, 152.14, 152.11, 151.20, 151.19, 149.96, 149.47, 148.08, 146.74, 143.19, 143.13, 140.01, 139.99, 135.48, 135.20, 128.00, 127.95, 127.05, 127.01, 126.85, 125.94, 125.90, 124.30, 124.16, 124.03, 123.09, 123.08, 122.48, 121.18, 121.13, 120.55, 120.48, 120.27, 120.19, 120.06, 120.03, 107.37, 66.00, 65.64,

55.44, 45.56, 40.35, 31.94, 31.91, 31.53, 29.71, 29.66, 29.51, 29.48, 29.38, 29.35, 26.47, 26.11, 23.82, 22.71, 22.69, 22.54, 13.91, 13.89, 13.76, 8.42.

DEPT 135 ^{13}C NMR (101 MHz, Dichloromethane- d_2) δ =CH-: 154.22, 149.96, 149.47, 148.08, 135.48, 128.00, 127.95, 127.05, 127.01, 126.85, 125.94, 125.90, 124.30, 124.16, 124.03, 123.09, 123.08, 122.48, 121.18, 121.13, 120.55, 120.48, 120.19, 120.06, 120.03, 107.37; -CH₂-: 66.00, 65.64, 55.44, 45.56, 40.35, 31.94, 31.91, 31.53, 29.71, 29.66, 29.51, 29.48, 29.38, 29.35, 26.47, 26.11, 23.82, 22.71, 22.69, 22.54; -CH₃: 13.91, 13.89, 13.76, 8.42.

HRMS (ESI): m/z =1689.9517 [M]⁺, (calculated for [RuC₁₀₆H₁₃₅N₆O₆]⁺ : m/z = 1689.7665).

[Ru(C[^]N)(33)(bpy(CO₂Me)₂)](PF₆) (SA281) was synthesized according to the general procedure. **33** (78.2 mg, 0.12 mmol), dimethyl 2,2'-bipyridine-4,4'-dicarboxylate (32.6 mg, 0.12 mmol) and [Ru(C[^]N)(CH₃CN)₄](PF₆) (112 mg, 0.12 mmol) were used. Yield: (51 mg, 25 %).

^1H NMR (400 MHz, Dichloromethane- d_2) δ 8.97 (s, 1H), 8.87 (s, 1H), 8.65 (d, J = 8.4 Hz, 1H), 8.47 (d, J = 6.0 Hz, 1H), 8.27 (d, J = 17.0 Hz, 2H), 8.09 (d, J = 5.7 Hz, 1H), 7.96 (d, J = 7.2 Hz, 1H), 7.69 (dd, J = 6.0, 1.7 Hz, 1H), 7.65 (t, J = 8.8 Hz, 1H), 7.59 (d, J = 3.9 Hz, 1H), 7.55 (d, J = 6.1 Hz, 1H), 7.48 (d, J = 3.9 Hz, 1H), 7.39 (d, J = 6.1 Hz, 1H), 7.33 (d, J = 6.4 Hz, 2H), 7.24 (dd, J = 6.2, 1.8 Hz, 1H), 7.18 (d, J = 3.8 Hz, 1H), 7.13 – 7.09 (m, 3H), 6.79 (t, J = 7.0 Hz, 1H), 6.76 – 6.74 (m, 2H), 5.65 (s, 1H), 4.52 – 4.42 (m, 2H), 4.21 – 4.10 (m, 2H), 4.01 (s, 6H), 2.82 (t, J = 6.4 Hz, 2H), 1.91 (p, J = 6.9 Hz, 2H), 1.74 – 1.64 (m, 4H), 1.64 – 1.48 (m, 4H), 1.46 – 1.12 (m, 46H), 0.94 – 0.81 (m, 12H).

^{13}C NMR (101 MHz, Dichloromethane- d_2) δ 165.39, 164.22, 164.17, 160.93, 159.75, 158.00, 156.50, 155.83, 155.33, 155.23, 149.71, 149.61, 149.37, 149.34, 147.55, 141.58, 141.55, 140.11, 140.03, 137.03, 136.50, 136.39, 136.23, 135.25, 133.51, 133.46, 128.08, 128.02, 126.65, 125.36, 125.31, 124.79, 124.44, 122.75, 122.61, 121.83, 121.81, 120.55, 119.81, 117.83, 117.69, 107.25, 66.18, 65.78, 53.28, 53.20, 31.93, 31.91, 31.56, 30.17, 29.71, 29.66, 29.63, 29.61, 29.50, 29.44, 29.37, 29.35, 29.29, 28.74, 26.45, 26.09, 22.70, 22.59, 13.89, 13.85.

DEPT 135 ^{13}C NMR (101 MHz, Dichloromethane- d_2) δ =CH-:155.33, 149.71, 149.61, 149.37, 149.34, 136.23, 128.08, 128.02, 126.65, 125.36, 125.31, 124.79, 124.44, 122.75, 122.61, 121.83, 121.81, 120.55, 117.83, 117.69, 107.25; -CH₂-: 66.18, 65.78, 31.93, 31.91, 31.56, 30.17, 29.71, 29.66, 29.63, 29.61, 29.50, 29.44, 29.37, 29.35, 29.29, 28.74, 26.45, 26.09, 22.70, 22.59; -CH₃: 53.28, 53.20, 13.89, 13.85.

HRMS (ESI): m/z =14549.4463 [M]⁺, (calculated for [RuC₈₆H₁₀₇N₆O₆S₄]⁺ : m/z = 1549.6200).

[Ru(C[^]N)(33)(bpy(CO₂H)₂)](PF₆) (SA284)

^1H NMR (400 MHz, Dichloromethane- d_2) δ 12.02 (s, 1H), 9.79 (s, 1H), 9.68 (s, 1H), 8.61 (d, J = 8.4 Hz, 1H), 8.29 (d, J = 5.9 Hz, 1H), 8.24 (d, J = 13.8 Hz, 2H), 7.98 (d, J = 5.5 Hz, 1H), 7.90 (d, J = 5.6 Hz, 1H), 7.73 (d, J = 5.0 Hz, 1H), 7.57 (m, 3H), 7.47 (dd, J = 12.3, 4.9 Hz, 2H), 7.39 (d, J = 5.6 Hz, 1H), 7.26 (d, J = 6.1 Hz, 1H), 7.21 – 7.03 (m, 5H), 6.78 – 6.70 (m, 3H), 5.63 (s, 1H), 4.45 (t, J = 6.7 Hz, 2H), 4.12 (d, J = 6.7 Hz, 2H), 2.85 – 2.77 (m, 4H), 1.95 – 1.82 (m, 2H), 1.73 – 1.47 (m, 16H), 1.42 – 1.09 (m, 38H), 0.95 – 0.77 (m, 12H).

HRMS (ESI): m/z =1521.4067 [M]⁺, (calculated for [RuC₈₄H₁₀₃N₆O₆S₄]⁺ : m/z = 1521.5886).

[Ru(C[^]N)(31)(bpy(CO₂Me)₂)](PF₆) (SA283) was synthesized according to the general procedure. **31** (120 mg, 0.118 mmol), dimethyl 2,2'-bipyridine-4,4'-dicarboxylate (32 mg, 0.118 mmol) and [Ru(C[^]N)(CH₃CN)₄](PF₆) (110 mg, 0.118 mmol) were used. Yield: (94 mg, 38 %).

¹H NMR (400 MHz, Dichloromethane-d₂) δ 8.98 (s, 1H), 8.88 (s, 1H), 8.63 (d, *J* = 8.4 Hz, 1H), 8.47 (d, *J* = 5.9 Hz, 1H), 8.29 (d, *J* = 9.1 Hz, 2H), 8.15 (d, *J* = 5.6 Hz, 1H), 7.96 (d, *J* = 5.6 Hz, 1H), 7.70 (d, *J* = 6.0 Hz, 1H), 7.63 (t, *J* = 7.9 Hz, 1H), 7.55 (d, *J* = 7.6 Hz, 2H), 7.50 (d, *J* = 6.2 Hz, 1H), 7.40 – 7.25 (m, 4H), 6.79 (t, *J* = 6.6 Hz, 1H), 6.73 (d, *J* = 2.8 Hz, 2H), 5.62 (s, 1H), 4.50 – 4.44 (m, 2H), 4.21 – 4.09 (m, 2H), 4.02 (s, 3H), 4.01 (s, 3H), 2.92 – 2.83 (m, 4H), 1.95 – 1.85 (m, 8H), 1.78 – 1.48 (m, 10H), 1.48 – 1.05 (m, 78H), 1.00 – 0.77 (m, 24H).

¹³C NMR (101 MHz, Dichloromethane-d₂) δ 165.49, 164.3, 164.24, 160.86, 160.09, 159.68, 158.40, 158.12, 156.35, 155.77, 155.41, 155.32, 150.14, 149.44, 149.37, 149.35, 149.23, 141.71, 141.50, 141.43, 137.16, 137.11, 136.78, 136.10, 134.96, 132.85, 132.84, 126.54, 125.27, 122.69, 122.59, 121.31, 121.28, 121.07, 120.44, 119.70, 119.34, 116.96, 116.89, 107.16, 66.10, 65.74, 53.26, 53.18, 37.83, 31.94, 31.91, 31.74, 31.64, 31.53, 31.00, 29.71, 29.63, 29.48, 29.49, 29.47, 29.37, 29.34, 29.31, 29.28, 28.63, 26.43, 26.09, 24.49, 22.70, 22.69, 22.59, 13.90, 13.89, 13.83.

DEPT 135 ¹³C NMR (101 MHz, Dichloromethane-d₂) δ =CH-: 155.41, 149.44, 149.37, 149.35, 149.23, 136.10, 126.54, 125.27, 122.69, 122.59, 121.31, 121.28, 121.07, 120.44, 119.34, 116.96, 116.89, 107.16; -CH₂-: 66.10, 65.74, 37.83, 31.94, 31.91, 31.74, 31.64, 31.53, 31.00, 29.71, 29.63, 29.48, 29.49, 29.47, 29.37, 29.34, 29.31, 29.28, 28.63, 26.43, 26.09, 24.49, 22.70, 22.69, 22.59; -CH₃: 53.26, 53.18, 13.90, 13.89, 13.83.

HRMS (ESI): *m/z* = 1909.7163 [M]⁺, (calculated for [RuC₁₁₂H₁₅₅N₆O₆S₄]⁺ : *m/z* = 1909.9963).

[Ru(C[^]N)(31)(bpy(CO₂H)₂)](PF₆) (SA285)

¹H NMR (400 MHz, Dichloromethane-d₂) δ 12.24 (s, 1H), 9.84 (s, 1H), 9.72 (s, 1H), 8.60 (d, *J* = 8.3 Hz, 1H), 8.28 (d, *J* = 6.2 Hz, 3H), 7.98 – 7.92 (m, 3H), 7.73 (d, *J* = 5.9 Hz, 1H), 7.59 – 7.49 (m, 4H), 7.45 (d, *J* = 6.2 Hz, 1H), 7.41 (dd, *J* = 5.8, 1.6 Hz, 1H), 7.30 (dd, *J* = 6.2, 1.9 Hz, 1H), 7.26 – 7.22 (m, 1H), 6.71 (d, *J* = 4.1 Hz, 3H), 5.64 (s, 1H), 4.45 (t, *J* = 6.7 Hz, 2H), 4.20 – 4.06 (m, 2H), 2.87 (q, *J* = 4.8 Hz, 4H), 1.94 – 1.83 (m, 8H), 1.78 – 1.48 (m, 16H), 1.48 – 1.05 (m, 72H), 1.02 – 0.73 (m, 24H).

¹³C NMR (101 MHz, Dichloromethane-d₂) δ 167.40, 167.34, 165.60, 162.20, 160.67, 159.80, 159.75, 159.56, 158.51, 158.29, 156.54, 156.36, 155.85, 154.22, 149.78, 149.67, 149.52, 148.42, 148.02, 141.15, 141.06, 140.55, 137.63, 137.59, 135.39, 132.96, 132.93, 130.91, 129.83, 128.71, 126.78, 125.67, 124.24, 124.19, 122.40, 121.04, 120.92, 120.81, 120.13, 119.29, 116.85, 107.27, 65.95, 65.64, 45.74, 38.11, 37.84, 36.18, 31.93, 31.91, 31.74, 31.63, 31.54, 31.00, 30.07, 29.70, 29.65, 29.51, 29.48, 29.37, 29.34, 28.63, 26.45, 26.10, 24.48, 22.70, 22.68, 22.59, 13.90, 13.89, 13.83, 8.41.

DEPT 135 ¹³C NMR (101 MHz, Dichloromethane-d₂) δ =CH-: 154.22, 149.52, 148.42, 148.02, 135.39, 130.91, 129.83, 128.71, 126.78, 125.67, 124.24, 124.19, 122.40, 121.04, 120.92, 120.81, 120.13, 116.85, 106.27; -CH₂-: 65.95, 65.64, 45.74, 38.11, 37.84, 36.18, 31.93, 31.91, 31.74, 31.63, 31.54, 31.00, 30.07, 29.70, 29.65, 29.51, 29.48, 29.37, 29.34, 28.63, 26.45, 26.10, 24.48, 22.70, 22.68, 22.59; -CH₃: 13.90, 13.89, 13.83, 8.41.

Below ^1H NMR and ^{13}C or ^{13}C -DEPT-135 are brought. DEPT-135 NMR are preferred when high concentrations for the ^{13}C NMR were not available. Note that for SA22 and SA25 NMRs for the non-hydrolyzed products are shown, since final products' amount were not enough to obtain NMR signals.

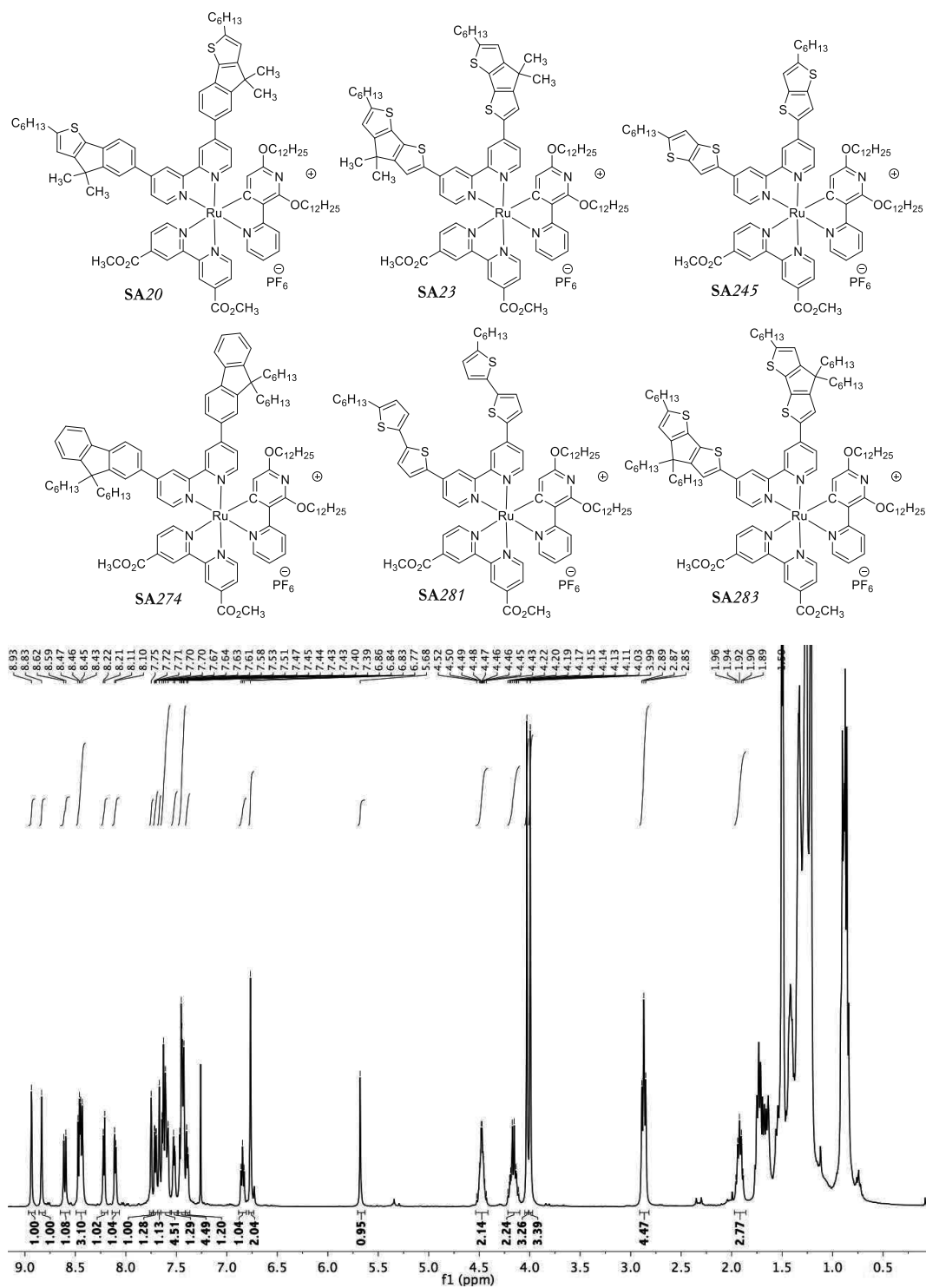


Figure 8.1. ^1H NMR of [Ru(C^N)(29)(bpy(CO₂Me)₂)](PF₆) (SA20) in *chloroform-d*

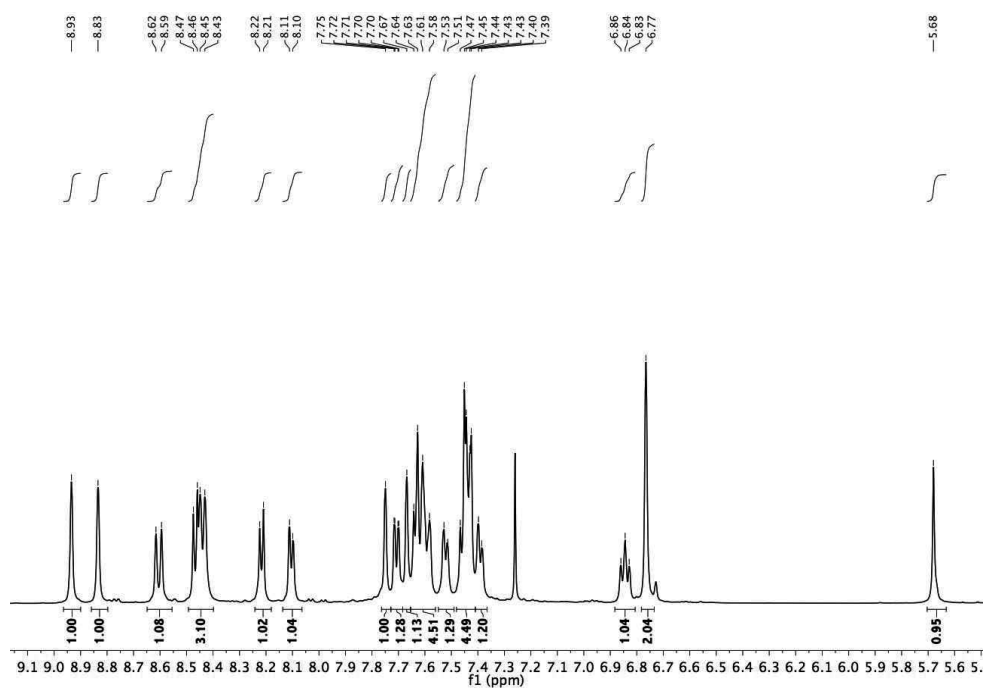


Figure 8.2. ^1H NMR (aromatic region) of $[\text{Ru}(\text{C}^{\wedge}\text{N})(29)(\text{bpy}(\text{CO}_2\text{Me})_2)](\text{PF}_6)$ (SA-20) in *chloroform-d*

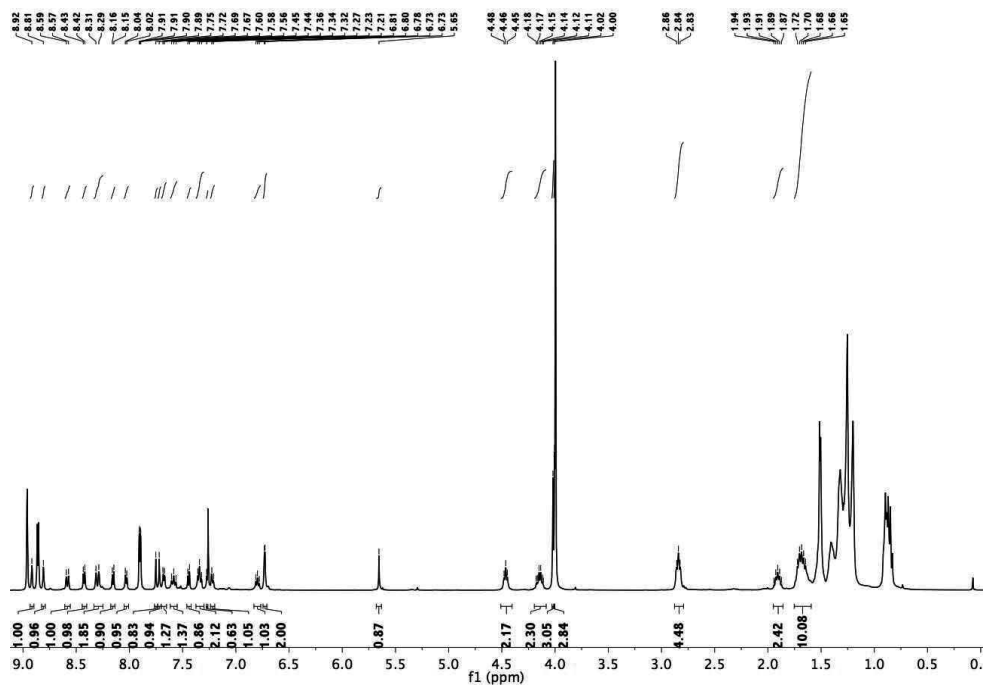
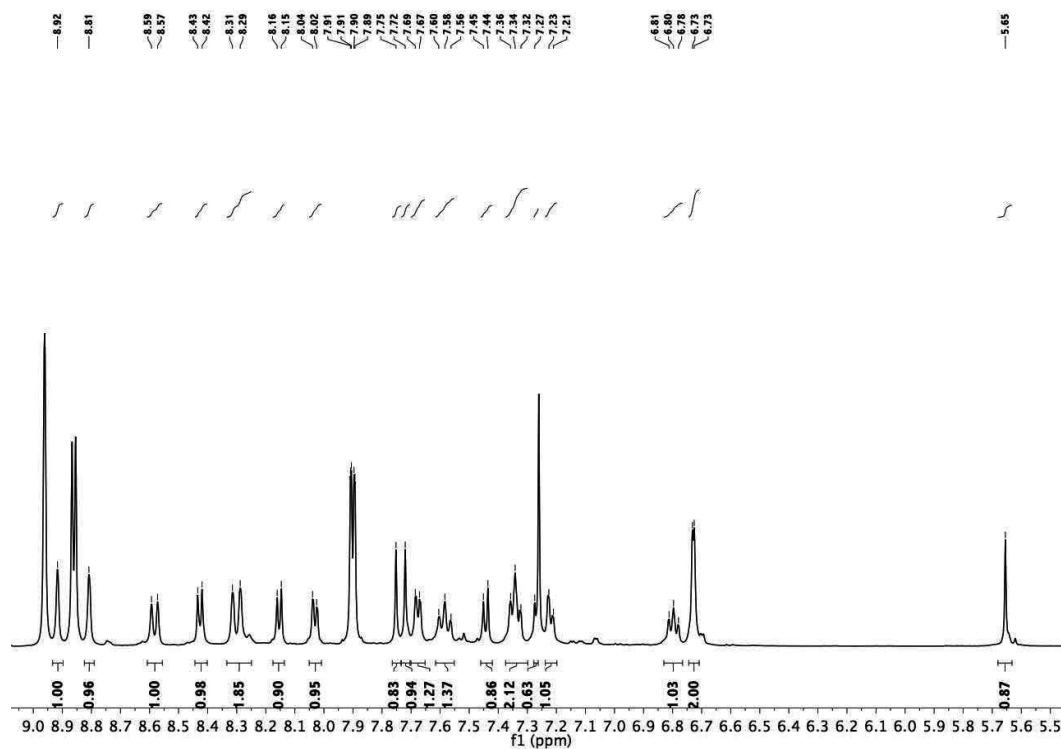
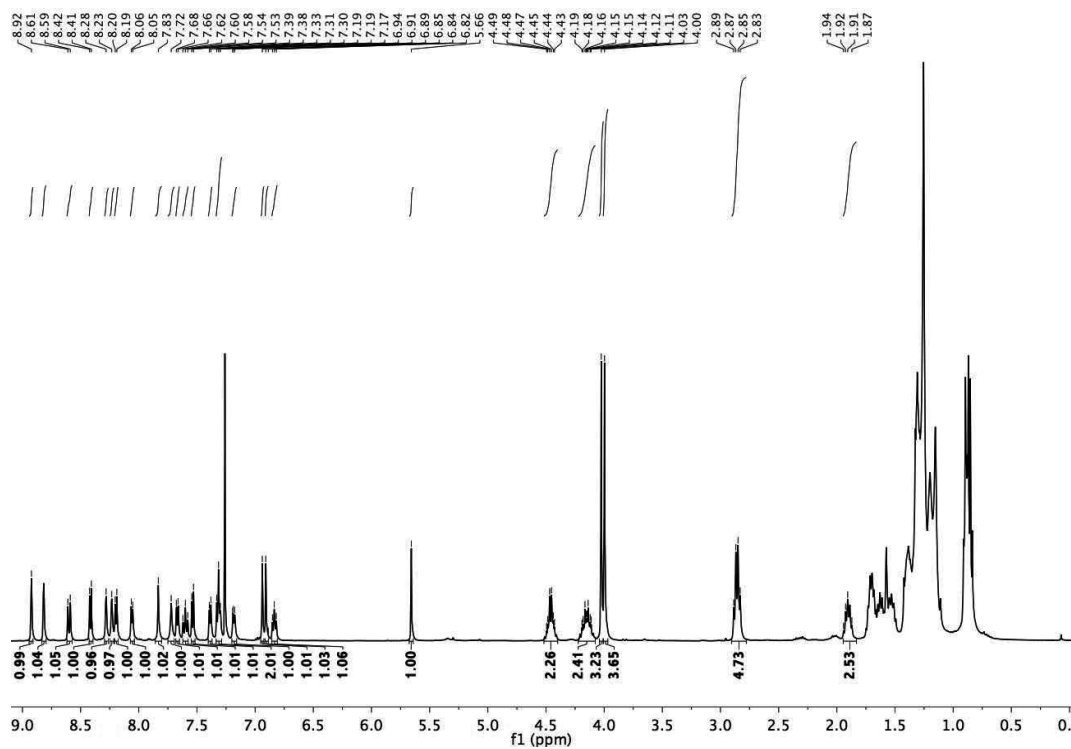


Figure 8.3. ^1H NMR of $[\text{Ru}(\text{C}^{\wedge}\text{N})(30)(\text{bpy}(\text{CO}_2\text{Me})_2)](\text{PF}_6)$ (SA-23) in *chloroform-d*. (Contains dimethyl-2,2'-bipyridine-4,4'-dicarboxylate, which were filtered from the final dye after hydrolysis to acidic form).

Figure 8.4. ^1H NMR (aromatic region) of $[\text{Ru}(\text{C}^{\text{N}})(30)(\text{bpy}(\text{CO}_2\text{Me})_2)](\text{PF}_6)$ (SA-23) in *chloroform-d*Figure 8.5. ^1H NMR of $[\text{Ru}(\text{C}^{\text{N}})(32)(\text{bpy}(\text{CO}_2\text{Me})_2)](\text{PF}_6)$ (SA245) in *chloroform-d*

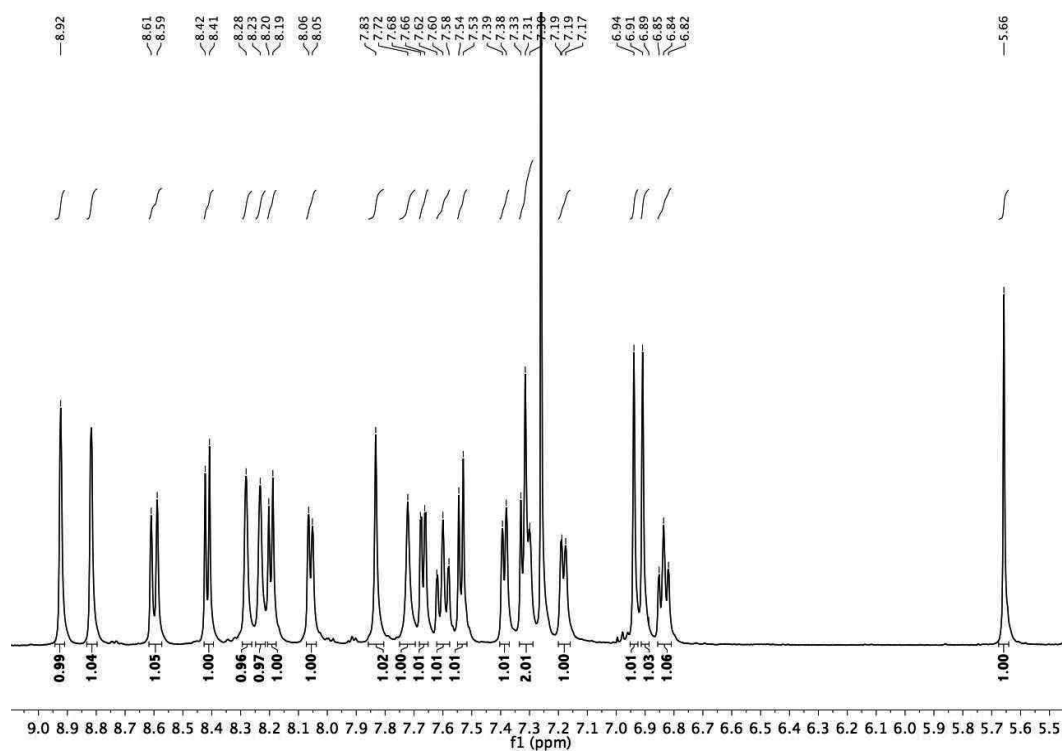


Figure 8.6. ^1H NMR (aromatic region) of $[\text{Ru}(\text{C}^{\wedge}\text{N})(32)(\text{bpy}(\text{CO}_2\text{Me})_2)](\text{PF}_6)$ (SA245) in *chloroform-d*

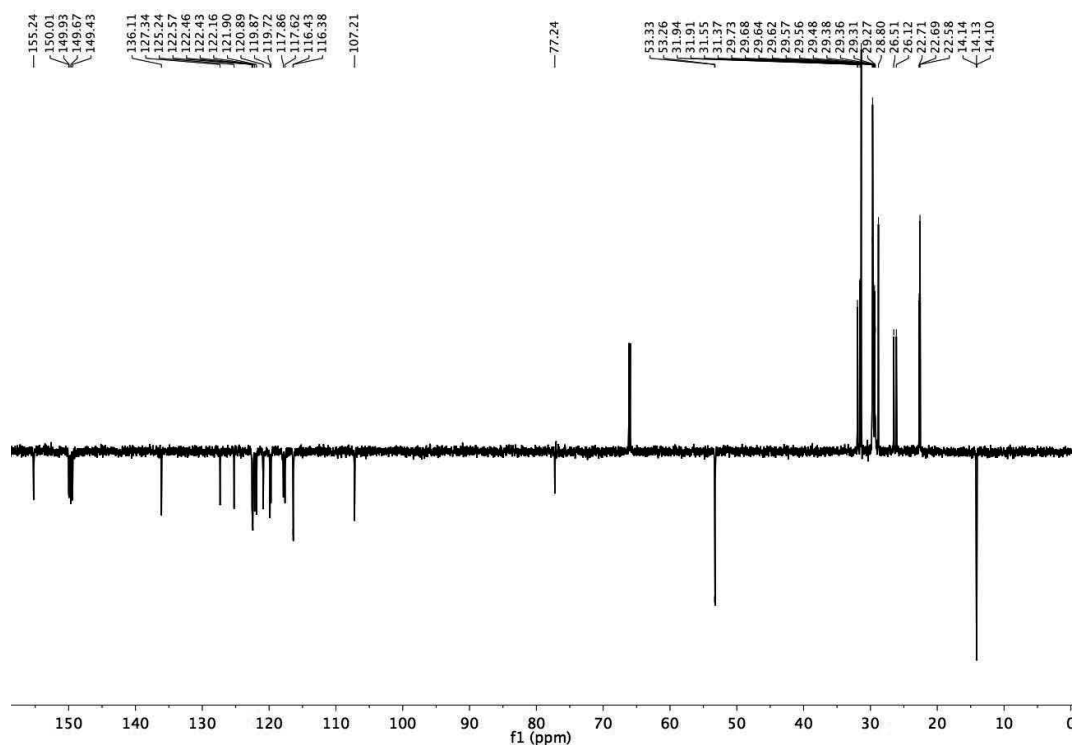


Figure 8.7. DEPT 135 ^{13}C NMR of $[\text{Ru}(\text{C}^{\wedge}\text{N})(32)(\text{bpy}(\text{CO}_2\text{Me})_2)](\text{PF}_6)$ (SA-245) in *chloroform-d*

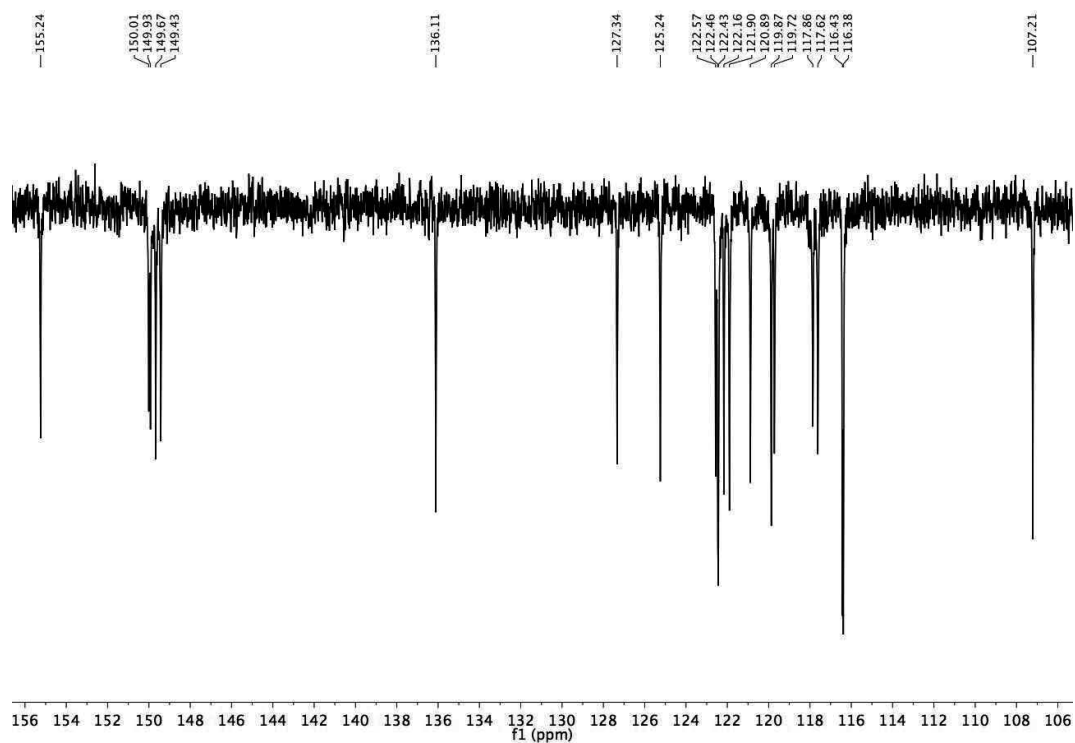


Figure 8.8. DEPT 135 ^{13}C NMR (aromatic region) of $[\text{Ru}(\text{C}^{\wedge}\text{N})(32)(\text{bpy}(\text{CO}_2\text{Me})_2)](\text{PF}_6)$ (SA-245) in *chloroform-d*

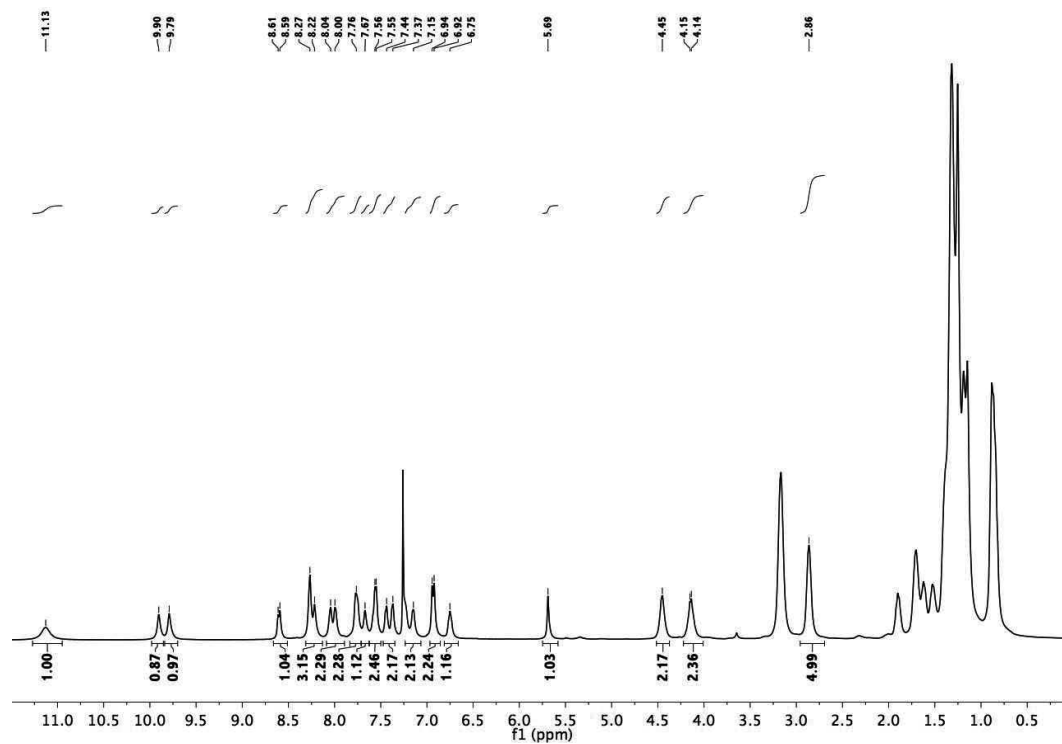


Figure 8.9. ^1H NMR of $[\text{Ru}(\text{C}^{\wedge}\text{N})(32)(\text{bpy}(\text{CO}_2\text{H})_2)](\text{PF}_6)$ (SA246) in *chloroform-d*

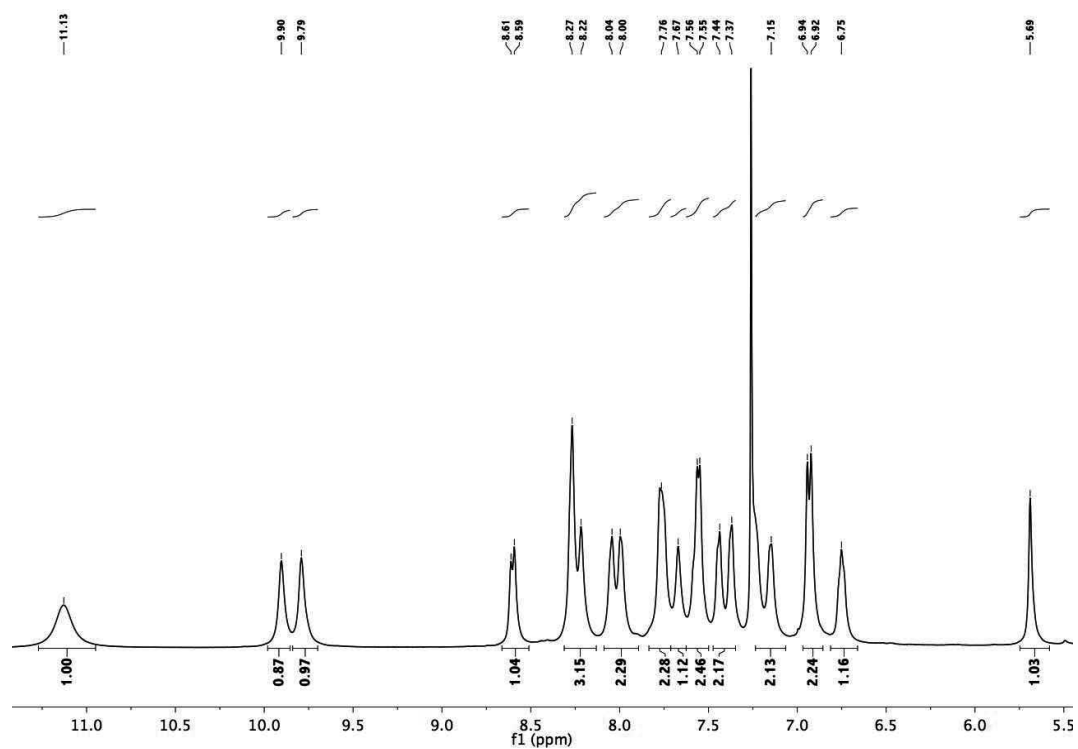


Figure 8.10. ^1H NMR (aromatic region) of $[\text{Ru}(\text{C}^{\wedge}\text{N})(32)(\text{bpy}(\text{CO}_2\text{H})_2)](\text{PF}_6)$ (SA246) in *chloroform-d*

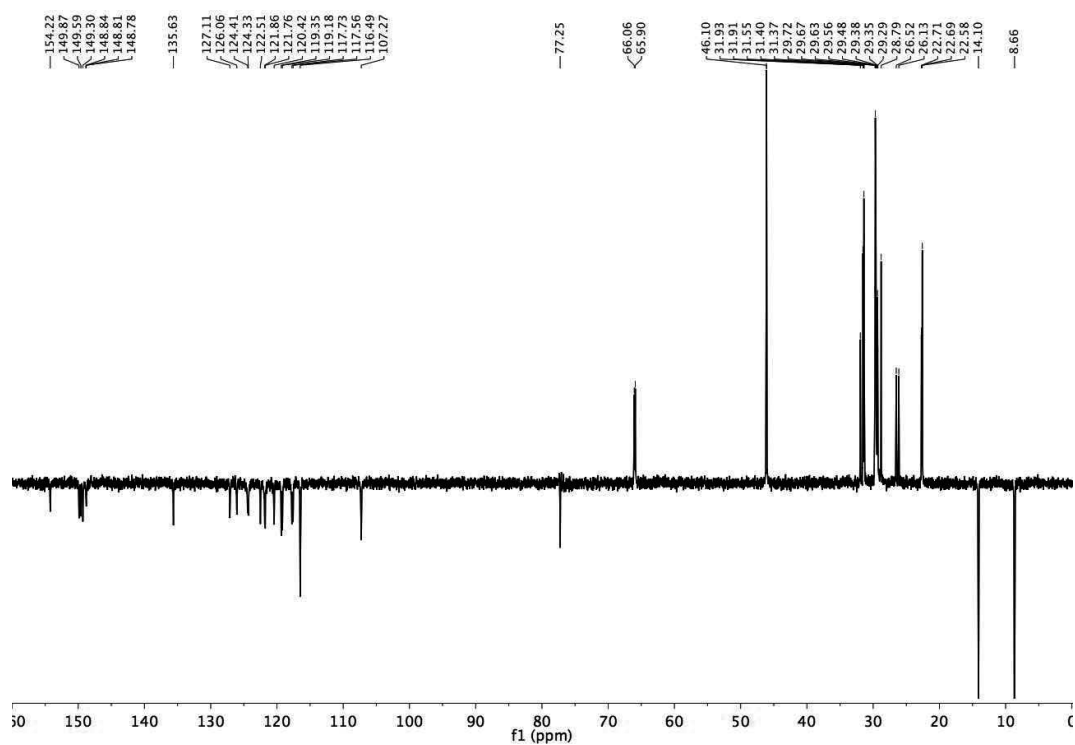


Figure 8.11. DEPT 135 ^{13}C NMR of $[\text{Ru}(\text{C}^{\wedge}\text{N})(32)(\text{bpy}(\text{CO}_2\text{H})_2)](\text{PF}_6)$ (SA246) in *dichloromethane-d*₂.

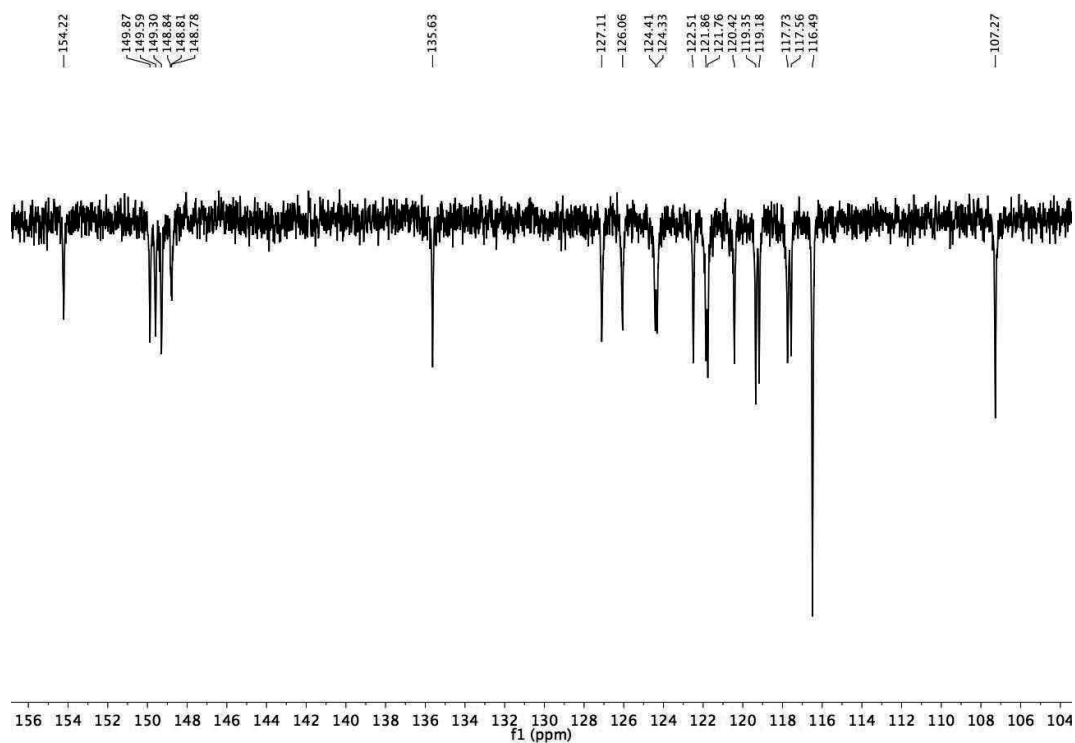


Figure 8.12. DEPT 135 ^{13}C NMR (aromatic region) of $[\text{Ru}(\text{C}^{\wedge}\text{N})(32)(\text{bpy}(\text{CO}_2\text{H})_2)](\text{PF}_6)$ (SA246) in *dichloromethane- d_2*

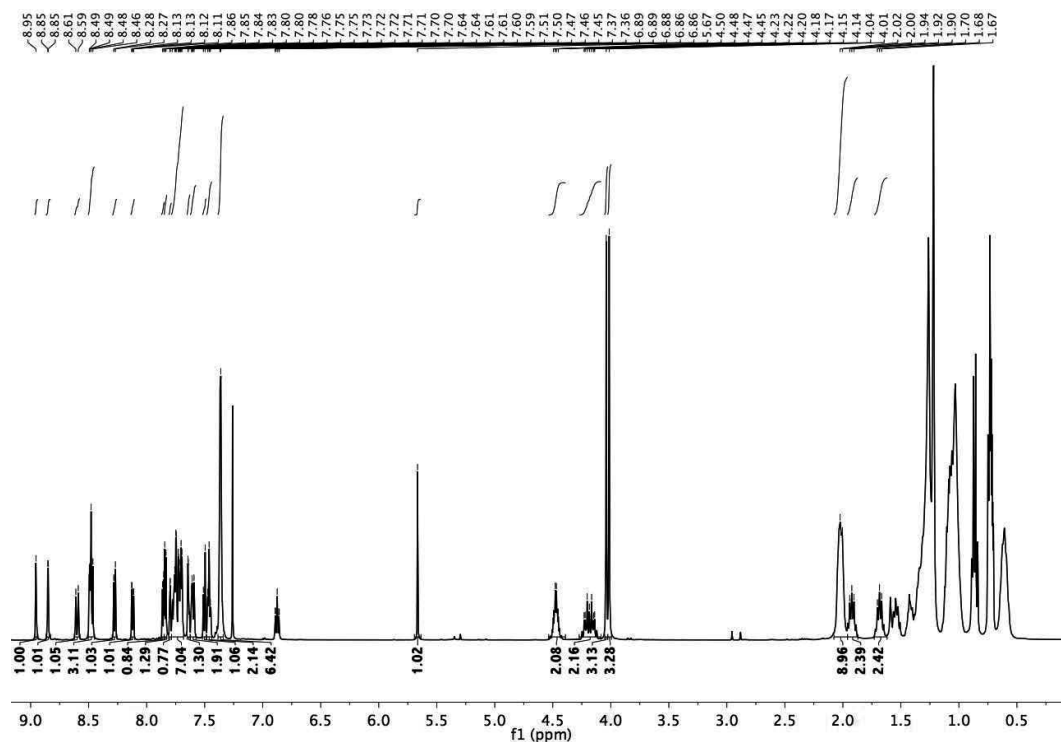
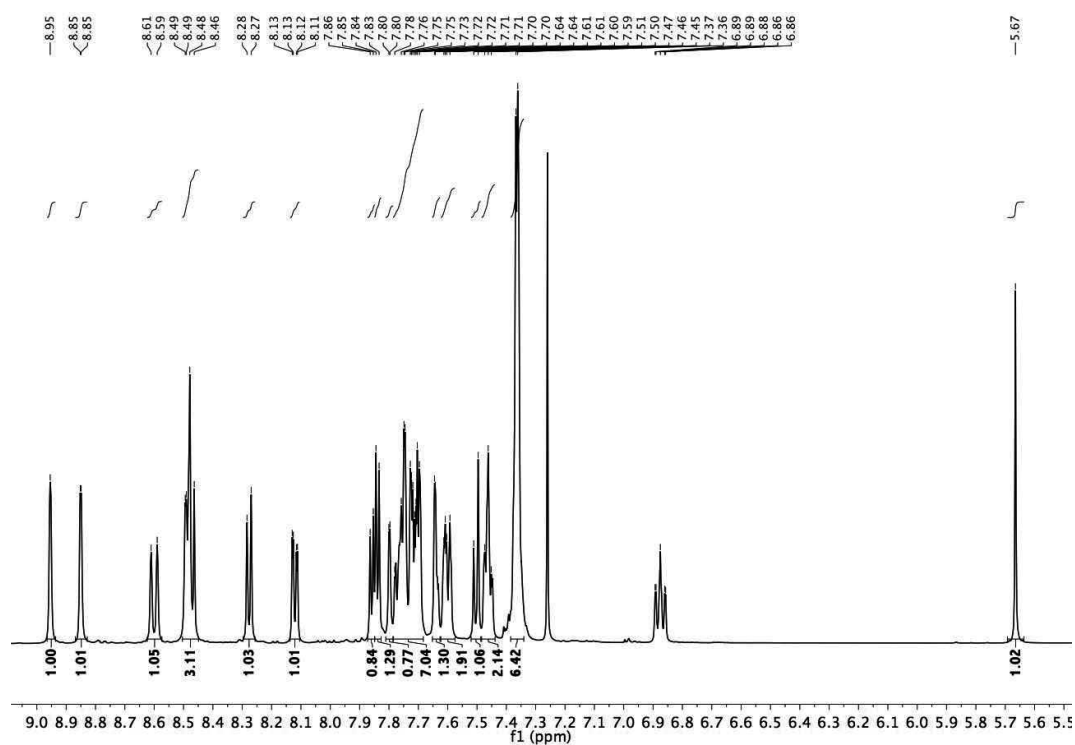
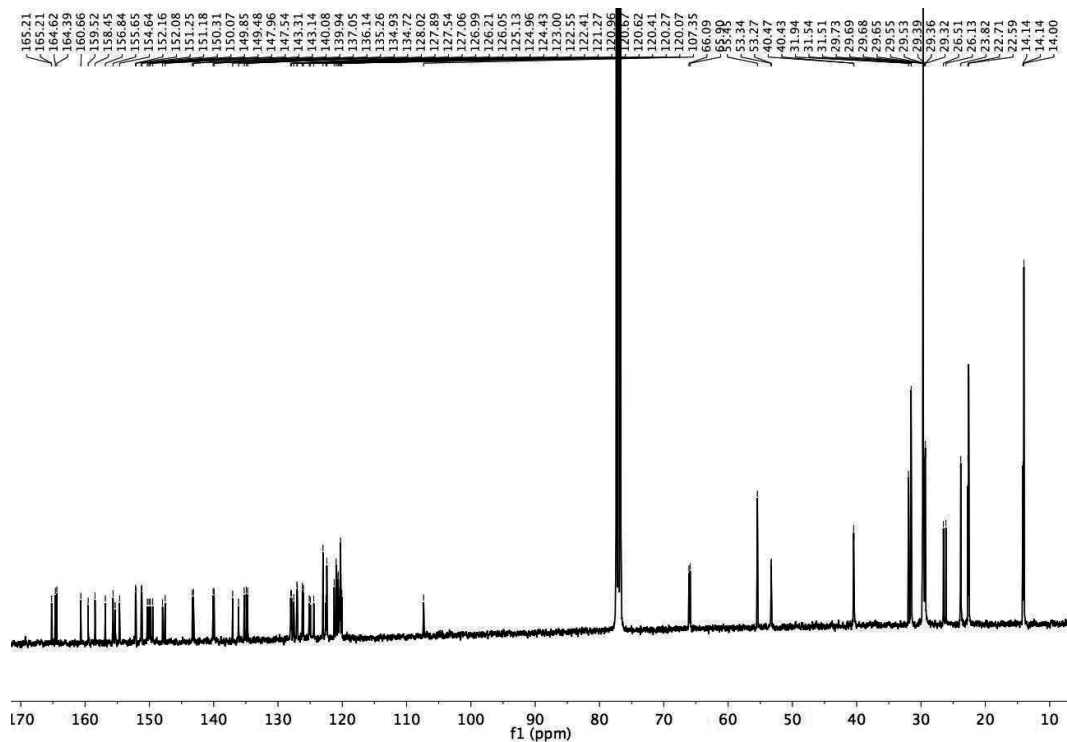
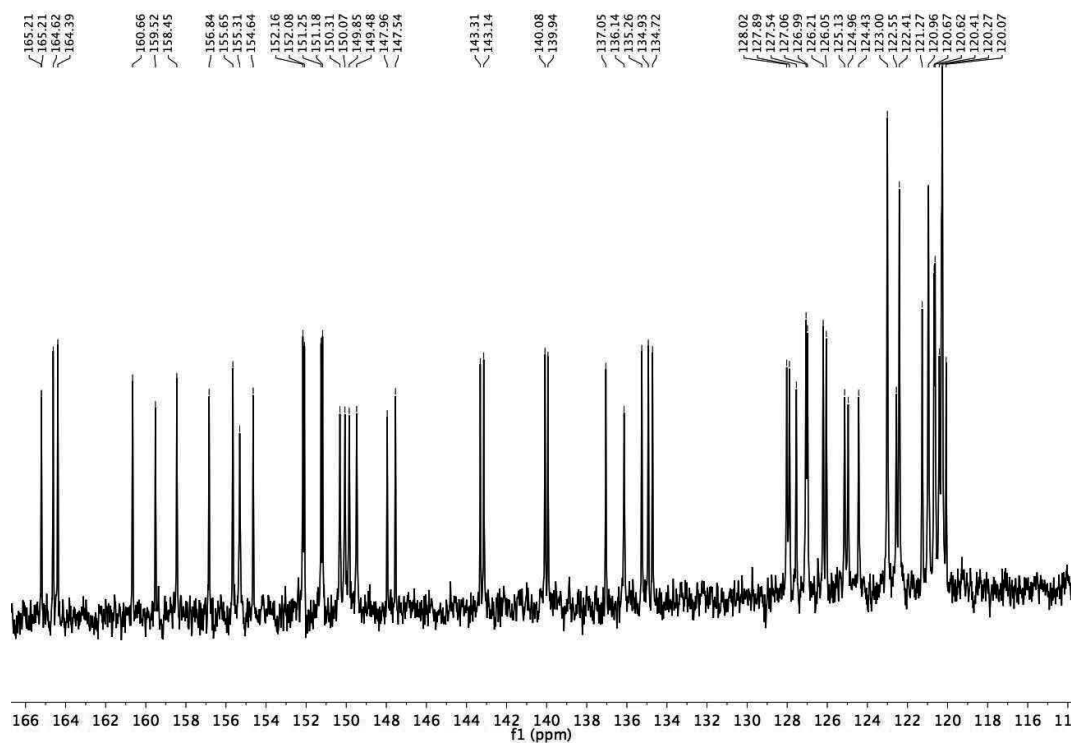
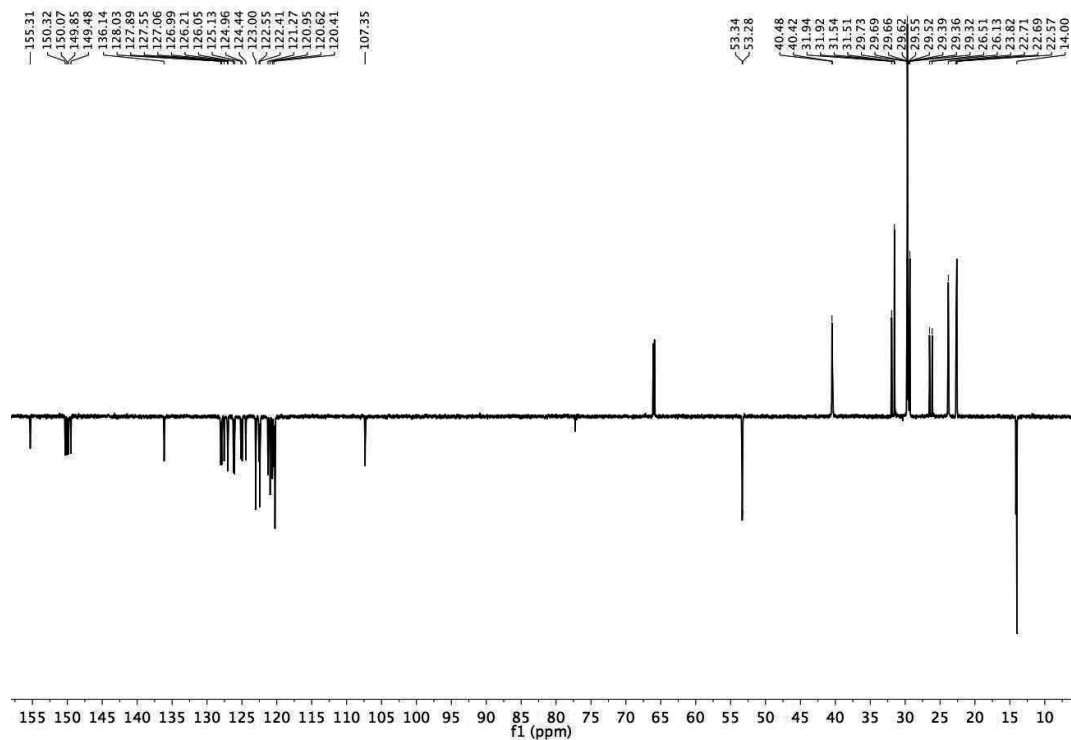


Figure 8.13. ^1H NMR of $[\text{Ru}(\text{C}^{\wedge}\text{N})(34)(\text{bpy}(\text{CO}_2\text{Me})_2)](\text{PF}_6)$ (SA274) in *chloroform- d*

Figure 8.14. ^1H NMR (aromatic region) of $[\text{Ru}(\text{C}^{\wedge}\text{N})(34)(\text{bpy}(\text{CO}_2\text{Me})_2)](\text{PF}_6)$ (SA-274) in *chloroform-d*Figure 8.15. ^{13}C NMR of $[\text{Ru}(\text{C}^{\wedge}\text{N})(34)(\text{bpy}(\text{CO}_2\text{Me})_2)](\text{PF}_6)$ (SA274) in *chloroform-d*

Figure 8.16. ^{13}C NMR (aromatic region) of $[\text{Ru}(\text{C}^{\wedge}\text{N})(34)(\text{bpy}(\text{CO}_2\text{Me})_2)](\text{PF}_6)$ (SA274) in *chloroform-d*Figure 8.17. DEPT 135 ^{13}C NMR of $[\text{Ru}(\text{C}^{\wedge}\text{N})(34)(\text{bpy}(\text{CO}_2\text{Me})_2)](\text{PF}_6)$ (SA274) in *chloroform-d*

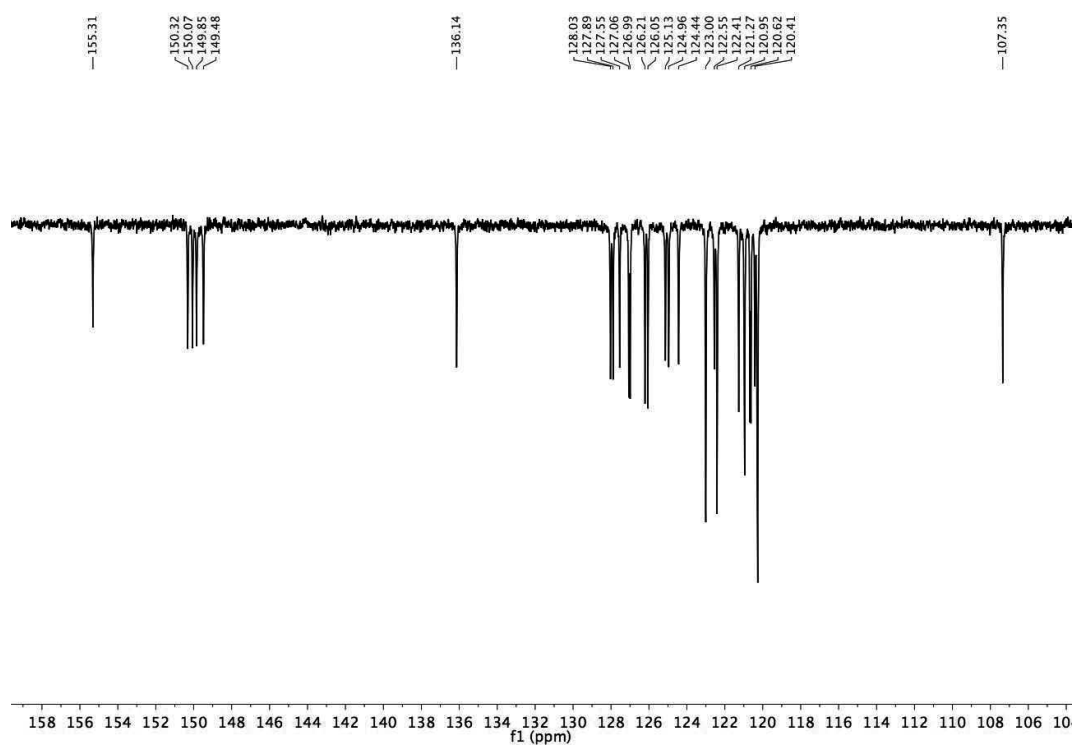


Figure 8.18. DEPT 135 ^{13}C NMR (aromatic region) of $[\text{Ru}(\text{C}^{\wedge}\text{N})(34)(\text{bpy}(\text{CO}_2\text{Me})_2)](\text{PF}_6)$ (SA274) in *chloroform-d*

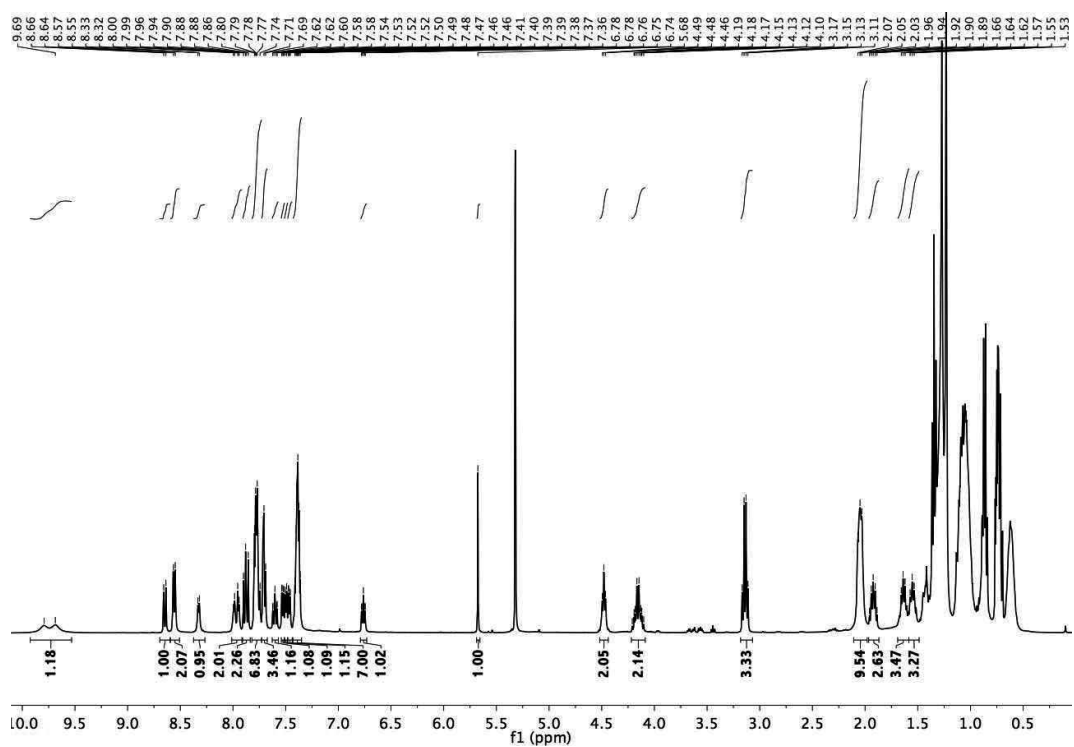


Figure 8.19. ^1H NMR of $[\text{Ru}(\text{C}^{\wedge}\text{N})(34)(\text{bpy}(\text{CO}_2\text{H})_2)](\text{PF}_6)$ (SA282) in *dichloromethane-d*₂

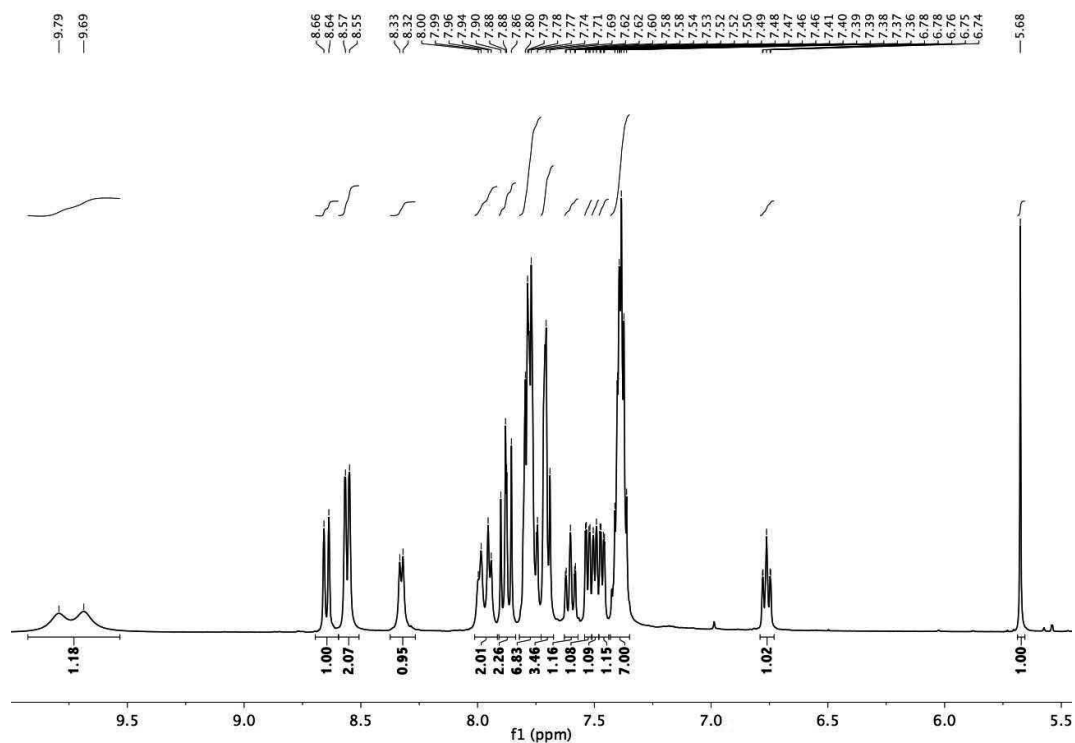


Figure 8.20. ^1H NMR (aromatic region) of $[\text{Ru}(\text{C}^{\wedge}\text{N})(34)(\text{bpy}(\text{CO}_2\text{H})_2)](\text{PF}_6)$ (SA282) in *dichloromethane- d_2*

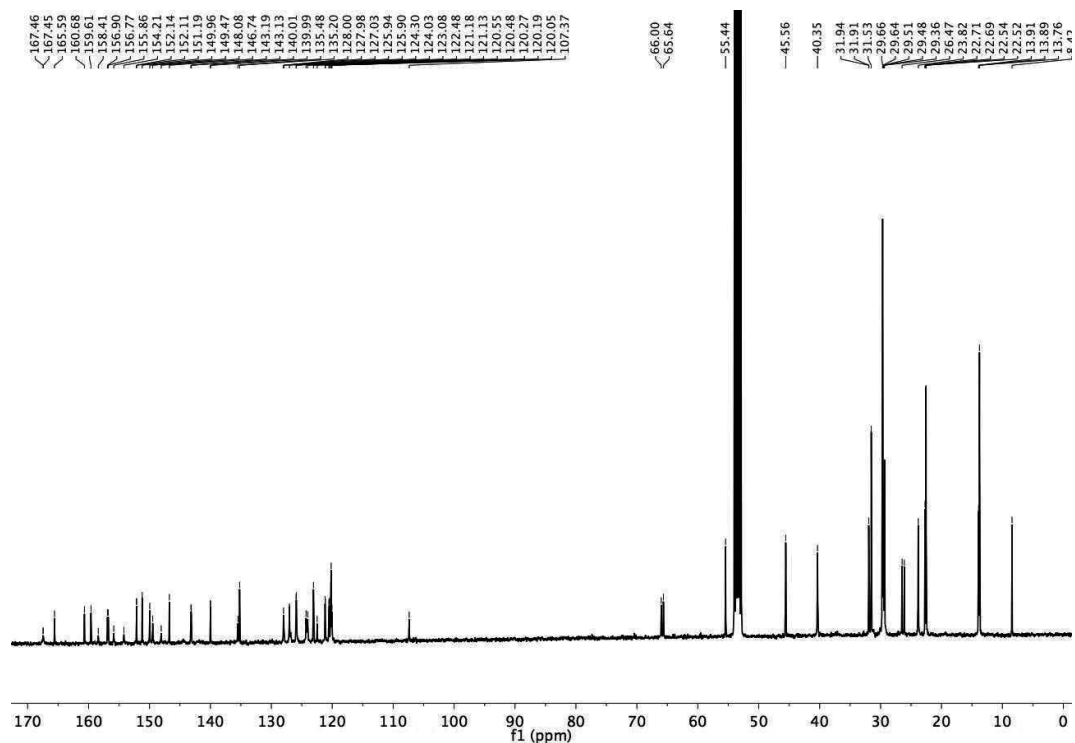


Figure 8.21. ^{13}C NMR of $[\text{Ru}(\text{C}^{\wedge}\text{N})(34)(\text{bpy}(\text{CO}_2\text{H})_2)](\text{PF}_6)$ (SA282) in *dichloromethane- d_2*

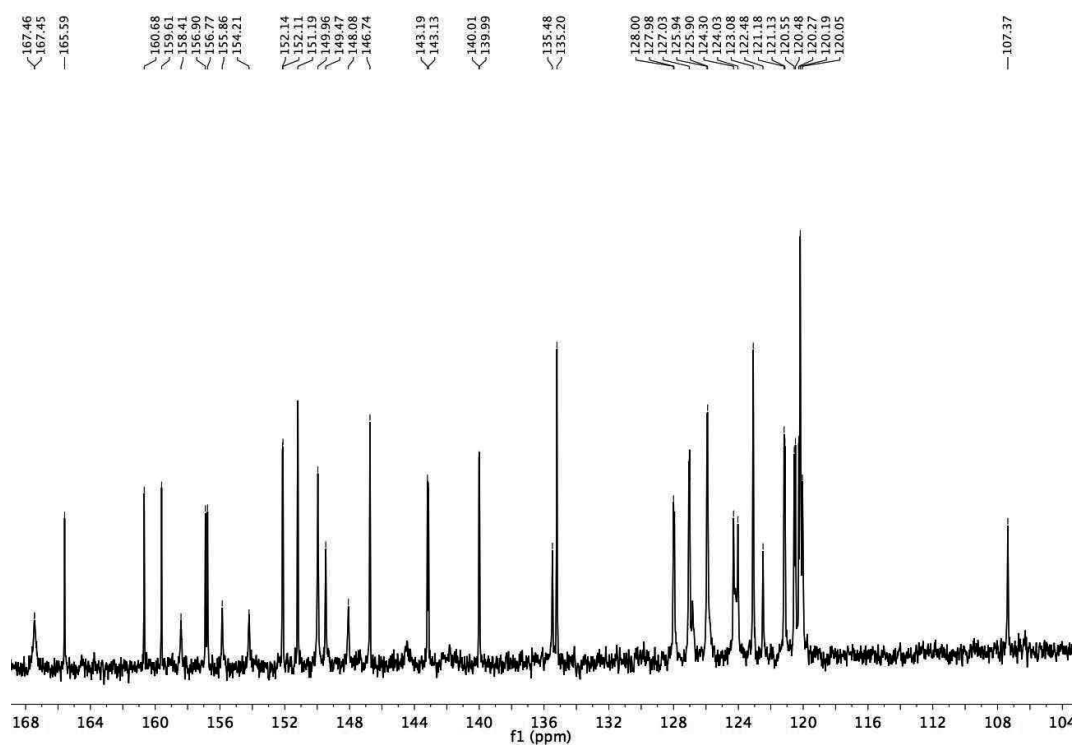


Figure 8.22. ^{13}C NMR (aromatic region) of $[\text{Ru}(\text{C}^{\wedge}\text{N})(34)(\text{bpy}(\text{CO}_2\text{H})_2)](\text{PF}_6)$ (SA282) in *dichloromethane- d_2*

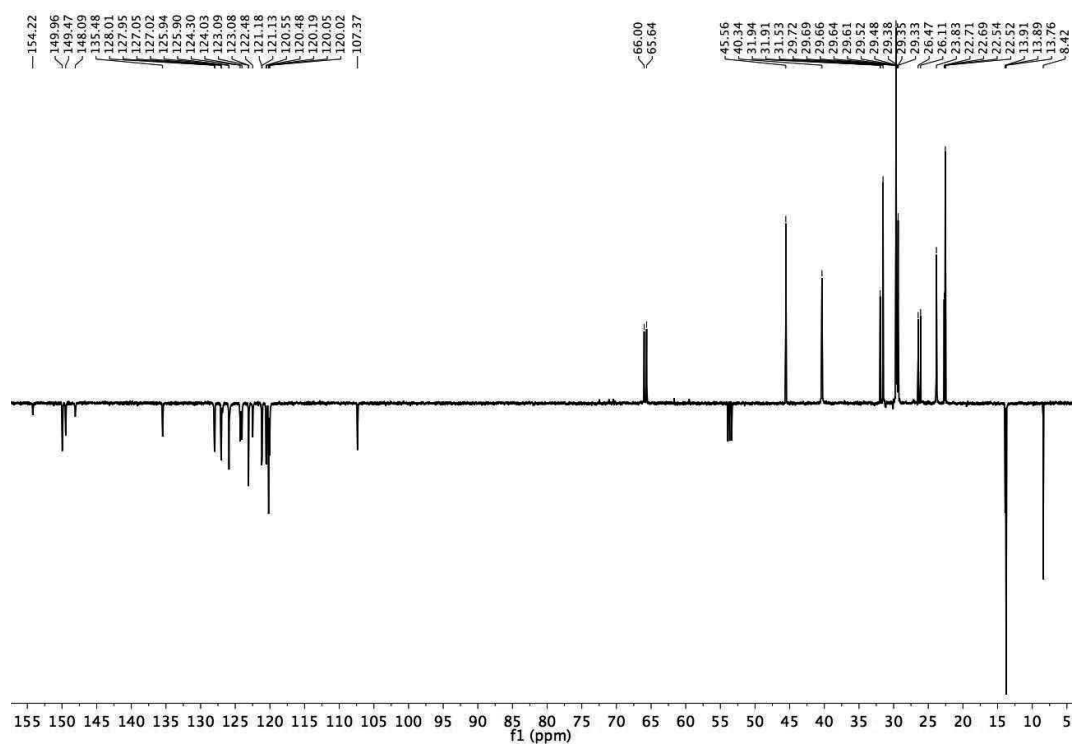


Figure 8.23. DEPT 135 ^{13}C NMR of $[\text{Ru}(\text{C}^{\wedge}\text{N})(34)(\text{bpy}(\text{CO}_2\text{H})_2)](\text{PF}_6)$ (SA282) in *dichloromethane- d_2*

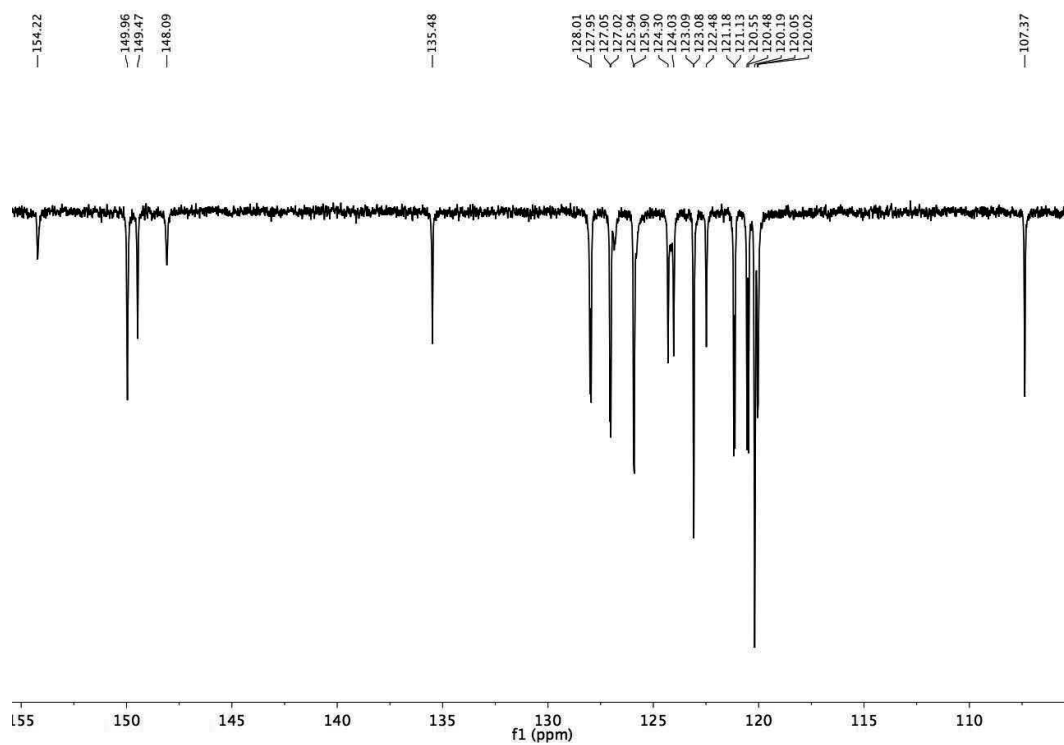


Figure 8.24. DEPT 135 ^{13}C NMR (aromatic region) of $[\text{Ru}(\text{C}^{\wedge}\text{N})(34)(\text{bpy}(\text{CO}_2\text{H})_2)](\text{PF}_6)$ (SA282) in *dichloromethane-d*₂

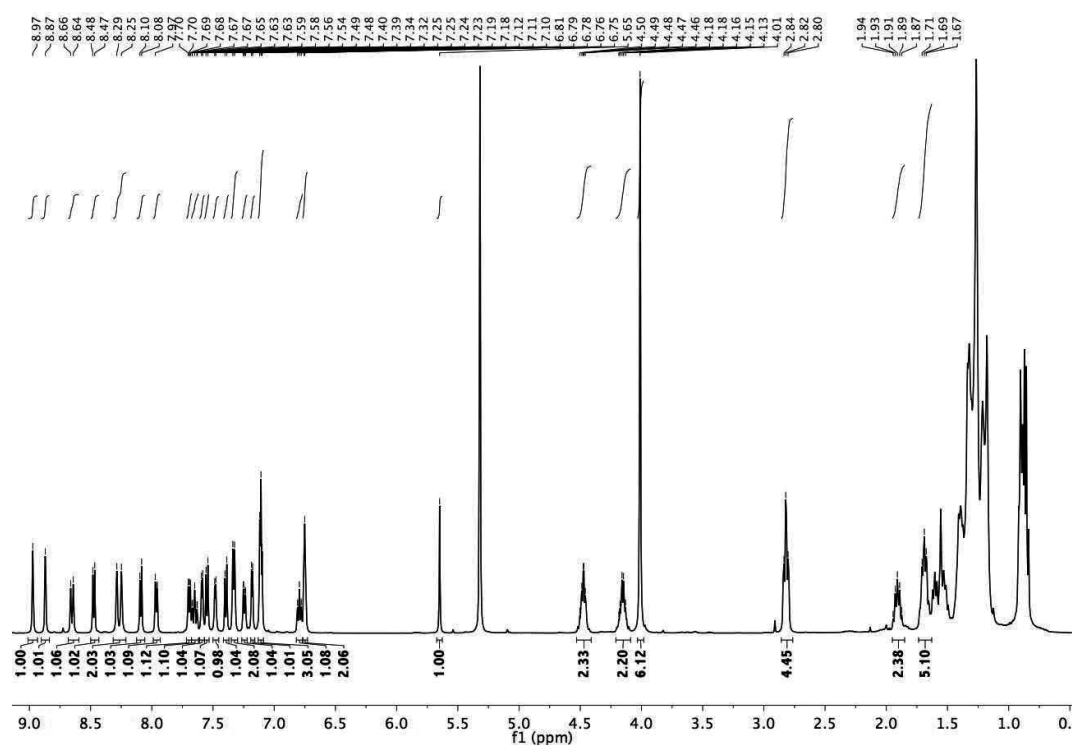


Figure 8.25. ^1H NMR of $[\text{Ru}(\text{C}^{\wedge}\text{N})(33)(\text{bpy}(\text{CO}_2\text{Me})_2)](\text{PF}_6)$ (SA-281) in *dichloromethane-d*₂

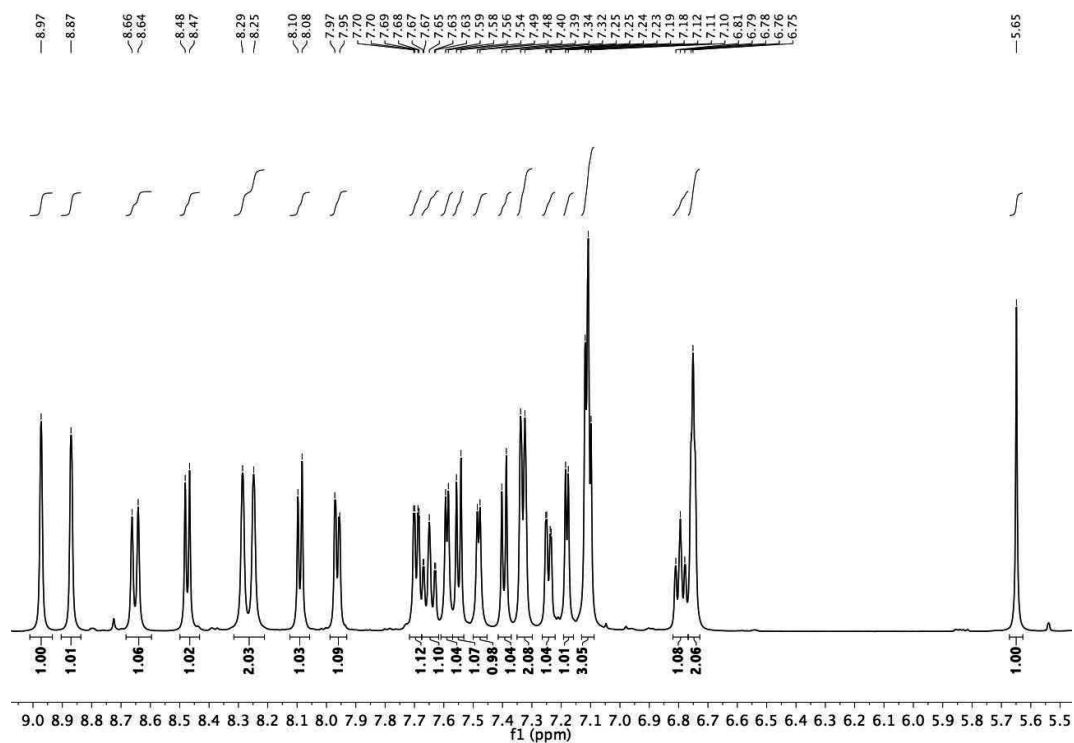


Figure 8.26. ^1H NMR (aromatic region) of $[\text{Ru}(\text{C}^{\wedge}\text{N})(33)(\text{bpy}(\text{CO}_2\text{Me})_2)](\text{PF}_6)$ (SA281) in *dichloromethane- d_2*

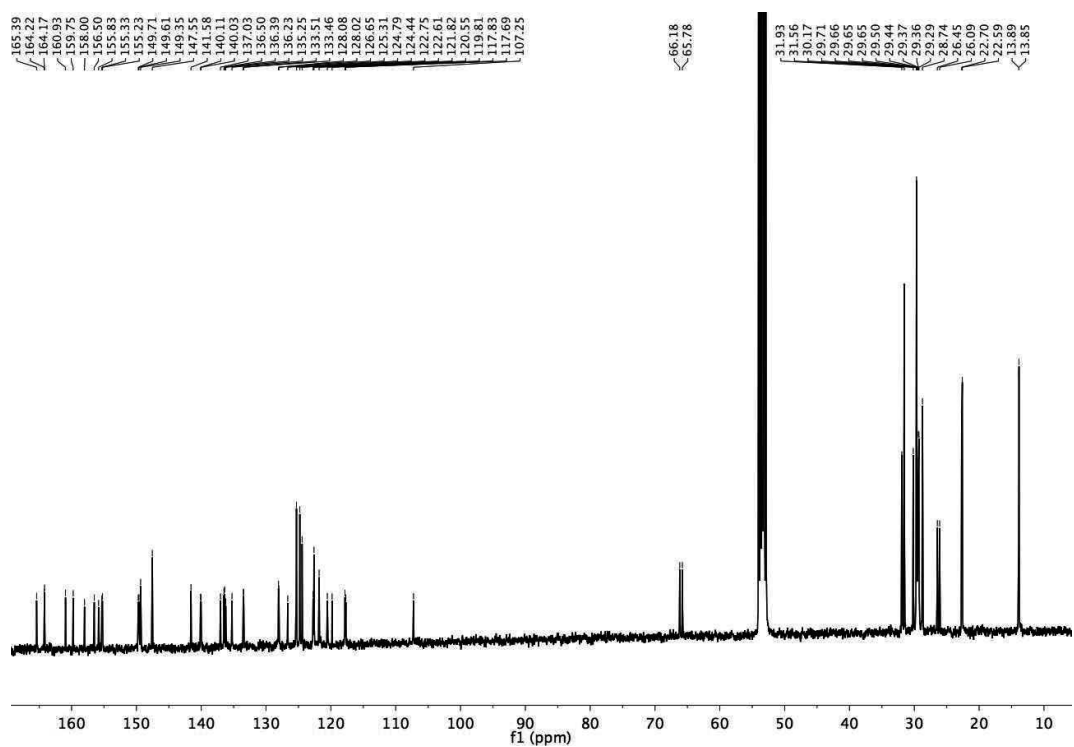


Figure 8.27. ^{13}C NMR of $[\text{Ru}(\text{C}^{\wedge}\text{N})(33)(\text{bpy}(\text{CO}_2\text{Me})_2)](\text{PF}_6)$ (SA-281) in *dichloromethane- d_2*

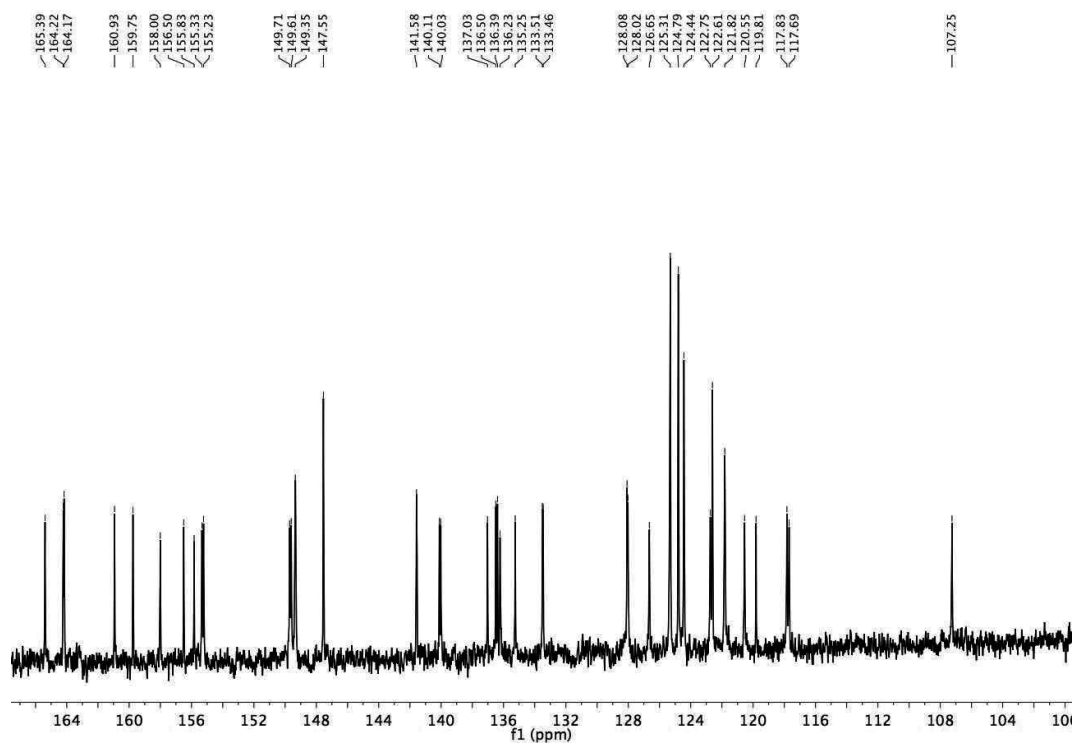


Figure 8.28. ^{13}C NMR (aromatic region) of $[\text{Ru}(\text{C}^{\wedge}\text{N})(33)(\text{bpy}(\text{CO}_2\text{Me})_2)](\text{PF}_6)$ (SA-281) in *dichloromethane- d_2*

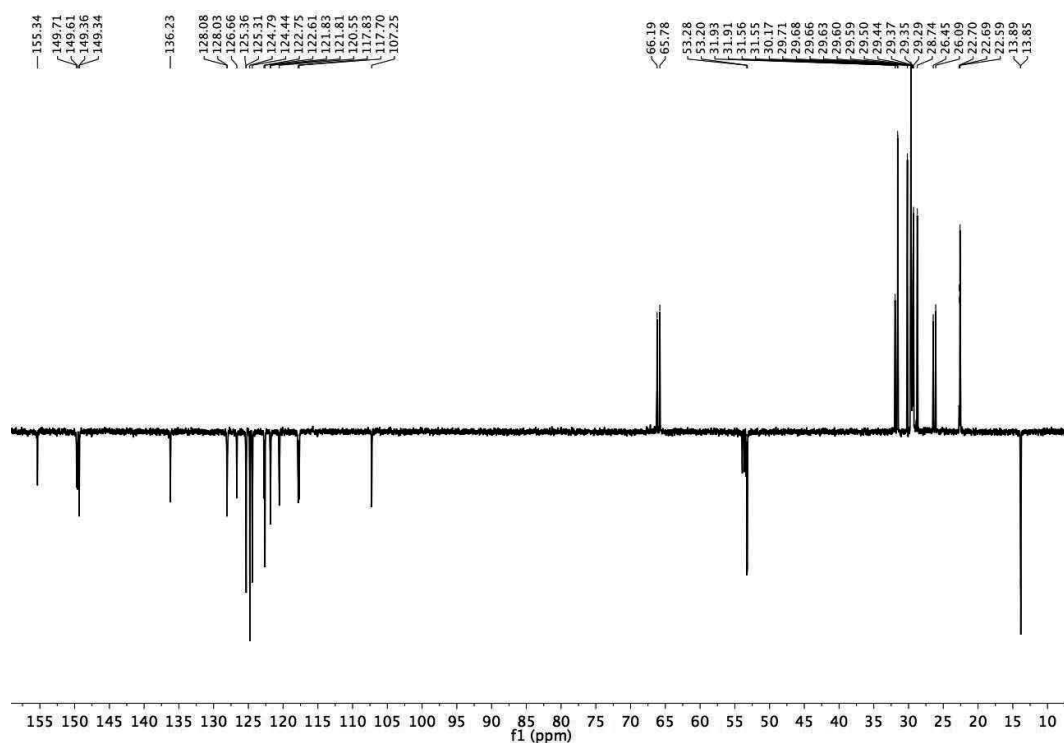


Figure 8.29. DEPT 135 ^{13}C NMR of $[\text{Ru}(\text{C}^{\wedge}\text{N})(33)(\text{bpy}(\text{CO}_2\text{Me})_2)](\text{PF}_6)$ (SA-281) in *dichloromethane- d_2*

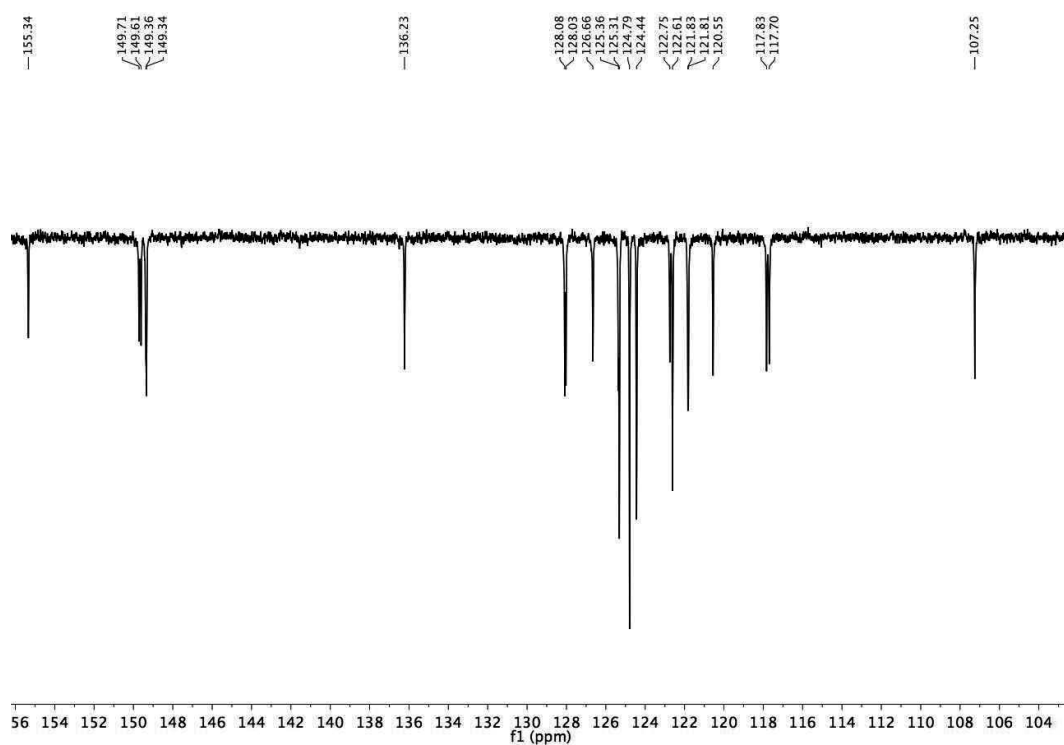


Figure 8.30. DEPT 135 ^{13}C NMR (aromatic region) of $[\text{Ru}(\text{C}^{\wedge}\text{N})(33)(\text{bpy}(\text{CO}_2\text{Me})_2)](\text{PF}_6)$ (SA-281) in dichloromethane- d_2

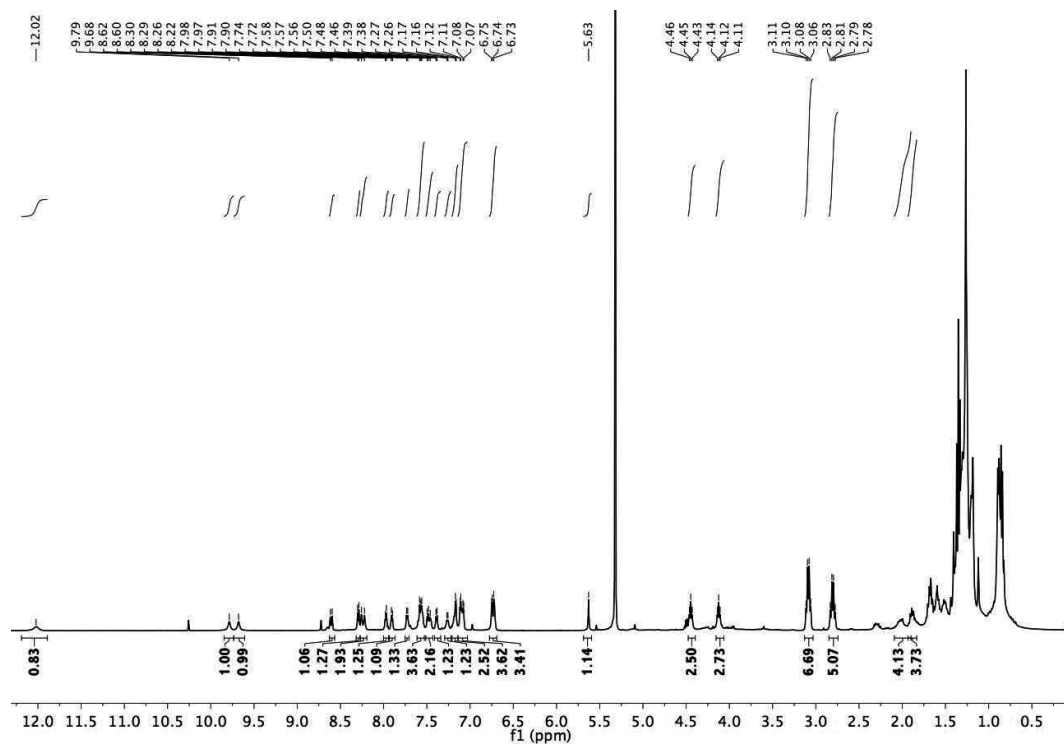


Figure 8.31. ^1H NMR of $[\text{Ru}(\text{C}^{\wedge}\text{N})(33)(\text{bpy}(\text{CO}_2\text{H})_2)](\text{PF}_6)$ (SA284) in dichloromethane- d_2

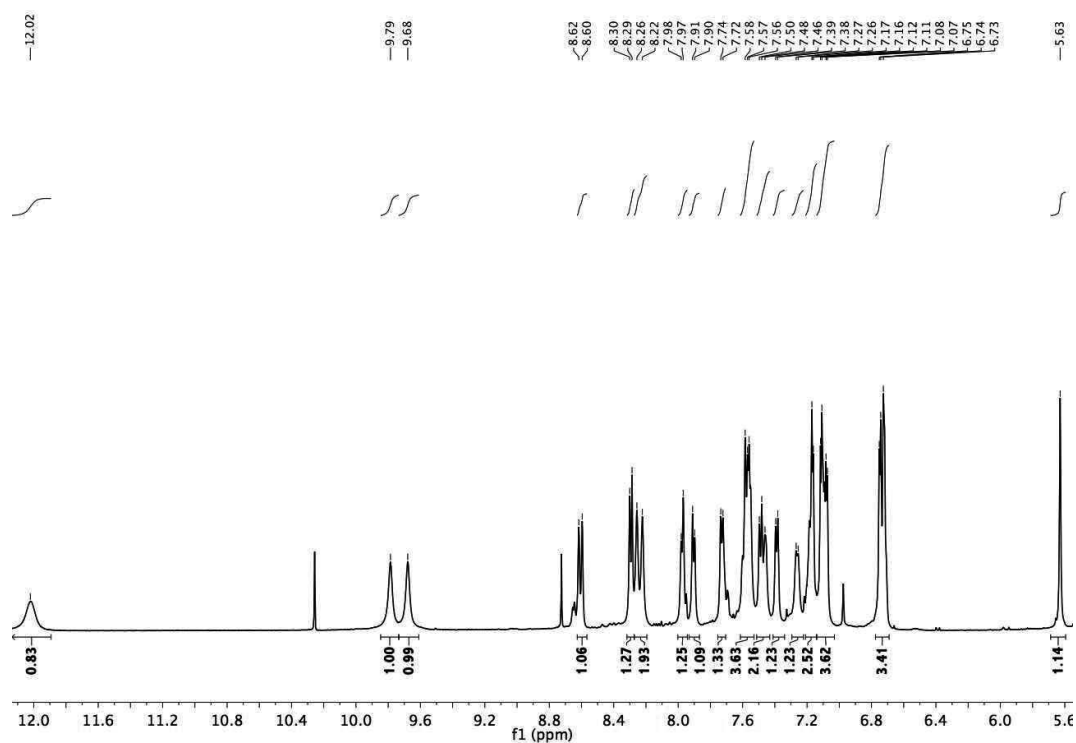


Figure 8.32. ^1H NMR (aromatic region) of $[\text{Ru}(\text{C}^{\text{N}})(33)(\text{bpy}(\text{CO}_2\text{H})_2)](\text{PF}_6)$ (SA284) in $\text{dichloromethane-}d_2$

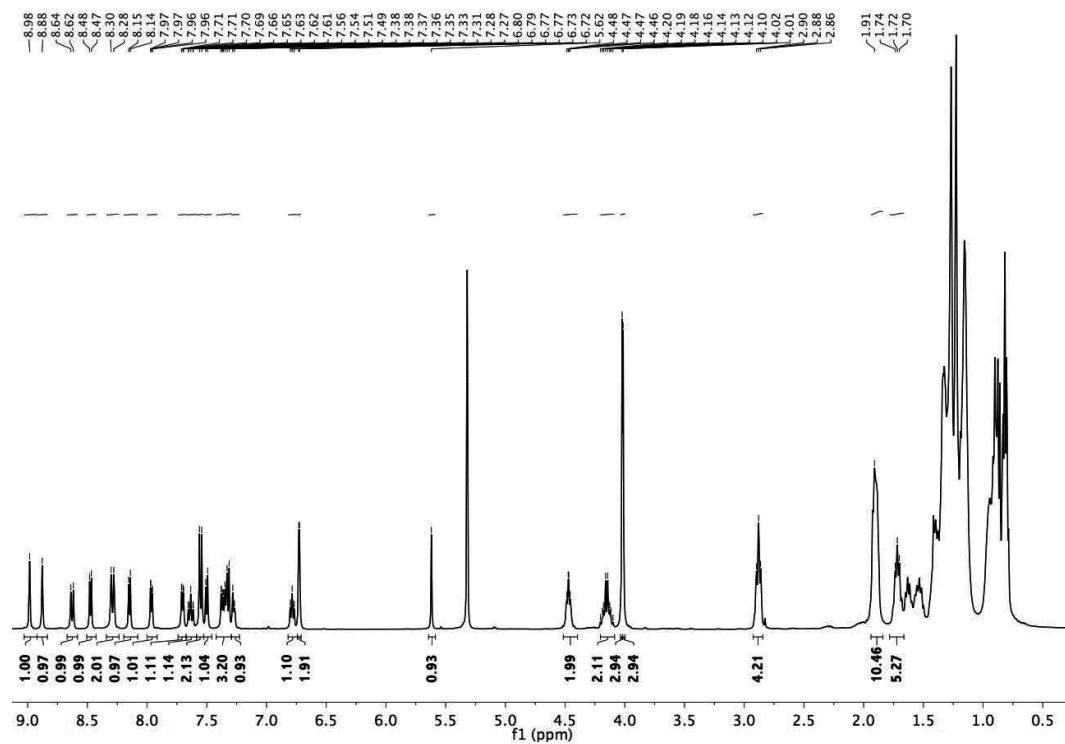


Figure 8.33. ^1H NMR of $[\text{Ru}(\text{C}^{\text{N}})(31)(\text{bpy}(\text{CO}_2\text{Me})_2)](\text{PF}_6)$ (SA283) in $\text{dichloromethane-}d_2$

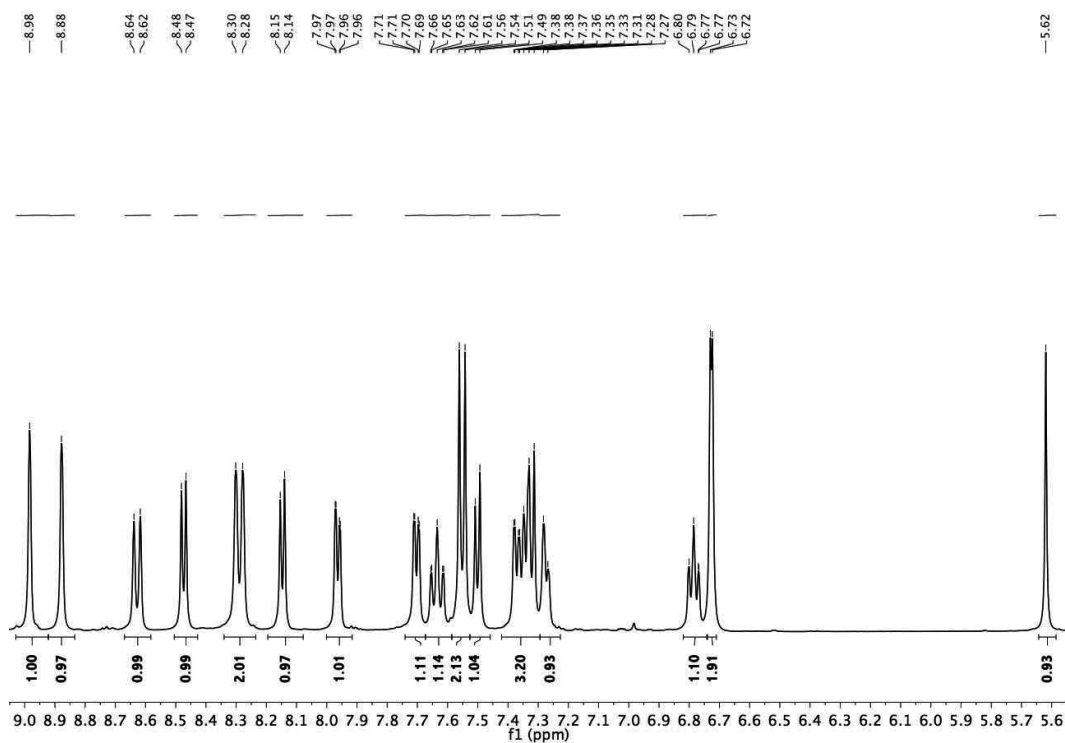


Figure 8.34. ^1H NMR (aromatic region) of $[\text{Ru}(\text{C}^{\wedge}\text{N})(31)(\text{bpy}(\text{CO}_2\text{Me})_2)](\text{PF}_6)$ (SA-283) in *dichloromethane- d_2*

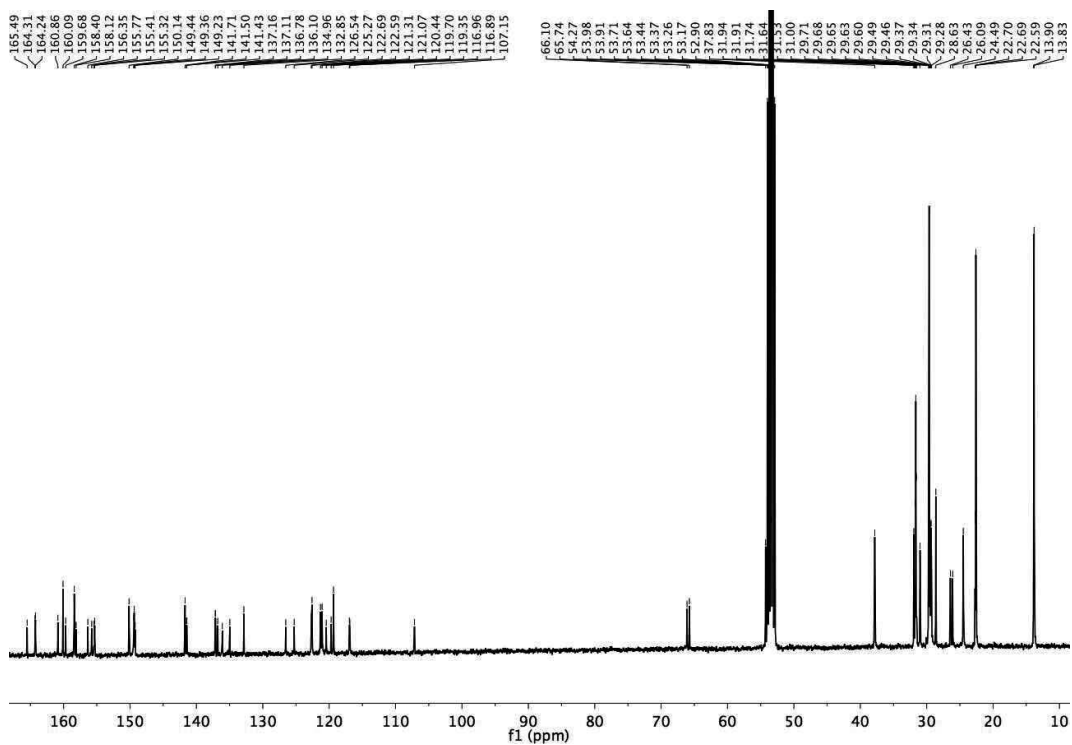


Figure 8.35. ^{13}C NMR of $[\text{Ru}(\text{C}^{\wedge}\text{N})(31)(\text{bpy}(\text{CO}_2\text{Me})_2)](\text{PF}_6)$ (SA-283) in *dichloromethane- d_2*

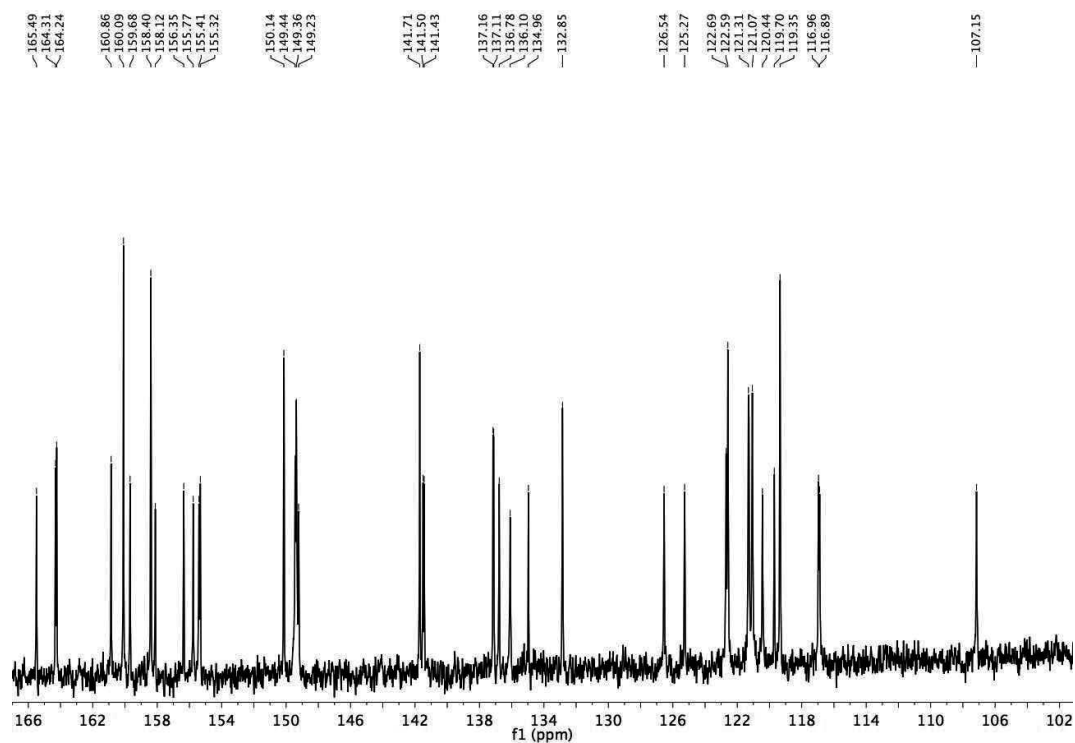


Figure 8.36. ^{13}C NMR (aromatic region) of $[\text{Ru}(\text{C}^{\wedge}\text{N})(31)(\text{bpy}(\text{CO}_2\text{Me})_2)](\text{PF}_6)$ (SA-283) in *dichloromethane- d_2*

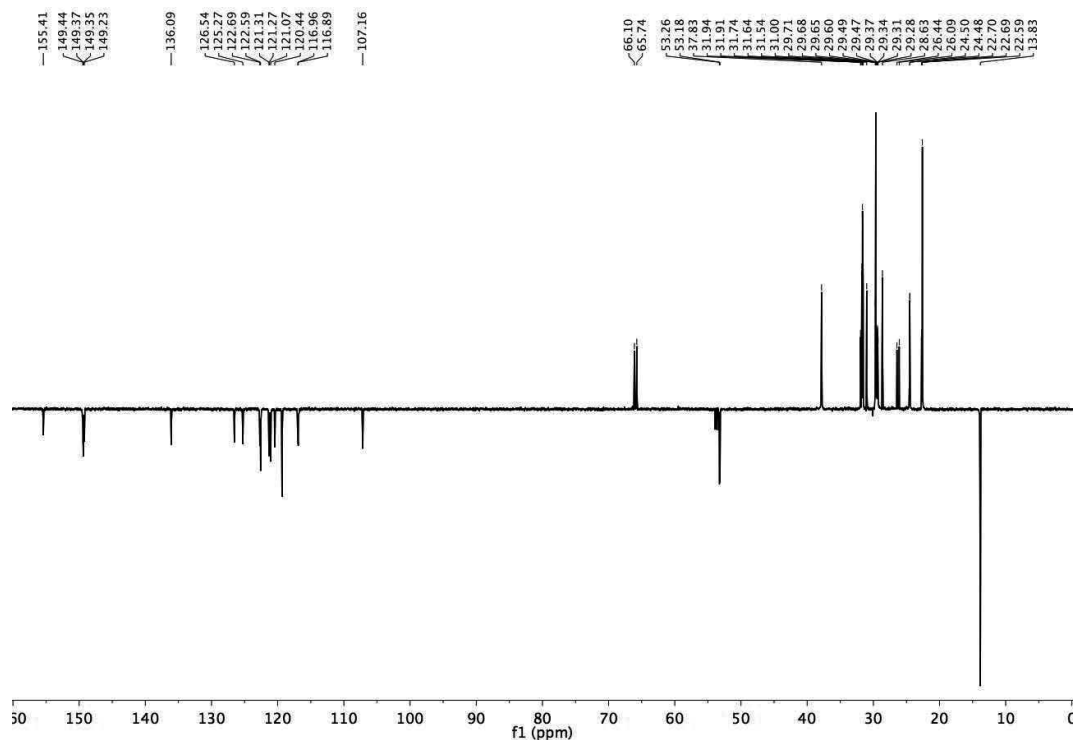


Figure 8.37. DEPT 135 ^{13}C NMR of $[\text{Ru}(\text{C}^{\wedge}\text{N})(31)(\text{bpy}(\text{CO}_2\text{Me})_2)](\text{PF}_6)$ (SA-283) in *dichloromethane- d_2*

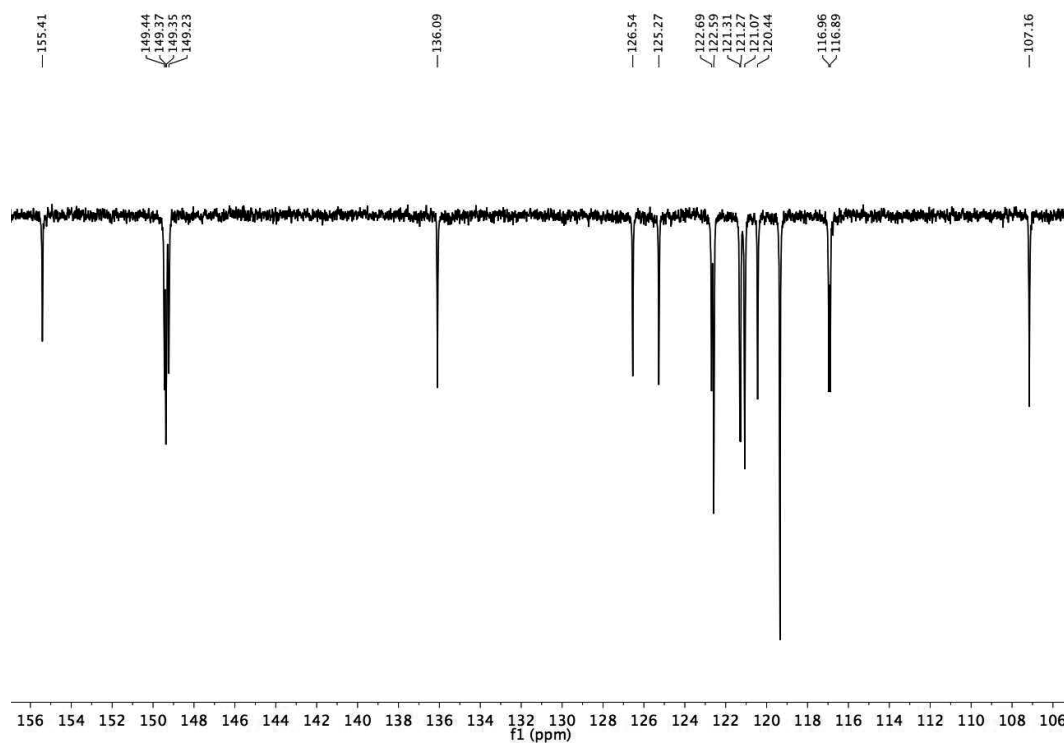


Figure 8.38. DEPT 135 ^{13}C NMR (aromatic region) of $[\text{Ru}(\text{C}^{\wedge}\text{N})(31)(\text{bpy}(\text{CO}_2\text{Me})_2)](\text{PF}_6)$ (SA-283) in *dichloromethane-d*₂

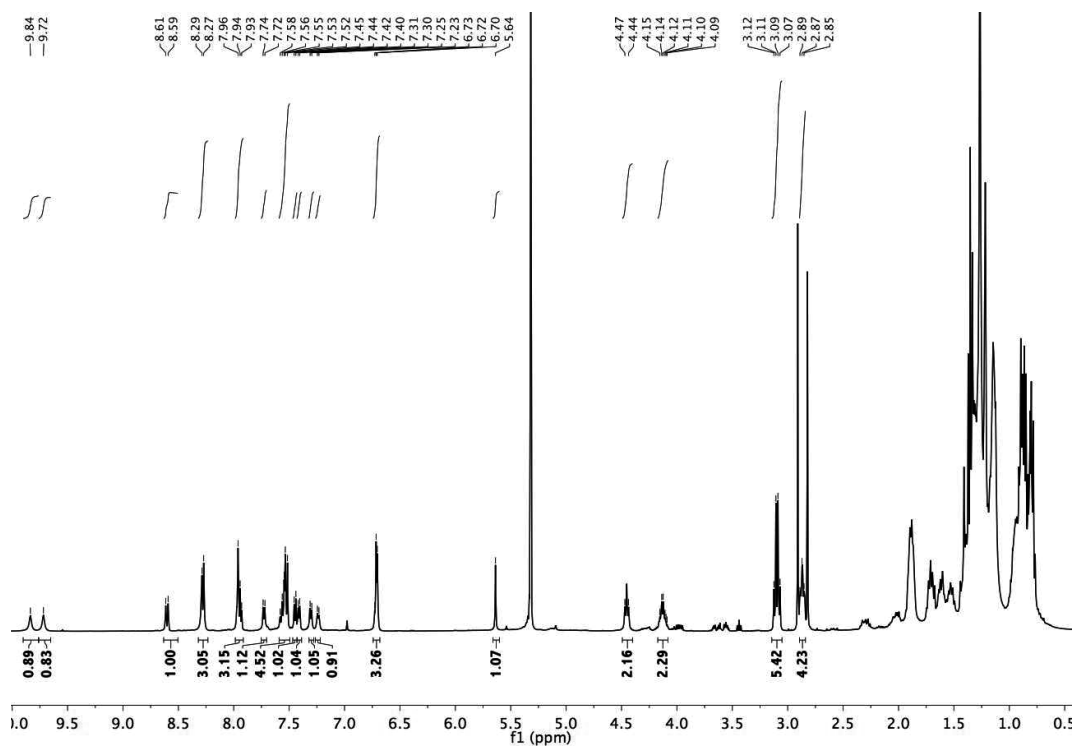


Figure 8.39. ^1H NMR of $[\text{Ru}(\text{C}^{\wedge}\text{N})(31)(\text{bpy}(\text{CO}_2\text{H})_2)](\text{PF}_6)$ (SA285) in *dichloromethane-d*₂

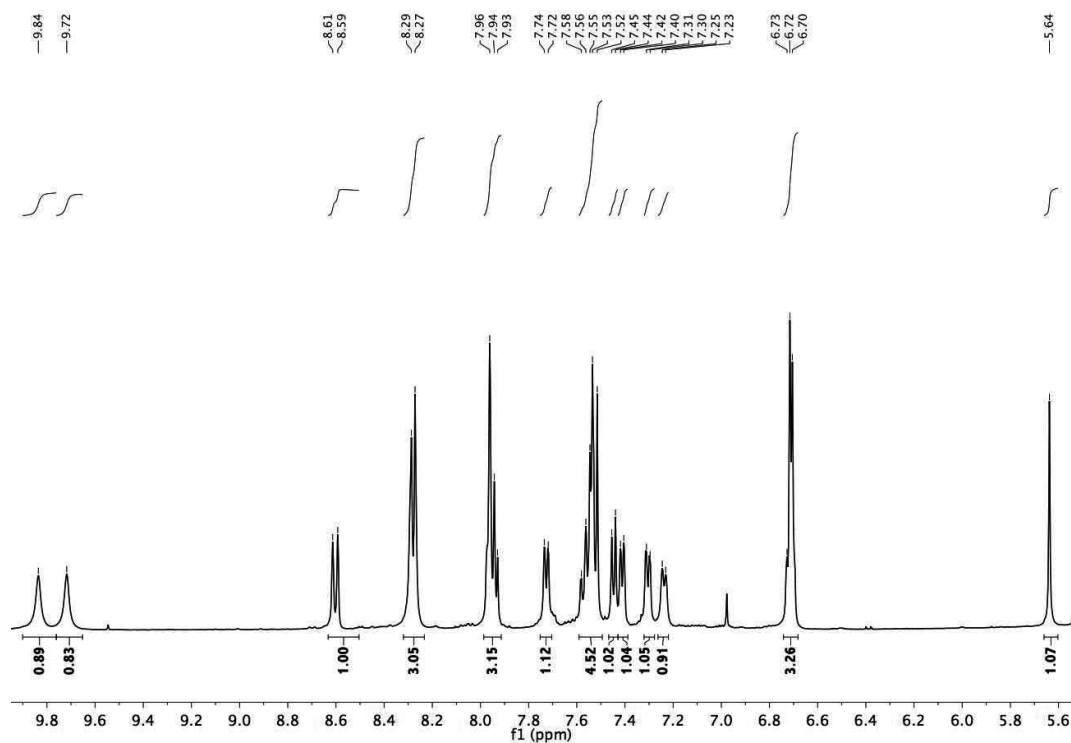


Figure 8.40. ^1H NMR (aromatic region) of $[\text{Ru}(\text{C}^{\wedge}\text{N})(31)(\text{bpy}(\text{CO}_2\text{H})_2)](\text{PF}_6)$ (SA285) in *dichloromethane- d_2*

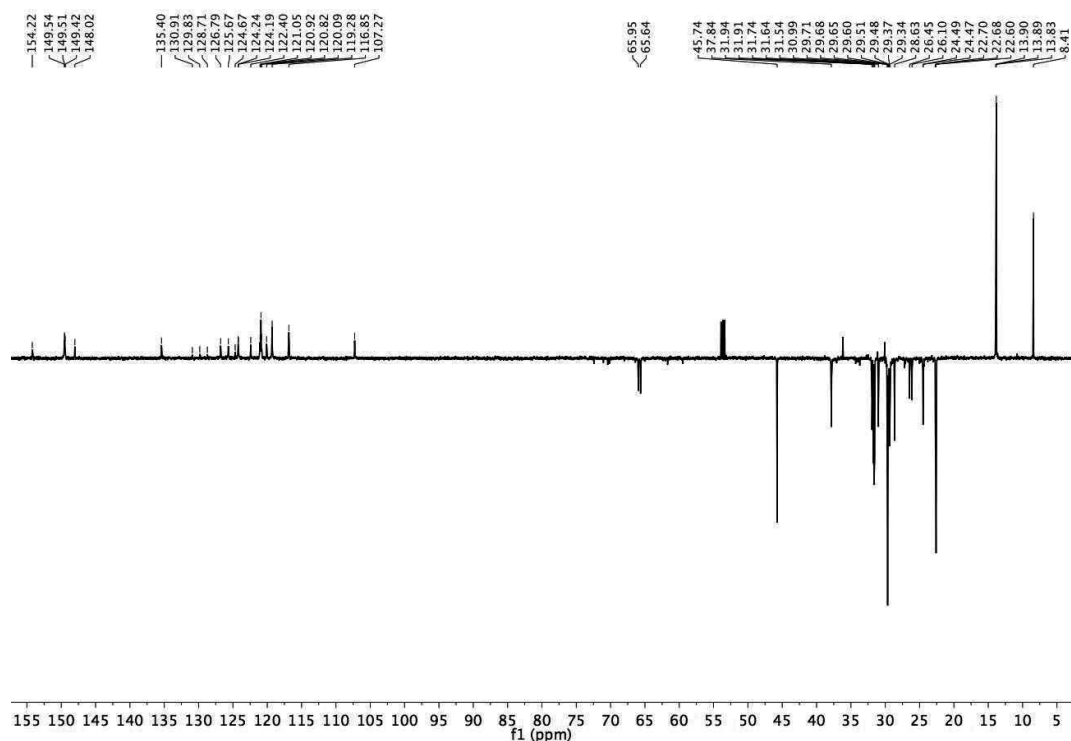


Figure 8.41. DEPT 135 ^{13}C NMR of $[\text{Ru}(\text{C}^{\wedge}\text{N})(31)(\text{bpy}(\text{CO}_2\text{H})_2)](\text{PF}_6)$ (SA285) in *dichloromethane- d_2*

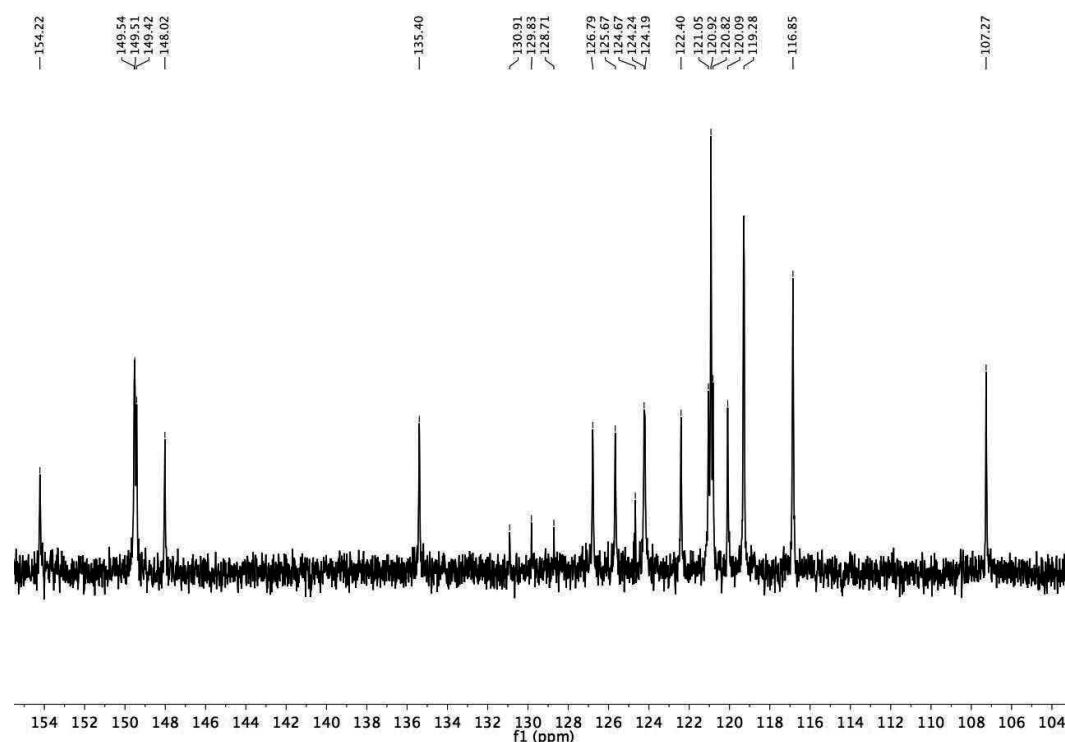


Figure 8.42. DEPT 135 ^{13}C NMR (aromatic region) of $[\text{Ru}(\text{C}^{\wedge}\text{N})(31)(\text{bpy}(\text{CO}_2\text{H})_2)](\text{PF}_6)$ (SA285) in *dichloromethane-d*₂

8.1.2 Optical and Electrochemical Characterization of Dyes.

Electronic absorption spectra of dyes were measured in dichloromethane with a Hewlett Packard Diode Array spectrophotometer. Emission spectra were recorded with a Fluorolog Horiba Jobin Yvon Model FL-1065. Absorption and emission spectra sensitized titania films were measured with the same instruments. For the absorption spectra measurements a mask with area lower than sensitized film area was used.

To determine dyes oxidation potentials cyclic voltammetry measurements were conducted. A PC controlled AutoLab PSTAT 10 electrochemical workstation was employed. Dyes were dissolved in 0.1 M solution of tetra-n-butylammonium hexafluorophosphate in dichloromethane using a glassy carbon electrode as working and Pt wires as a counter and pseudo-reference electrodes. Measurements were carried out under argon flux. Fc/Fc^+ was used as internal standard. Fc/Fc^+ 's oxidation potential was fixed at +0.70 V vs. NHE to convert potentials to NHE scale.

Time-Related Single Photon Counting (TCSPC) experiments were conducted using the setup for emission spectroscopy coupled with additional FluoroHub (Horiba) unit with TBX-04 photomultiplier as a detector. A NanoLed pulsed laser-diode emitting at 406 nm was used.

Spectroelectrochemical measurements were carried out using a PC controlled AutoLab PSTAT 10 electrochemical workstation coupled with a Hewlett Packard Diode Array spectrophotometer. A Pt-mesh working electrode inside a thin-layer quartz cuvette employed with Pt – wire counter electrode and Ag-wire pseudo-reference electrode was used for measurements. Dye was dissolved in 0.1 M solution of NBu_4PF_6 in dichloromethane. First, a potential by 50 mV higher than oxidation wave potential was applied and absorption spectra were measured every 10 second 16 times. Then, applied potential was fixed at a value by 50 mV lower than the reduction wave potential and absorption spectra were measured for every 10 second 16-20 times (Figure 8.43(A,B)).

Spectroelectrochemical studies of the complete devices lacking redox shuttle were carried out using the same station described above. The applied potentials for the dye oxidation and reduction were fixed at the potentials relevant to the onset of anodic and cathodic currents (Figure 8.43 (C)).

Worth to notice that unrecovered MLCT band intensity may result in a loss of a dye during the oxidation. This may cause a drop in J_{SC} and V_{OC} in a working device. However, one may argue that in the full device a photooxidized dye is regenerated with a reductant present in the electrolyte before going through detrimental destruction. The transient absorbance analysis showed that dye regeneration takes place in the microsecond time scale (vide infra), which competes with other destructive chemical processes.

8.1.3 Dye Desorption Measurements

To analyze the amount of the dye chemisorbed on the surface, we put dye-sensitized photoanodes into a vial containing 3 mL of DCM. Then few drops of 0.1 M NBu_4OH in ethanol were added. After 4 hours the electrode converted completely white. The electrode was taken out, washed with few milliliters of DCM and the volume of the dye solution was brought to 10 mL. Absorption spectra were measured and the amount of chemisorbed dye was calculated using Beer-Lambert-Bouguer law on the most redshifted MLCT band maximum. Due to dye deprotonation, blue shift of the absorption band maximum position within few nanometers were observed. We considered, that dye deprotonation is not changing the extinction coefficient significantly. Due to the inconsistencies in the electrode thickness, we have repeated the experiment at least three times with all dyes until obtaining the consistent result (error within 5 %).

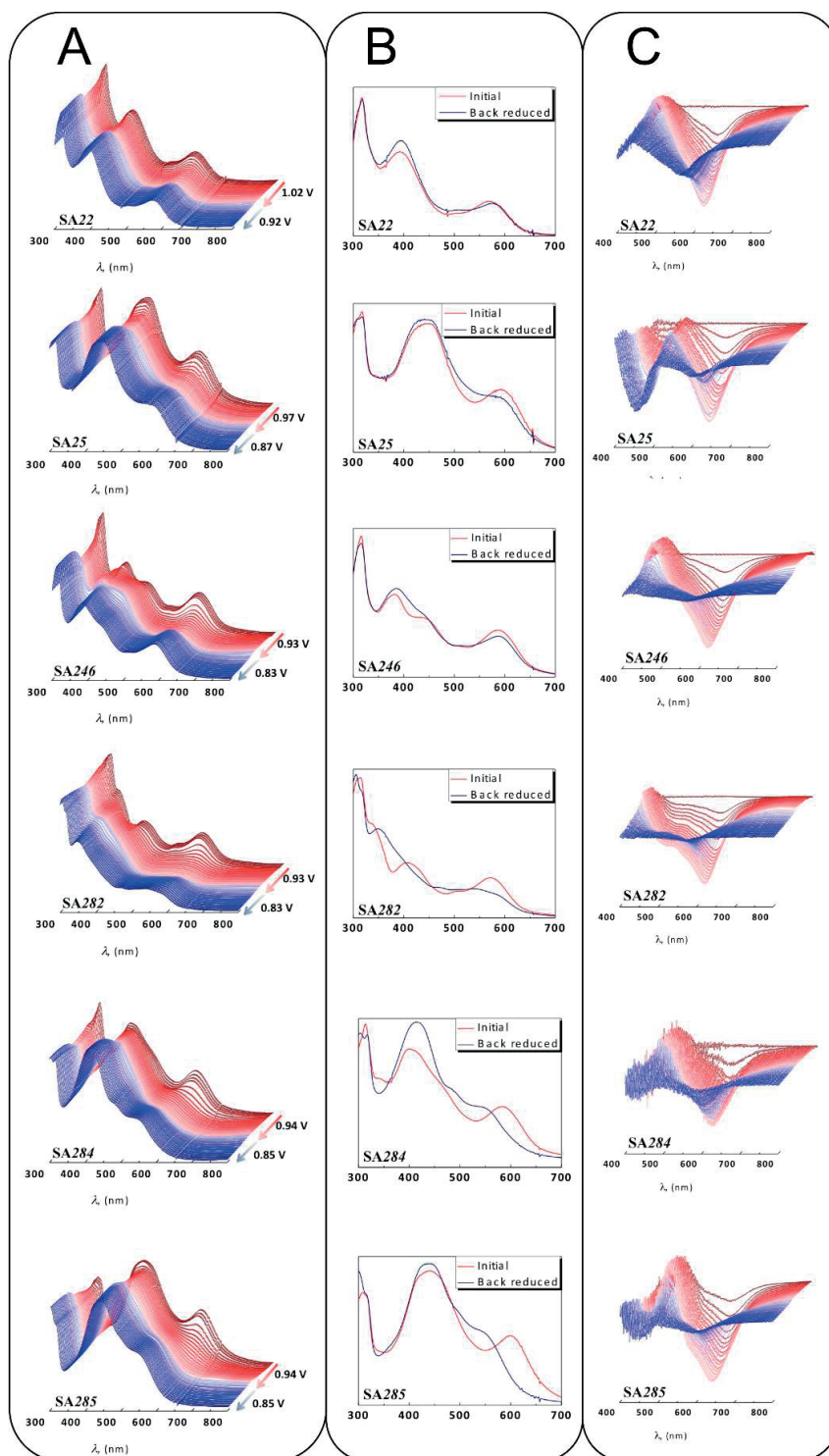


Figure 8.43. (A) Spectroelectrochemical measurements in 0.1 M NBu_4PF_6 DCM solution of SA dyes. Color change from the red to the pale red and then to the blue visualize the change in spectra during the oxidation and back reduction respectively; (B) Initial and final spectra obtained after back reduction; (C) Spectroelectrochemical measurements in a full device lacking redox shuttle with sensitized SA dyes titania films. Color change from the red to the pale red and then to the blue visualize the change in

spectra during the oxidation and back reduction respectively. The starting spectrum was taken as a baseline.

8.1.4 Computational Details

All the calculations have been performed by the GAUSSIAN 09 program package.¹⁸⁸ We optimized the molecular structure of the full protonated complexes in vacuum using the B3LYP exchange–correlation functional²²⁷ and a 3-21G* basis set.²²⁸ TDDFT calculations of the lowest singlet–singlet excitations were performed in DCM solution on the structure optimized in vacuum and using a DGDZVP basis set.²²⁹ The non-equilibrium version of C-PCM^{230–232} was employed for TDDFT calculations, as implemented in G09. To simulate the optical spectra, the 70 lowest spin-allowed singlet–singlet transitions were computed on the ground state geometry. Transition energies and oscillator strengths were interpolated by a Gaussian convolution with a σ value of 0.13 eV.

Optimized geometries of SA series dyes are shown in Figure 8.44. Cyclometalated pyridine ring was fixed in trans-position to the anchoring carboxypyridine ring.

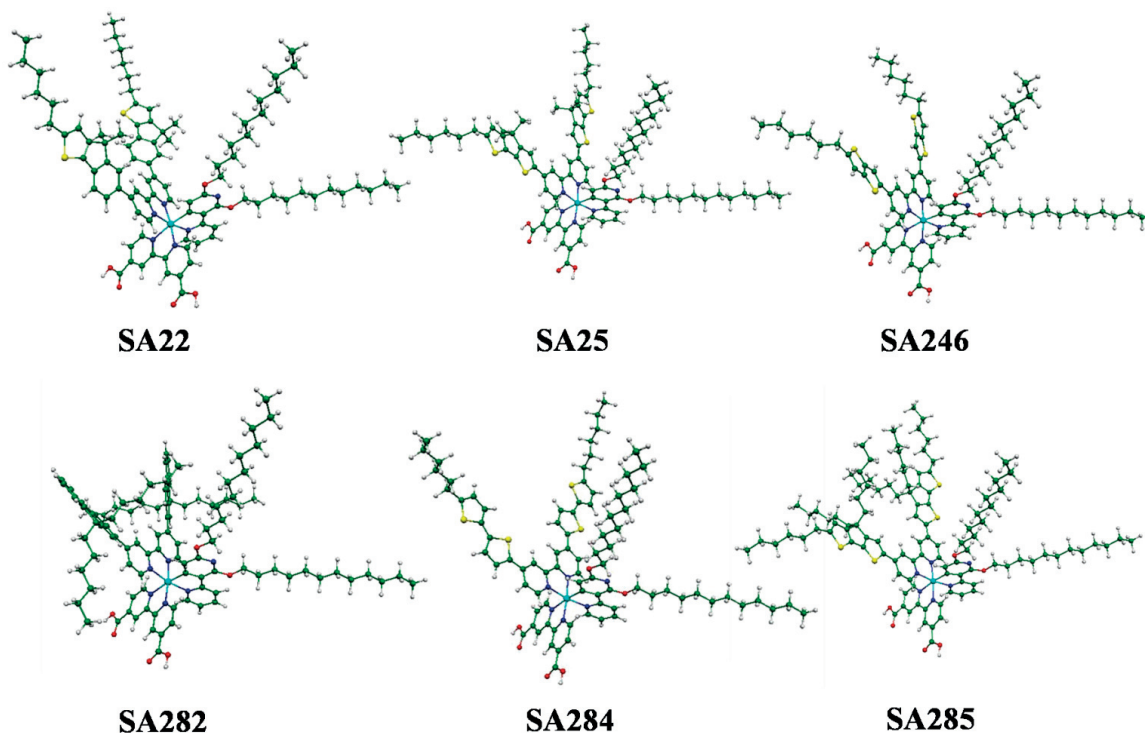


Figure 8.44. Optimized geometry of investigated SA dyes. Balls' colors: light blue (Ru), green (C), white (H), blue (N), yellow (S)

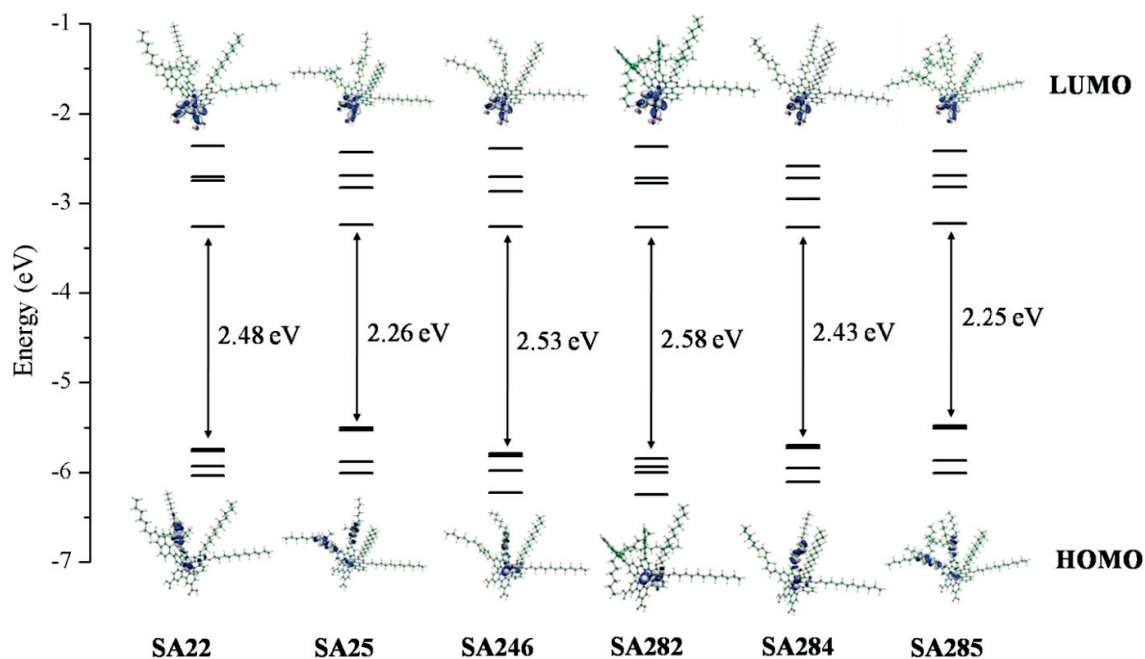


Figure 8.45. Plot of relevant molecular orbitals energy (in eV). HOMO and LUMO isodensity plots are also reported.

Table 8.1. Calculated molecular volume and the key dihedral angles.

	Molecular Volume (\AA^3)	Dihedral angle between the aromatic substituents and pyridine ring in the auxiliary ligands (in degrees)
SA22	2201	~36
SA25	2179	~9
SA246	1980	~0
SA282	2420	~38
SA284	2060	~1.5 and 10
SA285	2687	~8 and 10

Table 8.2. Calculated molecular orbitals energies (eV) in DCM solvent of investigated dyes. The energies were calculated at B3LYP/3-21G* level.

	SA22	SA25	SA246	SA282	SA284	SA285
L+3	-2.36	-2.43	-2.39	-2.37	-2.59	-2.42
L+2	-2.71	-2.69	-2.71	-2.72	-2.72	-2.69
L+1	-2.75	-2.83	-2.87	-2.78	-2.95	-2.82
L	-3.26	-3.24	-3.26	-3.27	-3.27	-3.23
H	-5.74	-5.50	-5.79	-5.85	-5.70	-5.48
H-1	-5.76	-5.53	-5.82	-5.94	-5.73	-5.51
H-2	-5.93	-5.88	-5.98	-6.00	-5.95	-5.87
H-3	-6.04	-6.01	-6.23	-6.25	-6.11	-6.01
H-L Gap	2.48	2.26	2.53	2.58	2.43	2.25

In Table 8.3 the comparison between experimental electrochemical potentials and calculated HOMO/LUMO energies is reported. To note that the experimental electrochemical potentials were converted using the value of -4.43 eV for the vacuum level with respect to the NHE electrode.²³³

Table 8.3. Experimental electrochemical potentials (in eV) and calculated HOMOs and LUMOs energies.

	Experimental		Calculated	
	$E^0(S^+/S)$ [eV]	$E^0(S^+/S^*)$ [eV]	HOMO [eV]	LUMO [eV]
SA22	-5.40	-3.63	-5.74	-3.26
SA25	-5.35	-3.64	-5.50	-3.24
SA246	-5.31	-3.59	-5.79	-3.26
SA282	-5.31	-3.54	-5.85	-3.27
SA284	-5.32	-3.61	-5.70	-3.27
SA285	-5.32	-3.61	-5.48	-3.23

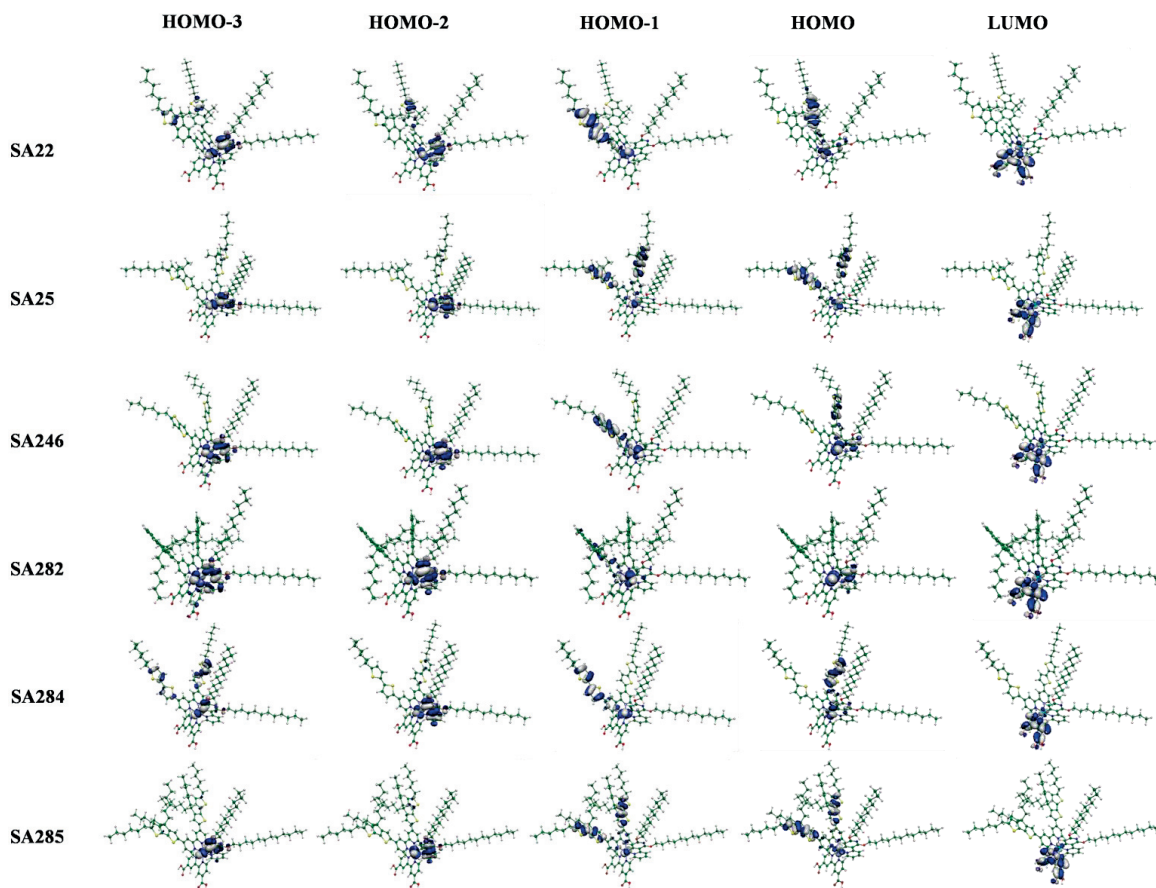


Figure 8.46. Isodensity plots of relevant molecular orbitals of SA dyes. The atoms colors is the same of optimized geometries in Figure 8.44.

The calculated absorption spectra of SA dyes are shown in Figure 8.47. Calculated UV-vis absorption spectra in DCM solvent of SA dyes. The calculated transitions (vertical sticks) are also reported. Figure 8.47 and the comparison between experimental and theoretical absorption maxima is reported in Table 8.4.

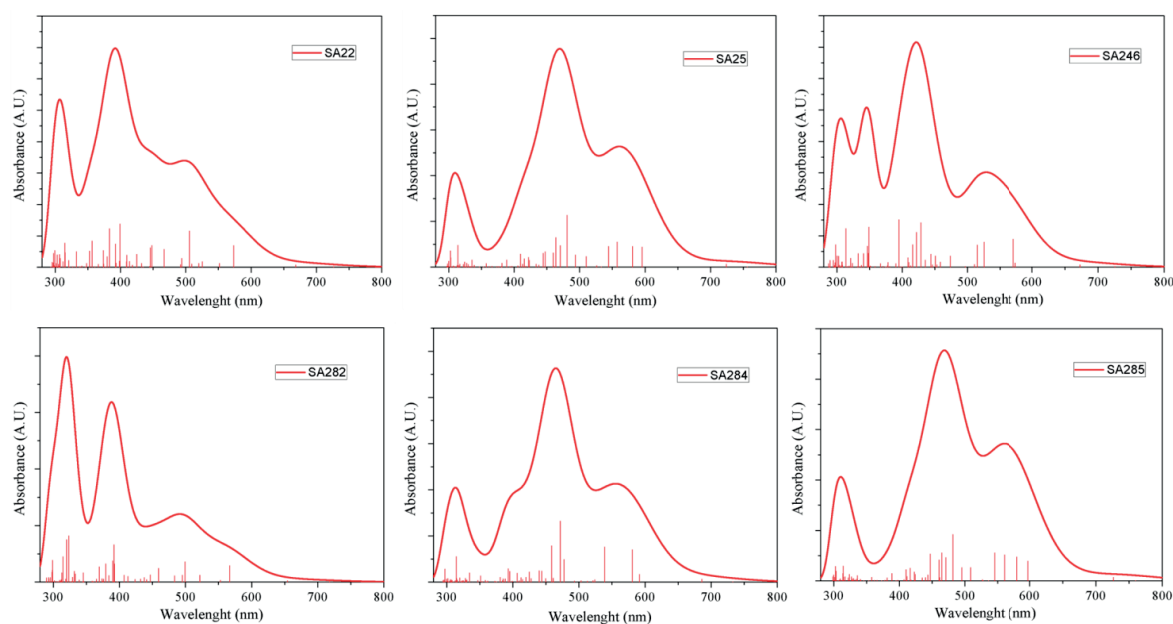


Figure 8.47. Calculated UV-vis absorption spectra in DCM solvent of SA dyes. The calculated transitions (vertical sticks) are also reported.

Table 8.4. Experimental and calculated absorption maxima wavelengths (in nm) and excitation energy (in eV).

	Experimental		Calculated	
	λ_{\max} (nm)	$E_{\text{ex.}}$ (eV)	λ_{\max} (nm)	$E_{\text{ex.}}$ (eV)
SA22	592	2.09	573	2.16
	511	2.42	506	2.45
	399	3.11	399	3.10
SA25	593	2.09	596	2.08
	448	2.77	464	2.67
SA246	585	2.12	572	2.17
	431 ^{sh}	2.88	429	2.89
	382	3.25	395	3.14
SA282	571	2.17	567	2.19
	508 ^{sh}	2.44	499	2.48
	411	3.02	392	3.16
SA284	592	2.09	581	2.13
	398	3.11	393	3.15
SA285	595	2.08	581	2.13
	456	2.72	465	2.67

Table 8.5. Excitation energies, oscillator strengths and excited state wave-function composition of the main calculated transitions for investigated dyes.

Complex	N state	E (eV)	WL (nm)	f	Composition					
SA22	3	2.1620	573.47	0.1737	47	H-2 →L				
					26	H-3 →L				
					10	H-1 →L				
SA25	8	2.4512	505.82	0.2892	34	H →L+2				
					23	H -1→L+1				
					11	H -4→L				
SA246	22	3.1048	399.33	0.3450	64	H →L+4				
					3	2.0809	595.81	0.2195	51	H-2 →L
					19	H-1 →L				
SA282	14	2.672	464.01	0.3244	36	H-1 →L+3				
					21	H-1 →L+4				
					15	H-2 →L+2				
SA284	4	2.1684	571.78	0.225	75	H-2 →L				
					16	2.891	428.86	0.3553	36	H-1 →L+4
					29	H-1 →L+3				
SA285	24	3.1384	395.06	0.3776	14	H →L+4				
					13	H →L+3				
					36	H-1 →L+5				
SA282	3	2.1864	567.06	0.1471	74	H-2 →L				
					10	H-1 →L				
					51	H →L+2				
SA282	6	2.4831	499.3	0.1818	30	H -1→L+1				
					19	3.1559	392.87	0.161	52	H →L+4
					19	H →L+5				
SA284	3	2.0962	591.48	0.0847	58	H -1→L+1				
					21	H →L+1				
					10	H-3 →L+1				
SA285	27	3.1547	393.02	0.1467	46	H-5 →L+2				
					28	H-3 →L+3				
					15	H-4 →L+2				
SA285	4	2.1339	581.03	0.2397	66	H -1→L+1				
					14	H -2→L+1				
					33	H -1→L+3				
SA285	14	2.6673	464.84	0.2803	28	H -1→L+4				
					10	H -2→L+2				

8.1.5 Device Fabrication

All materials were ordered from commercial suppliers and used without further purification. The DSCs were prepared according to literature procedures describe before. Electrolyte components – [Co(phen)₃](TFSI)₂ and [Co(phen)₃](TFSI)₃ were synthesized according to the literature methods.²³⁴

*Working electrode*²³⁵

Working electrode for the iodine-based and cobalt-based devices had different parameters. For the Co-based devices, working electrode was composed of FTO glass (Nippon Sheet Glass, NSG, 10 Ω /sq) treated twice with 60 mM aqueous solution of TiCl_4 at 70 °C for 30 minutes and washed thoroughly. 4 μm thick titania film with 32 nm size TiO_2 particles and another 4 μm thick layer onto with 400 nm size TiO_2 particles were applied according to the procedure described before. Afterwards, electrodes were treated with 25 mM aqueous solution of TiCl_4 at 70 °C for 30 minutes, washed thoroughly with water and dried. Electrodes were heated at 500 °C for 30 minutes before dipping into the 0.2 mM dye solution in THF/EtOH (3:7). Working electrode for the iodine-based devices were prepared similarly, however, 8 μm thick titania film with 18 nm size TiO_2 particles and another 5 μm thick layer onto with 400 nm size TiO_2 particles were used.

*Counter Electrode*²³⁵

Before preparation of the counter electrodes (CEs) FTO glass (TEC 7, Dyesol) pieces were heated at 410 °C for 15 minutes and cooled down to room temperature. For the Co-based devices the CEs were prepared by drop-casting a suspension of graphene nanoparticles (ABCR, Karlsruhe, 6-8 nm thick, 15 μm wide) in acetone (0.1 mg/mL) onto FTO glass. Then electrodes were dried at room temperature and heated at 410 °C for 2 minutes. For the iodine-based devices the CEs were prepared by drop-casting a solution of H_2PtCl_6 (5 mM in isopropanol) onto FTO glass (TEC 7, Dyesol, 7 Ω /sq). Then electrodes were dried at room temperature and heated at 410 °C for 20 minutes.

Electrolytes

The Co-based electrolytes consist of: 1) 0.25 M $[\text{Co(II)(phen)}_3](\text{TFSI})_2$, 0.05 M $[\text{Co(III)(phen)}_3](\text{TFSI})_3$, 0.25 M 4-(5-nonyl)pyridine (NP) and 0.1 M LiTFSI or 4) 0.25 M $[\text{Co(II)(phen)}_3](\text{TFSI})_2$, 0.05 M $[\text{Co(III)(phen)}_3](\text{TFSI})_3$, 0.5 M 4-(5-nonyl)pyridine (NP) and 0.1 M LiTFSI.

*Cell Assembly*²³⁵

Counter and working electrodes were sealed with a 25 μm thick hot-melt ionomer (Surlyn, DuPont) under heating at 120 °C. Then the electrolyte was introduced through predrilled holes in the CE, which were sealed with a piece of similar ionomer and thin glass at 120 °C. Cells active area was 0.28 cm^2 and a black mask with area 0.159 cm^2 was used for all photovoltaic studies to provide reliable results.

8.1.6 Device Characterization

J-V Characterization.

A solar simulator based on 450 W xenon light source (Osram XBO 450) with a sunlight filter Schott K113 Tempax (Präzisions Glas & Optik GmbH, Germany) was used to reduce the mismatch between the simulated and real solar spectra to less than 4 %. The lamp power was controlled in respect to the AM 1.5 solar standard employing a reference Si photodiode. The current–voltage characteristics of the device were measured at different sun intensities by applying external voltage bias to the device and measuring photocurrent with a Keithley digital source meter (Keithley 2400, USA). The delay time between applying voltage and measuring generated photocurrent was fixed to 80 ms.

Incident Photon-to-Collected Electron Conversion Efficiency (IPCE).

For IPCE measurements, light from a 300 W Xenon lamp (ILC Technology, U.S.A.) was focused by Gemini-180 double monochromator (Jobin Yvon Ltd., U.K.) onto the measured device. A white light bias (5 %) was used to ensure total light intensity close to working conditions. The incident light wavelength was incremented by 10 nm and IPCE was measure in visible region.

8.1.7 Transient absorption Spectroscopy

Device preparations for the TAS measurements were analogous to the solar cell preparations with only two differences: first, the scattering layer of titania consisting of 400 nm size nanoparticles was not used; second, the platinum catalysts were not deposited on the counter electrode. Devices were subjected to pulsed laser excitation from an Ekspla NT-342 Nd:YAG laser at 20 Hz, pumping an OPO tuned at 510 nm (full width at half-maximum (fwhm) \approx 5 ns). The laser pulse was attenuated to 40 $\mu\text{J cm}^{-2}$ pulse $^{-1}$. The beam was expanded by a planoconcave lens to irradiate the whole sample, whose surface was kept at a 45° angle to the excitation and probe beams. The probe light was produced by a 250 W halogen bulb (64655 HLX, Osram). It was passed through a series of cutoff filters up to 780 nm to remove unwanted light bias, focused onto the sample, and passed through a monochromator tuned at the desired wavelength (Omni- λ 150, Oriel) prior to being detected by a fast InGaAs diode (SM05PD5A, Thorlabs). Transient signals were measured through a 1 k Ω load with an oscilloscope (DPO 7104, Tektronix). Satisfactory signal-to-noise ratios were typically obtained by averaging over 1500 laser shots, and a Savitsky–Golay smoothing algorithm was applied to raw data.

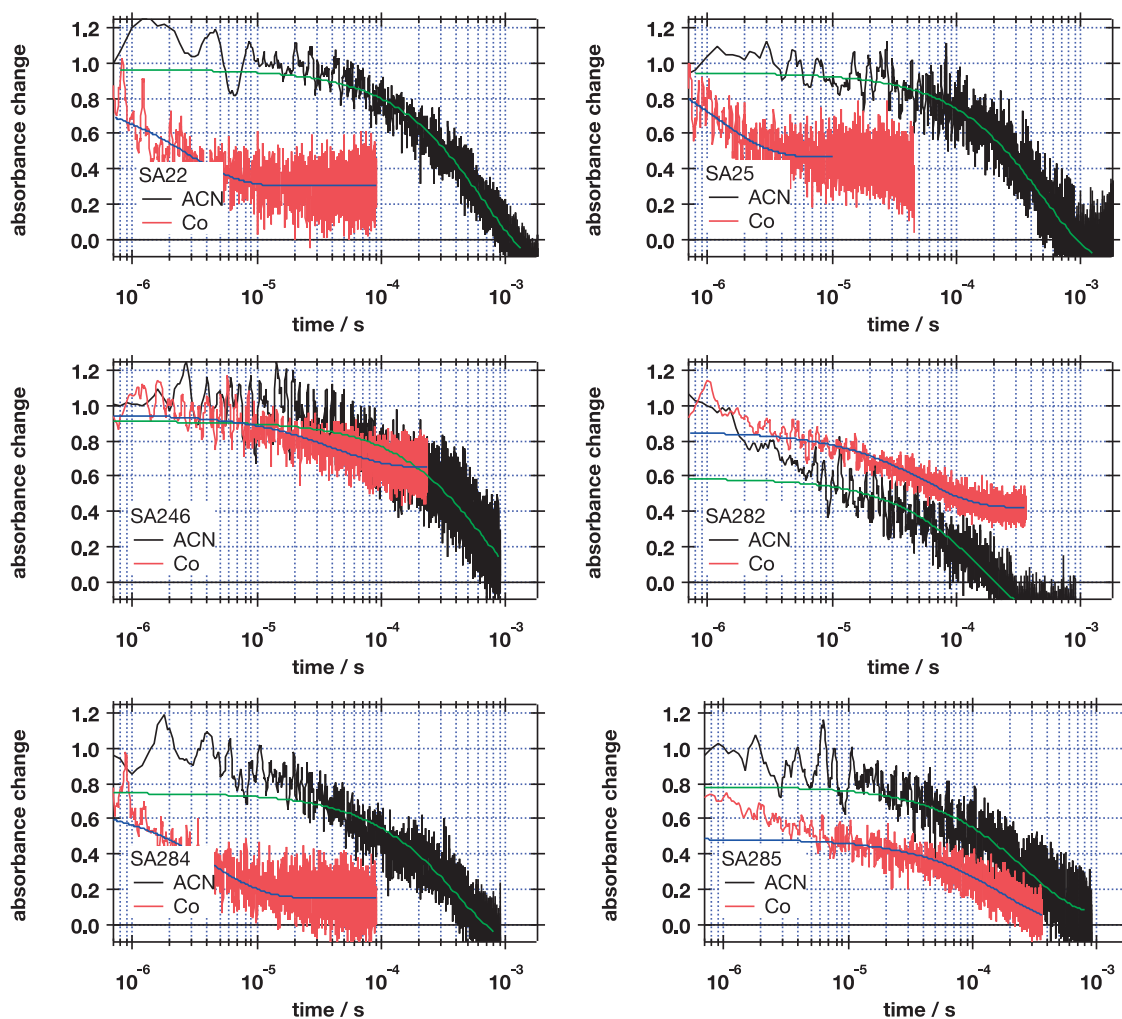


Figure 8.48. Nanosecond normalized transient absorbance decays of SA dyes at 900 nm in a DSC lacking (black) and containing (red) $\text{Co}^{3+/2+}$ redox couple in the electrolyte.

In the devices with pure acetonitrile the only possible way of dye regeneration is back electron recombination, which is indicative of photooxidized dye lifetime.

Table 8.6. The Summary of TAS Analysis

dye	τ_{rec} [μs]	τ_{reg} (cobalt) [μs]	η_{reg} (cobalt)
SA22	658	2.7	1
SA25	497	1.2	1
SA246	677	41	0.94
SA282	170	53	0.76
SA284	414	4.3	0.99
SA285	264	175	0.60

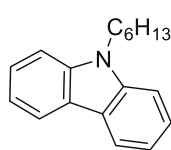
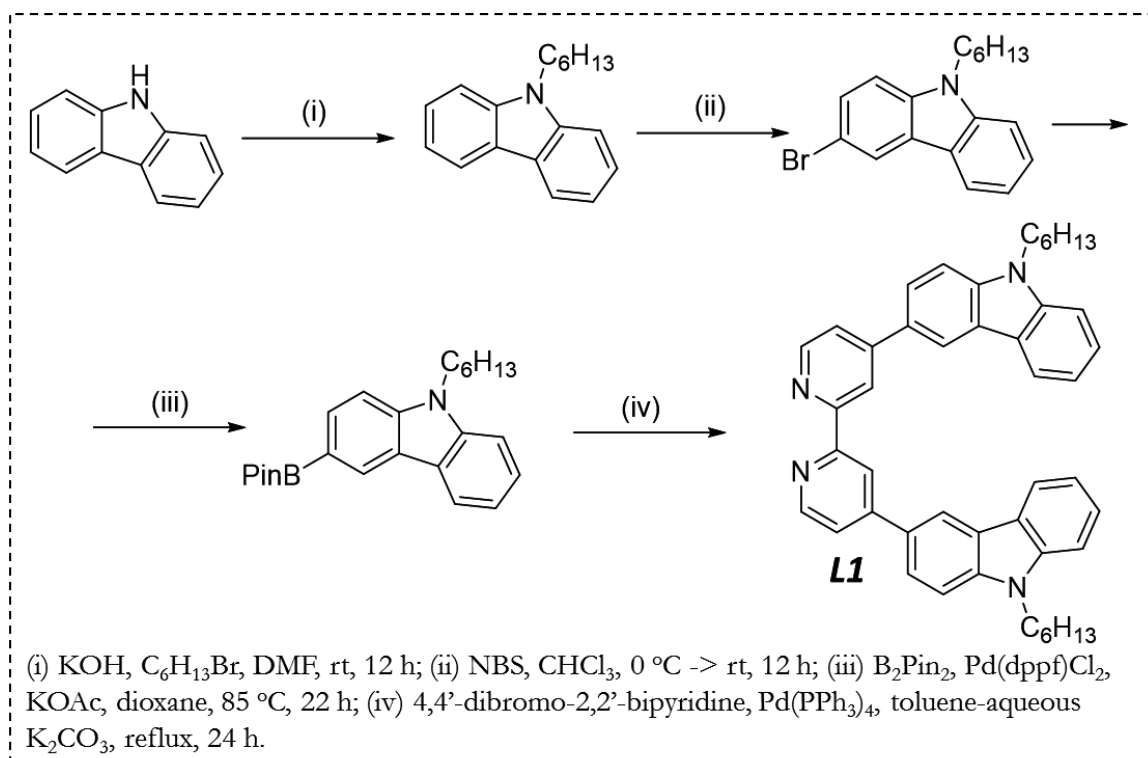
8.1.8 Electrochemical Impedance Spectroscopy

EIS measurements were performed by a Biologic SP300 (BioLogic, France) in a frequency range between 7 MHz and 0.1 Hz for potentials from 0 V to about V_{OC} (with a 20 mV sinusoidal ac perturbation) in 50 mV steps. A stabilization time of 20 s at each measurement potential was applied. The resulting impedance spectra were analyzed with the ZView software (Scribner Associate) on the basis of the transmission line model.²³⁶ The potentials of the EIS results are corrected for IR drop. The real potential (V_{real}) to the device is determined by the subtraction of the voltage drop (V_{Drop}) from the applied potential ($V_{applied}$). The voltage drop is calculated by the integration of the sum of all series resistances ($R_{Aseries}$) over the current passed ($V_{real} = V_{applied} - V_{Drop}$; with $V_{Drop} = \int R_{Aseries} dI$, where $R_{Aseries} = R_s + R_{ce} + R_{Electrolyte}$).

8.2 Appendix to chapter 3

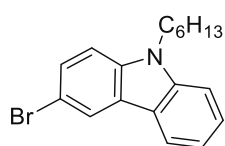
8.2.1 Synthetic Procedures and material characterization

All the commercially available materials were used as received. ^1H NMR spectra were recorded on a Bruker AVIII-HD (400 MHz), and are reported in ppm using solvent as an internal standard (CDCl_3 at 7.26/77.16 ppm or CD_3CN at 1.94/118.26 ppm for proton/carbon). Data reported as: s = singlet, d = doublet, t = triplet, q = quartet, p = pentet, m = multiplet, b = broad, ap = apparent; coupling constant(s) in Hz; integration. UV-Vis spectra were measured with an LS-55 spectrometer. Cyclic voltammetry was measured with a Biologic S-200 cyclic voltammeter. Mass spectra were recorded on a Bruker Microflex MALDI-TOF or ESI mass spectrometer.



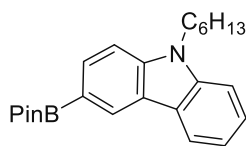
9-hexyl-9H-carbazole (1).²³⁷ Carbazole (2.5 g, 15 mmol, 1 equiv.) was added to the mixture of KOH (5.04 g, 90 mmol, 6 equiv.) and hexyl bromide (2.97 g, 18 mmol, 1.2 equiv.) in 20 mL of DMF . The mixture was stirred at room temperature for 12 hours. Afterwards, the reaction mixture was poured into 80 mL of deionized water, and neutralized with 10 % HCl . Organics were extracted with DCM , dried over MgSO_4 ,

filtered to remove solids and evaporated to little amount. Column chromatography (SiO_2) with hexane afforded the final product as a white powder (3.25 g, 86 %). ^1H NMR (200 MHz, $\text{Chloroform-}d$) δ 8.37 (d, $J = 7.7$ Hz, 2H), 7.77 – 7.45 (m, 6H), 4.41 (t, $J = 7.2$ Hz, 2H), 2.04 (p, $J = 7.1$ Hz, 2H), 1.53 (m, 6H), 1.26 – 1.04 (m, 3H).



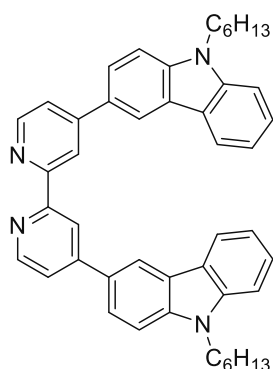
3-bromo-9-hexyl-9H-carbazole (2). In a 100 mL round-bottom flask, 9-hexyl-9H-carbazole (2.51 g, 10 mmol, 1 equiv.) was dissolved in 50 ml of CHCl_3 . The solution was cooled down to $0\text{ }^\circ\text{C}$ and N -bromosuccinimide (1.8 g, 10 mmol, 1 equiv.) was added portionwise in 30 minutes. The reaction was let to warm up to

room temperature and stirred for 12 hour. Afterwards, the mixture was washed with deionized water and extracted with DCM. Organic phase was dried with MgSO_4 , filtered and the volume of liquid was reduced by rotor evaporation. Column chromatography (SiO_2) with hexane afforded the final product as colorless oil (3.2 g, 97 %). ^1H NMR (200 MHz, Chloroform-*d*) δ 8.24 (d, J = 1.9 Hz, 1H), 8.07 (d, J = 7.8 Hz, 1H), 7.56 (dd, J = 8.7, 2.0 Hz, 1H), 7.53 – 7.39 (m, 2H), 7.33 – 7.23 (m, 2H), 4.26 (t, J = 7.2 Hz, 2H), 1.86 (p, J = 7.2 Hz, 2H), 1.33 (q, J = 4.3 Hz, 6H), 0.97 – 0.86 (m, 3H).



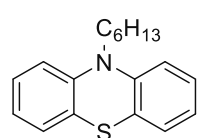
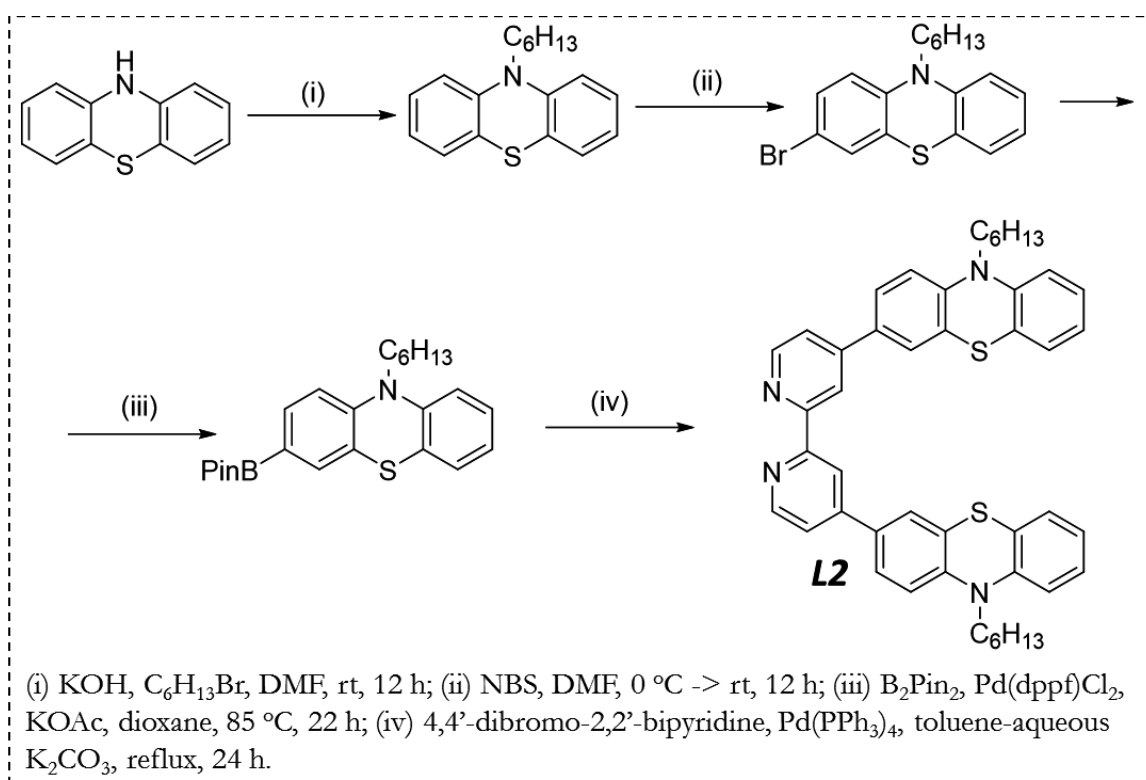
9-hexyl-3-(4,4,5,5-tetramethyl-1,3,2-dioxaborolan-2-yl)-9H-carbazole

(3). In 50 mL oven-dried two-neck round-bottom flask equipped with a stirring bar and a condenser, 3-bromo-9-hexyl-9H-carbazole (3.1 g, 9.4 mmol, 1 equiv.), B_2Pin_2 (2.86 g, 11.3 mmol, 1.2 equiv.), $\text{Pd}(\text{dppf})\text{Cl}_2$ (344 mg, 0.47 mmol, 0.05 equiv.), and KOAc (2.77g, 28.2 mmol, 3 equiv.) were mixed under nitrogen atmosphere. Dry dioxane 30 mL was added and the reaction mixture was stirred under nitrogen, at 85 °C, for 22 h. Afterwards, the mixture was washed with deionized water and extracted with DCM. The organic phase was dried with MgSO_4 , filtered and reduced to little volume by rotary evaporation. In column chromatography (SiO_2) purification with hexane:DCM (1:1) blue-fluorescent fraction under UV irradiation (365 nm) was collected, which afforded the final product as colorless oil (3.19 g, 90 %) upon solvent evaporation. ^1H NMR (200 MHz, Chloroform-*d*) δ 8.67 (s, 1H), 8.20 (d, J = 7.7 Hz, 1H), 7.99 (dd, J = 8.2, 1.2 Hz, 1H), 7.59 – 7.40 (m, 3H), 7.30 (t, J = 7.0, 6.5, 1.6 Hz, 1H), 4.35 (t, J = 7.2 Hz, 2H), 1.92 (p, J = 7.2 Hz, 2H), 1.46 (s, 18H), 0.98 – 0.86 (m, 3H).

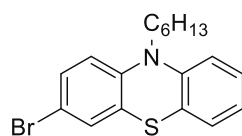


L1. 4,4'-dibromo-2,2'-bipyridine (366 mg, 1.17 mmol, 1 equiv.) and 9-hexyl-3-(4,4,5,5-tetramethyl-1,3,2-dioxaborolan-2-yl)-9H-carbazole (1.1 g, 2.92 mmol, 2.5 equiv.) were dissolved in 40 mL of toluene in round-bottom flask equipped with a stirring bar. To this solution, an aqueous solution (10 mL), containing K_2CO_3 (2.76 g, 20 mmol) was added. The mixture was deoxygenated by bubbling with nitrogen for 20 minutes and $\text{Pd}(\text{PPh}_3)_4$ (170 mg, 0.15 mmol, 0.05 equiv.) was added. The mixture was refluxed for 24 hours. Afterwards, it was cooled down to room temperature, washed with deionized water and extracted with DCM. The organic phase was dried with MgSO_4 , filtered and the volume of filtrate was reduced by rotary evaporation.

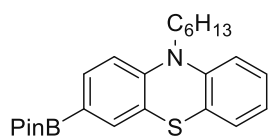
Column chromatography (SiO_2) with solvent of increasing polarity DCM to DCM:acetone (9:1) afforded the final product as yellow powder (670 mg, 88 %). ^1H NMR (400 MHz, Chloroform-*d*) δ 8.91 (d, J = 1.8 Hz, 2H), 8.81 (d, J = 5.1 Hz, 2H), 8.57 (d, J = 1.7 Hz, 2H), 8.22 (d, J = 7.7 Hz, 2H), 7.92 (dd, J = 8.5, 1.8 Hz, 2H), 7.70 (dd, J = 5.1, 1.8 Hz, 2H), 7.56 – 7.42 (m, 6H), 7.30 (t, J = 7.4 Hz, 2H), 4.31 (t, J = 7.2 Hz, 4H), 1.90 (p, J = 7.3 Hz, 4H), 1.47 – 1.22 (m, 12H), 0.89 (t, J = 6.9 Hz, 6H). ^{13}C NMR (101 MHz, Chloroform-*d*) δ 156.53, 150.25, 149.63, 140.94, 140.82, 128.55, 126.17, 124.99, 123.30, 122.79, 121.78, 120.79, 119.38, 119.32, 119.03, 109.26, 109.13, 43.27, 31.77, 29.14, 27.18, 22.80, 14.39.



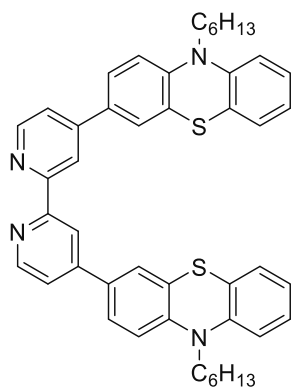
10-hexyl-10H-phenothiazine (4). KOH (5.04 g, 90 mmol, 6 equiv.) and hexyl bromide (0.94 g, 18 mmol, 1.2 equiv.) mixed with 20 mL of DMF. To this mixture phenothiazine (2.98 g, 15 mmol, 1 equiv.) was added. The reaction mixture was stirred at room temperature for 12 hours and then was poured into 50 mL of deionized water. Afterwards, organic material was extracted with DCM, dried over MgSO₄, filtered and the volume of filtrate was reduced by rotary evaporation. Column chromatography (SiO₂) with hexane afforded the final product as a yellowish oil, which was crystallizing over time (3.7 g, 87 %). ¹H NMR (400 MHz, Chloroform-*d*) δ 7.22 – 7.12 (m, 4H), 6.99 – 6.82 (m, 4H), 3.86 (t, *J* = 7.3 Hz, 2H), 1.82 (p, *J* = 7.5 Hz, 2H), 1.54 – 1.40 (m, 2H), 1.33 (m, 4H), 0.99 – 0.83 (m, 3H).



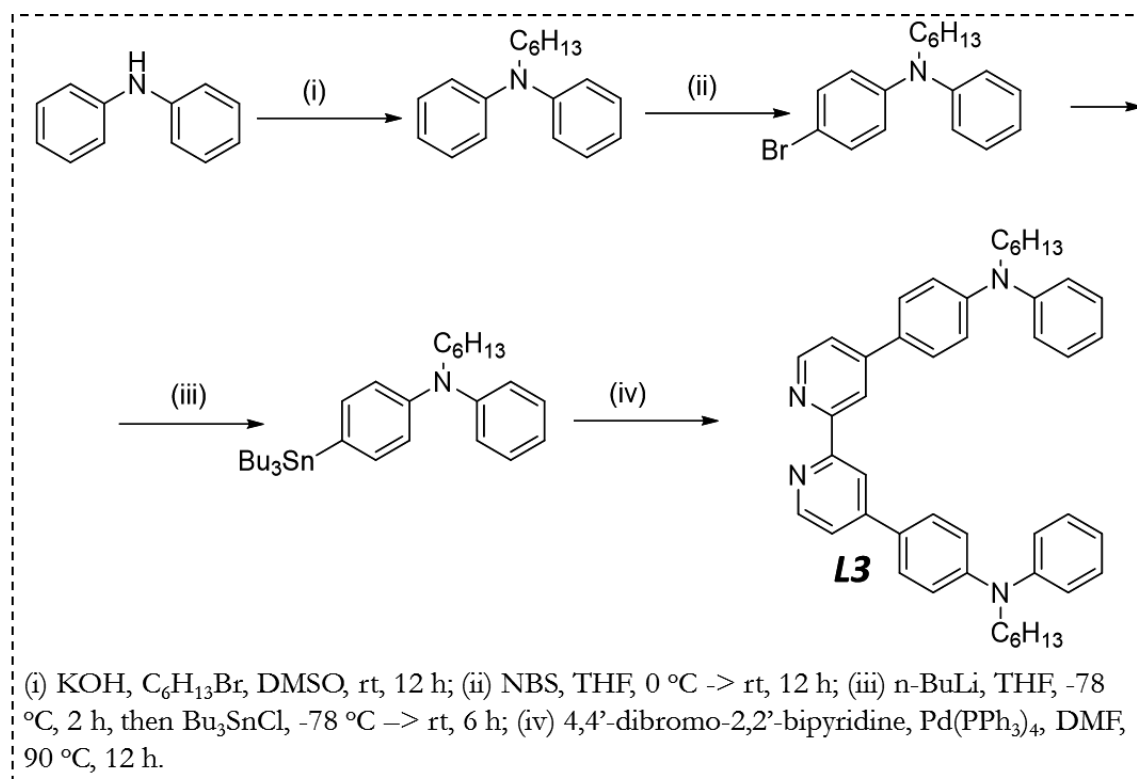
3-bromo-10-hexyl-10H-phenothiazine (5). 10-hexyl-10H-phenothiazine (2.58 g, 9.12 mmol, 1 equiv.) was dissolved in 50 mL of DMF and the solution was cooled down to 0 °C. N-bromosuccinimide (1.64 g, 9.12 mmol, 1equiv.) was dissolved in 20 mL of DMF, and this solution was added drop-wise into the first solution in 30 minutes. Afterwards, the reaction was let to warm up to room temperature and stirred for 12 hours. Then, the mixture was washed with deionized water and extracted with DCM. The organic phase was dried with MgSO₄, filtered and the volume of filtrate was reduced by rotary evaporation. Column chromatography (SiO₂) with hexane afforded product as colorless oil (1.9 g, 57 %). ¹H NMR (400 MHz, Chloroform-*d*) δ 7.26 – 7.21 (m, 2H), 7.19 – 7.13 (m, 1H), 7.12 (dd, *J* = 7.7, 1.5 Hz, 1H), 6.92 (t, *J* = 7.5 Hz, 1H), 6.86 (d, *J* = 8.1 Hz, 1H), 6.68 (dd, *J* = 8.4, 5.0 Hz, 1H), 3.87 – 3.70 (m, 2H), 1.77 (p, *J* = 7.5 Hz, 2H), 1.42 (p, *J* = 6.8 Hz, 2H), 1.35 – 1.25 (m, 4H), 0.91 – 0.86 (m, 3H).

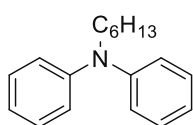


10-hexyl-3-(4,4,5,5-tetramethyl-1,3,2-dioxaborolan-2-yl)-10H-phenothiazine (6). Was synthesized in absolutely similar way as **3**. 3-bromo-10-hexyl-10H-phenothiazine (1.6 g, 4.42 mmol, 1 equiv.), B_2Pin_2 (1.35 g, 5.3 mmol, 1.2 equiv.), $Pd(dppf)Cl_2$ (162 mg, 0.22 mmol, 0.05 equiv.), KOAc (1.3 g, 13.3 mmol, 3 equiv.) in 20 mL of dry dioxane were used. In column chromatography (SiO_2) purification with hexane:DCM a strong blue-fluorescent fraction was collected, and which resulted in the product as a yellow oil (1.1 g, 61 %). 1H NMR (400 MHz, Chloroform-*d*) δ 7.62 – 7.54 (m, 2H), 7.16 – 7.07 (m, 2H), 6.95 – 6.80 (m, 3H), 3.84 (broad s, 2H), 1.79 (p, $J = 7.6$ Hz, 2H), 1.50 – 1.38 (m, 2H), 1.36 – 1.25 (m, 16H), 0.90 – 0.80 (m, 3H).

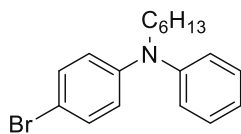


L2. Was synthesized in a similar way as L1. 4,4'-dibromo-2,2'-bipyridine (338 mg, 1.08 mmol, 1 equiv.), **6** (1.08 g, 2.7 mmol, 2.5 equiv.) in 40 mL of toluene and K_2CO_3 (2.76 g, 20 mmol) in 10 ml of water were used. $Pd(PPh_3)_4$ (156 mg, 0.135 mmol, 0.125 equiv.) was added after deoxygenation. Final product was obtained after column chromatography as a yellow powder (580 mg, 75 %). 1H NMR (400 MHz, Chloroform-*d*) δ 8.69 (d, $J = 5.1$ Hz, 2H), 8.66 (d, $J = 1.8$ Hz, 2H), 7.61 – 7.54 (m, 4H), 7.47 (dd, $J = 5.2, 1.9$ Hz, 2H), 7.20 – 7.12 (m, 4H), 6.98 – 6.88 (m, 4H), 6.87 (d, $J = 8.0$ Hz, 2H), 3.86 (t, $J = 7.2$ Hz, 4H), 1.83 (p, $J = 8.2, 7.8$ Hz, 4H), 1.45 (p, $J = 7.6$ Hz, 4H), 1.37 – 1.28 (m, 8H), 0.93 – 0.85 (m, 6H). ^{13}C NMR (101 MHz, Chloroform-*d*) δ 156.51, 149.56, 147.98, 146.15, 144.66, 131.97, 127.51, 127.38, 126.10, 125.71, 125.48, 124.16, 122.71, 120.73, 118.26, 115.51, 115.49, 47.62, 31.48, 26.82, 26.65, 22.63, 14.04.

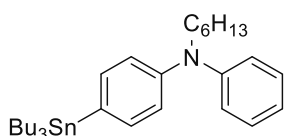




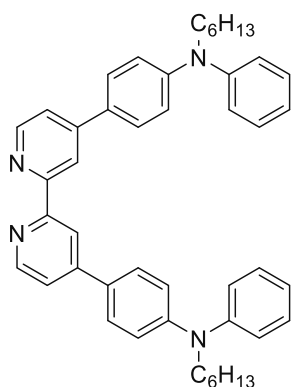
N-hexyl-N-phenylaniline (7). In a 100 mL round-bottom flask KOH (2.7 g, 48 mmol, 2 equiv.) and hexyl bromide (4.75 g, 28.8 mmol, 1.2 equiv.) were mixed in 60 mL of DMSO. To this mixture diphenyl amine (4 g, 24 mmol, 1 equiv.) was added and the reaction was stirred at room temperature for 12 hours. Then the mixture was poured in to 100 mL of deionized water, and organic material were extracted with DCM, and further washed with deionized water. The organic phase was separated, dried with MgSO_4 , filtered and the volume of filtrate was reduced by rotary evaporation. Column chromatography (SiO_2) with hexane afforded the product as a colorless oil (5.7 g, 94 %). $^1\text{H NMR}$ (400 MHz, Chloroform-*d*) δ 7.32 – 7.28 (m, 4H), 7.04 (d, $J = 7.4$ Hz, 4H), 6.98 (t, $J = 7.3$ Hz, 2H), 3.78 – 3.68 (m, 2H), 1.71 (p, $J = 7.5$ Hz, 2H), 1.36 (hd, $J = 7.2, 4.8, 3.6$ Hz, 6H), 0.97 – 0.90 (m, 3H).



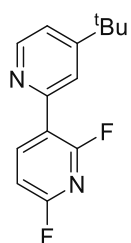
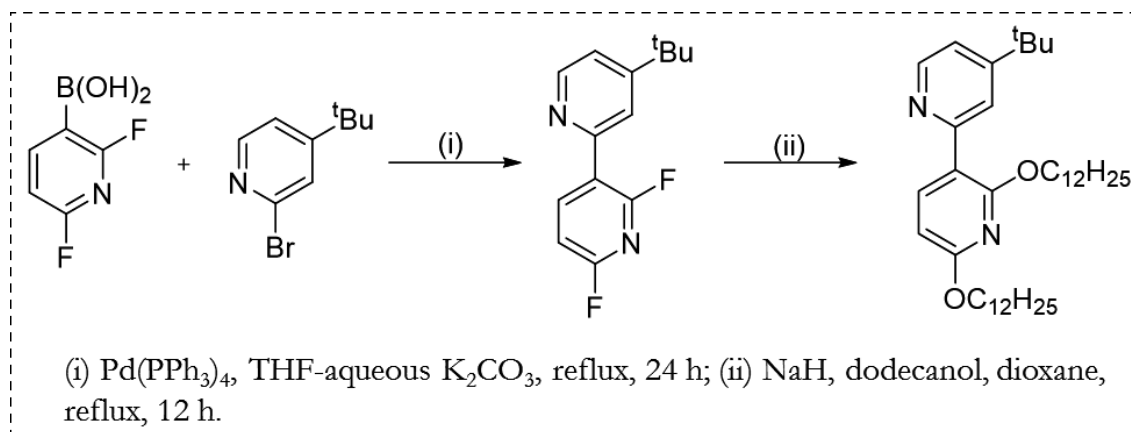
4-bromo-N-hexyl-N-phenylaniline (8). To the solution of 7 (3.0 g, 11.6 mmol, 1 equiv.) in 40 mL of THF, a solution of N-bromosuccinimide (2.13 g, 11.6 mmol, 1 equiv.) in 40 mL of THF was added drop-wise at 0 °C. The reaction was let to warm up to room temperature and stirred for 12 hours. Afterwards, the reaction was washed with deionized water and extracted with DCM. The organic phase was dried with MgSO_4 , filtered and the volume of filtrate was reduced by rotary evaporation. Column chromatography (SiO_2) with hexanes afforded the product as a colorless oil (3.65 g, 94 %). $^1\text{H NMR}$ (400 MHz, Chloroform-*d*) δ 7.41 – 7.28 (m, 4H), 7.09 – 7.02 (m, 3H), 6.91 – 6.79 (m, 2H), 3.72 – 3.63 (m, 2H), 1.67 (p, $J = 7.5$ Hz, 2H), 1.41 – 1.27 (m, 6H), 0.95 – 0.87 (m, 3H).



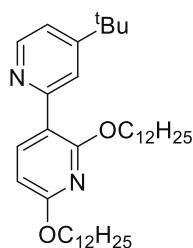
N-hexyl-N-phenyl-4-(tributylstannyl)aniline (9). In a 50 mL Schlenk flask, 8 (1.84 g, 5.54 mmol, 1 equiv.) was dissolved in 30 mL of dry THF under nitrogen. The solution was cooled down to -78 °C, and then 2.5 M solution of n-BuLi in hexanes (2.33 mL, 5.82 mmol, 1.05 equiv.) was added dropwise. The reaction was left to stir at -78 °C for 2 hours, and then Bu_3SnCl (1.89 g, 5.82 mmol, 1.05 equiv.) was added. The reaction was stirred for 6 hours during which it was left to warm up to room temperature. Afterwards, a few drops of methanol was added to ensure full quenching of BuLi, and then the mixture was washed with deionized water and extracted with DCM. The organic phase was separated, dried with MgSO_4 , filtered, and the filtrate was evaporated to dryness. No further purification was conducted and considering full conversion the product was directly used in the following step.



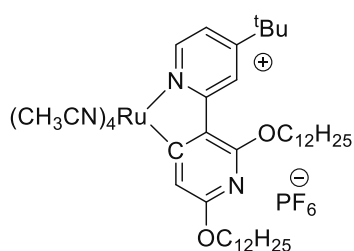
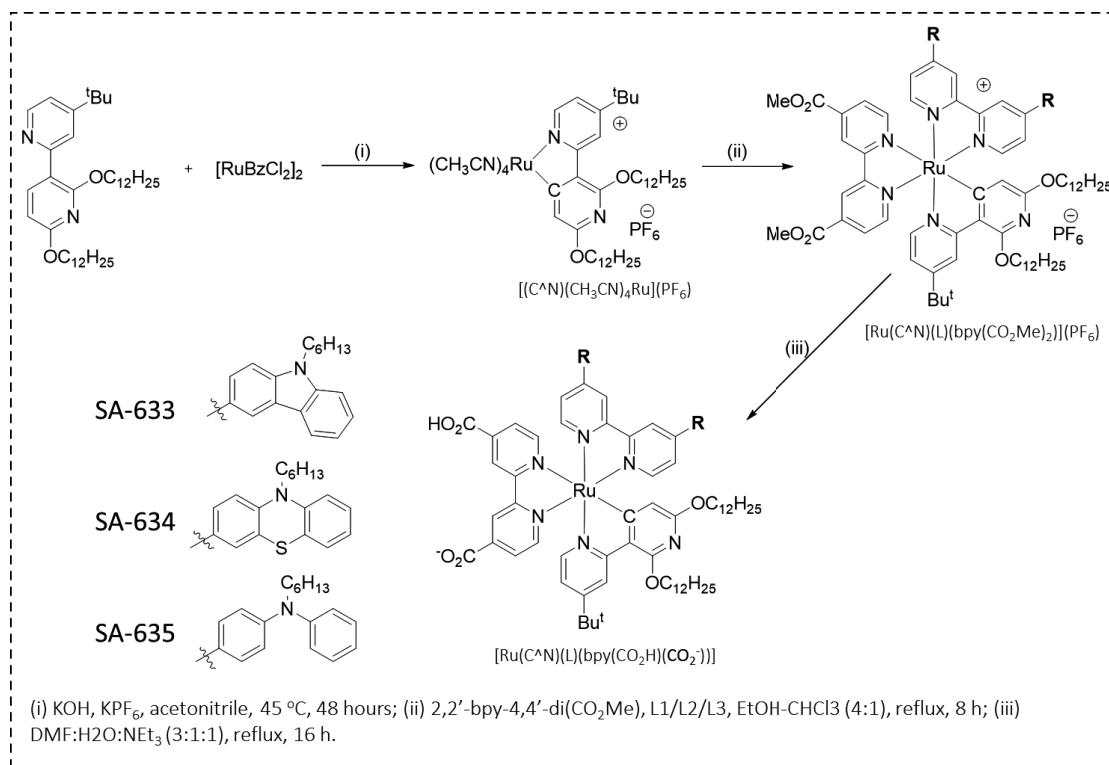
L3. In a Schlenk tube under nitrogen atmosphere, 9 (5.54 mmol, 4 equiv.), 4,4'-dibromo-2,2'-bipyridine (435 mg, 1.38 mmol, 1 equiv.) and $\text{Pd}(\text{PPh}_3)_4$ (320 mg, 0.2 equiv.) were dissolved in 40 mL of dry DMF. The reaction was stirred at 90 °C for 12 hours, then cooled down to room temperature, washed with water and organic material were extracted with DCM. The organic phase was separated, dried with MgSO_4 , filtered and the volume of filtrate was reduced with rotary evaporation. Column chromatography (SiO_2) with eluent of increasing polarity (from DCM to DCM:acetone 9:1) afforded the final product as a yellow powder (345 mg, 38 %). $^1\text{H NMR}$ (400 MHz, Chloroform-*d*) δ 8.76 (s, 2H), 8.73 (d, $J = 5.2$ Hz, 2H), 7.73 (d, $J = 8.3$ Hz, 4H), 7.54 (d, $J = 5.2$ Hz, 2H), 7.40 (t, $J = 7.7$ Hz, 4H), 7.22 (d, $J = 7.9$ Hz, 4H), 7.16 (t, $J = 7.4$ Hz, 2H), 7.01 (d, $J = 8.3$ Hz, 4H), 3.79 (t, $J = 7.8$ Hz, 4H), 1.81 – 1.66 (m, 4H), 1.49 – 1.30 (m, 12H), 1.08 – 0.88 (m, 6H). $^{13}\text{C NMR}$ (151 MHz, Chloroform-*d*) δ 156.56, 149.43, 149.16, 148.88, 147.22, 129.61, 128.10, 127.88, 124.47, 123.63, 120.50, 118.15, 117.44, 52.44, 31.66, 27.39, 26.77, 22.70, 14.09, 13.67.



4-(tert-butyl)-2',6'-difluoro-2,3'-bipyridine (10). This compound was synthesized according to procedure described in literature.²³⁸

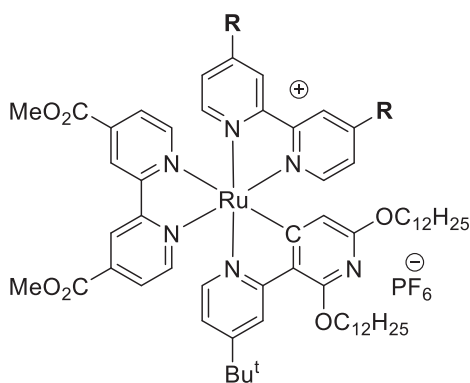


4-(tert-butyl)-2',6'-bis(dodecyloxy)-2,3'-bipyridine (11). This compound was synthesized according to procedure described in literature. 10 (2.66 g, 10.7 mmol, 1 equiv.), dodecanol (6 g, 32.2 mmol, 3 equiv.), NaH (60 % in mineral oil, 1.93 g, 48.3 mmol, 4.5 equiv), in 70 mL of dioxane were used. In column purification (SiO₂) with hexane:EtOAc as an eluent, a blue-fluorescent fraction was collected, which afforded the product upon evaporation and drying as yellowish oil, which was slowly crystallizing (5.21 g, 84 %). ¹H NMR (400 MHz, Chloroform-*d*) δ 8.54 (dd, *J* = 5.3, 0.8 Hz, 1H), 8.26 (d, *J* = 8.2 Hz, 1H), 8.06 (dd, *J* = 1.8, 0.8 Hz, 1H), 7.14 (dd, *J* = 5.3, 1.9 Hz, 1H), 6.41 (d, *J* = 8.2 Hz, 1H), 4.39 (t, *J* = 6.5 Hz, 2H), 4.30 (t, *J* = 6.7 Hz, 2H), 1.87 – 1.73 (m, 4H), 1.53 – 1.40 (m, 36H), 1.40 – 1.21 (m, 41H), 0.88 (t, *J* = 6.7 Hz, 6H).



$[(\text{C}^{\wedge}\text{N})(\text{CH}_3\text{CN})_4\text{Ru}](\text{PF}_6)$. In an oven-dried 100 mL Schlenk flask, $[\text{RuBzCl}_2]_2$ (421 mg, 0.84 mmol, 1 equiv.), 11 (1 g, 1.72 mmol, 2.05 equiv.), KOH (96 mg, 1.72 mmol, 2.05 equiv.) and KPF_6 (618 mg, 3.36 mmol, 4 equiv.) were mixed under nitrogen. The flask was protected from light, 25 mL of dry acetonitrile was added and the mixture was stirred at 45 °C for 48 hours. Afterwards, the mixture was filtered through celite and washed with additional DCM. The filtrate was evaporated and loaded on the column (basic-alumina) and using

an eluent of increasing polarity (from DCM to 3:1 mixture of DCM and acetonitrile), the yellow fraction was collected. Upon rotary evaporation and drying under high vacuum, yellow powder was obtained, which was later kept in a freezer (1 g, 59 %). (*Note: This powder becomes greenish over time, using of which didn't have apparent effect on the following step*). ^1H NMR (400 MHz, Acetonitrile- d_3) δ 8.75 (d, $J = 6.1$ Hz, 1H), 8.54 (d, $J = 2.2$ Hz, 1H), 7.09 (dd, $J = 6.1, 2.2$ Hz, 1H), 6.94 (s, 1H), 4.44 (t, $J = 6.4$ Hz, 2H), 4.29 (t, $J = 6.8$ Hz, 2H), 2.49 (s, 3H), 2.03 (s, 6H), 1.96 (s, 3H), 1.95 – 1.83 (m, 2H), 1.76 (p, $J = 6.9$ Hz, 2H), 1.56 (p, $J = 7.5$ Hz, 2H), 1.49 – 1.19 (m, 43H), 0.86 (t, $J = 6.5$ Hz, 6H). ^{13}C NMR (101 MHz, Acetonitrile- d_3) δ 163.64, 158.00, 157.33, 156.06, 149.35, 120.48, 120.08, 119.10, 116.23, 114.93, 108.52, 63.54, 63.13, 32.67, 29.72, 27.95, 27.48, 27.46, 27.42, 27.39, 27.28, 27.26, 27.17, 27.15, 24.62, 23.94, 20.46, 11.49, 1.34, 0.89.



General procedure for $[\text{Ru}(\text{C}^{\wedge}\text{N})(\text{L})(\text{bpy}(\text{CO}_2\text{Me})_2)](\text{PF}_6)$.

In a 100 mL round bottom flask equipped with a stirring bar and condenser, 4,4'-dicarboxy-2,2'-bipyridine (1 equiv.) and L (1 equiv.) were dissolved in a mixture of CHCl_3 (10 mL) and EtOH (40 mL) at 70 °C. Then, $[(\text{C}^{\wedge}\text{N})(\text{CH}_3\text{CN})_4\text{Ru}](\text{PF}_6)$ (1 equiv.) was added, and the solution was refluxed under nitrogen for 6 hours. Afterwards, the solvent was evaporated via rotary evaporation and column chromatography (SiO_2) using eluent of increasing polarity (from DCM to DCM:acetone

9:1) to separate three different products. First and last eluting fractions were of homoleptic complexes $[\text{Ru}(\text{C}^{\wedge}\text{N})(\text{L})_2](\text{PF}_6)$ and $[\text{Ru}(\text{C}^{\wedge}\text{N})(\text{bpy}(\text{CO}_2\text{Me})_2)_2](\text{PF}_6)$ respectively. The second eluting fraction of $[\text{Ru}(\text{C}^{\wedge}\text{N})(\text{L})(\text{bpy}(\text{CO}_2\text{Me})_2)](\text{PF}_6)$ was collected, evaporated and run 2 times through LH-20 Sephadex column eluting with DCM to ensure complete removal of free L. Solvent evaporation and drying under high vacuum resulted in a pure product.

$[\text{Ru}(\text{C}^{\wedge}\text{N})(\text{L})(\text{bpy}(\text{CO}_2\text{Me})_2)](\text{PF}_6)$ (SA617). According to the general procedure, 4,4'-dicarboxy-2,2'-bipyridine (49 mg, 0.182 mmol, 1 equiv.), L1 (119 mg, 0.182 mmol, 1 equiv.) and $[(\text{C}^{\wedge}\text{N})(\text{CH}_3\text{CN})_4\text{Ru}](\text{PF}_6)$ (180 mg, 0.182 mmol, 1 equiv.) were used. Product as a mauve powder was obtained (98 mg, 31 %).

^1H NMR (400 MHz, Chloroform-*d*) δ 8.95 (s, 1H), 8.85 (d, $J = 1.7$ Hz, 1H), 8.75 (d, $J = 2.0$ Hz, 1H), 8.55 (d, $J = 4.8$ Hz, 2H), 8.50 (d, $J = 5.9$ Hz, 1H), 8.44 (d, $J = 13.6$ Hz, 2H), 8.23 (d, $J = 5.5$ Hz, 1H), 8.15 (dd, $J = 7.8, 3.5$ Hz, 2H), 8.09 (d, $J = 5.5$ Hz, 1H), 7.84 (dd, $J = 22.9, 8.5$ Hz, 2H), 7.67 (t, $J = 6.4$ Hz, 2H), 7.62 – 7.39 (m, 9H), 7.27 (q, $J = 7.6, 7.0$ Hz, 4H), 6.89 (dd, $J = 6.1, 2.2$ Hz, 1H), 5.78 (s, 1H), 4.57 – 4.42 (m, 2H), 4.38 – 4.27 (m, 4H), 4.24 – 4.10 (m, 2H), 4.04 (s, 3H), 4.01 (s, 4H), 2.06 – 1.81 (m, 7H), 1.64 (dp, $J = 22.3, 7.2$ Hz, 5H), 1.50 – 1.09 (m, 65H), 0.96 – 0.79 (m, 14H).

^{13}C NMR (101 MHz, Chloroform-*d*) δ 164.83, 164.58, 164.53, 160.38, 158.41, 156.84, 155.79, 155.35, 154.99, 149.83, 149.80, 149.35, 149.00, 148.63, 148.39, 141.40, 141.04, 136.66, 134.40, 127.21, 127.16, 126.90, 126.45, 126.37, 125.20, 124.93, 124.72, 124.53, 124.20, 123.68, 123.66, 122.74, 122.67, 122.45, 122.38, 120.65, 120.41, 120.30, 120.14, 119.79, 119.61, 119.55, 119.24, 119.10, 118.63, 109.80, 109.77, 109.21, 109.17, 107.33, 66.18, 65.97, 53.31, 53.24, 43.33, 35.14, 31.94, 31.89, 31.58, 31.57, 30.56, 29.73, 29.67, 29.64, 29.61, 29.56, 29.49, 29.38, 29.33, 29.30, 28.98, 28.97, 26.97, 26.87, 26.12, 22.71, 22.67, 22.56, 22.54, 14.15, 14.11, 14.02, 14.01.

^{13}C DEPT 135 NMR (101 MHz, Chloroform-*d*) δ C-H: 155.35, 149.83, 149.80, 149.35, 149.00, 127.21, 127.16, 126.90, 126.45, 126.37, 125.20, 124.93, 124.72, 124.53, 124.20, 122.45, 122.38, 120.65, 120.30, 120.14, 119.79, 119.61, 119.55, 119.24, 119.10, 118.63, 109.80, 109.77, 109.21, 109.17, 107.33
 δ C-H₂: 66.18, 65.97, 43.33, 31.94, 31.89, 31.58, 31.57, 29.73, 29.67, 29.64, 29.61, 29.56, 29.49, 29.38, 29.33, 29.30, 28.98, 28.97, 26.97, 26.87, 26.12, 22.71, 22.67, 22.56, 22.54.
 δ C-H₃: 53.31, 53.24, 30.56, 14.15, 14.11, 14.02.

^{31}P NMR (162 MHz, Chloroform-*d*) δ -144.34 (hept, $J = 713.1$ Hz).

$[\text{Ru}(\text{C}^{\wedge}\text{N})(\text{L}2)(\text{bpy}(\text{CO}_2\text{Me})_2)](\text{PF}_6)$ (SA618). According to the general procedure, 4,4'-dicarboxy-2,2'-bipyridine (49 mg, 0.182 mmol, 1 equiv.), L1 (130 mg, 0.182 mmol, 1 equiv.) and $[(\text{C}^{\wedge}\text{N})(\text{CH}_3\text{CN})_4\text{Ru}](\text{PF}_6)$ (180 mg, 0.182 mmol, 1 equiv.) were used. Product as a mauve powder was obtained (96 mg, 29 %).

^1H NMR (400 MHz, Chloroform-*d*) δ 8.96 (s, 1H), 8.84 (d, $J = 1.7$ Hz, 1H), 8.74 (d, $J = 2.1$ Hz, 1H), 8.46 (d, $J = 6.0$ Hz, 1H), 8.33 (d, $J = 10.5$ Hz, 2H), 8.15 (d, $J = 5.6$ Hz, 1H), 8.09 (d, $J = 5.4$ Hz, 1H), 7.71 (dd, $J = 5.9, 1.7$ Hz, 1H), 7.65 (d, $J = 8.4$ Hz, 1H), 7.60 – 7.52 (m, 2H), 7.47 – 7.34 (m, 4H), 7.27 (s, 1H), 7.25 – 7.08 (m, 5H), 7.03 – 6.82 (m, 7H), 5.52 (s, 1H), 4.50 (qt, $J = 10.7, 6.5$ Hz, 2H), 4.17 (qt, $J = 10.5, 7.0$ Hz, 2H), 4.05 (s, 3H), 4.03 (s, 3H), 3.89 (broad s, 4H), 1.97 (p, $J = 6.7$ Hz, 2H), 1.88 – 1.78 (m, 4H), 1.74 – 1.57 (m, 4H), 1.52 – 1.21 (m, 55H), 0.96 – 0.85 (m, 12H).

^{13}C NMR (101 MHz, Chloroform-*d*) δ 164.60, 164.50, 164.46, 160.38, 158.34, 156.87, 155.79, 155.42, 154.95, 150.17, 150.00, 149.67, 149.12, 136.77, 134.54, 127.54, 127.50, 127.36, 127.20, 126.73, 126.51, 125.21, 123.60, 123.21, 122.95, 122.38, 122.27, 119.77, 119.35, 119.14, 118.65, 116.03, 115.99, 115.68, 66.15, 65.93, 53.29, 53.22, 47.63, 35.11, 31.94, 31.92, 31.45, 31.44, 30.52, 29.71, 29.66, 29.63, 29.58, 29.49, 29.37, 29.35, 29.27, 26.86, 26.59, 26.57, 26.11, 22.70, 22.61, 14.14, 14.01.

^{13}C DEPT135 NMR (101 MHz, Chloroform-*d*) δ C-H: 155.42, 150.17, 150.00, 149.67, 149.12, 127.54, 127.50, 127.36, 127.20, 126.73, 126.51, 125.21, 123.60, 123.21, 122.95, 122.38, 122.27, 119.77, 119.35, 119.14, 118.65, 116.03, 115.99, 115.68;
 δ C-H₂: 66.15, 65.93, 47.63, 31.94, 31.92, 31.45, 31.44, 30.52, 29.71, 29.66, 29.63, 29.58, 29.49, 29.37, 29.35, 29.27, 26.86, 26.59, 26.57, 26.11, 22.70, 22.61;
 δ C-H₃: 53.29, 53.22, , 14.14, 14.01.

^{31}P NMR (162 MHz, Chloroform-*d*) δ -144.46 (hept, $J = 713.2$ Hz).

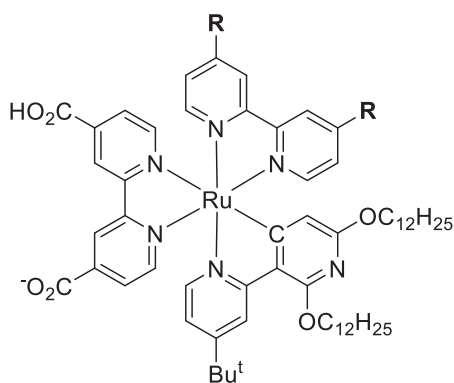
[Ru(C^{^N})(L3)(bpy(CO₂Me)₂)](PF₆) (SA631). According to the general procedure, 4,4'-dicarboxy-2,2'-bipyridine (49 mg, 0.182 mmol, 1 equiv.), L1 (120 mg, 0.182 mmol, 1 equiv.) and , [(C^{^N})(CH₃CN)₄Ru](PF₆) (180 mg, 0.182 mmol, 1 equiv.) were used. Product as a mauve powder was obtained (91 mg, 28 %).

^1H NMR (400 MHz, Chloroform-*d*) δ 8.92 (s, 1H), 8.82 (s, 1H), 8.68 (s, 1H), 8.46 (d, $J = 5.9$ Hz, 1H), 8.27 (d, $J = 9.3$ Hz, 2H), 8.14 (d, $J = 4.7$ Hz, 1H), 8.05 (d, $J = 4.6$ Hz, 1H), 7.69 (d, $J = 5.9$ Hz, 1H), 7.59 (d, $J = 8.5$ Hz, 2H), 7.54 (d, $J = 8.5$ Hz, 3H), 7.46 – 7.12 (m, 14H), 6.87 (t, $J = 8.7$ Hz, 5H), 5.62 (s, 1H), 4.44 (tt, $J = 10.7, 5.4$ Hz, 2H), 4.22 – 4.06 (m, 2H), 4.02 (s, 6H), 3.73 (dq, $J = 8.8, 4.4$ Hz, 4H), 1.93 (p, $J = 6.7$ Hz, 2H), 1.75 – 1.52 (m, 8H), 1.44 – 1.17 (m, 55H), 0.88 (m, 12H).

^{13}C NMR (151 MHz, Chloroform-*d*) δ 164.73, 164.63, 164.56, 160.25, 158.43, 156.67, 155.61, 155.38, 154.96, 150.00, 149.95, 149.75, 149.33, 149.02, 147.11, 146.86, 146.66, 146.56, 136.54, 134.22, 129.83, 129.80, 127.79, 127.65, 127.16, 126.06, 125.94, 125.18, 125.15, 124.96, 124.84, 124.79, 123.14, 122.76, 122.40, 122.33, 119.73, 118.84, 118.66, 118.59, 116.19, 116.03, 66.13, 65.95, 53.36, 53.25, 52.50, 35.09, 31.95, 31.94, 31.64, 30.52, 29.72, 29.70, 29.67, 29.66, 29.60, 29.57, 29.54, 29.39, 29.28, 27.36, 27.35, 26.87, 26.74, 26.72, 26.13, 22.72, 22.69, 14.17, 14.07.

^{13}C DEPT 135 NMR (151 MHz, Chloroform-*d*) δ C-H: 155.61, 150.00, 149.95, 149.33, 149.02, 129.83, 129.80, 127.79, 127.65, 127.16, 126.06, 125.94, 125.18, 124.96, 124.79, 123.14, 122.76, 122.40, 122.33, 119.73, 118.84, 118.66, 118.59, 116.19, 116.03;
 δ C-H₂: 66.13, 65.95, 52.50, 31.95, 31.94, 31.64, 29.72, 29.70, 29.67, 29.66, 29.60, 29.57, 29.54, 29.39, 29.28, 27.36, 27.35, 26.87, 26.74, 26.72, 26.13, 22.72, 22.69;
 δ C-H₃: 53.36, 53.25, 30.52, 14.17, 14.07.

^{31}P NMR (162 MHz, Chloroform-*d*) δ -144.50 (m).



General Procedure for $[\text{Ru}(\text{C}^{\wedge}\text{N})(\text{L})(\text{bpy}(\text{CO}_2\text{H})(\text{CO}_2^-))]$

$[\text{Ru}(\text{C}^{\wedge}\text{N})(\text{L}_2)(\text{bpy}(\text{CO}_2\text{Me})_2)](\text{PF}_6)$ was dissolved in 15 mL of DMF- H_2O - NEt_3 (3:1:1) and the solution was refluxed under nitrogen for 16 hours. Afterwards, the solvent was evaporated with rotary evaporation and the solid was dissolved in small amount of DCM. Addition of hexane precipitated the dark product, which was collected by filtration through the fritted glass filter. The solid was again dissolved in DCM and precipitation and filtration was repeated 2 more times. Afterwards, the product was run through LH-20 Sephadex column eluting with DCM, and

this column was repeated one more time. Rotary evaporation of solvent and drying under high vacuum provided the final product.

$[\text{Ru}(\text{C}^{\wedge}\text{N})(\text{L}_1)(\text{bpy}(\text{CO}_2\text{H})(\text{CO}_2^-))]$ (SA-633). Was synthesized according to the general procedure. $[\text{Ru}(\text{C}^{\wedge}\text{N})(\text{L}_1)(\text{bpy}(\text{CO}_2\text{Me})_2)](\text{PF}_6)$ (90 mg, 5.1×10^{-5} mol) was used. The product as a mauve powder was obtained (73 mg, 90 %).

^1H NMR (600 MHz, Chloroform-*d*) δ 10.15 (s, 1H), 10.02 (s, 1H), 8.79 (d, $J = 2.2$ Hz, 1H), 8.47 (dd, $J = 53.0, 26.9$ Hz, 4H), 8.29 (d, $J = 5.8$ Hz, 1H), 8.15 (t, $J = 8.1$ Hz, 2H), 8.07 (d, $J = 5.6$ Hz, 1H), 7.88 (d, $J = 5.6$ Hz, 1H), 7.82 (s, 1H), 7.76 (d, $J = 6.0$ Hz, 2H), 7.52 (tdd, $J = 34.7, 19.8, 8.9$ Hz, 8H), 7.37 – 7.26 (m, 5H), 6.80 (dd, $J = 6.1, 2.2$ Hz, 1H), 5.85 (s, 1H), 4.56 (dt, $J = 10.5, 6.5$ Hz, 1H), 4.47 (dt, $J = 10.7, 6.5$ Hz, 1H), 4.36 (dt, $J = 13.5, 7.2$ Hz, 4H), 4.23 (dt, $J = 10.6, 6.9$ Hz, 1H), 4.16 (dt, $J = 10.7, 6.9$ Hz, 1H), 2.03 – 1.96 (m, 2H), 1.95 – 1.86 (m, 4H), 1.70 – 1.59 (m, 4H), 1.38 – 1.14 (m, 55H), 0.93 – 0.84 (m, 12H).

^{13}C NMR (151 MHz, Chloroform-*d*) δ 167.52, 165.23, 160.57, 159.70, 159.51, 157.00, 156.89, 154.21, 150.01, 149.82, 148.73, 147.71, 147.43, 147.28, 141.37, 141.30, 141.18, 141.13, 135.89, 127.39, 126.69, 126.55, 125.65, 124.96, 124.68, 124.59, 124.32, 123.88, 123.78, 122.78, 122.72, 120.96, 120.77, 120.70, 119.91, 119.76, 119.68, 119.19, 118.16, 113.71, 109.70, 109.42, 109.28, 107.54, 66.16, 65.95, 43.49, 43.42, 35.17, 34.36, 32.06, 31.70, 30.73, 30.45, 29.89, 29.85, 29.79, 29.77, 29.74, 29.66, 29.59, 29.50, 29.44, 29.13, 29.10, 27.14, 27.10, 26.99, 26.25, 22.83, 22.78, 22.67, 14.26, 14.23, 14.14.

^{13}C DEPT 135 NMR (101 MHz, Chloroform-*d*) δ C-H: 154.21, 150.01, 149.82, 148.73, 147.71, 127.39, 126.69, 126.55, 125.65, 124.96, 124.68, 124.59, 124.32, 120.77, 120.70, 119.91, 119.76, 119.68, 119.19, 118.16, 113.71, 109.70, 109.42, 109.28, 107.54;

δ C-H₂: 66.16, 65.95, 43.49, 43.42, 35.17, 34.36, 32.06, 31.70, 29.89, 29.85, 29.79, 29.77, 29.74, 29.66, 29.59, 29.50, 29.44, 29.13, 29.10, 27.14, 27.10, 26.99, 26.25, 22.83, 22.78, 22.67;

δ C-H₃: 30.73, 30.45, 14.26, 14.23, 14.14.

^{31}P NMR (162 MHz, Chloroform-*d*) No signal.

$[\text{Ru}(\text{C}^{\wedge}\text{N})(\text{L}_2)(\text{bpy}(\text{CO}_2\text{H})(\text{CO}_2^-))]$ (SA-634). Was synthesized according to the general procedure. $[\text{Ru}(\text{C}^{\wedge}\text{N})(\text{L}_2)(\text{bpy}(\text{CO}_2\text{Me})_2)](\text{PF}_6)$ (90 mg, 5.0×10^{-5} mol) was used. The product as a mauve powder was obtained (71 mg, 87 %).

^1H NMR (600 MHz, Chloroform-*d*) δ 10.06 (s, 1H), 9.94 (s, 1H), 8.72 (d, $J = 2.2$ Hz, 1H), 8.25 (d, $J = 5.8$ Hz, 1H), 8.20 (d, $J = 20.7$ Hz, 2H), 8.00 (d, $J = 5.7$ Hz, 1H), 7.82 (dd, $J = 5.8, 1.6$ Hz, 1H), 7.74 (d, $J = 5.6$ Hz, 1H), 7.64 (d, $J = 6.0$ Hz, 1H), 7.54 (d, $J = 6.0$ Hz, 1H), 7.46 (d, $J = 8.4$ Hz, 1H), 7.38 – 7.33

(m, 3H), 7.23 (t, $J = 9.9$ Hz, 2H), 7.19 – 7.10 (m, 5H), 6.93 (dt, $J = 13.8, 6.9$ Hz, 3H), 6.88 (d, $J = 8.2$ Hz, 1H), 6.85 (d, $J = 8.2$ Hz, 2H), 6.75 (dd, $J = 6.1, 2.2$ Hz, 1H), 5.64 (s, 1H), 4.50 (dt, $J = 10.8, 6.5$ Hz, 1H), 4.42 (dt, $J = 10.7, 6.5$ Hz, 1H), 4.18 (dt, $J = 10.7, 7.0$ Hz, 1H), 4.10 (dt, $J = 10.6, 6.9$ Hz, 1H), 3.87 (dt, $J = 17.0, 7.2$ Hz, 4H), 1.94 (p, $J = 6.9$ Hz, 2H), 1.81 (dp, $J = 15.1, 7.4$ Hz, 4H), 1.66 – 1.56 (m, 4H), 1.50 – 1.38 (m, 6H), 1.37 – 1.15 (m, 49H), 0.90 – 0.83 (m, 12H).

^{13}C NMR (151 MHz, Chloroform-*d*) δ 167.45, 167.40, 165.07, 160.54, 159.83, 159.45, 158.45, 156.96, 156.80, 156.16, 154.13, 150.07, 150.00, 148.59, 147.71, 146.95, 146.82, 144.95, 144.82, 144.47, 144.40, 130.31, 130.26, 127.74, 127.63, 127.02, 126.09, 125.97, 125.42, 125.40, 124.83, 123.97, 123.83, 123.36, 123.18, 123.09, 122.99, 120.78, 119.80, 199.00, 118.93, 118.20, 115.90, 115.80, 115.75, 107.46, 66.17, 65.94, 53.56, 47.81, 47.75, 35.16, 32.06, 32.03, 31.56, 30.69, 29.87, 29.84, 29.83, 29.78, 29.75, 29.73, 29.68, 29.60, 29.49, 29.47, 29.41, 26.97, 26.89, 26.71, 26.23, 22.82, 22.81, 22.73, 14.26, 14.13.

^{13}C DEPT 135 NMR (101 MHz, Chloroform-*d*) δ C-H: 154.13, 150.07, 150.00, 148.59, 147.71, 127.74, 127.63, 127.02, 126.09, 125.97, 125.42, 125.40, 124.83, 123.36, 123.18, 123.09, 122.99, 119.80, 199.00, 118.93, 118.20, 115.90, 115.80, 115.75, 107.46;

δ C-H₂: 66.17, 65.94, 47.81, 47.75, 35.16, 32.06, 32.03, 31.56, 29.87, 29.84, 29.83, 29.78, 29.75, 29.73, 29.68, 29.60, 29.49, 29.47, 29.41, 26.97, 26.89, 26.71, 26.23, 22.82, 22.81, 22.73;

δ C-H₃: 30.69, 14.26, 14.13.

^{31}P NMR (162 MHz, Chloroform-*d*) No signal.

[Ru(C[^]N)(L3)(bpy(CO₂H)(CO₂⁻))] (SA-635). Was synthesized according to the general procedure. [Ru(C[^]N)(L2)(bpy(CO₂Me)₂)](PF₆) (85 mg, 4.8*10⁻⁵ mol) was used. The product as a mauve powder was obtained (68 mg, 89 %).

^1H NMR (400 MHz, Chloroform-*d*) δ 9.95 (s, 1H), 9.84 (s, 1H), 8.68 (d, $J = 2.2$ Hz, 1H), 8.25 (d, $J = 6.0$ Hz, 1H), 8.22 (dd, $J = 10.9, 2.0$ Hz, 2H), 7.99 (d, $J = 5.7$ Hz, 1H), 7.78 (d, $J = 5.5$ Hz, 2H), 7.59 (d, $J = 6.1$ Hz, 1H), 7.56 – 7.46 (m, 5H), 7.38 (dt, $J = 8.6, 6.8$ Hz, 4H), 7.32 (dd, $J = 6.2, 1.9$ Hz, 1H), 7.25 – 7.14 (m, 8H), 6.89 – 6.83 (m, 4H), 6.72 (dd, $J = 6.2, 2.2$ Hz, 1H), 5.66 (s, 1H), 4.55 – 4.36 (m, 2H), 4.13 (qt, $J = 10.6, 6.9$ Hz, 2H), 3.72 (td, $J = 8.0, 4.2$ Hz, 4H), 1.92 (p, $J = 6.7$ Hz, 2H), 1.74 – 1.53 (m, 8H), 1.39 – 1.19 (m, 55H), 0.91 – 0.83 (m, 12H).

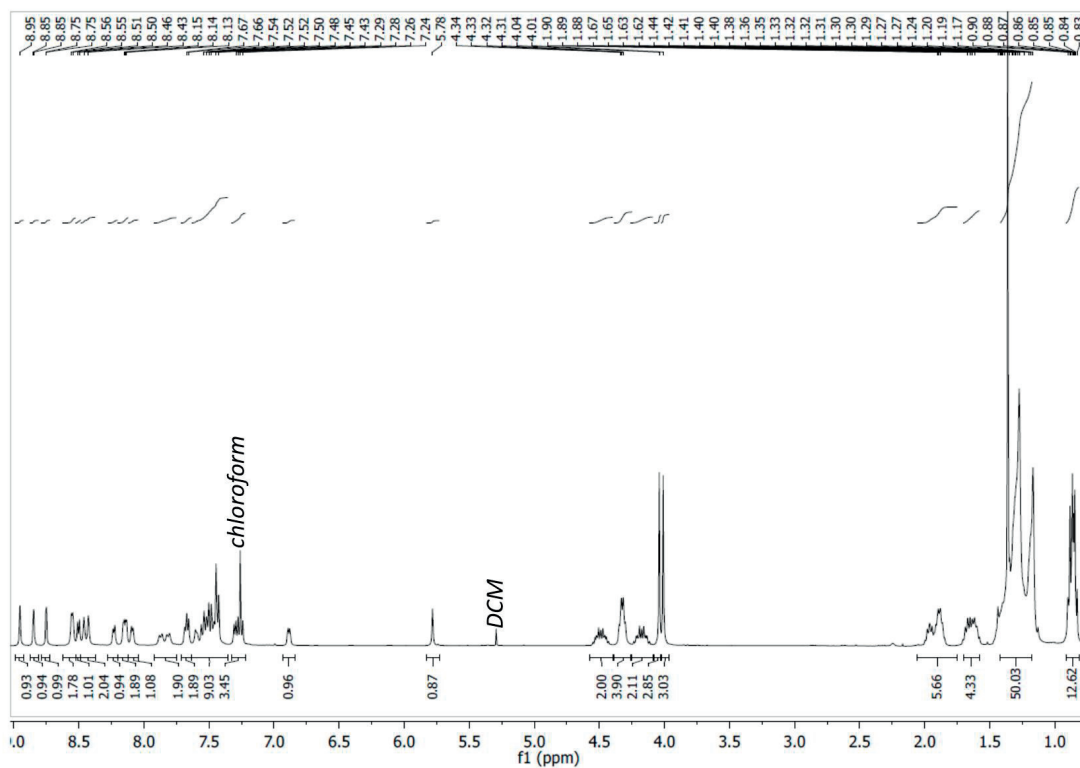
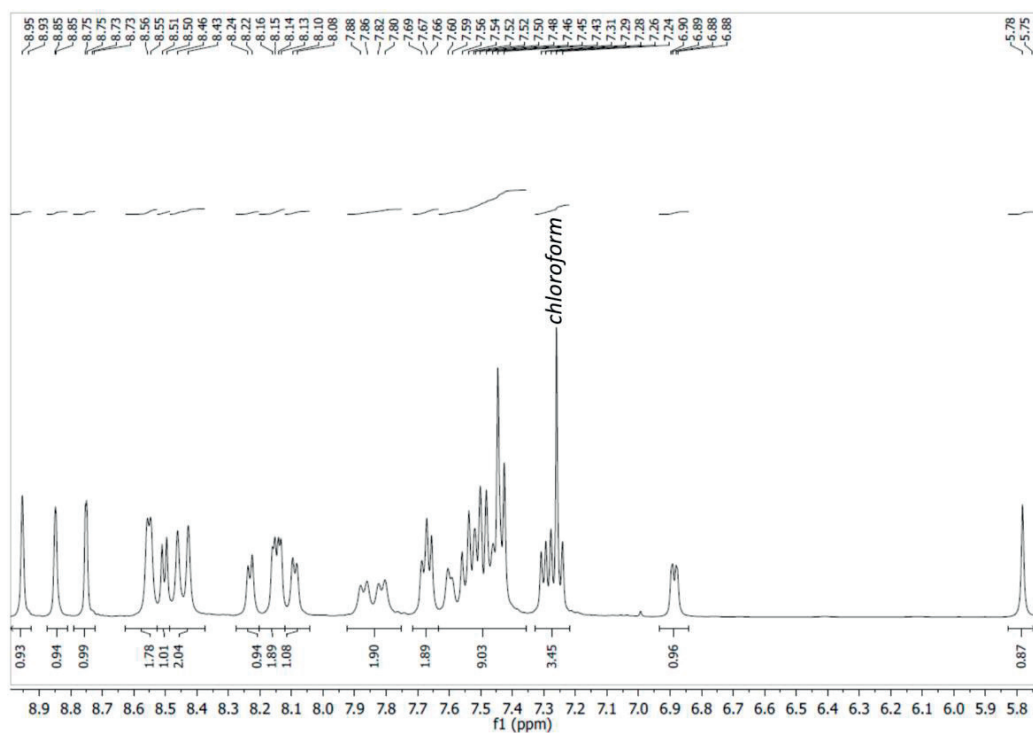
^{13}C NMR (151 MHz, Chloroform-*d*) δ 167.57, 167.48, 165.21, 162.67, 160.45, 159.64, 159.40, 158.56, 156.85, 156.67, 156.18, 154.31, 150.03, 149.94, 149.90, 149.80, 148.66, 147.82, 146.82, 146.75, 146.07, 145.91, 129.94, 129.90, 127.67, 127.59, 126.11, 125.95, 125.56, 125.36, 125.03, 124.88, 125.64, 122.94, 122.55, 120.77, 119.73, 118.66, 118.54, 118.07, 116.39, 116.27, 107.40, 66.09, 65.95, 52.62, 38.28, 36.62, 35.12, 32.06, 32.04, 31.74, 31.57, 31.37, 30.68, 29.83, 29.80, 29.77, 29.76, 29.71, 29.65, 29.49, 29.48, 29.43, 27.48, 26.98, 26.84, 26.26, 22.82, 22.78, 14.26, 14.15.

^{13}C DEPT 135 NMR (101 MHz, Chloroform-*d*) δ C-H: 162.67, 154.31, 149.90, 149.80, 148.66, 147.82, 129.94, 129.90, 127.67, 127.59, 126.11, 125.95, 125.03, 124.88, 124.64, 122.94, 122.55, 119.73, 118.66, 118.54, 118.07, 116.39, 116.27, 107.40;

δ C-H₂: 66.09, 65.95, 52.62, 38.28, 35.12, 32.06, 32.04, 31.74, 29.83, 29.80, 29.77, 29.76, 29.71, 29.65, 29.49, 29.48, 29.43, 27.48, 26.98, 26.84, 26.26, 22.82, 22.78;

δ C-H₃: 36.62, 31.57, 31.37, 30.68, 14.26, 14.15.

^{31}P NMR (162 MHz, Chloroform-*d*) δ -146.62 (m). Intensity is weak in compare to those obtained for ester analogues, which indicates, that partially SA635 is double protonated - [Ru(C[^]N)(L3)(bpy(CO₂H)₂)](PF₆).

$[Ru(C^{\wedge}N)(L1)(bpy(CO_2Me)_2)](PF_6)$ (SA617)

 Figure 8.49. 1H NMR spectrum of $[Ru(C^{\wedge}N)(L1)(bpy(CO_2Me)_2)](PF_6)$ in $chloroform-d$

 Figure 8.50. 1H NMR spectrum of $[Ru(C^{\wedge}N)(L1)(bpy(CO_2Me)_2)](PF_6)$ (aromatic region) in $chloroform-d$

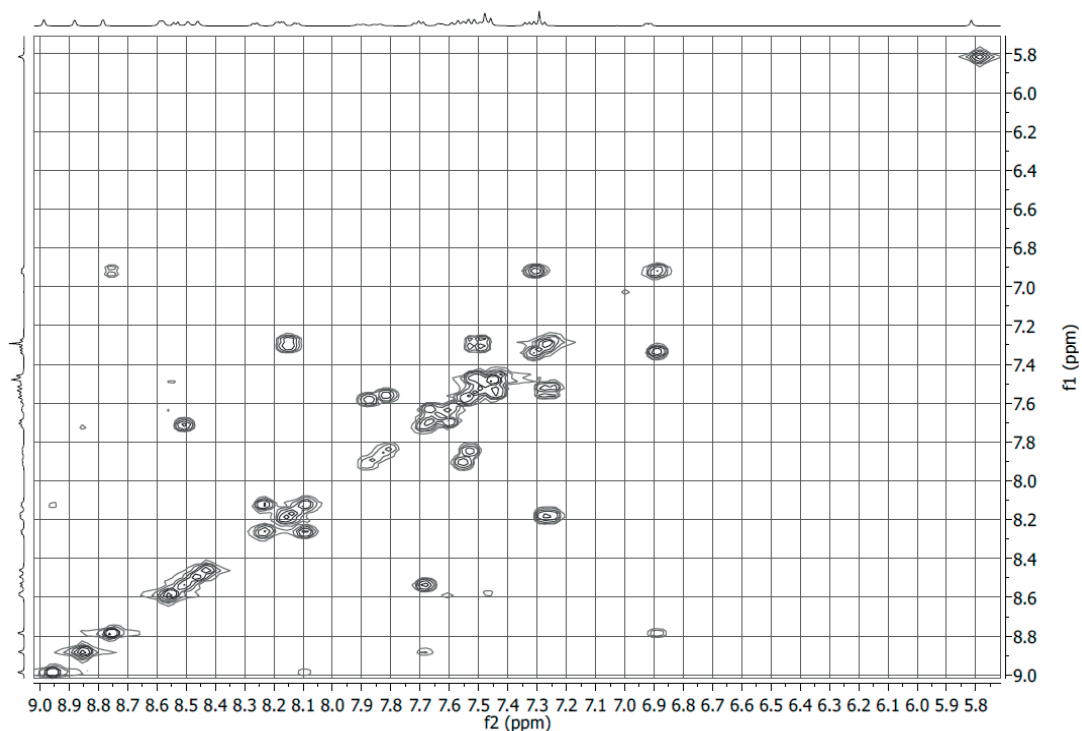


Figure 8.51. ^1H - ^1H COSY spectrum of $[\text{Ru}(\text{C}^{\text{N}})(\text{L1})(\text{bpy}(\text{CO}_2\text{Me})_2)](\text{PF}_6)$ (aromatic region) in *chloroform-d*

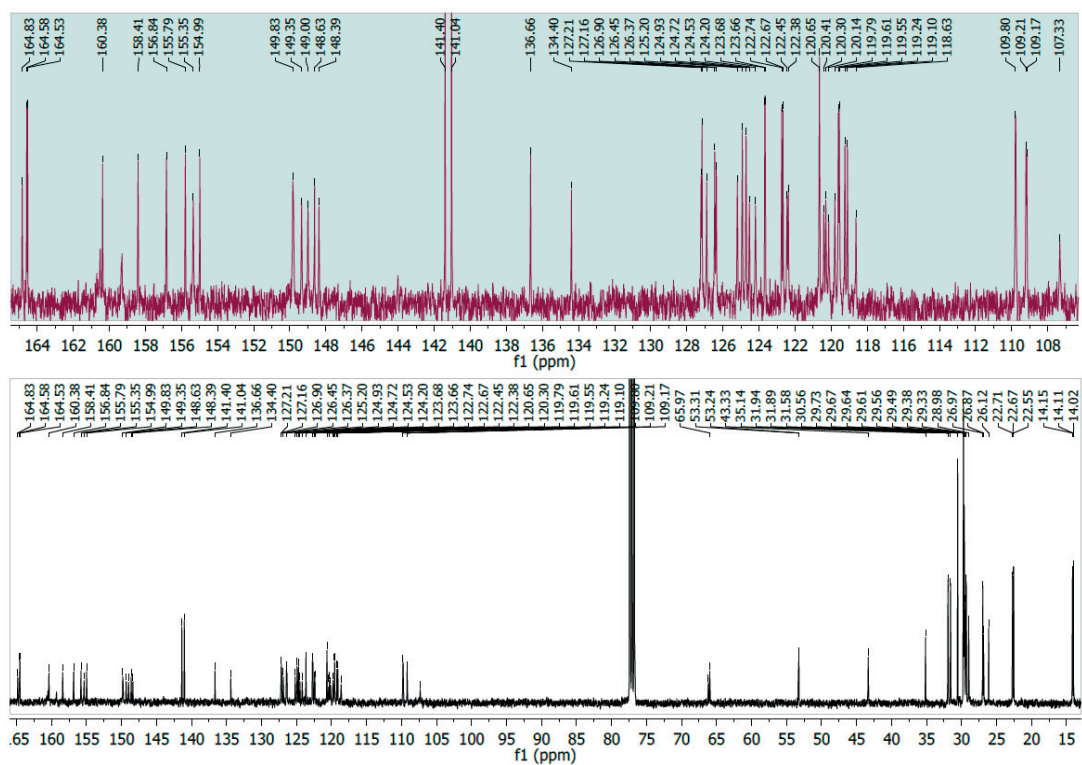


Figure 8.52. ^{13}C NMR spectrum of $[\text{Ru}(\text{C}^{\text{N}})(\text{L1})(\text{bpy}(\text{CO}_2\text{Me})_2)](\text{PF}_6)$ in *chloroform-d*

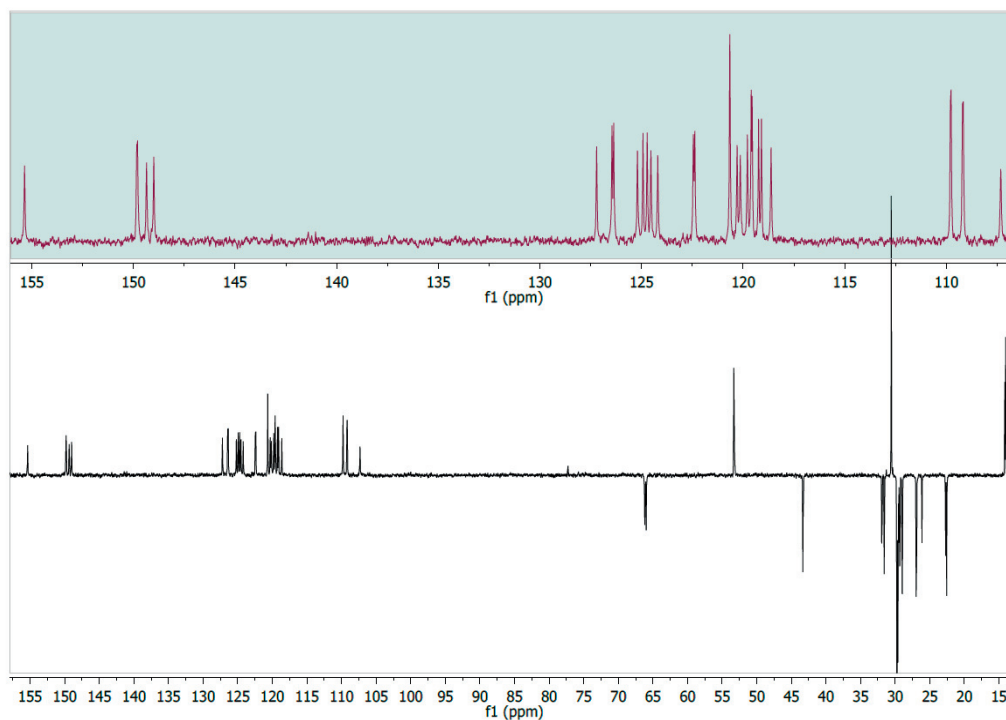


Figure 8.53. ^{13}C DEPT 135 NMR spectrum of $[\text{Ru}(\text{C}^{\wedge}\text{N})(\text{L1})(\text{bpy}(\text{CO}_2\text{Me})_2)](\text{PF}_6)$ in *chloroform-d*
 $[\text{Ru}(\text{C}^{\wedge}\text{N})(\text{L2})(\text{bpy}(\text{CO}_2\text{Me})_2)](\text{PF}_6)$ (SA-618)

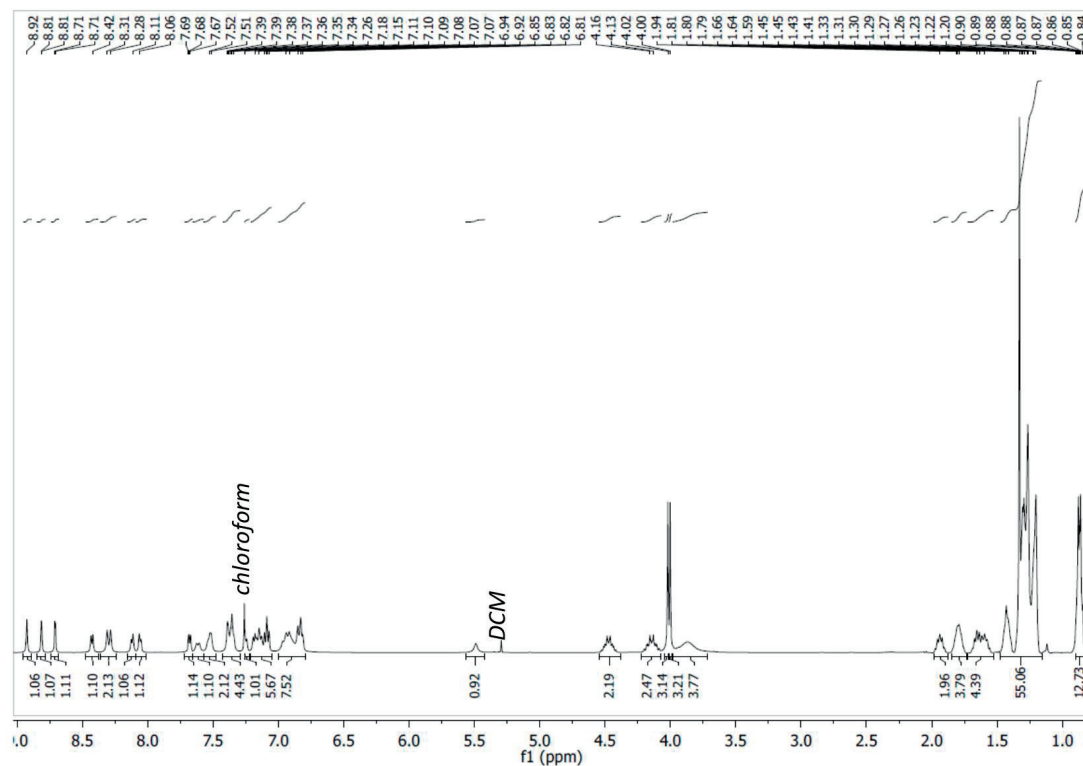


Figure 8.54. ^1H NMR spectrum of $[\text{Ru}(\text{C}^{\wedge}\text{N})(\text{L2})(\text{bpy}(\text{CO}_2\text{Me})_2)](\text{PF}_6)$ in *chloroform-d*

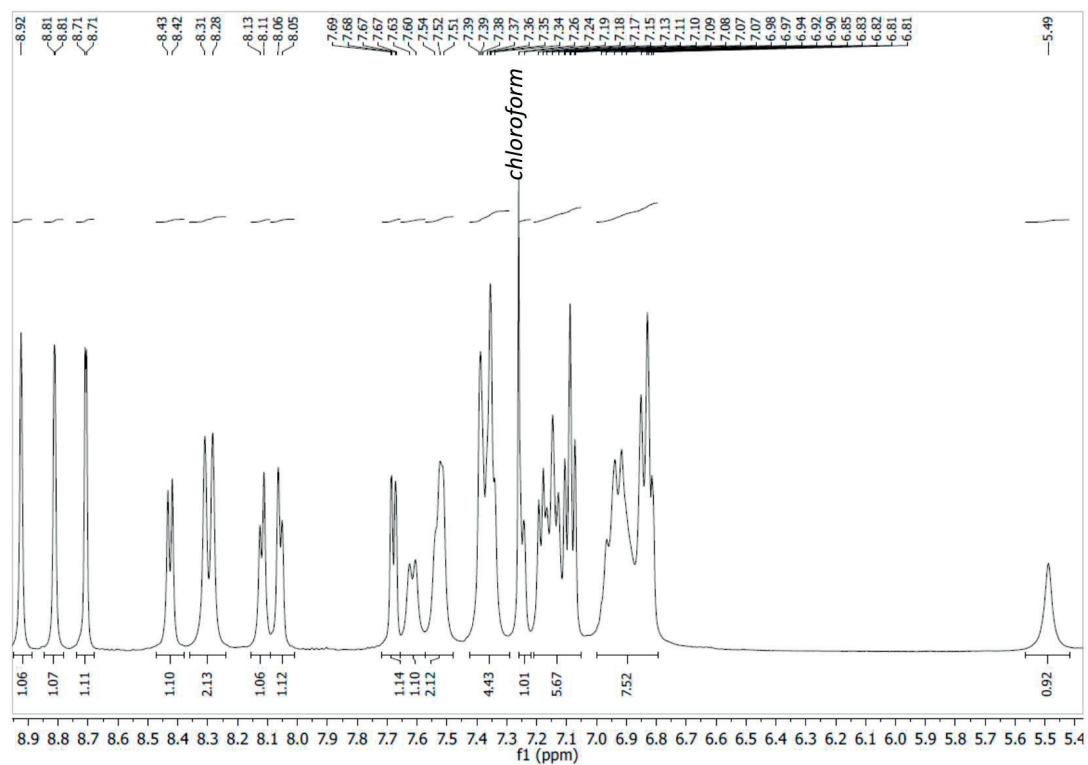


Figure 8.55. ^1H NMR spectrum of $[\text{Ru}(\text{C}^{\wedge}\text{N})(\text{L}2)(\text{bpy}(\text{CO}_2\text{Me})_2)](\text{PF}_6)$ (aromatic region) in *chloroform-d*

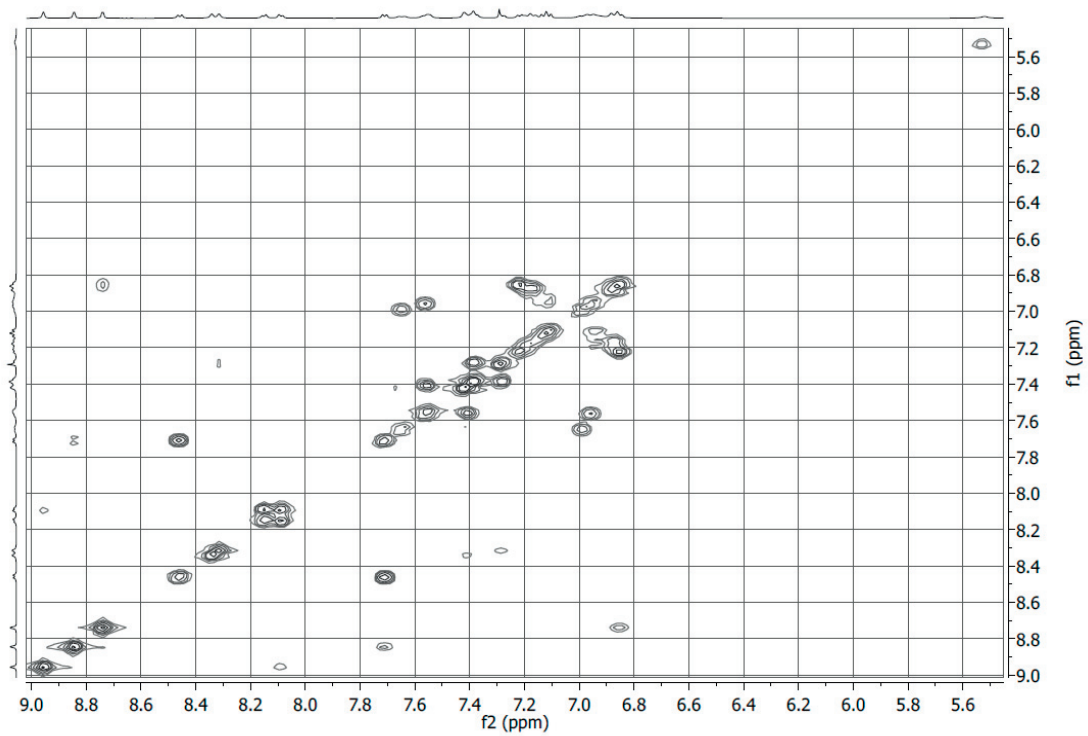
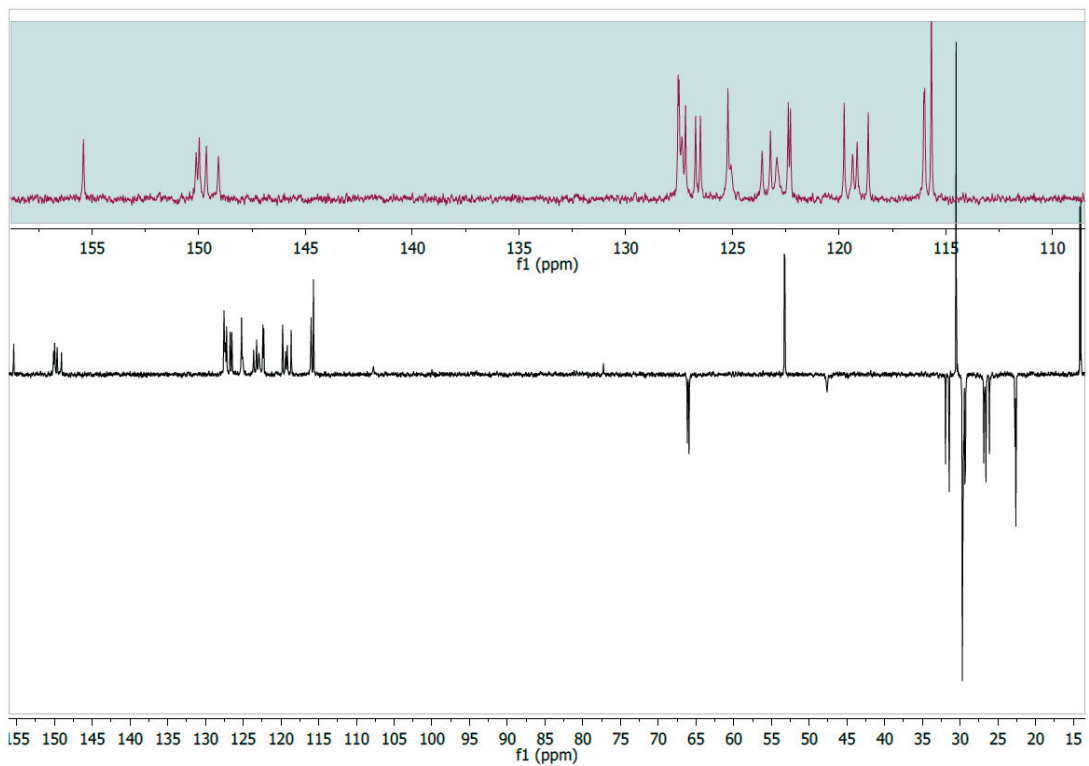
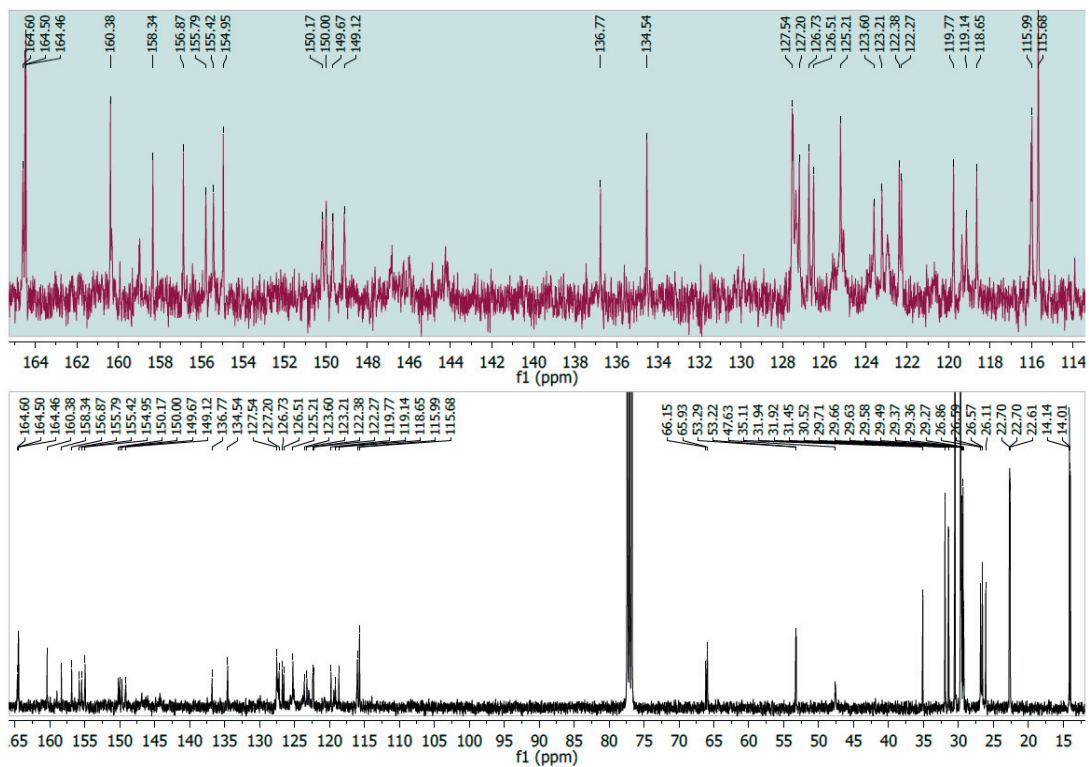
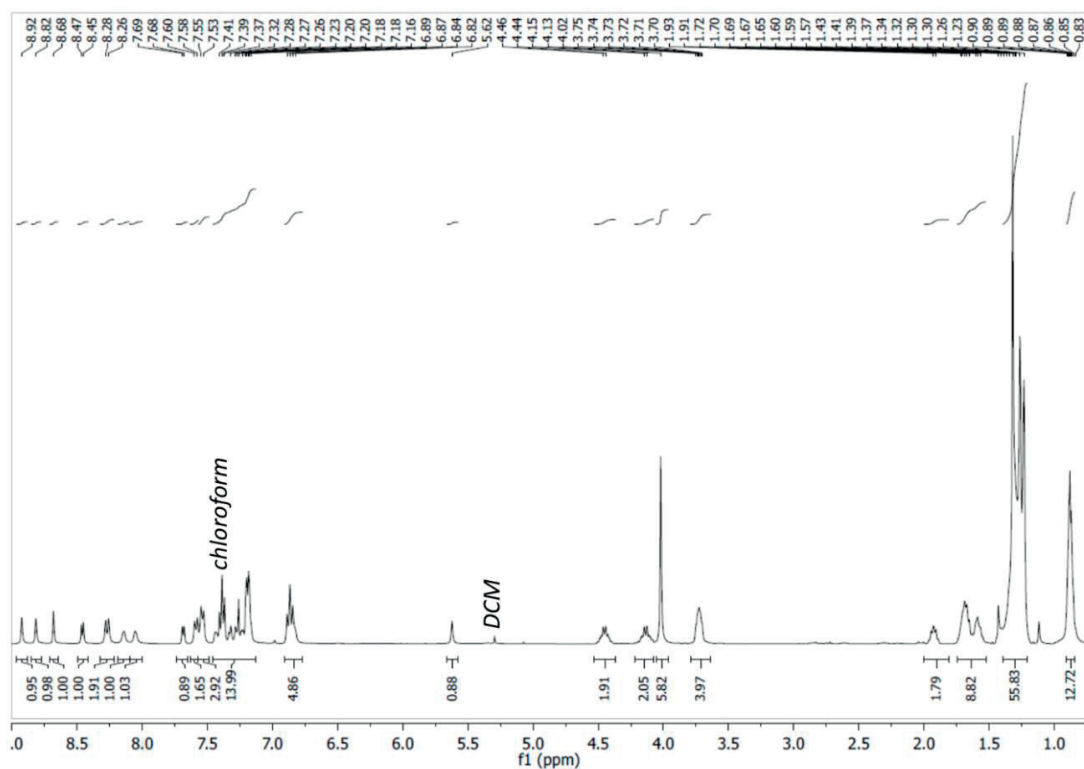
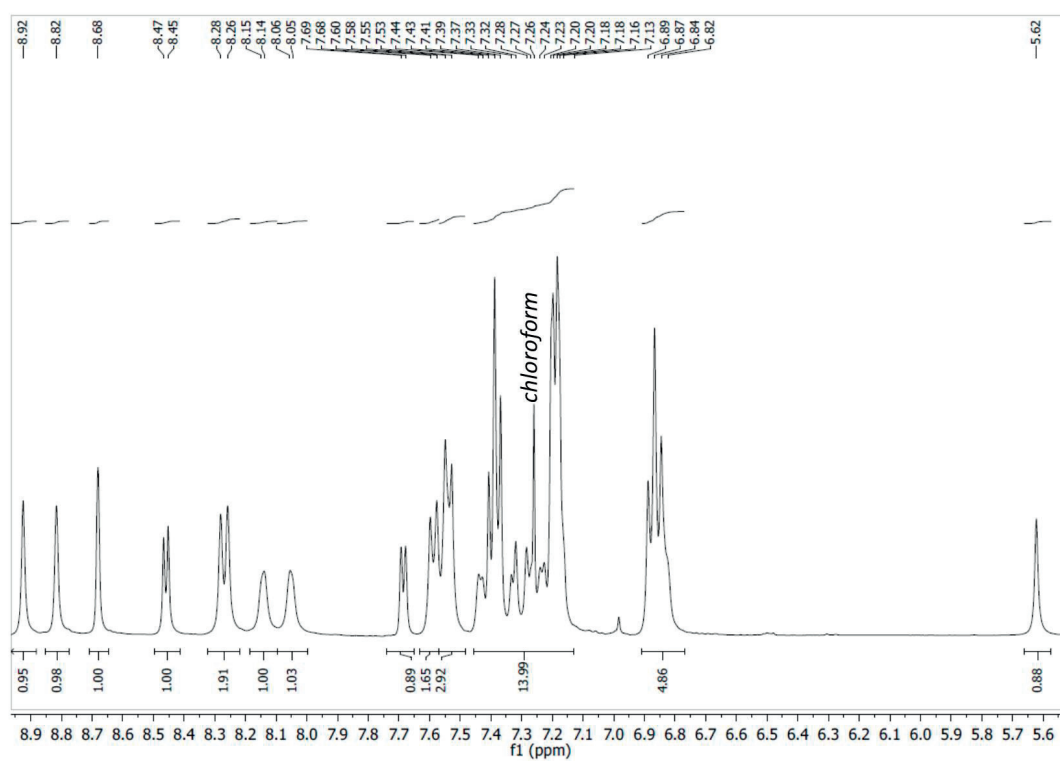


Figure 8.56. ^1H - ^1H COSY NMR spectrum of $[\text{Ru}(\text{C}^{\wedge}\text{N})(\text{L}2)(\text{bpy}(\text{CO}_2\text{Me})_2)](\text{PF}_6)$ in *chloroform-d*



$[Ru(C^{\wedge}N)(L2)(bpy(CO_2Me)_2)](PF_6)$ (SA-631)
Figure 8.59. 1H NMR spectrum of $[Ru(C^{\wedge}N)(L2)(bpy(CO_2Me)_2)](PF_6)$ in *chloroform-d*Figure 8.60. 1H NMR spectrum of $[Ru(C^{\wedge}N)(L3)(bpy(CO_2Me)_2)](PF_6)$ (aromatic region) in *chloroform-d*

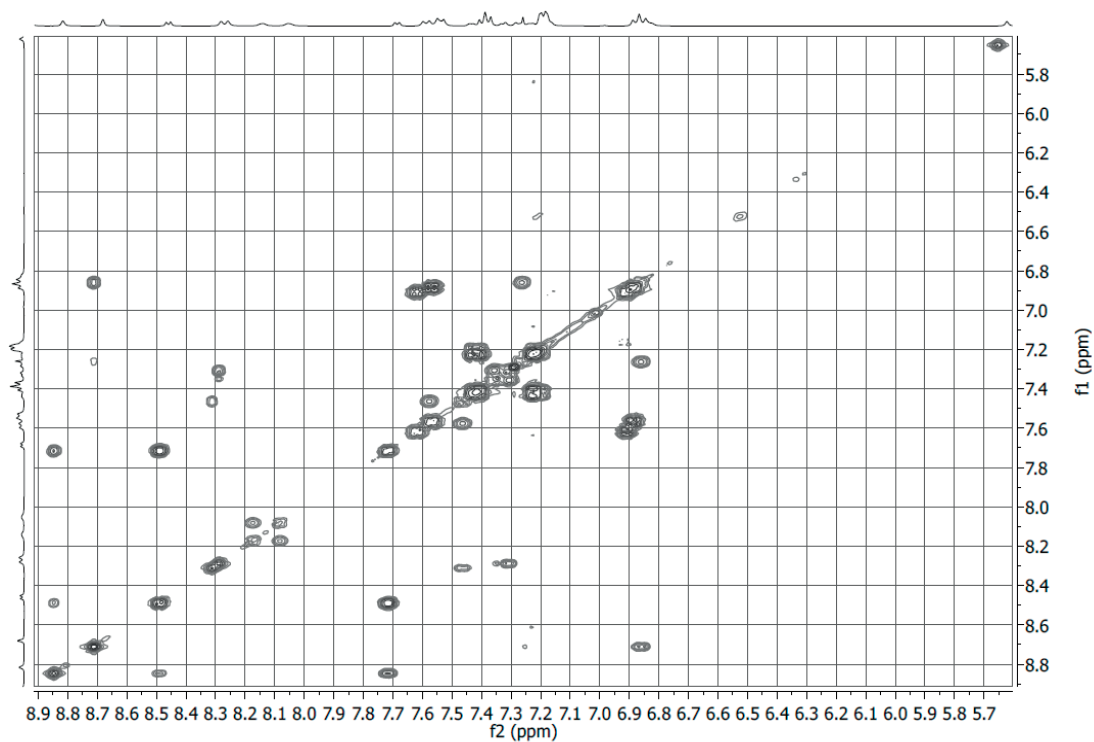


Figure 8.61. ^1H - ^1H COSY NMR spectrum of $[\text{Ru}(\text{C}^{\wedge}\text{N})(\text{L}3)(\text{bpy}(\text{CO}_2\text{Me})_2)](\text{PF}_6)$ (aromatic region) in *chloroform-d*

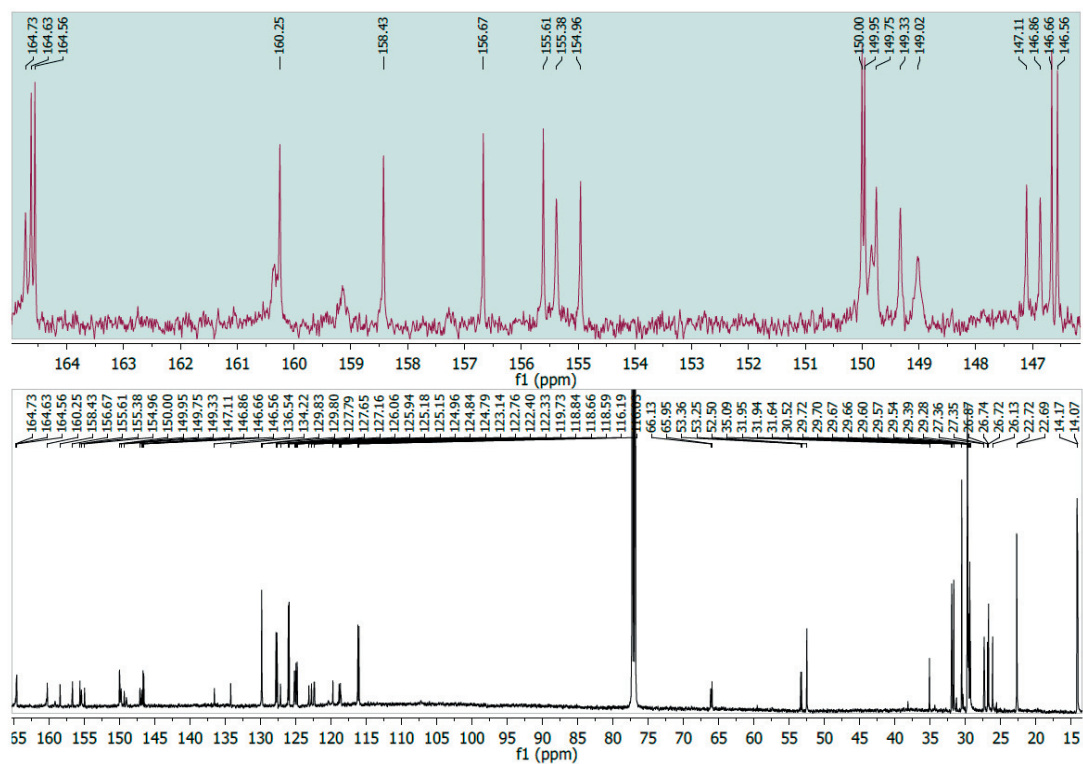


Figure 8.62. ^{13}C NMR spectrum of $[\text{Ru}(\text{C}^{\wedge}\text{N})(\text{L}3)(\text{bpy}(\text{CO}_2\text{Me})_2)](\text{PF}_6)$ in *chloroform-d*

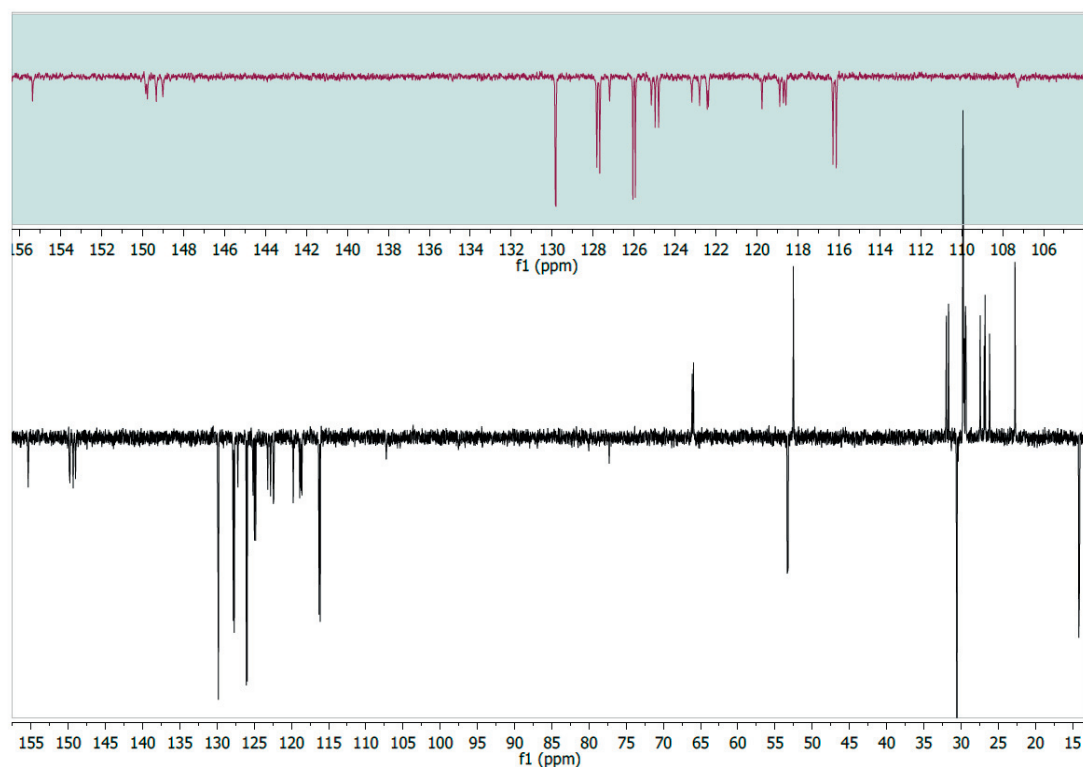


Figure 8.63. ^{13}C DEPT 135 NMR spectrum of $[\text{Ru}(\text{C}^{\wedge}\text{N})(\text{L3})(\text{bpy}(\text{CO}_2\text{Me})_2)](\text{PF}_6)$ in *chloroform-d* $[\text{Ru}(\text{C}^{\wedge}\text{N})(\text{L1})(\text{bpy}(\text{CO}_2\text{H})(\text{CO}_2^-))] (\text{SA633})$

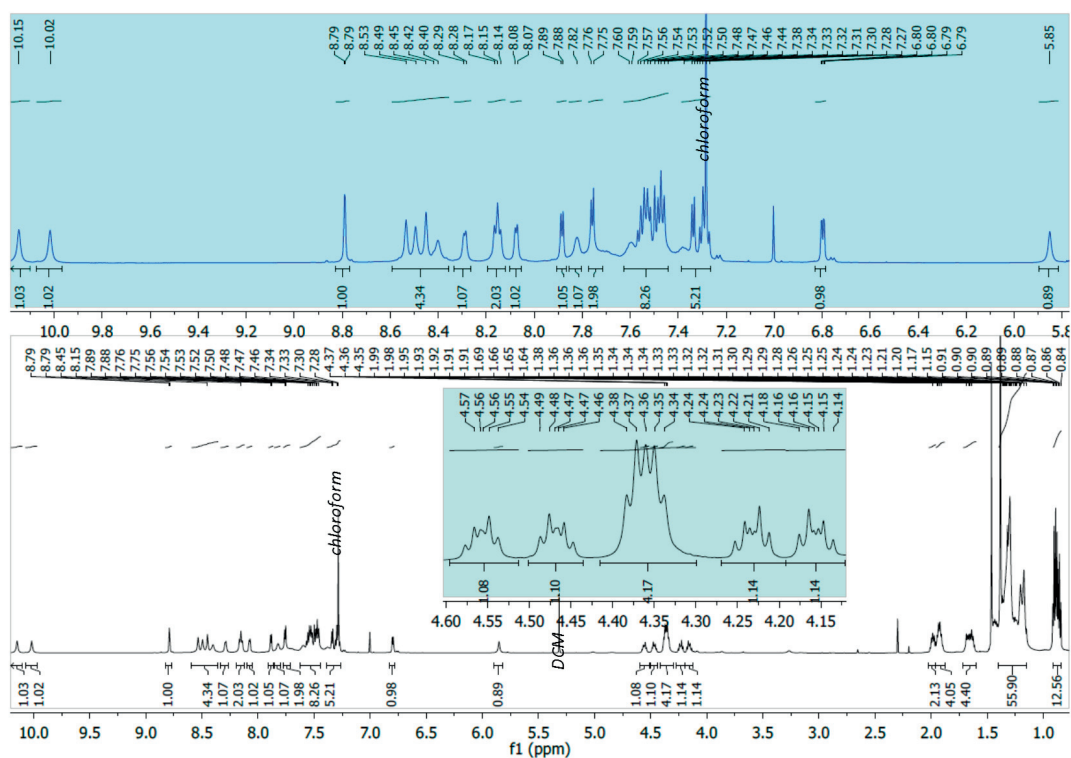


Figure 8.64. ^1H NMR spectrum of $[\text{Ru}(\text{C}^{\wedge}\text{N})(\text{L1})(\text{bpy}(\text{CO}_2\text{H})(\text{CO}_2^-))] (\text{SA633})$ in *chloroform-d*

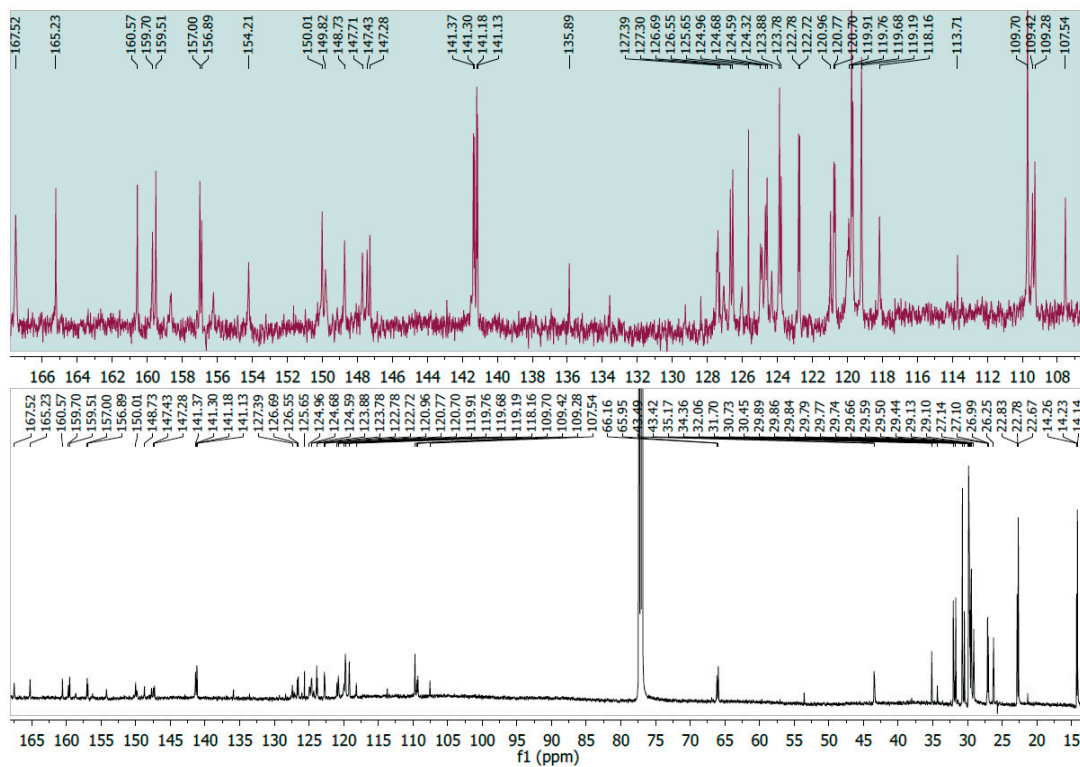


Figure 8.65. ^{13}C NMR spectrum of $[\text{Ru}(\text{C}^{\text{N}})(\text{L1})(\text{bpy}(\text{CO}_2\text{H})(\text{CO}_2))]$ (SA633) in $\text{chloroform-}d$

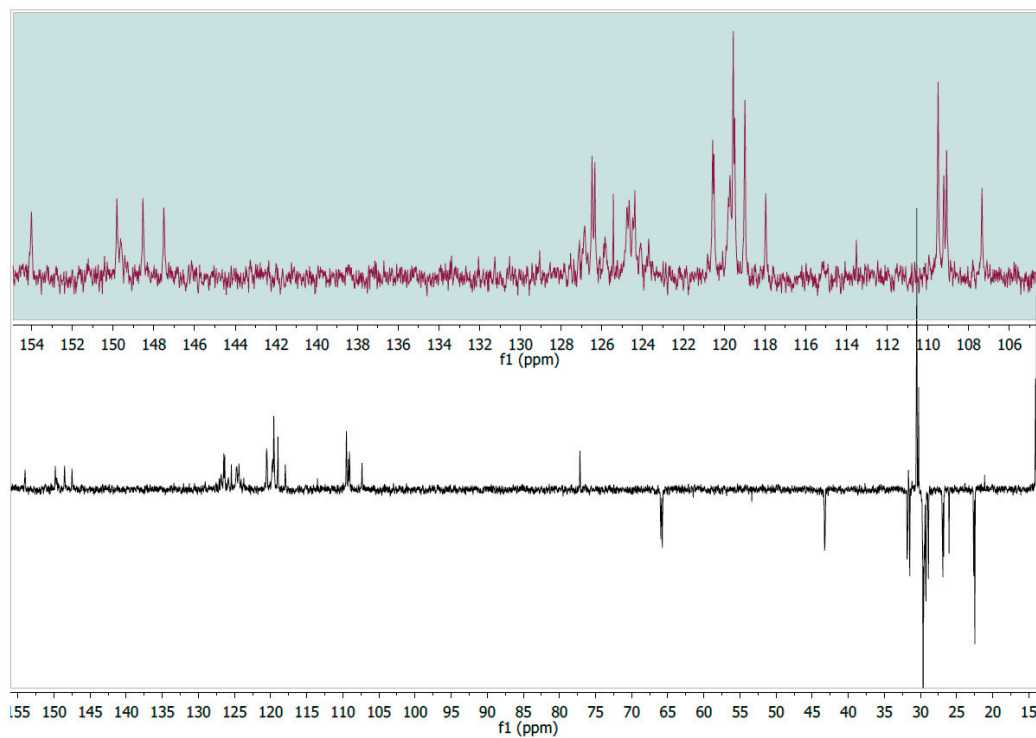


Figure 8.66. ^{13}C DEPT 135 NMR spectrum of $[\text{Ru}(\text{C}^{\text{N}})(\text{L1})(\text{bpy}(\text{CO}_2\text{H})(\text{CO}_2))]$ (SA633) in $\text{chloroform-}d$

$[\text{Ru}(\text{C}^{\wedge}\text{N})(\text{L}2)(\text{bpy}(\text{CO}_2\text{H})(\text{CO}_2))] (\text{SA634})$

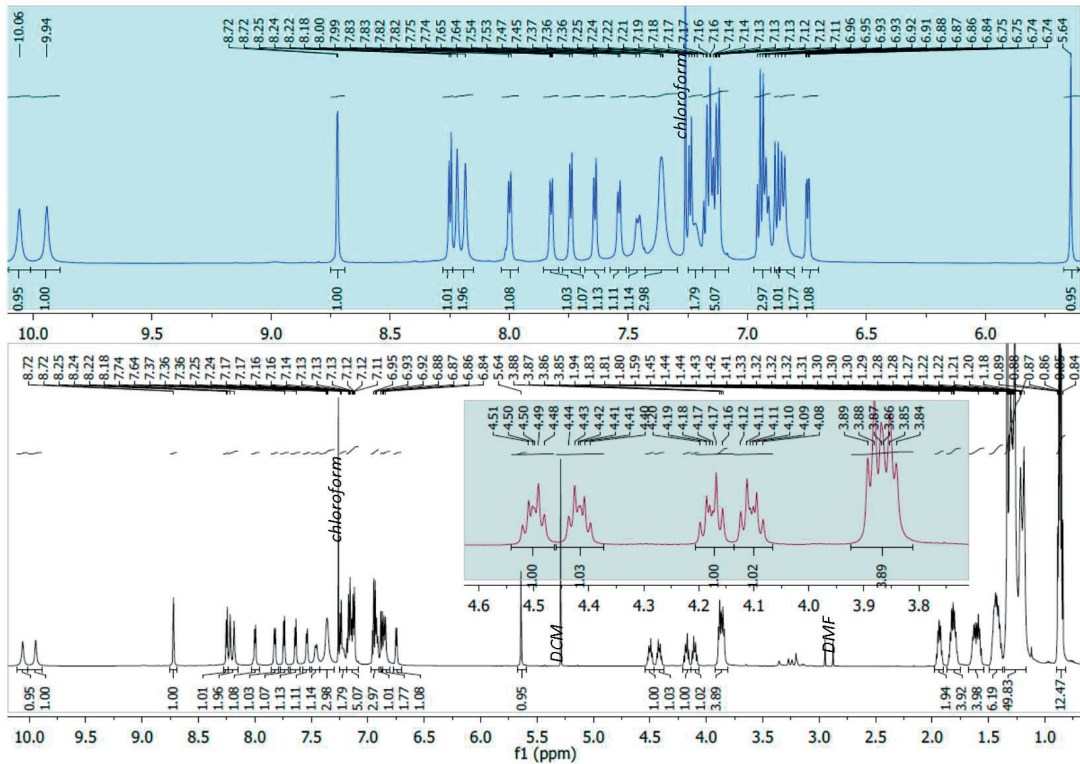


Figure 8.67. ^1H NMR spectrum of $[\text{Ru}(\text{C}^{\wedge}\text{N})(\text{L}2)(\text{bpy}(\text{CO}_2\text{H})(\text{CO}_2))] (\text{SA634})$ in $\text{chloroform-}d$

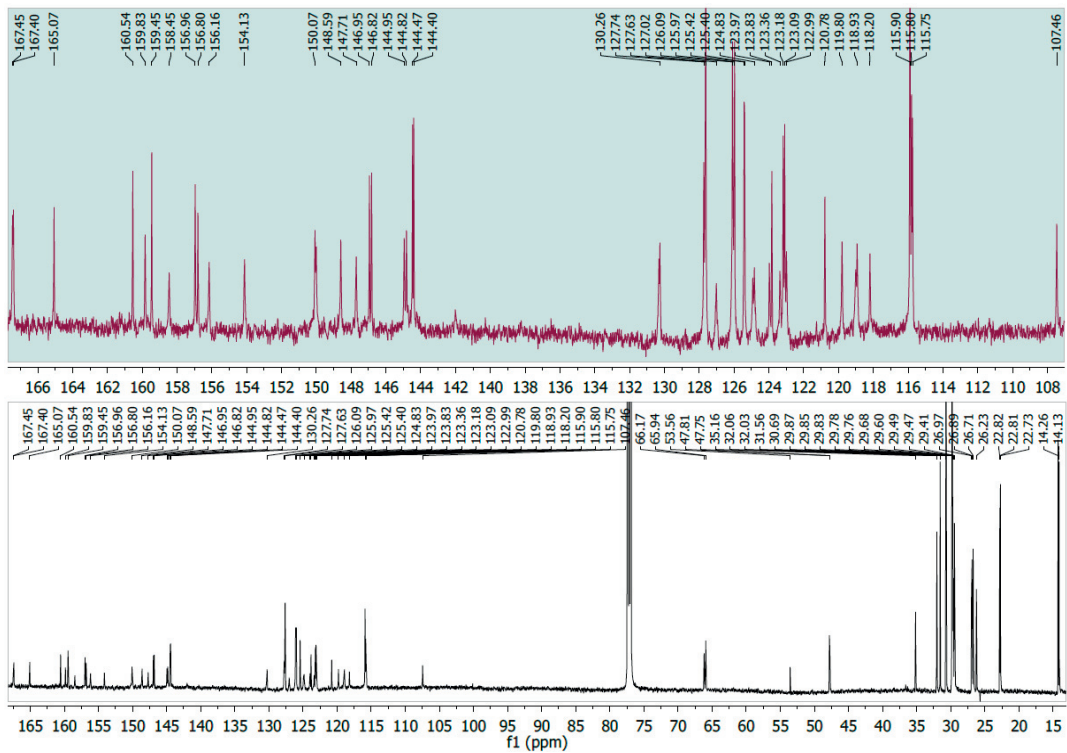


Figure 8.68. ^{13}C NMR spectrum of $[\text{Ru}(\text{C}^{\wedge}\text{N})(\text{L}2)(\text{bpy}(\text{CO}_2\text{H})(\text{CO}_2))] (\text{SA634})$ in $\text{chloroform-}d$

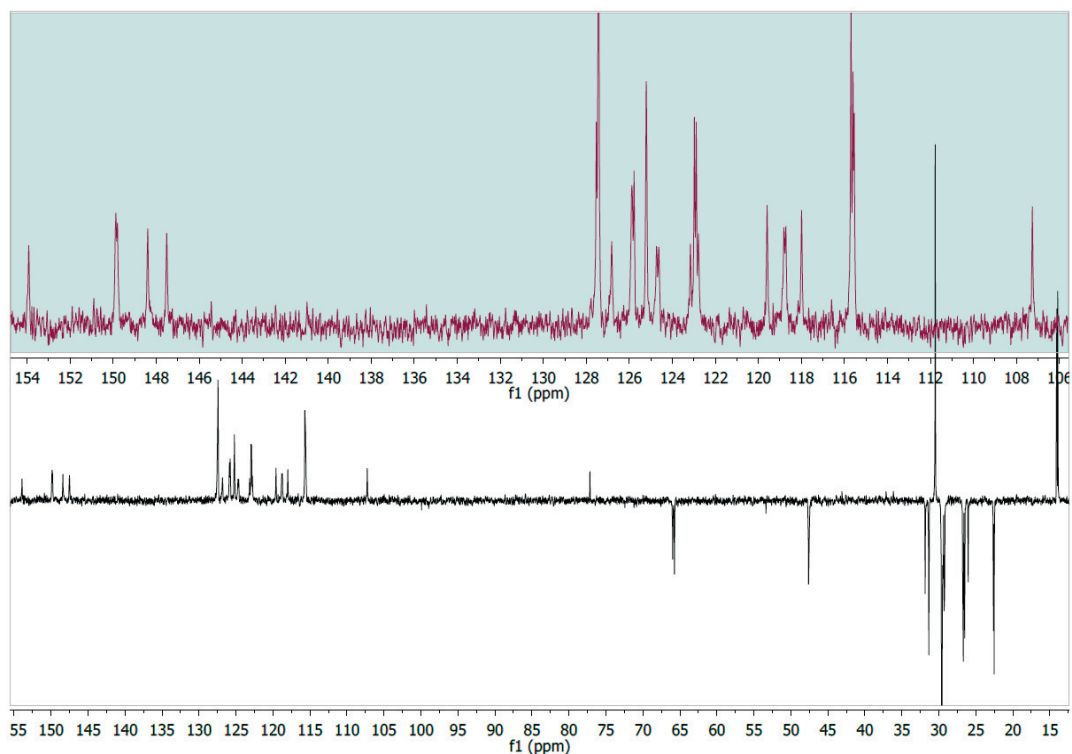


Figure 8.69. ^{13}C DEPT 135 NMR spectrum of $[\text{Ru}(\text{C}^{\text{N}})(\text{L}2)(\text{bpy}(\text{CO}_2\text{H})(\text{CO}_2))]$ (SA634) in *chloroform-d*

$[\text{Ru}(\text{C}^{\text{N}})(\text{L}3)(\text{bpy}(\text{CO}_2\text{H})(\text{CO}_2))]$ (SA635)

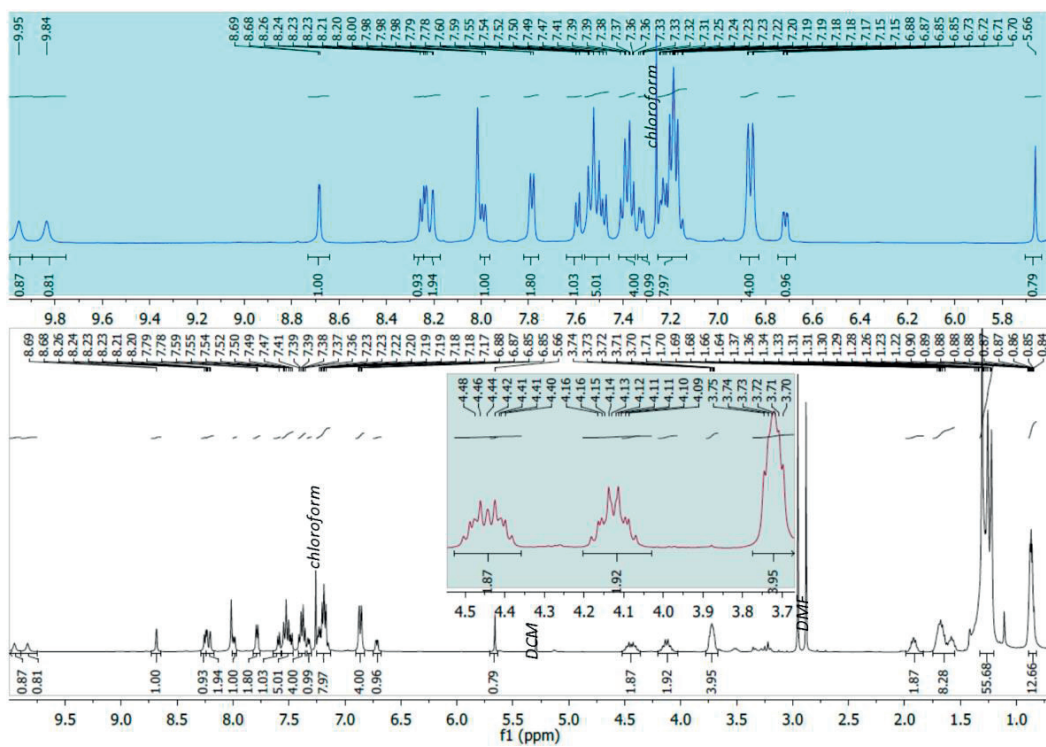


Figure 8.70. ^1H NMR spectrum of $[\text{Ru}(\text{C}^{\text{N}})(\text{L}3)(\text{bpy}(\text{CO}_2\text{H})(\text{CO}_2))]$ (SA635) in *chloroform-d*

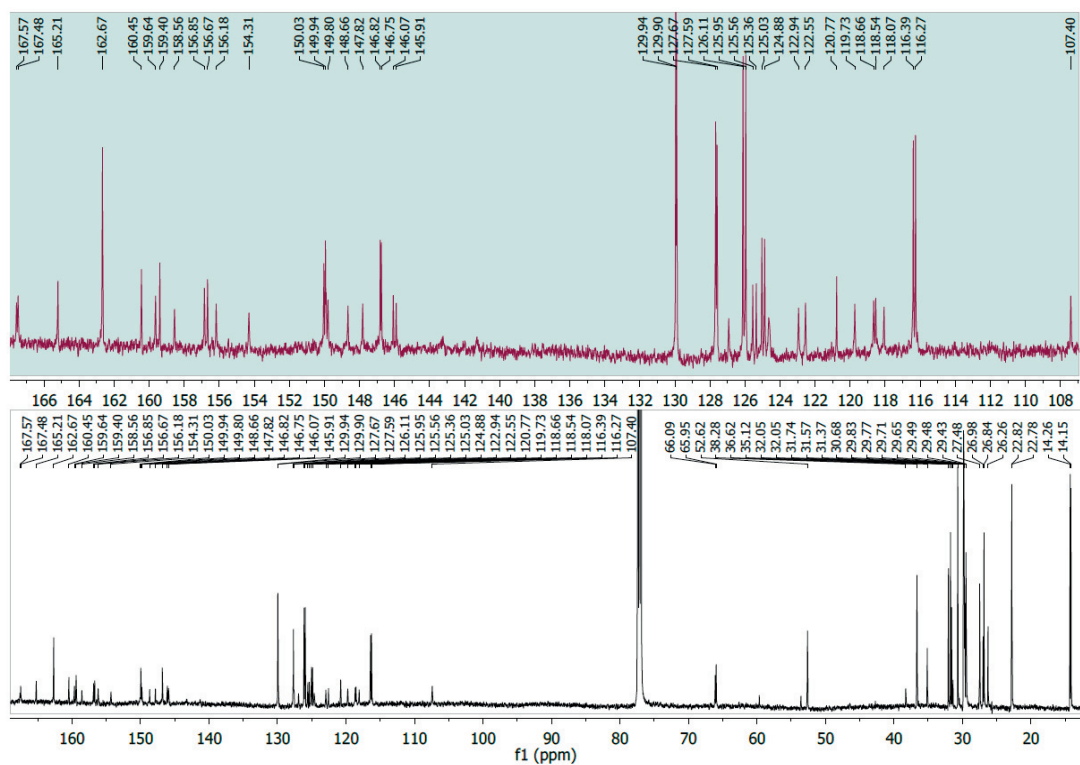


Figure 8.71. ^{13}C NMR spectrum of $[\text{Ru}(\text{C}^{\wedge}\text{N})(\text{L}3)(\text{bpy}(\text{CO}_2\text{H})(\text{CO}_2))]$ (SA635) in $\text{chloroform-}d$

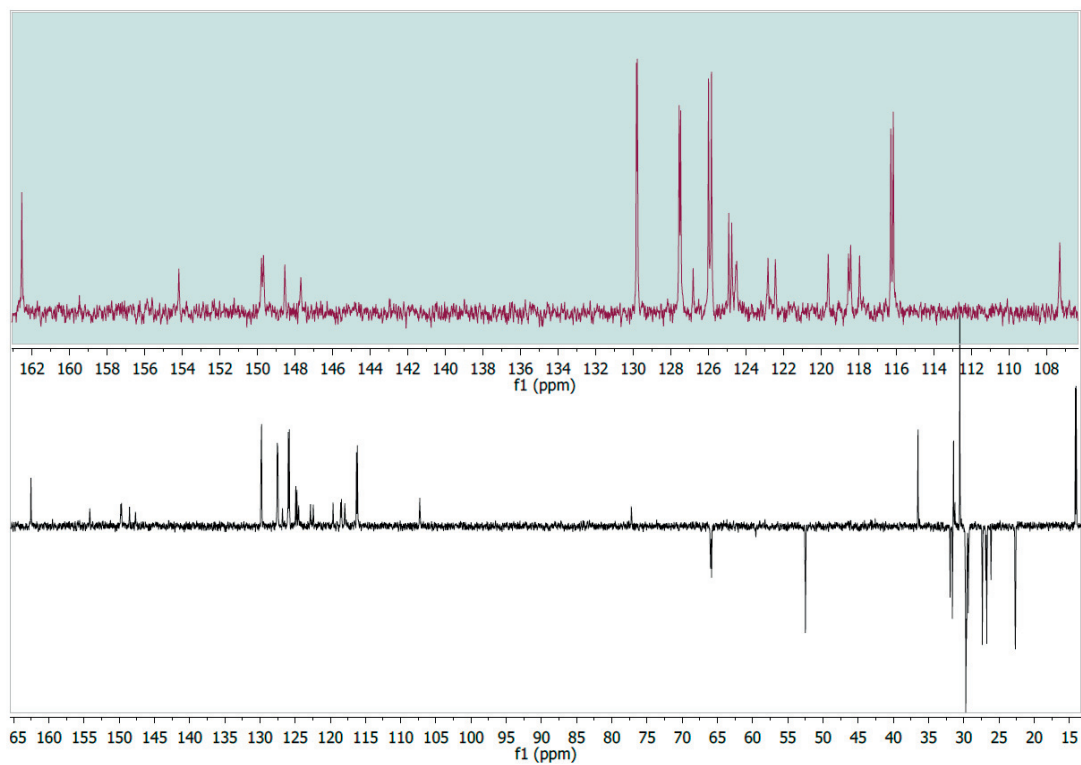


Figure 8.72. ^{13}C NMR spectrum of $[\text{Ru}(\text{C}^{\wedge}\text{N})(\text{L}3)(\text{bpy}(\text{CO}_2\text{H})(\text{CO}_2))]$ (SA635) in $\text{chloroform-}d$

8.2.2 Quantum Mechanical Calculations

Computational analysis of the ruthenium complexes was carried out with Gaussian 09 software package¹⁸⁸ using the functional mPW1PW91.¹⁸⁹ To reduce the computation time, hexyl chains were substituted by ethyl groups. Geometries in the ground state were optimized using LANL2DZ¹⁹⁰ basis set and effective core potential (ECP) for ruthenium and 6-31G* for nonmetal atoms.¹⁹¹ Single point energy calculations were performed at the optimized geometries employing the Stuttgart-Dresden SDD¹⁹² basis set and quasirelativistic effective core potential for ruthenium atom and TZVP¹⁹³ for nonmetal atoms. Solvation effects of acetonitrile were taken into account with implicit solvent model COSMO.¹⁹⁴ Frontier molecular orbitals of the ground state were plotted with GaussView 5.0.

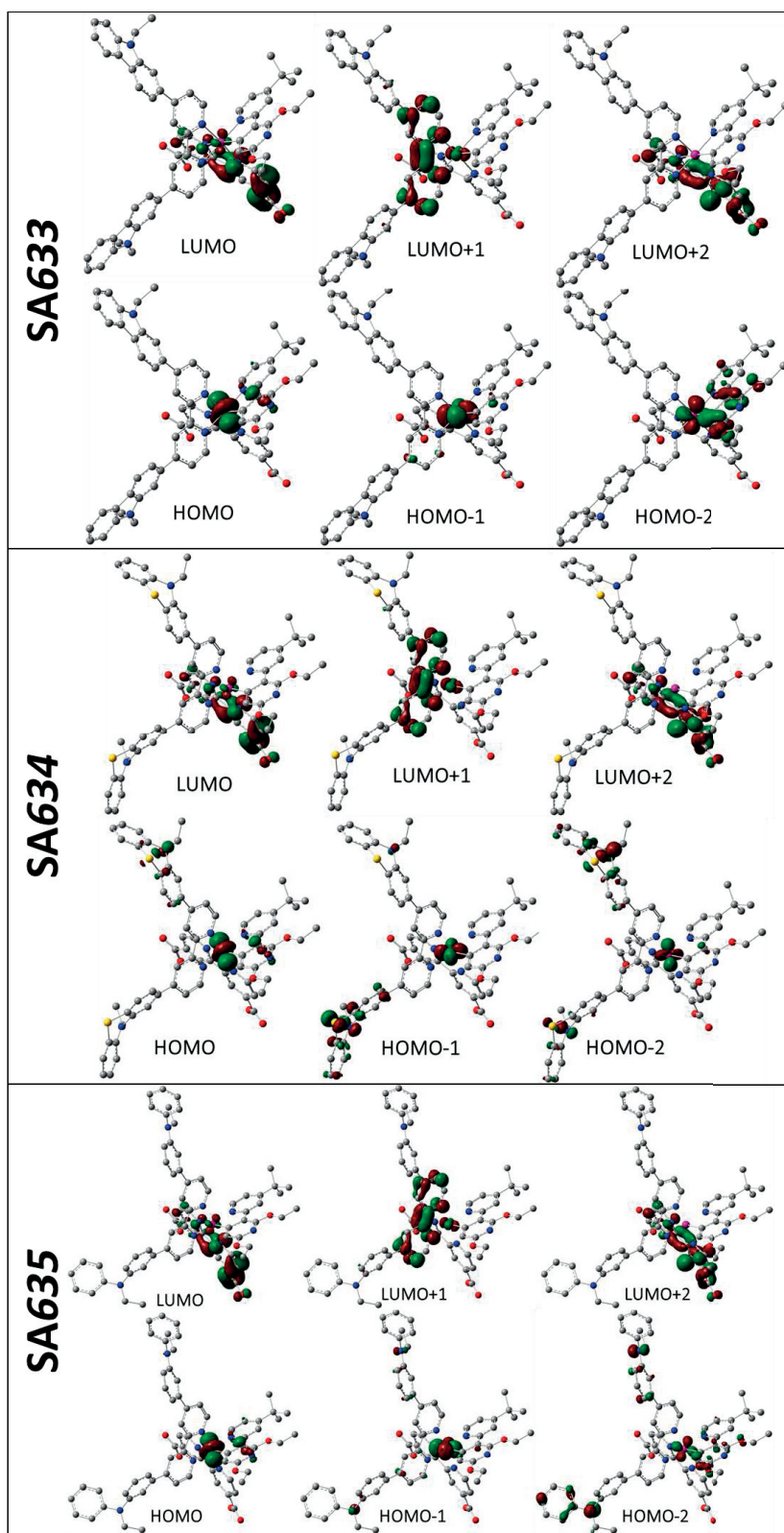


Figure 8.73. DFT calculated frontier orbitals of SA633, SA634 and SA635.

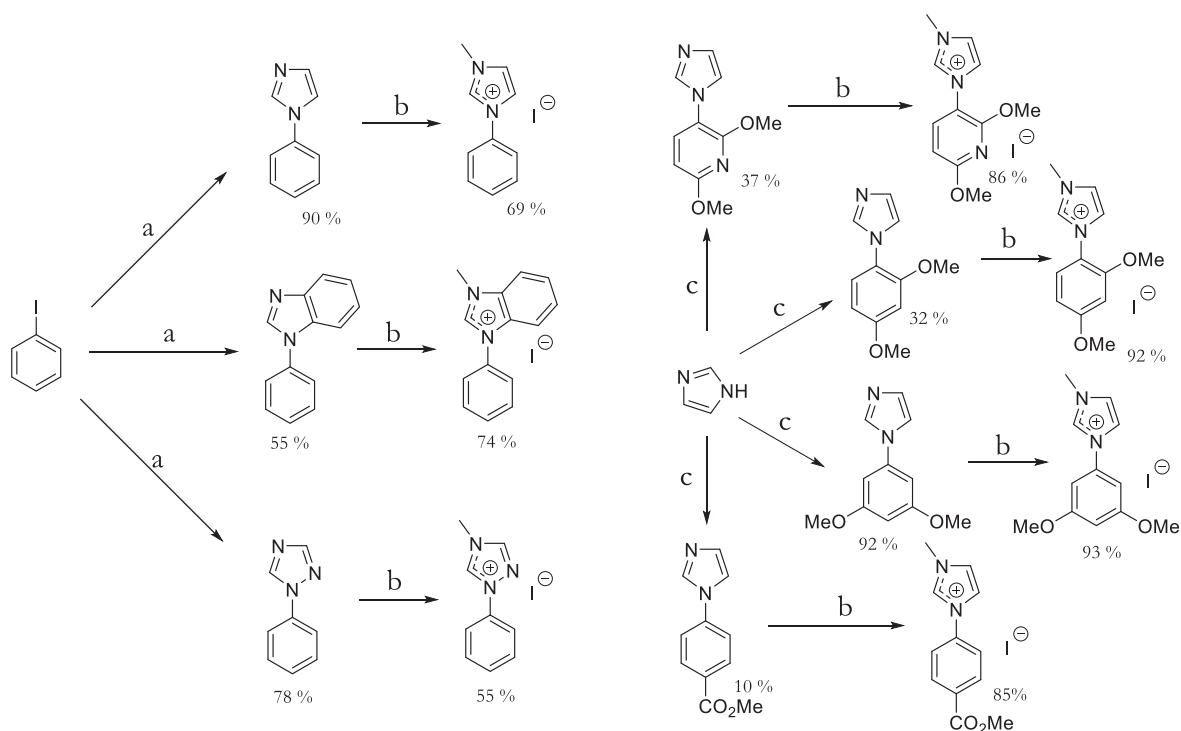
8.2.3 Device Fabrication

A 4.5+5- μm -thick, double layer titania film screen-printed on a pre-cleaned FTO conducting glass (NSG, Solar) was employed as the negative electrode of DSCs and further dye-loaded by immersing it into a dye solution made by dissolving 0.2 mM of dye in a tetrahydrofuran-ethanol mixture (*v/v*, 1/4) for 12 h. The details for film preparation were described in a previous paper.²³⁹ The dye-coated titania electrode was assembled with a thermally platinized FTO electrode by using a 25- μm -thick Surlyn ring to produce a thin-layer electrochemical cell. The Co-phen electrolyte is made from 0.25 M tris(1,10-phenanthroline)cobalt(II) di[bis(trifluoromethanesulfonyl)imide], 0.05 M tris(1,10-phenanthroline)cobalt(III) tris[bis(trifluoromethanesulfonyl)imide], 0.25 M TBP, and 0.1M LiTFSI in acetonitrile. Electrical measurements (EQE, $J-V$, CE, and TPD) were performed as reported in previous papers.^{240,241}

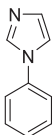
8.3 Appendix to chapter 5

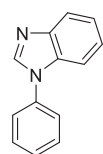
All the commercially available materials were used as received. ^1H NMR spectra were recorded on a Bruker AVIII-HD (400 MHz), and are reported in ppm using solvent as an internal standard (CDCl_3 at 7.26/77.16 ppm or CD_3CN at 1.94/118.26 ppm for proton/carbon). Data reported as: s = singlet, d = doublet, t = triplet, q = quartet, p = pentet, m = multiplet, b = broad, ap = apparent; coupling constant(s) in Hz; integration. UV-Vis spectra were measured with an LS-55 spectrometer. Cyclic voltammetry was measured with a Biologic S-200 cyclic voltammeter. Mass spectra were recorded on a Bruker Microflex MALDI-TOF or ESI mass spectrometer.

8.3.1 Synthesis of ligands and ruthenium complexes

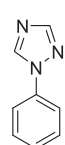


- a. Imidazole (benzimidazole, 1,2,4-triazole or the corresponding aryl halide), CuI , KOH , DMSO , $110\text{ }^\circ\text{C}$, 24h;
 b. CH_3I , THF or acetonitrile, $130\text{ }^\circ\text{C}$; c. corresponding aryl halide, K_3PO_4 , CuI , DMF , $130\text{ }^\circ\text{C}$, 24 h.

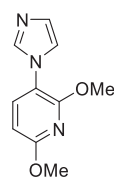
 *1-phenyl-1H-imidazole*. The synthesis was conducted according to the procedure described in literature.²⁴² In a round-bottom flask, phenyl iodide (1 g, 4.9 mmol, 1 equiv.), imidazole (0.5 g, 7.35 mmol, 1.5 equiv.), CuI (93 mg, 0.59 mmol, 0.05 equiv.) and KOH (550 mg, 9.8 mmol, 2 equiv.) were mixed in 10 mL of DMSO and the mixture was degassed with nitrogen. Then, the reaction mixture was heated up to $110\text{ }^\circ\text{C}$ and stirred for 24 h under nitrogen atmosphere. Afterwards, the reaction mixture was cooled down to RT, filtered through celite, washed few times with deionized water and extracted with DCM . Organic phase was dried over MgSO_4 . Column chromatography on silica with $\text{DCM}:\text{EtOAc}$ eluent (3:1) resulted in a pure product (630 mg, 90%). ^1H NMR (400 MHz, Chloroform-d) δ 7.87 (s, 1H), 7.50 – 7.42 (m, 2H), 7.40 – 7.16 (m, 5H).



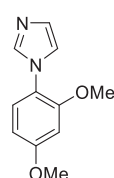
1-phenyl-1H-benzimidazole. The synthetic procedure was absolutely analogous to the synthesis of *1-phenyl-1H-imidazole*. Phenyl iodide (2g, 9.8 mmol, 1 equiv.), benzimidazole (1.73 g, 14.7 mmol, 1.5 equiv.), CuI (186 mg, 0.98 mmol, 0.1 equiv.) and KOH (1.1 g, 19.6 mmol, 2 equiv.) in 15 ml of DMSO were used. Column chromatography on silica with DCM:EtOAc (3:1) resulted in final product (1.05 g, 55 %). ¹H NMR (400 MHz, Methylene Chloride-*d*₂) δ 8.13 (s, 1H), 7.85 (m, 1H), 7.63 – 7.52 (m, 5H), 7.51 – 7.44 (m, 1H), 7.37 – 7.32 (m, 2H).



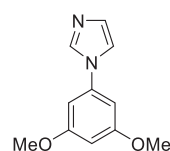
1-phenyl-1H-1,2,4-triazole. The synthetic procedure was absolutely analogous to the synthesis of *1-phenyl-1H-imidazole*. Phenyl iodide (2g, 9.8 mmol, 1 equiv.), 1,2,4-triazole (1 g, 14.7 mmol, 1.5 equiv.), CuI (186 mg, 0.98 mmol, 0.1 equiv.) and KOH (1.1 g, 19.6 mmol, 2 equiv.) in 20 ml of DMSO were used. Column chromatography on silica with DCM:EtOAc (3:1) resulted in final product (1.12 g, 78 %). ¹H NMR (400 MHz, Methylene Chloride-*d*₂) δ 8.58 (s, 1H), 8.07 (s, 1H), 7.70 (d, *J* = 7.3 Hz, 2H), 7.52 (t, *J* = 7.9 Hz, 2H), 7.41 (t, *J* = 7.5 Hz, 1H).



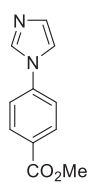
3-(1H-imidazol-1-yl)-2,6-dimethoxybenzimidazole. 3-bromo-2,6-dimethoxybenzimidazole (4.5 g, 20.6 mmol, 1 equiv.), imidazole (1.97 g, 29 mmol, 1.4 equiv.), K₃PO₄ (8.48 g, 40 mmol, 2 equiv.) and CuI (762 mg, 4 mmol, 0.2 equiv.) were mixed in a double-neck round-bottom flask and degassed. Afterwards, 20 mL of dry DMF was added the mixture was heated up to 130 °C and stirred for 1 day. Then, the mixture was cooled down to room temperature, filtered through celite, washed few times with deionized water and extracted with DCM. Combined organic phase was dried over MgSO₄, filtered and the filtrate was evaporated to small amount. Column chromatography on silica with acetone as eluent provided a final product (1.55 g, 37 %). ¹H NMR (400 MHz, Chloroform-*d*) δ 7.84 (broad s, 1H), 7.66 – 7.50 (broad s, 1H), 7.33 (d, *J* = 8.2 Hz, 1H), 7.09 – 6.93 (broad s, 1H), 6.23 (d, *J* = 8.2 Hz, 1H), 3.82 (s, 3H), 3.81 (s, 3H).



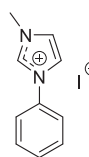
1-(2,4-dimethoxyphenyl)-1H-imidazole. The synthesis was conducted similarly to the synthesis of *3-(1H-imidazol-1-yl)-2,6-dimethoxybenzimidazole*. 1-bromo-2,4-dimethoxybenzene (2.2 g, 10 mmol, 1 equiv.), imidazole (952 mg, 14 mmol, 1.4 equiv.) K₃PO₄ (4.24 g, 20 mmol, 2 equiv.) and CuI (381 mg, 2 mmol, 0.2 equiv.) in 15 mL of dry DMF were used. Column chromatography on silica with DCM:EtOAc (4:1) provided the final product (650 mg, 32 %). ¹H NMR (400 MHz, Chloroform-*d*) δ 7.78 (s, 1H), 7.67 – 7.36 (broad, 1H), 7.20 – 6.80 (broad, 1H), 6.95 (d, *J* = 8.6 Hz, 1H), 6.39 (d, *J* = 2.6 Hz, 1H), 6.32 (dd, *J* = 8.6, 2.6 Hz, 1H), 3.62 (s, 3H), 3.56 (s, 3H).



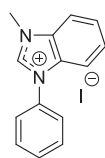
1-(3,5-dimethoxyphenyl)-1H-imidazole. The synthesis was analogous to that of *3-(1H-imidazol-1-yl)-2,6-dimethoxybenzimidazole* with the only modification that the reaction mixture was refluxed. 1-bromo-3,5-dimethoxybenzene (5 g, 23 mmol, 1 equiv.), imidazole (2.2 g, 32.3 mmol, 1.4 equiv.), K₃PO₄ (9.75 g, 46 mmol, 2 equiv.) and CuI (876 mg, 4.6 mmol, 0.2 equiv.) in 25 mL of dry DMF were used. Column chromatography on silica with DCM:acetone (1:3) as eluent afforded the final product (4.48 g, 92 %). ¹H NMR (400 MHz, Chloroform-*d*) δ 8.00 (s, 1H), 6.55 (s, 3H), 6.42 (s, 2H), 3.82 (s, 6H).



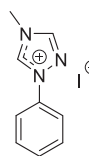
Methyl 4-(1H-imidazol-1-yl)benzoate. The synthesis was analogous to that of *3-(1H-imidazol-1-yl)-2,6-dimethoxyppyridine*. methyl 4-bromobenzoate (3.22 g, 15 mmol, 1 equiv.), imidazole (1.43 g, 21 mmol, 1.4 equiv.), K_3PO_4 (6.36 g, 30 mmol, 2 equiv.) and CuI (571 mg, 3 mmol, 0.2 equiv.) in 10 mL of dry DMF were used. Column chromatography on silica with DCM:acetone (4:1) as eluent afforded the final product (335 mg, 10 %). 1H NMR (200 MHz, Chloroform- d) δ 8.09 (d, J = 8.6 Hz, 2H), 7.91 (broad s, 1H), 7.42 (d, J = 8.6 Hz, 2H), 7.31 (broad s, 1H), 7.18 (broad s, 1H), 3.88 (s, 3H).



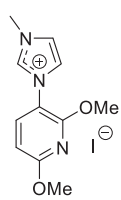
3-methyl-1-phenyl-1H-imidazol-1-ium iodide. 1-phenyl-1H-imidazole (630 mg, 4.4 mmol, 1 equiv.) was dissolved in 7 mL of THF in the high pressure reaction bomb and methyl iodide (2.5 g, 17.6 mmol, 4 equiv.) was added. The reaction bomb was capped and heated up to 110 °C for 12 hours, during what the white precipitate has formed. After the mixture was cooled down to room temperature, the precipitate was filtered and washed with DCM. The second portion of product was obtained after reducing the volume of filtrate (875 mg, 69 %). 1H NMR (400 MHz, Acetonitrile- d_3) δ 9.72 (s, 1H), 7.89 (s, 1H), 7.82 – 7.67 (m, 3H), 7.54 (m, 3H), 4.00 (s, 3H).



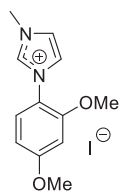
1-methyl-3-phenyl-1H-benzo[d]imidazol-3-ium iodide. The synthesis was similar to that of *3-methyl-1-phenyl-1H-imidazol-1-ium iodide*. 1-phenyl-1H-benzo[d]imidazole (1.05 g, 5.4 mmol, 1 equiv) and methyl iodide (1.53 g, 10.8 mmol, 2 equiv.) in 15 mL of THF were used. The product as a white solid was obtained (1.34 g, 74 %). 1H NMR (400 MHz, Acetonitrile- d_3) δ 9.52 (d, J = 8.1 Hz, 1H), 8.01 – 7.91 (m, 1H), 7.74 (m, 8H), 4.19 (s, 3H).



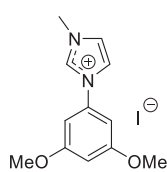
4-methyl-1-phenyl-1,2,4-triazol-1-ium iodide. The synthesis was similar to that of *3-methyl-1-phenyl-1H-imidazol-1-ium iodide*. 1-phenyl-1H-1,2,4-triazole (1.11 g, 7.7 mmol, 1 equiv) and methyl iodide (2.17 g, 15.3 mmol, 2 equiv.) in 15 mL of THF were used. The product as a off-white solid was obtained (1.21 g, 55 %). 1H NMR (400 MHz, Acetonitrile- d_3) δ 10.35 (s, 1H), 8.83 (s, 1H), 7.95 – 7.78 (m, 2H), 7.73 – 7.56 (m, 3H), 4.06 (s, 3H).



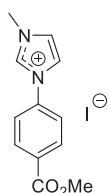
1-(2,6-dimethoxyppyridin-3-yl)-3-methyl-1H-imidazol-1-ium iodide. The synthesis was similar to that of *3-methyl-1-phenyl-1H-imidazol-1-ium iodide*. 3-(1H-imidazol-1-yl)-2,6-dimethoxyppyridine (1.46 g, 7.2 mmol, 1 equiv) and methyl iodide (1.53 g, 10.8 mmol, 1.5 equiv.) in 30 mL of acetonitrile were used. The product as a off-white solid was obtained (2.15 g, 86 %). 1H NMR (400 MHz, Acetonitrile- d_3) δ 8.87 (s, 1H), 7.78 (d, J = 8.5 Hz, 1H), 7.59 (d, J = 1.9 Hz, 1H), 7.52 (d, J = 1.8 Hz, 1H), 6.52 (d, J = 8.4 Hz, 1H), 4.01 (s, 3H), 3.98 (s, 3H), 3.94 (s, 3H).



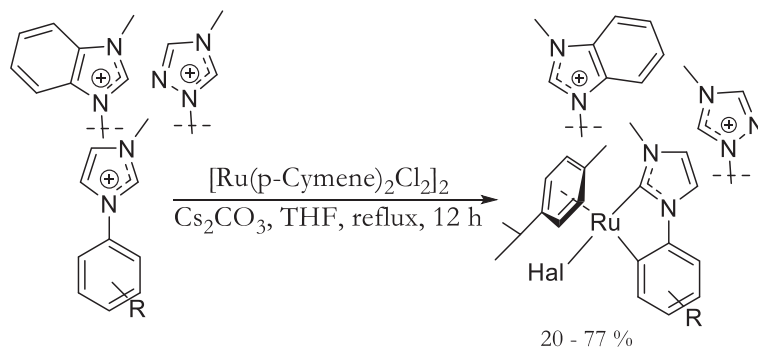
1-(2,4-dimethoxyphenyl)-3-methyl-1H-imidazol-1-ium iodide. The synthesis was similar to that of *3-methyl-1-phenyl-1H-imidazol-1-ium iodide*. 1-(2,4-dimethoxyphenyl)-1H-imidazole (640 mg, 3.1 mmol, 1 equiv) and methyl iodide (670 mg, 4.7 mmol, 1.5 equiv.) in 20 mL of acetonitrile were used. The product as an off-white solid was obtained and recrystallized from hexane-acetone (993 mg, 92 %). 1H NMR (400 MHz, Acetonitrile- d_3) δ 9.48 (s, 1H), 7.81 (m, 2H), 7.53 (d, J = 8.7 Hz, 1H), 6.76 (d, J = 2.6 Hz, 1H), 6.62 (dd, J = 8.8, 2.5 Hz, 1H), 4.10 (s, 3H), 3.84 (s, 3H), 3.80 (s, 3H).



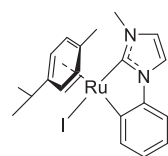
1-(3,5-dimethoxyphenyl)-3-methyl-3-methyl-1H-imidazol-1-ium iodide. The synthesis was similar to that of *3-methyl-1-phenyl-1H-imidazol-1-ium iodide*. 1-(3,5-dimethoxyphenyl)-1H-imidazole (3.83 g, 18.7 mmol, 1 equiv) and methyl iodide (4 g, 28 mmol, 1.5 equiv.) in 50 mL of acetonitrile were used. The product as an off-white solid was obtained and recrystallized from hexane-acetone (6 g, 93 %). $^1\text{H NMR}$ (400 MHz, Chloroform-*d*) δ 8.00 (s, 1H), 6.55 (broad s, 3H), 6.42 (s, 2H), 3.82 (s, 6H). $^1\text{H NMR}$ (400 MHz, Acetonitrile-*d*₃) δ 9.49 (broad s, 1H), 7.82 (s, 1H), 7.56 (s, 1H), 6.83 (s, 2H), 6.64 (s, 1H), 3.98 (s, 3H), 3.86 (s, 6H).



1-(4-(methoxycarbonyl)phenyl)-3-methyl-3-methyl-1H-imidazol-1-ium iodide. The synthesis was similar to that of *3-methyl-1-phenyl-1H-imidazol-1-ium iodide*. Methyl 4-(1H-imidazol-1-yl)benzoate (330 mg, 1.6 mmol, 1 equiv) and methyl iodide (1.5 g, 10.5 mmol, 6.5 equiv.) in 8 mL of THF were used. The product as an off-white solid was obtained (475 g, 85 %). $^1\text{H NMR}$ (200 MHz, Acetonitrile-*d*₃) δ 9.43 (s, 1H), 8.21 (m, 2H), 7.94 – 7.71 (m, 3H), 7.63 (s, 1H), 4.00 (s, 3H), 3.92 (s, 3H).

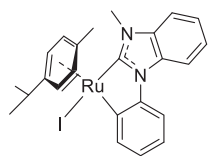


General procedure for $[\text{Ru}(\text{p-Cymene})(\text{C}^{\text{C}})\text{I}]$ synthesis.²⁴³ $[\text{Ru}(\text{p-Cymene})\text{Cl}_2]_2$ (1 equiv.), Cs_2CO_3 (8 equiv.) and the corresponding ligand (2 equiv.) were mixed in double-neck flask equipped with a condenser. The mixture was degassed and refilled with nitrogen and dry THF was added. The reaction mixture was refluxed for 12 hours and then cooled down and evaporated to a small amount. The column chromatography purification on silica or neutral alumina provided a final product.



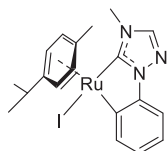
1a. Synthesis was conducted according to the general procedure. $[\text{Ru}(\text{p-Cymene})\text{Cl}_2]_2$ (300 mg, 0.49 mmol, 1 equiv.), 3-methyl-1-phenyl-1H-imidazol-1-ium iodide (280 mg, 0.98 mmol, 2 equiv.) and Cs_2CO_3 (1.28 g, 3.9 mmol, 8 equiv.) in 30 mL of THF were used. Column chromatography on neutral alumina with DCM as an eluent provided a pure product as an orange powder (396 mg, 77 %). $^1\text{H NMR}$ (400 MHz, Chloroform-*d*) δ 8.06 – 8.00 (m, 1H), 7.33 (d, $J = 2.1$ Hz, 1H), 7.10 – 7.04 (m, 1H), 6.96 (d, $J = 2.1$ Hz, 1H), 6.95 – 6.89 (m, 2H), 5.52 – 5.44 (m, 3H), 5.38 (dd, $J = 6.0, 1.2$ Hz, 1H), 4.04 (s, 3H), 2.35 (hept, $J = 7.0$ Hz, 1H), 2.29 (s, 3H), 0.92 (d, $J = 6.9$ Hz, 3H), 0.81 (d, $J = 6.9$ Hz, 3H). $^{13}\text{C NMR}$ (101 MHz, Chloroform-*d*) δ 187.21, 161.08, 145.54, 142.87, 124.18, 122.03, 121.98, 114.25, 111.00, 102.73, 102.53, 91.45, 89.35, 88.14, 84.58, 38.38, 31.56, 23.19, 21.90, 20.98.

HRMS (ESI): $m/z = 521.0033$ $[\text{M}+\text{H}]^+$, (calculated for $[\text{RuIN}_2\text{C}_{20}\text{H}_{23}+\text{H}]^+$: $m/z = 521.0028$).



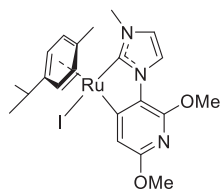
2a. Synthesis was conducted according to the general procedure. $[\text{Ru}(\text{p-Cymene})\text{Cl}_2]_2$ (300 mg, 0.49 mmol, 1 equiv.), 1-methyl-3-phenyl-1H-benzo[d]imidazol-3-ium iodide (329 mg, 0.98 mmol, 2 equiv.) and Cs_2CO_3 (1.28 g, 3.9 mmol, 8 equiv.) in 30 mL of THF were used. Column chromatography on neutral alumina with DCM as an eluent provided a pure product as an orange powder (300 mg, 64 %). ^1H NMR (400 MHz, Chloroform-*d*) δ 8.10 (dd, $J = 7.2, 1.6$ Hz, 1H), 7.99 – 7.92 (m, 1H), 7.67 (dd, $J = 7.6, 1.4$ Hz, 1H), 7.40 – 7.34 (m, 1H), 7.33 – 7.27 (m, 2H), 7.03 (td, $J = 7.5, 1.6$ Hz, 1H), 6.97 (td, $J = 7.3, 1.4$ Hz, 1H), 5.63 – 5.58 (m, 3H), 5.46 (d, $J = 6.4$ Hz, 1H), 4.24 (s, 3H), 2.34 (m, 4H), 0.92 (d, $J = 6.9$ Hz, 3H), 0.79 (d, $J = 6.9$ Hz, 3H). ^{13}C NMR (101 MHz, Chloroform-*d*) δ 161.03, 146.89, 142.81, 136.40, 131.69, 123.74, 122.96, 122.40, 122.19, 112.59, 111.21, 109.73, 104.27, 103.69, 93.29, 90.99, 89.71, 85.69, 35.77, 31.57, 23.14, 21.95, 20.98.

HRMS (ESI): $m/z = 571.0190$ $[\text{M}+\text{H}]^+$, (calculated for $[\text{RuIN}_2\text{C}_{24}\text{H}_{25}+\text{H}]^+$: $m/z = 571.0184$).



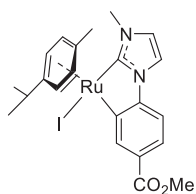
3a. Synthesis was conducted according to the general procedure. $[\text{Ru}(\text{p-Cymene})\text{Cl}_2]_2$ (300 mg, 0.49 mmol, 1 equiv.), 4-methyl-1-phenyl-1,2,4-triazol-1-ium iodide (281 mg, 0.98 mmol, 2 equiv.) and Cs_2CO_3 (1.28 g, 3.9 mmol, 8 equiv.) in 30 mL of THF were used. Column chromatography on neutral alumina with DCM as an eluent provided a pure product as an orange powder (230 mg, 45 %). ^1H NMR (400 MHz, Chloroform-*d*) δ 8.03 – 7.98 (m, 2H), 7.48 – 7.44 (m, 1H), 7.02 – 6.95 (m, 2H), 5.59 – 5.50 (m, 3H), 5.40 (dd, $J = 6.1, 1.3$ Hz, 1H), 4.05 (s, 3H), 2.42 (hept, $J = 6.9$ Hz, 1H), 2.28 (s, 3H), 0.97 (d, $J = 6.9$ Hz, 3H), 0.83 (d, $J = 6.9$ Hz, 3H). ^{13}C NMR (101 MHz, Chloroform-*d*) δ 144.66, 142.40, 142.18, 125.03, 122.34, 112.63, 104.20, 102.48, 99.98, 91.48, 89.59, 88.24, 84.36, 35.36, 31.59, 23.05, 21.88, 20.81.

HRMS (ESI): $m/z = 521.9985$ $[\text{M}+\text{H}]^+$, (calculated for $[\text{RuIN}_3\text{C}_{19}\text{H}_{22}+\text{H}]^+$: $m/z = 521.9980$).



4a. Synthesis was conducted according to the general procedure. $[\text{Ru}(\text{p-Cymene})\text{Cl}_2]_2$ (600 mg, 0.98 mmol, 1 equiv.), 1-(2,6-dimethoxypyridin-3-yl)-3-methyl-1H-imidazol-1-ium iodide (680 mg, 1.96 mmol, 2 equiv.) and Cs_2CO_3 (2.56 g, 7.8 mmol, 8 equiv.) in 50 mL of THF were used. Column chromatography on neutral alumina with DCM – acetone (5:1) as an eluent provided a pure product as an orange powder (220 mg, 20 %). ^1H NMR (400 MHz, Chloroform-*d*) δ 7.84 (d, $J = 2.0$ Hz, 1H), 7.06 (s, 1H), 6.91 (d, $J = 2.0$ Hz, 1H), 5.52 – 5.47 (m, 1H), 5.45 – 5.40 (m, 3H), 4.01 (s, 3H), 3.98 (s, 3H), 3.91 (s, 3H), 2.41 – 2.31 (m, 1H), 2.29 (s, 3H), 0.91 (d, $J = 7.0$ Hz, 3H), 0.82 (d, $J = 6.9$ Hz, 3H). ^{13}C NMR (101 MHz, Chloroform-*d*) δ 183.71, 182.15, 157.03, 148.09, 123.88, 120.78, 118.47, 114.20, 103.36, 103.01, 91.21, 89.54, 88.66, 85.63, 53.55, 52.98, 38.50, 31.52, 29.82, 23.17, 21.97, 20.94.

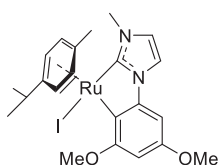
HRMS (ESI): $m/z = 582.0197$ $[\text{M}+\text{H}]^+$, (calculated for $[\text{RuIN}_3\text{O}_2\text{C}_{21}\text{H}_{26}+\text{H}]^+$: $m/z = 582.0192$).



5a. Synthesis was conducted according to the general procedure. $[\text{Ru}(\text{p-Cymene})\text{Cl}_2]_2$ (300 mg, 0.49 mmol, 1 equiv.), 1-(4-(methoxycarbonyl)phenyl)-3-methyl-1H-imidazol-1-ium iodide (337 mg, 0.98 mmol, 2 equiv.) and Cs_2CO_3 (1.28 g, 3.9 mmol, 8 equiv.) in 30 mL of THF were used. Column chromatography on neutral alumina with DCM – acetone (5:1) as an eluent provided a pure product as an orange powder (430 mg, 76 %). ^1H NMR (400 MHz, Chloroform-*d*) δ 8.70 (d, $J = 1.8$ Hz, 1H), 7.63 (dd, $J = 8.1, 1.8$ Hz, 1H), 7.36 (d, $J = 2.1$ Hz, 1H), 7.09 (d, $J = 8.1$ Hz, 1H), 6.98 (d, $J = 2.1$ Hz, 1H), 5.56 (d, $J = 6.0$ Hz, 1H), 5.54 – 5.51 (m, 2H), 5.40 (d, $J =$

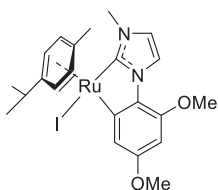
5.9 Hz, 1H), 4.03 (s, 3H), 3.91 (s, 3H), 2.40 – 2.24 (m, 4H), 0.90 (d, $J = 6.9$ Hz, 3H), 0.77 (d, $J = 6.9$ Hz, 3H). ^{13}C NMR (101 MHz, Chloroform- d) δ 188.83, 168.10, 149.47, 143.86, 125.25, 124.78, 122.65, 114.61, 110.52, 103.91, 102.74, 92.09, 89.82, 88.30, 84.62, 51.87, 38.46, 31.56, 23.19, 21.07.

HRMS (ESI): $m/z = 579.0077$ $[\text{M}+\text{H}]^+$, (calculated for $[\text{RuIN}_2\text{O}_2\text{C}_{22}\text{H}_{25}+\text{H}]^+$: $m/z = 579.0083$).



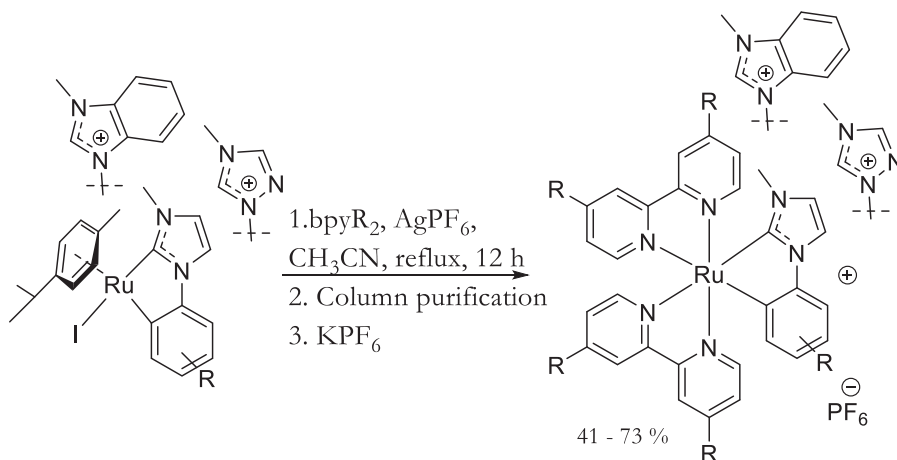
7a. Synthesis was conducted according to the general procedure. $[\text{Ru}(\text{p-Cymene})\text{Cl}_2]_2$ (300 mg, 0.49 mmol, 1 equiv.), 1-(3,5-dimethoxyphenyl)-3-methyl-3-methyl-1H-imidazol-1-ium iodide (339 mg, 0.98 mmol, 2 equiv.) and Cs_2CO_3 (1.28 g, 3.9 mmol, 8 equiv.) in 30 mL of THF were used. Column chromatography on neutral alumina with DCM – acetone (4:1) as an eluent provided a pure product as an orange powder (315 mg, 56 %). ^1H NMR (400 MHz, Chloroform- d) δ 7.29 (d, $J = 2.0$ Hz, 1H), 6.95 (d, $J = 2.0$ Hz, 1H), 6.46 (d, $J = 2.2$ Hz, 1H), 6.30 (d, $J = 2.2$ Hz, 1H), 5.73 (d, $J = 6.0$ Hz, 1H), 5.68 (d, $J = 6.0$ Hz, 1H), 5.55 (d, $J = 5.4$ Hz, 1H), 5.42 (d, $J = 5.9$ Hz, 1H), 4.03 (s, 3H), 3.91 (s, 3H), 3.80 (s, 3H), 2.41 (s, 3H), 2.21 – 2.09 (m, 1H), 0.81 (d, $J = 6.9$ Hz, 3H), 0.75 (d, $J = 6.9$ Hz, 3H). ^{13}C NMR (101 MHz, Chloroform- d) δ 187.89, 166.89, 157.61, 145.97, 135.05, 121.78, 114.31, 95.88, 92.26, 89.89, 87.65, 87.31, 84.96, 56.84, 55.46, 38.28, 31.45, 22.88, 22.17, 21.40.

HRMS (ESI): $m/z = 581.0262$ $[\text{M}+\text{H}]^+$, (calculated for $[\text{RuIN}_2\text{O}_2\text{C}_{22}\text{H}_{27}+\text{H}]^+$: $m/z = 581.0239$)

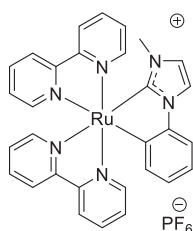


8a. Synthesis was conducted according to the general procedure. $[\text{Ru}(\text{p-Cymene})\text{Cl}_2]_2$ (300 mg, 0.49 mmol, 1 equiv.), 1-(3,5-dimethoxyphenyl)-3-methyl-3-methyl-1H-imidazol-1-ium iodide (339 mg, 0.98 mmol, 2 equiv.) and Cs_2CO_3 (1.28 g, 3.9 mmol, 8 equiv.) in 30 mL of THF were used. Column chromatography on neutral alumina with DCM – acetone (4:1) as an eluent provided a pure product as an orange powder (100 mg, 19 %). ^1H NMR (400 MHz, Chloroform- d) δ 7.90 (d, $J = 2.0$ Hz, 1H), 7.24 (d, $J = 2.3$ Hz, 1H), 6.88 (d, $J = 2.0$ Hz, 1H), 6.11 (d, $J = 2.3$ Hz, 1H), 5.47 (d, $J = 6.1$ Hz, 1H), 5.44 – 5.37 (m, 4H), 4.00 (s, 3H), 3.86 (s, 3H), 3.83 (s, 3H), 2.38 – 2.26 (m, 4H), 0.91 (d, $J = 6.9$ Hz, 3H), 0.81 (d, $J = 6.9$ Hz, 3H). ^{13}C NMR (101 MHz, Chloroform- d) δ 184.71, 164.77, 155.62, 147.41, 129.05, 128.06, 126.35, 120.31, 119.12, 118.78, 102.90, 102.04, 93.33, 91.49, 88.93, 88.22, 85.09, 55.62, 55.25, 38.48, 31.48, 23.19, 21.90, 20.95.

HRMS (ESI): $m/z = 581.0264$ $[\text{M}+\text{H}]^+$, (calculated for $[\text{RuIN}_2\text{O}_2\text{C}_{22}\text{H}_{27}+\text{H}]^+$: $m/z = 581.0239$)



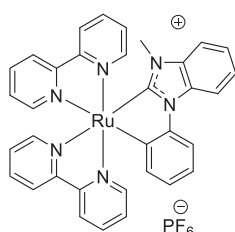
General Procedure for $[\text{Ru}(\text{C}_{\text{NHC}}^{\wedge}\text{C})(\text{bpyR}_2)](\text{PF}_6)$ preparation. $[\text{Ru}(\text{C}_{\text{NHC}}^{\wedge}\text{C})(\text{p-Cymene})\text{I}]$ (1 equiv.), bpyR_2 (2.2 equiv.) and AgPF_6 (1.1 equiv.) were mixed in the 50 mL round-bottom flask protected from lights. 20 mL of acetonitrile was added to the mixture, condenser was attached and the reaction mixture was refluxed under nitrogen atmosphere for 12 h. After, the reaction mixture was cooled down to room temperature, filtered through celite, and purified by column chromatography on alumina or silica. Consecutive anion exchange by washing the DCM solution of the complex few times with saturated solution of KPF_6 and then with deionized water afforded the final product. Which was precipitated 3 times from DCM with hexane.



1. Was synthesized according to the general procedure. **1a** (80 mg, 0.15 mmol, 1 equiv.), 2,2'-bipyridine (52 mg, 0.33 mmol, 2.2 equiv.) and AgPF_6 (42 mg, 0.165 mmol, 1.1 equiv.) were used. Column purification on alumina (neutral) with DCM:acetonitrile (4:1) as an eluent afforded a mauve product. After counterion exchange and reprecipitation a pure product was obtained (80 mg, 73 %). ^1H NMR (400 MHz, Acetonitrile- d_3) δ 8.37 (d, $J = 8.2$ Hz, 1H), 8.32 (ddt, $J = 9.4, 8.3, 1.1$ Hz, 2H), 8.22 (dt, $J = 8.2, 1.1$ Hz, 1H), 8.02 (m, 2H), 7.95 – 7.91 (m, 1H), 7.87 (dddd, $J = 8.2, 7.5, 1.6, 0.8$ Hz, 2H), 7.79 (ddd, $J = 8.2, 7.5, 1.6$ Hz, 1H), 7.71 (d, $J = 2.1$ Hz, 1H), 7.67 (ddd, $J = 8.1, 7.5, 1.5$ Hz, 1H), 7.56 – 7.53 (m, 1H), 7.33 – 7.24 (m, 3H), 7.14 (dddd, $J = 7.4, 6.0, 4.8, 1.4$ Hz, 2H), 6.97 (d, $J = 2.1$ Hz, 1H), 6.83 (td, $J = 7.5, 1.4$ Hz, 1H), 6.63 (td, $J = 7.3, 1.2$ Hz, 1H), 6.29 (dd, $J = 7.2, 1.4$ Hz, 1H), 3.01 (s, 3H). ^{13}C NMR (101 MHz, Acetonitrile- d_3) δ 195.73, 174.89, 158.31, 157.37, 156.32, 156.26, 155.07, 154.75, 150.05, 149.43, 149.07, 137.32, 136.26, 136.08, 134.99, 134.02, 127.42, 127.38, 126.97, 126.72, 124.75, 124.12, 124.05, 123.97, 123.72, 123.47, 121.94, 115.76, 111.42, 35.93.

Elemental analysis: Calculated for $\text{RuN}_6\text{C}_{30}\text{H}_{25}\text{PF}_6$: C, 50.35 %; H, 3.52 %; N, 11.74 %. Found: C, 49.96 %; H, 3.58 %; N, 10.83 %.

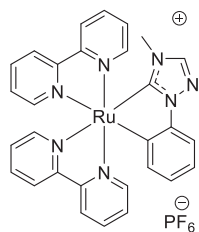
HRMS (ESI): $m/z = 571.1192$ $[\text{M}]^+$, (calculated for $[\text{RuN}_6\text{C}_{30}\text{H}_{25}]^+$: $m/z = 571.1184$).



2. Was synthesized according to the general procedure. **2a** (100 mg, 0.176 mmol, 1 equiv.), 2,2'-bipyridine (61 mg, 0.38 mmol, 2.2 equiv.) and AgPF_6 (49 mg, 0.194 mmol, 1.1 equiv.) were used. Column purification on alumina (neutral) with DCM:acetonitrile (4:1) as an eluent afforded a mauve product. After counterion exchange and reprecipitation a pure product was obtained (81 mg, 60 %). Was synthesized according to the general procedure. **2a** (100 mg, 0.176 mmol, 1 equiv.), 2,2'-bipyridine (61 mg, 0.38 mmol, 2.2 equiv.) and AgPF_6 (49 mg, 0.194 mmol, 1.1 equiv.) were used. Column purification on alumina (neutral) with DCM:acetonitrile (4:1) as an eluent afforded a mauve product. After counterion exchange and reprecipitation a pure product was obtained (81 mg, 60 %). ^1H NMR (400 MHz, Acetonitrile- d_3) δ 8.43 – 8.38 (m, 1H), 8.35 (d, $J = 8.2$ Hz, 2H), 8.25 (d, $J = 8.1$ Hz, 1H), 8.12 (d, $J = 8.1$ Hz, 1H), 8.08 (d, $J = 5.0$ Hz, 1H), 7.96 – 7.89 (m, 4H), 7.87 (dd, $J = 7.9, 1.1$ Hz, 1H), 7.80 (ddd, $J = 8.2, 7.5, 1.6$ Hz, 1H), 7.68 (ddd, $J = 8.2, 7.5, 1.5$ Hz, 1H), 7.52 (dd, $J = 5.5, 0.7$ Hz, 1H), 7.39 – 7.23 (m, 5H), 7.11 (ddd, $J = 7.3, 5.7, 1.4$ Hz, 1H), 7.03 (ddd, $J = 7.3, 5.7, 1.4$ Hz, 1H), 6.96 (td, $J = 7.6, 1.5$ Hz, 1H), 6.67 (td, $J = 7.3, 1.1$ Hz, 1H), 6.36 (dd, $J = 7.2, 1.5$ Hz, 1H), 3.26 (s, 3H). ^{13}C NMR (101 MHz, Acetonitrile- d_3) δ 175.29, 158.24, 157.10, 156.07, 155.73, 155.24, 154.75, 150.84, 150.03, 148.81, 137.90, 137.13, 136.85, 136.79, 135.80, 134.69, 133.33, 127.70, 127.57, 127.02, 126.86, 124.30, 124.25, 124.17, 123.58, 123.40, 122.95, 122.12, 113.04, 111.16, 110.12, 32.79.

Elemental analysis: Calculated for $\text{RuN}_6\text{C}_{34}\text{H}_{27}\text{PF}_6$: C, 53.34 %; H, 3.55 %; N, 10.98 %. Found: C, 54.13 %; H, 3.92 %; N, 10.36 %.

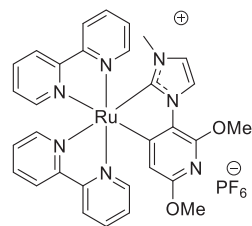
HRMS (ESI): $m/z = 621.1434 [M]^+$, (calculated for $[RuN_6C_{34}H_{27}]^+$: $m/z = 521.1341$).



3. Was synthesized according to the general procedure. **3a** (100 mg, 0.19 mmol, 1 equiv.), 2,2'-bipyridine (65 mg, 0.42 mmol, 2.2 equiv.) and $AgPF_6$ (53 mg, 0.21 mmol, 1.1 equiv.) were used. Column purification on alumina (neutral) with DCM:acetonitrile (4:1) as an eluent afforded a mauve product. After counterion exchange and reprecipitation a pure product was obtained (63 mg, 46 %). 1H NMR (400 MHz, Acetonitrile- d_3) δ 8.43 – 8.29 (m, 3H), 8.26 (d, $J = 8.0$ Hz, 1H), 8.08 – 8.02 (m, 2H), 7.99 (dd, $J = 5.6, 0.8$ Hz, 1H), 7.96 (dd, $J = 5.4, 0.7$ Hz, 1H), 7.91 (dddd, $J = 8.1, 7.5, 3.4, 1.5$ Hz, 2H), 7.84 (ddd, $J = 8.1, 7.5, 1.6$ Hz, 1H), 7.74 (ddd, $J = 8.1, 7.5, 1.5$ Hz, 1H), 7.58 (dd, $J = 5.6, 0.7$ Hz, 1H), 7.47 (dd, $J = 7.7, 1.3$ Hz, 1H), 7.36 – 7.30 (m, 2H), 7.20 (ddd, $J = 7.3, 5.7, 1.4$ Hz, 1H), 7.15 (ddd, $J = 7.3, 5.7, 1.4$ Hz, 1H), 6.88 (td, $J = 7.5, 1.4$ Hz, 1H), 6.70 (td, $J = 7.3, 1.3$ Hz, 1H), 6.33 (dd, $J = 7.2, 1.3$ Hz, 1H), 3.04 (s, 3H). ^{13}C NMR (101 MHz, Acetonitrile- d_3) δ 197.72, 172.01, 158.32, 157.27, 156.42, 156.19, 155.37, 155.15, 150.36, 149.15, 148.72, 144.64, 137.19, 136.75, 136.44, 135.66, 134.57, 127.51, 127.46, 127.13, 127.12, 125.62, 124.18, 124.15, 124.04, 123.63, 122.18, 112.23, 33.57.

Elemental analysis: Calculated for $RuN_7C_{29}H_{24}PF_6$: C, 48.61 %; H, 3.38 %; N, 13.68 %. Found: C, 48.65 %; H, 3.45 %; N, 12.65 %.

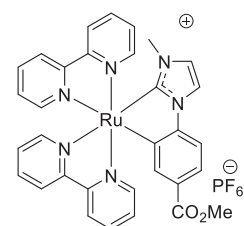
HRMS (ESI): $m/z = 572.1144 [M]^+$, (calculated for $[RuN_7C_{29}H_{24}]^+$: $m/z = 572.1137$).



4. Was synthesized according to the general procedure. **4a** (95 mg, 0.164 mmol, 1 equiv.), 2,2'-bipyridine (56 mg, 0.36 mmol, 2.2 equiv.) and $AgPF_6$ (46 mg, 0.18 mmol, 1.1 equiv.) were used. Column purification on alumina (neutral) with DCM:acetonitrile (3:1) as an eluent afforded a mauve product. After counterion exchange and reprecipitation a pure product was obtained (52 mg, 41 %). 1H NMR (400 MHz, Acetonitrile- d_3) δ 8.38 (d, $J = 8.0$ Hz, 1H), 8.36 – 8.31 (m, 2H), 8.26 (d, $J = 8.1$ Hz, 1H), 8.12 (d, $J = 2.0$ Hz, 1H), 8.04 (dd, $J = 5.7, 0.8$ Hz, 1H), 7.95 – 7.87 (m, 4H), 7.83 (ddd, $J = 8.2, 7.6, 1.5$ Hz, 1H), 7.79 – 7.75 (m, 1H), 7.56 – 7.50 (m, 1H), 7.31 (ddt, $J = 6.9, 5.5, 1.4$ Hz, 2H), 7.19 (ddd, $J = 7.3, 5.7, 1.4$ Hz, 2H), 6.93 (d, $J = 2.1$ Hz, 1H), 5.29 (s, 1H), 4.00 (s, 3H), 3.68 (s, 3H), 3.00 (s, 3H). ^{13}C NMR (101 MHz, Acetonitrile- d_3) δ 198.67, 192.99, 158.69, 158.05, 157.39, 156.40, 155.94, 155.11, 154.77, 150.06, 149.25, 148.42, 136.56, 136.53, 135.36, 134.93, 127.49, 127.43, 127.24, 126.96, 126.36, 124.20, 124.13, 124.03, 123.61, 122.45, 119.63, 109.21, 53.23, 53.16, 35.98.

Elemental analysis: Calculated for $RuN_7O_2C_{31}H_{28}PF_6$: C, 47.94 %; H, 3.63 %; N, 12.62 %. Found: C, 47.55 %; H, 3.55 %; N, 11.53 %.

HRMS (ESI): $m/z = 632.1356 [M]^+$, (calculated for $[RuN_7O_2C_{31}H_{28}]^+$: $m/z = 632.1348$).



5. Was synthesized according to the general procedure. **5a** (150 mg, 0.26 mmol, 1 equiv.), 2,2'-bipyridine (89 mg, 0.57 mmol, 2.2 equiv.) and $AgPF_6$ (72 mg, 0.28 mmol, 1.1 equiv.) were used. Column purification on alumina (neutral) with DCM:acetonitrile (3:1) as an eluent afforded a mauve product. After counterion exchange and reprecipitation a pure product was obtained (129 mg, 64 %). 1H NMR (400 MHz, Acetonitrile- d_3) δ 8.37 (d, $J = 8.2$ Hz, 1H), 8.37 – 8.28 (m, 2H), 8.19 (d, $J = 8.1$ Hz, 1H), 8.00 (d, $J = 5.0$ Hz, 1H), 7.96 (dd, $J = 5.7, 0.8$ Hz, 1H), 7.95 – 7.84 (m, 3H), 7.80 (td, $J = 8.0, 1.5$ Hz, 1H), 7.76 (d, $J = 2.2$ Hz, 1H), 7.64 (td, $J = 8.0, 1.5$ Hz, 1H), 7.56 (dd, $J = 5.5, 0.8$ Hz, 1H), 7.51 (dd, $J = 8.1, 1.9$ Hz, 1H),

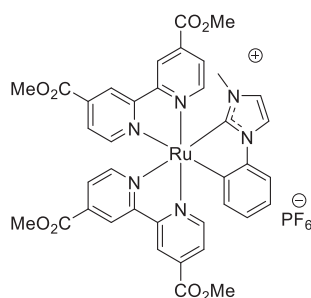
7.38 – 7.28 (m, 3H), 7.13 (dddd, $J = 7.3, 5.6, 4.2, 1.4$ Hz, 2H), 7.01 (t, $J = 2.0$ Hz, 2H), 3.64 (s, 3H), 3.03 (s, 3H).

^{13}C NMR (101 MHz, Acetonitrile- d_3) δ 197.46, 175.46, 168.40, 158.22, 157.25, 156.23, 156.19, 155.18, 154.91, 153.90, 150.08, 149.10, 138.23, 136.53, 136.44, 135.33, 134.47, 127.56, 127.49, 127.12, 126.90, 125.86, 124.42, 124.19, 124.11, 124.03, 123.59, 116.18, 110.97, 51.97, 36.02.

Elemental analysis: Calculated for $\text{RuN}_6\text{O}_2\text{C}_{32}\text{H}_{27}\text{PF}_6$: C, 49.68 %; H, 3.52 %; N, 10.86 %.

Found: C, 50.67 %; H, 3.92 %; N, 9.98 %.

HRMS (ESI): $m/z = 629.1239$ $[\text{M}]^+$, (calculated for $[\text{RuN}_6\text{O}_2\text{C}_{32}\text{H}_{27}]^+$: $m/z = 629.1234$).



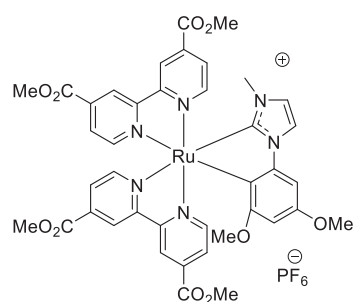
6. Was synthesized according to the general procedure. **1a** (200 mg, 0.38 mmol, 1 equiv.), dimethyl 4,4'-dicarboxy-2,2'-bipyridine (230 mg, 0.88 mmol, 2.2 equiv.) and AgPF_6 (107 mg, 0.42 mmol, 1.1 equiv.) were used. Column purification on silica with DCM:acetone (4:1) as an eluent afforded a green product. After counterion exchange and reprecipitation a pure product was obtained (215 mg, 59 %). ^1H NMR (400 MHz, Acetonitrile- d_3) δ 8.94 (d, $J = 0.8$ Hz, 1H), 8.90 (d, $J = 1.8$ Hz, 1H), 8.87 (s, 1H), 8.78 (d, $J = 2.1$ Hz, 1H), 8.25 (dd, $J = 6.2, 2.0$ Hz, 2H), 8.10 (d, $J = 5.6$ Hz, 1H), 7.76 (dd, $J = 5.7, 1.6$ Hz, 1H), 7.74 (d, $J = 1.5$ Hz, 3H), 7.66 (dd, $J = 6.0, 1.8$ Hz, 1H), 7.63 (dd, $J = 6.0, 1.8$ Hz, 1H), 7.30 (dd, $J = 7.8, 1.2$ Hz, 1H), 7.03 (d, $J = 2.1$ Hz, 1H), 6.86 (td, $J = 7.6, 1.4$ Hz, 1H), 6.63 (td, $J = 7.3, 1.2$ Hz, 1H), 6.17 (dd, $J = 7.3, 1.3$ Hz, 1H), 3.95 (s, 3H), 3.94 (s, 3H), 3.93 (s, 3H), 3.92 (s, 3H), 2.98 (s, 3H).

^{13}C NMR (101 MHz, Acetonitrile- d_3) δ 190.68, 170.23, 164.54, 164.49, 164.39, 157.47, 156.47, 155.76, 155.68, 154.82, 154.58, 150.30, 149.38, 147.74, 136.71, 136.36, 135.76, 135.28, 134.08, 125.85, 125.71, 125.16, 125.05, 124.49, 123.58, 122.87, 122.80, 122.75, 122.33, 122.28, 115.25, 111.22, 52.78, 52.67, 35.32.

Elemental analysis: Calculated for $\text{RuN}_6\text{O}_8\text{C}_{38}\text{H}_{33}\text{PF}_6$: C, 48.16 %; H, 3.51 %; N, 8.87 %.

Found: C, 48.23 %; H, 3.51 %; N, 8.24 %.

HRMS (ESI): $m/z = 803.1407$ $[\text{M}]^+$, (calculated for $[\text{RuN}_6\text{O}_8\text{C}_{38}\text{H}_{33}]^+$: $m/z = 803.1404$).



7. Was synthesized according to the general procedure. **1a** (80 mg, 0.14 mmol, 1 equiv.), dimethyl 4,4'-dicarboxy-2,2'-bipyridine (82 mg, 0.30 mmol, 2.2 equiv.) and AgPF_6 (38 mg, 0.15 mmol, 1.1 equiv.) were used. Column purification on silica with DCM:acetone (3:1) as an eluent afforded a green product. After counterion exchange and reprecipitation a pure product was obtained (60 mg, 43 %).

^1H NMR (400 MHz, Acetonitrile- d_3) δ 8.90 (d, $J = 3.9$ Hz, 2H), 8.79 (d, $J = 9.9$ Hz, 2H), 8.42 (d, $J = 5.9$ Hz, 1H), 8.03 (d, $J = 6.0$ Hz, 1H), 7.93 (d, $J = 5.7$ Hz, 1H), 7.75 (d, $J = 2.1$ Hz, 1H), 7.71 (td, $J = 5.8, 1.7$ Hz, 2H), 7.66 (d, $J = 5.8$ Hz, 1H), 7.64 – 7.59 (m, 2H), 6.97 (d, $J = 2.0$

Hz, 1H), 6.73 (d, $J = 2.1$ Hz, 1H), 5.95 (d, $J = 2.1$ Hz, 1H), 3.96 (s, 3H), 3.94 – 3.92 (m, 9H), 3.74 (s, 3H), 2.90 (s, 3H), 2.87 (s, 3H).

^{13}C NMR (101 MHz, Acetonitrile- d_3) δ 191.83, 169.56, 165.52, 165.50, 165.24, 159.41, 158.47, 157.92, 157.03, 156.42, 156.19, 155.37, 151.05, 150.72, 149.09, 141.81, 137.59, 136.75, 136.00, 134.55, 126.94, 125.89, 125.70, 124.88, 124.46, 123.75, 123.66, 123.18, 122.12, 116.38, 95.28, 93.11, 55.90, 55.29, 53.66, 53.54, 53.52, 36.23.

Elemental analysis: Calculated for $\text{RuN}_6\text{O}_{10}\text{C}_{40}\text{H}_{37}\text{PF}_6$: C, 49.24 %; H, 3.82 %; N, 8.61 %.

Found: C, 48.33 %; H, 4.06 %; N, 7.79 %.

HRMS (ESI): $m/z = 863.1633$ $[M]^+$, (calculated for $[\text{RuN}_6\text{O}_8\text{C}_{40}\text{H}_{37}]^+$: $m/z = 863.1626$)

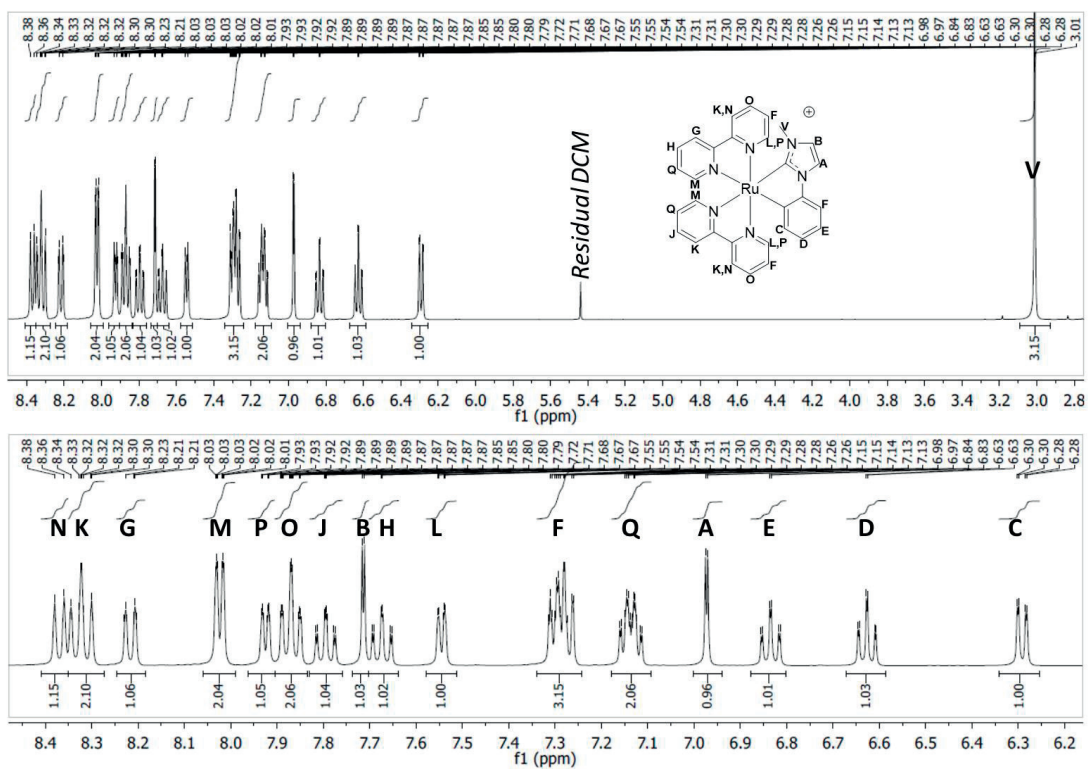


Figure 8.74. ^1H NMR spectrum of complex **1** in $\text{acetonitrile-}d_3$.

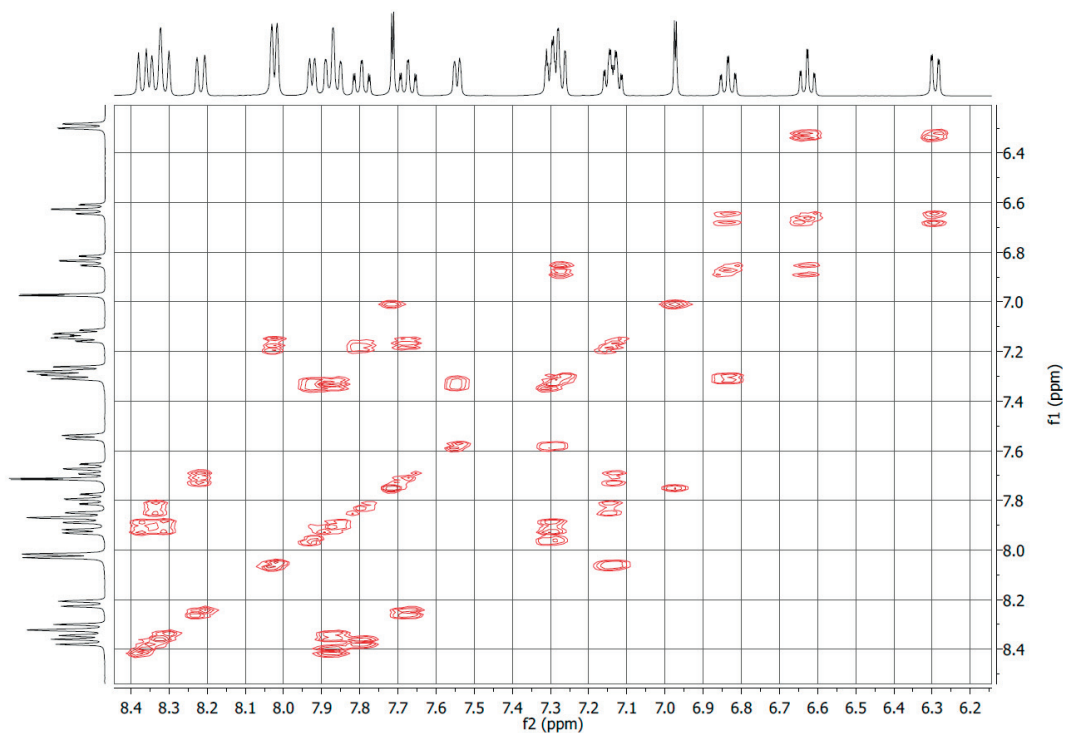
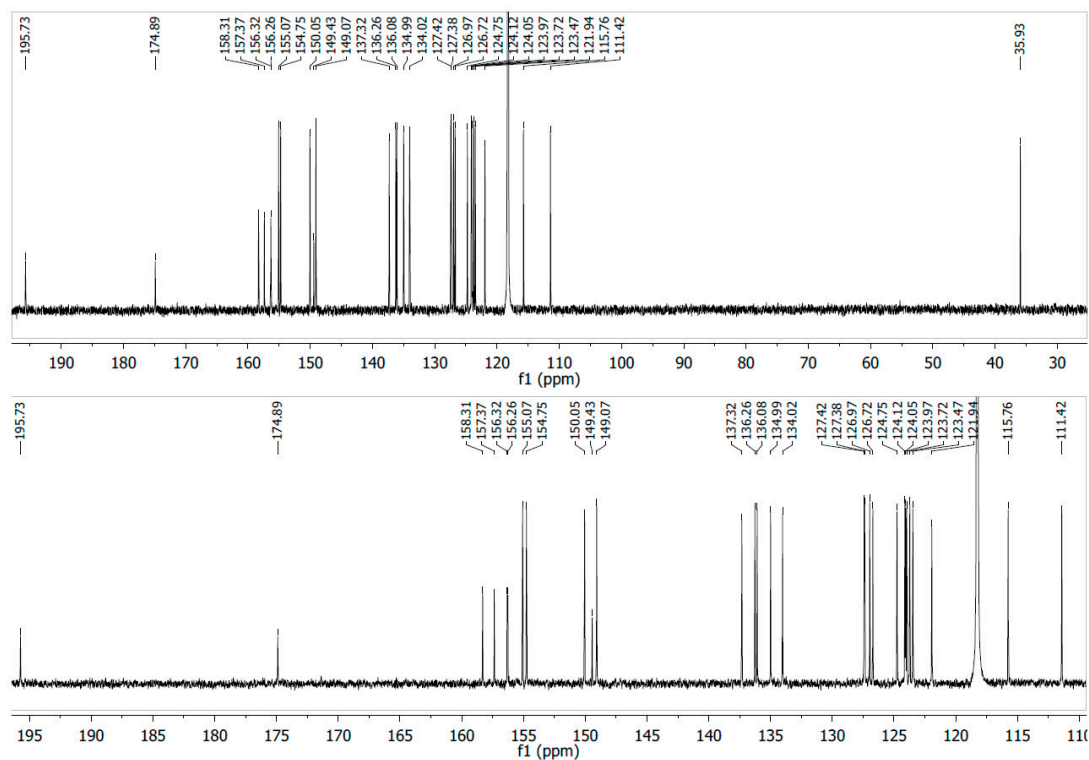
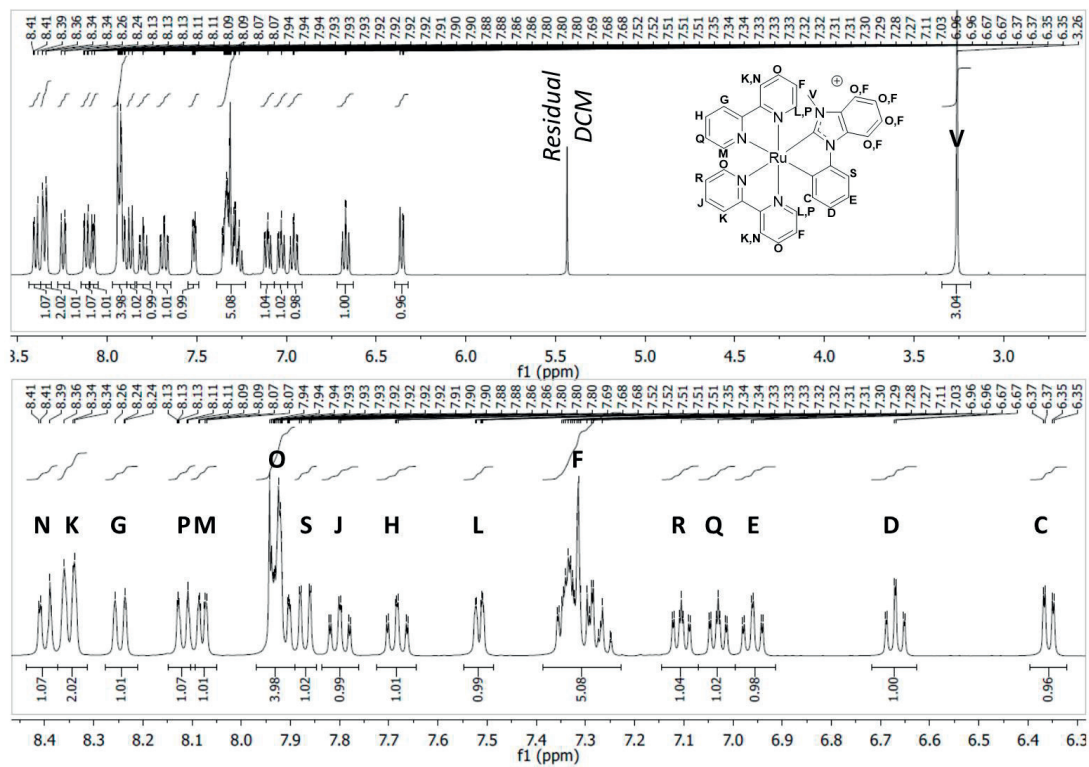
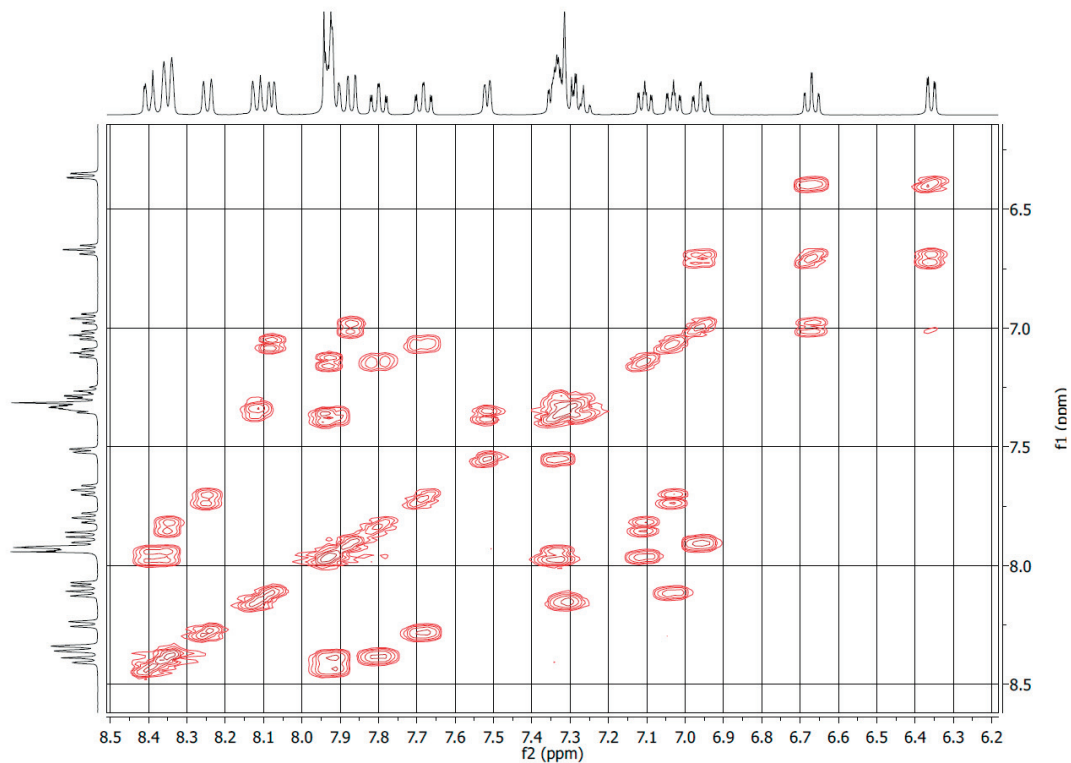
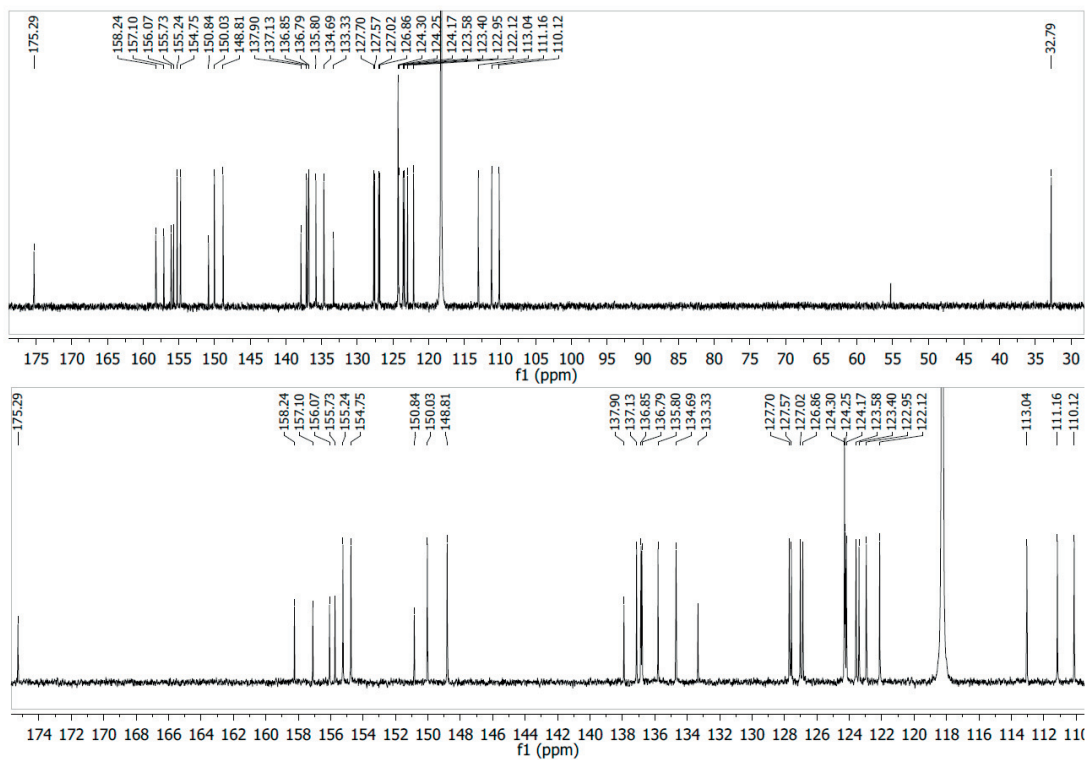
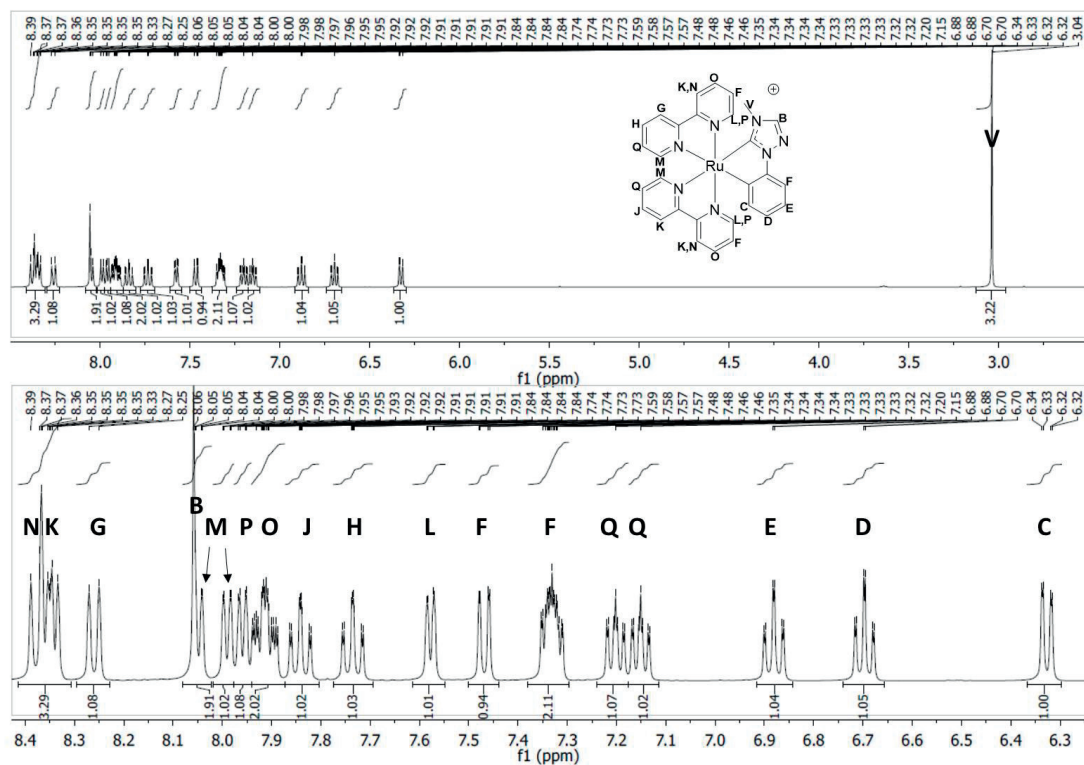
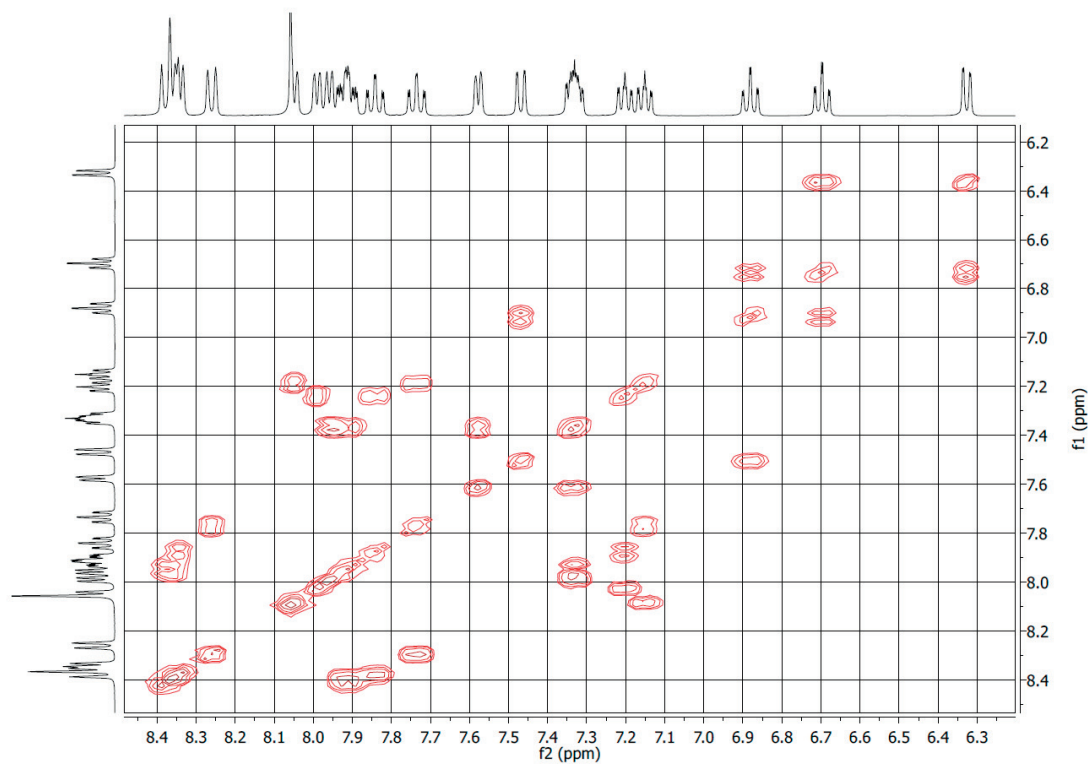
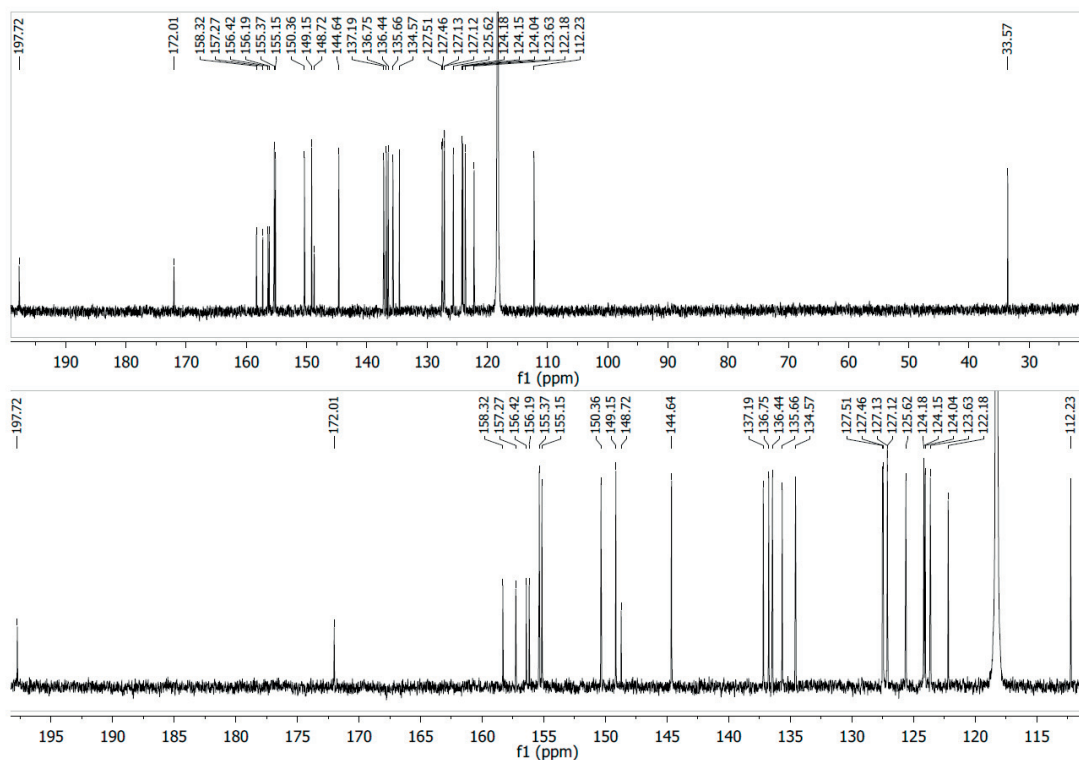
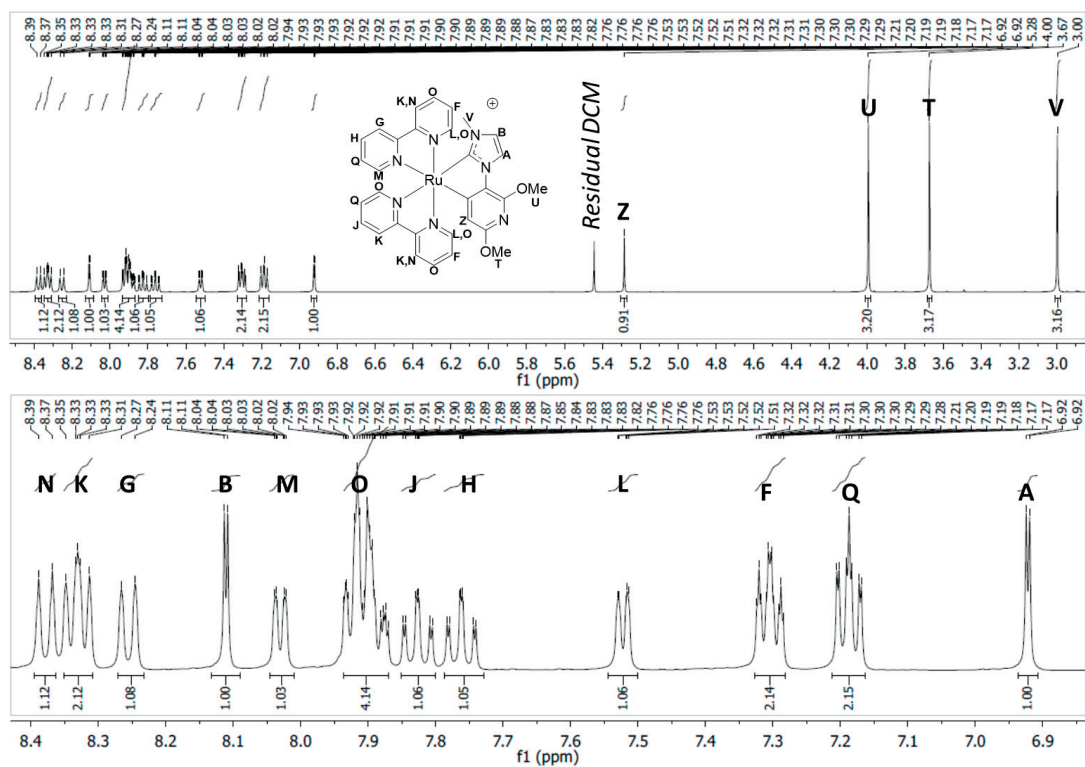


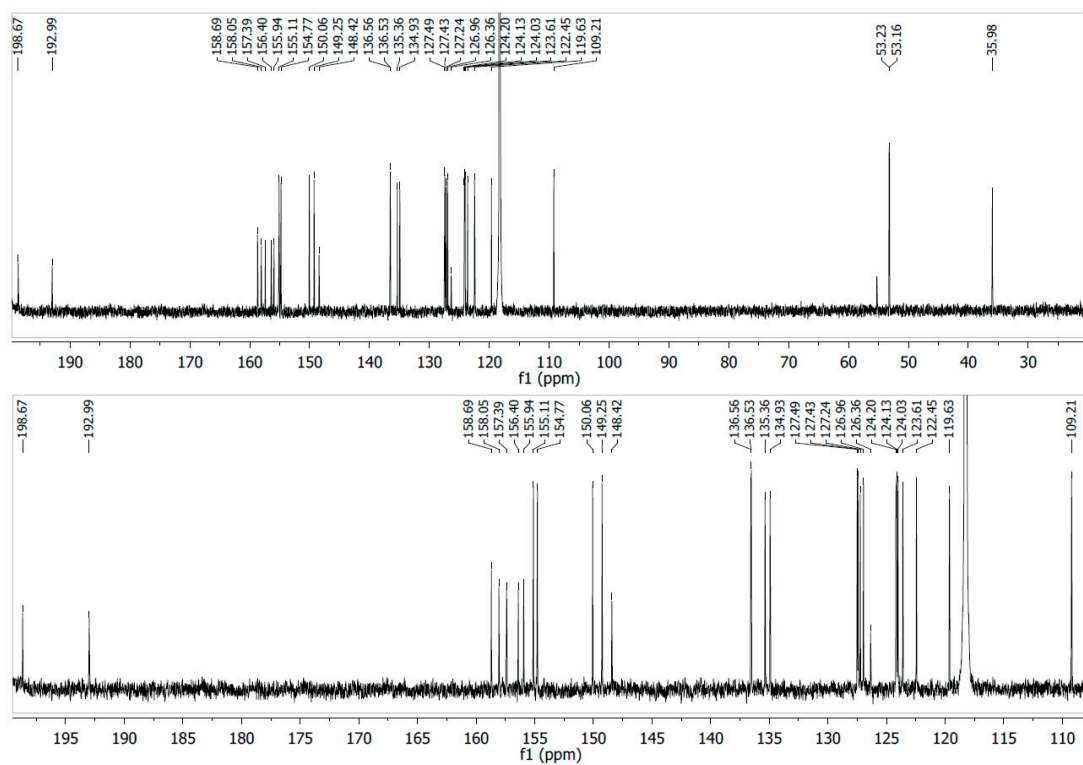
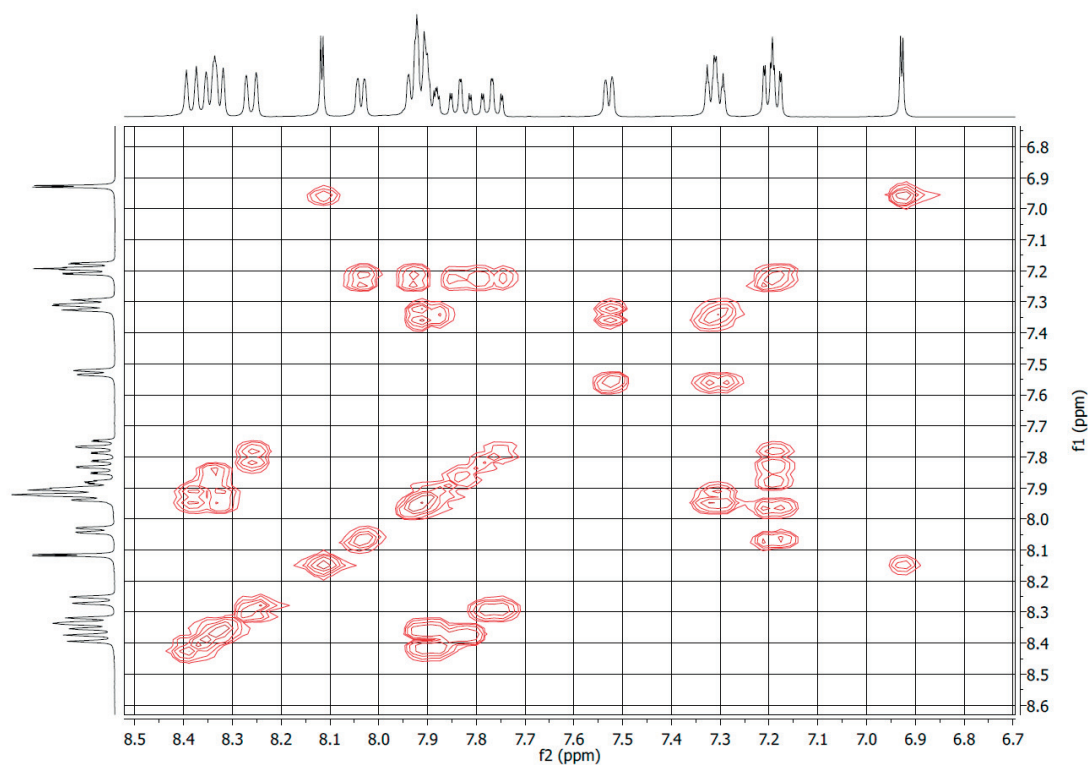
Figure 8.75. ^1H - ^1H COSY spectrum of complex **1** in $\text{acetonitrile-}d_3$.

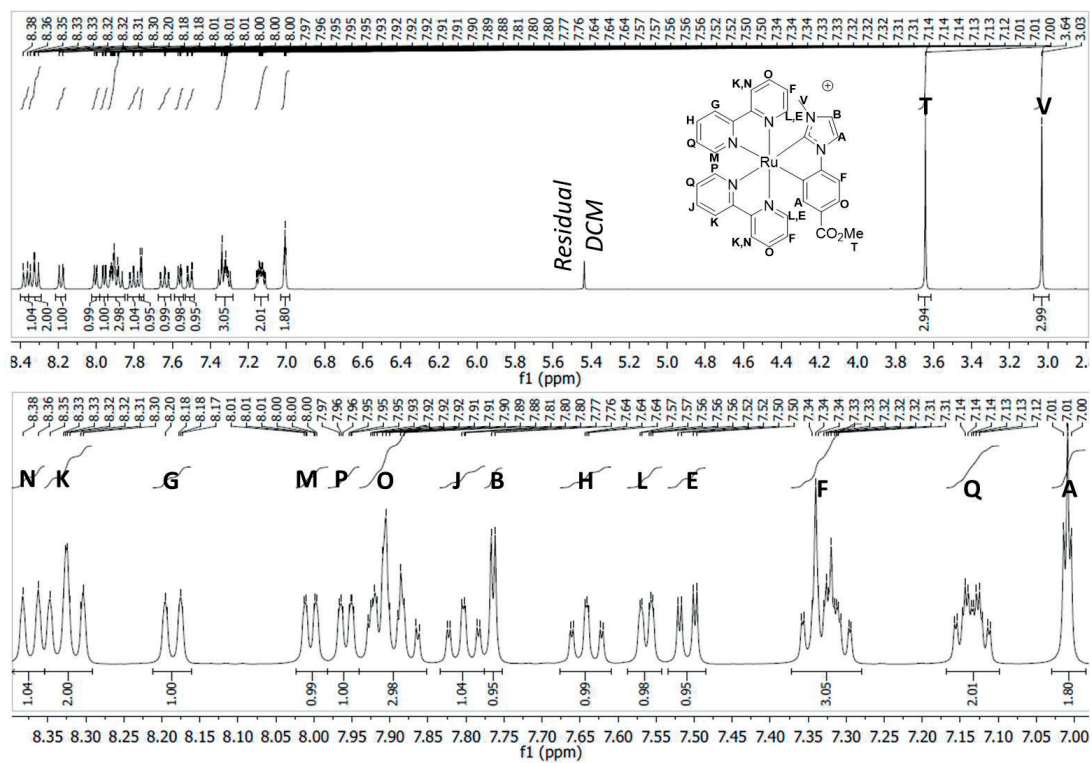
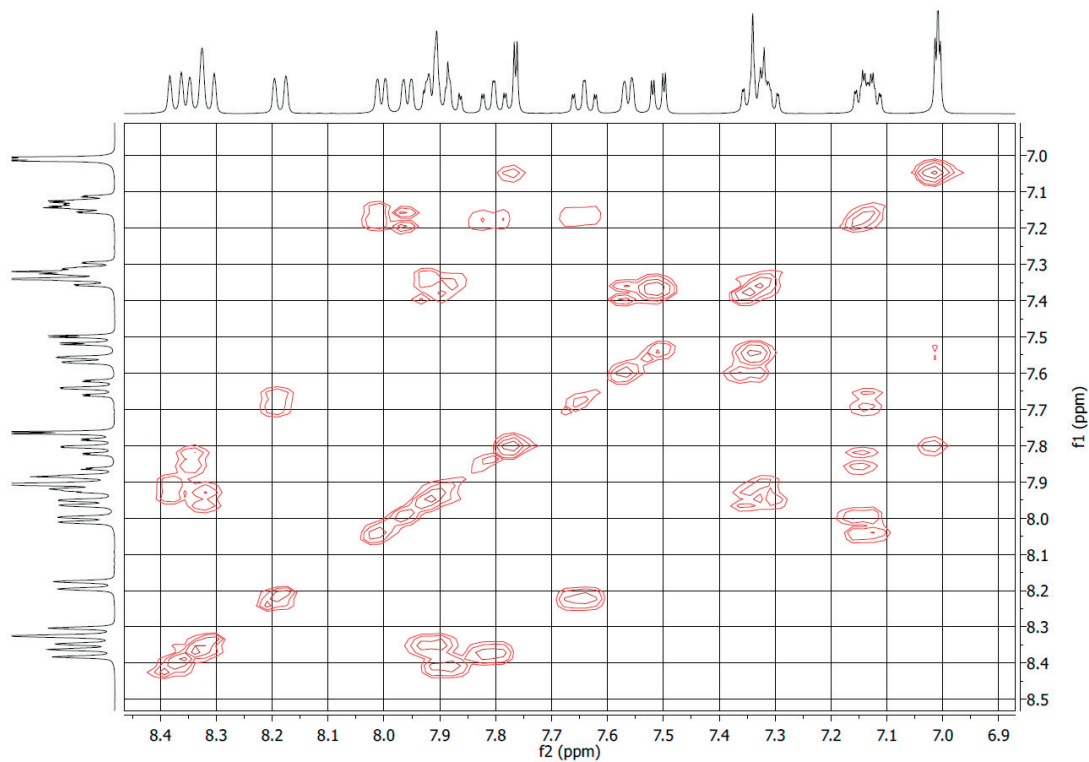
Figure 8.76. ^{13}C spectrum of complex **1** in $\text{acetonitrile-}d_3$.Figure 8.77. ^1H NMR spectrum of complex **2** in $\text{acetonitrile-}d_3$.

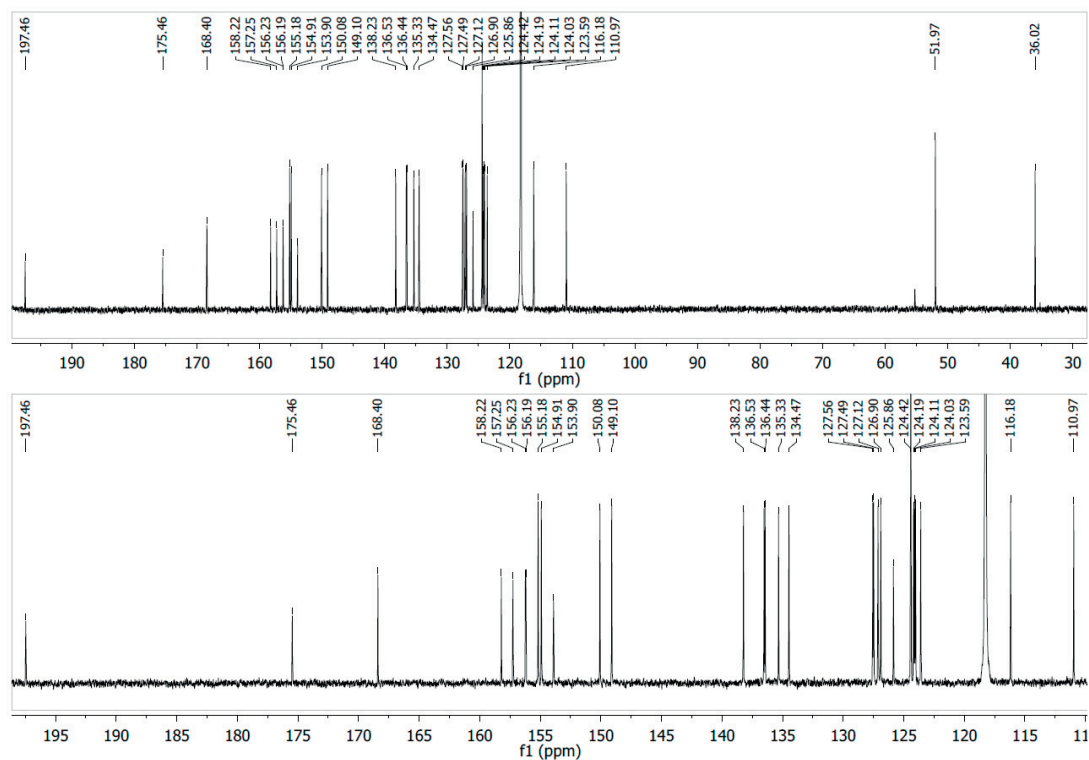
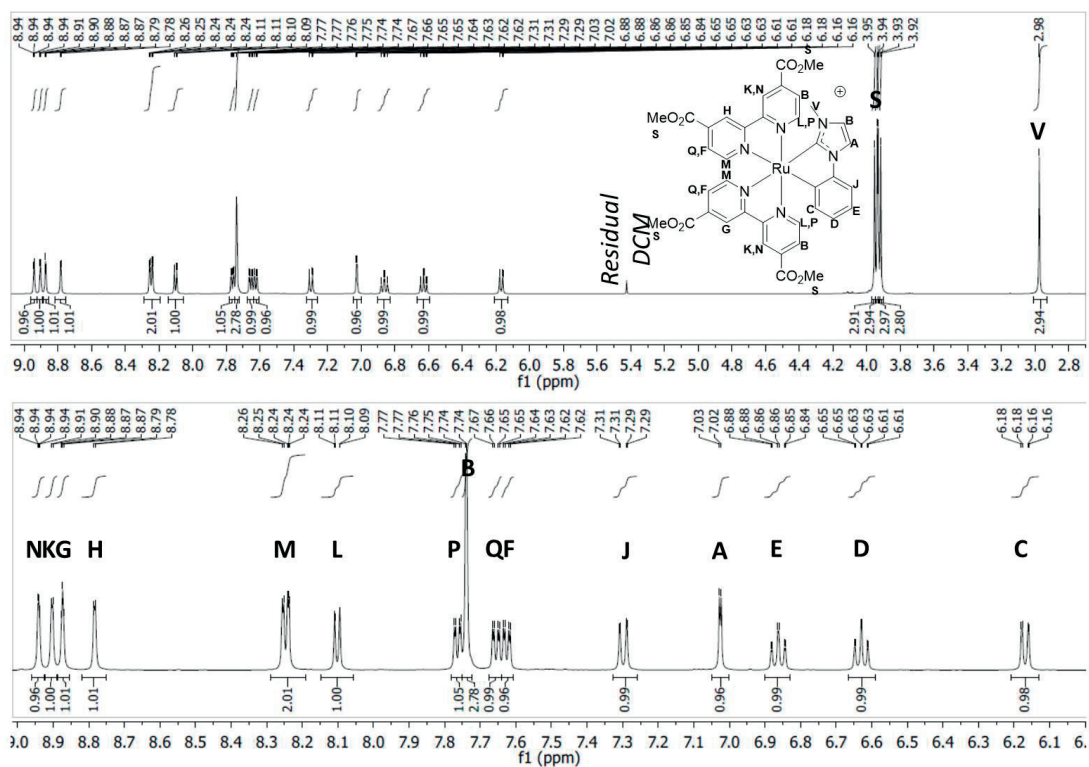
Figure 8.78. ^1H - ^1H COSY spectrum of complex **2** in *acetonitrile-d*₃.Figure 8.79. ^{13}C spectrum of complex **2** in *acetonitrile-d*₃.

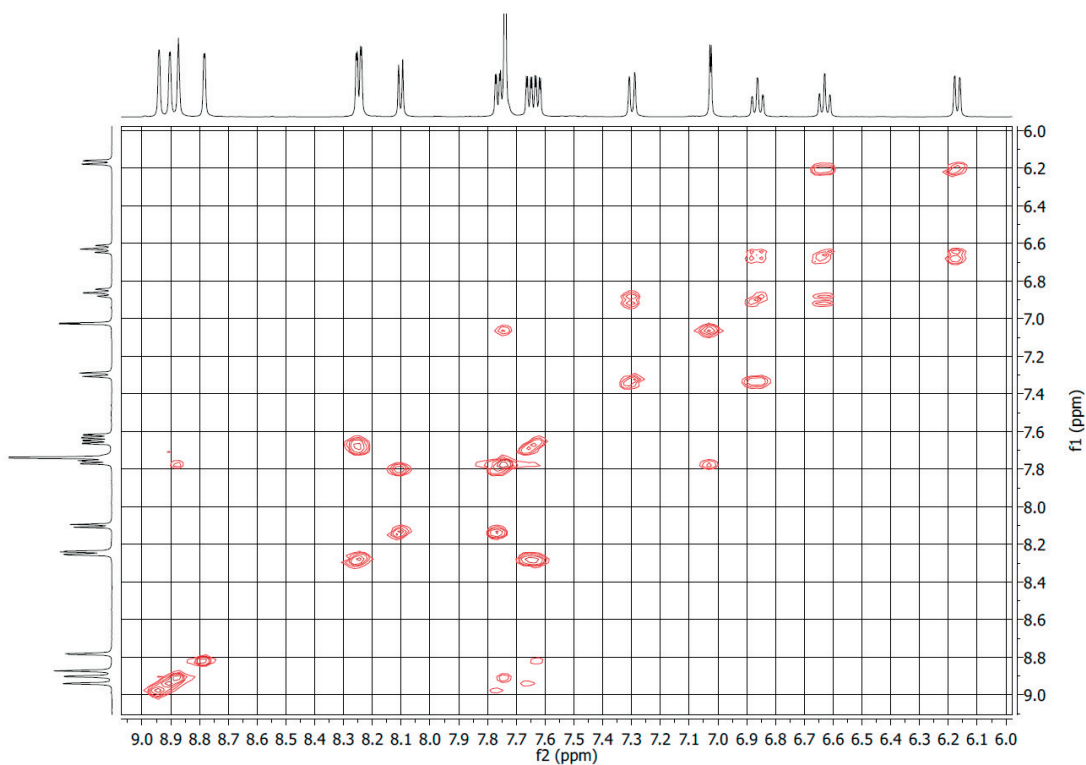
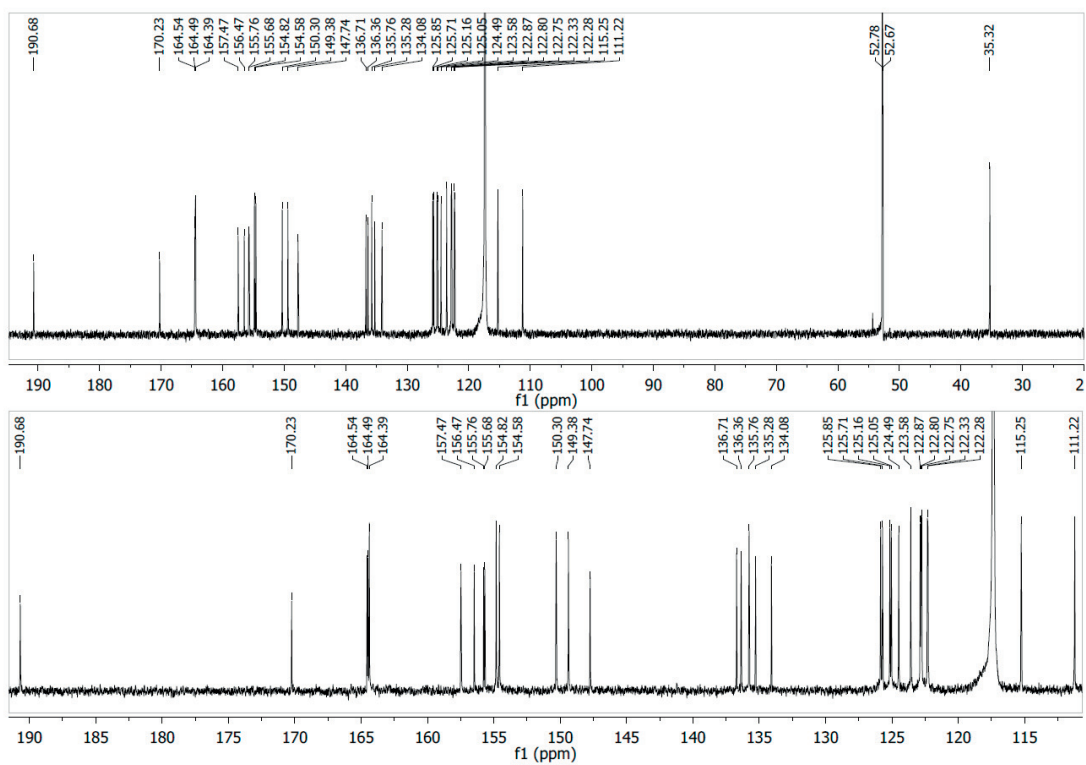
Figure 8.80. ^1H NMR spectrum of complex **3** in *acetonitrile-d*₃.Figure 8.81. ^1H - ^1H COSY spectrum of complex **3** in *acetonitrile-d*₃.

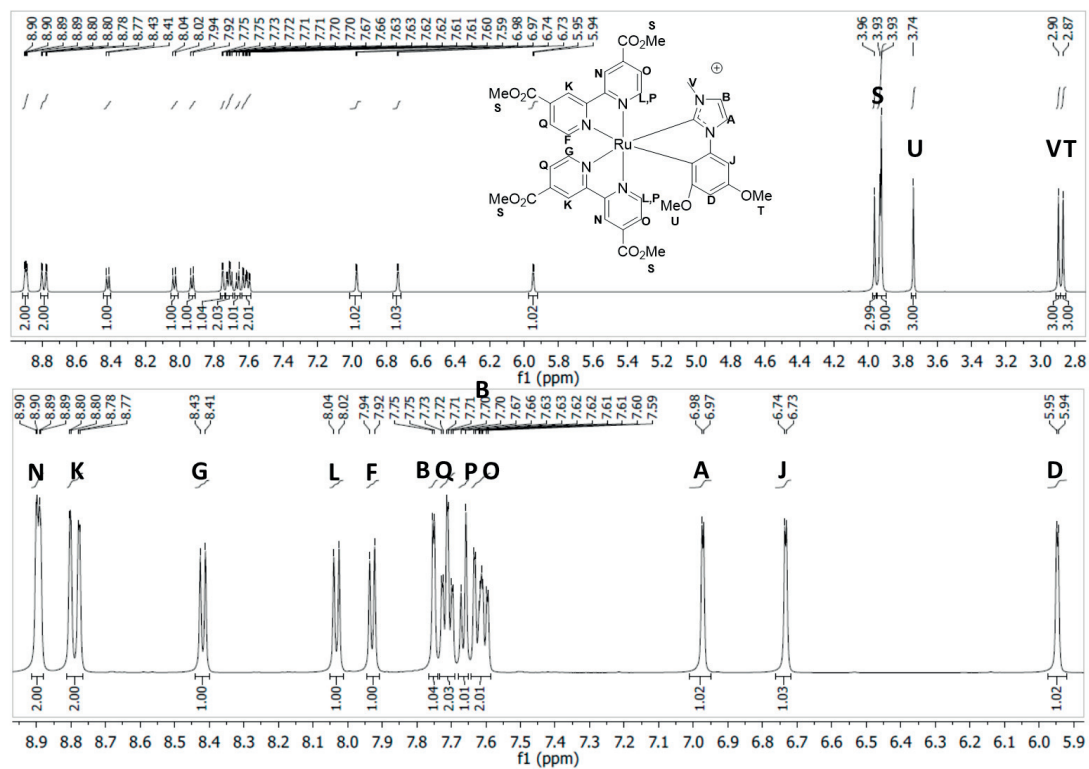
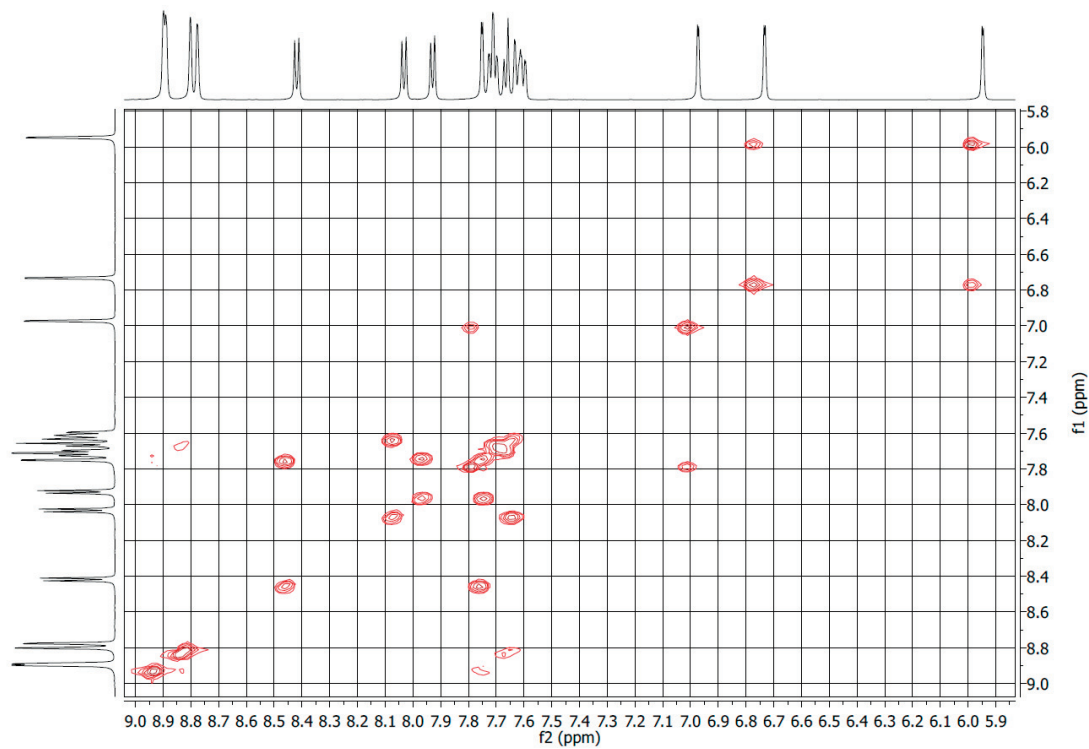
Figure 8.82. ^{13}C spectrum of complex **3** in $\text{acetonitrile-}d_3$.Figure 8.83. ^1H NMR spectrum of complex **4** in $\text{acetonitrile-}d_3$.



Figure 8.86. ^1H NMR spectrum of complex **5** in *acetonitrile-d*₃.Figure 8.87. ^1H - ^1H COSY spectrum of complex **5** in *acetonitrile-d*₃.

Figure 8.88. ^{13}C spectrum of complex **5** in $\text{acetonitrile-}d_3$.Figure 8.89. ^1H NMR spectrum of complex **6** in $\text{acetonitrile-}d_3$.

Figure 8.90. ^1H - ^1H COSY spectrum of complex **6** in $\text{acetonitrile-}d_3$.Figure 8.91. ^{13}C spectrum of complex **6** in $\text{acetonitrile-}d_3$.

Figure 8.92. ^1H NMR spectrum of complex **7** in *acetonitrile-d*₃.Figure 8.93. ^1H - ^1H COSY spectrum of complex **7** in *acetonitrile-d*₃.

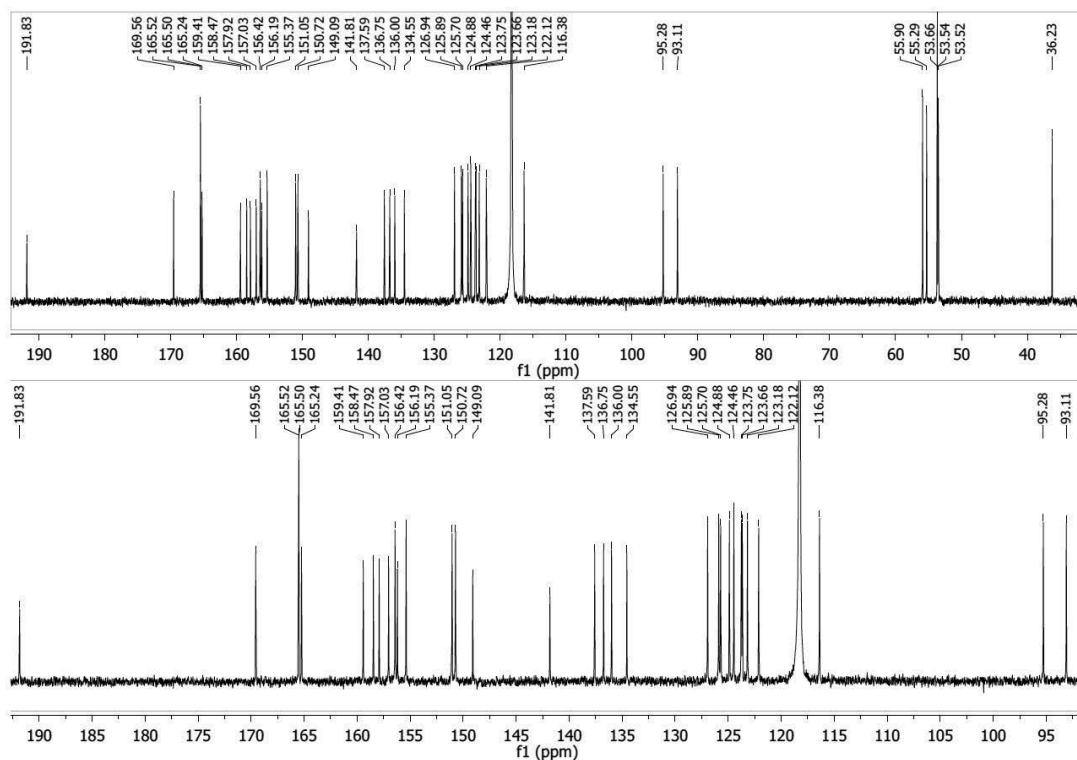


Figure 8.94. ^{13}C spectrum of complex 7 in $\text{acetonitrile-}d_3$.

8.3.2 XRD characterization

The data collection was performed at 293 K for 514, 110 K for 515 and 516 and at 100 K for 519 and 526 on a Bruker D8 Venture diffractometer using Mo K_α radiation. ($\lambda=0.71069$ nm) Data reduction and absorption correction were done with SAINT and SADABS integrated in the APEX 3 software package. The structure solution was carried out with SHELXS and the refinement with SHELXL-2014 in the WINGX environment. All atoms except hydrogens were refined anisotropically. Due to the poor crystal quality oxygen and nitrogen atoms of the compounds 514 and 516 were refined isotropically to avoid meaningless anisotropic temperature parameters. Hydrogen atoms were inserted on geometrically optimized positions and refined using the riding model. Structure drawings were made with the program Diamond 2.1e. Crystallographic data were submitted to Cambridge Crystallographic Data Centre (CCDC 1529867-1529871 for complexes 1a, 2a, 3a, 1 and 6).

Table 8.7. Summary of the crystallographic parameters for compound 1a, 2a, 3a, 1 and 6.

Compound	1a	2a	3a	1	6
Formula	C ₂₀ H ₂₃ IN ₂ Ru	C ₂₄ H ₂₅ IN ₂ Ru	C ₁₉ H ₂₂ IN ₃ Ru	C ₁₂₆ H ₁₀₀ Cl ₁₂ F ₃₀ N ₂₄ P ₅ Ru ₄	C ₃₈ H ₃₃ F ₆ N ₄ O ₈ PRu
Crystal system	Orthorhombic	Monoclinic	Orthorhombic	Triclinic	Triclinic
Space group	<i>Pna</i> 2 ₁	<i>P</i> 2 ₁ / <i>c</i>	<i>P</i> 2 ₁ 2 ₁ 2 ₁	<i>P</i> -1	<i>P</i> -1
Temperature / K	293(2)	110(2)	110(2)	100(2)	100(2)
Lattice constants / Å and °	<i>a</i> = 7.7179(13) <i>b</i> = 14.194(3) <i>c</i> = 17.506(3)	<i>a</i> = 10.3734(9) <i>b</i> = 12.4204(13) <i>c</i> = 17.3242(18) <i>β</i> = 105.10(3)	<i>a</i> = 10.634(3) <i>b</i> = 11.936(3) <i>c</i> = 14.358(4)	<i>a</i> = 15.144(5) <i>b</i> = 15.340(4) <i>c</i> = 18.042(5) <i>a</i> = 81.686(6) <i>β</i> = 74.189(6) <i>γ</i> = 73.145(7)	<i>a</i> = 8.4507(14) <i>b</i> = 11.955(2) <i>c</i> = 20.358(3) <i>a</i> = 95.461(3) <i>β</i> = 91.237(4) <i>γ</i> = 107.660(3)
Volume / Å ³	1917.8(6)	2155.0(5)	1822.4(9)	3849.5(10)	1948.2(6)
Z	4	4	4	1	2
D _{calculated} / g·cm ⁻³	1.80	1.76	1.90	1.51	1.62
Radiation	Mo-K _α (λ = 0.71069 Å)	Mo-K _α (λ = 0.71069 Å)	Mo-K _α (λ = 0.71069 Å)	Mo-K _α (λ = 0.71069 Å)	Mo-K _α (λ = 0.71069 Å)
Crystal habit	Plate	Block	Plate	Needle	Plate
Θ range / °	2.87 – 25.00	2.435 – 26.407	2.219 – 25.345	2.257 – 26.352	2.533 – 26.288
Min. / max. <i>b</i> <i>k</i> / <i>l</i>	-9 ≤ <i>b</i> ≤ 9 -16 ≤ <i>k</i> ≤ 16 -20 ≤ <i>l</i> ≤ 20	-12 ≤ <i>b</i> ≤ 12 -15 ≤ <i>k</i> ≤ 15 -21 ≤ <i>l</i> ≤ 21	-11 ≤ <i>b</i> ≤ 12 -12 ≤ <i>k</i> ≤ 14 -16 ≤ <i>l</i> ≤ 16	-17 ≤ <i>b</i> ≤ 17 -17 ≤ <i>k</i> ≤ 17 -21 ≤ <i>l</i> ≤ 21	-10 ≤ <i>b</i> ≤ 10 -14 ≤ <i>k</i> ≤ 14 -25 ≤ <i>l</i> ≤ 25
Reflections, measured	25354	47437	5698	54931	24945
Reflections, independent	3362	4399	3022	12638	6860
Absorption coefficient / mm ⁻¹	2.43	2.17	2.56	0.734	0.533
Absorption correction	Multi-Scan	Multi-Scan	Multi-Scan	Multi-Scan	Multi-Scan
Refined parameters	112	256	111	919	546
R1 [<i>I</i> > 2σ(<i>I</i>)]	0.0554	0.0262	0.0710	0.0837	0.0752
wR2 (all data)	0.15	0.0563	0.2216	0.2130	0.1357
Max. / min. Residual Density / e ⁻ / Å ³	3.518 and -2.078	0.550 and -0.708	1.805 and -3.088	1.536 and -1.419	0.616 and -0.505

Table 8.8. Bonding distances of the central Ru atom in complexes 1a, 2a and 3a. (All distances in Å)

Compound	Ru-C _{NHC}	Ru-C _{Cyd}	Ru-C _{ymene}	Ru-I
1a	2.028(16)	2.079(16)	1.729	2.7198(16)
2a	2.003(3)	2.066(3)	1.741	2.7063(5)
3a	2.01(2)	2.06(2)	1.739	2.705(2)

Table 8.9. Bonding distances of the central Ru atom in the complexes 1 and 6. (All distances in Å)

Compound	1	6
Ru-NHC	2.092(11) / 2.168(11)	2.030(7)
Ru-C _{cyclomet}	2.111(10) / 2.054(9)	2.002(7)
Ru-N1 / N5	2.149(7) / 2.077(7)	2.052(5)
Ru-N2 / N6	2.133(8) / 2.111(8)	2.107(6)
Ru-N3 / N7	2.159(7) / 2.251(8)	2.088(5)
Ru-N4 / N8	2.134(7) / 2.091(8)	2.017(5)

8.3.3 Electrochemical characterization

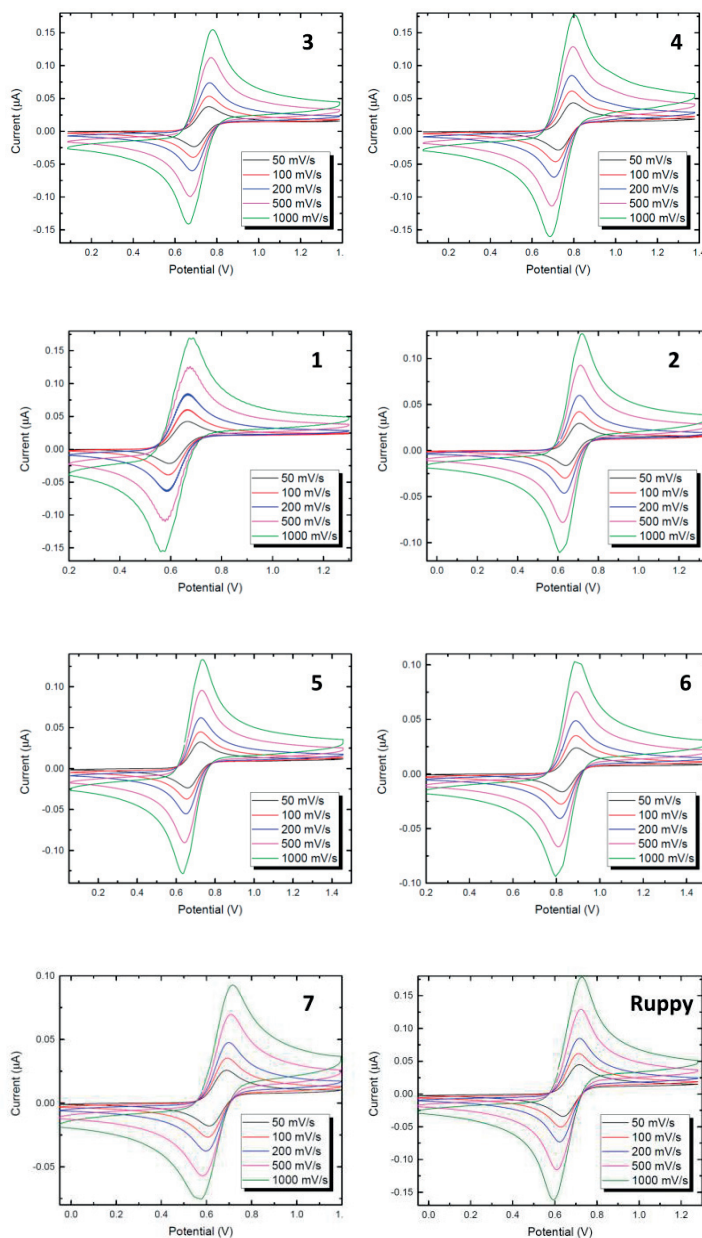
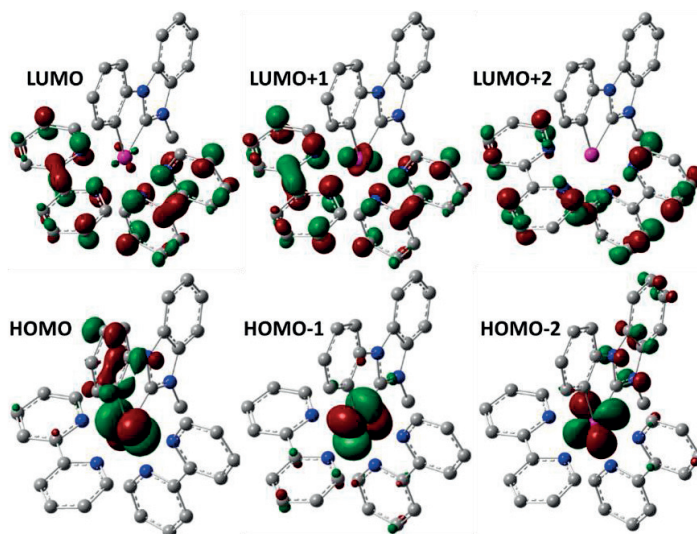
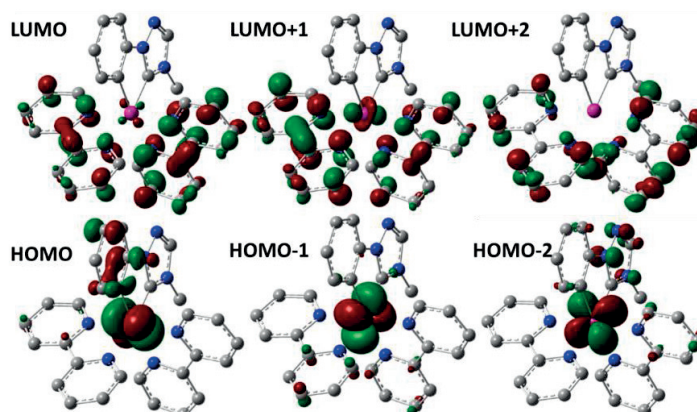


Figure 8.95. Cyclic voltammograms of the first oxidation of complex **1-7** and $[\text{Ru}(\text{ppy})(\text{bpy})_2](\text{PF}_6)$ measured in the same system as described in Figure 5.7 at different potential scan rates

8.3.4 Quantum mechanical calculations

Figure 8.96. Frontier molecular orbitals of 2^+ (mPW1PW91/SDD, TZVP in acetonitrile).Figure 8.97. Frontier molecular orbitals of 3^+ (mPW1PW91/SDD, TZVP in acetonitrile).Table 8.10. Frontier orbital energies of complexes 1^+ , 2^+ , 3^+ .

	1^+	2^+	3^+
LUMO+2	-1.51972	-1.54584	-1.54013
LUMO+1	-2.20461	-2.24107	-2.2272
LUMO	-2.29277	-2.32243	-2.32379
HOMO	-5.40513	-5.45765	-5.50962
HOMO-1	-5.73302	-5.81874	-5.81193
HOMO-2	-5.74037	-5.89302	-5.94717

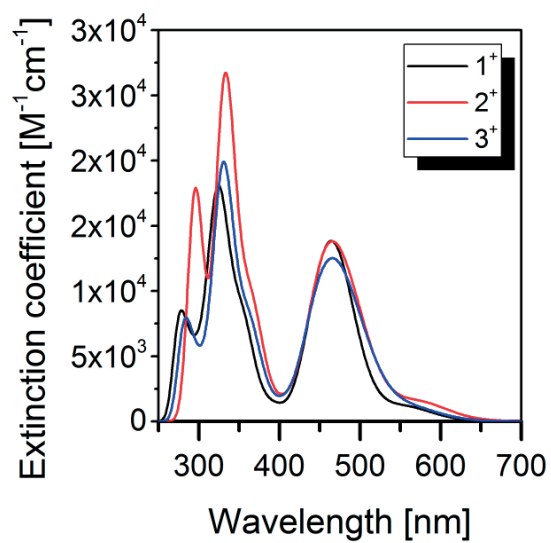
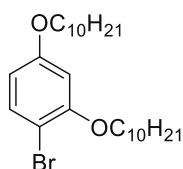
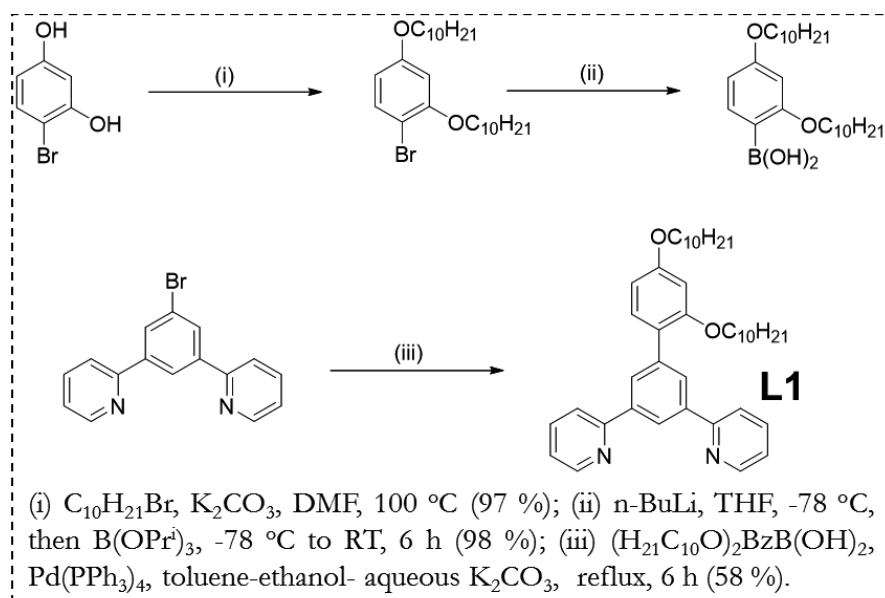


Figure 8.98. Theoretical absorption spectra of 1⁺ (blue), 2⁺ (red) and 3⁺ (green) computed with TD-DFT (30 excitations).

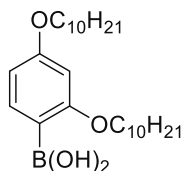
8.4 Appendix to chapter 6

8.4.1 Synthesis of ligands and ruthenium complexes

All the commercially materials were used as received. NMR spectra were collected on a Bruker AVIII-HD (400 MHz), and are reported in ppm using solvent as an internal standard (chloroform 7.26/77.16, dimethylformamide 2.75/163.15 and acetonitrile 1.94/118.69 ppm for proton/carbon). Data reported as: s = singlet, d = doublet, t = triplet, q = quartet, p = pentet, m = multiplet; coupling constants in Hz. UV-Vis spectra were collected on LS-55 spectrometer. Mass spectra were measured on a Bruker Microflex or Autoflex MALDI-TOF mass spectrometers.

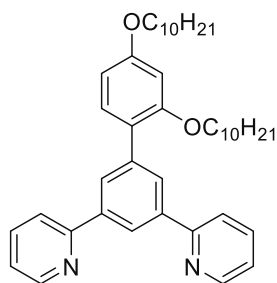


1-bromo-2,4-bis(decyloxy)benzene. 4-bromoresorcinol (3 g, 15.9 mmol, 1 equiv.), 1-bromodecane (8.77 g, 39.7 mmol, 2.5 equiv.) were dissolved in 100 mL of DMF in round-bottom flask. K_2CO_3 (8.77 g, 63.6 mmol, 4 equiv.) was added, and the mixture was stirred at 100 °C overnight. Afterwards, the reaction mixture was cooled down to room temperature, excess of deionized water was added and the organic compounds were extracted with DCM. The organic phase was dried on MgSO_4 , filtered and solvent was evaporated. Column chromatography (SiO_2) with gradient polarity eluent (hexane to hexane:DCM (9:1)) afforded the product as a colorless oil (7.86 g, 97 %). ^1H NMR (400 MHz, Chloroform- d) δ 7.37 (d, J = 8.7 Hz, 1H), 6.47 (d, J = 2.7 Hz, 1H), 6.37 (dd, J = 8.7, 2.7 Hz, 1H), 3.98 (t, J = 6.5 Hz, 2H), 3.91 (t, J = 6.6 Hz, 2H), 1.88 – 1.80 (m, 2H), 1.80 – 1.73 (m, 2H), 1.54 – 1.41 (m, 4H), 1.37 – 1.23 (m, 24H), 0.92 – 0.86 (m, 6H).



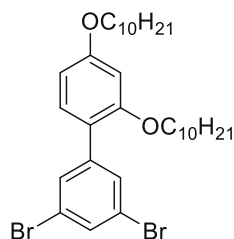
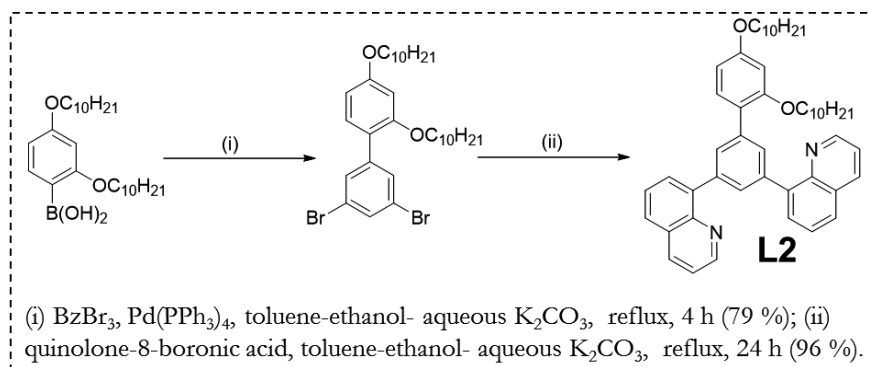
(2,4-bis(decyloxy)phenyl)boronic acid. In a 200 mL oven-dried Schlenk flask equipped with a stirring bar, 1-bromo-2,4-bis(decyloxy)benzene (3 g, 6.4 mmol, 1 equiv.) was dissolved in 100 mL of dry THF. Solution was cooled down to -78 °C and 1.6 M solution of $n\text{-BuLi}$ in hexanes (4.8 mL, 1.2 equiv.) was added drop-wise. The solution was stirred for 2 hours at -78 °C and tri-isopropyl borate (1.56 g, 1.3 equiv.) was added drop-wise. Afterwards, the reaction was let to warm up to room temperature and stirred for 6 hours. Then, the mixture was washed with water and the product was extracted with DCM. The organic phase was collected and dried with MgSO_4 . Solids were filtered and

the solvent was evaporated with rotary evaporation to afford the product as an off-white product (2.72 g, 98 %). Without analysis the product was used for the following step.



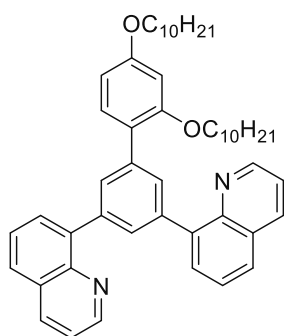
2,2'-(2',4'-bis(decyloxy)-[1,1'-biphenyl]-3,5-diyl)dipyridine (L1). 2,2'-(5-bromo-1,3-phenylene)dipyridine (746 mg, 2.4 mmol, 1 equiv.) and (2,4-bis(decyloxy)phenyl)boronic acid (1.25 g, 1.2 equiv.) were mixed in 5 mL of EtOH and 40 mL of toluene, and a 2 M aqueous solution of K_2CO_3 (10 mL) was added to the mixture. The reaction mixture was purged with nitrogen for 20 minutes and $Pd(PPh_3)_4$ (138 mg, 0.12 mmol, 0.05 equiv.) was added. The reaction mixture was refluxed for 6 hours. Then, it was cooled down to room temperature, the organic compounds were extracted with DCM, the organic phase was dried with $MgSO_4$, filtered, and the solvent was evaporated with rotary evaporation.

Column chromatography (SiO_2 , DCM-acetone (9:1)) afforded the final product as an off-white solid (865 mg, 58 %). 1H NMR (400 MHz, Chloroform-*d*) δ 8.72 (d, $J = 3.9$ Hz, 2H), 8.63 (t, $J = 1.8$ Hz, 1H), 8.26 (d, $J = 1.7$ Hz, 2H), 7.87 (d, $J = 8.0$ Hz, 2H), 7.73 (td, $J = 7.7, 1.8$ Hz, 2H), 7.42 (d, $J = 9.0$ Hz, 1H), 7.21 (ddd, $J = 7.4, 4.8, 1.1$ Hz, 2H), 6.61 – 6.56 (m, 2H), 4.04 – 3.93 (m, 4H), 1.81 (p, $J = 6.7$ Hz, 2H), 1.70 (p, $J = 6.7$ Hz, 2H), 1.49 (p, $J = 6.6$ Hz, 2H), 1.41 – 1.05 (m, 26H), 0.94 – 0.84 (m, 6H). ^{13}C NMR (101 MHz, Chloroform-*d*) δ 160.04, 157.59, 157.20, 149.65, 139.57, 139.50, 136.64, 131.34, 128.81, 123.64, 123.21, 122.09, 120.70, 105.41, 100.49, 68.52, 68.18, 31.99, 31.94, 29.68, 29.65, 29.64, 29.54, 29.52, 29.50, 29.42, 29.39, 29.36, 26.37, 26.17, 22.76 (d, $J = 2.4$ Hz), 14.20 (d, $J = 1.8$ Hz). HRMS (MALDI-TOF): $m/z = 621.524 [M+H]^+$, (calculated for $[N_2O_2C_{42}H_{56}+H]^+$: $m/z = 621.4426$).



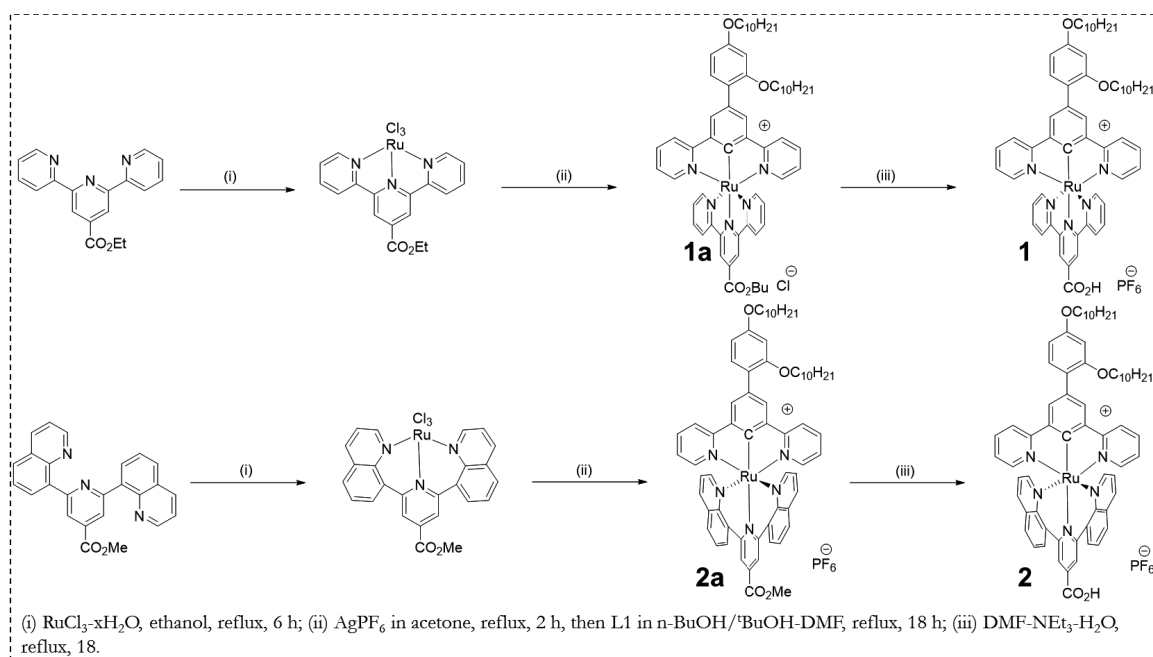
3',5'-dibromo-2,4-bis(decyloxy)-1,1'-biphenyl. 1,3,5-tribromobenzene (2 g, 6.4 mmol, 2.3 equiv.) and (2,4-bis(decyloxy)phenyl)boronic acid (1.2 g, 2.7 mmol, 1.2 equiv.) were mixed in 4 mL of EtOH and 40 mL of toluene, and a 2 M aqueous solution of K_2CO_3 (8 mL) was added to the mixture. The reaction mixture was purged with nitrogen for 20 minutes and $Pd(PPh_3)_4$ (156 mg, 0.13 mmol, 0.05 equiv.) was added. The reaction mixture was refluxed for 4 hours. Then, it was cooled down to room temperature, the organic compounds were extracted with DCM, the organic phase was dried with $MgSO_4$, filtered, and the

solvent was evaporated with rotary evaporation. Column chromatography (SiO_2 , hexane-DCM (6:1)) afforded the final product as a colorless oil (1.33 g, 79 %). 1H NMR (400 MHz, Chloroform-*d*) δ 7.69 (d, $J = 1.8$ Hz, 2H), 7.60 (t, $J = 1.8$ Hz, 1H), 7.21 (d, $J = 8.3$ Hz, 1H), 6.59 – 6.53 (m, 2H), 4.00 (q, $J = 6.3$ Hz, 4H), 1.90 – 1.74 (m, 4H), 1.58 – 1.47 (m, 4H), 1.38 (dd, $J = 14.7, 8.3$ Hz, 26H), 0.97 (t, $J = 6.6$ Hz, 6H). ^{13}C NMR (101 MHz, Chloroform-*d*) δ 160.75, 157.01, 142.14, 131.43, 131.18, 130.92, 122.24, 120.32, 105.46, 100.27, 68.39, 68.17, 32.09, 29.78, 29.76, 29.61, 29.57, 29.52, 29.45, 29.32, 26.48, 26.24, 22.87, 14.29, 14.28.



8,8'-(2',4'-bis(decyloxy)-[1,1'-biphenyl]-3,5-diyl)diquinoline (L2).

3',5'-dibromo-2,4-bis(decyloxy)-1,1'-biphenyl (668 mg, 1.07 mmol, 1 equiv.) and quinolone-8-boronic acid (426 mg, 2.5 mmol, 2.3 equiv.) were mixed in 4 mL of EtOH and 40 mL of toluene, and a 2 M aqueous solution of K_2CO_3 (8 mL) was added to the mixture. The reaction mixture was purged with nitrogen for 20 minutes and $\text{Pd}(\text{PPh}_3)_4$ (142 mg, 0.12 mmol, 0.05 equiv.) was added. The reaction mixture was refluxed for 24 hours. Then, it was cooled down to room temperature, the organic compounds were extracted with DCM, the organic phase was dried with MgSO_4 , filtered, and the solvent was evaporated with rotary evaporation. Column chromatography (SiO_2 , gradient polarity eluent starting with DCM and increasing a polarity up to DCM : acetone (3:1)) afforded the final product as a yellowish oil (740 mg, 96 %). ^1H NMR (400 MHz, Chloroform-*d*) δ 9.01 (dd, $J = 4.2, 1.8$ Hz, 2H), 8.17 (dd, $J = 8.3, 1.8$ Hz, 2H), 8.14 (d, $J = 1.7$ Hz, 1H), 8.09 (d, $J = 1.6$ Hz, 2H), 7.99 (dd, $J = 7.2, 1.4$ Hz, 2H), 7.81 (dd, $J = 8.2, 1.4$ Hz, 2H), 7.63 (t, $J = 7.6$ Hz, 2H), 7.57 (d, $J = 8.1$ Hz, 1H), 7.39 (d, $J = 4.2$ Hz, 1H), 7.37 (d, $J = 4.2$ Hz, 1H), 6.68 – 6.62 (m, 2H), 4.08 – 4.01 (m, 4H), 1.91 – 1.76 (m, 4H), 1.54 (p, $J = 6.9$ Hz, 2H), 1.48 – 1.13 (m, 24H), 1.08 – 1.01 (m, 2H), 1.00 – 0.92 (m, 6H). ^{13}C NMR (101 MHz, Chloroform-*d*) δ 159.64, 157.25, 150.02, 146.22, 141.43, 138.39, 137.72, 136.05, 131.68, 131.61, 131.00, 130.59, 128.68, 127.21, 126.24, 123.68, 120.78, 105.14, 100.19, 68.25, 68.02, 31.92, 29.62, 29.59, 29.44, 29.38, 29.35, 29.28, 26.33, 26.13, 22.72, 22.71, 14.17, 14.16. HRMS (MALDI-TOF): $m/z = 721.571$ $[\text{M}+\text{H}]^+$, (calculated for $[\text{N}_2\text{O}_2\text{C}_{50}\text{H}_{60}+\text{H}]^+$: $m/z = 721.4733$).



[Ru(L¹)(tpyCO₂Bu)]Cl (1a). In an oven-dried 50 mL round-bottom flask protected from light with aluminum foil, $\text{RuCl}_3(\text{tpyCO}_2\text{Et})$ (225 mg, 0.44 mmol, 1 equiv.) and AgPF_6 (377 mg, 1.49 mmol, 3.3 equiv.) were dissolved in 25 mL of dry acetone under nitrogen atmosphere. The reaction mixture was refluxed for 3 hours, and then cooled down to room temperature. The precipitated AgCl was filtered with celite, and the solvent was evaporated with rotary evaporator. To the remaining red material ligand (L¹) (307 mg, 0.49 mmol, 1.1 equiv.) and 10 mL of DMF-^tBuOH were added. The solution was refluxed for 18 hours. Afterwards, the solvent was evaporated with rotary evaporator, and the remaining material was purified by column chromatography (SiO_2 ; DCM-acetone (9:1)) provided the product as a mauve

solid. (90 mg, 19 %). ^1H NMR (400 MHz, DMF- d_7) δ 9.57 (s, 2H), 9.11 (d, J = 8.0 Hz, 2H), 8.70 (s, 2H), 8.40 (d, J = 8.0 Hz, 2H), 7.95 (t, J = 7.7 Hz, 2H), 7.76 (t, J = 7.6 Hz, 2H), 7.66 (d, J = 8.2 Hz, 1H), 7.42 (d, J = 5.5 Hz, 2H), 7.32 (t, J = 6.4 Hz, 2H), 7.23 (d, J = 5.5 Hz, 2H), 6.92 (d, J = 2.3 Hz, 1H), 6.86 (dd, J = 8.3, 2.3 Hz, 1H), 6.74 (t, J = 6.5 Hz, 2H), 4.63 (t, J = 6.6 Hz, 2H), 4.27 – 4.14 (m, 4H), 1.97 (p, J = 6.8 Hz, 2H), 1.92 – 1.79 (m, 4H), 1.72 – 1.61 (m, 2H), 1.61 – 1.15 (m, 16H), 1.13 – 0.99 (m, 6H), 0.97 – 0.82 (m, 9H), 0.73 (dt, J = 14.5, 7.2 Hz, 6H). ^{13}C NMR (101 MHz, DMF- d_7) δ 169.35, 166.23, 161.02, 160.12, 158.77, 155.66, 154.35, 153.26, 136.98, 136.59, 132.51, 128.18, 125.48, 123.31, 122.95, 121.24, 107.07, 101.24, 69.35, 69.06, 66.96, 32.90, 32.64, 31.87, 27.68, 27.15, 23.62, 23.47, 20.20, 14.79, 14.70, 14.54. HRMS (MALDI-TOF): m/z = 1054.520 $[\text{M}]^+$, (calculated for $[\text{RuN}_5\text{O}_4\text{C}_{62}\text{H}_{74}]^+$: m/z = 1054.4784).

$[\text{Ru}(\text{L}^1)(\text{dqpCO}_2\text{Me})](\text{PF}_6)$ (2a). This compound was synthesized according to the synthesis of $[\text{Ru}(\text{L}^1)(\text{tpyCO}_2\text{Et})]\text{Cl}$. $\text{RuCl}_3(\text{dqpCO}_2\text{Me})$ (187 mg, 0.31 mmol, 1 equiv.), AgPF_6 (260 mg, 1.03 mmol, 3.3 equiv.) and L^1 (262 mg, 0.34 mmol, 1.1 equiv.) were used. Before column chromatography, the counterion was exchanged to PF_6 by washing the material in DCM with saturated aqueous KPF_6 . This washing was repeated three times. Column chromatography (SiO_2 , DCM-acetone (9:1)) provided the final product as a green solid (164 mg, 42 %). ^1H NMR (400 MHz, DMF- d_7) δ 8.90 (s, 2H), 8.81 (d, J = 7.3 Hz, 2H), 8.67 (d, J = 5.5 Hz, 2H), 8.49 (s, 2H), 8.06 – 8.01 (m, 4H), 7.94 (d, J = 8.0 Hz, 2H), 7.89 (t, J = 7.7 Hz, 2H), 7.72 (t, J = 7.6 Hz, 2H), 7.38 (d, J = 8.3 Hz, 1H), 7.02 (d, J = 5.1 Hz, 2H), 6.91 (dd, J = 8.1, 5.1 Hz, 2H), 6.87 – 6.82 (m, 3H), 6.78 (dd, J = 8.4, 2.2 Hz, 1H), 4.24 – 4.09 (m, 7H), 1.89 – 1.80 (m, 2H), 1.80 – 1.70 (m, 2H), 1.57 – 1.49 (m, 2H), 1.47 – 1.25 (m, 14H), 1.21 – 0.85 (m, 15H), 0.76 (t, J = 7.2 Hz, 3H). ^{13}C NMR (101 MHz, DMF- d_7) δ 166.27, 165.94, 161.31, 159.47, 159.36, 158.68, 148.31, 147.67, 138.39, 137.37, 136.94, 136.82, 134.73, 133.65, 128.83, 127.91, 127.01, 123.62, 123.39, 122.70, 121.50, 121.40, 106.84, 100.95, 69.33, 69.04, 54.01, 32.90, 32.79, 27.71, 27.12, 23.62, 23.55, 14.82, 14.73. ^{31}P NMR (162 MHz, Chloroform- d) δ -144.32 (hept, J = 712.6 Hz). HRMS (MALDI-TOF): m/z = 1112.463 $[\text{M}]^+$, (calculated for $[\text{RuN}_5\text{O}_4\text{C}_{67}\text{H}_{72}]^+$: m/z = 1112.4628).

$[\text{Ru}(\text{L}^1)(\text{tpyCO}_2\text{H})](\text{PF}_6)$ (1). $[\text{Ru}(\text{L}^1)(\text{tpyCO}_2\text{Et})]\text{Cl}$ (85 mg, 0.08 mmol) was dissolved in 15 mL of DMF-NEt₃-H₂O (3:1:1), and the solution was refluxed for 18 hours. Afterwards, the reaction was cooled down to room temperature and washed with saturated aqueous KPF_6 , and extracted with DCM. The washing was repeated three times. The collected organic phase was dried with MgSO_4 and filtered. The volume of filtrate was reduced to small amount by rotary evaporator, and the remaining solution was subjected to size-exclusion chromatography (Sephadex, LH-20, DCM). The chromatography was repeated 3 times. To the collected mauve solution an excess of hexane was added to precipitate the product, which was then collected and dissolved again in small amount of DCM. The precipitation and collection step was repeated additional 2 times. At the end, the product was dried under high vacuum and mauve solid was obtained (64 mg, 70 %). ^1H NMR (400 MHz, DMF- d_7) δ 9.54 (s, 2H), 9.11 (d, J = 8.1 Hz, 2H), 8.64 (s, 2H), 8.45 (d, J = 8.1 Hz, 2H), 7.94 (td, J = 7.8, 1.5 Hz, 2H), 7.80 – 7.72 (m, 3H), 7.37 (dd, J = 5.6, 1.4 Hz, 2H), 7.26 (ddd, J = 13.0, 5.7, 1.3 Hz, 4H), 6.90 (d, J = 2.3 Hz, 1H), 6.86 (dd, J = 8.3, 2.3 Hz, 1H), 6.80 (ddd, J = 7.1, 5.6, 1.3 Hz, 2H), 4.26 – 4.16 (m, 4H), 1.93 – 1.80 (m, 4H), 1.62 – 1.51 (m, 4H), 1.48 – 1.17 (m, 14H), 1.04 (p, J = 7.0 Hz, 2H), 0.95 – 0.84 (m, 9H), 0.81 – 0.69 (m, 5H). ^{13}C NMR (101 MHz, DMF- d_7) δ 169.88, 167.41, 160.71, 160.19, 158.36, 155.08, 154.24, 153.30, 141.98, 136.98, 136.52, 133.93, 132.42, 132.24, 127.86, 126.57, 125.46, 125.38, 123.46, 122.81, 120.97, 107.14, 101.43, 69.30, 69.02, 32.87, 32.60, 30.64, 30.42, 27.65, 27.12, 23.58, 23.43, 14.76, 14.66. ^{31}P NMR (162 MHz, DMF- d_7) δ -127.56 – -159.21 (m). HRMS (MALDI-TOF): m/z = 998.415 $[\text{M}]^+$, (calculated for $[\text{RuN}_5\text{O}_4\text{C}_{58}\text{H}_{66}]^+$: m/z = 998.4158).

$[\text{Ru}(\text{L}^1)(\text{dqpCO}_2\text{H})](\text{PF}_6)$ (2). The synthesis was similar to the synthesis of $[\text{Ru}(\text{L}^1)(\text{tpyCO}_2\text{H})](\text{PF}_6)$. $[\text{Ru}(\text{L}^1)(\text{dqpCO}_2\text{Me})](\text{PF}_6)$ (155 mg, 0.123 mmol) was used. The product as a green solid was obtained

(98 mg, 64 %). ^1H NMR (400 MHz, DMF- d_7) δ 8.85 (dd, $J = 7.6, 1.3$ Hz, 2H), 8.79 (s, 2H), 8.56 (d, $J = 5.5$ Hz, 2H), 8.24 (s, 2H), 8.14 – 8.03 (m, 6H), 7.87 (t, $J = 7.8$ Hz, 2H), 7.68 (td, $J = 7.7, 1.5$ Hz, 2H), 7.46 (d, $J = 8.3$ Hz, 1H), 7.21 – 7.17 (m, 2H), 6.90 – 6.84 (m, 4H), 6.81 (d, $J = 2.4$ Hz, 1H), 6.75 (dd, $J = 8.4, 2.3$ Hz, 1H), 4.17 – 4.07 (m, 4H), 1.83 (p, $J = 6.7$ Hz, 2H), 1.79 – 1.71 (m, 2H), 1.57 – 1.48 (m, 2H), 1.46 – 1.24 (m, 14H), 1.23 – 0.83 (m, 15H), 0.75 (t, $J = 7.2$ Hz, 3H). ^{13}C NMR (101 MHz, DMF- d_7) δ 168.26, 167.09, 160.80, 158.56, 158.40, 158.31, 148.43, 145.28, 139.37, 137.07, 136.97, 136.40, 135.13, 133.34, 132.40, 129.13, 128.10, 127.82, 125.41, 124.84, 122.65, 121.44, 120.92, 107.01, 101.32, 69.27, 68.98, 32.84, 32.73, 30.66, 30.60, 30.28, 30.24, 27.66, 27.06, 23.56, 23.49, 14.74, 14.65. ^{31}P NMR (162 MHz, DMF- d_7) δ -126.16 – -161.31 (m). HRMS (MALDI-TOF): $m/z = 1098.460$ [M] $^+$, (calculated for $[\text{RuN}_5\text{O}_4\text{C}_{66}\text{H}_{70}]^+$: $m/z = 1098.4471$).

[Ru(tpy)(dqp'(CO₂Me))](PF₆) (3a). In a 50 mL round-bottom flask, Ru(dqp)Cl₃ (70 mg, 0.117 mmol, 1 equiv.) and 2:2',6':2''-terpyridine (33 mg, 0.14 mmol, 1.2 equiv.) were dissolved in a mixture of 15 mL DMF and 10 mL ethanol. Then, 5 drops of N-ethylmorpholine was added and the solution was refluxed for 6 hours under nitrogen atmosphere. Afterwards, the solvent was removed with the rotary evaporation and the remaining material was subjected to the column chromatography (SiO₂, acetonitrile-H₂O-KNO₃ (aqueous, saturated) 40:4:1) in which intense mauve fraction was collected. The solvent was evaporated and the remaining solids 30 mL of DCM was added and this mixture was washed three times with 50 mL of saturated aqueous solution of NH₄PF₆ and 2 times with deionized water. The organic phase was then dried with MgSO₄, solids were filtered and the solvent was evaporated to afford the final product as a mauve solid (48 mg, 47 %). ^1H NMR (400 MHz, Acetonitrile- d_3) δ 11.05 (d, $J = 1.8$ Hz, 1H), 8.89 (dd, $J = 4.3, 1.9$ Hz, 1H), 8.60 (dd, $J = 7.6, 1.5$ Hz, 1H), 8.58 – 8.54 (m, 3H), 8.27 (dt, $J = 8.0, 1.1$ Hz, 2H), 8.23 (dd, $J = 8.3, 1.7$ Hz, 1H), 8.15 (t, $J = 8.1$ Hz, 1H), 8.09 (dd, $J = 8.1, 1.4$ Hz, 1H), 7.96 (dd, $J = 8.1, 1.9$ Hz, 1H), 7.92 (t, $J = 7.8$ Hz, 1H), 7.71 (dd, $J = 4.9, 1.6$ Hz, 1H), 7.66 (td, $J = 8.1, 1.5$ Hz, 2H), 7.35 (ddd, $J = 5.6, 1.6, 0.8$ Hz, 2H), 7.25 (dd, $J = 8.1, 4.3$ Hz, 1H), 7.11 (dd, $J = 8.2, 4.9$ Hz, 1H), 7.05 (d, $J = 8.2$ Hz, 1H), 6.93 (ddd, $J = 7.2, 5.7, 1.4$ Hz, 2H), 6.22 (d, $J = 8.2$ Hz, 1H), 4.14 (s, 3H). ^{13}C NMR (101 MHz, Acetonitrile- d_3) δ 202.01, 167.82, 167.21, 157.97, 156.53, 156.39, 153.41, 151.98, 149.54, 147.51, 144.55, 139.61, 139.33, 137.90, 137.79, 136.56, 136.32, 135.29, 133.74, 133.24, 132.15, 129.97, 128.66, 127.67, 127.56, 125.72, 124.62, 124.09, 123.83, 123.33, 122.80, 119.36, 53.56. ^{31}P NMR (162 MHz, Acetonitrile- d_3) δ -124.42 – -170.27 (m). HRMS (ESI): $m/z = 725.127$ [M] $^+$, (calculated for $[\text{RuN}_6\text{O}_2\text{C}_{40}\text{H}_{27}]^+$: $m/z = 725.1239$).

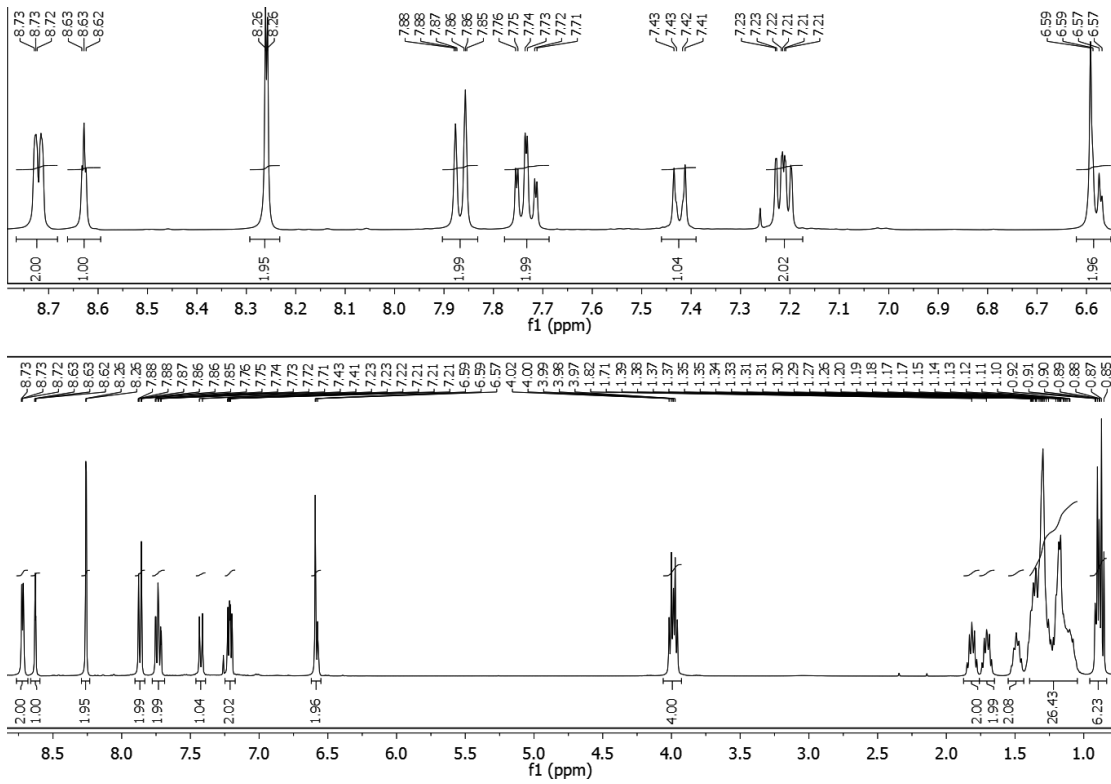


Figure 8.99. ^1H NMR spectrum of L1 *chloroform-d3*.

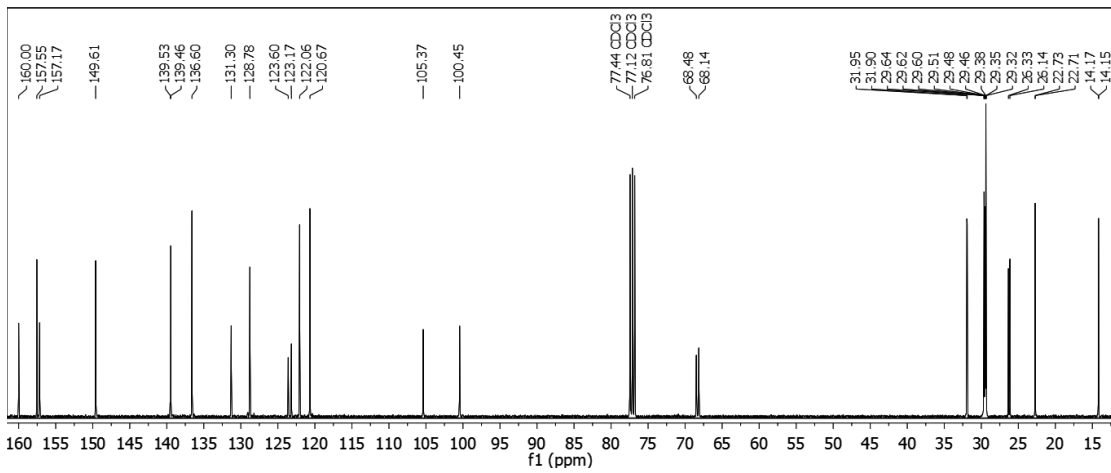
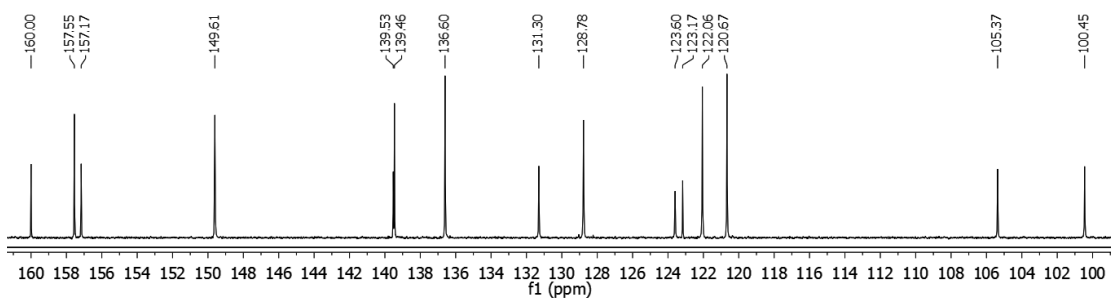
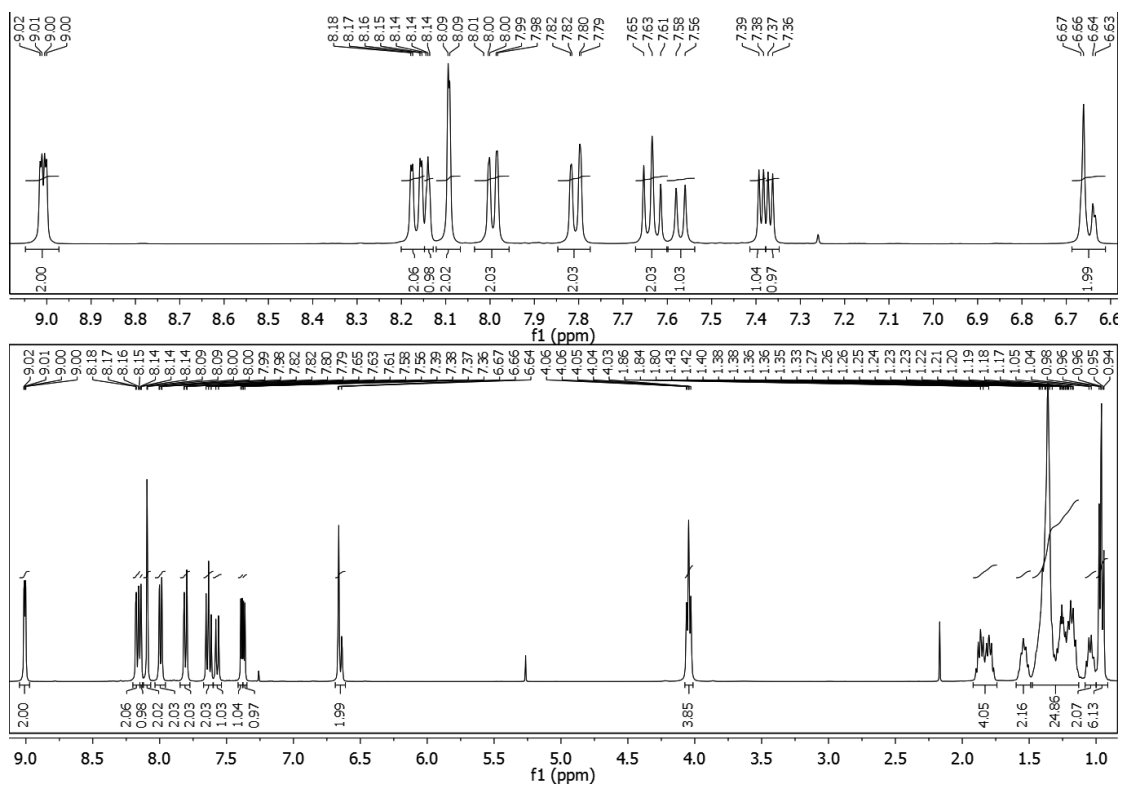
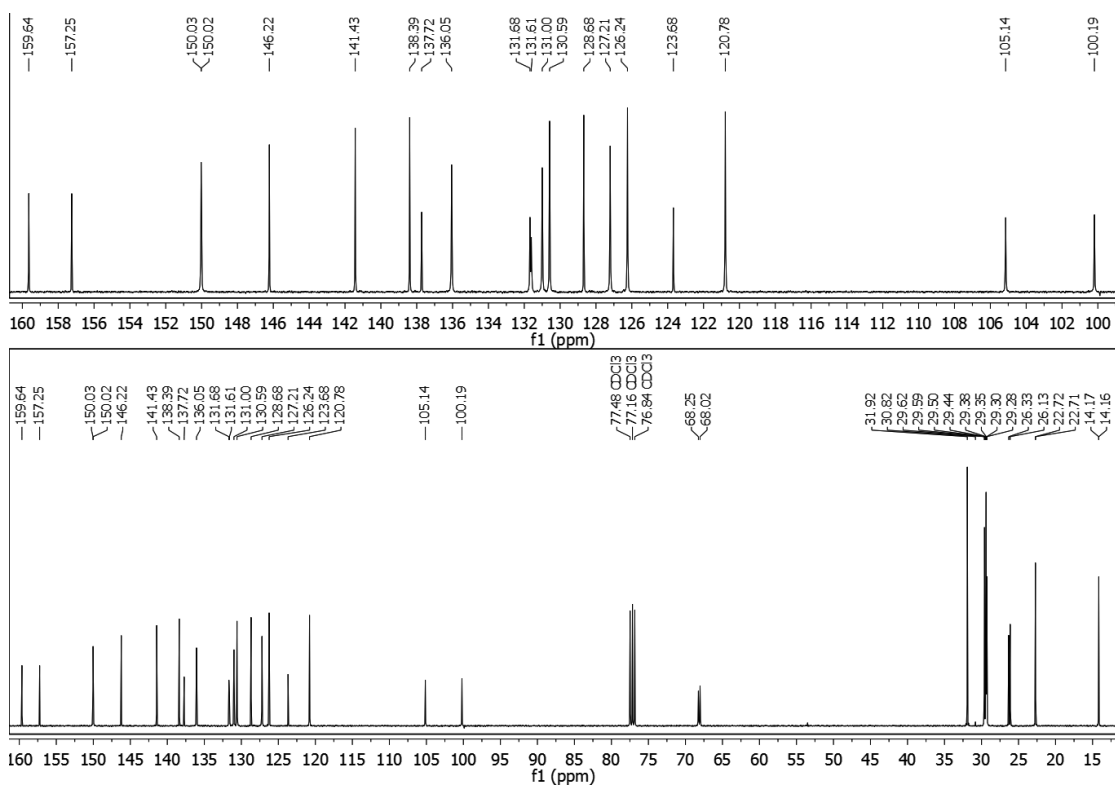
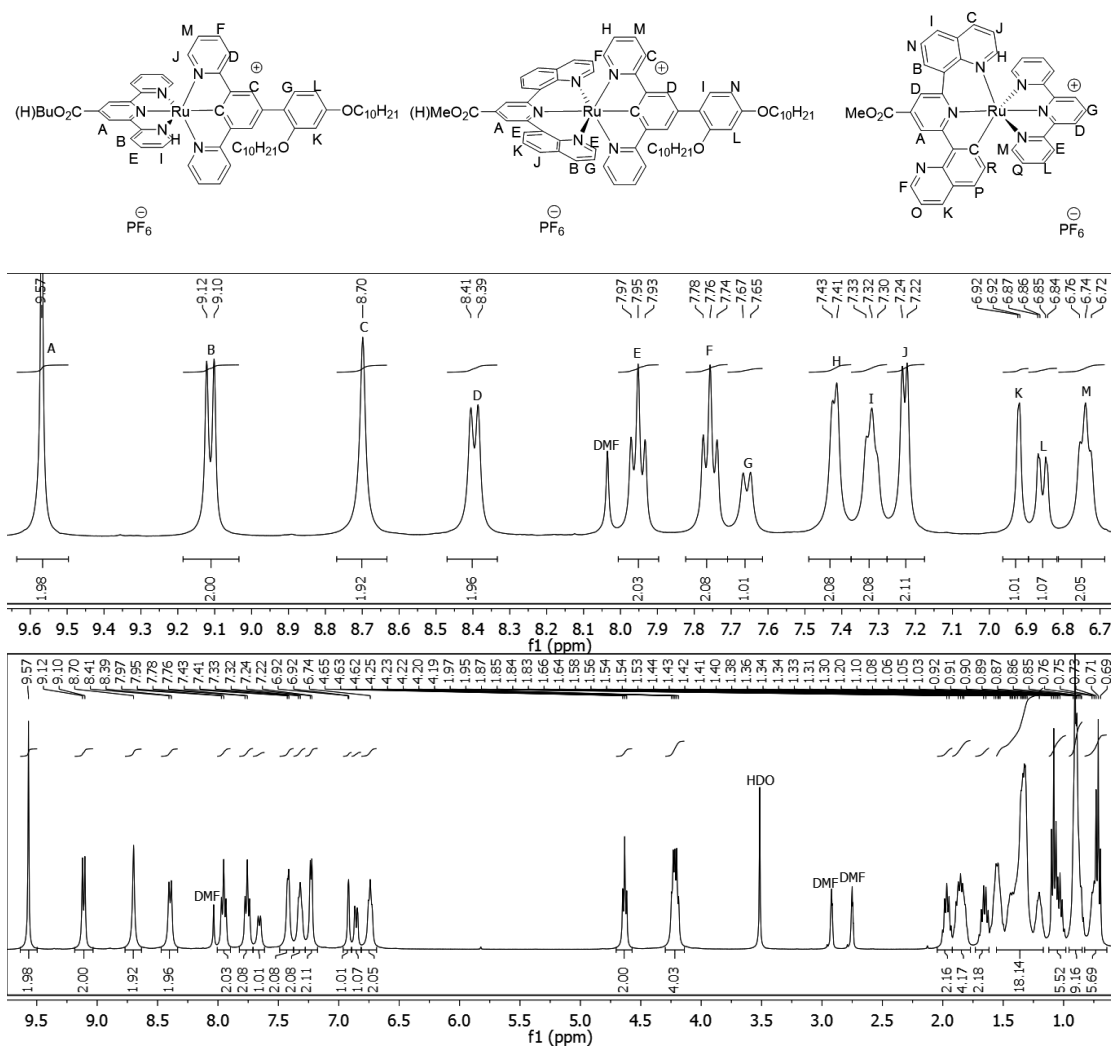
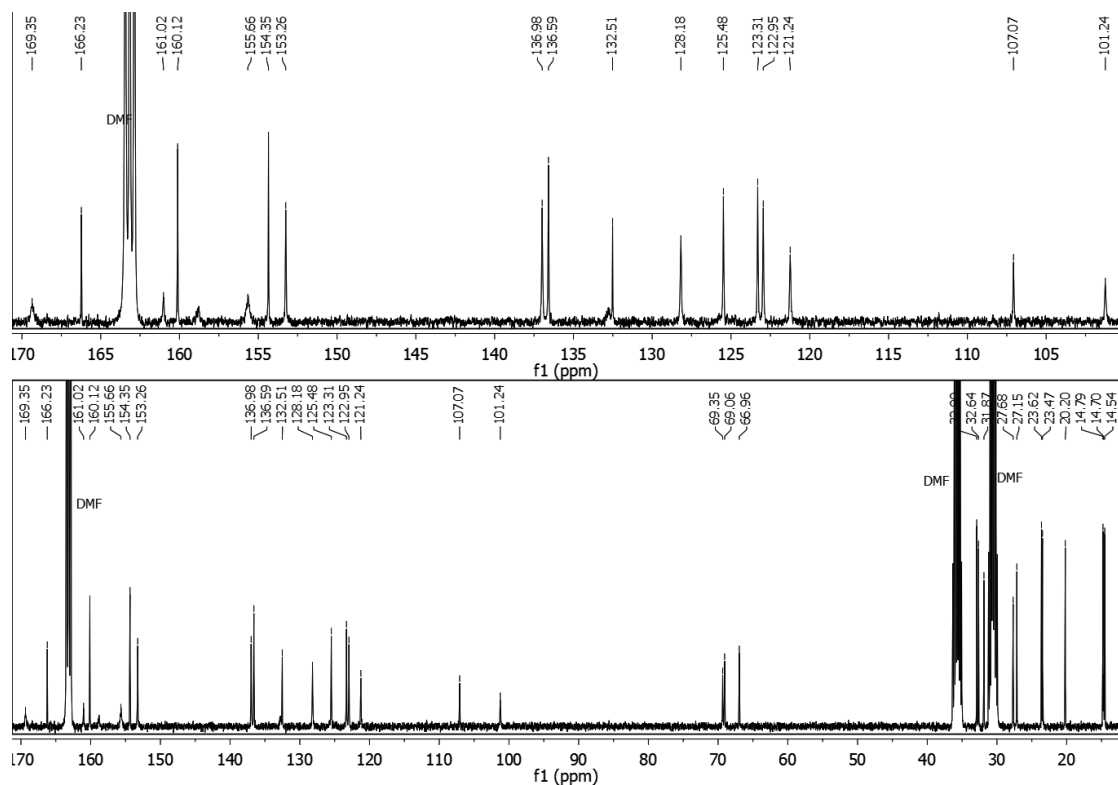
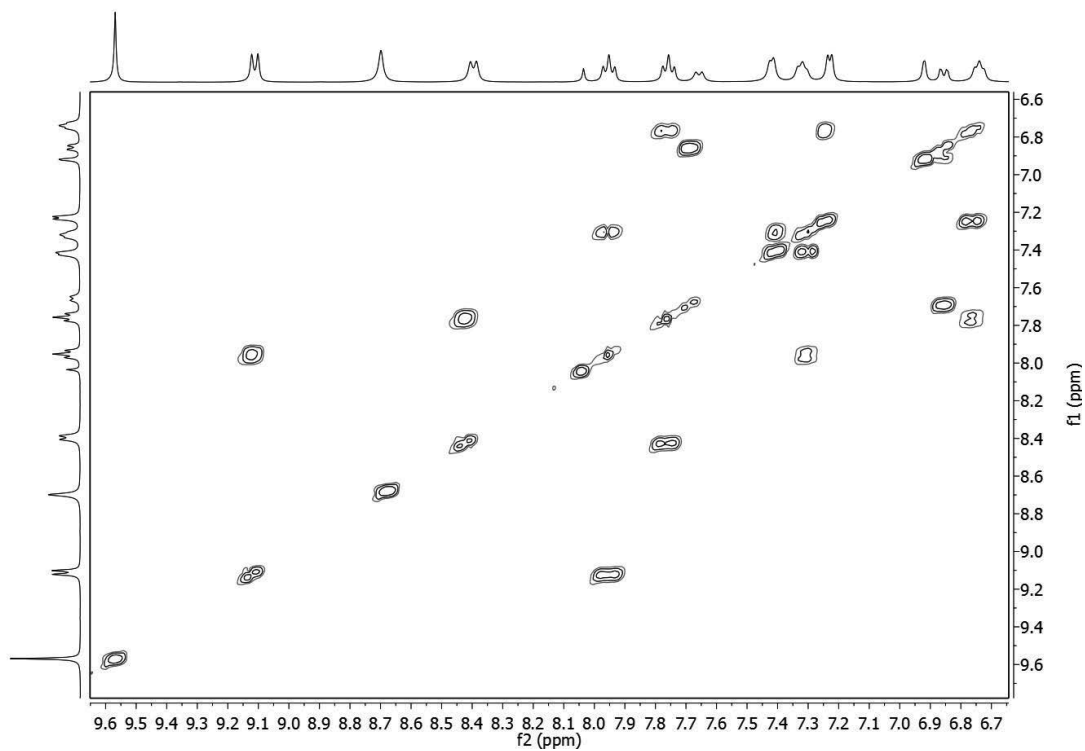
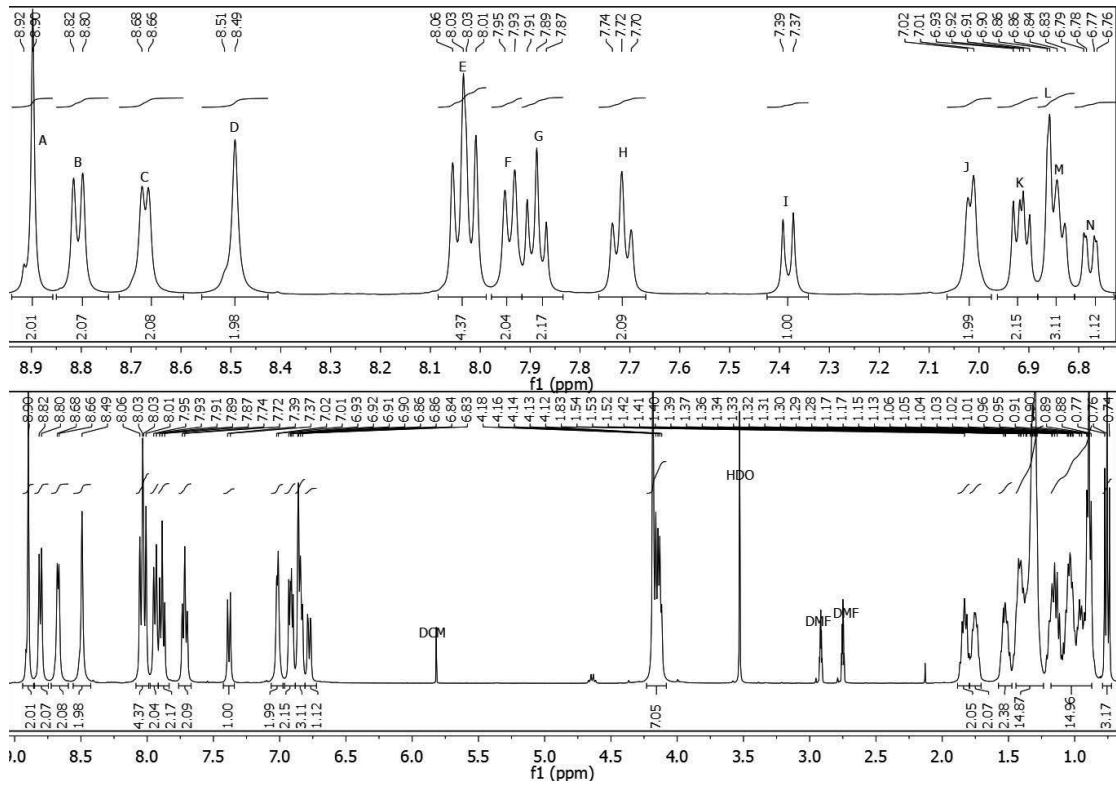
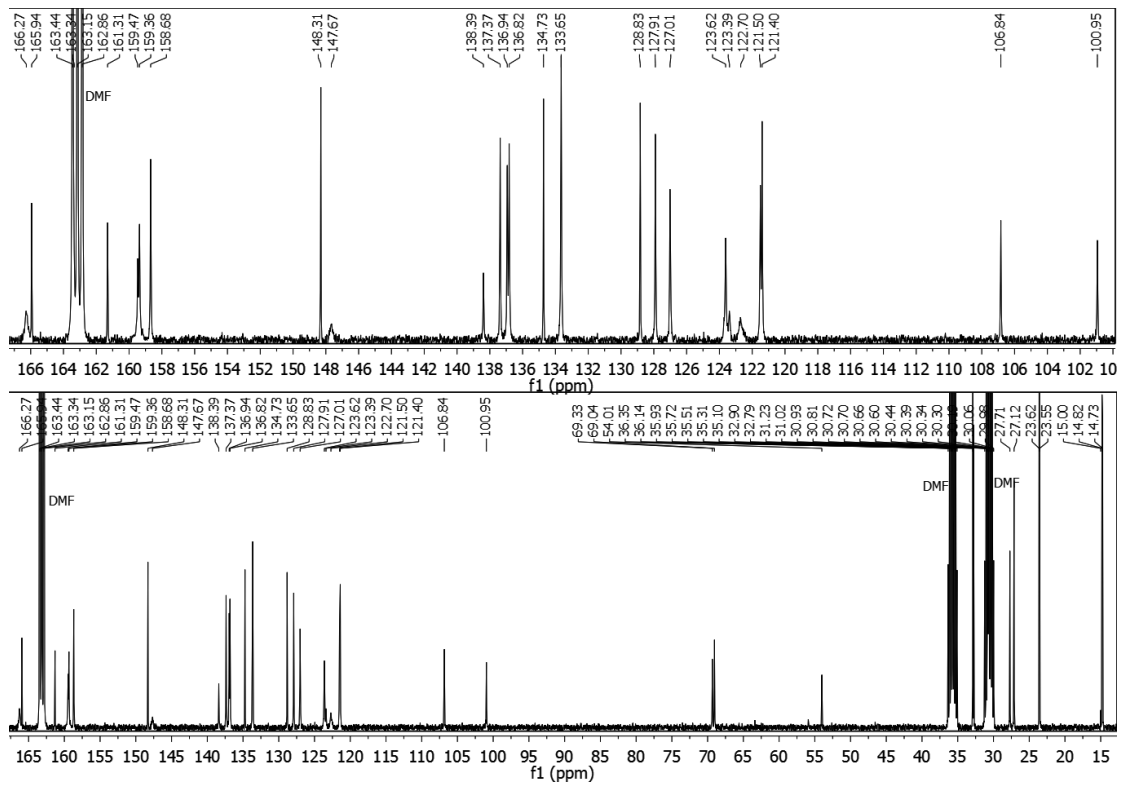


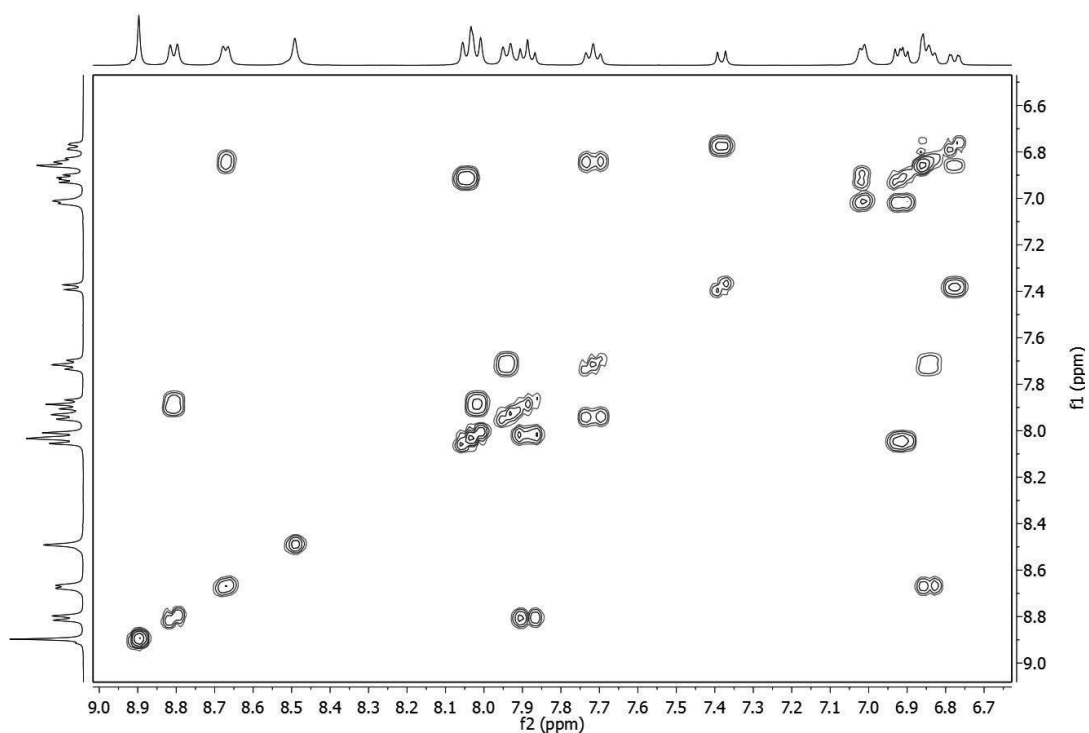
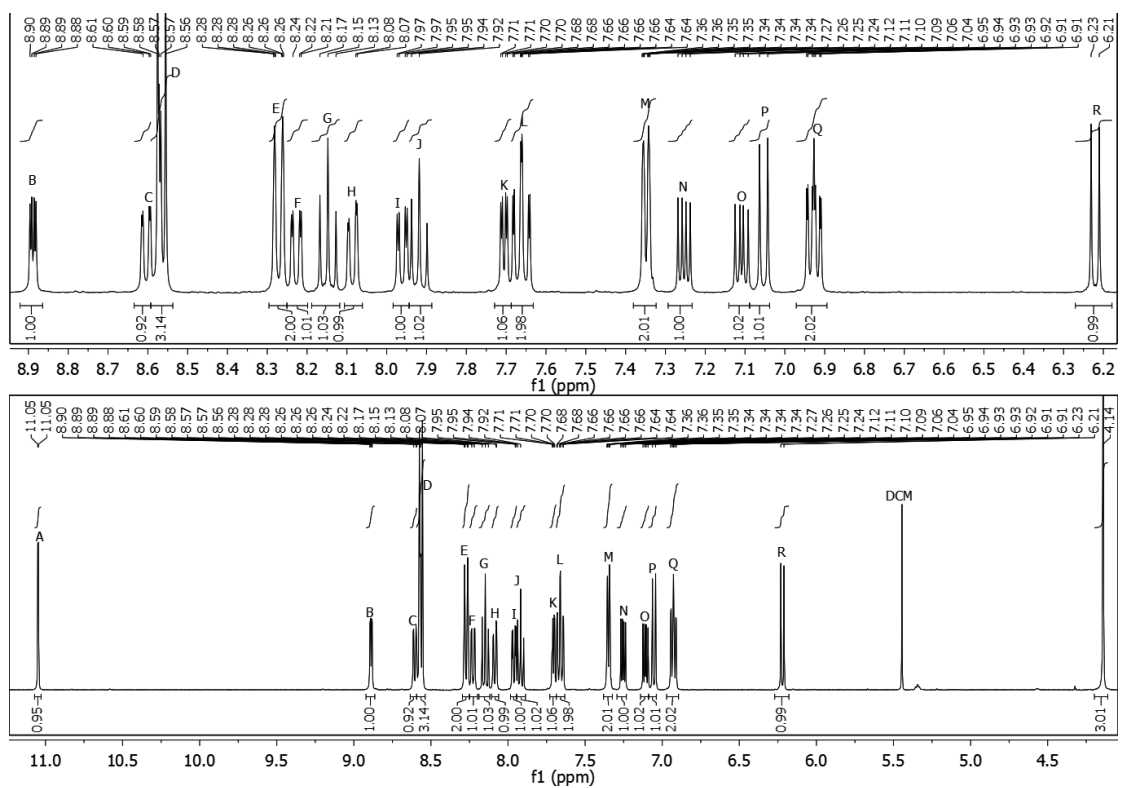
Figure 8.100. ^{13}C NMR spectrum of L1 *chloroform-d3*.

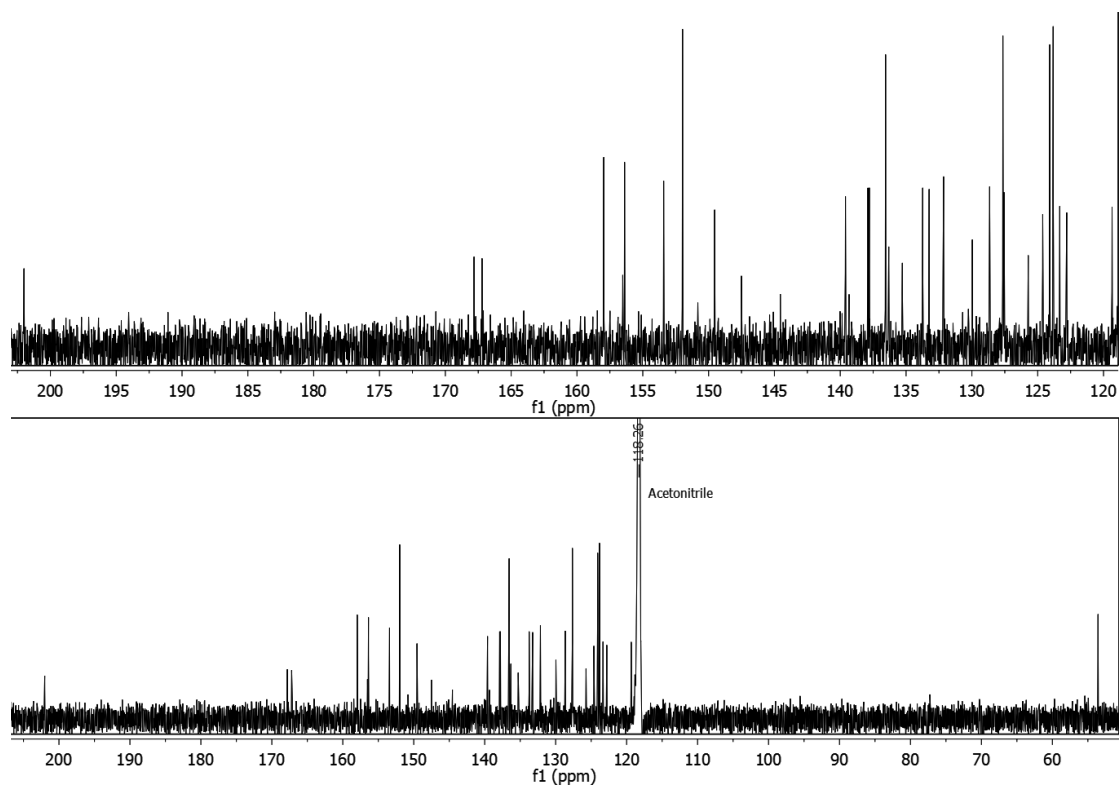
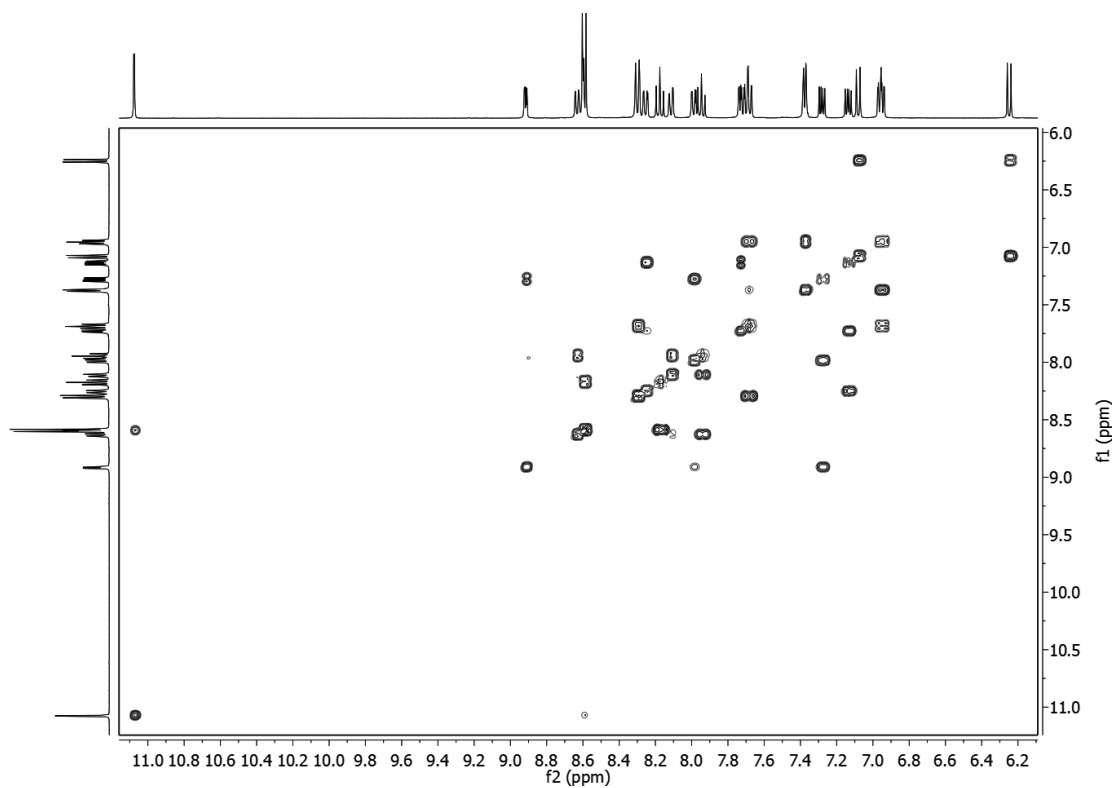
Figure 8.101. ^1H NMR spectrum of L2 *chloroform-d3*.Figure 8.102. ^{13}C NMR spectrum of L2 *chloroform-d3*.

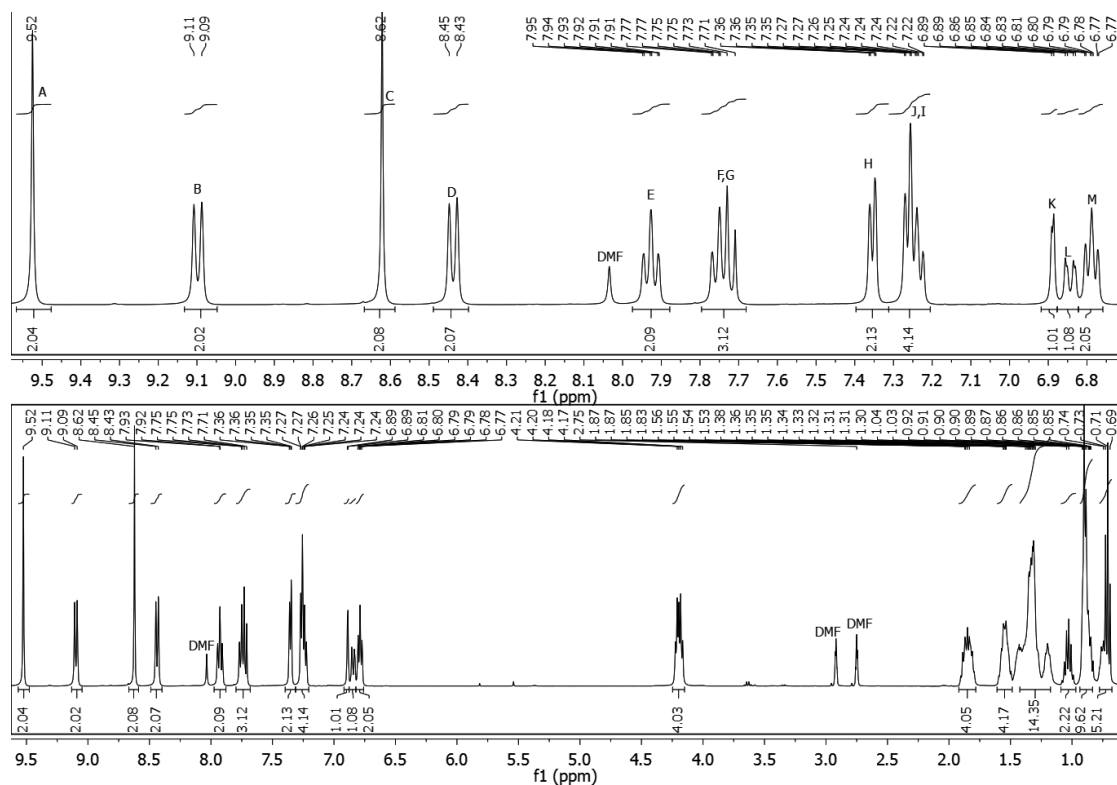
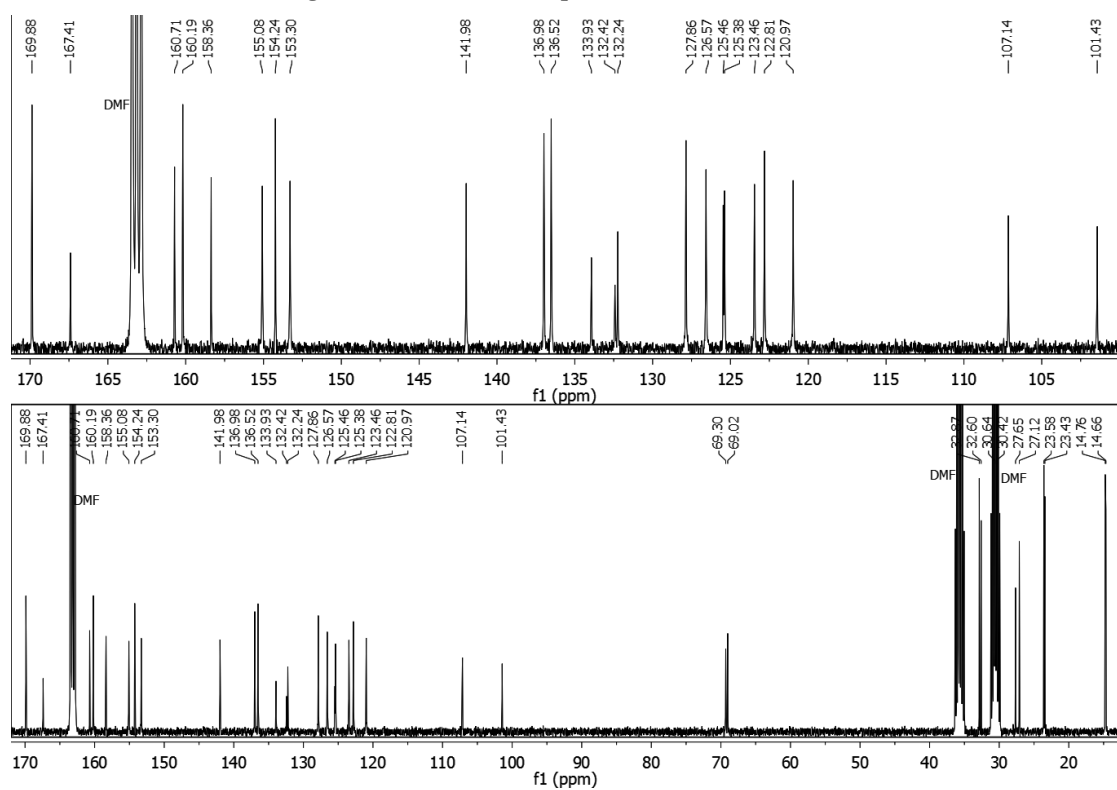
Figure 8.103. ^1H NMR spectrum of 1a in $\text{DMF-}d_7$.

Figure 8.104. ^{13}C NMR spectrum of 1a in DMF-d_7 .Figure 8.105. ^1H - ^1H COSY NMR spectrum of 1a in DMF-d_7 (aromatic region).

Figure 8.106. ^1H NMR spectrum of **2a** in $\text{DMF-}d_7$.Figure 8.107. ^{13}C NMR spectrum of **2a** in $\text{DMF-}d_7$.

Figure 8.108. ^1H - ^1H COSY NMR spectrum of 2a in DMF-d_7 (aromatic region).Figure 8.109. ^1H NMR spectrum of 3a in acetonitrile-d_3 .

Figure 8.110. ^{13}C NMR spectrum of 3a in *acetonitrile-d3*.Figure 8.111. ^1H - ^1H COSY NMR spectrum of 3a in *acetonitrile-d3* (aromatic region).

Figure 8.112. ^1H NMR spectrum of 1 in $\text{DMF-}d_7$.Figure 8.113. ^{13}C NMR spectrum of 1 in $\text{DMF-}d_7$.

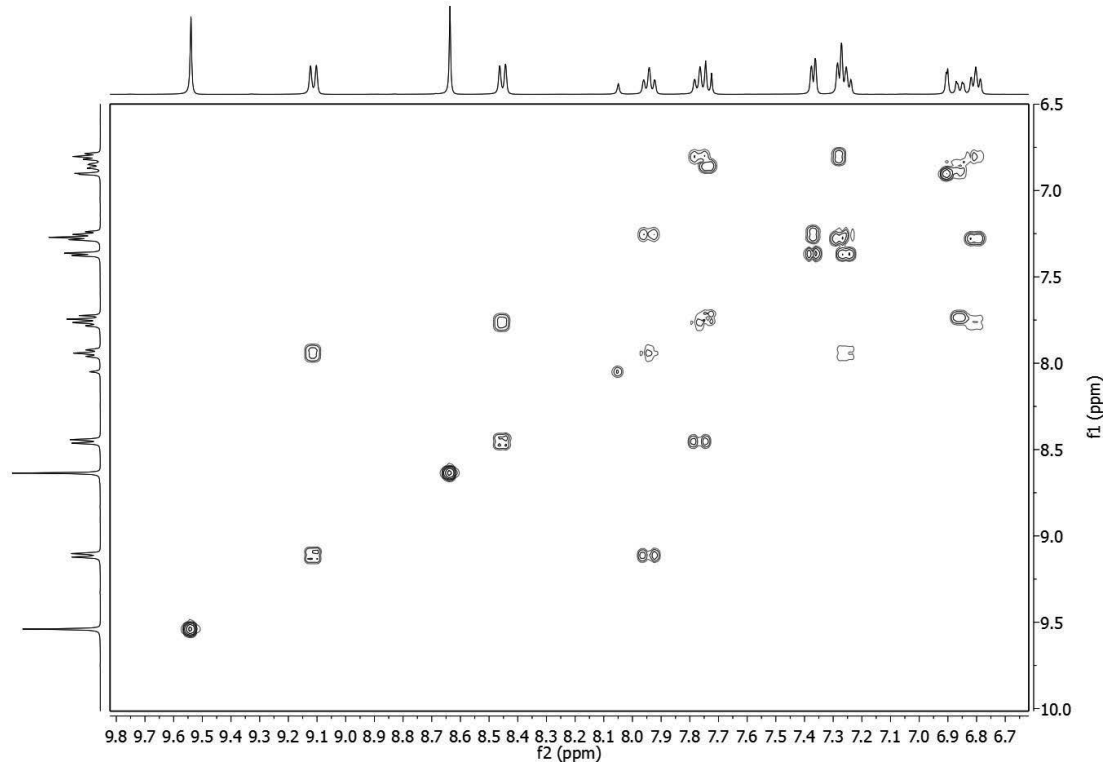


Figure 8.114. ^1H - ^1H COSY NMR spectrum of 1 in DMF-d_7 (aromatic region).

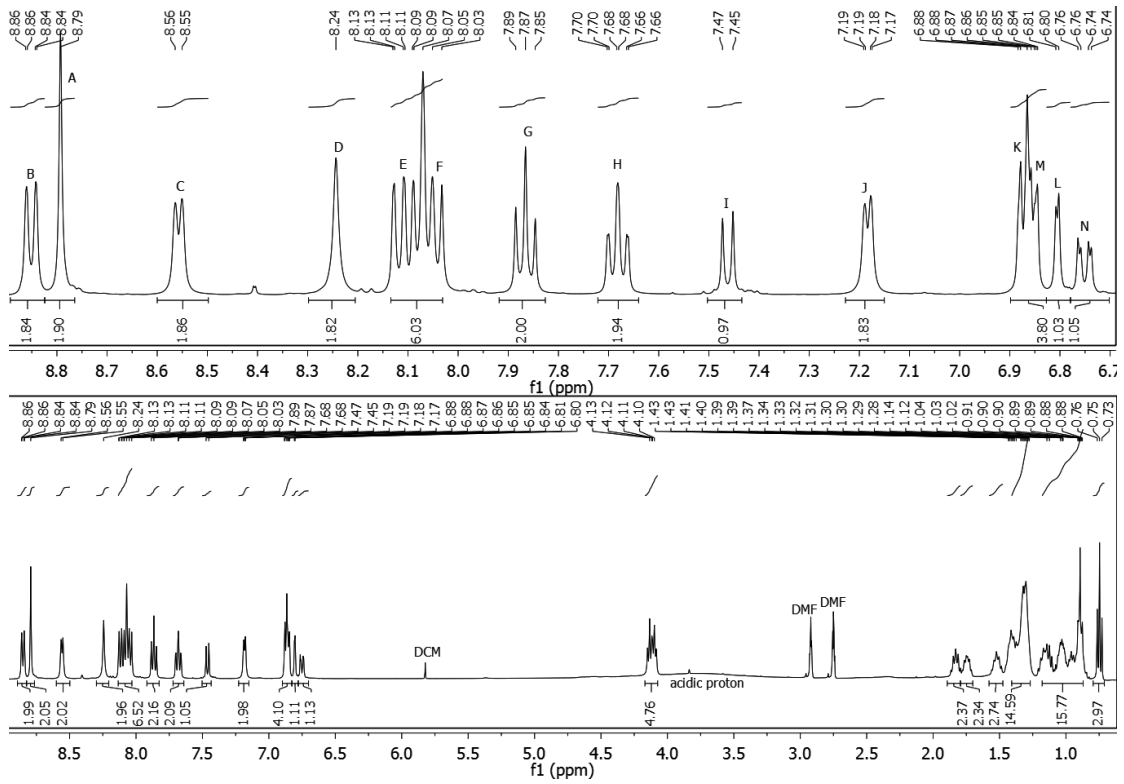
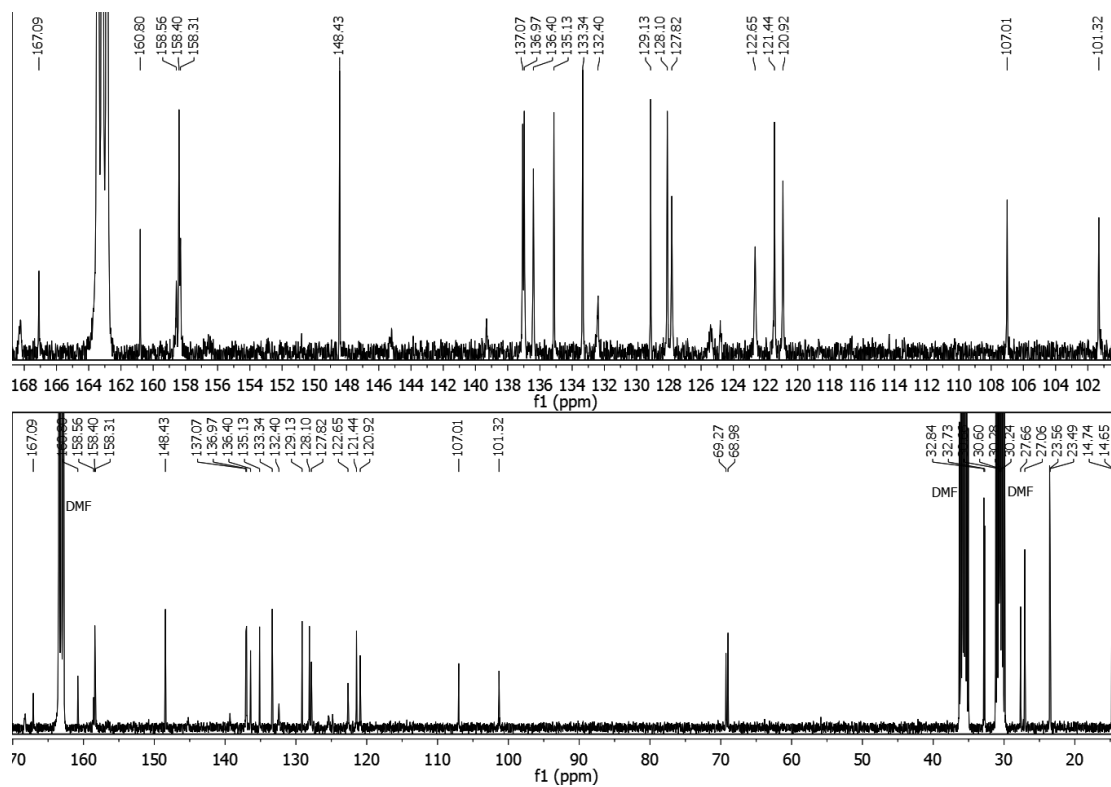
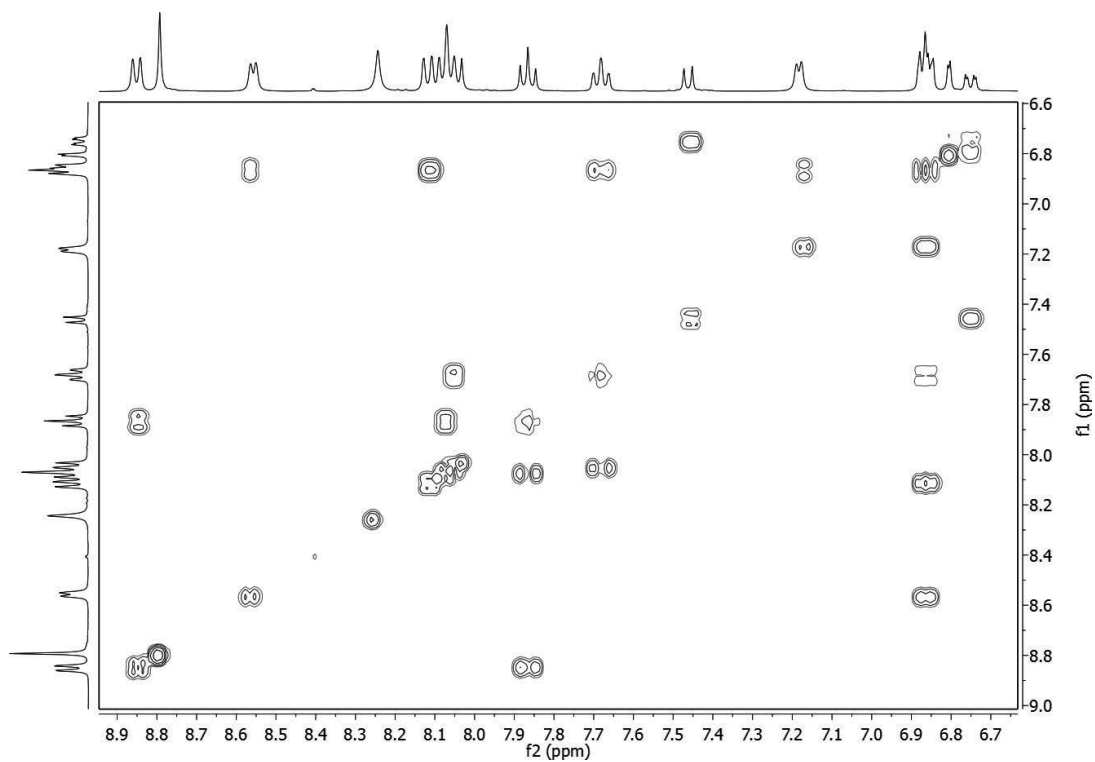


Figure 8.115. ^1H NMR spectrum of 2 in DMF-d_7 .

Figure 8.116. ^{13}C NMR spectrum of 2 in DMF-d_7 .Figure 8.117. ^1H - ^1H COSY NMR spectrum of 2 in DMF-d_7 (aromatic region).

8.4.2 X-ray Crystallography

The data collection was performed 100 at K on a Bruker D8 Venture diffractometer using Mo K α radiation. ($\lambda=0.71069$ nm) Data reduction and absorption correction were done with SAINT and SADABS integrated in the APEX 3 software package. The structure solution was carried out with SHELXS and the refinement with SHELXL-2014 in the WINGX environment. All atoms except hydrogens were refined anisotropically. Hydrogen atoms were inserted on geometrically optimized positions and refined using the riding model. Structure drawings were made with the program Mercury 3.7.

Table 8.11. Summary of the crystallographic parameters for 3a.

Compound	3a
Formula	C ₄₂ H ₃₁ Cl ₄ F ₆ N ₆ O ₂ PRu
Crystal system	Triclinic
Space group	<i>P</i> -1
Temperature / K	100(2)
Lattice constants / Å and °	<i>a</i> = 8.611(3) <i>b</i> = 13.775(6) <i>c</i> = 18.143(7) α = 105.889(15) β = 94.368(13) γ = 91.304(14)
Volume / Å ³	2061.8(14)
Z	2
D _{calculated} / g·cm ⁻³	1.67
Radiation	Mo-K α (λ = 0.71069 Å)
Crystal habit	Green plate
θ range / °	2.18 – 25.00
Min. / max. <i>h k l</i>	-10 ≤ <i>h</i> ≤ 10 -17 ≤ <i>k</i> ≤ 17 -22 ≤ <i>l</i> ≤ 22
Reflections, measured / independent	39817 / 8055
Refined parameters / restraints	561 / 18
R1 [<i>I</i> > 2 σ (<i>I</i>)]	0.1196
R _{sym}	0.0449
Max. / min. Residual Density / e ⁻ /Å ³	4.86 and -1.11

8.4.3 Electrochemistry

Cyclic voltammograms of final complexes were measured in 0.1 M solution of NBu₄PF₆ in DMF under argon atmosphere with a Biologic S-200 station. Glassy carbon working electrode, platinum wire reference and counter electrodes were used. Measurements at 100 mV/s were conducted with and without an internal standard. Ferrocene was used as the internal standard and its oxidation potential was fixed at 0.63 V versus NHE. Corrected cyclic voltammograms without ferrocene couple are presented in this work. To conduct the Randles-Sevcik analysis, in the same setup the cyclic voltammograms were collected at 20, 50, 100, 200, 400, 500, 750 and 1000 mV/s scan rates. Then the current maximum values were plotted versus the square root of the scan rate.

References

- (1) IEA. Key World Energy Statistics 2016. **2016**, 80 DOI: 10.1787/9789264039537-en.
- (2) Kahn, B. We just breached the 410 parts per million threshold <https://www.climatecentral.org/news/we-just-breached-the-410-parts-per-million-threshold-21372> (accessed Sep 15, 2017).
- (3) McNeil, B. I.; Sasse, T. P. Future Ocean Hypercapnia Driven by Anthropogenic Amplification of the Natural CO₂ Cycle. *Nature* **2016**, *529* (7586), 383–386 DOI: 10.1038/nature16156.
- (4) Sabine, C. L. The Oceanic Sink for Anthropogenic CO₂. *Science* **2004**, *305* (5682), 367–371 DOI: 10.1126/science.1097403.
- (5) Orr, J. C.; Fabry, V. J.; Aumont, O.; Bopp, L.; Doney, S. C.; Feely, R. A.; Gnanadesikan, A.; Gruber, N.; Ishida, A.; Joos, F.; Key, R. M.; Lindsay, K.; Maier-Reimer, E.; Matear, R.; Monfray, P.; Mouchet, A.; Najjar, R. G.; Plattner, G.-K.; Rodgers, K. B.; Sabine, C. L.; Sarmiento, J. L.; Schlitzer, R.; Slater, R. D.; Totterdell, I. J.; Weirig, M.-F.; Yamanaka, Y.; Yool, A. Anthropogenic Ocean Acidification over the Twenty-First Century and Its Impact on Calcifying Organisms. *Nature* **2005**, *437* (7059), 681–686 DOI: 10.1038/nature04095.
- (6) Shaw, E. C.; McNeil, B. I.; Tilbrook, B.; Matear, R.; Bates, M. L. Anthropogenic Changes to Seawater Buffer Capacity Combined with Natural Reef Metabolism Induce Extreme Future Coral Reef CO₂ Conditions. *Glob. Chang. Biol.* **2013**, *19* (5), 1632–1641 DOI: 10.1111/gcb.12154.
- (7) Lewis, N. S.; Nocera, D. G. Powering the Planet: Chemical Challenges in Solar Energy Utilization. *Proc. Natl. Acad. Sci.* **2006**, *103* (43), 15729–15735 DOI: 10.1073/pnas.0603395103.
- (8) Gray, H. B. Powering the Planet with Solar Fuel. *Nat. Chem.* **2009**, *1* (1), 7 DOI: 10.1038/nchem.141.
- (9) World Nuclear Association. Nuclear Power Today | Nuclear Energy - World Nuclear Association <http://www.world-nuclear.org/information-library/current-and-future-generation/nuclear-power-in-the-world-today.aspx> (accessed Sep 15, 2017).
- (10) GWEC. Global Wind Report 2015 | Gwec. *Wind energy Technol.* **2016**, 75.
- (11) Becquerel, A. E. Recherches Sur Les Effets de La Radiation Chimique de La Lumiere Solaire Au Moyen Des Courants Electriques. *Comptes Rendus L'Academie des Sci.* **1839**, *9*, 145–149.
- (12) Becquerel, E. Mémoire Sur Les Effets Électriques Produits Sous L'influence Des Rayons Solaires. *Ann. der Physik und Chemie* **1841**, *54*, 35–42 DOI: 10.1017/CBO9781107415324.004.
- (13) Smith, W. Effect of Light on Selenium During the Passage of An Electric Current. *Nature*. 1873, pp 303–303.
- (14) Adams, W. G.; Day, R. E. The Action of Light on Selenium. [Abstract]. *Proc. R. Soc. London* **1876**, *25* (ArticleType: research-article / Full publication date: 1876-1877 / Copyright © 1876 The Royal Society), 113–117 DOI: 10.2307/113462.

-
- (15) Fritts, C. E. On a New Form of Selenium Cell, and Some Electrical Discoveries Made by Its Use. *Am. J. Sci.* **1883**, *s3-26* (156), 465–472 DOI: 10.2475/ajs.s3-26.156.465.
- (16) Ohl, R. Light-Sensitive Electric Device. US 2402662 A, 1941.
- (17) Lashkaryov, V. E. Investigations of a Barrier Layer by the Thermoprobe Method. *Izv. Akad. Nauk SSSR, Ser. Fiz.* **1941**, *5* (4–5), 442–446.
- (18) Chapin, D. M.; Fuller, C. S.; Pearson, G. L. A New Silicon P-N Junction Photocell for Converting Solar Radiation into Electrical Power [3]. *Journal of Applied Physics*. American Institute of Physics May 14, 1954, pp 676–677.
- (19) Shockley, W.; Queisser, H. J. Detailed Balance Limit of Efficiency of P-N Junction Solar Cells. *J. Appl. Phys.* **1961**, *32* (3), 510–519 DOI: 10.1063/1.1736034.
- (20) Yoshikawa, K.; Kawasaki, H.; Yoshida, W.; Irie, T.; Konishi, K.; Nakano, K.; Uto, T.; Adachi, D.; Kanematsu, M.; Uzu, H.; Yamamoto, K. Silicon Heterojunction Solar Cell with Interdigitated Back Contacts for a Photoconversion Efficiency over 26%. *Nat. Energy* **2017**, *2* (5), 17032 DOI: 10.1038/nenergy.2017.32.
- (21) Alferov, Z. I. Nobel Lecture: The Double Heterostructure Concept and Its Applications in Physics, Electronics, and Technology. *Rev. Mod. Phys.* **2001**, *73* (3), 767–782 DOI: 10.1103/RevModPhys.73.767.
- (22) Green, M. A.; Emery, K.; Hishikawa, Y.; Warta, W.; Dunlop, E. D. Solar Cell Efficiency Tables (Version 46). *Progress in Photovoltaics: Research and Applications*. July 1, 2015, pp 805–812.
- (23) West, W. First Hundred Years of Spectral Sensitization. *Proc. Vogel. Sent. Symp. Photogr. Sci. Eng* **1974**, *18*, 35–48.
- (24) Moser, J. Notiz Über Verstärkung Photoelektrischer Ströme Durch Optische Sensibilisierung. *Monatsb. Chem.* **1887**, *8* (1), 373 DOI: 10.1007/BF01510059.
- (25) Namba, S.; Hishiki, Y. Color Sensitization of Zinc Oxide with Cyanine Dyes1. *J. Phys. Chem.* **1965**, *69* (3), 774–779 DOI: 10.1021/j100887a010.
- (26) Gerischer, H.; Tributsch, H. Elektrochemische Untersuchungen Zur Spektralen Sensibilisierung von ZnO-Einkristallen. *Ber. Bunsen-Ges. Phys. Chem.* **1968**, *72* (1), 437–445 DOI: 10.1002/bbpc.196800013.
- (27) Hauffe, K.; Danzmann, H. J.; Pusch, H.; Range, J.; Volz, H. New Experiments on the Sensitization of Zinc Oxide by Means of the Electrochemical Cell Technique. *J. Electrochem. Soc.* **1970**, *117* (8), 993–999 DOI: 10.1149/1.2407745.
- (28) Desilvestro, J.; Grätzel, M.; Kavan, L.; Moser, J.; Augustynski, J. Highly Efficient Sensitization of Titanium Dioxide. *J. Am. Chem. Soc.* **1985**, *107* (10), 2988–2990 DOI: 10.1021/ja00296a035.
- (29) O'Regan, B.; Grätzel, M. A Low-Cost, High-Efficiency Solar Cell Based on Dye-Sensitized Colloidal TiO₂ Films. *Nature* **1991**, *353* (6346), 737–740 DOI: 10.1038/353737a0.
- (30) Boschloo, G.; Hagfeldt, A. Characteristics of the Iodide/Triiodide Redox Mediator in Dye-Sensitized Solar Cells. *Acc. Chem. Res.* **2009**, *42* (11), 1819–1826 DOI: 10.1021/ar900138m.
- (31) Hagfeldt, A.; Boschloo, G.; Sun, L.; Kloo, L.; Pettersson, H. Dye-Sensitized Solar Cells. *Chem. Rev.* **2010**, *110* (11), 6595–6663 DOI: 10.1021/cr900356p.

- (32) O'Regan, B. C.; Durrant, J. R. Kinetic and Energetic Paradigms for Dye-Sensitized Solar Cells: Moving from the Ideal to the Real. *Acc. Chem. Res.* **2009**, *42* (11), 1799–1808 DOI: 10.1021/ar900145z.
- (33) Ramakrishna, G.; Jose, D. A.; Kumar, D. K.; Das, A.; Palit, D. K.; Ghosh, H. N. Strongly Coupled Ruthenium-Polypyridyl Complexes for Efficient Electron Injection in Dye-Sensitized Semiconductor Nanoparticles. *J. Phys. Chem. B* **2005**, *109* (32), 15445–15453 DOI: 10.1021/jp051285a.
- (34) Kuang, D.; Ito, S.; Wenger, B.; Klein, C.; Moser, J. E.; Humphry-Baker, R.; Zakeeruddin, S. M.; Grätzel, M. High Molar Extinction Coefficient Heteroleptic Ruthenium Complexes for Thin Film Dye-Sensitized Solar Cells. *J. Am. Chem. Soc.* **2006**, *128* (12), 4146–4154 DOI: 10.1021/ja058540p.
- (35) Benkő, G.; Kallioinen, J.; Korppi-Tommola, J. E. I.; Yartsev, A. P.; Sundström, V. Photoinduced Ultrafast Dye-to-Semiconductor Electron Injection from Nonthermalized and Thermalized Donor States. *J. Am. Chem. Soc.* **2002**, *124* (3), 489–493 DOI: 10.1021/ja016561n.
- (36) Asbury, J. B.; Ellingson, R. J.; Ghosh, H. N.; Ferrere, S.; Nozik, A. J.; Lian, T. Femtosecond IR Study of Excited-State Relaxation and Electron-Injection Dynamics of Ru(dcbpy)₂(NCS)₂ in Solution and on Nanocrystalline TiO₂ and Al₂O₃ Thin Films. *J. Phys. Chem. B* **1999**, *103* (16), 3110–3119 DOI: 10.1021/jp983915x.
- (37) Koops, S. E.; O'Regan, B. C.; Barnes, P. R. F.; Durrant, J. R. Parameters Influencing the Efficiency of Electron Injection in Dye-Sensitized Solar Cells. *J. Am. Chem. Soc.* **2009**, *131* (13), 4808–4818 DOI: 10.1021/ja8091278.
- (38) Kallioinen, J.; Benkő, G.; Sundström, V.; Korppi-Tommola, J. E. I.; Yartsev, A. P. Electron Transfer from the Singlet and Triplet Excited States of Ru(dcbpy)₂(NCS)₂ into Nanocrystalline TiO₂ Thin Films. *J. Phys. Chem. B* **2002**, *106* (17), 4396–4404 DOI: 10.1021/jp0143443.
- (39) Evans, M. G.; Polanyi, M. Some Applications of the Transition State Method to the Calculation of Reaction Velocities, Especially in Solution. *Trans. Faraday Soc.* **1935**, *31* (0), 875 DOI: 10.1039/tf9353100875.
- (40) Eyring, H. The Activated Complex in Chemical Reactions. *J. Chem. Phys.* **1935**, *3* (2), 107–115 DOI: 10.1063/1.1749604.
- (41) Anderson, N. A.; Lian, T. Ultrafast Electron Injection from Metal Polypyridyl Complexes to Metal-Oxide Nanocrystalline Thin Films. *Coordination Chemistry Reviews*. Elsevier July 1, 2004, pp 1231–1246.
- (42) Mori, S. N.; Kubo, W.; Kanzaki, T.; Masaki, N.; Wada, Y.; Yanagida, S. Investigation of the Effect of Alkyl Chain Length on Charge Transfer at TiO₂/dye/electrolyte Interface. *J. Phys. Chem. C* **2007**, *111* (8), 3522–3527 DOI: 10.1021/jp066261y.
- (43) Kuciauskas, D.; Freund, M. S.; Gray, H. B.; Winkler, J. R.; Lewis, N. S. Electron Transfer Dynamics in Nanocrystalline Titanium Dioxide Solar Cells Sensitized with Ruthenium or Osmium Polypyridyl Complexes. *J. Phys. Chem. B* **2001**, *105* (2), 392–403 DOI: 10.1021/jp002545l.
- (44) Pelet, S.; Moser, J.-E.; Grätzel, M. Cooperative Effect of Adsorbed Cations and Iodide on the Interception of Back Electron Transfer in the Dye Sensitization of Nanocrystalline TiO₂. *J. Phys. Chem. C* **2000**, *104* (8), 1791–1795 DOI: 10.1021/jp9934477.

- (45) Mosconi, E.; Yum, J.-H.; Kessler, F.; Gómez García, C. J.; Zuccaccia, C.; Cinti, A.; Nazeeruddin, M. K.; Grätzel, M.; De Angelis, F. Cobalt Electrolyte/Dye Interactions in Dye-Sensitized Solar Cells: A Combined Computational and Experimental Study. *J. Am. Chem. Soc.* **2012**, *134* (47), 19438–19453 DOI: 10.1021/ja3079016.
- (46) Cong, J.; Kinschel, D.; Daniel, Q.; Safdari, M.; Gabrielsson, E.; Chen, H.; Svensson, P. H.; Sun, L.; Kloo, L. Bis(1,1-bis(2-Pyridyl)ethane)copper(I / II) as an Efficient Redox Couple for Liquid Dye-Sensitized Solar Cells. *J. Mater. Chem. A* **2016**, *4* (38), 14550–14554 DOI: 10.1039/C6TA06782D.
- (47) Li, J.; Yang, X.; Yu, Z.; Gurzadyan, G. G.; Cheng, M.; Zhang, F.; Cong, J.; Wang, W.; Wang, H.; Li, X.; Kloo, L.; Wang, M.; Sun, L. Efficient Dye-Sensitized Solar Cells with [copper(6,6'-Dimethyl-2,2'-Bipyridine) 2]^{2+/1+} Redox Shuttle. *RSC Adv.* **2017**, *7* (8), 4611–4615 DOI: 10.1039/C6RA25676G.
- (48) Peter, L. “Sticky Electrons” transport and Interfacial Transfer of Electrons in the Dye-Sensitized Solar Cell. *Acc. Chem. Res.* **2009**, *42* (11), 1839–1847 DOI: 10.1021/ar900143m.
- (49) Peter, L. M. Dye-Sensitized Nanocrystalline Solar Cells. *Phys. Chem. Chem. Phys.* **2007**, *9* (21), 2630–2642 DOI: 10.1039/b617073k.
- (50) Bisquert, J.; Fabregat-Santiago, F.; Mora-Seró, I.; Garcia-Belmonte, G.; Giménez, S. Electron Lifetime in Dye-Sensitized Solar Cells: Theory and Interpretation of Measurements. *J. Phys. Chem. C* **2009**, *113* (40), 17278–17290 DOI: 10.1021/jp9037649.
- (51) Haque, S. A.; Palomares, E.; Cho, B. M.; Green, A. N. M.; Hirata, N.; Klug, D. R.; Durrant, J. R. Charge Separation versus Recombination in Dye-Sensitized Nanocrystalline Solar Cells: The Minimization of Kinetic Redundancy. *J. Am. Chem. Soc.* **2005**, *127* (10), 3455–3462 DOI: 10.1021/ja0460357.
- (52) Fabregat-Santiago, F.; Bisquert, J.; Garcia-Belmonte, G.; Boschloo, G.; Hagfeldt, A. Influence of Electrolyte in Transport and Recombination in Dye-Sensitized Solar Cells Studied by Impedance Spectroscopy. *Sol. Energy Mater. Sol. Cells* **2005**, *87* (1), 117–131 DOI: 10.1016/j.solmat.2004.07.017.
- (53) Yella, A.; Lee, H.-W.; Tsao, H. N.; Yi, C.; Chandiran, A. K.; Nazeeruddin, M. K.; Diau, E. W.-G.; Yeh, C.-Y.; Zakeeruddin, S. M.; Grätzel, M. Porphyrin-Sensitized Solar Cells with Cobalt (II/III)-Based Redox Electrolyte Exceed 12 Percent Efficiency. *Science* **2011**, *334* (6056).
- (54) Kakiage, K.; Aoyama, Y.; Yano, T.; Oya, K.; Fujisawa, J.; Hanaya, M. Highly-Efficient Dye-Sensitized Solar Cells with Collaborative Sensitization by Silyl-Anchor and Carboxy-Anchor Dyes. *Chem. Commun.* **2015**, *51* (88), 15894–15897 DOI: 10.1039/C5CC06759F.
- (55) Gerischer, H. Electrochemical Techniques for the Study of Photosensitization. *Photochem. Photobiol.* **1972**, *16* (4), 243–260 DOI: 10.1111/j.1751-1097.1972.tb06296.x.
- (56) Gerischer, H.; Willig, F. Reaction of Excited Dye Molecules at Electrodes. In *Physical and Chemical Applications of Dyestuffs*; Springer-Verlag: Berlin/Heidelberg, 1976; pp 31–84.
- (57) Ardo, S.; Meyer, G. J. Photodriven Heterogeneous Charge Transfer with Transition-Metal Compounds Anchored to TiO₂ Semiconductor Surfaces. *Chem. Soc. Rev.* **2009**, *38* (1), 115–164 DOI: 10.1039/B804321N.
- (58) Snaith, H. J. Estimating the Maximum Attainable Efficiency in Dye-Sensitized Solar Cells. *Adv.*

- Funct. Mater.* **2010**, *20* (1), 13–19 DOI: 10.1002/adfm.200901476.
- (59) Kalyanasundaram, K. *Dye-Sensitized Solar Cells*; CRC Press, 2010.
- (60) Amadelli, R.; Argazzi, R.; Bignozzi, C. A.; Scandola, F. Design of Antenna-Sensitizer Polynuclear Complexes. Sensitization of Titanium Dioxide with [Ru(bpy)₂(CN)₂]₂Ru(bpy(COO)₂)₂. *J. Am. Chem. Soc.* **1990**, *112* (20), 7099–7103 DOI: 10.1021/ja00176a003.
- (61) Nazeeruddin, M. K.; Liska, P.; Moser, J.; Vlachopoulos, N.; Grätzel, M. Conversion of Light into Electricity with Trinuclear Ruthenium Complexes Adsorbed on Textured TiO₂ Films. *Helv. Chim. Acta* **1990**, *73* (6), 1788–1803 DOI: 10.1002/hlca.19900730624.
- (62) Nazeeruddin, M. K.; Kay, A.; Rodicio, I.; Humphry-Baker, R.; Mueller, E.; Liska, P.; Vlachopoulos, N.; Grätzel, M. Conversion of Light to Electricity by Cis-X₂bis(2,2'-bipyridyl-4,4'-dicarboxylate)ruthenium(II) Charge-Transfer Sensitizers (X = Cl-, Br-, I-, CN-, and SCN-) on Nanocrystalline Titanium Dioxide Electrodes. *J. Am. Chem. Soc.* **1993**, *115* (14), 6382–6390 DOI: 10.1021/ja00067a063.
- (63) Nazeeruddin, M. K.; De Angelis, F.; Fantacci, S.; Selloni, A.; Viscardi, G.; Liska, P.; Ito, S.; Takeru, B.; Grätzel, M. Combined Experimental and DFT-TDDFT Computational Study of Photoelectrochemical Cell Ruthenium Sensitizers. *J. Am. Chem. Soc.* **2005**, *127* (48), 16835–16847 DOI: 10.1021/ja052467l.
- (64) Chen, C.-Y.; Wang, M.; Li, J.-Y.; Pootrakulchote, N.; Alibabaei, L.; Ngoc-le, C.; Decoppet, J.-D.; Tsai, J.-H.; Grätzel, C.; Wu, C.-G.; Zakeeruddin, S. M.; Grätzel, M. Highly Efficient Light-Harvesting Ruthenium Sensitizer for Thin-Film Dye-Sensitized Solar Cells. *ACS Nano* **2009**, *3* (10), 3103–3109 DOI: 10.1021/nn900756s.
- (65) Cao, Y.; Bai, Y.; Yu, Q.; Cheng, Y.; Liu, S.; Shi, D.; Gao, F.; Wang, P. Dye-Sensitized Solar Cells with a High Absorptivity Ruthenium Sensitizer Featuring a 2-(Hexylthio)thiophene Conjugated Bipyridine. DOI: 10.1021/jp9006872.
- (66) Chen, C. Y.; Pootrakulchote, N.; Wu, S. J.; Wang, M.; Li, J. Y.; Tsai, J. H.; Wu, C. G.; Zakeeruddin, S. M.; Grätzel, M. New Ruthenium Sensitizer with Carbazole Antennas for Efficient and Stable Thin-Film Dye-Sensitized Solar Cells. *J. Phys. Chem. C* **2009**, *113* (48), 20752–20757 DOI: 10.1021/jp9089084.
- (67) Pashaie, B.; Shahroosvand, H.; Grätzel, M.; Nazeeruddin, M. K. Influence of Ancillary Ligands in Dye-Sensitized Solar Cells. *Chemical Reviews*. American Chemical Society August 24, 2016, pp 9485–9564.
- (68) Nazeeruddin, M. K.; Péchy, P.; Renouard, T.; Zakeeruddin, S. M.; Humphry-Baker, R.; Comte, P.; Liska, P.; Cevey, L.; Costa, E.; Shklover, V.; Spiccia, L.; Deacon, G. B.; Bignozzi, C. A.; Grätzel, M. Engineering of Efficient Panchromatic Sensitizers for Nanocrystalline TiO₂-Based Solar Cells. *J. Am. Chem. Soc.* **2001**, *123* (8), 1613–1624 DOI: 10.1021/ja003299u.
- (69) Nguyen, P. T.; Degn, R.; Nguyen, H. T.; Lund, T. Thiocyanate Ligand Substitution Kinetics of the Solar Cell Dye Z-907 by 3-Methoxypropionitrile and 4-Tert-Butylpyridine at Elevated Temperatures. *Sol. Energy Mater. Sol. Cells* **2009**, *93*, 1939–1945 DOI: 10.1016/j.solmat.2009.07.008.
- (70) Nguyen, P. T.; Lam, B. X. T.; Andersen, A. R.; Hansen, P. E.; Lund, T. Photovoltaic Performance and Characteristics of Dye-Sensitized Solar Cells Prepared with the n719 Thermal Degradation Products [Ru(LH)₂(NCS)(4-Tert-butylpyridine)][N(Bu)₄] and [Ru(LH)₂(NCS)(1-

- methylbenzimidazole)][N(Bu)₄]. *Eur. J. Inorg. Chem.* **2011**, 2011 (16), 2533–2539 DOI: 10.1002/ejic.201000935.
- (71) Andersen, A. R.; Halme, J.; Lund, T.; Asghar, M. I.; Nguyen, P. T.; Miettunen, K.; Kemppainen, E.; Albrektsen, O. Charge Transport and Photocurrent Generation Characteristics in Dye Solar Cells Containing Thermally Degraded N719 Dye Molecules. *J. Phys. Chem. C* **2011**, 115 (31), 15598–15606 DOI: 10.1021/jp201658j.
- (72) Wu, K. L.; Clifford, J. N.; Wang, S. W.; Aswani, Y.; Palomares, E.; Lobello, M. G.; Mosconi, E.; De Angelis, F.; Ku, W. P.; Chi, Y.; Nazeeruddin, M. K.; Grätzel, M. Thiocyanate-Free ruthenium(II) Sensitizers for Dye-Sensitized Solar Cells Based on the Cobalt Redox Couple. *ChemSusChem* **2014**, 7 (10), 2930–2938 DOI: 10.1002/cssc.201402030.
- (73) Chi, Y.; Wu, K.-L.; Wei, T.-C. Ruthenium and Osmium Complexes That Bear Functional Azolate Chelates for Dye-Sensitized Solar Cells. *Chem. - An Asian J.* **2015**, 10 (5), 1098–1115 DOI: 10.1002/asia.201403261.
- (74) Albrecht, M. Cyclometalation Using D-Block Transition Metals: Fundamental Aspects and Recent Trends. *Chem. Rev.* **2010**, 110 (2), 576–623 DOI: 10.1021/cr900279a.
- (75) Kleiman, J. P.; Dubeck, M. The Preparation of Cyclopentadienyl [O-(Phenylazo)phenyl] Nickel. *Journal of the American Chemical Society*. American Chemical Society May 1963, pp 1544–1545.
- (76) Cope, A. C.; Siekman, R. W. Formation of Covalent Bonds from Platinum or Palladium to Carbon by Direct Substitution. *J. Am. Chem. Soc.* **1965**, 87 (14), 3272–3273 DOI: 10.1021/ja01092a063.
- (77) Djukic, J.-P.; Sortais, J.-B.; Barloy, L.; Pfeffer, M. Cycloruthenated Compounds - Synthesis and Applications. *Eur. J. Inorg. Chem.* **2009**, 2009 (7), 817–853 DOI: 10.1002/ejic.200801016.
- (78) Fernandez, S.; Pfeffer, M.; Ritleng, V.; Sirlin, C. An Effective Route to Cycloruthenated N-Ligands under Mild Conditions. *Organometallics* **1999**, 18 (12), 2390–2394 DOI: 10.1021/om9901067.
- (79) Revecó, P.; Medley, J. H.; Garber, A. R.; Bhacca, N. S.; Selbin, J. Study of a Cyclometalated Complex of Ruthenium by 400-MHz Two-Dimensional Proton NMR. *Inorg. Chem.* **1985**, 24 (7), 1096–1099 DOI: 10.1021/ic00201a027.
- (80) Constable, E. C.; Holmes, J. M. A Cyclometallated Analogue of tris(2,2'-bipyridine)ruthenium(II). *J. Organomet. Chem.* **1986**, 301 (2), 203–208 DOI: 10.1016/0022-328X(86)80011-0.
- (81) Constable, E. C.; Hannon, M. J. Solvent Effects in the Reactions of 6-Phenyl-2,2',2''-Bipyridine with ruthenium(II). *Inorganica Chim. Acta* **1993**, 211 (1), 101–110 DOI: 10.1016/S0020-1693(00)82850-9.
- (82) Hartshorn, C. M.; Steel, P. J. Cyclometalated Compounds. XI. 1 Single and Double Cyclometalations of Poly(pyrazolylmethyl)benzenes. *Organometallics* **1998**, 17 (16), 3487–3496 DOI: 10.1021/om9800851.
- (83) Revecó, P.; Schmehl, R. H.; Cherry, W. R.; Fronczek, F. R.; Selbin, J. Cyclometalated Complexes of Ruthenium. 2. Spectral and Electrochemical Properties and X-Ray Structure of bis(2,2'-bipyridine)(4-Nitro-2-(2-pyridyl)phenyl)ruthenium(II). *Inorg. Chem.* **1985**, 24 (24), 4078–4082 DOI: 10.1021/ic00218a023.

- (84) Maestri, M.; Balzani, V.; Deuschel-Cornioley, C.; Zelewsky, A. Von. Photochemistry and Luminescence of Cyclometallated Complexes. In *Advances in Photochemistry, Volume 17, John Wiley & Sons, Inc., Hoboken, NJ, USA*; John Wiley & Sons, Inc., 1992.
- (85) Reveco, P.; Cherry, W. R.; Medley, J.; Garber, A.; Gale, R. J.; Selbin, J. Cyclometalated Complexes of Ruthenium. 3. Spectral, Electrochemical, and Two-Dimensional Proton NMR of [Ru(bpy)₂(cyclometalating Ligand)]⁺. *Inorg. Chem.* **1986**, *25* (11), 1842–1845 DOI: 10.1021/ic00231a025.
- (86) Bessho, T.; Yoneda, E.; Yum, J. H.; Guglielmi, M.; Tavernelli, L.; Lmai, H.; Rothlisberger, U.; Nazeeruddin, M. K.; Grätzel, M. New Paradigm in Molecular Engineering of Sensitizers for Solar Cell Applications. *J. Am. Chem. Soc.* **2009**, *131* (16), 5930–5934 DOI: 10.1021/ja9002684.
- (87) Bomben, P. G.; Koivisto, B. D.; Berlinguette, C. P. Cyclometalated Ru Complexes of Type [Ru^{II}(N^AN)₂(C^AN)]^Z: Physicochemical Response to Substituents Installed on the Anionic Ligand. *Inorg. Chem.* **2010**, *49* (11), 4960–4971 DOI: 10.1021/ic100063c.
- (88) Martin, G. C.; Boncella, J. M.; Wucherer, E. J. Synthesis of Ruthenium Amide Complexes by Nucleophilic Attack on Ortho-Metalated I Mine Ligands. *Organometallics* **1991**, *10* (8), 2804–2811 DOI: 10.1021/om00054a051.
- (89) Abbenhuis, H. C. L.; Pfeffer, M.; Sutter, J. P.; de Cian, A.; Fischer, J.; Ji, H. L.; Nelson, J. H. Carbon-Carbon and Carbon-Nitrogen Bond Formation Mediated by Ruthenium(II) Complexes: Synthesis of (1H)-Isoquinolinium Derivatives. *Organometallics* **1993**, *12* (11), 4464–4472 DOI: 10.1021/om00035a034.
- (90) Ryabov, A. D.; Le Lagadec, R. Le; Estevez, H.; Toscano, R. A.; Hernandez, S.; Alexandrova, L.; Kurova, V. S.; Fischer, A.; Sirlin, C.; Pfeffer, M. Synthesis, Characterization, and Electrochemistry of Biorelevant Photosensitive Low-Potential Orthometalated Ruthenium Complexes. *Inorg. Chem.* **2005**, *44* (5), 1626–1634 DOI: 10.1021/ic048270w.
- (91) Bomben, P. G.; Gordon, T. J.; Schott, E.; Berlinguette, C. P. A Trisheteroleptic Cyclometalated RuII Sensitizer That Enables High Power Output in a Dye-Sensitized Solar Cell. *Angew. Chemie - Int. Ed.* **2011**, *50* (45), 10682–10685 DOI: 10.1002/anie.201104275.
- (92) Bomben, P. G.; Borau-Garcia, J.; Berlinguette, C. P. Three Is Not a Crowd: Efficient Sensitization of TiO₂ by a Bulky Trichromic Trisheteroleptic Cycloruthenated Dye. *Chem. Commun.* **2012**, *48* (45), 5599–5601 DOI: 10.1039/c2cc00136e.
- (93) Polander, L. E.; Yella, A.; Curchod, B. F. E.; Ashari Astani, N.; Teuscher, J.; Scopelliti, R.; Gao, P.; Mathew, S.; Moser, J.-E.; Tavernelli, I.; Rothlisberger, U.; Grätzel, M.; Nazeeruddin, M. K.; Frey, J. Towards Compatibility between Ruthenium Sensitizers and Cobalt Electrolytes in Dye-Sensitized Solar Cells. *Angew. Chemie Int. Ed.* **2013**, *52* (33), 8731–8735 DOI: 10.1002/anie.201304608.
- (94) Housecroft, C. E.; Constable, E. C. The Emergence of Copper(<sc>i</sc>)-Based Dye Sensitized Solar Cells. *Chem. Soc. Rev.* **2015**, *44* (23), 8386–8398 DOI: 10.1039/C5CS00215J.
- (95) Alonso-Vante, N.; Nierengarten, J.-F.; Sauvage, J.-P. Spectral Sensitization of Large-Band-Gap Semiconductors (Thin Films and Ceramics) by a Carboxylated bis(1,10-phenanthroline)copper(I) Complex. *J. Chem. Soc. Dalt. Trans.* **1994**, No. 11, 1649 DOI: 10.1039/dt9940001649.
- (96) Bessho, T.; Constable, E. C.; Grätzel, M.; Hernandez Redondo, A.; Housecroft, C. E.; Kylberg,

- W.; Nazeeruddin, M. K.; Neuburger, M.; Schaffner, S. An Element of Surprise—efficient Copper-Functionalized Dye-Sensitized Solar Cells. *Chem. Commun.* **2008**, 0 (32), 3717 DOI: 10.1039/b808491b.
- (97) Brauchli, S. Y.; Malzner, F. J.; Constable, E. C.; Housecroft, C. E. Copper(I)-Based Dye-Sensitized Solar Cells with Sterically Demanding Anchoring Ligands: Bigger Is Not Always Better. *RSC Adv.* **2015**, 5 (60), 48516–48525 DOI: 10.1039/C5RA07449E.
- (98) Brauchli, S. Y.; Malzner, F. J.; Constable, E. C.; Housecroft, C. E. Influence of a Co-Adsorbent on the Performance of Bis(diimine) copper(I)-Based Dye-Sensitized Solar Cells. *RSC Adv.* **2014**, 4 (107), 62728–62736 DOI: 10.1039/C4RA12284D.
- (99) Sandroni, M.; Favereau, L.; Planchat, A.; Akdas-Kilig, H.; Szuwarski, N.; Pellegrin, Y.; Blart, E.; Le Bozec, H.; Boujtita, M.; Odobel, F. Heteroleptic Copper(I)–polypyridine Complexes as Efficient Sensitizers for Dye Sensitized Solar Cells. *J. Mater. Chem. A* **2014**, 2 (26), 9944–9947 DOI: 10.1039/C4TA01755B.
- (100) Mishra, A.; Fischer, M. K. R.; Bäuerle, P. Metal-Free Organic Dyes for Dye-Sensitized Solar Cells: From Structure: Property Relationships to Design Rules. *Angew. Chemie Int. Ed.* **2009**, 48 (14), 2474–2499 DOI: 10.1002/anie.200804709.
- (101) Yu, Q.; Wang, Y.; Yi, Z.; Zu, N.; Zhang, J.; Zhang, M.; Wang, P. High-Efficiency Dye-Sensitized Solar Cells: The Influence of Lithium Ions on Exciton Dissociation, Charge Recombination, and Surface States. *ACS Nano* **2010**, 4 (10), 6032–6038 DOI: 10.1021/nn101384e.
- (102) Boschloo, G.; Hagfeldt, A. Characteristics of the Iodide/triiodide Redox Mediator in Dye-Sensitized Solar Cells. *Acc. Chem. Res.* **2009**, 42 (11), 1819–1826 DOI: 10.1021/ar900138m.
- (103) Zhang, Z.; Chen, P.; Murakami, T. N.; Zakeeruddin, S. M.; Grätzel, M. The 2,2,6,6-Tetramethyl-1-Piperidinyloxy Radical: An Efficient, Iodine- Free Redox Mediator for Dye-Sensitized Solar Cells. *Adv. Funct. Mater.* **2008**, 18 (2), 341–346 DOI: 10.1002/adfm.200701041.
- (104) Daeneke, T.; Kwon, T.-H.; Holmes, A. B.; Duffy, N. W.; Bach, U.; Spiccia, L. High-Efficiency Dye-Sensitized Solar Cells with Ferrocene-Based Electrolytes. *Nat. Chem.* **2011**, 3 (3), 211–215 DOI: 10.1038/nchem.966.
- (105) Feldt, S. M.; Gibson, E. A.; Gabrielsson, E.; Sun, L.; Boschloo, G.; Hagfeldt, A. Design of Organic Dyes and Cobalt Polypyridine Redox Mediators for High-Efficiency Dye-Sensitized Solar Cells. *J. Am. Chem. Soc.* **2010**, 132 (46), 16714–16724 DOI: 10.1021/ja1088869.
- (106) Feldt, S. M.; Wang, G.; Boschloo, G.; Hagfeldt, A. Effects of Driving Forces for Recombination and Regeneration on the Photovoltaic Performance of Dye-Sensitized Solar Cells Using Cobalt Polypyridine Redox Couples. *J. Phys. Chem. C* **2011**, 115 (43), 21500–21507 DOI: 10.1021/jp2061392.
- (107) Giribabu, L.; Bolligarla, R.; Panigrahi, M. Recent Advances of Cobalt(II/III) Redox Couples for Dye-Sensitized Solar Cell Applications. *Chem. Rec.* **2015**, 15 (4), 760–788 DOI: 10.1002/tcr.201402098.
- (108) Colombo, A.; Dragonetti, C.; Magni, M.; Roberto, D.; Demartin, F.; Caramori, S.; Bignozzi, C. A. Efficient Copper Mediators Based on Bulky Asymmetric Phenanthrolines for DSSCs. *ACS Appl. Mater. Interfaces* **2014**, 6 (16), 13945–13955 DOI: 10.1021/am503306f.
- (109) Magni, M.; Giannuzzi, R.; Colombo, A.; Cipolla, M. P.; Dragonetti, C.; Caramori, S.; Carli, S.;

- Grisorio, R.; Suranna, G. P.; Bignozzi, C. A.; Roberto, D.; Manca, M. Tetracoordinated Bis-Phenanthroline Copper-Complex Couple as Efficient Redox Mediators for Dye Solar Cells. *Inorg. Chem.* **2016**, *55* (11), 5245–5253 DOI: 10.1021/acs.inorgchem.6b00204.
- (110) Nusbaumer, H.; Jacques-E., M.; Shaik M., Z.; Nazeeruddin, M. K.; Grätzel, M. CoII(dbqip)22+ Complex Rivals Tri-iodide/Iodide Redox Mediator in Dye-Sensitized Photovoltaic Cells. *J. Phys. Chem. B* **2001**, *105*, 10561–10464 DOI: 10.1021/JP012075A.
- (111) Sapp, S. A.; Elliott, C. M.; Contado, C.; Caramori, S.; Bignozzi, C. A. Substituted Polypyridine Complexes of cobalt(II/III) as Efficient Electron-Transfer Mediators in Dye-Sensitized Solar Cells. *J. Am. Chem. Soc.* **2002**, *124* (37), 11215–11222 DOI: 10.1021/ja027355y.
- (112) Klahr, B. M.; Hamann, T. W. Performance Enhancement and Limitations of Cobalt Bipyridyl Redox Shuttles in Dye-Sensitized Solar Cells. *J. Phys. Chem. C* **2009**, *113* (31), 14040–14045 DOI: 10.1021/jp903431s.
- (113) Liu, Y.; Jennings, J. R.; Huang, Y.; Wang, Q.; Zakeeruddin, S. M.; Grätzel, M. Cobalt Redox Mediators for Ruthenium-Based Dye-Sensitized Solar Cells: A Combined Impedance Spectroscopy and Near-IR Transmittance Study. *J. Phys. Chem. C* **2011**, *115* (38), 18847–18855 DOI: 10.1021/jp204519s.
- (114) Omata, K.; Kuwahara, S.; Katayama, K.; Qing, S.; Toyoda, T.; Lee, K.-M.; Wu, C.-G. The Cause for the Low Efficiency of Dye Sensitized Solar Cells with a Combination of Ruthenium Dyes and Cobalt Redox. *Phys. Chem. Chem. Phys.* **2015**, *17* (15), 10170–10175 DOI: 10.1039/C4CP05981F.
- (115) Tsao, H. N.; Yi, C.; Moehl, T.; Yum, J.-H.; Zakeeruddin, S. M.; Nazeeruddin, M. K.; Grätzel, M. Cyclopentadithiophene Bridged Donor-Acceptor Dyes Achieve High Power Conversion Efficiencies in Dye-Sensitized Solar Cells Based on the Tris-Cobalt Bipyridine Redox Couple. *ChemSusChem* **2011**, *4* (5), 591–594 DOI: 10.1002/cssc.201100120.
- (116) Yella, A.; Lee, H.-W.; Tsao, H. N.; Yi, C.; Chandiran, A. K.; Nazeeruddin, M. K.; Diau, E. W.-G.; Yeh, C.-Y.; Zakeeruddin, S. M.; Grätzel, M. Porphyrin-Sensitized Solar Cells with Cobalt (II/III)-Based Redox Electrolyte Exceed 12 Percent Efficiency. *Science* **2011**, *334* (6056), 629–634.
- (117) Mathew, S.; Yella, A.; Gao, P.; Humphry-Baker, R.; Curchod, B. F. E.; Ashari-Astani, N.; Tavernelli, I.; Rothlisberger, U.; Nazeeruddin, M. K.; Grätzel, M. Dye-Sensitized Solar Cells with 13% Efficiency Achieved through the Molecular Engineering of Porphyrin Sensitizers. *Nat. Chem.* **2014**, *6* (3), 242–247 DOI: 10.1038/nchem.1861.
- (118) Yella, A.; Mai, C.-L.; Zakeeruddin, S. M.; Chang, S.-N.; Hsieh, C.-H.; Yeh, C.-Y.; Grätzel, M. Molecular Engineering of Push-Pull Porphyrin Dyes for Highly Efficient Dye-Sensitized Solar Cells: The Role of Benzene Spacers. *Angew. Chemie Int. Ed.* **2014**, *53* (11), 2973–2977 DOI: 10.1002/anie.201309343.
- (119) Yum, J.-H.; Baranoff, E.; Kessler, F.; Moehl, T.; Ahmad, S.; Bessho, T.; Marchioro, A.; Ghadiri, E.; Moser, J.-E.; Yi, C.; Nazeeruddin, M. K.; Grätzel, M. A Cobalt Complex Redox Shuttle for Dye-Sensitized Solar Cells with High Open-Circuit Potentials. *Nat. Commun.* **2012**, *3*, 631 DOI: 10.1038/ncomms1655.
- (120) Wu, K.-L.; Hu, Y.; Chao, C.-T.; Yang, Y.-W.; Hsiao, T.-Y.; Robertson, N.; Chi, Y. Dye Sensitized Solar Cells with Cobalt and Iodine-Based Electrolyte: The Role of Thiocyanate-Free Ruthenium Sensitizers. *J. Mater. Chem. A* **2014**, *2* (45), 19556–19565 DOI: 10.1039/C4TA04208E.

- (121) Barnes, P. R. F.; Anderson, A. Y.; Durrant, J. R.; O'Regan, B. C. Simulation and Measurement of Complete Dye Sensitized Solar Cells: Including the Influence of Trapping, Electrolyte, Oxidised Dyes and Light Intensity on Steady State and Transient Device Behaviour. *Phys. Chem. Chem. Phys. Phys. Chem. Chem. Phys.* **2011**, *13* (13), 5798–5816 DOI: 10.1039/c0cp01554g.
- (122) Jennings, J. R.; Liu, Y.; Wang, Q. Efficiency Limitations in Dye-Sensitized Solar Cells Caused by Inefficient Sensitizer Regeneration. *J. Phys. Chem. C* **2011**, *115*, 15109–15120 DOI: 10.1021/jp2053053.
- (123) Martiniani, S.; Anderson, A. Y.; Law, C.; O'Regan, B. C.; Barolo, C. New Insight into the Regeneration Kinetics of Organic Dye Sensitized Solar Cells. *Chem. Commun.* **2012**, *48* (18), 2406–2408 DOI: 10.1039/c2cc17100g.
- (124) Anderson, A. Y.; Barnes, P. R. F.; Durrant, J. R.; O'Regan, B. C. Quantifying Regeneration in Dye-Sensitized Solar Cells. *J. Phys. Chem. C* **2011**, *115* (5), 2439–2447 DOI: 10.1021/jp1101048.
- (125) Li, F.; Jennings, J. R.; Wang, Q. Determination of Sensitizer Regeneration Efficiency in Dye-Sensitized Solar Cells. *ACS Nano* **2013**, *7* (9), 8233–8242 DOI: 10.1021/nn403714s.
- (126) Fabregat-Santiago, F.; Garcia-Belmonte, G.; Mora-Seró, I.; Bisquert, J. Characterization of Nanostructured Hybrid and Organic Solar Cells by Impedance Spectroscopy. *Phys. Chem. Chem. Phys.* **2011**, *13* (20), 9083–9118 DOI: 10.1039/c0cp02249g.
- (127) Li, J.-Y.; Chen, C.-Y.; Chen, J.-G.; Tan, C.-J.; Lee, K.-M.; Wu, S.-J.; Tung, Y.-L.; Tsai, H.-H.; Ho, K.-C.; Wu, C.-G. Heteroleptic Ruthenium Antenna-Dye for High-Voltage Dye-Sensitized Solar Cells. *J. Mater. Chem.* **2010**, *20* (34), 7158–7164 DOI: 10.1039/c0jm01418d.
- (128) Kono, T.; Masaki, N.; Nishikawa, M.; Tamura, R.; Matsuzaki, H.; Kimura, M.; Mori, S. Interfacial Charge Transfer in Dye-Sensitized Solar Cells Using SCN-Free Terpyridine-Coordinated Ru Complex Dye and Co Complex Redox Couples. *ACS Appl. Mater. Interfaces* **2016**, *8* (26), 16677–16683 DOI: 10.1021/acsami.6b03712.
- (129) Robson, K. C. D.; Koivisto, B. D.; Yella, A.; Sporinova, B.; Nazeeruddin, M. K.; Baumgartner, T.; Grätzel, M.; Berlinguette, C. P. Design and Development of Functionalized Cyclometalated Ruthenium Chromophores for Light-Harvesting Applications. *Inorg. Chem.* **2011**, *50* (12), 5494–5508 DOI: 10.1021/ic200011m.
- (130) Chen, W. C.; Kong, F. T.; Ghadari, R.; Li, Z. Q.; Guo, F. L.; Liu, X. P.; Huang, Y.; Yu, T.; Hayat, T.; Dai, S. Y. Unravelling the Structural-Electronic Impact of Arylamine Electron-Donating Antennas on the Performances of Efficient Ruthenium Sensitizers for Dye-Sensitized Solar Cells. *J. Power Sources* **2017**, *346*, 71–79 DOI: 10.1016/j.jpowsour.2017.02.026.
- (131) Aghazada, S.; Gao, P.; Yella, A.; Marotta, G.; Moehl, T.; Teuscher, J.; Moser, J.-E.; De Angelis, F.; Grätzel, M.; Nazeeruddin, M. K. Ligand Engineering for the Efficient Dye-Sensitized Solar Cells with Ruthenium Sensitizers and Cobalt Electrolytes. *Inorg. Chem.* **2016**, *55* (13), 6653–6659 DOI: 10.1021/acs.inorgchem.6b00842.
- (132) Ryabov, A. D.; Estevez, H.; Alexandrova, L.; Pfeiffer, M.; Lagadec, R. Le. Unusual Phenomenon in the Chemistry of Orthometalated Ruthenium (II) Complexes. *Inorganica Chim. Acta* **2006**, *359* (3), 883–887 DOI: 10.1016/j.ica.2005.05.034.
- (133) Bard, A. J.; Faulkner, L. R. *Electrochemical Methods: Fundamentals and Applications*; Wiley, 2001.
- (134) Duffy, N. W.; Peter, L. M.; Rajapakse, R. M. G.; Wijayantha, K. G. U. A Novel Charge

- Extraction Method for the Study of Electron Transport and Interfacial Transfer in Dye Sensitized Nanocrystalline Solar Cells. *Electrochem. commun.* **2000**, *2* (9), 658–662 DOI: 10.1016/S1388-2481(00)00097-7.
- (135) O'Regan, B. C.; Scully, S.; Mayer, A. C.; Palomares, E.; Durrant, J. The Effect of Al₂O₃ Barrier Layers in TiO₂/Dye/CuSCN Photovoltage Cells Explored by Recombination and DOS Characterization Using Transient Photovoltage Measurements. *J. Phys. Chem. B* **2005**, *109* (10), 4616–4623 DOI: 10.1021/jp0468049.
- (136) Clifford, J. N.; Martez-Ferrero, E.; Viterisi, A.; Palomares, E. Sensitizer Molecular Structure-Device Efficiency Relationship in Dye Sensitized Solar Cells. *Chem. Soc. Rev* **2011**, *40*, 1635–1646 DOI: 10.1039/b920664g.
- (137) Yao, Z.; Zhang, M.; Li, R.; Yang, L.; Qiao, Y.; Wang, P. A Metal-Free N-Annulated Thienocyclopentaperylene Dye: Power Conversion Efficiency of 12 % for Dye-Sensitized Solar Cells. *Angew. Chemie* **2015**, *127* (20), 6092–6096 DOI: 10.1002/ange.201501195.
- (138) Yao, Z.; Zhang, M.; Wu, H.; Yang, L.; Li, R.; Wang, P. Donor/Acceptor Indenoperylene Dye for Highly Efficient Organic Dye-Sensitized Solar Cells. *J. Am. Chem. Soc.* **2015**, *137* (11), 3799–3802 DOI: 10.1021/jacs.5b01537.
- (139) Gao, P.; Kim, Y. J.; Yum, J.-H.; Holcombe, T. W.; Nazeeruddin, M. K.; Grätzel, M. Facile Synthesis of a Bulky BPTPA Donor Group Suitable for Cobalt Electrolyte Based Dye Sensitized Solar Cells. *J. Mater. Chem. A* **2013**, *1* (18), 5535–5544 DOI: 10.1039/c3ta10632b.
- (140) Gao, P.; Tsao, H. N.; Yi, C.; Grätzel, M.; Nazeeruddin, M. K. Extended π -Bridge in Organic Dye-Sensitized Solar Cells: The Longer, the Better? *Adv. Energy Mater.* **2014**, *4* (7), 1301485 DOI: 10.1002/aenm.201301485.
- (141) Ganesan, P.; Yella, A.; Holcombe, T. W.; Gao, P.; Rajalingam, R.; Al-Muhtaseb, S. a; Grätzel, M.; Nazeeruddin, M. K. Unravel the Impact of Anchoring Groups on the Photovoltaic Performances of Diketopyrrolopyrrole Sensitizers for Dye-Sensitized Solar Cells. *ACS Sustain. Chem. Eng.* **2015**, *3* (10), 2389–2396 DOI: 10.1021/acssuschemeng.5b00332.
- (142) Clark, C. C.; Marton, A.; Meyer, G. J. Evidence for Static Quenching of MLCT Excited States by Iodide. *Inorg. Chem.* **2005**, *44* (10), 3383–3385 DOI: 10.1021/ic050077u.
- (143) Marton, A.; Clark, C. C.; Srinivasan, R.; Freundlich, R. E.; Narducci Sarjeant, A. A.; Meyer, G. J. Static and Dynamic Quenching of Ru(II) Polypyridyl Excited States by Iodide. *Inorg. Chem.* **2006**, *45* (1), 362–369 DOI: 10.1021/ic051467j.
- (144) Rowley, J. G.; Farnum, B. H.; Ardo, S.; Meyer, G. J. Iodide Chemistry in Dye-Sensitized Solar Cells: Making and Breaking I-I Bonds for Solar Energy Conversion. *J. Phys. Chem. Lett* **2010**, *1*, 3132–3140 DOI: 10.1021/jz101311d.
- (145) Gardner, J. M.; Giaimuccio, J. M.; Meyer, G. J. Evidence for Iodine Atoms as Intermediates in the Dye Sensitized Formation of I–I Bonds. *J. Am. Chem. Soc.* **2008**, *130* (51), 17252–17253 DOI: 10.1021/ja807703m.
- (146) Clifford, J. N.; Martínez-Ferrero, E.; Palomares, E. Dye Mediated Charge Recombination Dynamics in Nanocrystalline TiO₂ Dye Sensitized Solar Cells. *J. Mater. Chem.* **2012**, *22* (25), 12415–12422 DOI: 10.1039/c2jm16107a.
- (147) O'Regan, B.; Walley, K.; Juozapavicius, M.; Anderson, A.; Matar, F.; Ghaddar, T.; Zakeeruddin,

- S. M.; Klein, C.; Durrant, J. R. Structure/function Relationships in Dyes for Solar Energy Conversion: A Two-Atom Change in Dye Structure and the Mechanism for Its Effect on Cell Voltage. *J. Am. Chem. Soc.* **2009**, *131* (10), 3541–3548 DOI: 10.1021/ja806869x.
- (148) Miyashita, M.; Sunahara, K.; Nishikawa, T.; Uemura, Y.; Koumura, N.; Hara, K.; Mori, A.; Abe, T.; Suzuki, E.; Mori, S. Interfacial Electron-Transfer Kinetics in Metal-Free Organic Dye-Sensitized Solar Cells: Combined Effects of Molecular Structure of Dyes and Electrolytes. *J. Am. Chem. Soc.* **2008**, *130* (52), 17874–17881 DOI: 10.1021/ja803534u.
- (149) Bai, Y.; Zhang, J.; Zhou, D.; Wang, Y.; Zhang, M.; Wang, P. Engineering Organic Sensitizers for Iodine-Free Dye-Sensitized Solar Cells: Red-Shifted Current Response Concomitant with Attenuated Charge Recombination. *J. Am. Chem. Soc.* **2011**, *133* (30), 11442–11445 DOI: 10.1021/ja203708k.
- (150) Zhang, M.; Liu, J.; Wang, Y.; Zhou, D.; Wang, P. Redox Couple Related Influences of π -Conjugation Extension in Organic Dye-Sensitized Mesoscopic Solar Cells. *Chem. Sci.* **2011**, *2* (C), 1401–1406 DOI: 10.1039/c1sc00199j.
- (151) Robson, K. C. D.; Hu, K.; Meyer, G. J.; Berlinguette, C. P. Atomic Level Resolution of Dye Regeneration in the Dye-Sensitized Solar Cell. *J. Am. Chem. Soc.* **2013**, *135* (5), 1961–1971 DOI: 10.1021/ja311640f.
- (152) Swords, W. B.; Simon, S. J. C.; Parlane, F. G. L.; Dean, R. K.; Kellett, C. W.; Hu, K.; Meyer, G. J.; Berlinguette, C. P. Evidence for Interfacial Halogen Bonding. *Angew. Chemie Int. Ed.* **2016**, *55* (20), 5956–5960 DOI: 10.1002/anie.201510641.
- (153) Malytskyi, V.; Simon, J.-J.; Patrone, L.; Raimundo, J.-M. Thiophene-Based Push–pull Chromophores for Small Molecule Organic Solar Cells (SMOSCs). *RSC Adv.* **2014**, *5*, 354–397 DOI: 10.1039/C4RA11664J.
- (154) Teuscher, J.; Marchioro, A.; Andrès, J.; Roch, L. M.; Xu, M.; Zakeeruddin, S. M.; Wang, P.; Grätzel, M.; Moser, J.-E. Kinetics of the Regeneration by Iodide of Dye Sensitizers Adsorbed on Mesoporous Titania. *J. Phys. Chem. C* **2014**, *118* (30), 17108–17115.
- (155) Jeon, J.; William A. Goddard, I.; Kim, H. Inner-Sphere Electron-Transfer Single Iodide Mechanism for Dye Regeneration in Dye-Sensitized Solar Cells. *J. Am. Chem. Soc.* **2013**, *135* (7), 2421–2434.
- (156) Jeon, J.; Park, Y. C.; Han, S. S.; William A. Goddard, I.; Lee, Y. S.; Kim, H. Rapid Dye Regeneration Mechanism of Dye-Sensitized Solar Cells. *J. Phys. Chem. Lett.* **2014**, *5* (24), 4285–4290.
- (157) Wang, Q.; Moser, J.-E.; Grätzel, M. Electrochemical Impedance Spectroscopic Analysis of Dye-Sensitized Solar Cells. *J. Phys. Chem. B* **2005**, *109* (31), 14945–14953 DOI: 10.1021/jp052768h.
- (158) Zhang ZY Cai, YC Yang, L Xu, MF Li, RZ Zhang, M Dong, XD Wang, P, J. Y. Conjugated Linker Correlated Energetics and Kinetics in Dithienopyrrole Dye-Sensitized Solar Cells. *ENERGY Environ. Sci.* **2013**, *6* (5), 1614 DOI: 10.1039/c3ee40375k.
- (159) Cai, N.; Li, R.; Wang, Y.; Zhang, M.; Wang, P. Organic Dye-Sensitized Solar Cells with a Cobalt Redox Couple: Influences of π -Linker Rigidity and Dye–bath Solvent Selection. *Energy Environ. Sci.* **2013**, *6* (1), 139–157 DOI: 10.1039/c2ee23592g.
- (160) Urbani, M.; Medel, M.; Kumar, S. A.; Ince, M.; Bhaskarwar, A. N.; González-Rodríguez, D.;

- Grätzel, M.; Nazeeruddin, M. K.; Torres, T. Synthesis of Amphiphilic Ru II Heteroleptic Complexes Based on Benzo[1,2- B :4,5- B]dithiophene: Relevance of the Half-Sandwich Complex Intermediate and Solvent Compatibility. *Chem. - Eur. J.* **2015**, *21* (45), 16252–16265 DOI: 10.1002/chem.201502417.
- (161) Wu, K.-L.; Ku, W.-P.; Clifford, J. N.; Palomares, E.; Ho, S.-T.; Chi, Y.; Liu, S.-H.; Chou, P.-T.; Nazeeruddin, M. K.; Grätzel, M. Harnessing the Open-Circuit Voltage via a New Series of Ru(ii) Sensitizers Bearing (Iso-)Quinoliny Pyrazolate Ancillaries. *Energy Environ. Sci.* **2013**, *6* (3), 859–870 DOI: 10.1039/c2ee23988d.
- (162) Wadman, S. H.; Kroon, J. M.; Bakker, K.; Havenith, R. W. A.; Van Klink, G. P. M.; Van Koten, G. Cyclometalated Organoruthenium Complexes for Application in Dye-Sensitized Solar Cells. *Organometallics* **2010**, *29* (7), 1569–1579 DOI: 10.1021/om900481g.
- (163) Kreitner, C.; Erdmann, E.; Seidel, W. W.; Heinze, K. Understanding the Excited State Behavior of Cyclometalated Bis(tridentate)ruthenium(II) Complexes: A Combined Experimental and Theoretical Study. *Inorg. Chem.* **2015**, *54* (23), 11088–11104 DOI: 10.1021/acs.inorgchem.5b01151.
- (164) Kreitner, C.; Heinze, K. The Photochemistry of Mono- and Dinuclear Cyclometalated Bis(tridentate)ruthenium(II) Complexes: Dual Excited State Deactivation and Dual Emission. *Dalt. Trans.* **2016**, *45* (13), 5640–5658 DOI: 10.1039/C6DT00384B.
- (165) Abboto, A.; Coluccini, C.; Dell’Orto, E.; Manfredi, N.; Trifiletti, V.; Salamone, M. M.; Ruffo, R.; Acciarri, M.; Colombo, A.; Dragonetti, C.; Ordanini, S.; Roberto, D.; Valore, A. Thiocyanate-Free Cyclometalated Ruthenium Sensitizers for Solar Cells Based on Heteroaromatic-Substituted 2-Arylpyridines. *Dalt. Trans.* **2012**, *41* (38), 11731–11738 DOI: 10.1039/c2dt31551c.
- (166) Hopkinson, M. N.; Richter, C.; Schedler, M.; Glorius, F. An Overview of N-Heterocyclic Carbenes. *Nature* **2014**, *510* (7506), 485–496 DOI: 10.1038/nature13384.
- (167) Chang, W.-C.; Chen, H.-S.; Li, T.-Y.; Hsu, N.-M.; Tingare, Y. S.; Li, C.-Y.; Liu, Y.-C.; Su, C.; Li, W.-R. Highly Efficient N-Heterocyclic Carbene/Pyridine-Based Ruthenium Sensitizers: Complexes for Dye-Sensitized Solar Cells. *Angew. Chemie Int. Ed.* **2010**, *49* (44), 8161–8164 DOI: 10.1002/anie.201001628.
- (168) Sanford, M. S.; Love, J. A.; Grubbs, R. H. Mechanism and Activity of Ruthenium Olefin Metathesis Catalysts. *J. Am. Chem. Soc.* **2001**, *123* (27), 6543–6554 DOI: 10.1021/ja010624k.
- (169) Endo, K.; Grubbs, R. H. Chelated Ruthenium Catalysts for Z -Selective Olefin Metathesis. *J. Am. Chem. Soc.* **2011**, *133* (22), 8525–8527 DOI: 10.1021/ja202818v.
- (170) Ortega, N.; Urban, S.; Beiring, B.; Glorius, F. Ruthenium NHC Catalyzed Highly Asymmetric Hydrogenation of Benzofurans. *Angew. Chemie Int. Ed.* **2012**, *51* (7), 1710–1713 DOI: 10.1002/anie.201107811.
- (171) Barbante, G. J.; Francis, P. S.; Hogan, C. F.; Kheradmand, P. R.; Wilson, D. J. D.; Barnard, P. J. Electrochemiluminescent Ruthenium(II) N -Heterocyclic Carbene Complexes: A Combined Experimental and Theoretical Study. *Inorg. Chem.* **2013**, *52* (13), 7448–7459 DOI: 10.1021/ic400263r.
- (172) Leigh, V.; Ghattas, W.; Lalrempuia, R.; Müller-Bunz, H.; Pryce, M. T.; Albrecht, M. Synthesis, Photo, and Electrochemistry of Ruthenium Bis(bipyridine) Complexes Comprising a N-Heterocyclic Carbene Ligand. *Inorg. Chem.* **2013**, *52* (9), 5395–5402 DOI: 10.1021/ic400347r.

- (173) Nussbaum, M.; Schuster, O.; Albrecht, M. Efficient Electronic Communication of Two Ruthenium Centers through a Rigid Ditopic N-Heterocyclic Carbene Linker. *Chem. - Eur. J.* **2013**, *19* (51), 17517–17527 DOI: 10.1002/chem.201302688.
- (174) Son, S. U.; Park, K. H.; Lee, Y. S.; Kim, B. Y.; Choi, C. H.; Lan, M. S.; Jang, Y. H.; Jang, D. J.; Chung, Y. K. Synthesis of Ru(II) Complexes of N-Heterocyclic Carbenes and Their Promising Photoluminescence Properties in Water. *Inorg. Chem.* **2004**, *43* (22), 6896–6898 DOI: 10.1021/ic049514f.
- (175) Zhang, C.; Zhao, Y.; Li, B.; Song, H.; Xu, S.; Wang, B. The Intramolecular sp² and sp³ C–H Bond Activation of (P-Cymene)ruthenium(ii) N-Heterocyclic Carbene Complexes. *Dalt. Trans.* **2009**, *21* (26), 5182–5189 DOI: 10.1039/b818091a.
- (176) Watson, D. F.; Meyer, G. J. Electron Injection at Dye-Sensitized Semiconductor Electrodes. *Annu. Rev. Phys. Chem.* **2005**, *56*, 119–156 DOI: 10.1146/annurev.physchem.56.092503.141142.
- (177) Romero, N. A.; Nicewicz, D. A. Organic Photoredox Catalysis. *Chem. Rev.* **2016**, *116* (17), 10075–10166 DOI: 10.1021/acs.chemrev.6b00057.
- (178) Van Houten, J.; Watts, R. J. Temperature Dependence of the Photophysical and Photochemical Properties of the tris(2,2'-bipyridyl)ruthenium(II) Ion in Aqueous Solution. *J. Am. Chem. Soc.* **1976**, *98* (16), 4853–4858 DOI: 10.1021/ja00432a028.
- (179) Van Houten, J.; Watts, R. J. Photochemistry of tris(2,2'-bipyridyl)ruthenium(II) in Aqueous Solutions. *Inorg. Chem.* **1978**, *17* (12), 3381–3385 DOI: 10.1021/ic50190a016.
- (180) Auböck, G.; Chergui, M. Sub-50-Fs Photoinduced Spin Crossover in [Fe(bpy)₃]²⁺. *Nat. Chem.* **2015**, *7* (8), 629–633 DOI: 10.1038/nchem.2305.
- (181) Zhang, W.; Alonso-Mori, R.; Bergmann, U.; Bressler, C.; Chollet, M.; Galler, A.; Gawelda, W.; Hadt, R. G.; Hartsock, R. W.; Kroll, T.; Kjær, K. S.; Kubiček, K.; Lemke, H. T.; Liang, H. W.; Meyer, D. a; Nielsen, M. M.; Purser, C.; Robinson, J. S.; Solomon, E. I.; Sun, Z.; Sokaras, D.; van Driel, T. B.; Vankó, G.; Weng, T.-C.; Zhu, D.; Gaffney, K. J. Tracking Excited-State Charge and Spin Dynamics in Iron Coordination Complexes. *Nature* **2014**, *509* (7500), 345–348 DOI: 10.1038/nature13252.
- (182) Shepard, S. G.; Fatur, S. M.; Rappé, A. K.; Damrauer, N. H. Highly Strained Iron(II) Polypyridines: Exploiting the Quintet Manifold To Extend the Lifetime of MLCT Excited States. *J. Am. Chem. Soc.* **2016**, *138* (9), 2949–2952 DOI: 10.1021/jacs.5b13524.
- (183) Monat, J. E.; McCusker, J. K. Femtosecond Excited-State Dynamics of an iron(II) Polypyridyl Solar Cell Sensitizer Model. *J. Am. Chem. Soc.* **2000**, *122* (17), 4092–4097 DOI: 10.1021/ja992436o.
- (184) McCusker, J. K.; Walda, K. N.; Dunn, R. C.; Simon, J. D.; Magde, D.; Hendrickson, D. N. Subpicosecond 1MLCT .fwdarw. 5T2 Intersystem Crossing of Low-Spin Polypyridyl Ferrous Complexes. *J. Am. Chem. Soc.* **1993**, *115* (1), 298–307 DOI: 10.1021/ja00054a043.
- (185) Zhang, Y.-M.; Shao, J.-Y.; Yao, C.-J.; Zhong, Y.-W. Cyclometalated ruthenium(II) Complexes with a Bis-Carbene CCC-Pincer Ligand. *Dalton Trans.* **2012**, *41* (31), 9280–9282 DOI: 10.1039/c2dt31015e.
- (186) Liu, Y.; Persson, P.; Sundström, V.; Wärnmark, K. Fe N-Heterocyclic Carbene Complexes as Promising Photosensitizers. *Acc. Chem. Res.* **2016**, *49* (8), 1477–1485 DOI:

- 10.1021/acs.accounts.6b00186.
- (187) Liu, L.; Duchanois, T.; Etienne, T.; Monari, A.; Beley, M.; Assfeld, X.; Haacke, S.; Gros, P. C. A New Record Excited State 3MLCT Lifetime for Metalorganic Iron(II) Complexes. *Phys. Chem. Chem. Phys.* **2016**, *18* (18), 12550–12556 DOI: 10.1039/C6CP01418F.
- (188) Frisch (Gaussian, Inc.), Michael J. Trucks (Gaussian, Inc.), G. W. Schlegel (Gaussian, Inc.), H. Bernhard (Gaussian, Inc.). Gaussian 09 Citation. 2009.
- (189) Adamo, C.; Barone, V. Exchange Functionals with Improved Long-Range Behavior and Adiabatic Connection Methods without Adjustable Parameters: The mPW and mPW1PW Models. *J. Chem. Phys.* **1998**, *108* (2), 664–675 DOI: 10.1063/1.475428.
- (190) Hay, P. J.; Wadt, W. R. *Ab Initio* Effective Core Potentials for Molecular Calculations. Potentials for the Transition Metal Atoms Sc to Hg. *J. Chem. Phys.* **1985**, *82* (1), 270–283 DOI: 10.1063/1.448799.
- (191) Hehre, W. J.; Ditchfield, R.; Pople, J. A. Self-Consistent Molecular Orbital Methods. XII. Further Extensions of Gaussian-Type Basis Sets for Use in Molecular Orbital Studies of Organic Molecules. *J. Chem. Phys.* **1972**, *56* (5), 2257–2261 DOI: 10.1063/1.1677527.
- (192) Andrae, D.; Häußermann, U.; Dolg, M.; Stoll, H.; Preuß, H. Energy-Adjusted *ab Initio* Pseudopotentials for the Second and Third Row Transition Elements. *Theor. Chim. Acta* **1990**, *77* (2), 123–141 DOI: 10.1007/BF01114537.
- (193) Schäfer, A.; Horn, H.; Ahlrichs, R. Fully Optimized Contracted Gaussian Basis Sets for Atoms Li to Kr. *J. Chem. Phys.* **1992**, *97* (4), 2571–2577 DOI: 10.1063/1.463096.
- (194) Klamt, A.; Schüürmann, G. COSMO: A New Approach to Dielectric Screening in Solvents with Explicit Expressions for the Screening Energy and Its Gradient. *J. Chem. Soc., Perkin Trans. 2* **1993**, No. 5, 799–805 DOI: 10.1039/P29930000799.
- (195) Stratmann, R. E.; Scuseria, G. E.; Frisch, M. J. An Efficient Implementation of Time-Dependent Density-Functional Theory for the Calculation of Excitation Energies of Large Molecules. *J. Chem. Phys.* **1998**, *109* (19), 8218–8224 DOI: 10.1063/1.477483.
- (196) Furche, F.; Ahlrichs, R. Adiabatic Time-Dependent Density Functional Methods for Excited State Properties. *J. Chem. Phys.* **2002**, *117* (16), 7433–7447 DOI: 10.1063/1.1508368.
- (197) Abrahamsson, M.; Jäger, M.; Österman, T.; Eriksson, L.; Persson, P.; Becker, H. C.; Johansson, O.; Hammarström, L. A 3.0 Ms Room Temperature Excited State Lifetime of a Bistridentate Ru(II)-Polypyridine Complex for Rod-like Molecular Arrays. *J. Am. Chem. Soc.* **2006**, *128* (39), 12616–12617 DOI: 10.1021/ja064262y.
- (198) Jäger, M.; Smeigh, A.; Lombeck, F.; Görls, H.; Collin, J. P.; Sauvage, J. P.; Hammarström, L.; Johansson, O. Cyclometalated Ru(II) Complexes with Improved Octahedral Geometry: Synthesis and Photophysical Properties. *Inorg. Chem.* **2010**, *49* (2), 374–376 DOI: 10.1021/ic9020788.
- (199) Jäger, M.; Kumar, R. J.; Görls, H.; Bergquist, J.; Johansson, O. Facile Synthesis of Bistridentate Ru(II) Complexes Based on 2,6-Di(quinolin-8-yl)pyridyl Ligands: Sensitizers with Microsecond 3MLCT Excited State Lifetimes. *Inorg. Chem.* **2009**, *48* (7), 3228–3238 DOI: 10.1021/ic802342t.
- (200) Parada, G. A.; Fredin, L. A.; Santoni, M. P.; Jäger, M.; Lomoth, R.; Hammarström, L.; Johansson, O.; Persson, P.; Ott, S. Tuning the Electronics of bis(tridentate)ruthenium(II) Complexes with Long-Lived Excited States: Modifications to the Ligand Skeleton beyond Classical Electron

- Donor or Electron Withdrawing Group Decorations. *Inorg. Chem.* **2013**, *52* (9), 5128–5137 DOI: 10.1021/ic400009m.
- (201) Schlotthauer, T.; Parada, G. A.; Görls, H.; Ott, S.; Jäger, M.; Schubert, U. S. Asymmetric Cyclometalated RuII Polypyridyl-Type Complexes with π -Extended Carbanionic Donor Sets. *Inorg. Chem.* **2017**, *56* (14), 7720–7730 DOI: 10.1021/acs.inorgchem.7b00392.
- (202) Breivogel, A.; Park, M.; Lee, D.; Klassen, S.; Kühnle, A.; Lee, C.; Char, K.; Heinze, K. Push-Pull Design of Bis(tridentate) ruthenium(II) Polypyridine Chromophores as Deep Red Light Emitters in Light-Emitting Electrochemical Cells. *Eur. J. Inorg. Chem.* **2014**, *2014* (2), 288–295 DOI: 10.1002/ejic.201301226.
- (203) Pal, A. K.; Hanan, G. S. Design, Synthesis and Excited-State Properties of Mononuclear Ru(II) Complexes of Tridentate Heterocyclic Ligands. *Chem. Soc. Rev.* **2014**, *43* (17), 6184–6197 DOI: 10.1039/c4cs00123k.
- (204) Shao, J.-Y.; Fu, N.; Yang, W.-W.; Zhang, C.-Y.; Zhong, Y.-W.; Lin, Y.; Yao, J. Cyclometalated Ruthenium(II) Complexes with Bis(benzimidazolyl)benzene for Dye-Sensitized Solar Cells. *RSC Adv.* **2015**, *5* (109), 90001–90009 DOI: 10.1039/C5RA20294A.
- (205) Bomben, P. G.; Robson, K. C. D.; Koivisto, B. D.; Berlinguette, C. P. Cyclometalated Ruthenium Chromophores for the Dye-Sensitized Solar Cell. *Coordination Chemistry Reviews*. Elsevier August 1, 2012, pp 1438–1450.
- (206) Kreitner, C.; Mengel, A. K. C.; Lee, T. K.; Cho, W.; Char, K.; Kang, Y. S.; Heinze, K. Strongly Coupled Cyclometalated Ruthenium Triarylamine Chromophores as Sensitizers for DSSCs. *Chem. - A Eur. J.* **2016**, *22* (26), 8915–8928 DOI: 10.1002/chem.201601001.
- (207) Yao, C. J.; Zhong, Y. W.; Nie, H. J.; Abrun, H. D.; Yao, J. Near-IR Electrochromism in Electropolymerized Films of a Biscyclometalated Ruthenium Complex Bridged by 1,2,4,5-Tetra(2-Pyridyl)benzene. *J. Am. Chem. Soc.* **2011**, *133* (51), 20720–20723 DOI: 10.1021/ja209620p.
- (208) Kreitner, C.; Heinze, K. Excited State Decay of Cyclometalated Polypyridine Ruthenium Complexes: Insight from Theory and Experiment. *Dalt. Trans.* **2016**, *45* (35), 13631–13647 DOI: 10.1039/C6DT01989G.
- (209) Nie, H. J.; Yao, C. J.; Sun, M. J.; Zhong, Y. W.; Yao, J. Ruthenium-Bis-Terpyridine Complex with Two Redox-Asymmetric Amine Substituents: Potential-Controlled Reversal of the Direction of Charge-Transfer. *Organometallics* **2014**, *33* (21), 6223–6231 DOI: 10.1021/om500904k.
- (210) Wadman, S. H.; Lutz, M.; Tooke, D. M.; Spek, A. L.; František Hartl; Havenith, R. W. A.; Van Klink, G. P. M.; Van Koten, G. Consequences of N, C, N'- and C, N, N'-Coordination Modes on Electronic and Photophysical Properties of Cyclometalated Aryl ruthenium(II) Complexes. *Inorg. Chem.* **2009**, *48* (5), 1887–1900 DOI: 10.1021/ic801595m.
- (211) Feldt, S. M.; Lohse, P. W.; Kessler, F.; Nazeeruddin, M. K.; Grätzel, M.; Boschloo, G.; Hagfeldt, A. Regeneration and Recombination Kinetics in Cobalt Polypyridine Based Dye-Sensitized Solar Cells, Explained Using Marcus Theory. *Phys. Chem. Chem. Phys.* **2013**, *15* (19), 7087–7097 DOI: 10.1039/c3cp50997d.
- (212) Xia, C.; Fan, X.; Locklin, J.; Advincula, R. C. A First Synthesis of Thiophene Dendrimers. *Org. Lett.* **2002**, *4* (12), 2067–2070 DOI: 10.1021/ol205943a.

- (213) Tian, N.; Thiessen, A.; Schiewek, R.; Schmitz, O. J.; Hertel, D.; Meerholz, K.; Holder, E. Efficient Synthesis of Carbazolyl- and Thienyl-Substituted β -Diketones and Properties of Their Red- and Green-Light-Emitting Ir(III) Complexes. *J. Org. Chem.* **2009**, *74* (7), 2718–2725 DOI: 10.1021/jo8025516.
- (214) Wu, K. L.; Li, C. H.; Chi, Y.; Clifford, J. N.; Cabau, L.; Palomares, E.; Cheng, Y. M.; Pan, H. A.; Chou, P. T. Dye Molecular Structure Device Open-Circuit Voltage Correlation in Ru(II) Sensitizers with Heteroleptic Tridentate Chelates for Dye-Sensitized Solar Cells. *J. Am. Chem. Soc.* **2012**, *134* (17), 7488–7496 DOI: 10.1021/ja300828f.
- (215) Yang, S. H.; Wu, K. L.; Chi, Y.; Cheng, Y. M.; Chou, P. T. Tris(thiocyanate) ruthenium(II) Sensitizers with Functionalized Dicarboxyterpyridine for Dye-Sensitized Solar Cells. *Angew. Chemie - Int. Ed.* **2011**, *50* (36), 8270–8274 DOI: 10.1002/anie.201103515.
- (216) Kim, J. J.; Lim, K.; Choi, H.; Fan, S.; Kang, M. S.; Gao, G.; Kang, H. S.; Ko, J. New Efficient Ruthenium Sensitizers with Unsymmetrical indeno[1,2-b]thiophene or a Fused Dithiophene Ligand for Dye-Sensitized Solar Cells. *Inorg. Chem.* **2010**, *49* (18), 8351–8357 DOI: 10.1021/ic1009658.
- (217) Hai, J.; Zhu, E.; Bian, L.; Wang, J.; Wang, Z.; Li, Y.; Yin, L.; Zhang, F.; Tang, W. Synthesis, Optical, Electrochemical and Electroluminescent Properties of Novel Fluorene-Alt-Bithiophene Copolymers Bearing Phenylvinyl Bridged Accepting Side Chains. *Eur. Polym. J.* **2013**, *49* (11), 3610–3618 DOI: 10.1016/j.eurpolymj.2013.07.030.
- (218) Barlow, S.; Odom, S. A.; Lancaster, K.; Getmanenko, Y. A.; Mason, R.; Coropceanu, V.; Brédas, J.-L.; Marder, S. R. Electronic and Optical Properties of 4H-cyclopenta[2,1-b:3,4-B']bithiophene Derivatives and Their 4-Heteroatom-Substituted Analogues: A Joint Theoretical and Experimental Comparison. *J. Phys. Chem. B* **2010**, *114* (45), 14397–14407 DOI: 10.1021/jp100774r.
- (219) Brusso, J. L.; Hirst, O. D.; Dadvand, A.; Ganesan, S.; Cicoira, F.; Robertsons, C. M.; Oakley, R. T.; Rosei, F.; Perepichka, D. F. Two-Dimensional Structural Motif in Thienoacene Semiconductors: Synthesis, Structure, and Properties of Tetrathienoanthracene Isomers. *Chem. Mater.* **2008**, *20* (7), 2484–2494 DOI: 10.1021/cm7030653.
- (220) Kawabata, K.; Takeguchi, M.; Goto, H. Optical Activity of Heteroaromatic Conjugated Polymer Films Prepared by Asymmetric Electrochemical Polymerization in Cholesteric Liquid Crystals: Structural Function for Chiral Induction. *Macromolecules* **2013**, *46* (6), 2078–2091 DOI: 10.1021/ma400302j.
- (221) Meng, Q.; Gao, J.; Li, R.; Jiang, L.; Wang, C.; Zhao, H.; Liu, C.; Li, H.; Hu, W. New Type of Organic Semiconductors for Field-Effect Transistors with Carbon-Carbon Triple Bonds. *J. Mater. Chem.* **2009**, *19* (10), 1477 DOI: 10.1039/b816590d.
- (222) Kim, H. S.; Kim, Y. H.; Kim, T. H.; Noh, Y. Y.; Pyo, S.; Yi, M. H.; Kim, D. Y.; Kwon, S. K. Synthesis and Studies on 2-hexylthieno[3,2-B]thiophene End-Capped Oligomers for OTFTs. *Chem. Mater.* **2007**, *19* (14), 3561–3567 DOI: 10.1021/cm070053g.
- (223) Ponomarenko, S. A.; Tatarinova, E. A.; Muzafarov, A. M.; Kirchmeyer, S.; Brassat, L.; Mourran, A.; Moeller, M.; Setayesh, S.; De Leeuw, D. Star-Shaped Oligothiophenes for Solution-Processible Organic Electronics: Flexible Aliphatic Spacers Approach. *Chem. Mater.* **2006**, *18* (17), 4101–4108 DOI: 10.1021/cm061104x.
- (224) Dudek, S. P.; Pouderoijen, M.; Abbel, R.; Schenning, A. P. H. J.; Meijer, E. W. Synthesis and

- Energy-Transfer Properties of Hydrogen-Bonded Oligofluorenes. *J. Am. Chem. Soc.* **2005**, *127* (33), 11763–11768 DOI: 10.1021/ja052054k.
- (225) Gao, F.; Wang, Y.; Zhang, J.; Shi, D.; Wang, M.; Humphry-Baker, R.; Wang, P.; Zakeeruddin, S. M.; Grätzel, M. A New Heteroleptic Ruthenium Sensitizer Enhances the Absorptivity of Mesoporous Titania Film for a High Efficiency Dye-Sensitized Solar Cell. *Chem. Commun.* **2008**, *107* (23), 2635 DOI: 10.1039/b802909a.
- (226) Chen, C.-Y.; Wu, S.-J.; Wu, C.-G.; Chen, J.-G.; Ho, K.-C. A Ruthenium Complex with Superhigh Light-Harvesting Capacity for Dye-Sensitized Solar Cells. *Angew. Chemie Int. Ed.* **2006**, *45* (35), 5822–5825 DOI: 10.1002/anie.200601463.
- (227) Becke, A. D. A New Mixing of Hartree–Fock and Local Density-functional Theories. *J. Chem. Phys.* **1993**, *98* (2), 1372–1377 DOI: 10.1063/1.464304.
- (228) Binkley, J. S.; Pople, J. A.; Hehre, W. J. Self-Consistent Molecular Orbital Methods. 21. Small Split-Valence Basis Sets for First-Row Elements. *J. Am. Chem. Soc.* **1980**, *102* (3), 939–947 DOI: 10.1021/ja00523a008.
- (229) Godbout, N.; Salahub, D. R.; Andzelm, J.; Wimmer, E. Optimization of Gaussian-Type Basis Sets for Local Spin Density Functional Calculations. Part I. Boron through Neon, Optimization Technique and Validation. *Can. J. Chem.* **1992**, *70* (2), 560–571 DOI: 10.1139/v92-079.
- (230) Cossi, M.; Barone, V.; Cammi, R.; Tomasi, J. Ab Initio Study of Solvated Molecules: A New Implementation of the Polarizable Continuum Model. *Chem. Phys. Lett.* **1996**, *255* (4), 327–335 DOI: 10.1016/0009-2614(96)00349-1.
- (231) Cossi, M.; Barone, V. Time-Dependent Density Functional Theory for Molecules in Liquid Solutions. *J. Chem. Phys.* **2001**, *115* (10), 4708–4717 DOI: 10.1063/1.1394921.
- (232) Miertuš, S.; Scrocco, E.; Tomasi, J. Electrostatic Interaction of a Solute with a Continuum. A Direct Utilization of AB Initio Molecular Potentials for the Prediction of Solvent Effects. *Chem. Phys.* **1981**, *55* (1), 117–129 DOI: 10.1016/0301-0104(81)85090-2.
- (233) Isse, A. A.; Gennaro, A. Absolute Potential of the Standard Hydrogen Electrode and the Problem of Interconversion of Potentials in Different Solvents. *J. Phys. Chem. B* **2010**, *114* (23), 7894–7899 DOI: 10.1021/jp100402x.
- (234) Nusbaumer, H.; Zakeeruddin, S. M.; Moser, J.-E.; Grätzel, M. An Alternative Efficient Redox Couple for the Dye-Sensitized Solar Cell System. *Chem. - A Eur. J.* **2003**, *9* (16), 3756–3763 DOI: 10.1002/chem.200204577.
- (235) Ito, S.; Murakami, T. N.; Comte, P.; Liska, P.; Grätzel, C.; Nazeeruddin, M. K.; Grätzel, M. Fabrication of Thin Film Dye Sensitized Solar Cells with Solar to Electric Power Conversion Efficiency over 10%. *Thin Solid Films* **2008**, *516* (14), 4613–4619 DOI: 10.1016/j.tsf.2007.05.090.
- (236) Fabregat-Santiago, F.; Bisquert, J.; Palomares, E.; Otero, L.; Kuang, D.; Zakeeruddin, S. M.; Grätzel, M. Correlation between Photovoltaic Performance and Impedance Spectroscopy of Dye-Sensitized Solar Cells Based on Ionic Liquids. *J. Phys. Chem. C* **2007**, *111* (17), 6550–6560 DOI: 10.1021/jp066178a.
- (237) Xie, N.; Wang, J.; Guo, Z.; Chen, G.; Li, Q. Fluorene/carbazole Alternating Copolymers Tethered with Polyhedral Oligomeric Silsesquioxanes: Synthesis, Characterization, and Electroluminescent Properties. *Macromol. Chem. Phys.* **2013**, *214* (15), 1710–1723 DOI:

10.1002/macp.201300290.

- (238) Yang, C. H.; Mauro, M.; Polo, F.; Watanabe, S.; Muenster, I.; Fröhlich, R.; De Cola, L. Deep-Blue-Emitting Heteroleptic iridium(III) Complexes Suited for Highly Efficient Phosphorescent OLEDs. *Chem. Mater.* **2012**, *24* (19), 3684–3695 DOI: 10.1021/cm3010453.
- (239) Wang, P.; Zakeeruddin, S. M.; Comte, P.; Charvet, R.; Humphry-Baker, R.; Grätzel, M. Enhance the Performance of Dye-Sensitized Solar Cells by Co-Grafting Amphiphilic Sensitizer and Hexadecylmalonic Acid on TiO₂ Nanocrystals. *J. Phys. Chem. B* **2003**, *107* (51), 14336–14341 DOI: 10.1021/jp0365965.
- (240) Liu, J.; Li, R.; Si, X.; Zhou, D.; Shi, Y.; Wang, Y.; Jing, X.; Wang, P. Oligothiophene Dye-Sensitized Solar Cells. *Energy Environ. Sci.* **2010**, *3* (12), 1924–1928 DOI: 10.1039/c0ee00304b.
- (241) Cai, N.; Wang, Y.; Xu, M.; Fan, Y.; Li, R.; Zhang, M.; Wang, P. Engineering of Push-Pull Thiophene Dyes to Enhance Light Absorption and Modulate Charge Recombination in Mesoscopic Solar Cells. *Adv. Funct. Mater.* **2013**, *23* (14), 1846–1854 DOI: 10.1002/adfm.201202562.
- (242) Huang, Y.-Z.; Miao, H.; Zhang, Q.-H.; Chen, C.; Xu, J. Cu₂O: A Simple and Efficient Reusable Catalyst for N-Arylation of Nitrogen-Containing Heterocycles with Aryl Halides. *Catal. Letters* **2008**, *122* (3–4), 344–348 DOI: 10.1007/s10562-007-9386-0.
- (243) Ma, C.; Ai, C.; Li, Z.; Li, B.; Song, H.; Xu, S.; Wang, B. Synthesis and Alkyne Insertion Reactions of NHC-Based Cyclometalated ruthenium(II) Complexes. *Organometallics* **2014**, *33* (19), 5164–5172 DOI: 10.1021/om500369g.

Acknowledgements

This work would not be possible without many people which I will not be able to mention. First of all, I would like to thank Professors Mohammad Khaja Nazeeruddin and Michael Grätzel for accepting me to the Ph.D. program. I thank Prof. Nazeeruddin for giving me a freedom in choosing the subject of my research, which I suspect would be hard at this particular time when a new 'hot' field of perovskite solar cells emerged. Besides this, in this four years, Prof. Nazeeruddin was always understanding and supporting. Does not matter what was my question or problem, every time he was finding a good solution.

I am grateful to Iwan and Paul for discussions and arguments at La Post, and other spots of Sion; for being patient with me in skiing; for long coffee breaks; and so on. I hope, our soon become long-distance-friendship, will never fade. I am grateful to Kasparas for all the fun we had in four years and for his incredible skills with Microsoft Word, which I favored a lot writing this thesis. I am deeply grateful to both Giulia and Nikita from who I learned a lot of photophysics and organic chemistry, respectively. Thanks to Valeriu, for all the fun time, and calculations of course. I thank Cristina, and I hope that you will find your teleportation machine.

None of us in the group would be able to do anything without secretaries, Ursula Gonthier and Heidi, back in Lausanne, and Geraldine in Sion. I am deeply grateful to Geraldine for taking all my small problems seriously and helping out; for organizing events to cheer up the group, and just for being very friendly and understanding.

I thank Peng, for helping me a lot with the organic synthesis, and for being always ready to discuss reactions and giving valuable advice. I thank Simon for setting high standards for me; I have gained many skills while observing you working, which you may not have noticed. I thank Chen Yi, Jiabao Yang, and Madeline for an excellent lab environment. I am grateful to Aswani, for fabricating solar cells for me; You have the best skills that always surprised me. I thank Aravind for explaining me a lot about devices. I thank Thomas for patiently explaining me the impedance spectroscopy and Joël for helping with transient spectroscopy. I also appreciate our colleagues from Italy, Gabriele and Prof. De Angelis for the help with the computations, and from China, Yameng and Prof. Wang for fabricating solar cells.

These four years would be boring without other very close students and postdocs. I thank Aron for very fruitful collaborations. I thank Yonghui, Kyung Taek, Manuel, Lee, Erfan, Ines, Ibrahim, Wolfgang, Neha, Michael, and Maryline for the nice lab atmosphere both in Lausanne and Sion. I thank Val for helping me with the French version of the abstract, and Mousa for introducing to me a fun of new generation.

I would also like to thank Mrs. Odegaard, Dr. Pascal Mieville, Mrs. Pache, Mrs. Carrupt, Laurent, and Annabelle for creating the best conditions for the students at ISIC. And Shafak, Mehrdad, Olga, Ilya, Daniel, Li, and Shuliang who made the Industrie 17 a fun place to work.

Sion, October 26, 2017

Curriculum Vitae

Sadig AGHAZADA

Date/Place of Birth : 8 October 1990 / Astara, Azerbaijan
Nationality : Azerbaijan
E-mail : sadig.aghazada@gmail.com
ORCID ID : orcid.org/0000-0002-7568-4481

EDUCATION

Ph.D. in Chemistry 2017
 École Polytechnique Fédérale de Lausanne, Switzerland Aug 2013 –
Thesis title: Cyclometalated Ruthenium Complexes for Dye-Sensitized Solar Cells Dec 2017
Thesis supervisors: Prof. Md. Khaja Nazeeruddin and Prof. Michael Grätzel

Specialist in Chemistry Sep 2008 –
Diploma with Honours June 2013
 Lomonosov Moscow State University, Moscow, Russia
 5th year diploma work on syntheses of organic ligands and ruthenium complexes

EMPLOYMENT

Doctoral Assistant Aug 2013 –
 École Polytechnique Fédérale de Lausanne, Switzerland Dec 2017
Group for Molecular Engineering of Functional Materials, ISIC
Supervisor: Prof. Md. Khaja Nazeeruddin and Prof. Michael Grätzel

Internship June 2012 –
 Oil and Chemical Processes Institute of Azerbaijan national Academy of Sciences, Sep 2012
 Baku,
Supervisor: Prof. Vagif Abbasov

PRIZES, AWARDS, FELLOWSHIPS

- The Teaching Excellence Award, EPFL, Lausanne, Switzerland 2017
- 40th International Chemistry Olympiad IChO, Budapest, Hungary – *Silver medal* 12-21 JULY 2008
- 42nd International Mendeleev Chemistry Olympiad, Tashkent, Uzbekistan – *Bronze medal.* 27 Apr – 4 May 2008
- Azerbaijan National Chemistry Olympiad, Baku, Azerbaijan – *Absolute first – Gold medal* Feb 2008.
- Scholarship of the President of the Republic of Azerbaijan Sep 2008 – May 2013

PRIZES, AWARDS, FELLOWSHIPS

- Experimental Molecular Sciences (projects, master) 2013-2014
- Chemistry Laboratory Work (experimental, bachelor) 2014-2015
- Chemical Thermodynamics 2015-2016
- Statistical Thermodynamics 2016-2017.

PROFESSIONAL MEMBERSHIPS

- Swiss Chemical Society
- American Chemical Society

LANGUAGES

- English – working proficiency
- Azerbaijani – native
- Russian – fluent speaker
- Turkish – full comprehension

PUBLICATIONS

- (1) **Aghazada, S.**; Zimmermann, I.; Ren, Y.; Wang, P.; Nazeeruddin, M. K. Bis-tridentate Cyclometalated Ruthenium Complexes with extended Anchoring Ligand and their Performance in Dye-Sensitized Solar Cells, *submitted*
- (2) **Aghazada, S.**; Ren, Y.; Wang, P.; Nazeeruddin, M. K. Effect of Donor Groups on the Performance of Cyclometalated Ruthenium Sensitizers in Dye-Sensitized Solar Cells. *Inorg. Chem.* 2017, DOI: 10.1021/acs.inorgchem.7b02164. <http://pubs.acs.org/doi/abs/10.1021/acs.inorgchem.7b02164>
- (3) **Aghazada, S.**; Zimmermann, I.; Scutelnic, V.; Nazeeruddin, M. K. Synthesis and Photophysical Characterization of Cyclometalated Ruthenium Complexes with N-Heterocyclic Carbene Ligands. *Organometallics* 2017, 36 (13), 2397–2403 DOI: 10.1021/acs.organomet.7b00354. <http://pubs.acs.org/doi/abs/10.1021/acs.organomet.7b00354>
- (4) **Aghazada, S.**; Gao, P.; Yella, A.; Marotta, G.; Moehl, T.; Teuscher, J.; Moser, J.-E.; De Angelis, F.; Grätzel, M.; Nazeeruddin, M. K. Ligand Engineering for the Efficient Dye-Sensitized Solar Cells with Ruthenium Sensitizers and Cobalt Electrolytes. *Inorg. Chem.* 2016, 55 (13), 6653–6659 DOI: 10.1021/acs.inorgchem.6b00842. <http://pubs.acs.org/doi/abs/10.1021/acs.inorgchem.6b00842>
- (5) **Aghazada, S.**; Gao, P.; Yella, A.; Moehl, T.; Teuscher, J.; Moser, J. E.; Grätzel, M.; Nazeeruddin, M. K. Unraveling the Dual Character of Sulfur Atoms on Sensitizers in Dye-Sensitized Solar Cells. *ACS Appl. Mater. Interfaces* 2016, 8 (40), 26827–26833 DOI: 10.1021/acsami.6b08882. <http://pubs.acs.org/doi/abs/10.1021/acsami.6b08882>
- (6) **Aghazada, S.**; Huckaba, A. J.; Pertegas, A.; Babaei, A.; Grancini, G.; Zimmermann, I.; Bolink, H.; Nazeeruddin, M. K. Molecular Engineering of Iridium Blue Emitters Using Aryl N-

- Heterocyclic Carbene Ligands. *Eur. J. Inorg. Chem.* 2016, 2016 (32), 5089–5097 DOI: 10.1002/ejic.201600971. <http://onlinelibrary.wiley.com/doi/10.1002/ejic.201600971/full>
- (7) Yella, A.; Mathew, S.; **Aghazada, S.**; Comte, P.; Grätzel, M.; Nazeeruddin, M. K.; Grätzel, M.; Roosmalen, J. A. M. van; Kay, A.; Nazeeruddin, M. K.; Grätzel, M.; Manca, M. Dye-Sensitized Solar Cells Using Cobalt Electrolytes: The Influence of Porosity and Pore Size to Achieve High-Efficiency. *J. Mater. Chem. C* 2017, 110, 17155–17160 DOI: 10.1039/C6TC05640G. <http://pubs.rsc.org/en/Content/ArticleLanding/2017/TC/C6TC05640G#divAbstract>
- (8) Saliba, M.; Orlandi, S.; Matsui, T.; **Aghazada, S.**; Cavazzini, M.; Correa-Baena, J.-P.; Gao, P.; Scopelliti, R.; Mosconi, E.; Dahmen, K.-H.; De Angelis, F.; Abate, A.; Hagfeldt, A.; Pozzi, G.; Graetzel, M.; Nazeeruddin, M. K. A Molecularly Engineered Hole-Transporting Material for Efficient Perovskite Solar Cells. *Nat. Energy* 2016, 1 (January), 15017 DOI: 10.1038/nenergy.2015.17. <https://www.nature.com/articles/nenergy201517>
- (9) Arora, N.; Orlandi, S.; Dar, M. I.; **Aghazada, S.**; Jacopin, G.; Cavazzini, M.; Mosconi, E.; Grätzel, M.; De Angelis, F.; Pozzi, G.; Graetzel, M.; Nazeeruddin, M. K. High Open-Circuit Voltage: Fabrication of Formamidinium Lead Bromide Perovskite Solar Cells Using Fluorene–Dithiophene Derivatives as Hole-Transporting Materials. *ACS Energy Lett.* 2016, 1 (1), 107–112 DOI: 10.1021/acsenenergylett.6b00077. <http://pubs.acs.org/doi/abs/10.1021/acsenenergylett.6b00077>
- (10) Molina-Ontoria, A.; Zimmermann, I.; Garcia-Benito, I.; Grätzel, M.; Roldan-Carmona, C.; **Aghazada, S.**; Graetzel, M.; Nazeeruddin, M. K.; Martin, N. Benzotrithiophene-Based Hole-Transporting Materials for 18.2 % Perovskite Solar Cells. *Angew. Chemie - Int. Ed.* 2016, 55 (21), 6270–6274 DOI: 10.1002/anie.201511877. <http://onlinelibrary.wiley.com/doi/10.1002/anie.201511877/full>
- (11) Gao, P.; Konrad, D.; **Aghazada, S.**; Nazeeruddin, M. K. Molecular Engineering of Functional Materials for Energy and Opto-Electronic Applications. *Chim. Int. J. Chem.* 2015, 69 (5), 253–263 DOI: 10.2533/chimia.2015.253. <http://www.ingentaconnect.com/content/scs/chimia/2015/00000069/00000005/art00003>
- (12) ElBatal, H. S.; **Aghazada, S.**; Al-Muhtaseb, S. A.; Grätzel, M.; Nazeeruddin, M. K. Quasi-Solid-State Dye-Sensitized Solar Cells based on Ru(II) Polypyridine Sensitizers. *Energy Technol.* 2016, 4, 380–384 DOI: 10.1002/ente.201500477. <http://onlinelibrary.wiley.com/doi/10.1002/ente.201500477/full>
- (13) Koksharov, Y. A.; Dolzhenko, V. D.; **Agazade, S. A.** Electron Magnetic Resonance of Synthetic Goethite in the Range of the Magnetic Transition. *Phys. Solid State* 2010, 52 (9), 1929–1934 DOI: 10.1134/S1063783410090246. <https://link.springer.com/article/10.1134/S1063783410090246>

PEER-REVIEWED CONFERENCE PROCEEDINGS -POSTERS

- (1) **Aghazada, S.**; Nazeeruddin, M. Kh. “Cyclometalated Ruthenium Complexes for Highly Efficient Dye-Sensitized Solar Cells”. Hybrid & Organic Photovoltaics (HOPV 17), *Lausanne, Switzerland*, 21st-24th May 2017.
- (2) **Aghazada, S.**; Yella, A.; Marotta, G.; Gao, P.; Moehl, T.; Teuscher, J.; Xanthopoulos, N.; De Angelis, F.; Grätzel, M.; Nazeeruddin, M. Kh. “Efficient Dye-Sensitized Solar Cells with Ruthenium Sensitizers and Cobalt Electrolytes: Ligand Structures to Look for and to Avoid”. International Conference on Solution Processed Innovation Solar cells (SPINS15), *Santiago de Compostela, Spain*, 9-11 September 2015.

PEER-REVIEWED CONFERENCE PROCEEDINGS – ORAL PRESENTATIONS

- (1) **Aghazada, S.**; Grätzel, M.; Nazeeruddin, M. Kh. “Molecular engineering of ruthenium complexes for highly efficient dye-sensitized solar cells”. 253rd American Chemical Society National Meeting & Exposition, *San Francisco, California, US*, April 2-6, **2017**.
- (2) **Aghazada, S.**; Dolzhenko, V. D.; Koksharov, Yu. A. “Magnetoresonance Properties of iron Oxohydroxides Stabilized with oleic acid”. XVIII International student, postgraduate and young scientists’ conference “Lomonosov”, “Inorganic chemistry” section, *Moscow, Russia*, 11-15 April 2011. Book of abstracts **2011** (*in Russian*).
- (3) **Aghazada, S.**; Dolzhenko, V. D.; Koksharov, Yu. A. “Synthesis and Study of Magnetic Properties of Goethite and Ferrhydrite Nanoparticles”. XVII International student, postgraduate and young scientists’ conference “Lomonosov”, “Inorganic chemistry” section, *Moscow, Russia*, 12-15 April 2010. Book of abstracts **2010** (*in Russian*).

